ADVANCEMENTS IN BIOMASS FEEDSTOCK PREPROCESSING: CONVERSION READY FEEDSTOCKS, VOLUME II

EDITED BY: Timothy G. Rials, Allison E. Ray and J. Richard Hess

frontiers Research Topics

About Frontiers

Frontiers is more than just an open-access publisher of scholarly articles: it is a pioneering approach to the world of academia, radically improving the way scholarly research is managed. The grand vision of Frontiers is a world where all people have an equal opportunity to seek, share and generate knowledge. Frontiers provides immediate and permanent online open access to all its publications, but this alone is not enough to realize our grand goals.

Frontiers Journal Series

The Frontiers Journal Series is a multi-tier and interdisciplinary set of open-access, online journals, promising a paradigm shift from the current review, selection and dissemination processes in academic publishing. All Frontiers journals are driven by researchers for researchers; therefore, they constitute a service to the scholarly community. At the same time, the Frontiers Journal Series operates on a revolutionary invention, the tiered publishing system, initially addressing specific communities of scholars, and gradually climbing up to broader public understanding, thus serving the interests of the lay society, too.

Dedication to Quality

Each Frontiers article is a landmark of the highest quality, thanks to genuinely collaborative interactions between authors and review editors, who include some of the world's best academicians. Research must be certified by peers before entering a stream of knowledge that may eventually reach the public - and shape society; therefore, Frontiers only applies the most rigorous and unbiased reviews.
Frontiers revolutionizes research publishing by freely delivering the most outstanding research, evaluated with no bias from both the academic and social point of view. By applying the most advanced information technologies, Frontiers is catapulting scholarly publishing into a new generation.

What are Frontiers Research Topics?

Frontiers Research Topics are very popular trademarks of the Frontiers Journals Series: they are collections of at least ten articles, all centered on a particular subject. With their unique mix of varied contributions from Original Research to Review Articles, Frontiers Research Topics unify the most influential researchers, the latest key findings and historical advances in a hot research area! Find out more on how to host your own Frontiers Research Topic or contribute to one as an author by contacting the Frontiers Editorial Office: frontiersin.org/about/contact

ADVANCEMENTS IN BIOMASS FEEDSTOCK PREPROCESSING: CONVERSION READY FEEDSTOCKS, VOLUME II

Topic Editors:
Timothy G. Rials, The University of Tennessee, Knoxville, United States
Allison E. Ray, Idaho National Laboratory (DOE), United States
J. Richard Hess, Idaho National Laboratory (DOE), United States

Table of Contents

Image Analysis for Rapid Assessment and Quality-Based Sorting of Corn Stover

Ling Ding[1]*, Amber N. Hoover[1], Rachel M. Emerson[1], Kuan-Ting Lin[1], Josephine N. Gruber[2], Bryon S. Donohoe[2], Jordan L. Klinger[1], Rachel D. Colby[1], Brad J. Thomas[1], William A. Smith[1] and Allison E. Ray[3]*

[1]Energy and Environmental Science and Technology, Idaho National Laboratory, Idaho Falls, ID, United States, [2]Biosciences Center, National Renewable Energy Laboratory, Golden, CO, United States, [3]Science and Technology, Idaho National Laboratory, Idaho Falls, ID, United States

Imaging in the visible spectrum is a low-cost tool that can be readily deployed for in-field or over-belt monitoring of biomass quality for bio-refining operations. Rapid image analysis coupled with innovative preprocessing may reduce the impacts of feedstock variability through identification of contaminants or other material attributes to guide selective sorting and quality management. Image analysis was employed to evaluate the quality of corn stover in red-green-blue (RGB) chromatic space. This study used controlled, bench-scale imaging as a proof-of-concept for rapid quality assessment of corn stover based on variations in material attributes, including chemical and physical attributes, that relate to biological degradation and soil contamination. Logistic regression-based classification algorithms were used to develop a method for biomass screening as a function of biological degradation or soil contamination. This study demonstrated the use of image analysis to extract features from RGB color space to investigate variations in critical material attributes from chemical composition of corn stover. Fourier transform infrared (FT-IR) suggested a correlation between red band intensity and biological degradation, while detailed surface texture analysis was found to distinguish among variations in ash. These insights offer promise for development of a rapid screening tool that could be deployed by farmers for in-field assessment of biomass quality or biorefinery operators for in-line sorting and process optimization.

Keywords: image analysis, rapid detection, corn stover, biological degradation, chemical composition, feedstock variability, FT-IR

INTRODUCTION

The 2016 Billioin Tons Report (BT16) estimates that by 2040, more than 1 billion tons of biomass will be available to achieve a vision of a sustainable bioeconomy (US DOE, 2016). Lignocellulosic biomass has been considered a promising feedstock for biofuels production; therefore, tremendous research efforts have been made to enhance different aspects of the related processes (Cheah et al., 2020). Increases in fuel prices have challenged all countries around the world to develop their own biofuels from renewable resources such as lignocellulosic crops (Qureshi et al., 2010). *Zea mays* is a significant agricultural crop with potential as a biofuel feedstock due to its high carbohydrate content, low production cost, and high availability in the US corn belt (Li et al., 2020). Biomass variability

originating from production and field conditions propagates with the feedstock through the value chain, posing a challenge to the emerging biorefinery industry (Ray et al., 2020). Variations in lignocellulosic biomass material and quality attributes are often overlooked when assessing feedstock value and pathways for conversion to fuels, chemicals, and products (Ray et al., 2020). Variations in cell wall composition, extractives, moisture content, inorganic species, and soil contaminants have been identified as critical factors affecting biomass quality, process uptime, and product yields (Ray et al., 2020; Sievers et al., 2020; Ding et al., 2021a). Hoover et al. (2019) developed several multiple regression models where five chemical characteristics could be used to estimate biochemical conversion performance. Using these models, an approach for a grading system was demonstrated that could be used to inform markets on the impacts of biomass variability. Hartley et al. (2020) used discrete event simulation that investigated feedstock quality on plant uptime and overall impact to biofuel cost through feedstock delivery cost. These works show how fundamental biomass information might enable real-time decision making on plant profitability and operability. Storage is an essential component of the biomass logistics supply chain, which can have significant impacts to the overall feedstock supply cost and operational reliability (Rentizelas, 2016). Many studies have established that the combination of living cell respiration, biological degradation, and thermo-chemical oxidative reactions bring about significant changes to critical biomass feedstock attributes and process efficiency during storage (Bose et al., 2020; Groenewold et al., 2020; Li et al., 2020). Changes that may occur in stored biomass feedstock include dry mass loss (up to 5.5% per month) (Thornqvist, 1985; Eisenbies et al., 2016), drying, decomposition, and energy content loss (Krigstin and Wetzel, 2016). In addition to capital and operational costs, it is imperative to consider the impact of storage method and format on chemical properties of biomass and overall process efficiency.

Image analysis techniques have been widely applied to measure lignocellulosic biomass features. Image analysis techniques for assessing crops and plant material involve extracting information from digital images of the lignocellulosic biomass (Yan et al., 2020). Unique features of the materials, such as shape, color, and surface texture, can be recognized. Recent research found that crop biomass is highly correlated with different crop parameters, such as leaf area index, crop height, and canopy volume (Lati et al., 2013; Bendig et al., 2014; Tilly et al., 2014), and is also correlated with different vegetation indices based on hyperspectral and red, green, blue (RGB) images (Gupta et al., 2000; Gitelson et al., 2003; Swain et al., 2010; Gitelson et al., 2014; Jannoura et al., 2015). Crop biomass yield has been estimated from spectral information from an unmanned aerial vehicle using standard RGB and multispectral or hyperspectral cameras (Jiang et al., 2019). Image analysis has also been used to estimate the distribution of plants in fields of a clover-grass mixture by using convolutional neural networks trained to predict semantic segmentation maps of clover, grass, and weeds in RGB images containing clover-grass mixtures (Skovsen et al., 2017). Further, Wang et al. found a strong positive correlation between the grayscale values of

biochar and its methylene blue and iodine adsorption capacity, and the Pearson's correlation coefficient range was 0.685–0.977 (Wang et al., 2015). In addition, surface texture can be measured directly from images taken with a laser profilometer (Chinga et al., 2007; Wagner and Horn, 2017), stereomicroscope (Mitra et al., 2014; Piselli et al., 2017), photographic scanner (Aguirre et al., 2018), or scanning electron microscope (Yan et al., 2020). The image analysis can also provide information on the surface roughness based on grayscale values of the image or height map (Chinga et al., 2007).

There are limited publications on visible, red-green-blue (RGB) analysis of biomass variability relevant to biorefineries and lack of such a study limits the ability to develop rapid screening tools for in-field assessment of biomass quality based on physical and chemical attributes. The novelty of this paper was to design and use controlled, bench-scale imaging, employing an off-the-shelf digital camera, as a proof-of-concept for rapid, quality-based assessment of corn stover in visible, red-green-blue (RGB) space based on variability derived from soil contamination and biological degradation. Logistic regression classification algorithms were used to develop an image screening of biomass as a function of soil contamination and biological degradation. In addition, FTIR was used with a more detailed surface analysis to investigate variation in critical material attributes that arise from chemical composition. Finally, surface texture analysis of the same images distinguished among variable ash levels and degradation. The qualitative results presented in this study show promise for developing rapid screening tools to deploy in-field or in-line for rapid assessment of feedstock quality.

MATERIALS AND METHODS
Corn Stover Bale Collection and Sample Preparation

Two sets of corn stover samples were imaged and analyzed in this study. The first was a set of 216 core samples from 24 bales obtained from four fields in different central Iowa counties: Hamilton (4 bales), Hardin (6 bales), Story (6 bales), and Poweshiek (8 bales) described in Ray et al. (2020). Baling occurred between October 12 and 27, 2017, using an AGCO 2270XD large square baler, except for Poweshiek County, where a Heston 2270XD square baler was used. Preliminary screening for moisture and ash content was performed by taking three cores per bale to select the 24 bales used in this study. Selected bales were more thoroughly sampled by collecting nine cores per bale, illustrated in a previous study (Ray et al., 2020). Corn stover samples were dried at 40°C and milled with a 2 mm screen in a Thomas Model 4 Wiley Mill (Thomas Scientific, Swedesboro, NJ) for chemical composition analysis. Additional milling using a Retsch ZM200 (Haan, Germany) with a 0.2 mm screen was done to analyze inorganics. For surface analysis, the bales were size reduced through a Vermeer BG480 bale processor with a 75-mm screen, then a Bliss Hammermill with a 25-mm screen, and samples were collected and milled to pass a 2-mm screen for evaluation of surface properties.

FIGURE 1 | (A) Image workflow sample template with internal color standards and biomass samples; **(B)** Examples of the region of interest selection to measure and output RGB channel data.

The second set of 12 corn stover samples was selected to evaluate material attributes influenced by aging and degradation in storage operations. Bales were from Hardin County, IA (2 bales) and Story County, IA (3 bales) with harvest and baling information described for each county previously. Bale sections exhibiting visual evidence of biological degradation were selected

for sampling as described in previous studies (Li et al., 2020; Groenewold et al., 2020; Bose et al., 2020). Samples were collected from bale flakes displaying variable extents of biological degradation—moderate biological degradation (medium brown coloration), severe biological degradation (dark brown to almost black), and mild-or negligible biological degradation (light brown). The two bales from Hardin County were size reduced using a Vermeer BG480 bale processer with a 75-mm screen, samples were collected following size reduction, and one sample per bale was visually identified as severely biologically degraded or mild/negligible biologically degraded. The three bales from Story County were manually deconstructed and dissected to collect samples from flakes of the bale that were observed to have mild/negligible biological degradation or moderate/severe biological degradation (Groenewold et al., 2020). For subsequent characterization, samples were milled to pass through a 2 mm and a 0.2 mm screen as described above.

Image Processing and Analysis

An imaging workflow was developed that uses a Panasonic Lumix G camera with a 88.9-cm square light shed and Metz Mecablitz 52 AF-1 digital flashes. Camera location and settings, as well as flash position, were kept consistent for all images. Each 2-mm sample was imaged using a standardized sample template with internal color standards in each sample photo and a consistent set of biomass samples in each photo (**Figure 1A**). The image processing workflow included post-processing in SilkyPix Developer Studio 8 SE and data extraction with ImageJ (https://imagej.nih.gov/ij/). Each photo's exposure and gray balance were set individually using the X-Rite ColorChecker Passport Photo 2 with color reference targets included in each image. Regions of interest were defined in each image, as displayed in **Figure 1B**. The digital photos were decomposed into red, green, and blue channel values ranging from 0 to 255 in relative intensity. The mean, median, standard deviation, minimum, and maximum for the red, green, and blue values range from the regions of interest for all samples were included in the data sets available in the Bioenergy Feedstock Library (Ding et al., 2021b). The image results were aligned with sample metadata, total inorganics, inorganic speciation, and chemical composition (NIRS predicted composition or wet chemical composition) (Ding et al., 2021b). In addition to analytical characterization, three independent observers inspected each sample to assist with positive classification of samples into qualitative sample categories: 1) clean and not degraded, 2) soil contaminated, or 3) degraded (Ding et al., 2021b). This is further discussed below.

Chemical Analysis

Inorganic speciation for Al, Ca, Fe, K, Mg, Mn, Na, P, Si, Ti, and S oxides were measured according to ASTM standards D3174, D3682, D6349 by a Huffman Hazen Laboratories in Golden, CO and represented on a % dry biomass basis. The chemical composition, including total inorganics, glucan, xylan, lignin, and total extractives, was measured using near-infrared spectroscopy (NIRS) predicted composition or wet chemical composition. For NIRS, predicted composition samples at 2 mm particle size were

dried in a desiccator for a minimum of 72 h prior to NIRS analysis. Previous publications have described spectral analysis and NIRS calibration models in detail (Payne and Wolfrum, 2015; Ray et al., 2020). Wet chemical composition was performed in duplicate following the National Renewable Energy Laboratory's laboratory analytical procedures for standard biomass analysis (Sluiter et al., 2010), as described in a previous study (Hoover et al., 2019). The NIRS chemical composition predictive models were built on these same wet chemical procedures.

Observational Dataset

Three independent researchers performed an observational assessment of each sample and categorized sample quality on the basis of soil contamination and degradation due to biological heating. The surveyed researchers were highly experienced in biomass sampling, preparation, and analytical characterization for assessment of biomass quality, as well as identification of degraded samples that have undergone biological heating or biomass materials with soil contamination. Observational assessment consisted of a -visual (color and clear decay, soil contamination), tactile (texture from grit, soil, silt and/or sand entrapment, and fiber integrity), and odor (presence of astringent odors common to biological degradation) material inspection of each sample and recorded whether it was 1) not soil contaminated and not biologically degraded 2) soil contaminated, or 3) biologically degraded. Samples were assessed with a scale of 0–3 for soil contamination, and biological degradation with 0 = not observed, 1 = low, 2 = moderate, and 3 = high. The observational values were summed for each category for a minimum value of 0 (i.e., each observer selected 0) and a maximum of 9 (i.e., each observer selected 3) [(Ray et al., 2020) **Supplementary Material**]. Observational data are aggregated in the dataset (Ding et al., 2021b).

Statistical Analysis

JMP® Pro 16.0.0 was used to analyze the combined information from the image analysis, chemical analysis, and observational dataset as described above. Hierarchical cluster analysis using the Ward method was used to group the 222 samples with chemical composition data into four organic chemically distinct groups using glucan, xylan, lignin, and extractives contents (Ding et al., 2021b) along with four inorganic chemically distinct groups for the 191 samples in the dataset with inorganic speciation contents for 191 samples (Ding et al., 2021b). Principal component analysis (PCA) was also used for each organic and inorganic dataset to visualize and interpret the hierarchically defined clusters. Four linear regression models using least squares were generated relating 1) organic chemical components—glucan, xylan, lignin, a 2-way interaction between glucan and xylan, and a 3-way interaction between glucan, xylan, and lignin along with total inorganics—to the median red channel values (Ding et al., 2021b) as described in the image processing and analysis section, 2) the same organic chemical components along with SiO_2 and SO_3 inorganic constituents to the median red channel values 3) organic chemical components to the observed biological degradation dataset as described in the Observational

dataset section and 4) the observed biological degradation levels to median red channel value. For the development of these models, factors were retained if they significantly contributed to the response variable ($p \leq 0.05$) and were not highly correlated to other factors in the model except for cases when single factors were retained regardless of their significance if they were included in any interaction terms. Multicollinearity between model explanatory factors was determined based on the Variance Inflation Scores (VIF). A VIF score >10 was considered high multicollinearity between model factors. Nominal logistic fit regression models were used to develop predictive models for biological degradation and soil contamination levels, using the established hierarchical cluster groups as response variables and median values from the red, green, blue channels and 2-way interactions between these values. The dataset used for these models included the 222 samples for predicting the levels of biological degradation with organic chemical data available and 176 samples for predicting levels of soil contamination using samples with both organic chemical and inorganic speciation data available. Factors for each model were removed based on p-values greater than 0.05. The datasets were randomly split into 80% training and 20% validation for these predictive models.

Fourier-Transform Infrared Spectroscopy Characterization

Corn stover samples for Sample Set 1 were milled using a Retsch ZM200 (Haan, Germany) to 0.2 mm, extractives were retained in the samples. Corn stover samples were extracted with 95:5 acetone/water on a Soxhlet apparatus (~70°C) to remove extractives for Sample Set 2. Corn stover samples for Sample Set 2 were milled in Retsch PM 100 mill fitted with one or two 50 ml ZrO_2 grinding jars and 10*10 mm ball bearings 10 h to less or equal to 45 μm (5 min mill with 10 min interval test). FTIR spectra of all corn stover samples were collected using a Bruker Vertex 70 FTIR spectrometer, equipped with a diamond ATR accessory (Bruker Corporation). Spectra were collected in the spectral range 4000-600 cm^{-1}, using 64 scans and 1 cm^{-1} resolution. Spectra were baseline corrected at 1840 cm^{-1} and advanced diamond ATR fixed with the angle at 45^0.

Surface Texture Analysis

Textural features of cropped images were quantified using the plugins SurfChar J 1q (Chinga et al., 2007), GLCM Texture Too (Haralick, 1979; Lan and Liu, 2018), and FracLac (Smith et al., 1996; Karperien et al., 2013). Before textural analysis, the original color corrected images were cropped to isolate a 900x900-pixel region-of-interest (ROI) centered on the sample cup. Then, the color information was discarded in the image of all subsequent texture analyses and used either 32-bit (SurfCharJ) or 8-bit (GLCM and FracLac) greyscale images. The SurfCharJ 1q package calculated an estimate for the root mean square deviation (Rq), arithmetical mean deviation (Ra), skewness (Rsk), Kurtosis (Rku), lowest valley (Rv), the highest peak (Rp), total profile height (Rt), the mean height of surface

profile (Rc), mean polar facet orientation (FPO), variation of the polar facet orientation (MFOV), the direction of azimuthal facets (FAD), mean resultant vector (MRV), and surface area (SA) from the image. The GLCM Texture Too plugin calculated angular second moment (ASM), inverse difference moment (IDM), contrast, entropy, homogeneity, variance, shade, prominence, inertia, and correlation. The FracLac plugin analyzed the fractal dimensions of the images. Local connected fractal dimension analysis was used, and the Dm output was collected. In total, 27 different surface texture parameters were calculated.

RESULTS AND DISCUSSION

Biological Degradation

Figure 2 shows the results and distribution of chemical compositions and inorganic speciation variability of all samples used for image analysis (detailed dataset in (Ding et al., 2021b). Total inorganics, SiO_2, and Al_2O_3 revealed substantial variation on a % dry matter basis. Both Si and Al-based inorganic species are potential contributions from levels of soil contamination.

Image Analysis Biological Degradation

Hierarchical cluster analysis based on chemical components was used to glean key insights about sources of variability (i.e., degradation and soil contamination) that affect quality, with samples grouping into four distinct clusters observed through principal component analysis (PCA) (**Figure 3**). These chemical composition constituents vary by level of biological degradation (Andrews et al., 1999; Brand et al., 2011; Krigstin and Wetzel, 2016; Groenewold et al., 2020). The loading plot in **Figure 3B** shows how each of these chemical components is driving the observed cluster in the PCA score plot demonstrated in **Figure 3A**.

Figure 4A shows a linear relationship between the median red channel and the chemical properties of the samples and was used throughout the analyses. The red channel had the largest range of variability when compared to blue and green, high correlation to other factors used in regression analyses and was correlated to green and blue channels (**Supplementary Figure S1**, supporting information). Linear relationship factors were identified from chemical data using a stepwise technique as a function of their contributions toward explaining variability in the median red channel output, while minimizing multicollinearity between explanatory factors. For example, extractives and the interaction factor of (glucan x xylan) are highly correlated (**Supplementary Figure S1**, supporting information). Therefore, both were not necessary to explain the variability in the median red channel. The relationship between these chemical properties and the median red channel exceeds an R^2 value of 0.7. Interaction terms between glucan, xylan, and lignin content were included in this analysis. **Table 1** displays the standardized coefficients and relative significance level for each chemical material attribute from linear relationships in **Figure 4A**. These coefficients suggest that xylan was the highest

FIGURE 2 | Boxplots for **(A)** chemical composition; $n = 222$, and **(B)** inorganic speciation; $n = 191$. SiO_2 is broken out for a clearer view of the variable ranges of the other inorganic species.

FIGURE 3 | Principal component analysis of biological degradation **(A)** score plot and **(B)** loading plot for chemical composition. $n = 222$.
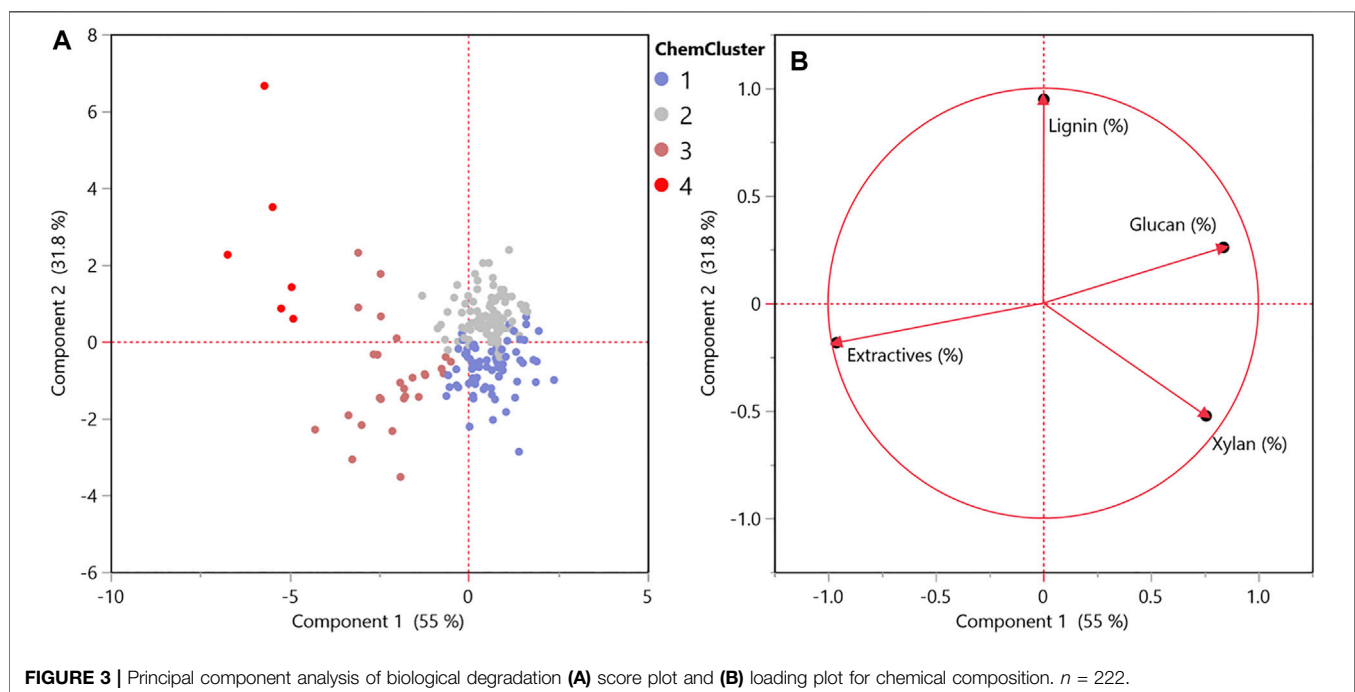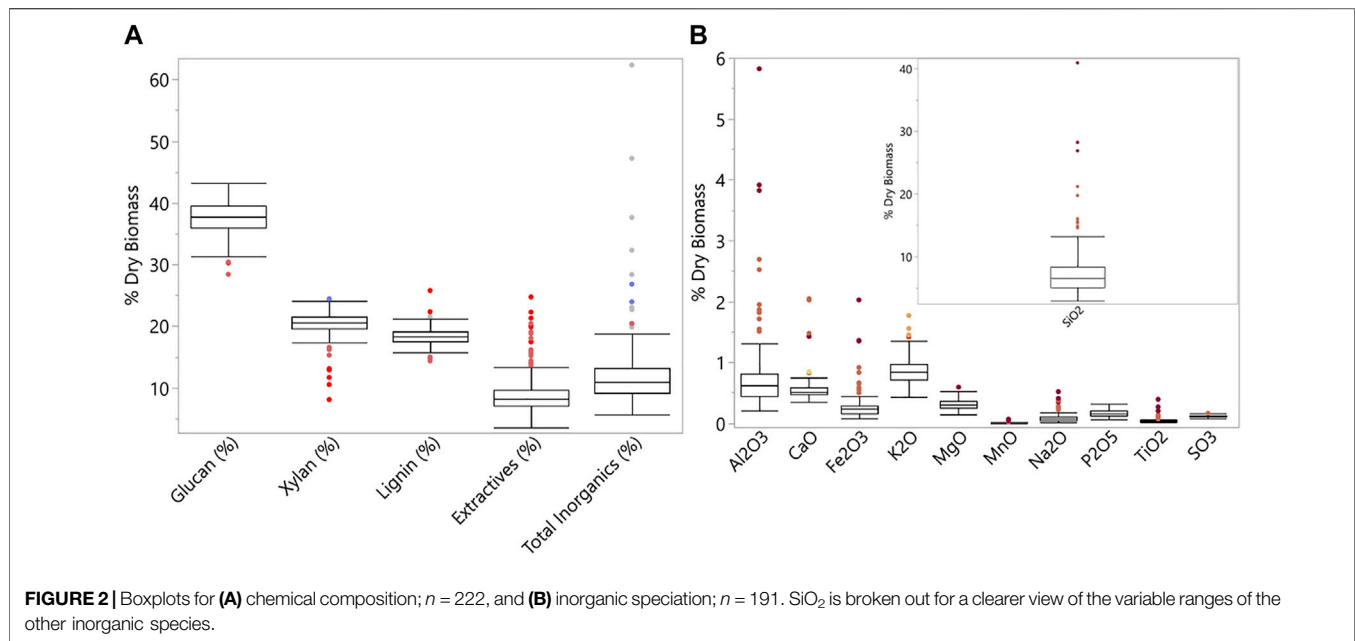
contributor to explaining the variability seen in the red channel. At the same time, changes in glucan contribute the least in comparison to the other factors. This is consistent with prior work that demonstrated selective degradation of hemicellulose in response to biological heating during storage with cellulosic components involved to a lesser extent (Groenewold et al., 2020). Both factors indicate that as glucan and xylan contents decrease, the red channel signal decreases.

It should be noted that extractives were not used in the model due to the high correlation with glucan and xylan; however, as extractive content increases in the data set, the red channel decreases. Previous studies have demonstrated that extractives content increases with the extent of biological degradation (Groenewold et al., 2020; Li et al., 2020; Ray et al., 2020), consistent with reductions in hemicellulose and to a lesser extent, cellulosic components, as a function of biological
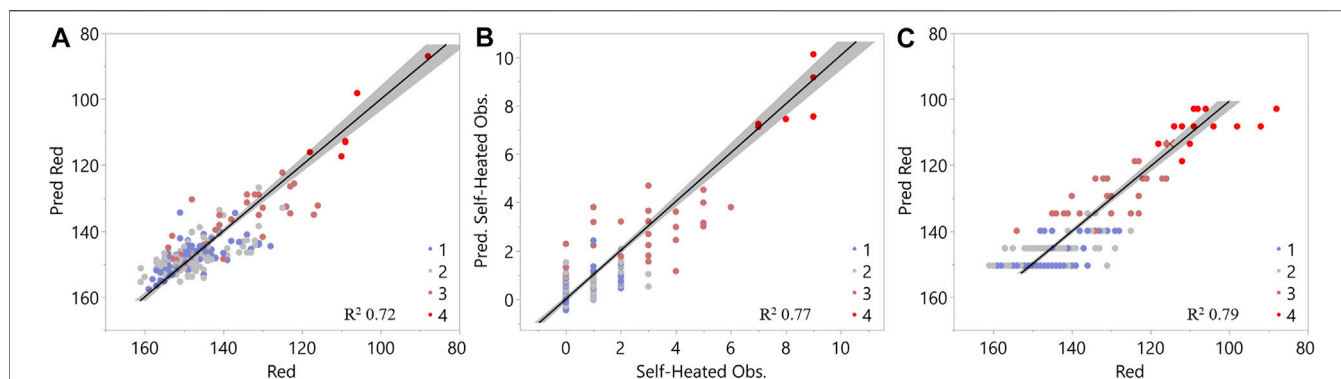
FIGURE 4 | Least squares regression analysis of **(A)** red band intensity as a function of chemical composition, **(B)** biological degradation/self-heating observation as a function of chemical composition, and **(C)** red band intensity as a function of biological degradation/self-heating observation. Legend gives results of cluster analysis from chemical composition in **Figures 3A,B**.

TABLE 1 | Chemical properties are used to form linear regressions for explaining the red-band and biological degradation/self-heating observation variability.

Chemical property	Red band coefficient[a]	Self-heating observation coefficient[a]
Glucan	0.10*	−0.26**
Xylan	0.44**	−0.49**
Lignin	0.25**	−0.18**
Glucan x Xylan	−0.26**	0.34**
Glucan x Xylan x Lignin	−0.15**	not significant
Total Inorganics	−0.35**	N/A

[a]*Standardized coefficients.*
Indicates significance $0.01 < p \leq 0.05$.
Indicates highly significant $p < 0.01$.

degradation. The interaction terms between glucan and xylan suggest that with increases in both, the impact of xylan on the red channel output decreases. During degradation, xylan content, representing the hemicellulose fraction, is more reduced than glucan content (Qing and Wyman, 2011). This interaction term reflects the changing ratio between cellulose and hemicellulose. The same conclusion can be drawn from the interaction between glucan, xylan, and lignin, representing the changing ratios between these chemical attributes in response to degradation. Total inorganics also significantly contributed to changes in the median red channel response. This relationship is further discussed in the following section on soil contamination.

Linear regression analysis was used to relate organic components of glucan, xylan, and lignin to the severity of biological degradation. **Figure 4B** shows the resulting linear relationship, and the coefficients are shown in **Table 1**. The R^2 was 0.77 for this regression, similar to the regression formed between chemical properties and the red band in **Figure 4A**. This relationship also indicates that xylan is the highest contributor, suggesting that lower concentrations of xylan content correspond to higher biological degradation levels. The only organic-based significant factor not shared between

the two regressions (**Figures 4A,B**) was the interaction between glucan, xylan, and lignin (**Table 1**). This factor did not significantly contribute to explaining the biological degradation observations. Researcher observations of biological degradation less resolved (scale from 0-9 with each researcher selecting between 0-3) compared to the red channel range (88-161 measured); therefore, observational data may not be able to capture the changes in glucan-xylan-lignin property relationships, suggesting the basis for differing explanatory factors in **Figures 4A,B**. The similarities between the linear regressions formed between the red channel and chemical properties and observed levels of biological degradation and chemical properties suggest that the red channel from the image analysis identifies biological degradation in the samples. **Figure 4C** further corroborates this by showing the strong linear relationship between the red channel outputs and the biological degradation observations ($R^2 = 0.79$).

The relationships observed between the chemical changes, image analysis of the red channel, and biological degradation observations generally align with the overarching hierarchical cluster grouping. Cluster 1 and 2 (**Figure 3A**) correspond with no or mild biological degradation, group 3 as moderate, and group 4 as the severely biological degradation samples.

Structural Properties of Biologically Degraded Corn Stover Biomass

To gain a more comprehensive understanding of the impacts of biological degradation on the structural properties of biomass, FT-IR was applied to characterize corn stover with different extents of degradation. Corn stover biomass was selected based on the degree of degradation classified as mild, moderate, and severe or scaled from 1 to 9. The detailed information for the red band values and chemical composition is listed in **Table 2**. The more severely biologically degraded biomass resulted in a lower red band value. **Figure 5** shows the FT-IR spectrum of selected corn stover biomass (Bales 5, 1, and

TABLE 2 | Biological degradation properties, red band value, and chemical composition of corn stover for samples characterized using FT-IR.

Sample	Degree of biological degradation	Red band	Glucan (%)	Xylan (%)	Lignin (%)	Total Inorganics (%)
Sample set 2, biologically degraded corn stover[a]						
Bale 5[b]	Mild	148	33.39	18.19	14.70	12.24
Bale 5[b]	Moderate	110	32.23	13.08	18.69	8.81
Bale 5[b]	Severe	106	30.23	10.51	20.41	10.43
Sample set 1, corn stover[c]						
Bale 1 core 3[d]	1	141	36.0	19.0	16.2	8.3
Bale 1 core 7[d]	4	130	31.8	18.7	16.2	9.6
Bale 1 core 6[d]	7	116	NP	NP	NP	NP
Bale 1 core 4[d]	8	104	NP	NP	NP	NP
Bale 6 core 1[d]	1	149	41.2	19.5	17.2	9.5
Bale 6 core 3[d]	3	138	32.1	19.2	15.8	9.1
Bale 6 core 8[d]	6	123	NP	18.5	15.0	10.4
Bale 6 core 7[d]	8	108	31.9	10.1	23.8	12.9
Bale 6 core 6[d]	9	92	NP	NP	NP	NP

[a]Obtained by wet chemistry.
[b]Extractives free for FT-IR, measurement, <45 μm.
[c]Obtained by NIR.
[d]Extractives retained for FT-IR, measurement, <0.2 mm.
NP, no prediction, samples fell outside of the NIRS prediction calibration.
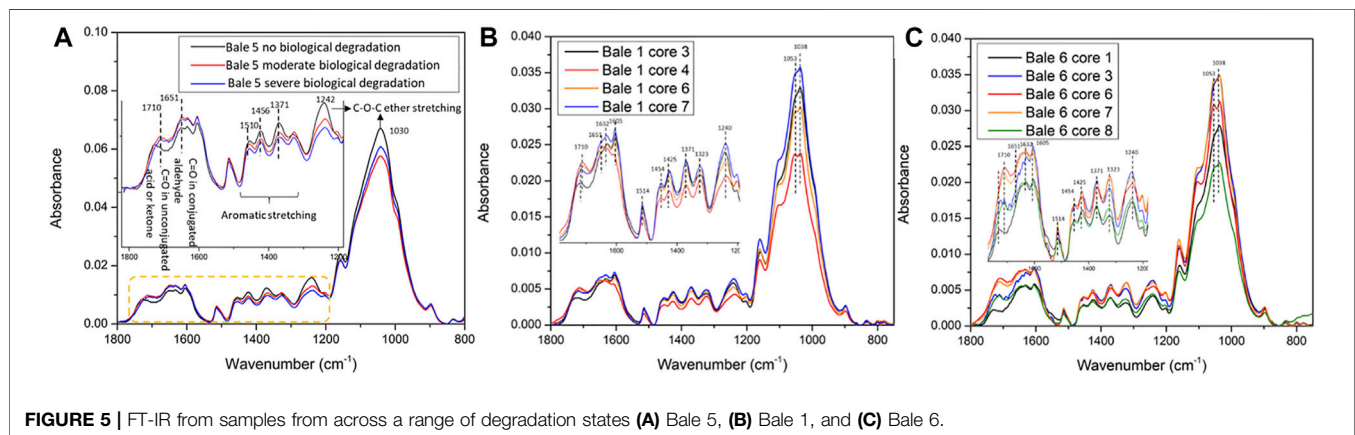
FIGURE 5 | FT-IR from samples from across a range of degradation states **(A)** Bale 5, **(B)** Bale 1, and **(C)** Bale 6.

6) (See image analysis dataset bale ID (Ding et al., 2021b)) and focuses on the region from 1800-800 cm^{-1} reflecting the critical structural properties of biomass (Ma et al., 2018). Remarkable differences were observed in Bale 5. The C-O-C ether stretching at 1030 cm^{-1} and 1242 cm^{-1} decreased after biological degradation indicating the carbohydrates were hydrolyzed during biological degradation, which corresponded to the decrease of xylan. The absorbance of aromatic C-H stretching of lignin in 1510-1300 cm^{-1} also decreased after degradation, suggesting that lignin condensation reactions happened during the biological degradation process. It was hypothesized that the biological oxidation reactions that occur during the degradation result in chromophore formation, such as conjugated carbonyl and quinone, leading to the darkened color of the biomass. In **Figure 5A**, the absorbance of unconjugated (1710 cm^{-1}) and conjugated (1651 cm^{-1}) carbonyl (C=O) increased and shifted with the reducing value of the red band, implying that lignin was oxidized during the biological degradation process supporting this hypothesis. **Figures 5B,C** show the FT-IR spectrum of the Sample Set 1 corn stover samples. Unlike the degraded samples, the extractives and soils were not removed, and the particle size was 0.2 mm, which is much larger than that used for the Sample Set 2 samples. The FT-IR spectra of the samples show similar results with the degraded samples. However, some samples, such as Bale 6 Cores1 and 8, have weaker absorbance caused by the particle size or soil contaminants. Also, the overall absorbance of Sample Set 1 is lower than the degraded samples (Sample Set 2). Therefore, the particle size of biomass and soil removal is essential for FT-IR ATR

FIGURE 6 | Principal component analysis of soil contamination **(A)** score plot and **(B)** loading plot for ash speciation represented on a % dry biomass basis.

FIGURE 7 | Linear regression of measured versus predicted red channel value explained by chemical composition and select inorganic species (SO$_3$ and SiO$_2$) visualizing **(A)** ash clusters and **(B)** chemical clusters.
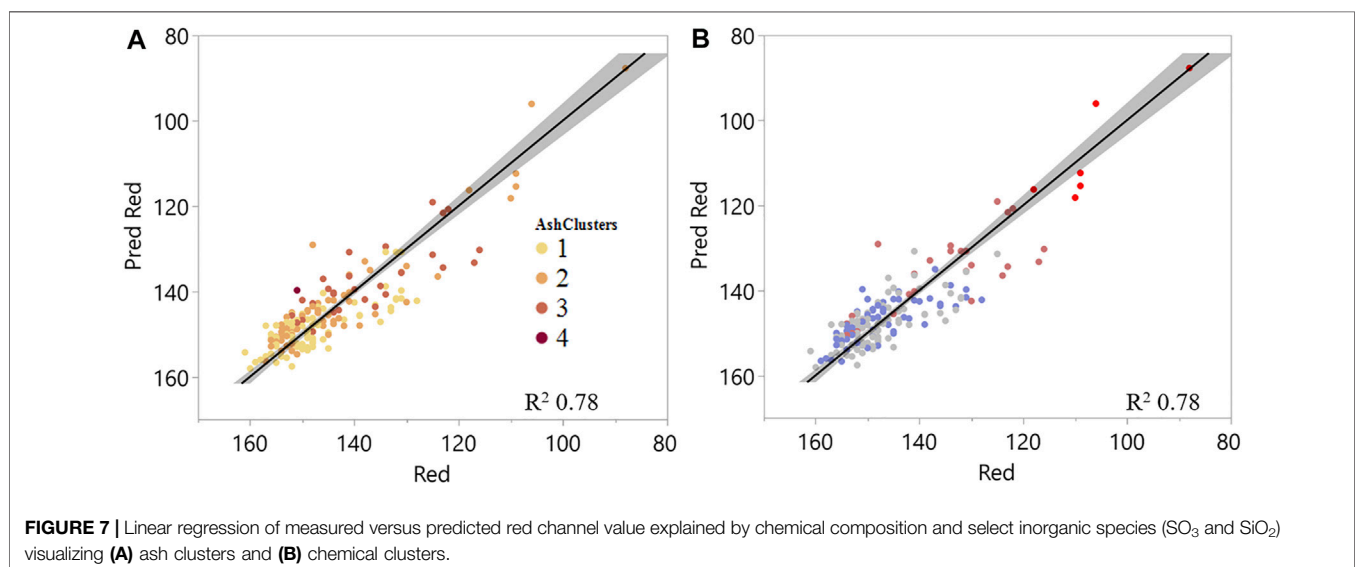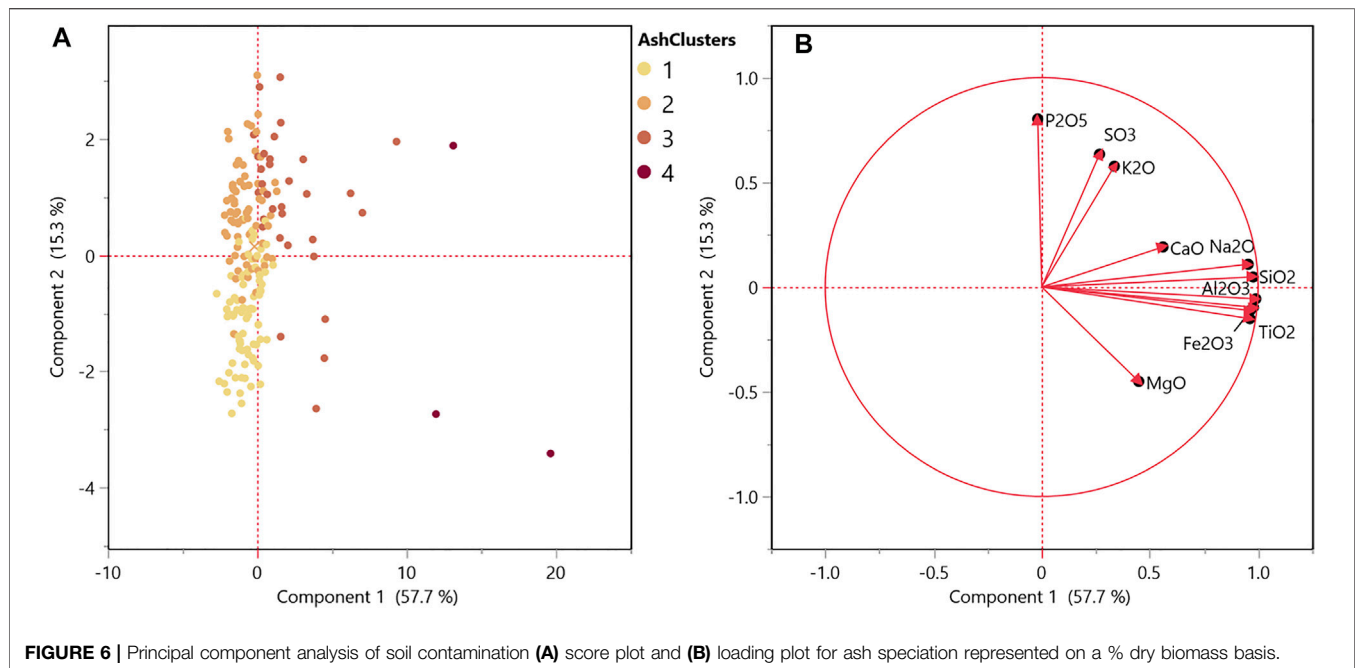
characterization. The FT-IR results demonstrated a potential correlation between the hydrolyzed carbohydrates and the condensed and oxidized lignin in biologically degraded corn stover. These results provide further insights into biopolymer degradation and modification mechanisms during storage, which could correlate to the red band intensity detected through image analysis.

Image Analysis of Soil Contamination

As shown in **Table 1** and **Figure 4A**, the total inorganics content significantly contributes to changes observed in the red channel, suggesting that image analysis could provide a valuable tool for identifying levels of soil contamination. Hierarchical cluster analysis was used similarly on ash speciation data to identify distinct clusters based on inorganic features. Cluster 1 represents limited or no soil contamination, and cluster 4 represents high soil contamination. The PCA score plot (**Figure 6A**) displays these clusters. The variability in the 1st principal component suggests a relationship to inorganic species derived from soil contamination, including silicon and aluminum (Lacey et al., 2018). The second principal component relates to inorganic components that serve structural and physiological functions within the plant (i.e., biogenic ash), including sulfur, nitrogen, potassium, calcium, magnesium, and phosphorus (Thy et al.,

TABLE 3 | Chemical properties, including select ash species (SO$_3$ and SiO$_2$), were used to form linear regressions to explain the red-band variability.

Chemical property	Red band coefficient[a]
Glucan	0.06
Xylan	0.33**
Lignin	0.22**
Glucan x Xylan	−0.36**
Glucan x Xylan x Lignin	−0.17**
SiO$_2$	−0.17**
SO$_3$	−0.30**

[a]*Standardized coefficients.*
(*) indicates significance 0.01 < p< 0.05.
**indicates highly significant p < 0.01.

2013; Li et al., 2020). The inorganic clusters 1 and 2 vary primarily based on intrinsic inorganic species inherent to plant biomass, and clusters 3 and 4 show relationships to soil contaminant inorganic species (i.e., silicon and aluminum).

Figure 7A shows the resulting regression with the ash speciation clusters labeled, and Figure 7B shows the same regression with the chemical clusters, that were based on glucan, xylan, lignin, and extractives contents. Regression analyses highlight that for this dataset, the red channel relationships are being driven by the biological degradation severity, even with the highest ash sample in the data representing close to 62% total inorganics. The regression shown in Figure 7A includes SO$_3$ and SiO$_2$ content instead of total inorganics, as was included in the regression represented in Figure 4A, to represent the relationship of these intrinsic and extrinsic ash species to the image red channel intensity. Phosphorus and potassium oxides were not selected for the linear regression as representatives of intrinsic ash, as suggested by the principal component 2 in the principal component loadings plot (Figure 6B) as they did not significantly contribute to explaining the red variability. It should be noted that fewer samples in the dataset contained ash speciation compared to the organic composition data available (191 samples compared to 222 samples). Therefore, the coefficient changes cannot be directly compared to the model in Figure 4A; however, the general trends remain consistent. Both SO$_3$ (representative of intrinsic ash) and SiO$_2$ content (representative of soil contamination) significantly explain variability in the red channel (Table 3).

In summary, regression analyses associated with both biological degradation and soil contamination identified relationships among chemical components in corn stover, namely xylan, glucan, lignin, total inorganics, Si, and S, strongly correlated to the red band intensity detected through image analysis. The variations in organic chemical attributes xylan, glucan, and lignin were attributed to biological degradation. In contrast, variations in inorganic attributes, Si and S, corresponded to the extent of soil contamination and intrinsic inorganic content in the sample. Although a mechanistic understanding of the biological degradation (Groenewold et al., 2020; Ding et al., 2021a) and thermo-chemical oxidative reactions that alter

biomass quality attributes during storage (Krigstin and Wetzel, 2016) is required to sort out confounding signals from the degradation and accumulation of inorganic species, qualitative results presented here show promise for developing rapid screening tools to deploy in-field or in-line for rapid assessment of quality (Ray et al., 2020).

Screening Prediction Development

The purpose of the regression analyses and relationships, as previously discussed, was to demonstrate that aspects of the images, the median red channel intensity specifically, could be quantitatively related to the chemical changes known to be impacted by biological degradation and soil contamination. Here the red channel along with the blue and green channels from the images was used to demonstrate potential screening methods for corn stover samples to predict the presence of biological degradation and soil contamination. For this demonstration, logistic regression was used to predict the hierarchical groups of chemical clusters representing biological degradation and inorganics clusters representing soil contamination considering the median red, blue and, green channel outputs and interactions between these color channels as predictors. For the organic chemical cluster logistic regression, the receiver operator characteristics (ROC) curve (Figures 8A,B) demonstrates the diagnostic ability of image analysis properties to correctly identify the organic chemical cluster, representing levels of biological degradation, that each sample belongs to by comparing the sensitivity, true identification rate, versus the specificity, false-positive identification rate. These plots, along with the confusion matrix, give the actual number of samples predicted to be in each group versus their actual group (Table 4) for both the training and validation sets. The confusion matrix indicates that this model correctly identified the severely biologically degraded samples (cluster 4) 100% of the time with no false identifications. However, the identification accuracy was lower for cluster group 3, moderate levels of biological degradation, and reduced further for clusters 1 and 2, representing no and mild biological degradation. The validation sample results from this logistic regression follow the same trend. Samples with severe biological degradation (cluster 4) are accurately predicted 100% with no false positives and show progressive decreases in the sensitivity and specificity for clusters 3, 2, and 1. This preliminary model indicates that this approach could be employed to identify biomass samples exhibiting moderate to severe biological degradation, but requires expanded datasets and further refinement to distinguish between samples with mild or limited biological degradation and samples without degradation.

Linear regression analysis indicated that biological degradation was the primary factor driving variaitions in the red-channel intensity, with soil contamination contributing secondarily. Based on this knowledge, the proposed process for screening feedstock for soil contamination is to the first screen for evidence of moderate and severe biological degradation and then use
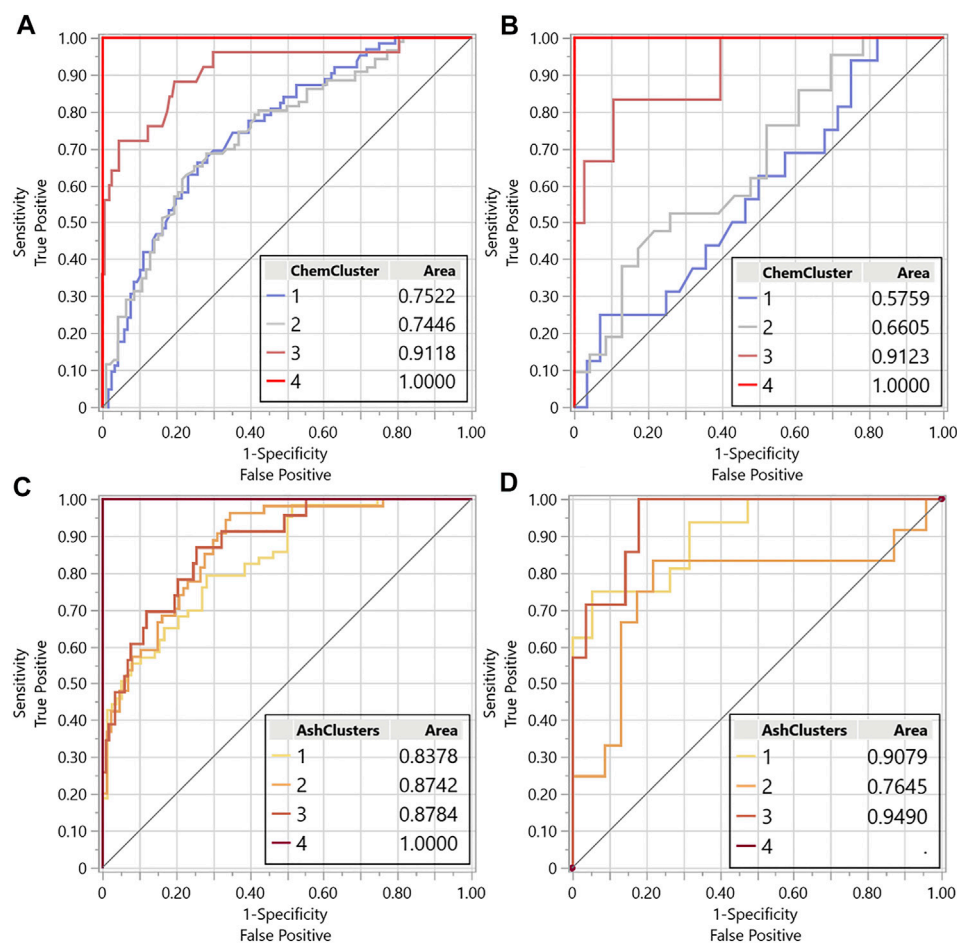
FIGURE 8 | Receiver operator characteristic (ROC) curves for the logistics regression training sets using image analysis data red, green, blue channels to predict the chemical cluster (associated with levels of biological degradation) **(A)** training set and **(B)** validation set and ash cluster (associated with levels of soil contamination) **(C)** training set and **(D)** validation set.

TABLE 4 | Confusion matrix for chemical cluster logistics regression using red, green, and blue channels image analysis data.

Actual	Predicted			
Training	**1**	**2**	**3**	**4**
1	31 (50%)	30	1	0
2	20	62 (72%)	4	0
3	3	6	16 (65%)	0
4	0	0	0	5 (100%)
Validation				
1	4 (25%)	12	0	0
2	5	15 (71%)	1	0
3	1	1	4 (67%)	0
4	0	0	0	1 (100%)

This table shows the actual number of samples predicted to be in each group versus their actual group and the true positive percentages for accurate prediction.

TABLE 5 | Confusion matrix for ash cluster logistics regressions using image analysis data red, green, and blue channels, and chemical cluster input.

Actual	Predicted			
Training	**1**	**2**	**3**	**4**
1	47 (75%)	11	5	0
2	14	39 (72%)	1	0
3	7	4	12 (52%)	0
4	0	0	0	1 (100%)
Validation				
1	13 (81%)	2	0	1
2	3	7 (58%)	0	2
3	1	2	4 (57%)	0
4	0	0	0	0 (.)

This table shows the actual number of samples predicted to be in each group versus their actual group, along with the true positive percentages for accurately predicted.
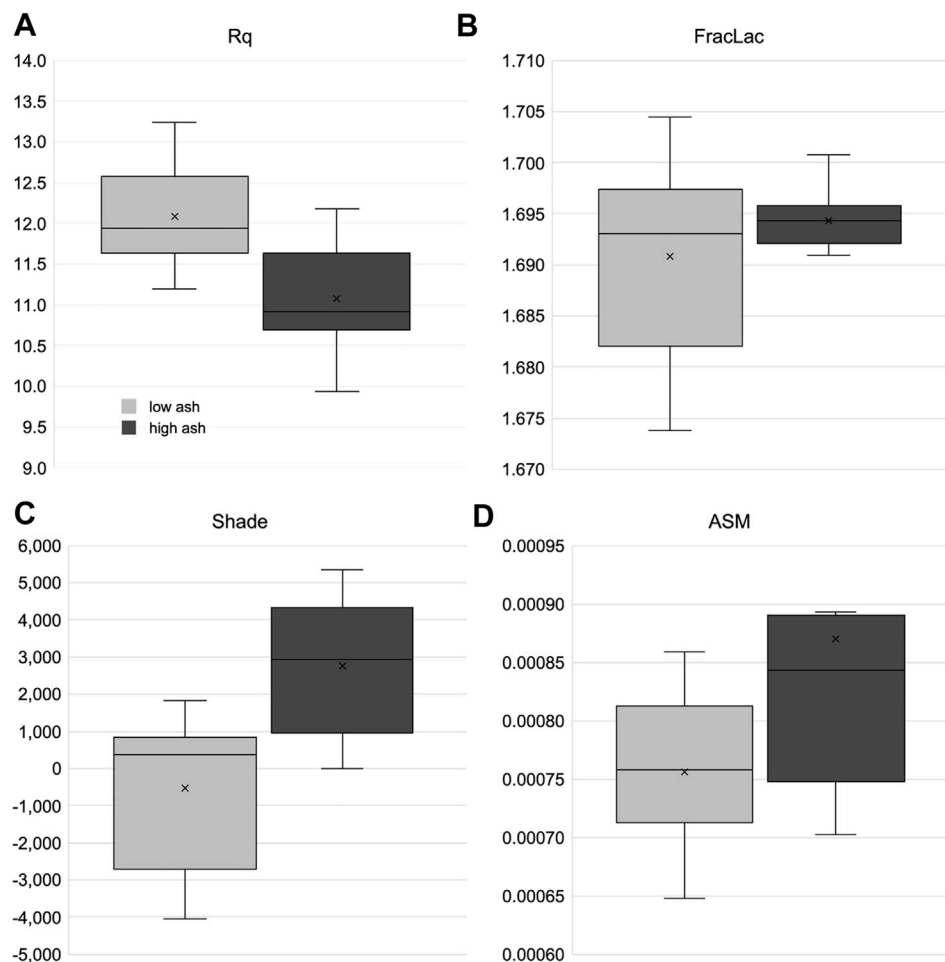
FIGURE 9 | A subset of textural feature image analysis results from bale core samples taken corn stover bales with variable ash content. **(A)** Rq is the root mean square deviation. **(B)** FracLac is the local connected fractal dimension. **(C,D)** Shade and angular second moment (ASM) are grey-level co-occurrence matrix analysis parameters.

the outputs of the biological degradation prediction levels to screen for the additional presence of soil contamination. The resulting ROC curve and confusion matrices from this soil contamination logistics regression are shown in **Figures 8C,D** and **Table 5**. These results indicate enhanced diagnostic ability to predict higher levels of soil contamination (cluster group 4), representing a sample with 38% total ash and 28% SiO_2 content. As only one sample was available at this level, no validation samples were used for this cluster group. Cluster 1 samples representing the lowest ash samples with on average 10% ash content and 6% SiO_2 content was accurately 75 and 81% for the training and validation sets, respectively. The model had relatively equal power for identifying the lower levels of soil contamination representing average total ash 18 and 11% and SiO_2 contents of 11 and 6% for clusters 3 and 2, respectively. These results show the potential for the image

analysis to be used as a screening tool for soil contamination after considering color changes due to biological degradation; however, a larger dataset with known validation samples are necessary to improve modelaccuracy.

Surface Texture Analysis

The image analysis based on color variability was used to identify biological degradation and soil contamination levels. In this research, image analysis of surface properties was also investigated to identify soil contamination, biological degradation, and additional properties impacting particle flow. For the samples with variable ash content, samples were selected with ash content of 5–10% (low ash) and 10–20% (high ash) (Sievers et al., 2020), surface roughness calculated as Rq (**Figure 9A**), and the GLCM parameter Shade (**Figure 9C**) appear to distinguish between high and low ash samples. The

FIGURE 10 | A subset of textural feature image analysis results from bale core samples taken corn stover bales with variable biological degradation. **(A)** Rq is the root mean square deviation. **(B)** FracLac is the local connected fractal dimension. **(C,D)** Shade and angular second moment (ASM) are grey-level co-occurrence matrix analysis parameters.

pattern, however, was different between Rq and Shade, with the high ash sample measuring low Rq and higher Shade values. Rq is a measure of surface roughness that is positively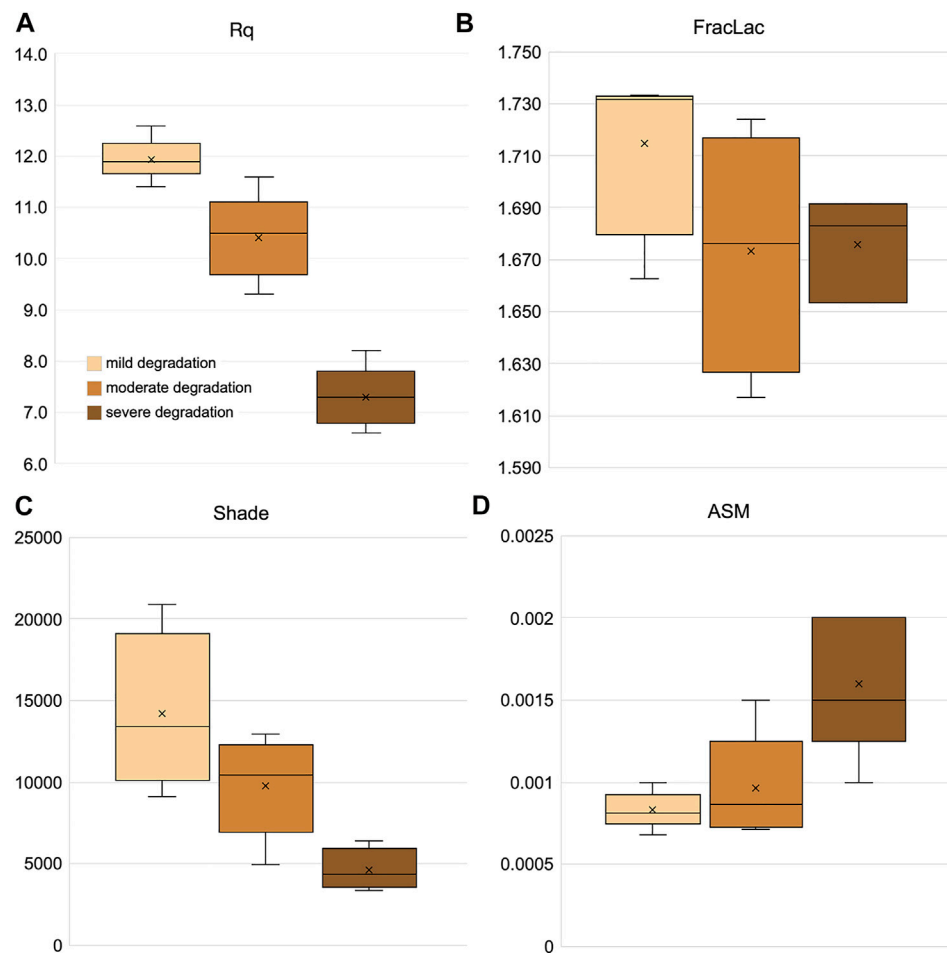 correlated with inter-particle friction and could impede flowability. However, surface roughness is also correlated with hydrophobicity. Therefore, particles that trap less water should have better flowability. Shade characterizes the tendency of clustering of pixels as a measure of asymmetry. In our previous work using images of hammer-milled biomass, the asymmetric clustering that shade describes was positively related to poor conveyance (Gudavalli et al., 2020). The fractal analysis (**Figure 9B**) or the GLCM parameter ASM (**Figure 9D**) differed among the ash variable samples (Sample Set 1).

Mild, moderately, and severely degraded samples (Sample Set 2) were partly distinguished by three of the four texture parameters shown in **Figure 10**. The surface roughness (Rq, **Figure 10A**) reveals the most separation. Shade and ASM (**Figures 10C,D**) showed differences between mild and severe samples. These differences can be generated by how the

samples fracture during milling, causing subtle differences in particle size and shape distributions—these differences in particles present as differences in the texture of biomass piles. For example, surface texture analysis could distinguish among variable ash levels or levels of degradation.

CONCLUSION

This study used image analysis in visible, red-green-blue (RGB) chromatic space to evaluate the quality of corn stover across four Iowa counties representing a realistic supply shed in the US corn belt. Linear regression relationships with $R^2 > 0.7$ were found between the red channel values from images of corn stover and changes in chemical properties resulting from biological degradation (xylan, glucan, and lignin) and soil contamination (Si and S). The FT-IR results demonstrated a potential correlation between the hydrolyzed carbohydrates and the condensed and oxidized lignin in biologically degraded corn stover, which could

correlate to the red band intensity detected through image analysis. In addition, surface texture analysis of for these same images was found to distinguish among variable levels of ash and degradation.

Further, logistic regression classification algorithms were used to develop an image analysis method for screening and classifying levels of biological degradation and soil contamination in corn stover. This prototype supports research and development that uses image analysis and other rapid characterization tools to further understand and describe corn stover and bioenergy feedstock quality during in-field or over-belt applications to support industrial operations for sorting biomass based on quality or presence of contaminants.

DATA AVAILABILITY STATEMENT

The datasets presented in this study can be found in online repositories. The names of the repository/repositories and accession number(s) can be found in the article/**Supplementary Material**.

AUTHOR CONTRIBUTIONS

LD and K-TL contributed to investigation, methodology, formal analysis, and writing the original draft manuscript. AH and RE contributed to conceptualization, methodology, formal analysis, data curation, and writing—draft, reviewing and editing. JG and BD performed the surface texture analysis and contributed to writing the original draft, reviewing, and editing; BD contributed to funding acquisition. RC and BT were involved in investigation and formal analysis. JK contributed to conceptualization and editing. WS contributed to conceptualization. AR contributed to funding acquisition, supervision, conceptualization, writing—reviewing and editing.

SUPPLEMENTARY MATERIAL

The Supplementary Material for this article can be found online at: https://www.frontiersin.org/articles/10.3389/fenrg.2022.837698/full#supplementary-material

REFERENCES

Aguirre, A., Karwe, M. V., and Borneo, R. (2018). Effect of High Pressure Processing on Sugar-Snap Cookie Dough Preservation and Cookie Quality. *J. Food Process. Preserv.* 42 (1), e13407. doi:10.1111/jfpp.13407

Andrews, J. A., Siccama, T. G., and Vogt, K. A. (1999). The Effect of Soil Nutrient Availability on Retranslocation of Ca, Mg and K from Senescing Sapwood in Atlantic white Cedar. *Plant Soil* 208, 117–123. doi:10.1023/A:1004512317397

Bendig, J., Bolten, A., Bennertz, S., Broscheit, J., Eichfuss, S., and Bareth, G. (2014). Estimating Biomass of Barley Using Crop Surface Models (CSMs) Derived from UAV-Based RGB Imaging. *Remote Sensing* 6, 10395–10412. doi:10.3390/rs61110395

Bose, E., Leal, J. H., Hoover, A. N., Zeng, Y., Li, C., Ray, A. E., et al. (2020). Impacts of Biological Heating and Degradation during Bale Storage on the Surface Properties of Corn Stover. *ACS Sustain. Chem. Eng.* 8, 13973–13983. doi:10.1021/acssuschemeng.0c03356

Brand, M. A., Bolzon de Muñiz, G. I., Quirino, W. F., and Brito, J. O. (2011). Storage as a Tool to Improve wood Fuel Quality. *Biomass Bioenerg.* 35, 2581–2588. doi:10.1016/J.BIOMBIOE.2011.02.005

Cheah, W. Y., Sankaran, R., Show, P. L., Tg. Ibrahim, T. N. B., Chew, K. W., Culaba, A., et al. (2020). Pretreatment Methods for Lignocellulosic Biofuels Production: Current Advances, Challenges and Future Prospects. *Biofuel Res. J.* 7, 1115–1127. doi:10.18331/BRJ2020.7.1.4

Chinga, G., Johnsen, P. O., Dougherty, R., Berli, E. L., and Walter, J. (2007). Quantification of the 3D Microstructure of SC Surfaces. *J. Microsc.* 227, 254–265. doi:10.1111/j.1365-2818.2007.01809.x

Ding, L., Gruber, J. N., Ray, A. E., Donohoe, B. S., and Li, C. (2021a). Distribution of Bound and Free Water in Anatomical Fractions of Pine Residues and Corn Stover as a Function of Biological Degradation. *ACS Sustain. Chem. Eng.* 9 (47), 15884–15896. doi:10.1021/acssuschemeng.1c05606

Ding, L., Hoover, A. N., Emerson, R. M., Lin, K., Ray, A. E., Donohoe, B. S., et al. (2021b). Image Analysis for Rapid Assessment and Quality-Based Sorting of Corn Stover Dataset. Idaho National Laboratory. Bioenergy Feedstock Library. Available at: https://bioenergylibrary.inl.gov/data/dataset.aspx?id=1006. (Accessed March 12, 2021).

Eisenbies, M. H., Volk, T. A., and Patel, A. (2016). Changes in Feedstock Quality in Willow Chip Piles Created in winter from a Commercial Scale Harvest. *Biomass Bioenerg.* 86, 180–190. doi:10.1016/j.biombioe.2016.02.004

Gitelson, A. A., Viña, A., Arkebauer, T. J., Rundquist, D. C., Keydan, G., and Leavitt, B. (2003). Remote Estimation of Leaf Area index and green Leaf Biomass in maize Canopies. *Geophys. Res. Lett.* 30 (5), 1248–1251. doi:10.1029/2002GL016450

Gitelson, A. A., Peng, Y., Arkebauer, T. J., and Schepers, J. (2014). Relationships between Gross Primary Production, green LAI, and Canopy Chlorophyll Content in maize: Implications for Remote Sensing of Primary Production. *Remote Sensing Environ.* 144, 65–72. doi:10.1016/j.rse.2014.01.004

Groenewold, G. S., Hodges, B., Hoover, A. N., Li, C., Zarzana, C. A., Rigg, K., et al. (2020). Signatures of Biologically Driven Hemicellulose Modification Quantified by Analytical Pyrolysis Coupled with Multidimensional Gas Chromatography Mass Spectrometry. *ACS Sustain. Chem. Eng.* 8, 1989–1997. doi:10.1021/acssuschemeng.9b06524

Gudavalli, C., Bose, E., Donohoe, B. S., and Sievers, D. A. (2020). Real-time Biomass Feedstock Particle Quality Detection Using Image Analysis and Machine Vision. *Biomass Conv. Bioref.*, 1–12. doi:10.1007/s13399-020-00904-w

Gupta, R. K., Prasad, T. S., and Vijayan, D. (2000). Relationship between LAI and NDVI for IRS LISS and LANDSAT TM Bands. *Adv. Space Res.* 26, 1047–1050. doi:10.1016/S0273-1177(99)01115-1

Haralick, R. M. (1979). Statistical and Structural Approaches to Texture. *Proc. IEEE* 67, 786–804. doi:10.1109/PROC.1979.11328

Hartley, D. S., Thompson, D. N., Griffel, L. M., Nguyen, Q. A., and Roni, M. S. (2020). Effect of Biomass Properties and System Configuration on the Operating Effectiveness of Biomass to Biofuel Systems. *ACS Sustain. Chem. Eng.* 8 (19), 7267–7277. doi:10.1021/acssuschemeng.9b06551

Hoover, A., Emerson, R., Williams, C. L., Ramirez-Corredores, M. M., Ray, A., Schaller, K., et al. (2019). Grading Herbaceous Biomass for Biorefineries: a Case Study Based on Chemical Composition and Biochemical Conversion. *Bioenerg. Res.* 12, 977–991. doi:10.1007/s12155-019-10028-3

Jannoura, R., Brinkmann, K., Uteau, D., Bruns, C., and Joergensen, R. G. (2015). Monitoring of Crop Biomass Using True Colour Aerial Photographs Taken from a Remote Controlled Hexacopter. *Biosyst. Eng.* 129, 341–351. doi:10.1016/j.biosystemseng.2014.11.007

Jiang, Q., Fang, S., Peng, Y., Gong, Y., Zhu, R., Wu, X., et al. (2019). UAV-based Biomass Estimation for Rice-Combining Spectral, TIN-Based Structural and Meteorological Features. *Remote Sensing* 11 (7), 890. doi:10.3390/rs11070890

Karperien, A., Ahammer, H., and Jelinek, H. F. (2013). Quantitating the Subtleties of Microglial Morphology with Fractal Analysis. *Front. Cel. Neurosci.* 7, 3. doi:10.3389/fncel.2013.00003

Krigstin, S., and Wetzel, S. (2016). A Review of Mechanisms Responsible for Changes to Stored Woody Biomass Fuels. *Fuel* 175, 75–86. doi:10.1016/j.fuel.2016.02.014

Lacey, J. A., Aston, J. E., and Thompson, V. S. (2018). Wear Properties of Ash Minerals in Biomass. *Front. Energ. Res.* 6, 119. doi:10.3389/fenrg.2018.00119

Lan, Z., and Liu, Y. (2018). Study on Multi-Scale Window Determination for GLCM Texture Description in High-Resolution Remote Sensing Image Geo-Analysis Supported by GIS and Domain Knowledge. *Int. J. Geo. Inf.* 7 (5), 175. doi:10.3390/ijgi7050175

Lati, R. N., Filin, S., and Eizenberg, H. (2013). Estimating Plant Growth Parameters Using an Energy Minimization-Based Stereovision Model. *Comput. Electron. Agric.* 98, 260–271. doi:10.1016/j.compag.2013.07.012

Li, C., Kerner, P., Williams, C. L., Hoover, A., and Ray, A. E. (2020). Characterization and Localization of Dynamic Cell Wall Structure and Inorganic Species Variability in Harvested and Stored Corn Stover Fractions as Functions of Biological Degradation. *ACS Sustain. Chem. Eng.* 8, 6924–6934. doi:10.1021/acssuschemeng.9b06977

Ma, R., Zhang, X., Wang, Y., and Zhang, X. (2018). New Insights toward Quantitative Relationships between Lignin Reactivity to Monomers and Their Structural Characteristics. *Chemsuschem* 11, 2146–2155. doi:10.1002/cssc.201800550

Mitra, A., Li, Y.-F., Klämpfl, T. G., Shimizu, T., Jeon, J., Morfill, G. E., et al. (2014). Inactivation of Surface-Borne Microorganisms and Increased Germination of Seed Specimen by Cold Atmospheric Plasma. *Food Bioproc. Technol* 7, 645–653. doi:10.1007/s11947-013-1126-4

Payne, C. E., and Wolfrum, E. J. (2015). Rapid Analysis of Composition and Reactivity in Cellulosic Biomass Feedstocks with Near-Infrared Spectroscopy. *Biotechnol. Biofuels* 8 (1), 1–14. doi:10.1186/s13068-015-0222-2

Piselli, A., Basso, M., Simonato, M., Furlanetto, R., Cigada, A., De Nardo, L., et al. (2017). Effect of Wear from Cleaning Operations on Sintered Ceramic Surfaces: Correlation of Surface Properties Data with Touch Perception and Digital Image Processing. *Wear* 390-391, 355–366. doi:10.1016/j.wear.2017.09.003

Qing, Q., and Wyman, C. E. (2011). Supplementation with Xylanase and β-xylosidase to Reduce Xylo-Oligomer and Xylan Inhibition of Enzymatic Hydrolysis of Cellulose and Pretreated Corn stover. *Biotechnol. Biofuels* 4 (1), 18–12. doi:10.1186/1754-6834-4-18

Qureshi, N., Saha, B. C., Hector, R. E., Dien, B., Hughes, S., Liu, S., et al. (2010). Production of Butanol (A Biofuel) from Agricultural Residues: Part II - Use of Corn stover and Switchgrass Hydrolysates☆. *Biomass and Bioenergy* 34, 566–571. doi:10.1016/j.biombioe.2009.12.023

Ray, A. E., Williams, C. L., Hoover, A. N., Li, C., Sale, K. L., Emerson, R. M., et al. (2020). Multiscale Characterization of Lignocellulosic Biomass Variability and its Implications to Preprocessing and Conversion: a Case Study for Corn Stover. *ACS Sustain. Chem. Eng.* 8, 3218–3230. doi:10.1021/acssuschemeng.9b06763

Rentizelas, A. A. (2016). Biomass Storage. *Biomass Supply Chains for Bioenergy and Biorefining*, 127–146. doi:10.1016/B978-1-78242-366-9.00006-X

Sievers, D. A., Kuhn, E. M., Thompson, V. S., Yancey, N. A., Hoover, A. N., Resch, M. G., et al. (2020). Throughput, Reliability, and Yields of a Pilot-Scale Conversion Process for Production of Fermentable Sugars from Lignocellulosic Biomass: A Study on Feedstock Ash and Moisture. *ACS Sustain. Chem. Eng.* 8, 2008–2015. doi:10.1021/acssuschemeng.9b06550

Skovsen, S., Dyrmann, M., Mortensen, A., Steen, K., Green, O., Eriksen, J., et al. (2017). Estimation of the Botanical Composition of Clover-Grass Leys from RGB Images Using Data Simulation and Fully Convolutional Neural Networks. *Sensors* 17 (12), 2930. doi:10.3390/s17122930

Sluiter, J. B., Ruiz, R. O., Scarlata, C. J., Sluiter, A. D., and Templeton, D. W. (2010). Compositional Analysis of Lignocellulosic Feedstocks. 1. Review and Description of Methods. *J. Agric. Food Chem.* 58, 9043–9053. doi:10.1021/jf1008023

Smith, T. G., Lange, G. D., and Marks, W. B. (1996). Fractal Methods and Results in Cellular Morphology - Dimensions, Lacunarity and Multifractals. *J. Neurosci. Methods* 69, 123–136. doi:10.1016/S0165-0270(96)00080-5

Swain, K. C., Thomson, S. J., and Jayasuriya, H. P. W. (2010). Adoption of an Unmanned Helicopter for Low-Altitude Remote Sensing to Estimate Yield and Total Biomass of a Rice Crop. *Trans. Asabe* 53, 21–27. doi:10.13031/2013.29493

Thörnqvist, T. (1985). Drying and Storage of forest Residues for Energy Production. *Biomass* 7, 125–134. doi:10.1016/0144-4565(85)90038-1

Thy, P., Yu, C., Jenkins, B. M., and Lesher, C. E. (2013). Inorganic Composition and Environmental Impact of Biomass Feedstock. *Energy Fuels* 27, 3969–3987. doi:10.1021/ef400660u

Tilly, N., Hoffmeister, D., Cao, Q., Huang, S., Lenz-Wiedemann, V., Miao, Y., et al. (2014). Multitemporal Crop Surface Models: Accurate Plant Height Measurement and Biomass Estimation with Terrestrial Laser Scanning in Paddy rice. *J. Appl. Remote Sens* 8 (1), 083671. doi:10.1117/1.JRS.8.083671

US DOE (2016). *2016 Billion-Ton Report: Advancing Domestic Resources for a Thriving Bioeconomy, Volume 1: Economic Availability of Feedstocks*. Editors M. H. Langholtz, B. J. Stokes, and L. M. Eaton (Oak Ridge: Oak Ridge National Laboratory). ORNL/TM-2016/160.

Wagner, M., and Horn, H. (2017). Optical Coherence Tomography in Biofilm Research: A Comprehensive Review. *Biotechnol. Bioeng.* 114, 1386–1402. doi:10.1002/bit.26283

Wang, M. F., Chen, X. K., Jiang, E. C., Wu, Y. J., Zhang, S. J., and Li, S. B. (2015). Biochar Absorption Characteristics Based on RGB Analysis of Scanned Images. *Trans. Chin. Soc. Agric. Machinery* 12, 12. doi:10.6041/j.issn.1000-1298.2015.12.028

Yan, J., Oyedeji, O., Leal, J. H., Donohoe, B. S., Semelsberger, T. A., Li, C., et al. (2020). Characterizing Variability in Lignocellulosic Biomass: A Review. *ACS Sustain. Chem. Eng.* 8, 8059–8085. doi:10.1021/acssuschemeng.9b06263

Investigation of Cutter–Woodchip Contact Pressure in a New Biomass Comminution System

Lianshan Lin[1]*, David Lanning[2], James R. Keiser[1] and Jun Qu[1]*

[1]Oak Ridge National Laboratory, Materials Science and Technology Division, Oak Ridge, TN, United States, [2]Forest Concepts, Auburn, WA, United States

A Crumbler® rotary shear system was recently developed to process fuel-grade woodchips into feedstocks having more uniform particle sizes for improved flowability and higher thermochemical output yield than a traditional hammer mill. It represents a significant innovation in the state of the art of biomass comminution equipment. However, the milling unit has experienced significant abrasive wear of the feeding teeth and cutters when processing hard and dusty feedstocks, such as logging residue and corn stover. Here, we present initial simulation results from a finite-element stress analysis of the rotary shear, which is used to investigate the dynamics of interaction between the cutters and woodchips. This is the first step for optimizing the cutter design to improve the system lifetime and processing efficiency, thus reducing downtime and improving overall productivity.

Keywords: biomass comminution, finite element simulation, tool wear, woodchip, contact pressure

INTRODUCTION

Variability in the size and shape of fuel-grade woodchips is a major source of inconsistent feed rate, flow plug, and poor flow into bioconversion reactors. Biomass flowability is one of the major barriers for efficient supply of feedstock (Mani et al., 2006; Shaw, 2008; Felix and Tilley, 2009; Miao et al., 2011; Rezaei et al., 2016). In addition to flow issues, particle length and thickness variability makes it difficult to achieve optimal yields of condensable vapors or non-condensable gases in thermochemical reactors (Schell and Harwood, 1994; Bitra et al., 2009; Oyedeji et al., 2016; Oyedeji et al., 2020). The particle size and shape of biomass particles after grinding are important for downstream processing (Mani et al., 2004; Lam et al., 2008; Guo et al., 2012; Ämmälä et al., 2018). The International Organization for Standardization (ISO) Solid Biofuel Standard 17,225-9 "Graded hog fuel and woodchips for industrial use" allows a percentage of chips up to 150 mm length in each liter of the sample (International Organizatio, 2020). Although allowable, such chips trigger bridging and jams in feed-handling systems. The solution is to replace the traditional hammer or knife mills with rotary shear mills, which can reduce the size and shape variability such that yields of desired chemicals are maximized and feeding issues are minimized.

Wide particle size distribution and a high aspect ratio are characteristic features of hammer-milled lignocellulosic biomass (Oyedeji et al., 2020). The undesired flatter particle size distributions and undesired shardy particle shapes exacerbate flowability issues. Hammermills consume more energy than desired due to high frictional losses within the grinding chamber. Hammermills are also operationally unworkable at a chip moisture content of about over 20 wt%.

Forest Concepts (FC), LLC has developed comminution and screening equipment, commercially known as the Crumbler® rotary shear system, which can process fuel-grade woodchips into much
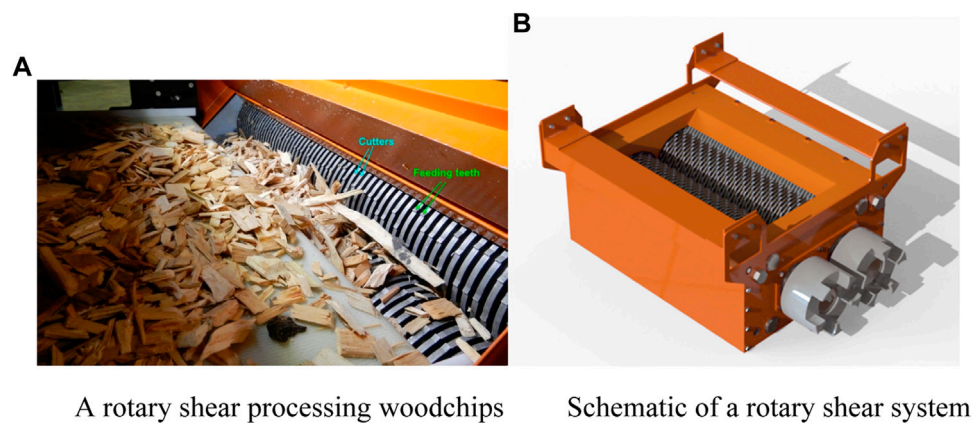
FIGURE 1 | Crumbler® rotary shear biomass comminution system.
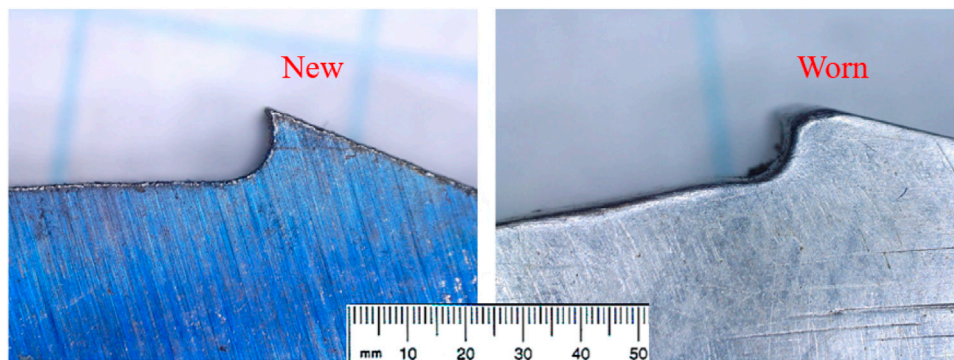
FIGURE 2 | New and worn A2 tool steel cutter tooth.

more uniform feedstocks with improved flowability and improved thermochemical output yields (Oyedeji et al., 2020). The Crumbler® rotary shear system (see **Figure 1A**) is more efficient than the traditional hammermills in comminuting high moisture biomass and producing very narrow particle size distributions to maximize reactor yields, low aspect ratios to improve flowability, and minimal fines that are not useful in the reactor. All of these factors represent significant innovations in biomass comminution equipment.

However, the rotary shear unit experiences significant abrasive wear, especially when processing hard and dirty biomass, such as dirty logging residue and recycled railroad ties. **Figure 2** shows an example of worn cutters, and more detailed worn component characterization can be found in our earlier report (Lee et al., 2021). The desired cutter life is in excess of 1,200 operating hours. However, in as few as 300 h, cutter worn out had been observed in Forest Concepts (FC), LLC's field experience in processing dirty southern hardwood. The current cutters and teeth are made of through-hardened A2 tool steel heat treated to a hardness of HRC 60. The specified HRC 60 hardness was selected as a trade-off

between brittleness and abrasion resistance for this tool steel. Several cutter materials have been tested in search of optimized wear-resistance components, but it has not been possible to identify the controlling wear mechanisms or to identify "economically maximum-life" cutters and other wear parts because of lack of resources and expertise.

The objective of this article is to present initial FEA simulation results to investigate the contact pressures at the cutter–biomass interface. Based on the rotary shear system's CAD model, loading data, and material properties of woodchips (Glass, Zelinka; David), finite element models of a representative rotary tribosystem were built to establish the baseline design of the feeding teeth and cutters and to determine the ranges of contact pressure at the cutter–biomass interfaces. The dynamic simulations provide the means for revealing various ways that cutters break woodchips into smaller pieces, which provides useful information for identifying and implementing advanced materials and/or surface treatments for improved cutter life. Details and results are reported in the following sections.
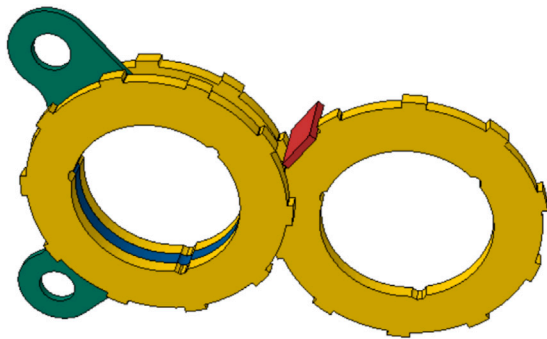
FIGURE 3 | Tribosystem model for a 3-mm thick woodchip (red) sitting on three 6.35-mm thick cutters (yellow), assembled with a clearing plate (green) and a spacer (blue).

GEOMETRY

Three rotary cutters (**Figure 3**) were exported from full CAD geometry to build representative components of the tribosystem. Cutter diameter, thickness, and tooth shape are tailored to the processed material and target output particle size. In the first analysis, 1.6- and 6.35-mm thick cutters with square corner teeth evenly distributed around the circumference were selected to investigate their dynamic behavior. These cutters with different thicknesses have the same outer diameter of approximately 54 mm and inner diameter of approximately 35 mm. Different shapes (sheet, plate, cubic, and bar) and dimensions of woodchips were investigated. **Figure 4** shows a plate-shaped woodchip particle with a representative dimension of $27.5 \times 17.5 \times 3$ mm. In addition, woodchip

particles of dimensions $27.5 \times 17.5 \times 1$, $27.5 \times 16 \times 6$, and $27.5 \times 14.5 \times 10$ mm were used in this investigation in order to cover the statistical range of thicknesses. In addition, bar-like $6 \times 3 \times 3$ mm and cubic-shaped ($6 \times 6 \times 6$ mm) woodchips were considered with the thin cutter ($1/16''$ or 1.6 mm) system and parallelepiped-shaped $15 \times 6 \times 6$ mm and plate-like $50 \times 20 \times 10$ mm woodchip particles were considered with the thick cutter ($1/4''$ or 6.35 mm) system. Consideration of these additional woodchip geometries (shown in **Figure 5**) addresses the real woodchips flowing in a two-stage rotary cutter system in a real working scenario: larger woodchips (thickness of 6–10 mm) from the upper stream go through the first-stage cutter (thick cutter, ¼"); smaller woodchips (thickness of 3–6 mm) sheared by first-stage cutters then go through the second stage cutters (thin cutter, 1/16"), which are broken into even smaller particles (e.g., thickness <3 mm). The size of new particles generated by the cutters should be closer to the cutters' thickness since the gap between every pair of cutters is almost equal to the thickness of the cutter. A two-stage cutter system might put the 6.35-mm cutters on the upstream and the 1.6-mm cutters on the downstream, which can break large woodchips more efficiently while avoiding jams in the woodchip stream.

Initial simulations were focused on the contact pressure between the steel cutters and woodchip. As shown in **Figure 6**, the possible contact interfaces between a single woodchip and three 6.35-mm thick cutters are identified as regions 1, 2, 3, and 4. The rotation direction and speed (315 rpm) are also illustrated in **Figure 6**, which drive the woodchip into contact with the cutters' teeth and edges. The 1.6-mm thick cutters have the same rotation direction, speed, and contact regions.
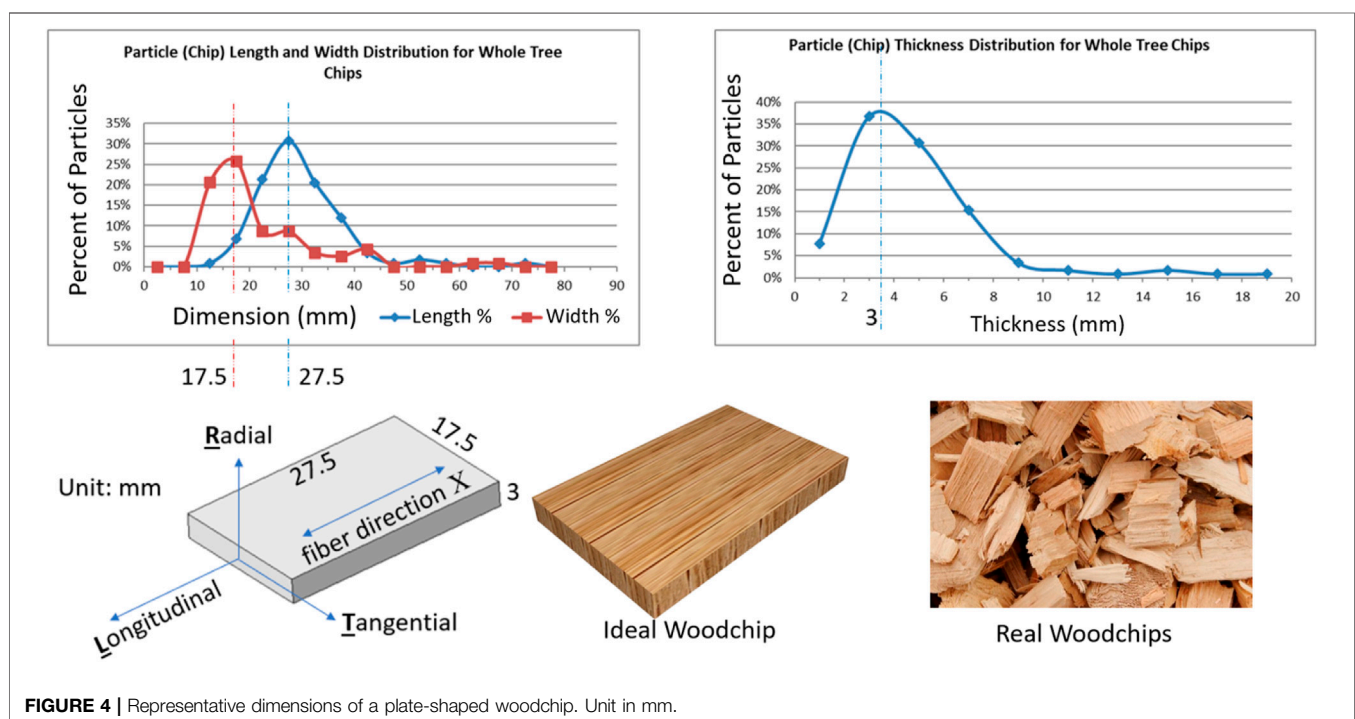
FIGURE 4 | Representative dimensions of a plate-shaped woodchip. Unit in mm.
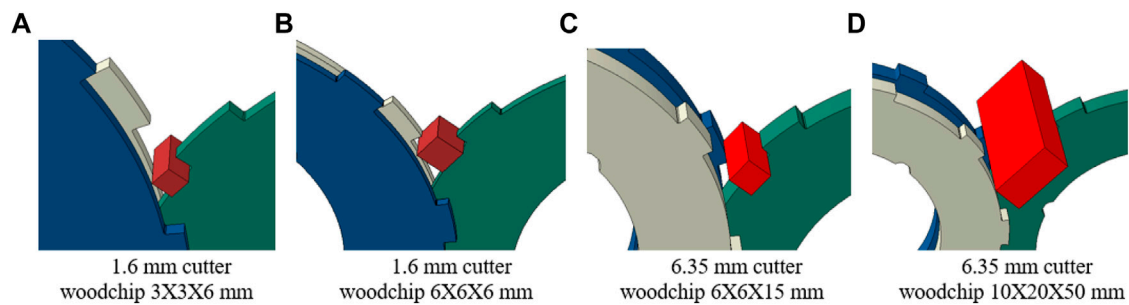
FIGURE 5 | Woodchips in parallelepiped and cubic shapes (cutters in green, blue, and gray, and woodchips in red).
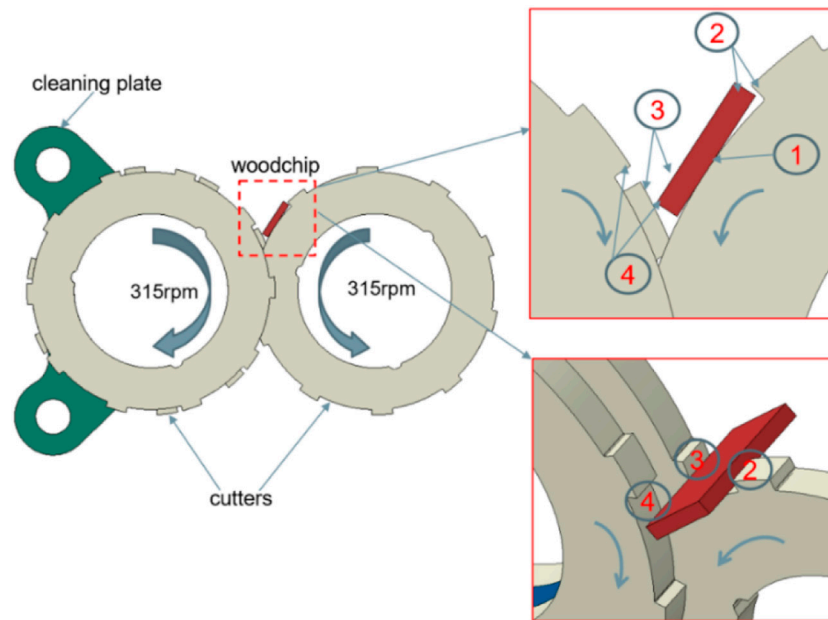
FIGURE 6 | Contact regions between a woodchip and three cutters.

FE MODEL

Based on the geometry illustrated in **Figure 3**, the tribosystem is meshed into a finite element model to investigate the contact pressure between the steel cutter and woodchip. **Figure 7** shows the meshes of three cutters and a woodchip in this finite element model. Since a hexahedral mesh with reduced integration points is preferred for dynamic simulation (ABAQUS Interactions, 2017), ABAQUS's C3D8R elements have been used to mesh both the cutter and woodchip. A total of 30,500 elements and 39,444 nodes were used to model the three 6.35-mm thick cutters, while 1,725 elements and 2,304 nodes were used to model the 27.5 × 17.5 × 3 mm woodchip. Mesh size sensitivity and convergence were not the major concern of this work, but the contact area on the cutter blade edges were refined with smaller size elements than most of the other locations to capture the contact pressure distribution. The woodchip had homogenous size of elements, and the size

was also fine enough to capture the large deformation and stress distribution. Due to the shaped edges, the mesh kept away from using superfine elements at the contact regions to avoid any stress singularity. More importantly, the mesh size was kept consistent for all the cases in the simulation, therefore making the results comparable.

The rotation speed of three cutters was applied on their centers, which are shown in **Figure 7** as the local coordinate origin for each cutter. Through kinematic coupling between each rotating center and corresponding cutter, the entire cutter body rotates along with its geometry center in the working speed of 315 rpm. The explicit dynamics analysis of this rotary cutters and woodchip system follows the govern equation of motion

$$\dot{u}^{\left(i+\frac{1}{2}\right)} = \dot{u}^{\left(i+\frac{1}{2}\right)} + \frac{\Delta t^{(i+1)} + \Delta t^{(i)}}{2} \ddot{u}^{(i)}; \qquad (1)$$
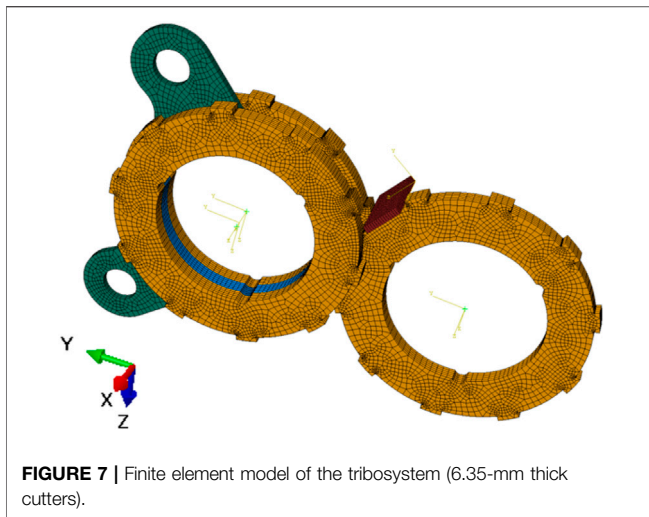
$$u^{(i+1)} = u^{(i)} + \Delta t^{(i+1)} \dot{u}^{\left(i+\frac{1}{2}\right)}, \tag{2}$$

where u is displacement, $\dot{u}$ is velocity, and $\ddot{u}$ is acceleration. The superscript (i) refers to the increment number and $i - \frac{1}{2}$ and $i + \frac{1}{2}$ refer to midincrement values, and t denotes time and Δt is the time increment. The key to the computational efficiency of the explicit procedure is the use of diagonal element mass matrices because the inversion of the mass matrix that is used in the computation for the accelerations at the beginning of the increment is triaxial:

$$\ddot{u}^{(i)} = M^{-1} \Delta \left(F^{(i)} - I^{(i)} \right), \tag{3}$$

where M is the diagonal lumped mass matrix, F is the applied load vector, and I is the internal force vector. More details of these equations can be found in reference to Explicit dynamics, (2017).

To set up the four contact regions between woodchip and three cutters, three contact pairs were created in this FE model. **Figure 8** illustrates these contact pairs, with red square dots for the first/master surface and pink area for the second/slave surface in one pair. The contact regions ① and ② are included in **Figure 8A**, while **Figures 8B,C** have contact regions ③ and ④, respectively. All these contact pairs used the kinematic contact method and finite sliding setting, along with the tangential friction coefficient of 0.5 and normal behavior in "hard" contact for pressure overclosure.

General Technical Report FPL–GTR–190 Chapter 4 (Glass, Zelinka) states that coefficients of kinetic friction for smooth, dry wood against hard, smooth surfaces commonly range from 0.3 to 0.5; at intermediate moisture content, 0.5 to 0.7; and near fiber saturation, 0.7 to 0.9. Considering the woodchip's moisture level in this analysis, which is neither the dry case nor the near fiber saturation case, an intermediate value of 0.5 was assumed to be a reasonable start point for the calculations.

The "hard" contact pressure–overclosure relationship in ABAQUS implies that (ABAQUS Interactions, 2017) 1) the surfaces transmit no contact pressure unless the nodes of the slave (second) surface contact the master (first) surface; 2) no penetration is allowed at each constraint location (depending on the constraint enforcement method used, this condition will either be strictly satisfied or approximated); and 3) there is no limit to the magnitude of contact pressure that can be transmitted when the surfaces are in contact. This "hard" contact mode agrees with the assumed behavior on the normal interface between woodchip and cutters; therefore, we adopt it for all the dynamic simulations in this project.

The current cutters and teeth are made of through-hardened A2 tool steel, which was heat treated to RC 60. The basic material properties of the A2 tool steel are listed in **Table 1**, according to the Granta's CES Selector database (GRANTA, 2014). As for the strength of A2 tool steel, its yield strength (YS) is 1.97 GPa, and ultimate tensile strength (UTS) is 2.36 GPa. Unlike isotropic elastic behavior of the tool steel, the mechanical properties of woodchips are anisotropic and thus are presented by multiple parameters. Five woodchips ranking by their hardness, i.e., 12% moisture yellow birch, 12% moisture red oak, 12% moisture coast Douglas-fir, green coast Douglas-fir, and green northern white cedar were selected as representatives of the very strong, strong, medium strong, medium soft, and very soft wood species, respectively (David). Geometry of the woodchip is determined by the particle size distribution in **Figure 4**. The parallelepiped and cubic shapes of the woodchip model (shown in **Figure 5**) cannot include all the features shown in a real woodchip but still be very close. The fiber direction of the woodchip is aligned with the rotary axis of cutter blades, which will produce the strongest resistance when the woodchip is stuck into two or three cutter edges. The woodchip material properties are extracted from references ((Glass, Zelinka) and (David)). Basically, the references provide big tables to cover all the wood species and available moisture conditions, and their mechanical properties are decided by the specific species and moisture level by looking
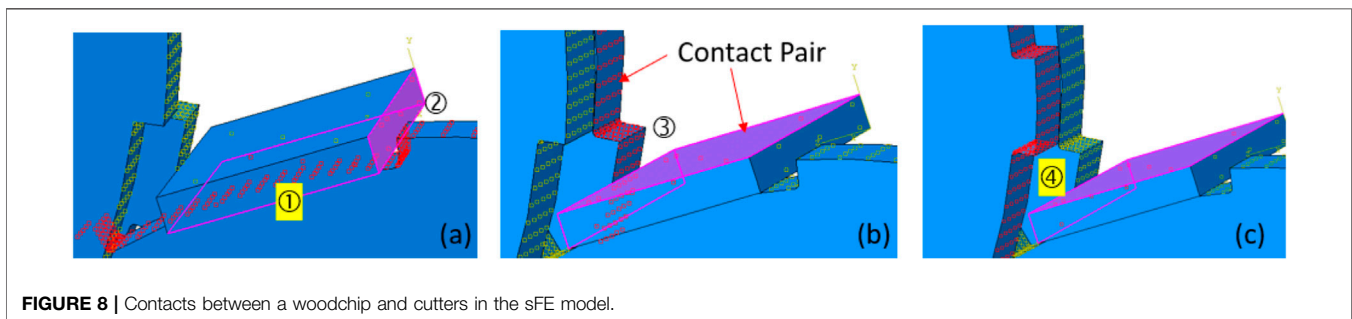
FIGURE 8 | Contacts between a woodchip and cutters in the sFE model.

TABLE 1 | Mechanical properties of the cutter and wood materials used in the FE model (Glass, Zelinka; David).

Material	Density (kg/m³)	Elastic modulus (moduli) (GPa)							Poisson's ratio		$E_{rupture}$ (MPa)
A2 tool steel	7,870	214							0.29		
		E_L	E_T	E_R	G_{LR}	G_{LT}	G_{RT}	μ_{LR}	μ_{LT}	μ_{RT}	
Birch, yellow, 12% moisture	762	13.9	0.695	1.084	1.029	0.945	0.236		0.451	0.697	114
								0.426			
Oak, red, 12% moisture	661	10.3	0.845	1.586	0.917	0.834	0.216		0.448	0.560	75
								0.350			
Douglas-fir, coast, 12% moisture	582	13.4	0.670	0.911	0.858	1.050	0.094		0.449	0.390	85
								0.292			
Douglas-fir, coast, green	612	10.8	0.540	0.734	0.691	0.842	0.076		0.449	0.390	53
								0.292			
Cedar, northern white, green	432	4.4	0.356	0.805	0.924	0.823	0.066		0.340	0.458	29
								0.337			

for data in the tables. Their mechanical properties are listed in **Table 1** (Glass, Zelinka; David).

A total of nine independent constants are needed to describe the elastic behavior of wood: three moduli of elasticity E, three moduli of rigidity G, and six Poisson's ratios μ (David). The subscripts L, R, and T in **Table 1** represent the three principal axes (Longitudinal, Radial, and Tangential as shown in **Figure 4**) of the woodchip with respect to its grain direction and growth rings. The longitudinal direction is parallel to the fiber grain direction or axis X in the FE model, which has the highest elastic modulus. The radial direction is perpendicular to the circle rings, while the tangential direction is the one perpendicular to radial direction in the wood's cross-section surface. The moduli of wood in R and T directions are generally much lower than the strongest E_L. The Poisson's ratios are denoted by μ_{LR}, μ_{LT}, and μ_{RT}. The first letter of the subscript refers to the direction of applied stress and the second letter to the direction of lateral deformation. For example, μ_{LR} is the Poisson's ratio for deformation along the radial axis caused by stress along the longitudinal axis. Similar combinations of subscripts are used in wood's shear moduli such as G_{LR}, G_{LT}, and G_{RT}. $E_{rupture}$ in **Table 1** stands for the rupture modulus on the woodchip's strongest direction, the fiber direction. In the finite element model, the direction of the wood fiber, i.e., direction of E_L in **Table 1**, was aligned with the X-axis in **Figure 7**. The other two directions, T and R, were locally lined up with the width and thickness directions of the woodchip model. A local coordinate system for the woodchip was used for these direction assignments.

The finite element model simulates the dynamic behavior of this tribosystem for 0.0002 s. All the simulations were performed using the 2019 Golden (base) version of FEA software ABAQUS/Explicit ([©] Dassault Systèmes, 2018). The results shown later suggest that at about 0.14 ms the maximum contact pressure in the linear elastic regime (**Figure 10**, tension stress reached the rupture strength of 114 MPa) was recorded for the cutter–woodchip reaction from the initial contact. Based on the practice, a fine time interval of 4–5 µs is set to collect the stress change throughout the simulation.

SIMULATION RESULTS

The stress results of the woodchip and cutter interaction were collected to verify the contact pressures at the interface during the simulation time span of 0.2 ms. **Figures 9A–F** show the stress along the fiber direction at different times. Without cutters displayed in these figures, contact regions 2 and 3 are pointed out in **Figure 9A** to indicate the woodchip's location in this system. The contact regions illustrated in **Figure 6** with the corresponding regions in **Figure 9** show that the woodchip was first contacted by a cutter tooth in region 2, and then sheared in region 3. **Figure 10** plots the history of the maximum tensile stress of the woodchip along the fiber direction (S11 in ABAQUS). Considering the 12% moisture yellow birch's modulus of rupture 114 MPa, we believe that at 0.140 ms the tensile stress on the woodchip reached its elastic limit. Through the time span between 0 and 0.140 ms, a small-time interval (Δt) of 5 µs was set to trace the contact pressure between the cutter and woodchip interface. The maximum contact pressure due to shear was observed at 0.12 ms in contact region 3, which was 187.7 MPa as shown in **Figure 11**.

By repeating the workflow, we identified the components' elastic regime of 26 cases and collected the maximum contact pressures while the cutter and woodchip contacted through either cutter's tooth or edge. **Figure 12** shows another example of the maximum contact pressure on the thin cutters (1.6 mm thickness) while shearing a 3-mm thick green northern white cedar woodchip, which is 215.9 MPa at the moment of 16 µs. **Table 2** summarizes the maximum contact pressure for these two different thickness cutter designs in cutting woodchips of various thicknesses.

DISCUSSION

In summary, sliding velocity has been calculated, and dynamic analysis has been conducted for the Crumbler® rotary shear system to understand the contact pressure at the cutter–biomass interface. A finite element model based on the
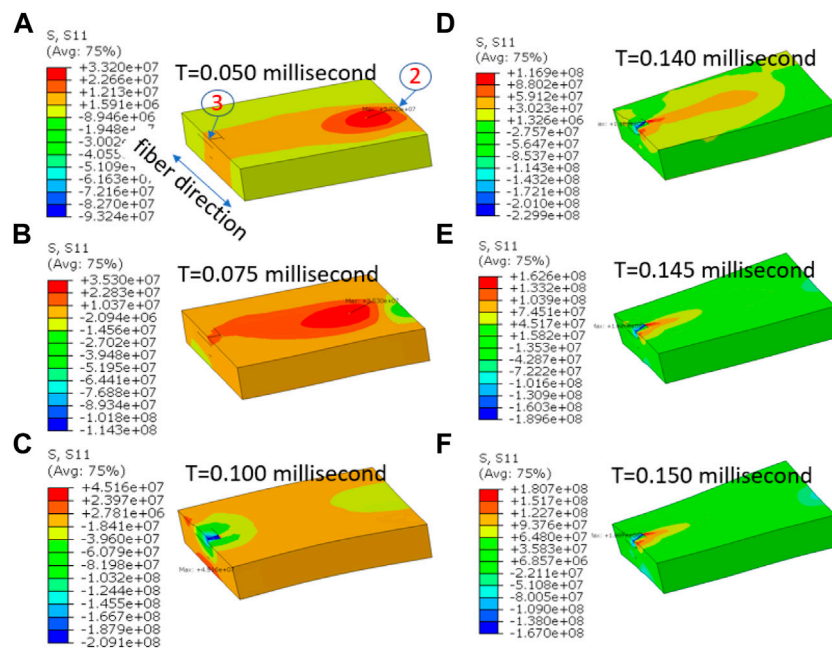
FIGURE 9 | Woodchip stress in the fiber direction. Stress unit in MPa.
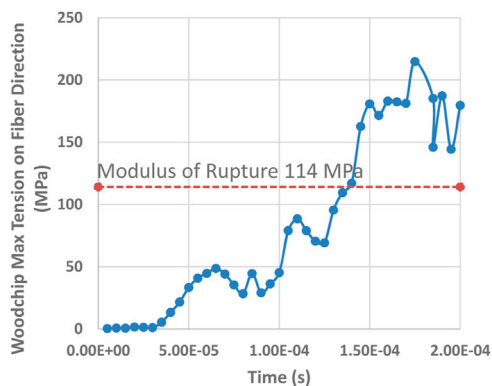
FIGURE 10 | Maximum tensile stress on woodchip's fiber direction, Δt = 5 μs

FC's cutter design, loading data, and materials' mechanical properties was established. The relative sliding velocity between the cutter and woodchip was calculated to be 1.78 m/s at the cutting edge and 1.86 m/s at the tooth tip, for a 4″ diameter cutter and specified rotation speed of 315 rpm. The dynamic simulation results showed different contact pressures for 4″ diameter and 1/16″ (1.6 mm) thickness cutters processing different species of woodchips, for e.g., up to 1284 MPa for 12% moisture yellow birch in case 3, and low to 23 MPa for green northern white cedar in case 12. For thicker cutters (1/4″ or 6.35 mm), the maximum contact pressure went up to 1284 MPa as well in case 19 with 10-mm thick 12% moisture yellow birch and down to 55 MPa in case 5 with 1-m thick 12% moisture

yellow birch. In general, a thicker woodchip will result in a higher contact pressure given the same wood species and similar shape. The only exceptions are cases 3 and 4, where the thicker woodchip (10 mm) in case 4 had a lower maximum contact pressure (831 MPa) than the thinner woodchip (6 mm) in case 3 (1284 MPa). The reversed tendency between woodchip thickness and maximum contact pressure could be explained by the location of maximum contact pressure (highlighted as red spots in **Figure 13**). Due to the thickness difference, the cutter contact was on the tooth edge with the 10-mm woodchip's rim in case 4, while in case 3 the contact pressure was more focused on the cutter's tooth corner.

All these simulation cases revealed another correlation between the wood species and the maximum contact pressures in the linear elastic stage. The ranking of the five types of woodchips, from the hardest to softest is the 12% moisture yellow birch, 12% moisture red oak, 12% moisture coast Douglas-fir, green coast Douglas-fir, and green northern white cedar. Harder woodchips seemed to induce a higher maximum contact pressure against the cutters. This correlation is illustrated in **Figure 14** by using one series of thin cutters and one series of thick cutters. Given the same dimension of woodchips (50 × 20 × 10 mm) and the same 6.35-mm thick cutters, the strongest 12% moisture yellow birch had the highest maximum contact pressure, while the softest green white cedar had the lowest value. A similar trend was observed for the 6 × 6 × 6 mm cubic woodchips being processed by 1.6-mm thick cutters. Case 15 (green white cedar, 6 × 6 × 6 mm woodchip, 1.6-mm cutter) appears to be an exception that had a higher maximum contact pressure than the equivalent green coast Douglas-fir one (case 23). This could be caused by the different locations of the
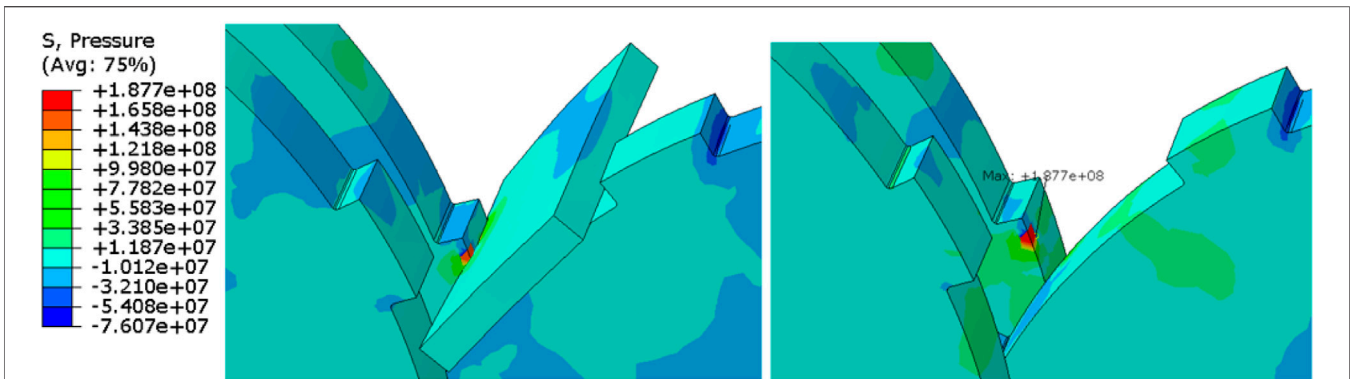
FIGURE 11 | Maximum contact pressure 187.7 MPa on 6.35-mm cutters. The woodchip used is 12% moisture yellow birch and time = 0.12e-3 s, left, woodchip displayed; right, woodchip hidden.
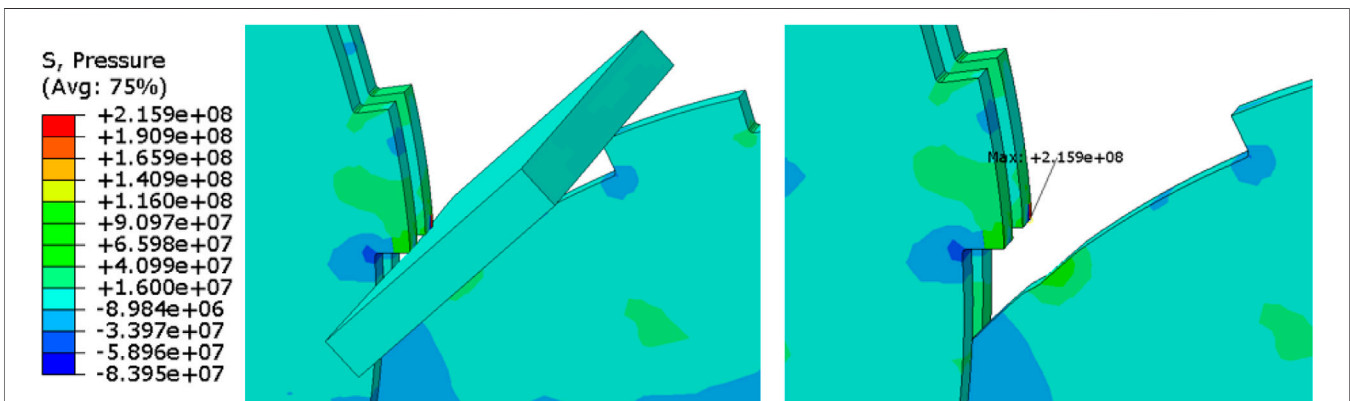
FIGURE 12 | Maximum contact pressure 215.9 MPa on 1.6-mm cutters. The woodchip used is green northern white cedar and time = 0.016e-3 s, left, woodchip displayed; right, woodchip hidden.

maximum contact pressure in cases 15 and 23. Initial investigation also indicated that the relative position between the woodchip and cutters would lead to woodchip's local failure initiated at different contact regions, such as the cutter's tooth corner (case 2), tooth edge (case 6 in **Figure 11** and case 3 and case 4 in **Figure 13**), or circumferential edge.

As shown in **Figure 14**, the contact pressure is higher than the strength of the wood but still below that of the steel material. The major reason of such high contact pressure here is that we consider both woodchip and steel materials as elastic materials, so the stress increases linearly with strain. We understand the drawback of such an assumption. First, the actual contact pressures would be different from current simulation results because of the linear elastic assumption on all material directions for the anisotropic wood materials. Furthermore, due to the linear elastic material assumption, the calculated normal stress for the woodchip at the contact region is above its compressive strength. Specifically, the calculated high contact pressures in radial and tangential directions are not realistic. The actual contact pressure should be significantly lower since the woodchip will rupture on the normal contact

direction much earlier than reaching the elastic limit in the fiber direction. The dash line in **Figure 14** shows that the rupture stress for each wood species is much lower than the maximum contact pressure recorded in simulation. Based on the linear elastic material assumption, what we really focused on was the tensile stress applied on the woodchip's fiber direction due to the shear or bending effect from nearby cutter blades, which provided the strongest resistance to the rotary cutters. The tensile stress on the woodchip's fiber direction has been carefully tracked against time to record the maximum contact pressure before the moment when fiber's tensile stress is larger than its tensile strength.

High contact pressure at these contact locations brings up continuum damage to the cutters and gradually downgrades their functionality. The wear mechanisms could include several types, such as abrasive wear, surface fatigue, erosive wear, and corrosion wear, as detailed in Lee et al., (2021). However, a high contact pressure on the cutter surface is expected to result in high tangential friction on the cutter surface and accumulate more heat under continuous working conditions. Therefore, the contact pressure, particularly the maximum value that cutter can experience in each rotation is a good metric to evaluate the

TABLE 2 | Maximum contact pressure between the woodchip and cutters in the elastic regime.

Case	Cutter thickness (mm)	Woodchip dimension LxWxT (mm)	Wood species	Woodchip stress in failure direction (MPa)	Maximum contact pressure (MPa)	Location of max pressure
1	1.6	27.5 × 17.5 × 1	Yellow birch, 12%	119	123	Cutter edge
2	1.6	27.5 × 17.5 × 3	Yellow birch, 12%	122	337	Tooth corner
3	1.6	27.5 × 16 × 6	Yellow birch, 12%	127	1284	Tooth edge
4	1.6	27.5 × 14.5 × 10	Yellow birch, 12%	118	831	Tooth edge
5	6.35	27.5 × 17.5 × 1	Yellow birch, 12%	132	55	Tooth edge
6	6.35	27.5 × 17.5 × 3	Yellow birch, 12%	122	188	Tooth edge
7	6.35	27.5 × 16 × 6	Yellow birch, 12%	127	527	Tooth corner
8	6.35	27.5 × 14.5 × 10	Yellow birch, 12%	118	452	Tooth root
9	1.6	27.5 × 17.5 × 3	White cedar, green	33	216	Tooth corner
10	1.6	6 × 3 × 3	Yellow birch, 12%	129	299	Tooth root
11	1.6	6 × 3 × 3	Red oak, 12%	78	191	Tooth root
12	1.6	6 × 3 × 3	White cedar, green	32	23	Cutter edge
13	1.6	6 × 6 × 6	Yellow birch, 12%	119	1038	Tooth corner
14	1.6	6 × 6 × 6	Red oak, 12%	81	627	Tooth corner
15	1.6	6 × 6 × 6	White cedar, green	29	486	Tooth corner
16	6.35	15 × 6 × 6	Yellow birch, 12%	126	276	Tooth edge
17	6.35	15 × 6 × 6	Red oak, 12%	77	263	Tooth edge
18	6.35	15 × 6 × 6	White cedar, green	35	66	Tooth edge
19	6.35	50 × 20 × 10	Yellow birch, 12%	118	1284	Tooth corner
20	6.35	50 × 20 × 10	Red oak, 12%	82	1209	Tooth corner
21	6.35	50 × 20 × 10	White cedar, green	30	384	Tooth edge
22	1.6	6 × 6 × 6	Douglas-fir, 12%	91	528	Tooth corner
23	1.6	6 × 6 × 6	Douglas-fir, green	60	356	Tooth corner
24	6.35	50 × 20 × 10	Douglas-fir, 12%	83	996	Tooth edge
25	6.35	50 × 20 × 10	Douglas-fir, green	59	444	Tooth corner

FIGURE 13 | Contact pressure difference between case 3 **(A)** and case 4 **(B)**.
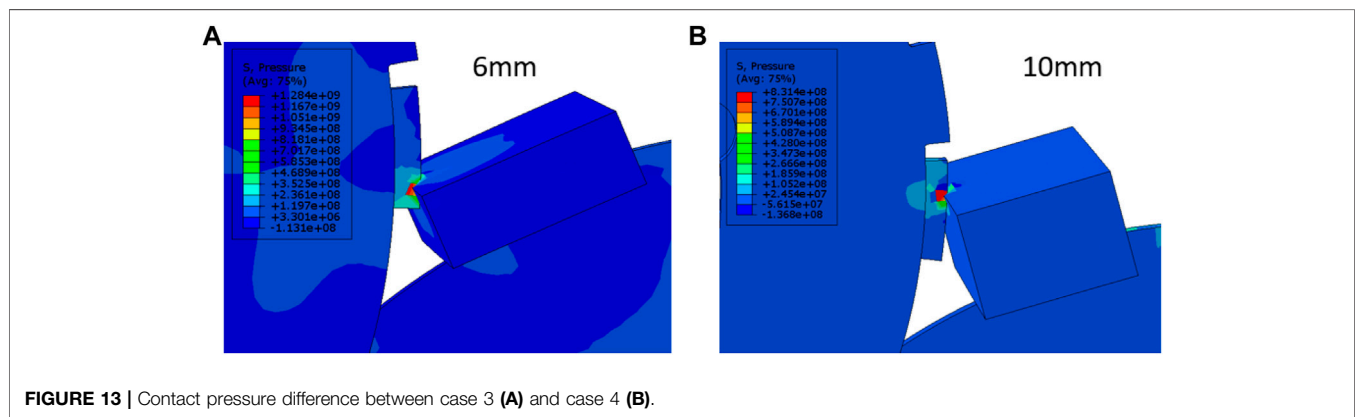
cutter's loading level. The identified high contact pressure locations on the cutter teeth and edges also indicate the most needed regions for material enhancement for cutters to improve the useful life. In terms of fatigue wear, the maximum contact pressure can be used as a peak value to predict the fatigue life at those local regions since the cutter's cycling speed is known. Dynamic simulations provide a way to correlate the maximum contact pressure from simulation results with experimental observations in future work. Once the numerical method is validated, the well-configured FE model will help understand the wear mechanisms more rapidly.

Experimental validation of the cutter–woodchip contact pressure on an actual rotary cutting machine is difficult due to

the following reasons: 1) it is too difficult, if not impossible, to install a sensor on either the cutter blade or woodchip to measure the pressure/force; 2) the woodchip breaks into pieces after touching the blades in a very short time, making it rather challenging to capture the real contact response in the elastic stage. Still, this finite element analysis made it possible to compare the contact pressures for different wood species and/or woodchip shapes, thereafter to provide useful information for the cutter blade design. For example, such an analysis suggested that the current square cutter tooth (DZ design) can break woodchips more efficiently than the previous sharp curvy tooth design in our earlier report (Lee et al., 2021). The improved performance of the DZ design has been validated on actual rotary shear systems at
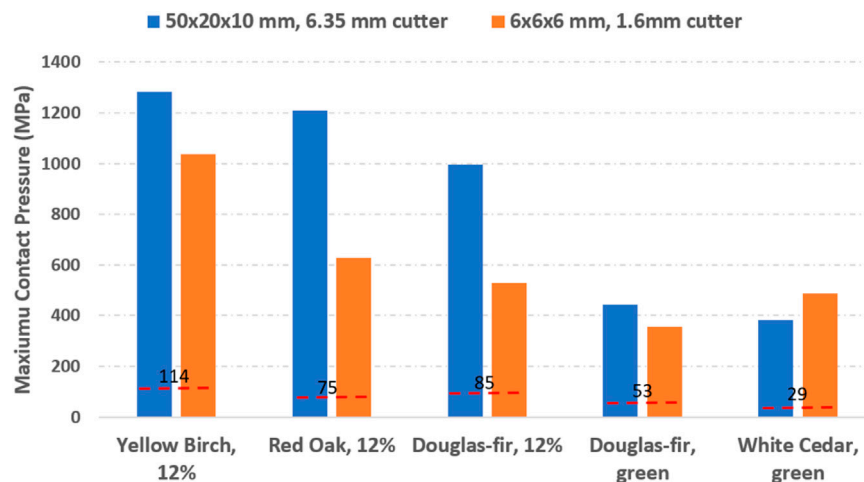
FIGURE 14 | Correlation between woodchip species and maximum contact pressure, dash line for wood species' rupture stress.
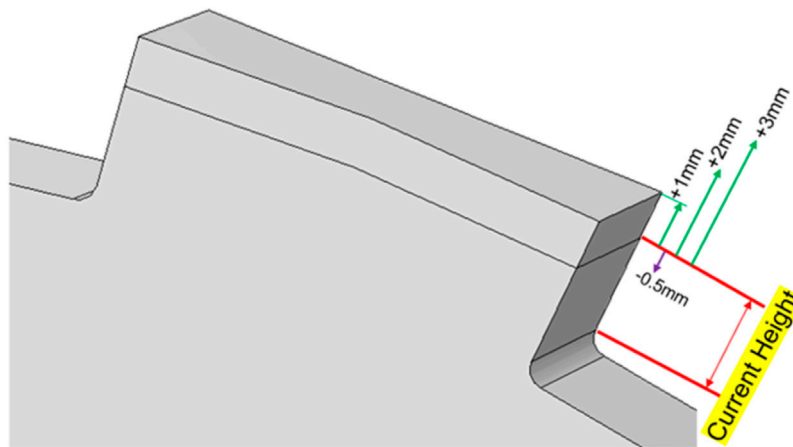
FIGURE 15 | Proposed design idea for cutters: adjusting cutter tooth height.

Forest Concepts, and the new version of Crumbler® now is equipped with DZ design cutters.

Utilizing this finite element simulation method, initial effort has been carried out for optimizing the DZ tooth design. As shown in **Figure 15**, four different tooth height adjustments are proposed: from reduction by 0.5 mm to increases by 1, 2, and 3 mm. Calculated contact pressures against Douglas-fir with 12% moisture are listed in **Table 3** for both the thick (6.35 mm) and thin (1.6 mm) cutters. For the thick cutter processing the large woodchip ($10 \times 20 \times 50 \, mm^3$), the current DZ tooth height (0 mm) results in the highest contact pressure (996 MPa), and either increasing or decreasing the tooth height is expected to substantially reduce the contact pressure (450–550 MPa). For the thin cutter processing small woodchip ($6 \times 6 \times 15 \, mm^3$), a lower tooth would increase the contact pressure, but a taller tooth would reduce the contact pressure with a significant drop for a 3 mm height increase. Since a taller tooth is also expected to provide better grip for feeding the woodchip based, the DZ

tooth height is proposed to increase by 1–3 mm for the thick cutter and by 3 mm for the thin cutter (3 mm is maximum restricted by the clearance between two adjacent set of cutters in the assembly). Further simulations with different types of woodchips are underway to confirm the tooth height optimization, and corresponding prototype cutters will be fabricated for experimental validation. Such a simulation–optimization–validation approach will be applied for optimizing other key components, for e.g., clearing plate of the rotary shear system as well.

Current simulation of the rotary shear tribosystem includes only three cutters and one model woodchip. While significantly simplified, the simulation sets a foundation for further analysis for finding potential geometrical changes or loading conditions that could reduce the cutter wear. The simulation model can be used to optimize the cutter design, such as the shape of the tooth, to reduce the contact pressure. Simulations of various cutter designs shearing the same model woodchip will provide a clear comparison for extending cutter working life, improving cutter

TABLE 3 | Max contact pressures for cutters with various tooth height adjustments.

Cutter/tooth thickness (mm)	Woodchip size (mm)	Wood species and moisture	Cutter tooth height adjustment (mm)	DZ tooth design maximum contact pressure (MPa)
6.35	10 × 20 × 50	Douglas-fir, 12%	−0.5	469.2 (corner)
			0	995.9 (corner)
			1	550.5 (corner)
			2	542.7 (corner)
			3	451.1 (near root)
1.6	6 × 6 × 15	Douglas-fir, 12%	−0.5	1180 (corner)
			0	1025 (corner)
			1	980.8 (corner)
			2	914.0 (corner)
			3	434.2 (corner)

efficiency, and reducing costs, etc. Investigation on woodchip behavior under contact, such as the time needed to reach its elastic rupture limit, the possible deformation, and failure modes from this FE model can also be utilized to optimize the woodchip breaking.

Though various sizes of the woodchip were used in the current simulations, they are still "ideal" cases that cannot match with the actual woodchips with irregular shapes. The metric of maximum contact pressures assumes that the strongest resistance comes from tension in the woodchip's fiber direction. More experimental work is needed to validate this assumption. The simulation considers woodchip's anisotropic behavior in the elastic stage only in this material model, which differs from real woodchip's intrinsic behavior. Woodchips might delaminate earlier along the weaker direction before reaching such a maximum contact pressure; however, the local failure has not been taken into consideration yet. The complex woodchip material behavior beyond the elastic stage could also bring variance in the maximum contact pressure. In all these simulations, only one woodchip was employed in the model. In actual operation, there are always multiple groups of cutters working against bunches of randomly orientated woodchips (see **Figure 1**). Examination of the used cutters also indicated that extrinsic inorganic particles included in the woodchips could bring severe abrasive wear or polishing wear on the cutters' edge and surfaces. All these limitations in current FE models point to the direction of our future work. Further studies in cutter wear tests, surface coating design, structural optimization design, and numerical simulations will be combined to reveal the wear mechanisms and improve the lifetime of this rotary shear system.

CONCLUSION

A FEA model was built for the Crumbler® rotary shear system. Taking the assumption of woodchip's elastic orthotropic behavior before reaching its rupture stress in the strongest fiber direction, dynamic analysis has been conducted for this rotary shear system to understand the contact pressure between the interface of the woodchip and cutter. Simulation cases showed ranges and trends of maximum contact pressures for different cutter designs and different species of woodchips.

From dynamic simulation, it can be concluded that the highest contact pressure was observed in the case with the hardest woodchip, the 12% moisture yellow birch, for the same cutters and the same size of woodchips. Similarly, the softest case, green northern white cedar, had the lowest contact pressure in the elastic stage. The woodchip's thickness also played an important role in the contact pressure. In general, a thicker woodchip introduces more resistance to tension, compression, bending, and shear, leading to a higher contact pressure. In addition, the woodchip's shape and relative location to the cutters also had some effects on the amplitude and position of the contact pressure on the cutters.

In conclusion, such a finite element analysis is an effective, quantitative approach to evaluate the interaction between the tool and feedstock in absence of direct contact measurement to guide tool design optimization.

DATA AVAILABILITY STATEMENT

The original contributions presented in the study are included in the article/Supplementary Material, further inquiries can be directed to the corresponding authors.

AUTHOR CONTRIBUTIONS

LL is the major contributor of this manuscript who did most of the simulation work and data analysis; DL provided original rotary cutter design geometry, working parameters, material properties, and all the other information related to cutter's wear; JK and JQ guided the research work in this project and gave important revisions to this manuscript.

FUNDING

ACKNOWLEDGMENTS

REFERENCES

ABAQUS Explicit dynamics analysis *SIMULIA User Assistance 2017*.

Abaqus Interactions *SIMULIA User Assistance 2017*.

Ämmälä, A., Pääkkönen, T. M., and Illikainen, M. (2018). Role of Screen Plate Design in the Performance of a Rotor Impact Mill in fine Grinding of Biomass. *Ind. Crops Prod.* 122, 384–391.

Bitra, V. S. P., Womac, A. R., Chevanan, N., Miu, P. I., Igathinathane, C., Sokhansanj, S., et al. (2009). Direct Mechanical Energy Measures of Hammer Mill Comminution of Switchgrass, Wheat Straw, and Corn stover and Analysis of Their Particle Size Distributions. *Powder Techn.* 193, 32–45. doi:10.1016/j.powtec.2009.02.010

David, E. *Kretschmann, General Technical Report FPL–GTR–190 Chapter 5 Mechanical Properties of Wood*.

Felix, E., and Tilley, D. R. (2009). Integrated Energy, Environmental and Financial Analysis of Ethanol Production from Cellulosic Switchgrass. *Energy* 34 (4), 410–436. doi:10.1016/j.energy.2008.10.013

Glass, Samuel. V., and Zelinka, Samuel. L. *General Technical Report FPL–GTR–190 Chapter 4 Moisture Relations and Physical Properties of Wood*.

Granta, D. E. S. I. G. N. (2014). *CES Selector*.

Guo, Q., Chen, X., and Liu, H. (2012). Experimental Research on Shape and Size Distribution of Biomass Particle. *Fuel* 94, 551–555. doi:10.1016/j.fuel.2011.11.041

International Organization for Standardization (2020). *Solid Biofuels — Fuel Specifications and Classes — Part 9: Graded Hog Fuel and wood Chips for Industrial Use*. Available at: https://www.iso.org/standard/75158.html.

Lam, P. S., Sokhansanj, S., Bi, X., and Lim, C. J. (2008). *Effect of Particle Size and Shape on Physical Properties of Biomass Grinds*. Providence, Rhode Island: American Society of Agricultural and Biological Engineers. doi:10.13031/2013.24879

Lee, K., Lanning, D., Lin, L., Cakmak, E., Keiser, J. R., and Qu, J. (2021). Wear Mechanism Analysis of a New Rotary Shear Biomass Comminution System. *ACS Sust. Chem. Eng.* 9 (35), 11652–11660. doi:10.1021/acssuschemeng.1c02542

Mani, S., Tabil, L. G., and Sokhansanj, S. (2006). Effects of Compressive Force, Particle Size and Moisture Content on Mechanical Properties of Biomass Pellets from Grasses. *Biomass and bioenergy* 30 (7), 648–654. doi:10.1016/j.biombioe.2005.01.004

Mani, S., Tabil, L. G., and Sokhansanj, S. (2004). Grinding Performance and Physical Properties of Wheat and Barley Straws, Corn stover and Switchgrass. *Biomass and Bioenergy* 27, 339–352. doi:10.1016/j.biombioe.2004.03.007

Miao, Z., Grift, T. E., Hansen, A. C., and Ting, K. C. (2011). Energy Requirement for Comminution of Biomass in Relation to Particle Physical Properties. *Ind. Crops Prod.* 33, 504–513. doi:10.1016/j.indcrop.2010.12.016

Oyedeji, O., Fasina, O., Adhikari, S., McDonald, T., and Taylor, S. (2016). The Effect of Storage Time and Moisture Content on Grindability of Loblolly pine (Pinus Taeda L.). *Eur. J. Wood Prod.* 74, 857–866. doi:10.1007/s00107-016-1070-x

Oyedeji, O., Gitman, P., Qu, J., and Webb, E. (2020). Understanding the Impact of Lignocellulosic Biomass Variability on the Size Reduction Process: A Review. *ACS Sust. Chem. Eng.* 8, 2327–2343. doi:10.1021/acssuschemeng.9b06698

Rezaei, H., Lim, C. J., Lau, A., and Sokhansanj, S. (2016). Size, Shape and Flow Characterization of Ground wood Chip and Ground wood Pellet Particles. *Powder Technol.* 301, 737–746. doi:10.1016/j.powtec.2016.07.016

Schell, D. J., and Harwood, C. (1994). Milling of Lignocellulosic Biomass. *Appl. Biochem. Biotechnol.* 45-46, 159–168. doi:10.1007/bf02941795

Shaw, M. (2008). *Feedstock and Process Variables Influencing Biomass Densification*. Saskatoon, Saskatchewan, Canada: Master thesis of University of Saskatchewan.

Conflict of Interest: DL was employed by Forest Concepts.

The remaining authors declare that the research was conducted in the absence of any commercial or financial relationships that could be construed as a potential conflict of interest.

Publisher's Note: All claims expressed in this article are solely those of the authors and do not necessarily represent those of their affiliated organizations, or those of the publisher, the editors, and the reviewers. Any product that may be evaluated in this article, or claim that may be made by its manufacturer, is not guaranteed or endorsed by the publisher.

Near-Infrared Spectroscopy can Predict Anatomical Abundance in Corn Stover

Dylan S. Cousins[1], William G. Otto[1], Asif Hasan Rony[2], Kristian P. Pedersen[1], John E. Aston[2] and David B. Hodge[1,3]*

[1]Department of Chemical and Biological Engineering, Montana State University, Bozeman, MT, United States, [2]Idaho National Laboratory, Idaho Falls, ID, United States, [3]Division of Sustainable Process Engineering, Luleå University of Technology, Luleå, Sweden

Feedstock heterogeneity is a key challenge impacting the deconstruction and conversion of herbaceous lignocellulosic biomass to biobased fuels, chemicals, and materials. Upstream processing to homogenize biomass feedstock streams into their anatomical components *via* air classification allows for a more tailored approach to subsequent mechanical and chemical processing. Here, we show that differing corn stover anatomical tissues respond differently to pretreatment and enzymatic hydrolysis and therefore, a one-size-fits-all approach to chemical processing biomass is inappropriate. To inform on-line downstream processing, a robust and high-throughput analytical technique is needed to quantitatively characterize the separated biomass. Predictive correlation of near-infrared spectra to biomass chemical composition is such a technique. Here, we demonstrate the capability of models developed using an "off-the-shelf," industrially relevant spectrometer with limited spectral range to make strong predictions of both cell wall chemical composition and the relative abundance of anatomical components of the corn stover, the latter for the first time ever. Gaussian process regression (GPR) yields stronger correlations (average R_v^2 = 88% for chemical composition and 95% for anatomical relative abundance) than the more commonly used partial least squares (PLS) regression (average R_v^2 = 84% for chemical composition and 92% for anatomical relative abundance). In nearly all cases, both GPR and PLS outperform models generated using neural networks. These results highlight the potential for coupling NIRS with predictive models based on GPR due to the potential to yield more robust correlations.

Keywords: near-infrared spectrocopy, corn stover, bioenergy, biomass pre-processing, biomass characterization

INTRODUCTION

Lignocellulosic biomass offers enormous potential as a renewable feedstock for biorefining processes that can yield sustainable fuels, chemicals, and materials (Sharma et al., 2020). A wide range of technological approaches are available for biorefining of lignocellulose that include thermochemical, catalytic, chemical, and biological processes for deconstruction and conversion of the cell wall biopolymers contained within lignocellulose to these bio-based fuels and products (Brown and Brown, 2013; Qureshi et al., 2014). One approach for biorefining of lignocellulosic biomass involves a chemical pretreatment to facilitate the subsequent depolymerization of plant cell wall

polysaccharides using cellulolytic enzymes to yield monosaccharides that can be further processed to biofuels or biobased chemicals (Kumar et al., 2016). Additional pre-processing operations on the biomass may be necessary to facilitate optimal storage, transport, and processing of heterogeneous, geographically dispersed biomass feedstocks. These feedstock pre-processing operations can include comminution, cleaning, physical or chemical fractionation, drying, pretreatment, and densification (Carolan et al., 2007; Lamers et al., 2015).

Corn stover is a high-volume co-product of corn production that has been identified as having significant potential for sustainable biofuel production in the U.S. (Langholtz et al., 2016). Importantly, corn stover, like other gramineous feedstocks for biorefining processes, exhibits significant within-plant heterogeneity as a consequence of the differences in the cell wall composition and higher order structures between different cell types, tissues, or anatomical fractions (e.g., cob, leaf, husk, stem). In addition to this heterogeneity, variability within a single feedstock can arise from differences in feedstock biological origin, agronomic practices, local environment during growth, harvest time and approach, and biomass storage time and conditions (Morrison et al., 1998).

Feedstock variability resulting from differences in chemical composition and physical properties can significantly impact process performance during both pre-processing and downstream biorefining operations. Moreover, differences in the physical properties of individual corn stover particles are largely derived from anatomical differences in the tissues. Such differences can impact the mechanical handling of biomass, have been shown to contribute to process upsets and can be detrimental to overall process throughput (Sievers et al., 2020). Since different anatomical tissues respond differently to both pre-processing (e.g., comminution) and deconstruction (e.g., chemical pretreatment and enzymatic hydrolysis), on-line knowledge of the tissue type, composition, and moisture content could prove to be a fundamental requirement for commercial-scale biorefineries (Garlock et al., 2009; Crowe et al., 2017; Li et al., 2018). To this end, a high-throughput analytical technique that is potentially deployable as an on-line measurement, would be needed to inform not only the feedstock chemical composition, but also anatomical relative abundance for a given sample of corn stover.

A suite of laboratory analysis procedures developed by the National Renewable Energy Laboratory (NREL) have become the *de facto* analysis techniques to determine the composition of both feedstocks and pretreated biomass slurries (Sluiter and Sluiter, 2011a; b). However, the wet laboratory procedures for these techniques are time consuming and expensive (Lupoi et al., 2014; Sykes et al., 2015). Therefore, near-infrared (NIR) spectroscopy (NIRS) has become widely used to characterize the composition of biomass (Xu et al., 2013). Predictions of cell wall composition *via* NIRS have been developed for corn stover (Hames et al., 2003; Templeton et al., 2009), pretreated corn stover (Wolfrum and Sluiter, 2009; Sluiter and Wolfrum, 2013), sorghum (Wolfrum et al., 2013; Li et al., 2017a), switchgrass (Vogel et al., 2011; Park et al., 2012), poplar

(Robinson and Mansfield, 2009; Nkansah et al., 2010) and cereal grains (Bruno-Soares et al., 1998; Caporaso et al., 2018). However, cell wall composition alone cannot predict other physical properties of the feedstock, yet this information would benefit biomass processing. Therefore, a principal objective of the present work is to demonstrate the predictive capability of NIRS for not only cell wall composition in corn stover, but also feedstock anatomical origin (e.g., husk, cob, or stalk rind) that greatly impacts both response to mechanical operations (e.g., comminution and feeding) and subsequent biorefining operations.

NIRS gained widespread use in the food industry in the 1980s due to advancement in chemometric techniques to correlate convoluted absorbance peaks to the chemical composition of the analytes using various mathematical tools like principal component analysis (PCA) and partial least squares (PLS) regression (Scotter, 1990). NIR is a commonly used technology for quality control in grain processing facilities (Gradenecker, 2003) as well as crude protein content in livestock forage and feeds (Vincent and Dardenne, 2021). Early work on analysis of biomass energy feedstocks showed the viability of NIRS with PLS to accurately predict corn stover cell wall composition (glucan, xylan, lignin, acetate, and ash) (Sanderson et al., 1996; Gao et al., 2018). Quantification of cell wall composition by NIRS demonstrated varying polysaccharide levels of anatomical fractions of corn stover (Ye et al., 2008) and differences between feedstock corn stover and that pretreated with dilute sulfuric acid (Wolfrum and Sluiter, 2009). Further work at NREL demonstrated a large variation in the cell wall composition of corn stover from various harvests as predicted by NIRS (Templeton et al., 2009). Lately, the same group has demonstrated that potentially low-cost and portable spectrometers with limited spectral range provide predictions that are nearly as accurate as those of well-developed laboratory instruments (Wolfrum et al., 2020). Here, we demonstrate that a comparable "off the shelf" instrument is adequate to predict not only composition, but further extend the predictive capability to anatomical tissue type.

Various chemometric tools have been implemented to make predictions of chemical composition from NIR spectra with PLS being the most common technique. Neural networks (NNs) (Li X. et al., 2015; Jin et al., 2017; Ahmed et al., 2019), support vector machines (SVMs) (Balabin and Lomakina, 2011) and Gaussian process regression (GPR) have also been applied to NIR spectra to predict the moisture content of biomass. GPR is commonly used to predict biomass properties in remote sensing but lacks any significant use in NIRS predictions of biomass properties (Hultquist et al., 2014). In this work, we investigate the efficacy of PLS, GRP, and NN for prediction of chemical composition and anatomical abundance in corn stover.

Air classification is a preprocessing technique of great interest that separates corn stover based on differences in density and surface area (Bilanski and Lai, 1965; Stessel Richard and Peirce, 1983; Lacey et al., 2015). These physical characteristics differ within the anatomical tissue types of corn stover. Additionally,

FIGURE 1 | Images of the harvested corn stover and respective plant fractions of interest for further isolation. These include (A) the corn stover rectangular bale as harvested, (B) cob, (C) stalk, (D) sheath, (E) leaf fractions pulverized during harvesting operations, (F) pith isolated from stalk fractions, (G) is the husk with attached shank, and (H) isolated shank found attached to the stalk and husk plant fractions.

since chemical composition varies with anatomy, we aim to demonstrate that models developed from NIRS can predict not only chemical composition of fractionated biomass, but also the relative abundance of tissue type. The utility of this technique is two-fold: 1) from an experimental perspective, NIRS is a high-throughput tool to validate air classification during process development and 2) in an applied setting, NIRS can inform downstream processes about the relative abundance of incoming corn stover (i.e., "stringy" with many husks vs. more "chip-like" with many stalk rinds and cobs). In the present work, we compare the predictive capabilities of NIRS by traditional PLS methods then explore the use of GPR and NNs to expand the state-of-the-art. Further, we demonstrate that NIRS can provide reliable predictions for not only composition, but also a further level of abstraction to anatomical tissue type.

EXPERIMENTAL

Materials

A diverse range of corn stover samples were used in the present study. Corn stover diversity panel samples were the same as those described in previous work (Li et al., 2017b). Briefly, the maize was grown at a different density and plants were harvested at grain maturity using a single pass, Case IH® 2144 axial-flow, combine for better separation of corn stover and grain. The samples for NIR scanning were taken from a commercial hybrid corn stover bale harvested on 28 October 2017 from Story, Iowa using an AGCO 2270 XD Large Square Baler (Duluth, Georgia) set to a 4-inch cut. The bales were sent to Iowa State University for storage under dry, stable conditions until 24 October 2019, when they were delivered to Idaho National Laboratory (INL). At INL, they continued to be stored under dry (moisture content 8.7 to 9.7 wt%), stable conditions until use.

Methods
Sample Preparation

To generate manually sorted anatomical fractions, 50 kg of flakes from the end sections of unprocessed, square corn stover bales was set aside. As detailed in **Figure 1**, the plant fractions of corn stover isolated consisted of leaf, sheath, stalk, pith, husk, shank, and cob. However, shank was not investigated in this study due to lower occurrence and similarity with the stalk fraction. The leaf fraction (**Figure 1E**) is often pulverized during the baling process and will usually be found in smaller pieces and fines. They are darker than most other tissues with a thick mid-rib. Husks (**Figure 1G**) are broad, thin tissues, lighter in color than the leaves, and do not fracture during the baling process. The sheath (**Figure 1D**) is usually found attached to the stalk. This is a thick, waxy, rigid tissue that must be broken off the stalk to collect. The stalk (**Figure 1C**) is long and usually cylindrical and consists of a rigid outer layer (rind), and spongy inner tissue (pith). The shank (**Figure 1H**) is a branch-like structure that grows out from a leaf node and it is from this shank that an ear of corn will grow. Cobs (**Figure 1B**) are usually found in larger pieces and have a "fuzzy" outer layer (beeswing/chaff) and contain pith inside a rigid ring of tissue (woody ring).

To further separate and isolate 25 g for subsequent testing of each anatomical fraction, 50 kg of the whole stover was slowly removed and manually sorted to provide a near-pure baseline of the different anatomical fractions. The larger plant fractions were isolated to control mass loss and minimize variance in overall anatomical composition of the unprocessed bale. To isolate 25 g of pith (**Figure 1F**), the tissue was scraped off the rind portion and reviewed for purity of anatomy. The cobs were mostly unattached to the husk and stalk from harvest operations and are the densest of the fractions, making manual separation quickly identifiable. The husks identified in **Figure 1G** tend to segregate from the other plant fractions and were hand-picked off the remaining unprocessed material. The shanks were pulled

from the broad husk portion of the plant and separated as seen in **Figure 1H**. To ensure purity and integrity of the leaf isolation, the darker and scattered pieces were gently brushed from the collapsed section of the bale. Any contaminates such as twine, plastic, and metal objects were identified and removed.

Composition analysis was conducted on both alkaline pretreated (see **Section 2.2.2**) and raw milled (#20 standard mesh, 0.85 mm) pure anatomical fractions (sheath, leaf, pith, husk, rind, and cob) of corn stover to determine structural polysaccharides, lignin, extractive, and ash content according to NREL/TP-510-42618 and 510-48087 with modifications as reported in our prior work (Sluiter et al., 2008; Sluiter and Sluiter, 2011a; Templeton et al., 2016; Singh et al., 2019). For composition analysis of pure tissues, several dozen pieces of a given tissue were milled and placed into a sealed bag. These were mixed by shaking and subsequently, aliquots of the mixture were taken for composition analysis which was done in triplicate. **Supplementary Table S2** provides summary data for samples used for prediction of chemical composition and **Supplementary Table S5** gives complete composition information for all samples used for NIR modeling.

To generate anatomical tissues with varying moisture content to enhance predictive models, samples of unmilled anatomical fractions were hydrated at varying relative humidity. To achieve different relative humidity, samples were equilibrated in five separate sealed containers containing saturated aqueous solutions of various ionic compounds in the bottom of the container. These compounds govern the water activity, and therefore, relative humidity. By varying the species of the ionic compound, the relative humidity can be altered to cover a wide range. Samples were allowed to equilibrate for at least 72 h and until the mass change due to moisture uptake no longer increased (maximum 96 h). **Supplementary Table S1** provides the salts and associated relative humidity used for moisture sorption experiments (Greenspan, 1977). **Supplementary Table S3** provides the associated moisture content of anatomical tissues that were equilibrated at varying relative humidity.

Alkaline Pretreatment

Anatomical tissues milled to #20 standard mesh using a benchtop Wiley mill were separately treated in an aqueous alkaline solution at 10% solids (w/v) with 10% sodium hydroxide (w/w) on a 3 g dry biomass basis in a 100 ml AMAR reactor. The vessel was continuously stirred at 200 rpm and temperature was ramped to 90°C over the course of 20 min where it was then held for an additional 60 min and then cooled to room temperature over the course of 10 min. The biomass was then vacuum filtered and washed with DI water until the effluent was of neutral pH. Prior to enzymatic hydrolysis, the pH was adjusted to 5 by adding the biomass to 300 ml of water and titrating with sulfuric acid. Pretreated samples were then vacuum filtered and stored in this moist state in a sealable polyethylene bag at 4°C until further use. **Supplementary Table S4** presents the moisture content during storage of these materials.

Enzymatic Hydrolysis

Enzymatic hydrolysis was performed on both raw and pretreated samples according to the procedure described by Yuan et al (Yuan et al., 2019). Briefly, pure anatomical tissues of corn stover (sheath, leaf, stalk pith, husk, stalk rind, and cob) were milled to pass a 20-mesh screen using a Wiley mini-mill (Thomas Scientific, Swedesboro, NJ). Hydrolysis was carried out in 15-ml centrifuge tubes at 10% (w/v) solids loading with 15 mg CTec3 enzyme per g of glucan buffered using a 50 mM sodium citrate buffer (pH 5) in a rotating incubator (198° of rotation) at 60 rpm for 72 h at 50°C. Glucose yields were determined by diluting the hydrolysis liquor ten-fold and measuring the concentration on an Agilent 1260 series HPLC equipped with an Aminex HPX-87H column (Bio-Rad, Hercules, CA) using 5 mM aqueous H_2SO_4 as the mobile phase coupled with RI detection. Hydrolysis yields are given in terms of percent of maximum theoretical glucose produced. Enzymatic hydrolysis was conducted on both raw and alkaline pretreated samples. Pretreated samples were used for enzymatic hydrolysis no more than 5 days after pretreatment to limit microbial growth.

Spectra Acquisition

NIR spectra were collected on a Foss InfraXact 7,500 non-contact spectrometer over wavelengths from 570 to 1850 nm in reflectance with the empty cup (air) serving as a baseline. This is a reduced wavelength range compared to many studies using NIR for chemical composition prediction (typically covering the full NIR range from 800 to 2500 nm), but recent work has confirmed little reduction in model predictive capability when using reduced spectral range (Wolfrum et al., 2020). For correlation of chemical composition (i.e. glucan, xylan, etc.) specimens from the corn stover diversity panel were used in addition to pure fractions that were isolated from the bale described above. In total, there were 62 specimens available for correlation of chemical composition (only 36 for extractives and moisture content). It should be noted that some of these specimens were milled (those from corn stover diversity and ambient humidity anatomical fractions) to #20 standard mesh, while some were not (those tissues that were hydrated at varying relative humidity as previously described).

Milled specimens were added to a cup with a transparent bottom (approximately 2 inches in diameter) to a depth of no less than 1 cm. Specimens were measured over three replicates except for hydrated tissues, for which spectra were collected in duplicate to minimize water loss due to drying. These hydrated tissues were not milled prior to scanning, but all other samples were milled to pass a #20 standard mesh. Specimens were stirred between replicate measurements. Hydrated, unmilled tissues were removed from their sealed containers and duplicate scans were performed quickly to limit moisture desorption from the material, though the samples were briefly mixed between scans. The duration of each scan is approximately 30 s, therefore relatively little time was available for desorption of water during the measurement. Nevertheless, inconsistency due to effects of moisture desorption means that these results should

be interpreted for their trends rather than as tabulations of well-defined thermodynamic hydration states.

In general, the anatomical relative abundance of a given sample of corn stover is not explicitly known, therefore, to generate a dataset for calibration of the models, mixtures of pure anatomical fractions which had been previously manually sorted and subsequently milled to pass a #20 standard mesh screen were prepared by "remixing" to obtain samples with known anatomical quantities. These mixtures were at least 3 g in quantity and were thoroughly agitated in sealed plastic bags prior to scanning. Thus, 60 total specimens were combined and scanned to generate the data set for determining anatomical relative abundance.

Modeling

Several techniques were used to process spectra prior to training models for prediction. Standard normal variate (SNV) pretreatment was applied to the absorbance spectra by subtracting the mean of absorbances over all wavelengths for a given observation and normalizing by the standard deviation. In this way, the mean values of all spectra were normalized to zero with a standard deviation of one. The second derivative of the absorbance spectra with respect to wavelength was calculated numerically over the sampling increment of the instrument (2 nm). Another common preprocessing technique is multiplicative scatter correction (MSC) to reduce the effects of scattering and differing path length between measurements (Rinnan et al., 2009). MSC regresses each spectrum to the mean spectrum of the dataset by ordinary least squares, then corrects each spectrum by the regressed linear parameters. The second derivative (2D) of the absorbance spectra is used to achieve higher correlations between the actual and predicted composition values. For all regressed spectra and correlations compared here, SNV, MSC, and the second derivative were applied.

Preliminary model screening was conducted using the Regression Learner Application in MATLAB (release R2021b; MathWorks, Natick, MA), which can quickly screen linear regression, decision trees, known nearest neighbor, SVMs, and GPR. Of these methods, GPR yielded the lowest mean squared error in preliminary screening when predicting both chemical and anatomical composition of corn stover. Therefore, in this work, GPR is compared to more commonly used PLS regression and NNs using MATLAB's *fitrgp*, *plsregress*, and *fitrnet* functions, respectively. For model testing in each training case, the data were partitioned into training and test data with a 70/30 split for holdout cross-validation. Root-mean-squared-error of validation (RMSEV) and R_v^2 (coefficient of determination of validation) were used to assess model performance on the holdout sets. In the case of the cell wall composition, the RMSE was normalized by the range of the predicted values. For each algorithm, the model was trained 100 times each with a new training/test split. R_v^2 and RMSEV are those for the average of the 100 model runs.

Gaussian processes leverage the expectation that samples with similar predictors will have similar targets. In this case the predictors are the absorbance values at varying wavelengths and the targets are the chemical or anatomical composition.

Briefly, the process fits a distribution of functions to the predictors in order to predict a target (e.g., chemical or anatomical composition). The variance of the assumed distribution of functions (prior) is designated by a kernel, which can take various forms. We screened common kernels and found that the rational quadratic form outperformed the Matern 5/2 and 3/2, squared exponential, and exponential kernels as screened by the Regression Learner Application in MATLAB. Therefore, in the *fitrgp* MATLAB function, the rational quadratic kernel was used to describe the covariance between predictors. All other hyperparameters were held at default settings.

plsregress implements the SIMPLS algorithm developed by de Jong (de Jong, 1993). All default parameters were used for *plsregress* and the number of components was varied from 1 to 20. The R_v^2 and RMSEV values tabulated for PLS are the maxima and minima over this range of components, respectively. Standard deviations over the 100 model runs were calculated at the number of components that maximized the R_v^2 value or minimized the RMSEV.

NNs trained using *fitrnet* used Bayesian optimization, with the default NN structure for the function: two fully connected layers with the first having 10 nodes and the second having a single output. The first fully connected layer has a rectified linear unit activation function while the second layer corresponds to the output target. The training iteration limit was set to 1,000 and both the gradient tolerance and the tolerance for the function loss were set to 10^{-6}. Principal component analysis was conducted using the *pca* function in MATLAB. Default parameters for the function were used (data are centered and singular value decomposition is the algorithm).

RESULTS AND DISCUSSION

Composition, Enzymatic Hydrolysis, and Moisture of Corn Stover Anatomical Tissues

While NIRS has been used in a number of studies and applications in the past to predict the composition of corn stover, the three objectives of the present study differentiate this work from the prior literature. The first objective is to identify differences in composition and responses to pretreatment and enzymatic hydrolysis between manually fractionated corn stover anatomical fractions. The second objective is to employ these corn stover samples to develop models for prediction of differences in chemical composition, relative abundance of anatomical fractions, and response to pretreatment and enzymatic hydrolysis using an industrially relevant NIR system with limited spectral range. The final objective is to compare both the utility and performance of three chemometric/machine learning algorithms (PLS, NN, GPR) to make these predictions from the NIR data sets. For correlative models to be useful, the dataset must cover the desired prediction range. To achieve this, we use anatomically pure samples to bound the design space for all samples of corn stover. That is, no mixture of corn stover will have chemical composition (e.g., glucan content) that is greater or lesser than the pure anatomical fractions that have the maximum or minimum

TABLE 1 | Summary of composition data for the specimens analyzed in this work. Maximum, minimum, range and average for chemicals are given as wt% on a dry basis. N refers to the number of NIR spectra available for correlation with a given parameter.

	Glucan	Xylan	Klason Lignin	Acetate	Ash	Water extractives	Ethanol extractives	Moisture
Max	42.3	41.1	20.4	5.0	12.4	26.7	6.5	38.0
Min	28.7	16.4	7.0	2.7	0.4	5.1	1.8	2.6
Range	13.6	24.7	13.4	2.3	12.0	21.6	4.7	35.4
Average	34.1	23.1	15.0	3.6	2.7	13.7	3.5	11.3
N	234	234	234	234	234	78	78	78
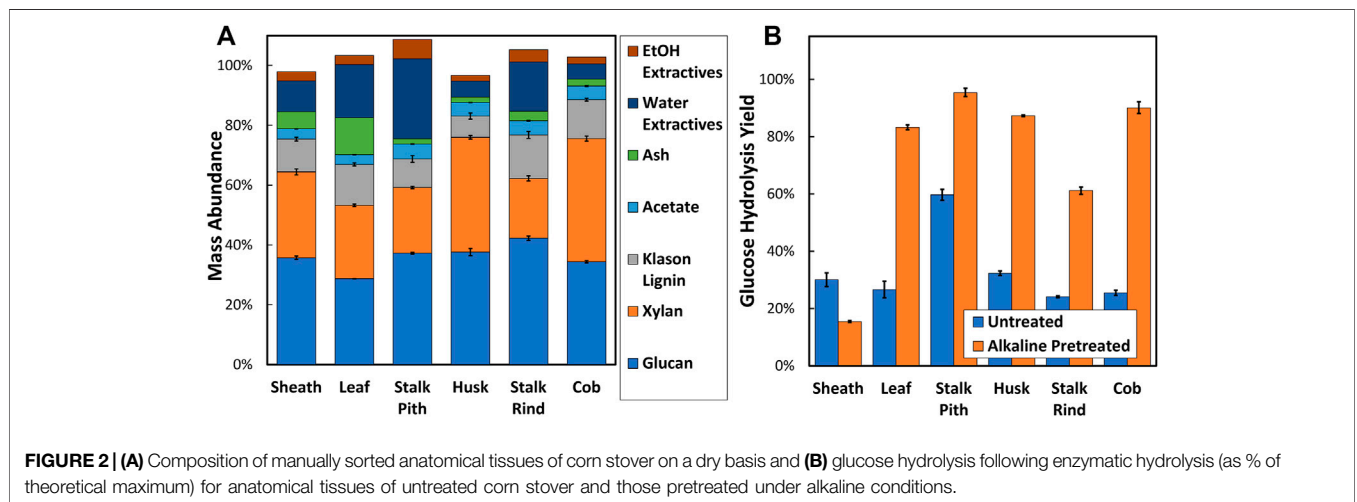
FIGURE 2 | (A) Composition of manually sorted anatomical tissues of corn stover on a dry basis and **(B)** glucose hydrolysis following enzymatic hydrolysis (as % of theoretical maximum) for anatomical tissues of untreated corn stover and those pretreated under alkaline conditions.

chemical content. Corn stover from our previous work was also used to develop correlations of chemical composition (Li et al., 2017b). **Table 1** shows the summary composition data for the corn stover samples used in this study and **Figure 2A** shows the composition for manually sorted anatomical tissues on a dry basis. The range of compositions found here are comparable to other studies (Hames et al., 2003; Templeton et al., 2009).

Several key differences in composition between the anatomical fractions can be observed within this data (**Figure 2A**). First, it can be observed that the stalk rind fraction had the highest glucan content (42.3% by mass), which is consistent with other prior work for the stems of graminaceous feedstocks such as corn stover (Li et al., 2012) and *Miscanthus × giganteus* (Williams et al., 2015). Another key observation is that the cob fraction exhibits the highest xylan content. It is well-established that cobs are more highly enriched in xylan (Takada et al., 2018) and the lower recalcitrance and potential for collection/recovery have made cobs a target feedstock for biorefining (Brown and Brown, 2013). The leaf fraction exhibits the highest ash content and is consistent with prior studies that have found the most abundant ash content in leaf fractions of corn stover (Li et al., 2012) and wheat straw (Atik and Ates, 2012), presumably due to the abundance of structural inorganics such as silicates. A final observation is the low lignin contents observed in stalk pith (9.5%), sheath (11.0%), and husk (7.0%). Low lignin contents for pith has been

observed in corn stover (Li et al., 2012) and have been linked to high enzymatic hydrolysis yields in sorghums (Li et al., 2018). Results for the response to enzymatic hydrolysis show significant differences between the six anatomical fractions for both untreated and following pretreatment (**Figure 2B**). From these results it can be observed that the stalk pith has the highest yield (59.7%) of the untreated anatomical fractions. It has been well-documented that untreated pith from diverse grasses are known to be more susceptible to digestion by rumen microbiota or cellulolytic enzymes due to their lower lignin content (Akin, 2008). Following pretreatment, the leaf, pith, husk, and cob fractions exhibit glucose yields greater than 80%. Leaf, husk, and cob show the most improvement in glucose yields between untreated and pretreated samples, while the sheath is particularly recalcitrant. Since this recalcitrance is fundamentally rooted in cell wall structure and chemical composition, we investigate later whether yields can be correlated to NIR spectra. Because different tissues of corn stover have different responses to pretreatment and hydrolysis, a preprocessing technique that can enrich the process streams in various anatomies would be highly advantageous.

In addition to chemical composition and enzymatic hydrolysis yields, moisture content is a critical parameter affecting both mechanical processes (e.g., comminution, conveying) and (bio)chemical processes (e.g., pretreatment,
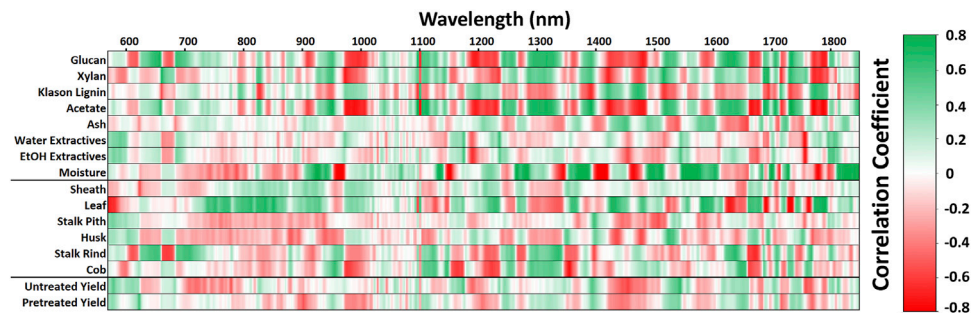
FIGURE 3 | Pearson correlation coefficients between NIR absorption from 570 to 1850 nm and corn stover compositional components, relative abundance of anatomical components, and response to pretreatment and enzymatic hydrolysis.
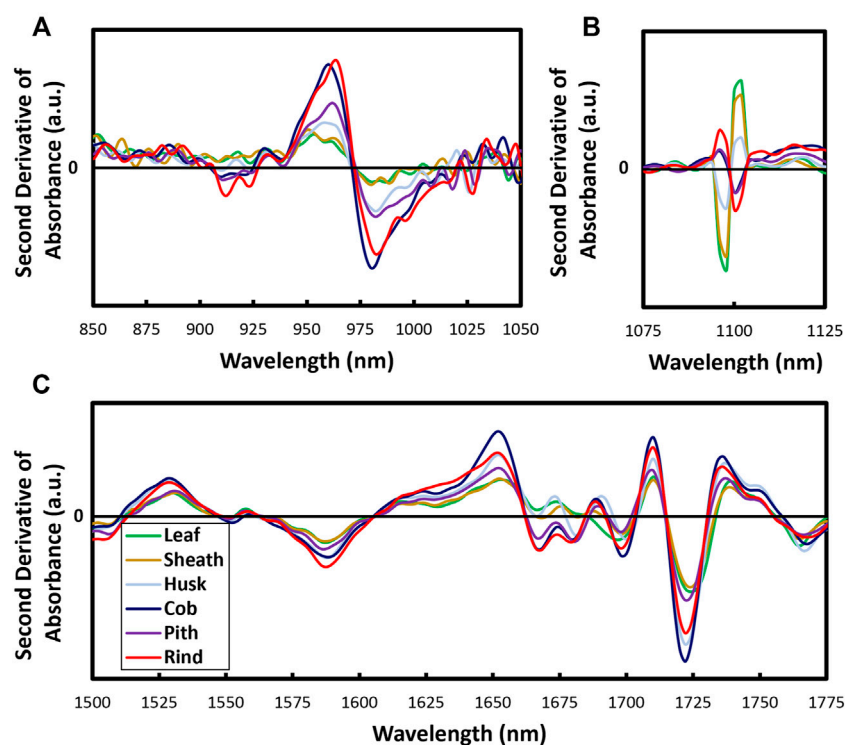
FIGURE 4 | Second derivative of NIR absorbance spectra for anatomically pure fractions of corn stover in the region from **(A)** 850–1,050 nm, **(B)** 1,075 nm–1,125 nm, and **(C)** 1,500 nm–1775 nm.

enzymatic hydrolysis) (Laureano-Perez et al., 2005; Liebmann et al., 2010; Ozaki, 2012; Sievers et al., 2020). Indeed, many processes utilizing materials of biological origin have utilized NIRS for decades to monitor moisture content. Therefore, it is a sensible candidate for prediction; strong correlations for moisture content are expected so it acts as a baseline check for model development. To obtain a range of moisture content across anatomical tissues, unmilled corn stover tissues were equilibrated at varying relative humidity as presented in **Supplementary Figure S1**. Generally, the moisture content increases rapidly at the

end of the moisture sorption curves and the stalk components (rind and pith) demonstrating the greatest hygroscopicity.

Correlation of Spectra to Chemical and Anatomical Composition

The principal focus of this work is to demonstrate that an "off the shelf" NIR spectrometer with limited spectral range (570–1850 nm) can be used to generate predictive models on a relatively small sample set of corn stover. Chemical functional

groups govern absorbance of NIR spectra and these groups appear in different quantities in the cell wall biopolymers that make up anatomical tissues. Therefore, chemical composition predictions can be made from the spectral signatures. Predictions of anatomical relative abundance are also rooted in the fact that the varying chemicals absorb IR radiation differently and different tissues have varying quantities of these chemicals. A correlation map was developed (**Figure 3**) to first identify NIR spectral correlations to the cell wall composition, relative abundance of anatomical fractions, and responses to pretreatment and enzymatic hydrolysis. This plot shows the strength of the Pearson correlation coefficient between these quantities and the second derivative of wavelength absorbance. Red areas indicate negative correlations while green areas indicate positive correlations. The magnitude of the second derivative gives an indication of the degree of concavity in the raw spectra. A larger magnitude of the second derivative in the negative direction corresponds to a more defined absorbance peak in the raw spectra. Positive peaks in the second derivative spectra are often coupled with negative peaks. These coupled peaks are often correlated to chemical composition or anatomical tissues (**Figure 3**) as transitions from positive to negative correlation (or vice versa). Such transitions are observed at 970 nm, 1,100 nm, and 1,238 nm, among others, and are important for model prediction. Chemical structures (polysaccharides, lignin, etc.) and anatomical tissues that share similar correlation patters are likely to be correlated (e.g., xylan and cob).

Several key differences within the NIR spectra contributing these correlations can be highlighted (**Figure 4**). First, starting at the lower end of the spectra, the first peak of interest occurs at 970 nm (**Figure 3**), where matching correlations between glucan, xylan, acetate, stalk rind, and cob can be observed. This peak is associated with amorphous hydroxyl content (Ahmed et al., 2019) and stronger peak signals are observed for rind and cob compared to other tissues (**Figure 4A**). These specimens are dried to approximately 5% moisture content so the signal increased hydroxyl absorbance may be due to higher relative abundance of these groups present on polysaccharides. Though weaker than the correlations previously described, lignin and water extractives show similar positive correlations to sheath, leaf, and husk. Because the second derivative of the spectra is negative for wavelengths greater than 970 nm (up to about 1,015 nm), a positive correlation between the absorbance and the chemical composition implies that the relative chemical quantity is decreasing with an increasing absorbance peak.

The peak that appears at 1,100 nm (**Figure 4B**) shows unique properties in that related tissues display similar behavior as the peaks transition from negative to positive. For example, sheath, leaf, and husk group together and have matching correlation patterns to lignin at 1,100 nm (**Figure 3**). Similarly, stalk rind, stalk pith, and cob group together and have matching correlation patterns to polysaccharides at 1,100 nm (**Figure 3**). Other reports have also shown positive correlation between absorbance and reference compositions of hemicellulose and cellulose at 1,096 nm and 1,100 nm, respectively, and negative correlation at 1,098 nm for lignin (Jin et al., 2017). The peak at 1,100 nm is one of the only significant peaks observed in this spectrum that

shows a segregation of anatomical tissues into positive and negative second derivatives of absorbance.

Prediction of chemical composition is one key component of feedstock quality and can be used to inform pre-processing or downstream pretreatment. Peaks in NIR spectra associated with crystalline cellulose can be observed at 1,592 nm (**Figure 4C**) for which stalk rind is observed to have the sharpest absorbance (Tsuchikawa et al., 2003). Higher up the spectrum, the segregation of the data into positive and negative peaks at 1,668 nm distinguishes anatomical tissues in a similar way to the peak at 1,100 nm. These two areas appear to be the only two significant wavelengths at which this phenomenon occurs. In previous work, our group has shown guaiacyl lignin to be correlated to a negative peak at 1726 nm (Li et al., 2017b). Previous authors have attributed this peak to pentose sugars (furanose or pyranose) from the presence of hemicellulose (Tsuchikawa et al., 2003). That the xylan-rich cob shows the largest peak is therefore likely attributable to the polysaccharides rather than the guaiacyl lignin in the present case.

Besides the spectra of specific anatomical fractions, it is informative to investigate the spectra for a single anatomical tissue that has been equilibrated at varying relative humidity. Our results show (**Figure 5**) the effect of moisture sorption on the amorphous hydroxyl band that is associated with wavelengths from 1,350 to 1,450 nm (Henri et al., 2002) for stalk pith that has been equilibrated at varying relative humidity. The band between 1,400 and 1,420 nm is related to the O-H first bending overtone (Gergely and Salgó, 2005). Increased moisture content is observed to lower the wavelength at which radiation is absorbed. In the raw spectra (**Supplementary Figure S2**), the magnitude of absorbance in this region is also observed to increase with increasing moisture content. At low moisture content, the water molecules can strongly associate with biopolymers through hydrogen bonding but as the moisture content increases, available sites for such interactions are decreased and the spectra becomes more dominated by unbound or amorphous water molecules. The contributions to the absorbance from hydroxyl groups present on the biopolymers are also diminished as the moisture content increases. These subtle shifts in absorbance enable predictive models to be developed from these spectra later in this work.

Of principal interest for the present study is identification of corn stover samples which may be more amenable to subsequent processing. For example, stalk pith requires no pretreatment to achieve the same glucose yields during enzymatic hydrolysis compared to pretreated stalk rind (**Figure 2A**). Therefore, samples enriched in pith can be targeted in upstream processing and the anatomical composition could be verified by NIR predictive models. Though correlation of chemical components to NIR spectra has been previously shown using PLS, here we also investigate GPR and NN to test whether these can provide more accurate predictions. The chemical components of interest are glucan, xylan, Klason lignin, acetate, ash, water extractives, ethanol extractives, and moisture content.

Use of high throughput screening for determination of biomass composition could be used in various applications
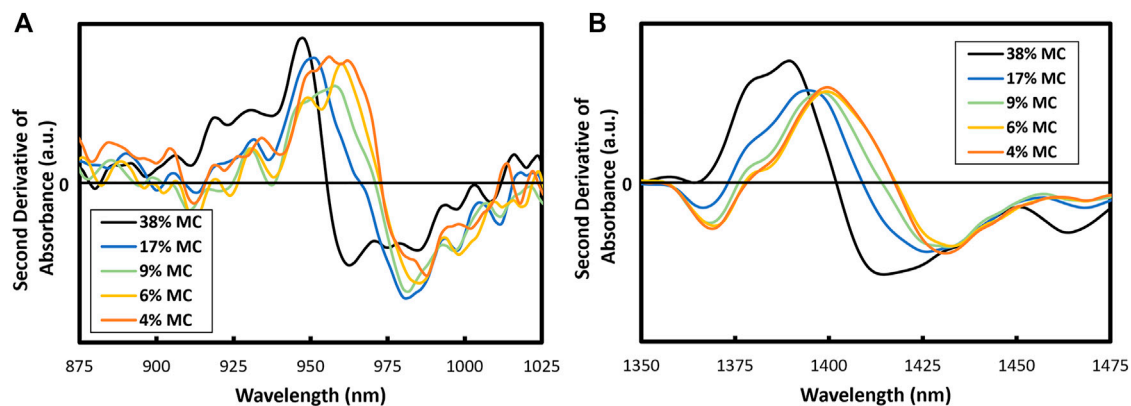
FIGURE 5 | Second derivative of NIR absorbance spectra for stalk pith in the range of the amorphous -OH groups at 970 nm **(A)** and 1,424 nm **(B)** equilibrated at varying % moisture content (MC).
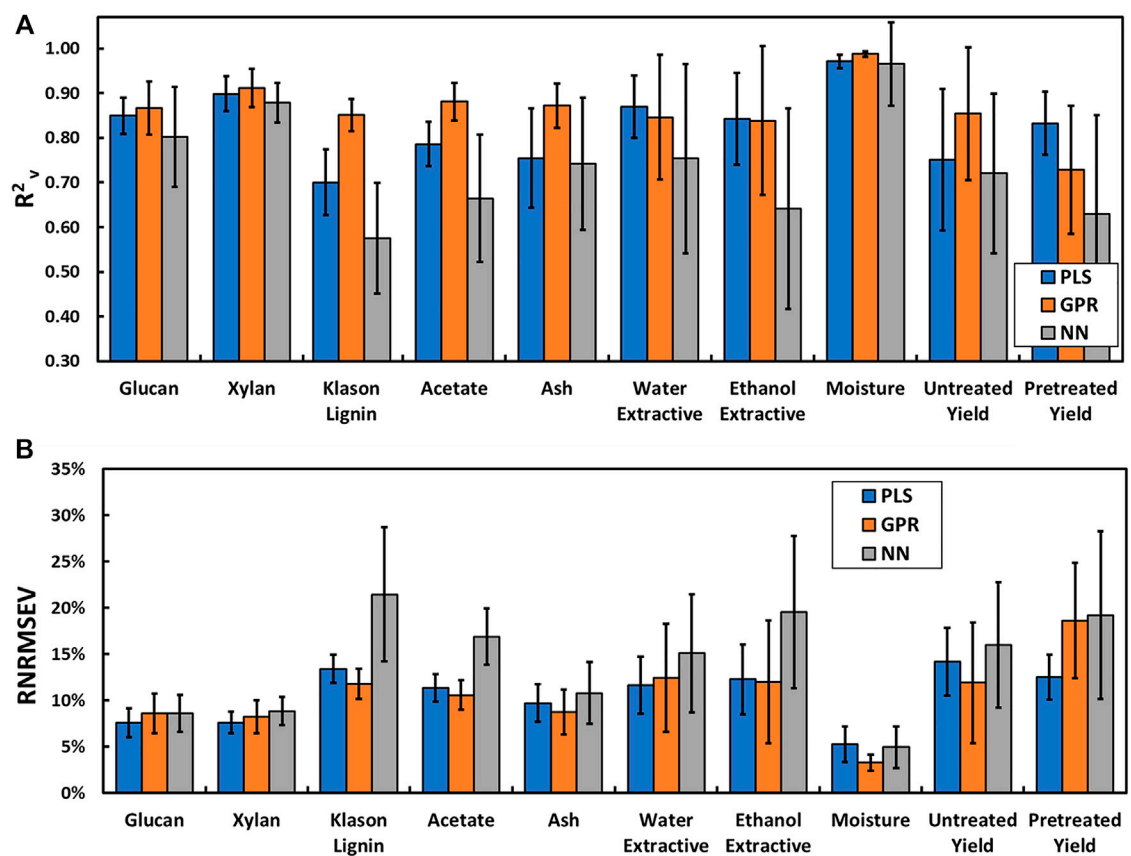
FIGURE 6 | R_v^2 **(A)** and RNRMSEV **(B)** for chemical composition and response to pretreatment and enzymatic hydrolysis of corn stover predicted from NIR spectra using partial least squares (PLS), Gaussian process regression (GPR) and neural networks (NN). Bars represent standard deviations over 100 model runs. Tabular data are provided in the **Supplementary Material**.

within a biorefinery process. Variability of lignocellulosic biomass poses a challenge for scale-up; but on-line NIRS could be used to predict composition, such as glucan, to inform downstream process parameters, such as enzyme loading for hydrolysis.

The average R_v^2 value and range-normalized RMSEV (RNRMSEV) between the actual and predicted responses for cell wall composition for models that could inform such predictions are presented in **Figure 6** (full data set in

Supplementary Tables S8, S9, S14). For PLS, the reported R_v^2 values are those that are the averages of the maximum R_v^2 for any loop over varying number of components in the model (up to 20 components). **Supplementary Figure S3** demonstrates how the number of components affects the correlation between the actual and predicted values. Generally, R_v^2 for the correlation plateaus at its maximum value by 10 PLS components.

Of the chemical composition parameters, it is observed that moisture content is the most easily predicted parameter. Indeed, NIR has been used extensively for moisture content prediction (Cozzolino et al., 2013). Well-defined peak shifts associated with increasing moisture content (**Figure 5**) at 970 and 1,420 nm likely contribute to these strong correlations. Polysaccharides (glucan and xylan) as well as extractives (both ethanol- and water-extractable) show relatively strong correlations between predicted and actual values ($R_v^2 > 0.80$). In all model cases, xylan is the best-predicted chemical component besides moisture content. Minor components (lignin, acetate and ash) have weaker correlation coefficients. The correlation between actual and predicted values for minor components (lignin, acetate, and ash) are about 10–15% higher for GPR compared to PLS. That these minor components can be well-predicted by GPR is an advancement of the state of the art. Ash can be difficult to correlate due to the fact that the mineral components that make up ash do not directly absorb NIR radiation and only affect the absorbance of proximal functional groups (Gao et al., 2018). This trend can be observed in **Figure 3** where ash has comparatively weak correlations when compared to major components like glucan, xylan, and lignin. Nevertheless, even subtle correlations prove useful for predictive modeling as ash content still has a relatively high R_v^2 value (0.87 for GPR).

The first three component loadings from PLS regression show strong positive and negative correlations for both anatomical and compositional components at 1,100 nm (**Supplementary Figure S4**), which correspond to the behavior of the positive and negative spectral derivatives at that wavelength (**Figure 4B**). Only a few wavelengths appear to have high or low loadings in the first three PLS components for chemical composition. Interestingly, loadings are extreme in the visible spectra (from 570 nm to about 720 nm). The first PLS component for composition regression also shows a strong loading around 1,394 nm. This pattern is observed for the moisture content present in the biomass samples. Importantly, this transition is slightly lower than those observed for polysaccharides (approximately 1,404 nm) so this may provide an important wavelength to distinguish the difference between hydroxyl content associated with water vs. those associated with polysaccharides that are not well-distinguished at 970 nm. Range-normalized PLS regression coefficients do not have similar patterning between observations (anatomical or chemical composition) (**Supplementary Figures S5, S6A,B**) unlike the Pearson correlation coefficients of those values.

GPR is able to achieve an R_v^2 of 0.85 for the raw yield from enzymatic hydrolysis and PLS is able to achieve an R_v^2 of 0.83 for the pretreated enzymatic hydrolysis yield. This ability to predict hydrolysis yields of corn stover by spectral analysis of incoming feedstock could be of great utility in an industrial setting. Prior work has employed PLS coupled to NIR to predict *in vitro*

digestibility in corn stover fractionated by anatomy (Hansey et al., 2010) and our previous work for predicted enzymatic hydrolysis yields in corn stover both before and after alkaline pretreatment (Li et al., 2017b). Notably, our previous work was not able to obtain robust prediction models for enzymatic hydrolysis yields following pretreatment.

While composition is useful to inform downstream chemical processing, knowledge of the anatomical tissue type can also inform process operations. Particularly, work from the Integrated Biorefinery Research Facility at NREL showed that certain anatomical types can be problematic for conveyance machinery (Sievers et al., 2020). That work found husk material from corn stover tends to form "bird nests" that can overload rotating equipment and cause large spikes in machinery energy requirements. Foreknowledge of the tissue type and quantity would be advantageous so that material flow or equipment specifications could be altered to prevent process bottlenecks or equipment damage. Moreover, corn stover feedstock quality can be improved *via* air classification, which separates different anatomical tissues based on surface area and density (Lacey et al., 2016; Thompson et al., 2016). To that end, **Figure 7** presents the goodness-of-fit (full data set in **Supplementary Tables S11, S12, S13, S15**) and RMSEV between actual and predicted model values for the relative abundance of differing anatomical fractions, which has hitherto not been described in the literature, despite instances of anatomical separation used to introduce variation in the cell wall composition to the sample dataset (Pordesimo et al., 2005; Liu et al., 2010; Gao et al., 2018). Prior work found that the first three principal components of NIR spectra of remixed anatomical fractions of *Miscanthus × giganteus* were able to predict the structural carbohydrate, lignin, and ash content (Williams et al., 2015). However, that work stopped short of making predictions of the anatomical relative abundance of the remixed anatomical samples. Because the dataset for anatomical composition covers the complete range (mass fraction from 0 to 1), the RMSEV does not require normalization. The anatomical relative abundance is well-predicted by all methods with average R_v^2 values of 0.92, 0.95, and 0.89 for PLS, GPR, and NN, respectively.

Because the chemical composition of biomass can be discerned by the principal components of NIR spectra, we applied principal component analysis to the spectra for pure anatomical fractions of corn stover (**Figure 8**). In this analysis, the first three principal components explained 92.9% of the variance in the NIR spectra. The anatomical fractions are shown to segregate into distinct bundles besides cob and husk which tend to group together. That husk and cob have distinct overlap of their principal component grouping is counterintuitive because their correlations with NIR absorbance are generally opposite (**Figure 3**).

Interestingly, the average correlation coefficient is higher for the anatomical relative abundance predictions than for the composition. Since the anatomical relative abundance can be thought of as another level of abstraction from composition, which governs NIR absorbance, one might expect these parameters to correlate less strongly. Composition analysis of corn stover for this study was
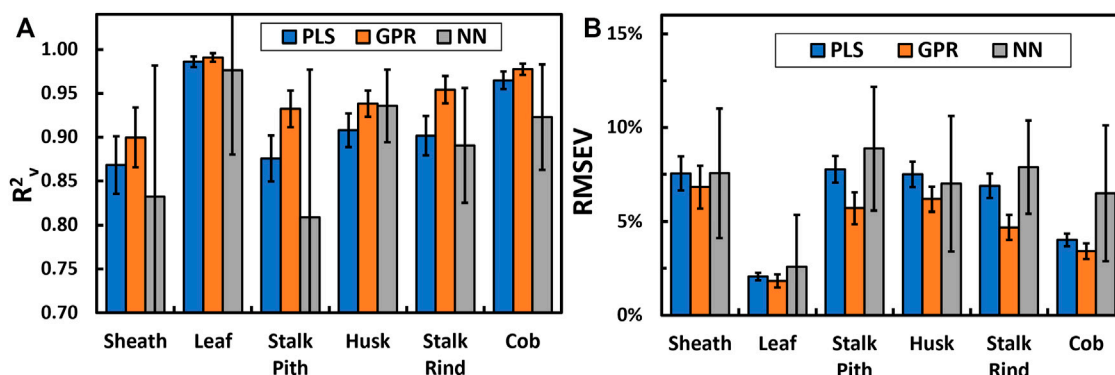
FIGURE 7 | R^2_v **(A)** and RMSEV **(B)** for anatomical relative abundance of corn stover predicted by various modeling algorithms. Bars represent standard deviations over 100 model runs. Tabular data are provided in the **Supplementary Material**.
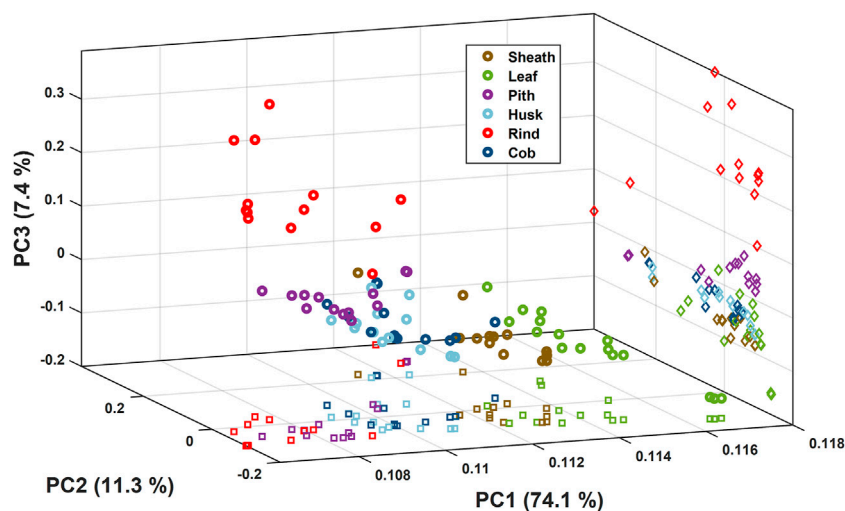
FIGURE 8 | First three principal components of the NIR spectra for pure components of corn stover. Circles represent the position in the 3-dimensional space, squares represent the position in the PC1-PC2 plane and diamonds represent the position in the PC2-PC3 plane.

conducted at Michigan State University in 2014 for corn stover diversity panel specimens (Li M. et al., 2015) and in 2021 for anatomical fractions at Montana State University. Measurements of chemical composition of biomass can vary by up to 20% between laboratories (Templeton et al., 2016), though other studies found much less error (Templeton et al., 2010). However, the quantity of corn stover anatomical tissues can be accurately and precisely controlled when preparing mixtures. Therefore, the higher correlation coefficient and lower RMSEV for the anatomical relative abundance compared to composition may be due in part to interlaboratory data variance in the composition. Nonetheless, these models still demonstrate utility to predict the chemical and anatomical constituents of corn stover over a relatively small data set. Here, we show that GPR as modeling approach may yield better predictions for both chemical composition and anatomical relative abundance in corn stover, but many different algorithmic approaches and other hyperparameter tuning options exist for

each of the three models presented here. It is beyond the scope of this study to investigate these parameters; we aim to demonstrate that GPR is a viable and presently under-investigated modeling technique that should be given more attention in the NIRS community.

CONCLUSION

In this work, we show for the first time that anatomical relative abundance can be predicted by NIRS models. This has important implications for the biomass processing by adding additional information about the feedstock beyond chemical composition. We demonstrate the stalk pith has the highest glucose hydrolysis yield (60% and 95% of theoretical for untreated and alkaline pretreated, respectively) among anatomical fractions of corn stover. If coupled with a physical fractionation strategy to recover fractions enriched or

depleted in select features such as the relative abundance of a target anatomical fraction, those streams can be treated differently to improve overall conversion. Despite the limited spectral range of the spectrometer used in this work, strong correlative models were still developed with a relatively small data set. We show that predictive models from GPR give the strongest correlations for these data; this regression technique should certainly garner more attention in future investigations. Future work will demonstrate the utility of these models on predicting composition, anatomical relative abundance, response to pretreatment, and hydrolysis yields for air-classified fractions of biomass.

DATA AVAILABILITY STATEMENT

The original contributions presented in the study are included in the article/**Supplementary Material**, further inquiries can be directed to the corresponding author.

AUTHOR CONTRIBUTIONS

DC developed the design of experiments, prepared and scanned samples, developed and implemented correlative models and wrote the working draft of the manuscript. WO prepared samples and conducted experiments and data analysis for pretreatment and enzymatic hydrolysis. AR prepared manually fractionated anatomical tissues. KP prepared samples and scanned them on the NIR instrument. JA supervised the project and provided critical advice to advance the ideas and methods. DH is the principal investigator and conceived of the project plan, supervised its implementation and provided major edits to the writing.

SUPPLEMENTARY MATERIAL

The Supplementary Material for this article can be found online at: https://www.frontiersin.org/articles/10.3389/fenrg.2022.836690/full#supplementary-material

REFERENCES

Ahmed, M. U., Andersson, P., Andersson, T., Aparicio, E. T., Baaz, H., Barua, S., et al. (2019). A Machine Learning Approach for Biomass Characterization. *Energ. Proced.* 158, 1279–1287. doi:10.1016/j.egypro.2019.01.316

Akin, D. E. (2008). Plant Cell wall Aromatics: Influence on Degradation of Biomass. *Biofuels, Bioprod. Bioref.* 2 (4), 288–303. doi:10.1002/bbb.76

Atik, C., and Ates, S. (2012). Mass Balance of Silica in Straw from the Perspective of Silica Reduction in Straw Pulp. *BioResources* 7 (3), 3274–3282. doi:10.15376/BIORES.7.3.3274-3282

Balabin, R. M., and Lomakina, E. I. (2011). Support Vector Machine Regression (SVR/LS-SVM)-an Alternative to Neural Networks (ANN) for Analytical Chemistry Comparison of Nonlinear Methods on Near Infrared (NIR) Spectroscopy Data. *Analyst* 136 (8), 1703–1712. doi:10.1039/C0AN00387E

Bilanski, W. K., and Lai, R. (1965). Behavior of Threshed Materials in a Vertical Wind Tunnel. *Trans. ASAE* 8 (3), 411–0413. doi:10.13031/2013.40533

Brown, T. R., and Brown, R. C. (2013). A Review of Cellulosic Biofuel Commercial-Scale Projects in the United States. *Biofuels, Bioprod. Bioref.* 7 (3), 235–245. doi:10.1002/bbb.1387

Bruno-Soares, A. M., Murray, I., Paterson, R. M., and Abreu, J. M. F. (1998). Use of Near Infrared Reflectance Spectroscopy (NIRS) for the Prediction of the Chemical Composition and Nutritional Attributes of green Crop Cereals. *Anim. Feed Sci. Tech.* 75 (1), 15–25. doi:10.1016/S0377-8401(98)00190-4

Caporaso, N., Whitworth, M. B., and Fisk, I. D. (2018). Near-Infrared Spectroscopy and Hyperspectral Imaging for Non-destructive Quality Assessment of Cereal Grains. *Appl. Spectrosc. Rev.* 53 (8), 667–687. doi:10.1080/05704928.2018.1425214

Carolan, J. E., Joshi, S. V., and Dale, B. E. (2007). Technical and Financial Feasibility Analysis of Distributed Bioprocessing Using Regional Biomass Pre-processing Centers. *J. Agric. Food Ind. Organ.* 5 (2), 1203. doi:10.2202/1542-0485.1203

Cozzolino, D., Roumeliotis, S., and Eglinton, J. (2013). Monitoring Water Uptake in Whole Barley (*Hordeum vulgare* L.) Grain during Steeping Using Near Infrared Reflectance Spectroscopy. *J. Food Eng.* 114 (4), 545–549. doi:10.1016/j.jfoodeng.2012.09.010

Crowe, J. D., Feringa, N., Pattathil, S., Merritt, B., Foster, C., Dines, D., et al. (2017). Identification of Developmental Stage and Anatomical Fraction Contributions to Cell wall Recalcitrance in Switchgrass. *Biotechnol. Biofuels* 10 (1), 184. doi:10.1186/s13068-017-0870-5

de Jong, S. (1993). SIMPLS: An Alternative Approach to Partial Least Squares Regression. *Chemometrics Intell. Lab. Syst.* 18 (3), 251–263. doi:10.1016/0169-7439(93)85002-X

Gao, L., Chen, S., and Zhang, D. (2018). Neural Network Prediction of Corn Stover Saccharification Based on its Structural Features. *Biomed. Res. Int.* 2018, 9167508. doi:10.1155/2018/9167508

Garlock, R. J., Chundawat, S. P., Balan, V., and Dale, B. E. (2009). Optimizing Harvest of Corn stover Fractions Based on Overall Sugar Yields Following Ammonia Fiber Expansion Pretreatment and Enzymatic Hydrolysis. *Biotechnol. Biofuels* 2 (1), 29. doi:10.1186/1754-6834-2-29

Gergely, S., and Salgó, A. (2005). Changes in Carbohydrate Content during Wheat Maturation-What Is Measured by Near Infrared Spectroscopy. *J. Near Infrared Spectrosc.* 13 (1), 9–17. doi:10.1255/jnirs.452

Gradenecker, F. (2003). NIR On-Line Testing in Grain Milling. *Cereal foods world* 48 (1), 18.

Greenspan, L. (1977). Humidity Fixed Points of Binary Saturated Aqueous Solutions. *J. Res. Natl. Bur. Stan. Sect. A.* 81A (1), 89–96. doi:10.6028/jres.081a.011

Hames, B. R., Thomas, S. R., Sluiter, A. D., Roth, C. J., and Templeton, D. W. (2003). Rapid Biomass Analysis. *Appl. Biochem. Biotechnol.* 105 (1), 5–16. doi:10.1385/ABAB10.1007/978-1-4612-0057-4_1

Hansey, C. N., Lorenz, A. J., and de Leon, N. (2010). Cell wall Composition and Ruminant Digestibility of Various Maize Tissues across Development. *Bioenerg. Res.* 3 (1), 28–37. doi:10.1007/s12155-009-9068-4

Henri, B., Fabrice, D., and Frédérique, H.-P. (2002). Near Infrared Analysis as a Tool for Rapid Screening of Some Major wood Characteristics in a Eucalyptus Breeding Program. *Ann. For. Sci.* 59 (5-6), 479–490. doi:10.1051/forest.:2002032

Hultquist, C., Chen, G., and Zhao, K. (2014). A Comparison of Gaussian Process Regression, Random Forests and Support Vector Regression for Burn Severity Assessment in Diseased Forests. *Remote Sensing Lett.* 5 (8), 723–732. doi:10.1080/2150704X.2014.963733

Jin, X., Chen, X., Shi, C., Li, M., Guan, Y., Yu, C. Y., et al. (2017). Determination of Hemicellulose, Cellulose and Lignin Content Using Visible and Near Infrared Spectroscopy in *Miscanthus sinensis*. *Bioresour. Tech.* 241, 603–609. doi:10.1016/j.biortech.2017.05.047

Kumar, R., Tabatabaei, M., Karimi, K., and Sárvári Horváth, I. (2016). Recent Updates on Lignocellulosic Biomass Derived Ethanol - A Review. *Biofuel Res. J.* 3 (1), 347–356. doi:10.18331/BRJ2016.3.1.4

Lacey, J. A., Aston, J. E., Westover, T. L., Cherry, R. S., and Thompson, D. N. (2015). Removal of Introduced Inorganic Content from Chipped Forest Residues via Air Classification. *Fuel* 160, 265–273. doi:10.1016/j.fuel.2015.07.100

Lacey, J. A., Emerson, R. M., Thompson, D. N., and Westover, T. L. (2016). Ash Reduction Strategies in Corn stover Facilitated by Anatomical and Size Fractionation. *Biomass and Bioenergy* 90, 173–180. doi:10.1016/j.biombioe.2016.04.006

Lamers, P., Roni, M. S., Tumuluru, J. S., Jacobson, J. J., Cafferty, K. G., Hansen, J. K., et al. (2015). Techno-economic Analysis of Decentralized Biomass Processing Depots. *Bioresour. Technol.* 194, 205–213. doi:10.1016/j.biortech.2015.07.009

Langholtz, M. H., Stokes, B. J., and Eaton, L. M. (2016). Economic Availability of Feedstock. Oak Ridge National Laboratory, Oak Ridge, Tennessee, Managed by UT-Battelle, LLC for the US Department of Energy. *Advancing Domest. Resour. a thriving bioeconomy* Vol. 1, 1–411.

Laureano-Perez, L., Teymouri, F., Alizadeh, H., and Dale, B. E. (2005). Understanding Factors that Limit Enzymatic Hydrolysis of Biomass: Characterization of Pretreated Corn stover. *Appl. Biochem. Biotechnol.* 121-124 (1), 1081–1099. doi:10.1385/ABAB10.1385/abab:124:1-3:1081

Li, M., Heckwolf, M., Crowe, J. D., Williams, D. L., Magee, T. D., Kaeppler, S. M., et al. (2015a). Cell-wall Properties Contributing to Improved Deconstruction by Alkaline Pre-treatment and Enzymatic Hydrolysis in Diverse Maize (*Zea mays* L.) Lines. *J. Exp. Bot.* 66 (14), 4305–4315. doi:10.1093/jxb/erv016

Li, M., Wang, J., Du, F., Diallo, B., and Xie, G. H. (2017a). High-throughput Analysis of Chemical Components and Theoretical Ethanol Yield of Dedicated Bioenergy Sorghum Using Dual-Optimized Partial Least Squares Calibration Models. *Biotechnol. Biofuels* 10 (1), 206. doi:10.1186/s13068-017-0892-z

Li, M., Williams, D. L., Heckwolf, M., de Leon, N., Kaeppler, S., Sykes, R. W., et al. (2017b). Prediction of Cell Wall Properties and Response to Deconstruction Using Alkaline Pretreatment in Diverse Maize Genotypes Using Py-MBMS and NIR. *Bioenerg. Res.* 10 (2), 329–343. doi:10.1007/s12155-016-9798-z

Li, M., Yan, G., Bhalla, A., Maldonado-Pereira, L., Russell, P. R., Ding, S.-Y., et al. (2018). Physical Fractionation of Sweet Sorghum and Forage/energy Sorghum for Optimal Processing in a Biorefinery. *Ind. Crops Prod.* 124, 607–616. doi:10.1016/j.indcrop.2018.07.002

Li, X., Sun, C., Zhou, B., and He, Y. (2015b). Determination of Hemicellulose, Cellulose and Lignin in Moso Bamboo by Near Infrared Spectroscopy. *Sci. Rep.* 5 (1), 17210. doi:10.1038/srep17210

Li, Z., Zhai, H., Zhang, Y., and Yu, L. (2012). Cell Morphology and Chemical Characteristics of Corn stover Fractions. *Ind. Crops Prod.* 37 (1), 130–136. doi:10.1016/j.indcrop.2011.11.025

Liebmann, B., Friedl, A., and Varmuza, K. (2010). Applicability of Near-Infrared Spectroscopy for Process Monitoring in Bioethanol Production. *Biochem. Eng. J.* 52 (2), 187–193. doi:10.1016/j.bej.2010.08.006

Liu, L., Ye, X. P., Womac, A. R., and Sokhansanj, S. (2010). Variability of Biomass Chemical Composition and Rapid Analysis Using FT-NIR Techniques. *Carbohydr. Polym.* 81 (4), 820–829. doi:10.1016/j.carbpol.2010.03.058

Lupoi, J. S., Singh, S., Simmons, B. A., and Henry, R. J. (2014). Assessment of Lignocellulosic Biomass Using Analytical Spectroscopy: an Evolution to High-Throughput Techniques. *Bioenerg. Res.* 7 (1), 1–23. doi:10.1007/s12155-013-9352-1

Morrison, T. A., Jung, H. G., Buxton, D. R., and Hatfield, R. D. (1998). Cell-Wall Composition of Maize Internodes of Varying Maturity. *Crop Sci.* 38 (2). doi:10.2135/cropsci1998.0011183X003800020031x

Nkansah, K., Dawson-Andoh, B., and Slahor, J. (2010). Rapid Characterization of Biomass Using Near Infrared Spectroscopy Coupled with Multivariate Data Analysis: Part 1 Yellow-poplar (*Liriodendron tulipifera* L.). *Bioresour. Tech.* 101 (12), 4570–4576. doi:10.1016/j.biortech.2009.12.046

Ozaki, Y. (2012). Near-Infrared Spectroscopy-Its Versatility in Analytical Chemistry. *Anal. Sci.* 28 (6), 545–563. doi:10.2116/analsci.28.545

Park, J. I., Liu, L., Philip Ye, X., Jeong, M. K., and Jeong, Y.-S. (2012). Improved Prediction of Biomass Composition for Switchgrass Using Reproducing Kernel Methods with Wavelet Compressed FT-NIR Spectra. *Expert Syst. Appl.* 39 (1), 1555–1564. doi:10.1016/j.eswa.2011.05.012

Philip Ye, X., Liu, L., Hayes, D., Womac, A., Hong, K., and Sokhansanj, S. (2008). Fast Classification and Compositional Analysis of Cornstover Fractions Using Fourier Transform Near-Infrared Spectroscopy. *Bioresour. Tech.* 99 (15), 7323–7332. doi:10.1016/j.biortech.2007.12.063

Pordesimo, L. O., Hames, B. R., Sokhansanj, S., and Edens, W. C. (2005). Variation in Corn stover Composition and Energy Content with Crop Maturity. *Biomass and Bioenergy* 28 (4), 366–374. doi:10.1016/j.biombioe.2004.09.003

Qureshi, N., Hodge, D., and Vertes, A. (2014). *Biorefineries: Integrated Biochemical Processes for Liquid Biofuels* Amsterdam: Elsevier.

Rinnan, Å., Berg, F. v. d., and Engelsen, S. B. (2009). Review of the Most Common Pre-processing Techniques for Near-Infrared Spectra. *Trac Trends Anal. Chem.* 28 (10), 1201–1222. doi:10.1016/j.trac.2009.07.007

Robinson, A. R., and Mansfield, S. D. (2009). Rapid Analysis of poplar Lignin Monomer Composition by a Streamlined Thioacidolysis Procedure and Near-Infrared Reflectance-Based Prediction Modeling. *Plant J.* 58 (4), 706–714. doi:10.1111/j.1365-313X.2009.03808.x

Sanderson, M. A., Agblevor, F., Collins, M., and Johnson, D. K. (1996). Compositional Analysis of Biomass Feedstocks by Near Infrared Reflectance Spectroscopy. *Biomass and Bioenergy* 11 (5), 365–370. doi:10.1016/S0961-9534(96)00039-6

Scotter, C. (1990). Use of Near Infrared Spectroscopy in the Food Industry with Particular Reference to its Applications to On/in-Line Food Processes. *Food Control* 1 (3), 142–149. doi:10.1016/0956-7135(90)90006-X

Sharma, B., Larroche, C., and Dussap, C.-G. (2020). Comprehensive Assessment of 2G Bioethanol Production. *Bioresour. Tech.* 313, 123630. doi:10.1016/j.biortech.2020.123630

Sievers, D. A., Kuhn, E. M., Thompson, V. S., Yancey, N. A., Hoover, A. N., Resch, M. G., et al. (2020). Throughput, Reliability, and Yields of a Pilot-Scale Conversion Process for Production of Fermentable Sugars from Lignocellulosic Biomass: A Study on Feedstock Ash and Moisture. *ACS Sust. Chem. Eng.* 8 (4), 2008–2015. doi:10.1021/acssuschemeng.9b06550

Singh, S. K., Savoy, A. W., Yuan, Z., Luo, H., Stahl, S. S., Hegg, E. L., et al. (2019). Integrated Two-Stage Alkaline-Oxidative Pretreatment of Hybrid Poplar. Part 1: Impact of Alkaline Pre-extraction Conditions on Process Performance and Lignin Properties. *Ind. Eng. Chem. Res.* 58 (35), 15989–15999. doi:10.1021/acs.iecr.9b01124

Sluiter, A. D., Hames, B. R., Ruiz, R., Scarlata, C., Sluiter, J., Templeton, D. W., et al. (2008). Determination of Structural Carbohydrates and Lignin in Biomass. National Renewable Energy Laboratory, Technical Report NREL/TP-510-42618. doi:10.17504/protocols.io.bumtnu6n

Sluiter, A., and Wolfrum, E. (2013). Near Infrared Calibration Models for Pretreated Corn Stover Slurry Solids, Isolated and *In Situ*. *J. Near Infrared Spectrosc.* 21 (4), 249–257. doi:10.1255/jnirs.1065

Sluiter, J. B., and Sluiter, A. D. (2011a). Laboratory Analytical Procedure (LAP) Review and Integration. National Renewable Energy Laboratory, Technical Report NREL/TP-510-48087.

Sluiter, J. B., and Sluiter, A. D. (2011b). Summative Mass Closure Laboratory Analytical Procedure (LAP) Review and Integration: Pretreated Slurries. National Renewable Energy Laboratory, Technical Report NREL/TP-510-48825.

Stessel, R. I., and Peirce, J. J. (1983). Pulsed-Flow Air Classification for Waste-to-Energy. *J. Energ. Eng.* 109 (2), 60–73. doi:10.1061/(ASCE)0733-9402(1983)10910.1061/(asce)0733-9402(1983)109:2(60)

Sykes, R. W., Gjersing, E. L., Doeppke, C. L., and Davis, M. F. (2015). High-Throughput Method for Determining the Sugar Content in Biomass with Pyrolysis Molecular Beam Mass Spectrometry. *Bioenerg. Res.* 8 (3), 964–972. doi:10.1007/s12155-015-9610-5

Takada, M., Niu, R., Minami, E., and Saka, S. (2018). Characterization of Three Tissue Fractions in Corn (Zea mays) Cob. *Biomass and Bioenergy* 115, 130–135. doi:10.1016/j.biombioe.2018.04.023

Templeton, D. W., Scarlata, C. J., Sluiter, J. B., and Wolfrum, E. J. (2010). Compositional Analysis of Lignocellulosic Feedstocks. 2. Method Uncertainties. *J. Agric. Food Chem.* 58 (16), 9054–9062. doi:10.1021/jf100807b

Templeton, D. W., Sluiter, A. D., Hayward, T. K., Hames, B. R., and Thomas, S. R. (2009). Assessing Corn stover Composition and Sources of Variability via NIRS. *Cellulose* 16 (4), 621–639. doi:10.1007/s10570-009-9325-x

Templeton, D. W., Wolfrum, E. J., Yen, J. H., and Sharpless, K. E. (2016). Compositional Analysis of Biomass Reference Materials: Results from an Interlaboratory Study. *Bioenerg. Res.* 9 (1), 303–314. doi:10.1007/s12155-015-9675-1

Thompson, V. S., Lacey, J. A., Hartley, D., Jindra, M. A., Aston, J. E., and Thompson, D. N. (2016). Application of Air Classification and Formulation to Manage Feedstock Cost, Quality and Availability for Bioenergy. *Fuel* 180, 497–505. doi:10.1016/j.fuel.2016.04.040

Tsuchikawa, S., Murata, A., Kohara, M., and Mitsui, K. (2003). Spectroscopic Monitoring of Biomass Modification by Light-Irradiation and Heat Treatment. *J. Near Infrared Spectrosc.* 11 (5), 401–405. doi:10.1255/jnirs.391

Vincent, B., and Dardenne, P. (2021). *Application of NIR in Agriculture*. Singapore: Springer, 331–345. doi:10.1007/978-981-15-8648-4_14

Vogel, K. P., Dien, B. S., Jung, H. G., Casler, M. D., Masterson, S. D., and Mitchell, R. B. (2011). Quantifying Actual and Theoretical Ethanol Yields for Switchgrass Strains Using NIRS Analyses. *Bioenerg. Res.* 4 (2), 96–110. doi:10.1007/s12155-010-9104-4

Williams, D. A., Danao, M.-G. C., Rausch, K. D., Paulsen, M. R., and Singh, V. (2015). Variability in Composition of Individual Botanical Fractions of *Miscanthus giganteus* and Their Blends. *Biofuels* 6 (1-2), 63–70. doi:10.1080/17597269.2015.1050641

Wolfrum, E. J., Payne, C., Schwartz, A., Jacobs, J., and Kressin, R. W. (2020). A Performance Comparison of Low-Cost Near-Infrared (NIR) Spectrometers to a Conventional Laboratory Spectrometer for Rapid Biomass Compositional Analysis. *Bioenerg. Res.* 13 (4), 1121–1129. doi:10.1007/s12155-020-10135-6

Wolfrum, E. J., and Sluiter, A. D. (2009). Improved Multivariate Calibration Models for Corn Stover Feedstock and Dilute-Acid Pretreated Corn stover. *Cellulose* 16 (4), 567–576. doi:10.1007/s10570-009-9320-2

Wolfrum, E., Payne, C., Stefaniak, T., Rooney, W., Dighe, N., Bean, B., et al. (2013). Multivariate Calibration Models for Sorghum Composition Using Near-Infrared Spectroscopy. National Renewable Energy Laboratory, Technical Report NREL/TP-5100-56838. doi:10.2172/1071953

Xu, F., Yu, J., Tesso, T., Dowell, F., and Wang, D. (2013). Qualitative and Quantitative Analysis of Lignocellulosic Biomass Using Infrared Techniques: A Mini-Review. *Appl. Energ.* 104, 801–809. doi:10.1016/j.apenergy.2012.12.019

Yuan, Z., Singh, S. K., Bals, B., Hodge, D. B., and Hegg, E. L. (2019). Integrated Two-Stage Alkaline-Oxidative Pretreatment of Hybrid Poplar. Part 2: Impact of Cu-Catalyzed Alkaline Hydrogen Peroxide Pretreatment Conditions on Process Performance and Economics. *Ind. Eng. Chem. Res.* 58 (35), 16000–16008. doi:10.1021/acs.iecr.9b00901

Combined Sugarcane Pretreatment for the Generation of Ethanol and Value-Added Products

Sidnei Emilio Bordignon[1], Eduardo Ximenes[2], Olavo Micali Perrone[3], Christiane da Costa Carreira Nunes[1], Daehwan Kim[4], Maurício Boscolo[3], Eleni Gomes[1], Edivaldo Ximenes Ferreira Filho[5], Roberto da Silva[1] and Michael R. Ladisch[2]*

[1]Laboratory of Biochemistry and Applied Microbiology, Department of Food Engineering and Science, UNESP—University Estadual Paulista—IBILCE, Sao José do Rio Preto, Brazil, [2]Laboratory of Renewable Resources Engineering, Department of Agricultural and Biological Engineering, Purdue University, West Lafayette, IN, United States, [3]Laboratory of Sucrochemistry and Analytical Chemistry, Department of Chemistry and Environmental Sciences, UNESP—University Estadual Paulista—IBILCE, Sao José do Rio Preto, Brazil, [4]Hodson Science and Technology Center, Department of Biology, Hood College, Frederick, Brazil, [5]Laboratory of Enzymology, Department of Cellular Biology, University of Brasília, Brasília, Brazil

In this work, we have tested individual and combination of applications of ozonolysis and liquid hot water (LHW) to pretreat sugarcane bagasse (SCB) for the removal of enzyme and/or microbial inhibitors and generation of potential value-added chemicals. A solid content with 80% cellulose and a liquid phase (liquor) rich in phenolic derived compounds $(3\,g{\cdot}L^{-1})$ from lignin, sugars $(>20\,g{\cdot}L^{-1})$, and other compounds, such as furfural and hydroxymethylfurfural (HMF), were generated. Maximal (59%) glucan conversion occurred in the presence of double-pretreated bagasse, which had 32–50% more glucan available than the samples that were individually LHW or ozone-pretreated, resulting in maximal ethanol production (92% after 42 h) from double-pretreated SCB enzyme hydrolyzate. In summary, this work showed that ozone reacts effectively with lignin without the use of any other chemical reagent, and LHW pretreatment, followed by a washing step, was effective in solubilizing and cleaning up the fiber enzyme and microbial inhibitory compounds with ozone being effective against phenolics. Moreover, the generated cellulose-rich substrate is readily fermentable. The acidic liquor fraction removed by sequential washings and containing mainly sugars and phenolic compounds may be evaluated for use in green chemistry bioconversions processes.

Keywords: ozone, liquid hot water, pretreatment, enzyme hydrolysis, ethanol fermentation, value-added chemicals, inhibitors

INTRODUCTION

The high resistance of cellulose to degradation is the main biological barrier to lignocellulosic processing on a large scale (Ximenes et al., 2021). To overcome that, the application of mild and eco-friendly pretreatment techniques have been preferred instead of traditional acid or alkali pretreatments that have been previously proposed for lignocelluloses. Compared to the latter two pretreatments, hydrothermal pretreatment can be performed in a large scale under more gentle conditions (Pedersen and Meyer, 2010; Ruiz et al., 2020).

Liquid hot water (LHW) and to a lesser extent ozonolysis have been tested for the pretreatment of different lignocellulosic materials with LHW pretreatment being one of the leading pretreatments

since it improves cellulose digestibility at lower cost, and is carried out once without chemicals (Kim et al., 2009; Kim et al., 2011; Kim et al., 2013; Ximenes et al., 2017; Ruiz et al., 2020; 2021). When choosing operational conditions of pretreatment, it is important to consider the type of biomass as well as the formed lignocellulosic degradation products that are inhibitory to downstream biochemical reactions (Ko et al., 2015a,b,c; Jonsson and Martin, 2016, Ximenes et al., 2017; Ruiz et al., 2021). In this sense, LHW pretreatment of a variety of lignocellulosic materials has included a wide range of operational conditions, including temperature, resident time, particle size, and water-to-solid biomass ratio, among others, and aims to avoid the formation of enzyme and/or microbial inhibitors. Hydrothermal pretreatment is generally performed under conditions of 150–230°C for 10–50 min and pressures corresponding to about 4.9–20 bars (Kim et al., 2009; Rasmussen et al., 2014; Ximenes et al., 2017; Aguilar et al., 2018; Pino et al., 2018; Ruiz et al., 2021). Hydronium ions act as catalysts to hydrolyze and solubilize hemicellulose at an elevated temperature, while acetic acid and other organic acids generated from hemicellulose also facilitate this process (Weil et al., 1998; Kim I. J. et al., 2014; Kim Y. et al., 2014; Ximenes et al., 2017; Ruiz et al., 2020).

Ozonolysis is a less studied pretreatment than LHW and represents another promising approach for lignocellulosic treatment since it has a high specificity of reaction with ozone gas being readily obtained at atmospheric pressure and room temperature. Other benefits are moderate cost of production and no wastewater generation (Barros et al., 2013; Gitifar et al., 2013; Panneerselvam et al., 2013; Travaini et al., 2013; Perrone et al., 2016).

Combined pretreatments of lignocellulosic substrates have recently been proposed for different types of biomass aiming at a more effective result when individual features of the two pretreatments are combined. A more effective recovery of lignin and hemicellulose is possible with the potential of maximizing their application in a biorefinery concept (Sun et al., 2016). The estimated global production of bio-based chemicals and polymers is about 50 million metric tonnes per year (mtpy), but most chemicals and polymers are still produced from petroleum sources (Jong et al., 2012; Rosales-Calderon and Arantes, 2019).

Lignocellulosic materials consist of ~30% lignin by weight and 40% by energy (Perlack et al., 2005; Beauchet et al., 2012). In this sense, lignin is a valuable resource that merits further study to increase the commercial viability of a biorefinery (Agrawal et al., 2014), although technologies aiming to convert lignin to macromolecules and aromatic chemicals are still under development (Rosales-Calderon and Arantes, 2019). Potential uses of lignin-derived products already include production of activated carbon, binders, carbon fibers, motor fuel, plastic materials, and sorbents (Demuner et al., 2019). The combination of ozonolysis and LHW pretreatments tested here to enhance enzymatic hydrolysis, and alleviate inhibition during saccharification and fermentation of sugarcane bagasse (SCB) is also attractive for generating valued compounds from phenolic compounds derived from lignin.

MATERIAL AND METHODS

Material

SCB from 2013/2014 period of harvesting was supplied by Alta Mogiana sugarcane mill (São Joaquim da Barra, Brazil). The experimental work was developed between 2015 and 2017. The biomass was washed six times with deionized (DI) water, dried in an oven at 45°C to 10% or lower humidity, and milled to a particle size of about 1.0 mm before use. Enzymatic cocktails Cellic^{TM} CTec2$^{®}$ and HTec2$^{®}$ were provided by Novozymes Latin America (Araucária, Brazil). All other reagents and chemicals, unless otherwise noted, were purchased from Sigma-Aldrich (St. Louis, MO, United States). The fermentative industrial strain (*Saccharomyces cerevisiae* JP1) was provided by AEB Latin America (Sao José dos Pinhais, Brazil).

Pretreatments of Biomass

Two types of pretreatments were evaluated individually and/or in a combined sequence. Ozonolysis was performed using O_3 gas to chemically oxidize biomass components, and LHW was employed as a physical process using water as the reagent. Combined ozonolysis was performed first to degrade lignin, and then followed by LHW. Operational conditions of each one are described.

Ozonolysis

Ozonolysis was performed at room temperature and atmospheric pressure, according to Travaini et al. (2013), with few modifications. In total, 25.0 g of dry SCB were humidified at 50% (w/v) with DI water, filled in a fixed bed glass column (2.7 × 50.0 cm), and kept under saturated gas O_3 (flux of 32.0 mg min^{-1}) for 60 min. Ozone was produced from atmospheric air by the corona process (Radast 10C, Ozoxi-Ozonio). Ozone flux was monitored according to the Standard Methods for the Examination of Water and Wastewater (APHA, 1998). After pretreatment, SCB was air-dried at room temperature prior to cold water washing, performed by a five-step sequential procedure. Each step was carried out mixing 5.0% (w/v) of pretreated SCB with DI water under 30 min of agitation at room temperature, followed by filtration to separate washed solids, which were dried at 45°C for 24 h before enzymatic hydrolysis. The supernatants of each washing were stored at 4°C protected from light until analysis of total phenolics.

Liquid Hot Water

LHW pretreatment was conducted as described previously (Kim et al., 2009; Ko et al., 2015a) with few modifications. Each batch was performed by mixing 3.5 g of dry SCB (untreated or ozonized SCB) with DI water for a final concentration of 10% solids (w/v). The resulting material was placed in a metal column (2.2 × 13.5 cm) for heating in a sand bath at 190°C for 15 min. It was heated for 5 min. The tube was quenched in water for 20 s and then placed in an ice bucket for 25 min to stop the reaction. The pretreated material was then vacuum filtered using Whatman$^{®}$ no 1 filter paper to separate the solids from liquor (suspension).

Same five washing steps at room temperature described before were performed in the LHW-pretreated solids. The liquor from pretreatment and supernatants of each washing were stored at 4°C protected from light until analysis of total phenolics.

Enzymatic Hydrolysis

Hydrolysis experiments were conducted using 10% (w/v) of pretreated SCB as a substrate. SCB was suspended in 0.05M sodium citrate buffer at pH 5.0. The reaction was conducted in an incubator at 50°C and 150 rpm, using a 4:1 mixture of Cellic CTec2 and HTec2 (180 FPU mL^{-1} FPase activity; 13,213 UI mL^{-1} xylanase activity; 7,240 UI mL^{-1} β-glucosidase activity) diluted into two enzyme loadings. Loadings were calculated based on the chemical characterization of samples, that is, 9.1 and 17.5 mg protein g^{-1} of glucan. At 96 h of hydrolysis, aliquots from supernatant were taken every 24 h in duplicate and analyzed for soluble carbohydrates, reported here as an average with an indicated standard deviation. The final volume of hydrolyzate from each replicate unit was recovered after the separation from solid residues by centrifugation (12,096 × g, 10 min), combined in a single unit, corresponding to individual pretreatments, and kept frozen until the fermentative step.

Alcoholic Fermentation

The fermentability of selected hydrolyzate obtained after the hydrolysis of double-pretreated SCB was tested using two *Saccharomyces cerevisiae* strains. The first (JP1) is an industrial strain selected by its roughness and adaptability to perform alcoholic fermentation under adverse conditions in the first-generation production of ethanol, which is also already in use in Brazilian mills. The second yeast, Y150, is a strain obtained by the adaptive laboratory evolution method following similar protocol described by Vasconcellos et al. (2019). Yeast reactivation was made by pre-cultivation of freeze-stored cells in the YEPD medium (10 g L^{-1} yeast extract; 10 g L^{-1} peptone; 20 g·L^{-1} glucose) in an incubator at 28°C, 200 rpm, and 24 h prior use.

Three hydrolyzates were obtained from each pretreated material (ozonolysis; LHW; and combined ozonolysis + LHW, respectively) as substrates for alcoholic fermentations. Substrates were sterilized by vacuum filtering through a 0.22-μm membrane, and 0.5 g fresh cells was added per liter as inoculum. The inoculum standardization was carried out through measuring the cell density of precultured suspension in a colorimeter, followed by two steps of centrifugation (12,096 × g, 10 min), washing and resuspension in sterilized DI water. The washed cells were inoculated in 40 ml of each hydrolyzate substrate. The fermentation experiments were carried out in an incubator at 32°C and 150 rpm in duplicate at a semi-anaerobic condition. The concentration of cells, ethanol production, and glucose consumption were systematically monitored by sampling at 6, 12, 20, 24, 30, and 40 h of fermentation, respectively. Glucose to ethanol conversion yields (%) were calculated at the endpoint of each fermentation experiment by assuming: *[(g·L^{-1} of ethanol produced)/(g·L^{-1} of initial glucose * 0.511)] * 100.*

Analytical Methods

The chemical composition of SCB was determined according to LAP-010—determination of extractives in biomass (Sluiter et al., 2012) and the LAP for the determination of structural carbohydrates and lignin in biomass (Sluiter et al., 2012). Glucose and ethanol concentrations were measured by HPLC analysis as described previously (Cao et al., 2013) using an Aminex HPX-87H ion exchange column (300 × 7.8 mm, Bio-Rad Laboratories Inc., Hercules, CA). The column was connected with a Milton Roy mini pump (Milton Roy Co., Ivyland, PA), a Waters^{TM} 717 plus autosampler, and a Waters^{TM} 2,414 refractive index detector (Waters Corp., Milford, MA). The procedure for total phenolic analyses was adapted from the study by Singleton et al. (1999) to a micro-scale analysis using Folin–Ciocalteu reagent.

The results were expressed in milligrams per liter (mg L^{-1}) of gallic acid equivalent (GAE). The protein content of commercial enzymes used in hydrolysis assays was determined using the Pierce BCA Protein Assay Kit (Thermo Scientific, Rockford, IL). Filter paper activity was measured according to Mandels et al. (1976). Cell concentration was estimated by optical density in a spectrophotometer at 630 nm, using 1:10 dilution with sterile DI water, in comparison to the dry weight curve of cellular growth, previously determined to JP1 strain.

Infrared spectroscopy data (FTIR-ATR) were collected using a Perkin Elmer FTIR Spectrum Two. Both FTIR-ATR and powder X-ray diffraction (XRD) patterns of SCB were obtained on a Model 300 miniFlex Rigaku® diffractometer according to Perrone et al. (2016). The crystallinity index was calculated by the method proposed by Segal et al. (1959).

Scanning electron microscopy (SEM) was carried out using a FEI Quanta 200 scanning electron microscope (FEI Company, Eindhoven, Netherlands) with an accelerating voltage of 12.5 kV. Sample preparation comprised 1) mixing bagasse in 2.5% (v/v) glutaraldehyde in 0.1 M phosphate buffer (pH 7.3) for 48 h at room temperature; and 2) washing the sample in distilled water and after fixing it in 1% (v/v) osmium tetroxide diluted in distilled water for 30 min at room temperature. Bagasse was dehydrated by a series of ethanol washes and then critical point-dried with CO_2, and sputter-coated with gold (Bal-Tec SCD 050) (Perrone et al., 2016).

RESULTS AND DISCUSSION

Chemical Characterization of Pretreated Sugarcane Bagasse

Three different samples of pretreated SCB were obtained from individual ozonolysis and LHW pretreatments or a combination. Chemical characterization shows that ozonolysis and LHW have distinct effects on SCB, as summarized in **Table 1**. Ozone acted mostly on delignification, causing about 37% reduction of acid insoluble lignin (AIL) and partially decreasing the hemicellulose portion (components determined as xylose, arabinose, and acetyl groups) as a secondary effect (20% solubilization). Delignification by ozonolysis was relevant to overcome the recalcitrant character of lignin through its separation and the breakdown of lignin

TABLE 1 | Compositional analysis of sugarcane bagasse generated by different pretreatment approaches and the untreated sample. Solid composition is presented as dry weight on a free extractive basis (%).

Component	Composition of sugarcane bagasse (%)			
	Untreated	Liquid hot water pretreated	Ozonolysis pretreated	Ozonolysis + liquid hot water pretreated
Cellulose	45.9 ± 0.10	53.6 ± 0.49	61.2 ± 1.64	80.5 ± 1.44
Hemicellulose	24.5	19.1	19.5	4.1
Xylan	20.2 ± 0.59	17.5 ± 0.17	18.6 ± 0.53	4.1 ± 0.11
Arabinose	2.6 ± 0.11	1.5 ± 0.07	1.0 ± 0.05	0.0
Acetyl group	1.7 ± 0.15	0.0	0.0	0.0
Lignin	26.9	25.1	18.0	14.1
Acid-insoluble lignin	22.9 ± 0.36	21.8 ± 0.04	14.3 ± 0.30	12.5 ± 0.27
Acid-soluble lignin	4.0 ± 0.29	3.3 ± 0.01	3.7 ± 0.08	1.7 ± 0.03
Ashes	0.5 ± 0.12	0.9 ± 0.06	1.1 ± 0.32	1.3 ± 0.27
Total	97.8	98.7	99.8	100.1

FIGURE 1 | XRD patterns and the corresponding results of crystallinity index (Icr) for in nature sugarcane bagasse, ozonolysis, LHW, and ozonolysis + LHW pretreatments.

FIGURE 2 | FTIR-ATR spectra in natural and ozonolysis + LHW sugarcane bagasse samples.
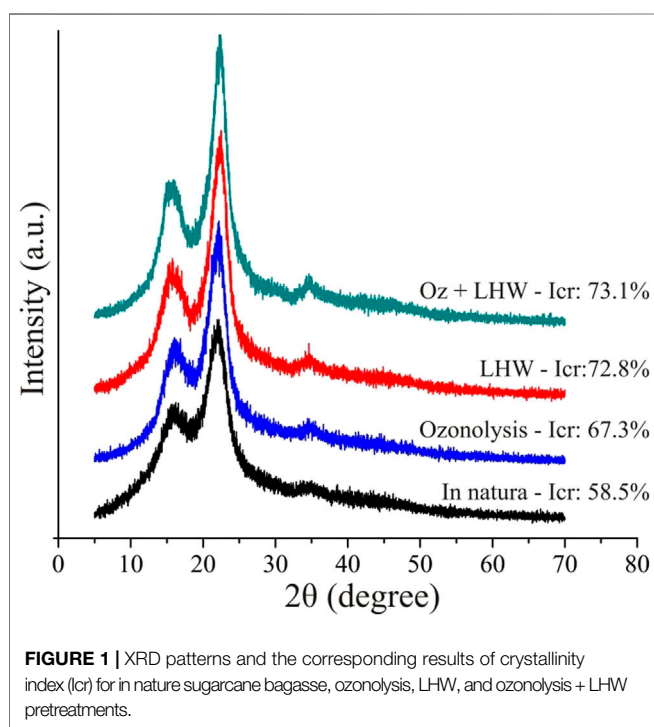
(Santos et al., 2019; Ázar et al., 2019). It also generated a rich fraction of phenolics and other compounds with potential use in green chemistry bioconversions, while also removing their enzyme and the microbial potential inhibitory effect in subsequent steps of enzyme hydrolysis and microbial fermentation (Kim et al., 2011, 2016; Ximenes et al., 2011; Michelin et al., 2016). Although the individual LHW pretreatment reduced the hemicellulose content (22% of solubilization), it had little effect on lignin (about 5% reduction of AIL).

The double-pretreated SCB (ozonolysis and LHW combined) generated the highest cellulose (80.5%) and the lowest hemicellulose (4.1%) contents among all samples, indicating an intensive solubilization (up to 80%) of hemicellulose into liquor and reaching a maximal delignification rate (45% reduction of AIL). In that sense, even taking into consideration all the pretreatments increased the glucan availability, its availability in the ozone + LHW-pretreated biomass was 75, 50, and 32% higher than that of the initial content (comparing only untreated LHW and ozone-pretreated SCB), respectively. The action on the lignin barrier observed in double-pretreated SCB helps to reduce enzyme adsorption on lignin and increase the accessibility of cellulose to enzyme (Zanchetta et al., 2018), which can also lead to a reduction of enzyme loading and cost.
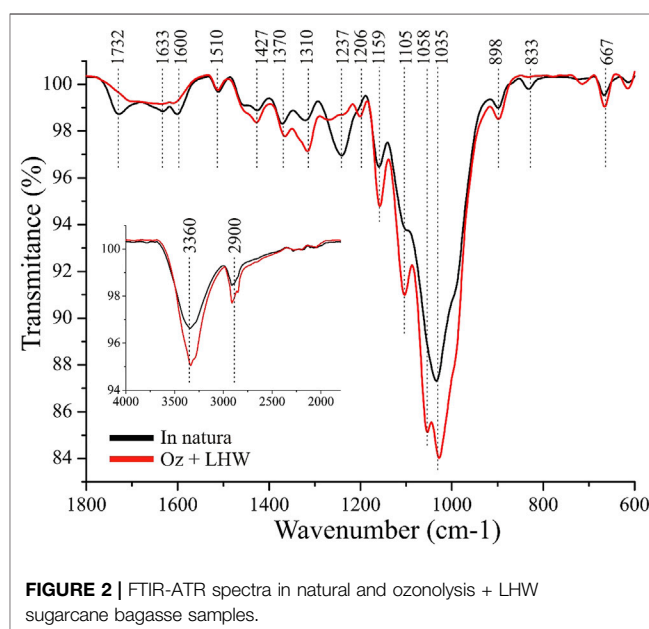
We observed an increase of the crystallinity index (CrI) according to the intensity of pretreatments in the following order: untreated < ozonolysis < LHW < Oz + LHW (**Figure 1**). We observed the highest CrI (73.1%) in the most intensive pretreatment (combined ozonolysis + LHW), possibly associated with lignin and hemicellulose degradation. In agreement with that reported in the literature (Gabhane et al.,
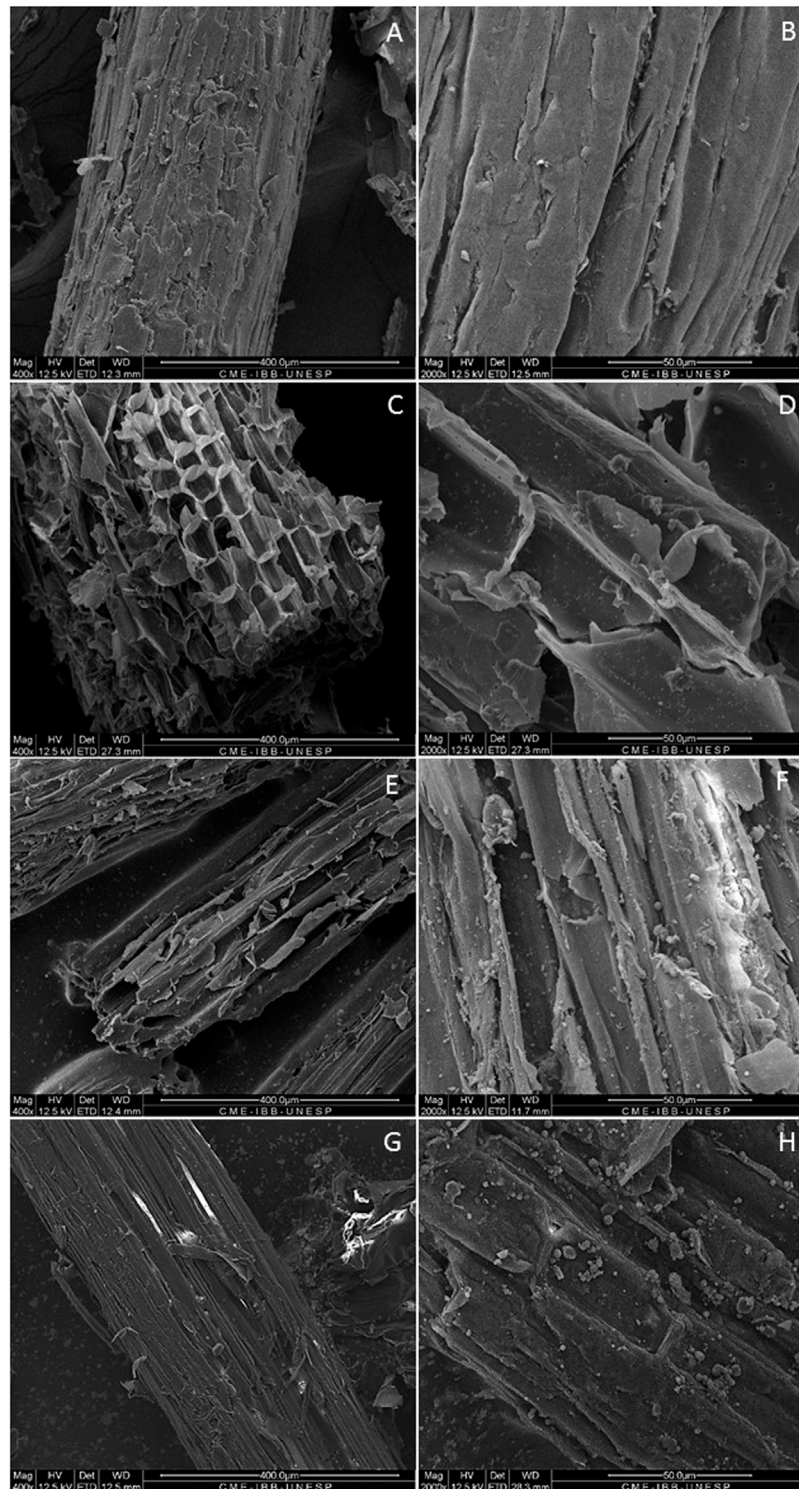
FIGURE 3 | Scanning electron microscopy of untreated bagasse **(A,B)**, ozone-treated bagasse **(C,D)**, LHW-treated bagasse **(E,F)**, and combined pretreatment ozone + LHW **(G,H)**.

2015; Pereira et al., 2016; Perrone et al., 2016), it seems that the increase in CrI observed here is more a function of removal of non-crystalline components from the biomass.

FTIR Analysis

Infrared spectrometry (FTIR-ATR) was used to analyze changes in functional groups that compose the fibers of SCB after

pretreatment, indicating possible targets of reaction in the material (**Figure 2**). A pronounced reduction in the intensity of infrared absorption bands found at 1,732 cm^{-1} and 1,237 cm^{-1} in the pretreated sample confirmed the strong removal of hemicellulose (Liu et al., 2007), which is also detected by compositional characterization analysis (**Table 1**). The increase of the cellulose content is also shown by FTIR-ATR, especially by the increase of infrared absorption bands at 1,427 cm^{-1} and 1,370 cm^{-1} (assigned to the crystalline cellulose structure), and amorphous cellulose at 898 cm^{-1} (Pereira et al., 2016).

A decrease in the lignin content in the double-pretreated sample was observed based on the presence of bands related to functional groups or specific lignin linkages, such as aromatic rings at 1,600 cm^{-1} and 1,510 cm^{-1} (Pereira et al., 2016), and carbonyl groups conjugated with aromatic rings at 1,633 cm^{-1} (Zhou et al., 2016). Also, the band at 833 cm^{-1} is associated to [C-H] vibrations out of a plane in *p*-hydroxyphenyl units (Hoareau et al., 2004). The presence of these bands indicates a clear decrease of the intensities in the spectra corresponding to the combined pretreatments, which is again in agreement with the large extent of lignin removal (compositional characterization, **Table 1**).

Ultrastructural Changes in Pretreated Sugarcane Bagasse

Scanning electron microscopy (SEM) was performed to analyze possible tissue damage and ultrastructural changes on the bagasse surface after each pretreatment (ozone, LHW, and ozone + LHW) in comparison to the untreated sample (**Figures 3A,B**). The initial smooth and intact structure of fibers was strongly affected by both ozone and hot water pretreatments (**Figures 3C–F**). Cell walls were ruptured by the ozone gas, generating opened cells with increased porosity and surface area (**Figures 3C,D**). Similar effects were observed with hot water. A cracked surface characterized by holes formed in the cell wall is noted; the holes may be caused by the high pressure experienced during LHW processing (**Figures 3E,F**).

A disorganized structure with greater exposure of fibers was also present in SCB pretreated with SO$_2$ and CO$_2$ steam (Corrales et al., 2012). The presence of globular structures on the surface of samples exposed to high temperature is probably related to the formation and accumulation of globular lignin at 190°C. It is known that lignin softens and agglomerates at a relatively low temperature (<200°C) (Hamdan et al., 2000; Zhang et al., 2015). All these observations also apply to the double-pretreated sample, which showed a random breaking along the fibers, and a total collapse of the cellular structure due to the combined process (**Figures 3G,H**). These morphological changes of SCB obtained after combined pretreatment enhance the accessibility of cellulose-degrading enzymes and facilitate the hydrolysis of cellulose.

Effect of Pretreatments on Phenolic Compound Releasing

When LHW pretreatment alone was performed, 1,462 mg L^{-1} of phenolics were solubilized through liquor, and 857 mg L^{-1} remained on solids, reaching a total of 2,320 mg L^{-1} of released phenolics. The lowest concentration was observed when ozonolysis was performed as a single pretreatment. Here, 936 mg L^{-1} of total phenolic compounds were released. Although delignification is stronger in ozonolysis than in LHW pretreatment, as previously demonstrated by biomass compositional and FTIR-ART analysis, the lower release of phenols may be explained by the conversion of acid-insoluble lignin (AIL) preferentially into acids with low molecular weight, such as formic, acetic, oxalic, and carboxylic acids (Travaini et al., 2016). This hypothesis is further supported by the intense acidification of the ozonized solids, which regularly had a pH near to 2.0 after ozonolysis. The highest concentration of total phenolics released was almost 3,000 mg·L^{-1} when combining ozonolysis and LHW pretreatments, with 2,300 mg·L^{-1} solubilized in the liquor and 681 mg·L^{-1} remaining in solids. Thus, the use of this combined pretreatment approach resulted in a maximal release of phenolic compounds.

Effect of Phenolic Compound Removal on 96-h Enzymatic Hydrolysis

The low molecular weight phenolic compounds derived from lignin depolymerization had a negative impact on enzyme performance, possibly due to both non-productive adsorption and inhibitory effects during saccharification and microbial fermentation (Ximenes et al., 2010; Nakagame et al., 2011; Ximenes et al., 2011; Jönsson and Martín, 2016). Therefore, phenolic compounds must be removed from pretreated solids prior to enzymatic hydrolysis to enhance the yields of both the saccharification and the fermentation steps (Kim et al., 2013; Xiros and Olsson, 2014).

Sequential washing of the material at room temperature (see Material and Methods section 2.2.1, section 2.2.2) significantly reduced phenolics embedded in the pretreated fibers (**Figure 3**). A maximum of 33 g·L^{-1} of glucose was reached in 24 h during hydrolysis of washed ozone-pretreated SCB (**Figure 4A**), which represented a conversion of about 75% of cellulose into glucose vs. 44% for the enzymatic hydrolysis of the non-washed pretreated sample. Similarly, high cellulose conversion was observed for washed LHW-pretreated SCB samples (**Figure 4B**), although lower yields were obtained than washed ozone-pretreated samples (compare **Figures 4A,B**). This suggests better accessibility of substrate to enzyme hydrolysis in the ozone-pretreated sample and the presence of more enzyme inhibitors, including remaining phenolic compounds in the LHW-pretreated samples, or both.

Kinetics of Enzymatic Hydrolysis of Pretreated Sugarcane Bagasse

A kinetic study was performed using reduced enzyme loading (9 mg of total protein per gram of glucan) for hydrolysis of untreated and pretreated SCB under different conditions for 96 h. The double pretreated SCB was also tested under non- and washed conditions.
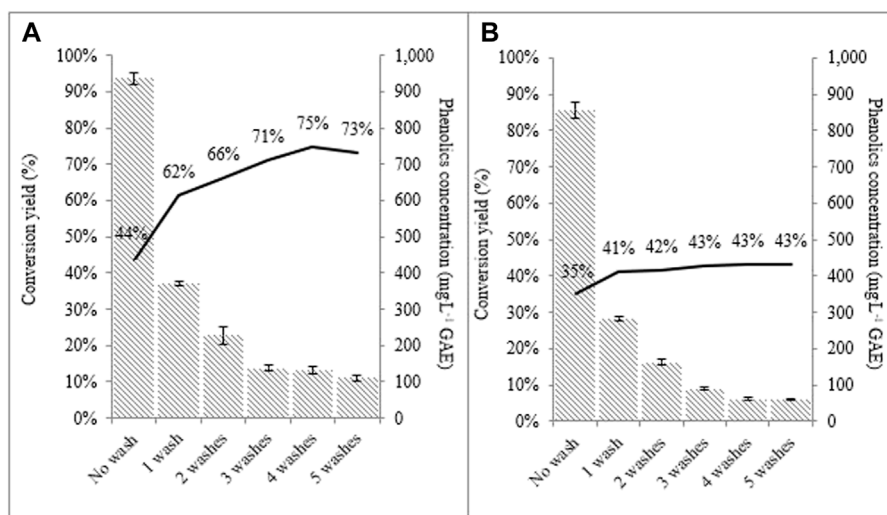
FIGURE 4 | Concentration of phenolic compounds (bars) and cellulose conversion yield (lines) in enzymatic hydrolysis (17.5 mg protein × g^{-1} glucan; 10% total solids loading, 96 h) related to sequential room temperature washes. **(A)** ozone-pretreated sugarcane bagasse; **(B)** LHW-pretreated sugarcane bagasse.
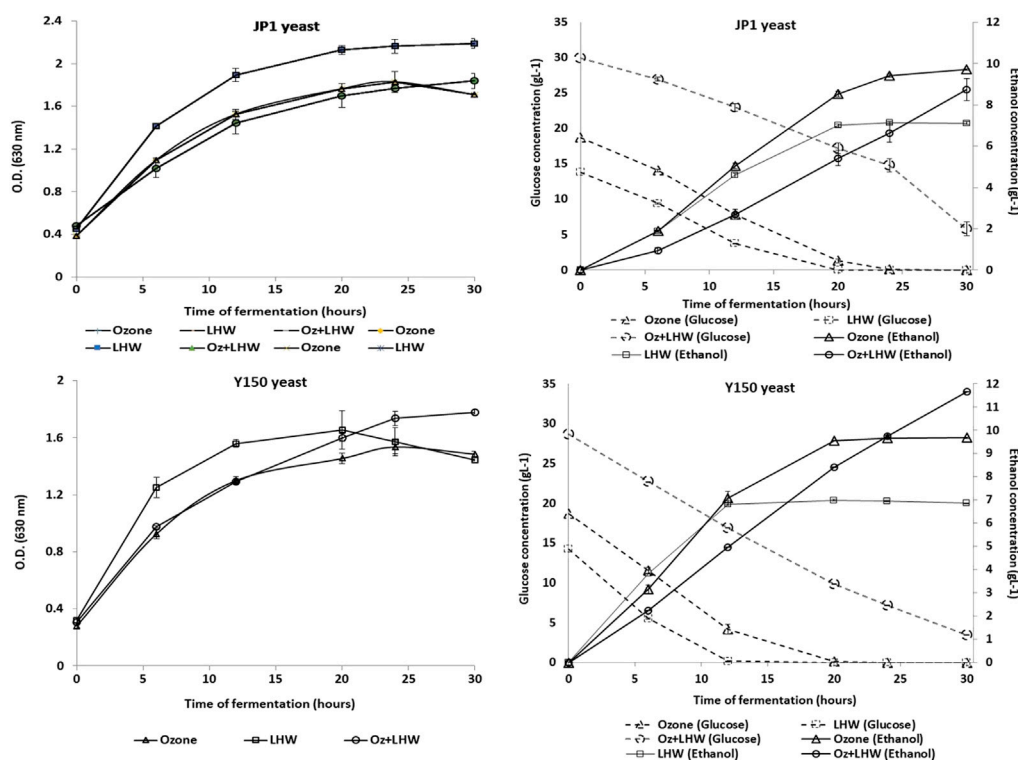
FIGURE 5 | Kinetics of yeasts JP1 and Y150 in alcoholic fermentation of sugarcane bagasse hydrolysate pretreated by individual and combined Ozonolysis and LHW approaches.

The kinetics of hydrolysis of different SCB samples showed that the yield increase was consistent with the increase of the cellulose content after pretreatment and washes, relative to the decline of hemicellulose removal (in LWH-pretreated bagasse), or lignin reduction (in ozone-pretreated bagasse), or associated to both effects (in combined pretreatments). For the combined pretreatments, 43.0 g L^{-1} of glucose was generated after enzymatic hydrolysis of double-pretreated SCB, corresponding

to 59% of conversion from initial glucan vs. 20, 47, 37, and 10% for untreated, ozone, LHW, and double pretreated samples, respectively. The hydrolyzate from double pretreated samples was tested by fermentation experiments that are reported and discussed in the next section. A strong inhibitory effect of pretreatment by-products was observed over cellulolytic and hemicellulolytic enzymes when the hydrolysis was performed in the presence of liquor derived from combined pretreatment, reducing cellulose conversion to about 10%, probably due to potential enzyme inhibitors mentioned before (Ximenes et al., 2010, 2011; Kim et al., 2011; Gabhane et al., 2015).

Alcoholic Fermentation of Hydrolyzate

JP1 and Y150 yeast strains were able to ferment the selected hydrolyzate without nutrient supplementation, with all glucose available exhausted after 42 h (**Figure 5**), while xylose concentration remained constant. This latter result was expected since these yeast strains cannot ferment xylose to ethanol. The final yield of glucose to ethanol was similar for both strains, 87% for JP1 vs. 92% for Y150 (**Figure 5**). However, Y150 strain was faster on the fermentation (conversion yield of 67% for Y150 after 24 h vs. 43% for JP1), indicating some possible adaptation advantage to the microbial inhibitory compounds still present in the hydrolyzate, including phenolics (Larsson et al., 2000; Palmqvist and Hahn-Hägerdal, 2000a, 2000b). Since the cellular density in all replicates of fermentations was similar, Y150 cells were found to be more efficient on ethanol production.

CONCLUSIONS

The effects of ozonolysis and LHW sugarcane bagasse pretreatment were observed in individual and combined pretreatment processes that resulted in a new approach for achieving a high amount of cellulose for hydrolysis purposes while generating an acid liquor fraction rich in sugars and phenolic compounds. The double pretreatment removed enzyme and microbial inhibitors, and generated water-soluble products that can be explored in green chemistry bioconversions processes. The combined ozonolysis and LHW pretreatment also generated, after enzyme hydrolysis, a hydrolyzate rapidly fermented by *S. cerevisiae* without the need for detoxification steps or nutrient supplementation. The maximal conversion yield by strain Y150 in fermenting glucose to ethanol was 92% in 42 h. This approach and results obtained are in agreement with a proposed model of the lignocellulosic biorefinery (Silva et al.,

2018), in which sugars from cellulose and hemicellulose are used to generate biofuels and bioproducts, while lignin components are utilized in the synthesis of other bioproducts and act as an alternative heat and energy source.

DATA AVAILABILITY STATEMENT

The original contributions presented in the study are included in the article/Supplementary Material, further inquiries can be directed to the corresponding author.

AUTHOR CONTRIBUTIONS

SB: experimental design, performance and manuscript writing; EX: experimental design, manuscript writing, review, and formatting; OP: experimental design, performance, and manuscript writing; CC: experimental design and performance; DK: experimental design and performance; MB: experimental design and manuscript writing; EG: experimental design and manuscript writing; EF: manuscript writing, review, and formatting; RS: experimental design and manuscript writing; ML: experimental design, manuscript writing, and review.

ACKNOWLEDGMENTS

REFERENCES

Agrawal, A., Kaushik, N., and Biswas, S. (2014). Derivatives and Applications of Lignin— an Insight. *Scitech. J.* 1, 30–36.

Aguilar, D. L., Rodríguez-Jasso, R. M., Zanuso, E., Lara-Flores, A. A., Aguilar, C. N., Sanchez, A., et al. (2018). "Operational Strategies for Enzymatic Hydrolysis in a Biorefinery," in *Biorefining Biomass to Biofuels -Opportunities and Perception*. Editors S. Kumar and R. Sani (Cham: Springer), 223–248. doi:10.1007/978-3-319-67678-4_10

APHA (1998). *Standard Methods for the Examination of Water and Wastewater*. Washington: American Public Health Association, 202–242.

Ázar, R. I. S. L., Morgan, T., Barbosa, M. H. P., Guimarães, V. M., Ximenes, E., and Ladisch, M. (2019). Impact of Protein Blocking on Enzymatic Saccharification of Bagasse from Sugarcane Clones. *Biotechnol. Bioeng.* 116 (7), 1584–1593. doi:10.1002/bit.26962

Barros, R. d. R. O. d., Paredes, R. d. S., Endo, T., Bon, E. P. d. S., and Lee, S.-H. (2013). Association of Wet Disk Milling and Ozonolysis as Pretreatment for Enzymatic Saccharification of Sugarcane Bagasse and Straw. *Bioresour. Tech.* 136, 288–294. doi:10.1016/j.biortech.2013.03.009

Beauchet, R., Monteil-Rivera, F., and Lavoie, J. M. (2012). Conversion of Lignin to Aromatic-Based Chemicals (L-Chems) and Biofuels (L-Fuels). *Bioresour. Tech.* 121, 328–334. doi:10.1016/j.biortech.2012.06.061

Cao, G., Ximenes, E., Nichols, N. N., Zhang, L., and Ladisch, M. (2013). Biological Abatement of Cellulase Inhibitors. *Bioresour. Tech.* 146, 604–610. doi:10.1016/j.biortech.2013.07.112

Corrales, R. C. N. R., Mendes, F. M. T., Perrone, C. C., Sant'Anna, C., de Souza, W., Abud, Y., et al. (2012). Structural Evaluation of Sugar Cane Bagasse Steam Pretreated in the Presence of CO2 and SO2. *Biotechnol. Biofuels* 5, 36. doi:10.1186/1754-6834-5-36

Demuner, I. F., Colodette, J. L., Demuner, A. J., and Jardim, C. M. (2019). Biorefinery Review: Wide-Reaching Products through Kraft Lignin. *BioRes.* 14, 7543–7581. doi:10.15376/biores.14.3.demuner

dos Santos, A. C., Ximenes, E., Kim, Y., and Ladisch, M. R. (2019). Lignin-Enzyme Interactions in the Hydrolysis of Lignocellulosic Biomass. *Trends Biotechnol.* 37, 518–531. doi:10.1016/j.tibtech.2018.10.010

Gabhane, J., William, S. P. M. P., Vaidya, A. N., Das, S., and Wate, S. R. (2015). Solar Assisted Alkali Pretreatment of Garden Biomass: Effects on Lignocellulose Degradation, Enzymatic Hydrolysis, Crystallinity and Ultra-structural Changes in Lignocellulose. *Waste Manag.* 40, 92–99. doi:10.1016/j.wasman.2015.03.002

Gitifar, V., Eslamloueyan, R., and Sarshar, M. (2013). Experimental Study and Neural Network Modeling of Sugarcane Bagasse Pretreatment with H2SO4 and O3 for Cellulosic Material Conversion to Sugar. *Bioresour. Tech.* 148, 47–52. doi:10.1016/j.biortech.2013.08.060

Hamdan, S., Dwianto, W., Morooka, T., and Norimoto, M. (2000). Softening Characteristics of Wet wood under Quasi Static Loading. *Holzforschung* 54, 557–560. doi:10.1515/hf.2000.094

Hoareau, W., Trindade, W. G., SiegmundCastellana, B., Castellan, A., and Frollini, E. (2004). Sugar Cane Bagasse and Curaua Lignins Oxidized by Chlorine Dioxide and Reacted with Furfuryl Alcohol: Characterization and Stability. *Polym. Degrad. Stab.* 86, 567–576. doi:10.1016/j.polymdegradstab.2004.07.005

Jong, E., Higson, A., Walsh, P., and Wellisch, M. (2012). *Biobased Chemicals—Value Added Products from Biorefineries*, 42. Wageningen, Netherlands: IEA Bioenergy Task. www.iea-bioenergy.taks42-biorefineries.com.

Jönsson, L. J., and Martín, C. (2016). Pretreatment of Lignocellulose: Formation of Inhibitory By-Products and Strategies for Minimizing Their Effects. *Bioresour. Tech.* 199, 103–112. doi:10.1016/j.biortech.2015.10.009

Kim, D., Ximenes, E. A., Nichols, N. N., Cao, G., Frazer, S. E., and Ladisch, M. R. (2016). Maleic Acid Treatment of Biologically Detoxified Corn stover Liquor. *Bioresour. Tech.* 216, 437–445. doi:10.1016/j.biortech.2016.05.086

Kim, I. J., Lee, H. J., Choi, I.-G., and Kim, K. H. (2014a). Synergistic Proteins for the Enhanced Enzymatic Hydrolysis of Cellulose by Cellulase. *Appl. Microbiol. Biotechnol.* 98 (20), 8469–8480. doi:10.1007/s00253-014-6001-3

Kim, Y., Kreke, T., Hendrickson, R., Parenti, J., and Ladisch, M. R. (2013). Fractionation of Cellulase and Fermentation Inhibitors from Steam Pretreated Mixed Hardwood. *Bioresour. Tech.* 135, 30–38. doi:10.1016/j.biortech.2012.10.130

Kim, Y., Kreke, T., Mosier, N. S., and Ladisch, M. R. (2014b). Severity Factor Coefficients for Subcritical Liquid Hot Water Pretreatment of Hardwood Chips. *Biotechnol. Bioeng.* 111 (2), 254–263. doi:10.1002/bit.25009

Kim, Y., Mosier, N. S., and Ladisch, M. R. (2009). Enzymatic Digestion of Liquid Hot Water Pretreated Hybrid poplar. *Biotechnol. Prog.* 25, 340–348. doi:10.1002/btpr.137

Kim, Y., Ximenes, E., Mosier, N. S., and Ladisch, M. R. (2011). Soluble Inhibitors/deactivators of Cellulase Enzymes from Lignocellulosic Biomass. *Enzyme Microb. Tech.* 48, 408–415. doi:10.1016/j.enzmictec.2011.01.007

Ko, J. K., Kim, Y., Ximenes, E., and Ladisch, M. R. (2015a). Effect of Liquid Hot Water Pretreatment Severity on Properties of Hardwood Lignin and Enzymatic Hydrolysis of Cellulose. *Biotechnol. Bioeng.* 112 (2), 252–262. doi:10.1002/bit.25349

Ko, J. K., Um, Y., Park, Y.-C., Seo, J.-H., and Kim, K. H. (2015b). Compounds Inhibiting the Bioconversion of Hydrothermally Pretreated Lignocellulose. *Appl. Microbiol. Biotechnol.* 99 (10), 4201–4212. doi:10.1007/s00253-015-6595-0

Ko, J. K., Ximenes, E., Kim, Y., and Ladisch, M. R. (2015c). Adsorption of Enzyme onto Lignins of Liquid Hot Water Pretreated Hardwoods. *Biotechnol. Bioeng.* 112 (3), 447–456. doi:10.1002/bit.25359

Larsson, S., Quintana-Sáinz, A., Reimann, A., Nilvebrant, N.-O., and Jönsson, L. J. (2000). Influence of Lignocellulose-Derived Aromatic Compounds on Oxygen-Limited Growth and Ethanolic Fermentation by *Saccharomyces cerevisiae*. *Abab* 84-86, 617–632. doi:10.1385/abab:84-86:1-9:617

Mandels, M., Andreotti, R., and Roche, C. (1976). Measurement of Saccharifying Cellulase. *Biotechnol. Bioeng. Symp.* 6, 21–33.

Michelin, M., Ximenes, E., de Lourdes Teixeira de Moraes Polizeli, M., and Ladisch, M. R. (2016). Effect of Phenolic Compounds from Pretreated Sugarcane Bagasse on Cellulolytic and Hemicellulolytic Activities. *Bioresour. Tech.* 199, 275–278. doi:10.1016/j.biortech.2015.08.120

Nakagame, S., Chandra, R. P., Kadla, J. F., and Saddler, J. N. (2011). The Isolation, Characterization and Effect of Lignin Isolated from Steam Pretreated Douglas-fir on the Enzymatic Hydrolysis of Cellulose. *Bioresour. Tech.* 102, 4507–4517. doi:10.1016/j.biortech.2010.12.082

Palmqvist, E., and Hahn-Hägerdal, B. (2000a). Fermentation of Lignocellulosic Hydrolysates. I: Inhibition and Detoxification. *Bioresour. Tech.* 74, 17–24. doi:10.1016/s0960-8524(99)00160-1

Palmqvist, E., and Hahn-Hägerdal, B. (2000b). Fermentation of Lignocellulosic Hydrolysates. II: Inhibitors and Mechanisms of Inhibition. *Bioresour. Tech.* 74, 25–33. doi:10.1016/s0960-8524(99)00161-3

Panneerselvam, A., Sharma-Shivappa, R. R., Kolar, P., Ranney, T., and Peretti, S. (2013). Potential of Ozonolysis as a Pretreatment for Energy Grasses. *Bioresour. Tech.* 148, 242–248. doi:10.1016/j.biortech.2013.08.129

Pedersen, M., and Meyer, A. S. (2010). Lignocellulose Pretreatment Severity - Relating pH to Biomatrix Opening. *New Biotechnol.* 27, 739–750. doi:10.1016/j.nbt.2010.05.003

Pereira, S. C., Maehara, L., Machado, C. M. M., and Farinas, C. S. (2016). Physical-chemical-morphological Characterization of the Whole Sugarcane Lignocellulosic Biomass Used for 2G Ethanol Production by Spectroscopy and Microscopy Techniques. *Renew. Energ.* 87, 607–617. doi:10.1016/j.renene.2015.10.054

Perlack, R. D., Wright, L. L., Turhollow, A. F., and Grahm, L. L. (2005). *Biomass as Feedstock for a Bioenergy and Bioproducts Industry: The Technical Feasibility of a Billion-Ton Annual Supply.* Oak Ridge, TN: U.S. Department of Energy (DOE), U.S. Department of Agriculture (USDA). http://www.osti.gov./bridge.

Perrone, O. M., Colombari, F. M., Rossi, J. S., Moretti, M. M. S., Bordignon, S. E., Nunes, C. d. C. C., et al. (2016). Ozonolysis Combined with Ultrasound as a Pretreatment of Sugarcane Bagasse: Effect on the Enzymatic Saccharification and the Physical and Chemical Characteristics of the Substrate. *Bioresour. Tech.* 218, 69–76. doi:10.1016/j.biortech.2016.06.072

Pino, M. S., Rodríguez-Jasso, R. M., Michelin, M., Flores-Gallegos, A. C., Morales-Rodriguez, R., Teixeira, J. A., et al. (2018). Bioreactor Design for Enzymatic Hydrolysis of Biomass under the Biorefinery Concept. *Chem. Eng. J.* 347, 119–136. doi:10.1016/j.cej.2018.04.057

Rasmussen, H., Sørensen, H. R., and Meyer, A. S. (2014). Formation of Degradation Compounds from Lignocellulosic Biomass in the Biorefinery: Sugar Reaction Mechanisms. *Carbohydr. Res.* 385, 45–57. doi:10.1016/j.carres.2013.08.029

Rosales-Calderon, O., and Arantes, V. (2019). A Review on Commercial-Scale High-Value Products that Can Be Produced Alongside Cellulosic Ethanol. *Biotechnol. Biofuels* 12, 240. doi:10.1186/s13068-019-1529-1

Ruiz, H. A., Conrad, M., Sun, S.-N., Sanchez, A., Rocha, G. J. M., Romaní, A., et al. (2020). Engineering Aspects of Hydrothermal Pretreatment: From Batch to Continuous Operation, Scale-Up and Pilot Reactor under Biorefinery Concept. *Bioresour. Tech.* 299, 122685. doi:10.1016/j.biortech.2019.122685

Ruiz, H. A., Galbe, M., Garrote, G., Ramirez-Gutierrez, D. M., Ximenes, E., Sun, S.-N., et al. (2021). Severity Factor Kinetic Model as a Strategic Parameter of Hydrothermal Processing (Steam Explosion and Liquid Hot Water) for Biomass Fractionation under Biorefinery Concept. *Bioresour. Tech.* 342, 125961. doi:10.1016/j.biortech.2021.125961

Segal, L., Creely, J. J., Martin, A. E., Jr., and Conrad, C. M. (1959). An Empirical Method for Estimating the Degree of Crystallinity of Native Cellulose Using the X-Ray Diffractometer. *Textile Res. J.* 29, 786–794. doi:10.1177/004051755902901003

Silva, C. O. G., Vaz, R. P., and Filho, E. X. F. (2018). Bringing Plant Cell wall-degrading Enzymes into the Lignocellulosic Biorefinery Concept. *Biofuels, Bioprod. Bioref.* 12, 277–289. doi:10.1002/bbb.1832

Singleton, V. L., Orthofer, R., and Lamuela-Raventós, R. M. (1999). [14] Analysis of Total Phenols and Other Oxidation Substrates and Antioxidants by Means of Folin-Ciocalteu Reagent. *Methods Enzymol.* 299, 152–178. doi:10.1016/s0076-6879(99)99017-1

Sluiter, A., Hames, A. B., RuizScarlata, R. C., Sluiter, J., Templeton, D., and Crocker, D. (2012). *Determination of Structural Carbohydrates and Lignin in Biomass*. Golden, CO: Laboratory Analytical Procedure, National Renewable Energy Laboratory (NREL). Version 08-03-2012.

Sun, S., Sun, S., Cao, X., and Sun, R. (2016). The Role of Pretreatment in Improving the Enzymatic Hydrolysis of Lignocellulosic Materials. *Bioresour. Tech.* 199, 49–58. doi:10.1016/j.biortech.2015.08.061

Travaini, R., Barrado, E., and Bolado-Rodríguez, S. (2016). Effect of Ozonolysis Pretreatment Parameters on the Sugar Release, Ozone Consumption and Ethanol Production from Sugarcane Bagasse. *Bioresour. Tech.* 214, 150–158. doi:10.1016/j.biortech.2016.04.102

Travaini, R., Otero, M. D. M., Coca, M., Da-Silva, R., and Bolado, S. (2013). Sugarcane Bagasse Ozonolysis Pretreatment: Effect on Enzymatic Digestibility and Inhibitory Compound Formation. *Bioresour. Tech.* 133, 332–339. doi:10.1016/j.biortech.2013.01.133

Vasconcellos, V. M., Farinas, C. S., Ximenes, E., Slininger, P., and Ladisch, M. (2019). Adaptive Laboratory Evolution of Nanocellulose-producing Bacterium. *Biotechnol. Bioeng.* 116, 1923–1933. doi:10.1002/bit.26997

Weil, J. R., Sarikaya, A., Rau, S.-L., Goetz, J., Ladisch, C. M., Brewer, M., et al. (1998). Pretreatment of Corn Fiber by Pressure Cooking in Water. *Appl. Biochem. Biotechnol.* 73, 1–17. doi:10.1007/bf02788829

Ximenes, E., Farinas, C., Baldino, A., and Ladisch, M. (2021). Moving from Residual Lignocellulosic Biomass into High-Value Products: Outcomes from a Long-Term International Cooperation. *Biofuels, Bioprod. Biorefin.* 15 (2), 563–573. doi:10.1002/bbb.2179

Ximenes, E., Farinas, C. S., and Kim, Y., and (2017) *Hydrothermal Processing in Biorefineries - Production of Bioethanol and High Added-Value Compounds of Second and Third Generation Biomass*. Editors, H. L. Trajano and M. H. Thomsen (Springer International Publishing Switzerland), 181–206. 978-3-319-56456-2. doi:10.1007/978-3-319-56457-9_7

Ximenes, E., Kim, Y., Mosier, N., Dien, B., and Ladisch, M. (2011). Deactivation of Cellulases by Phenols. *Enzyme Microb. Tech.* 48, 54–60. doi:10.1016/j.enzmictec.2010.09.006

Ximenes, E., Kim, Y., Mosier, N., Dien, B., and Ladisch, M. (2010). Inhibition of Cellulases by Phenols. *Enzyme Microb. Tech.* 46, 170–176. doi:10.1016/j.enzmictec.2009.11.001

Xiros, C., and Olsson, L. (2014). Comparison of Strategies to Overcome the Inhibitory Effects in High-Gravity Fermentation of Lignocellulosic Hydrolysates. *Biomass and Bioenergy* 65, 79–90. doi:10.1016/j.biombioe.2014.03.060

Zanchetta, A., Santos, A. C. F., Ximenes, E., Nunes, C. C. C., BoscoloGomes, M. E., and Ladisch, M. R. (2018). Temperature Dependent Cellulase Adsorption on Lignin from Sugarcane Bagasse. *Bioresour. Technol.* 252, 143–149. doi:10.1016/j.biortech.2017.12.061

Zhang, Q., Chen, Q., Chen, J., Wang, K., Yuan, S., and Sun, R. (2015). Morphological Variation of Lignin Biomacromolecules during Acid-Pretreatment and Biorefinery-Based Fractionation. *Ind. Crop Prod.* 77, 527–534. doi:10.1016/j.indcrop.2015.09.021

Zhou, Z., Cheng, Y., Jiang, J., and Lei, F. (2016). Characterization of Lignins from Sugarcane Bagasse Pretreated with green Liquor Combined Ethanol and Hydrogen Peroxide. *BioRes* 11, 3191–3203. doi:10.15376/biores.11.2.3191-3203

Decontamination of Mixed Paper and Plastic Municipal Solid Waste Increases Low and High Temperature Conversion Yields

Rebecca M. Brown[1]*, Amber N. Hoover[2], Jordan L. Klinger[2], Bradley D. Wahlen[1], Damon Hartley[3], Hyeonseok Lee[4] and Vicki S. Thompson[1]

[1]Biological Processing, Idaho National Laboratory, Idaho Falls, ID, United States, [2]Biomass Characterization, Idaho National Laboratory, Idaho Falls, ID, United States, [3]Operations Research and Analysis, Idaho National Laboratory, Idaho Falls, ID, United States, [4]Chemical Separations, Idaho National Laboratory, Idaho Falls, ID, United States

With the implementation of China's Green Fence Policy and the following National Sword Policy, there is a need to divert previously accepted waste materials away from the landfill. Mixed plastic and paper wastes that are too contaminated to be economically recycled can be used for conversion into fuels and products. The effect of common contaminants present in waste streams must be determined to make municipal solid waste (MSW) a viable alternative to agricultural feedstocks for conversion. In this study, MSW was sourced from a dual stream materials recovery facility (MRF) in Emmet County, Michigan and characterized *via* mass balance. The most common contaminants in mixed paper and plastic were quantified and targeted for decontamination when mixed paper was explored for low temperature conversion pathways and plastics for high temperature conversion pathways. Ink, stickies, and plastic contamination were sorted out of the mixed paper stream and did not have an impact on sugar yields during enzymatic hydrolysis (EH). Although no improvement in yield was found, it was noted that copy paper within the mixed paper stream had an elevated pH and higher concentration of fermentation inhibitors, suggesting that intrinsic properties of some paper types may not be ideal for EH and fermentation conversion. Dilute alkaline pretreatment and mechanical refining of mixed paper increased the EH yield of mixed paper, suggesting this previously established process could be used as a decontamination method. "Dirt" and particulates were washed from mixed plastic using either an aqueous detergent or a non-aqueous chemical washing method. Liquid oil yields were increased during microwave assisted fast pyrolysis. All decontamination techniques met the cost target of less than $30/dry ton with plastic decontamination ranging from $18.16 to $24.81/dry ton. Because dilute alkaline pretreatment and mechanical refining is considered part of the conversion process, the decontamination cost during feedstock preprocessing was considered $0/dry ton.

Keywords: enzymatic hydrolysis, pyrolysis, bio-oil, dimethyl ether (DME), dilute alkaline pretreatment

INTRODUCTION

The waste and recycling industry in the United States has drastically changed since China implemented the Green Fence and National Sword policies. Due to these policy changes, recycling programs in many areas were scaled back or completely discontinued (Beitsch, 2019). The waste materials that were previously imported into China are now accumulating at materials recovery facilities (MRFs) in the US and are often too contaminated or expensive to recycle. Because these materials represent a zero or negative value, they are eventually landfilled. The US Environmental Protection Agency (EPA) estimated that about 27 million tons of plastic and 17 million tons of paper were landfilled in the US in 2018 (EPA, 2018). These MSW fractions could potentially be diverted from the landfill and used as feedstocks for conversion into value-added fuels and products via low temperature and high temperature pathways.

Because MSW paper closely resembles lignocellulosic biomass, low temperature conversion processes can be used to screen the performance of these materials. Enzymatic hydrolysis is a low temperature conversion method traditionally used for agricultural biomass, such as corn stover, that makes their sugars available for fermentation into fuels and products. Due to the recalcitrance of many agricultural feedstock types, a pretreatment step is often needed to remove lignin and make cellulose more accessible to the enzymes used in enzymatic hydrolysis (Avila-Lara et al., 2015).

MSW paper has been found to be an economically viable feedstock for biochemical conversion (Wang et al., 2013). Previous studies have shown that blending mixed paper waste with corn stover can lower costs while maintaining sugar yield in ionic liquid pretreatment and enzymatic hydrolysis (Sun et al., 2015). However, more recent studies have shown that MSW paper had lower enzymatic hydrolysis yields compared to corn stover and corn stover/paper blends (Li et al., 2017; Thompson et al., 2019). This could be indicative of some type of inhibition, likely due to the presence of contaminants.

Alternately, MSW plastics are polymers of chemical building blocks such as ethylene and propylene and are rich in carbon-to-carbon bonds. These bonds are difficult to break biologically, and the monomer units are not suitable for fermentation. Pyrolysis is a high temperature process for converting biomass to fuels and would be more suitable for plastics. Fast pyrolysis is a high temperature degradation process that occurs between 450–700°C in the absence of oxygen. During this process, biomass is converted to liquid bio-oil, solid char, and gas. Bio-oil produced from this process can be further refined into fuels or chemicals (Zhang et al., 2019). The chemical composition of the bio-oil varies widely depending on reaction conditions and feedstock type. In addition, gaseous products rich in hydrocarbons can be used for energy recovery (Sipra et al., 2018).

There are many factors that can render MSW plastic unsuitable for traditional mechanical recycling. MSW plastic is a heterogenous mixture of resin types that are often contaminated with exogenous materials such as food residue, chemicals, metal, and glass (Qureshi et al., 2020). Heavily contaminated plastic

FIGURE 1 | Flow diagram depicting MSW sample preparation and experimentation.
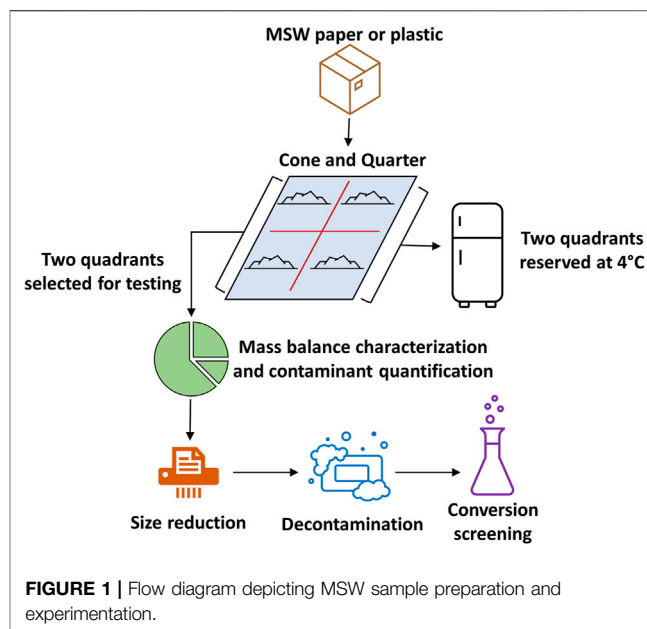
waste cannot be recycled and is usually landfilled or incinerated. Degradation caused by factors like UV radiation and temperature conditions can also make plastic unsuitable for recycling (Shah et al., 2008). Pyrolysis can tolerate high levels of contamination and can convert degraded plastic products to fuels and chemicals. Although pyrolysis can tolerate a wider array of feedstock types and contaminants, it is possible that these contaminants can negatively affect conversion yields. For example, MSW may contain large amounts of alkali metals, which can cause cracking reactions that result in a higher yield of gaseous products and a lower yield of liquid oil products (Wang et al., 2015; Alcazar-Ruiz et al., 2021).

This is the first study to investigate the effect of decontamination methods to increase conversion yields of MSW. Low and high temperature conversion methods were used to assess the impact of common contaminants on the conversion of mixed MSW paper and plastic, respectively. Decontamination strategies for the paper and plastic streams were developed and analyzed using enzymatic hydrolysis and microwave assisted fast pyrolysis. The added cost of decontamination to preprocessing of MSW is analyzed and compared to corn stover.

MATERIALS AND METHODS

Sampling and Characterization

Municipal solid waste (MSW) samples were sourced from a materials recovery facility (MRF) in Emmet County, Michigan through Resource Recycling Systems (RRS). The samples were non-recyclable residuals that were sorted from dual stream recycling collection. Mixed paper and mixed plastic waste streams were received at Idaho National Laboratory in Idaho Falls, Idaho and refrigerated at 4°C for future experimentation. Approximately 21.7 kg of mixed paper and 23.5 kg of mixed

FIGURE 2 | Representative images of MSW during sampling and sorting. Plastic as received **(A)** and coned and quartered **(B)**. Plastic was sorted into non-plastic contaminants **(C)**, films and baggies **(D)**, food containers **(E)**, bottles **(F)**, other **(G)**, and durable goods **(H)**.
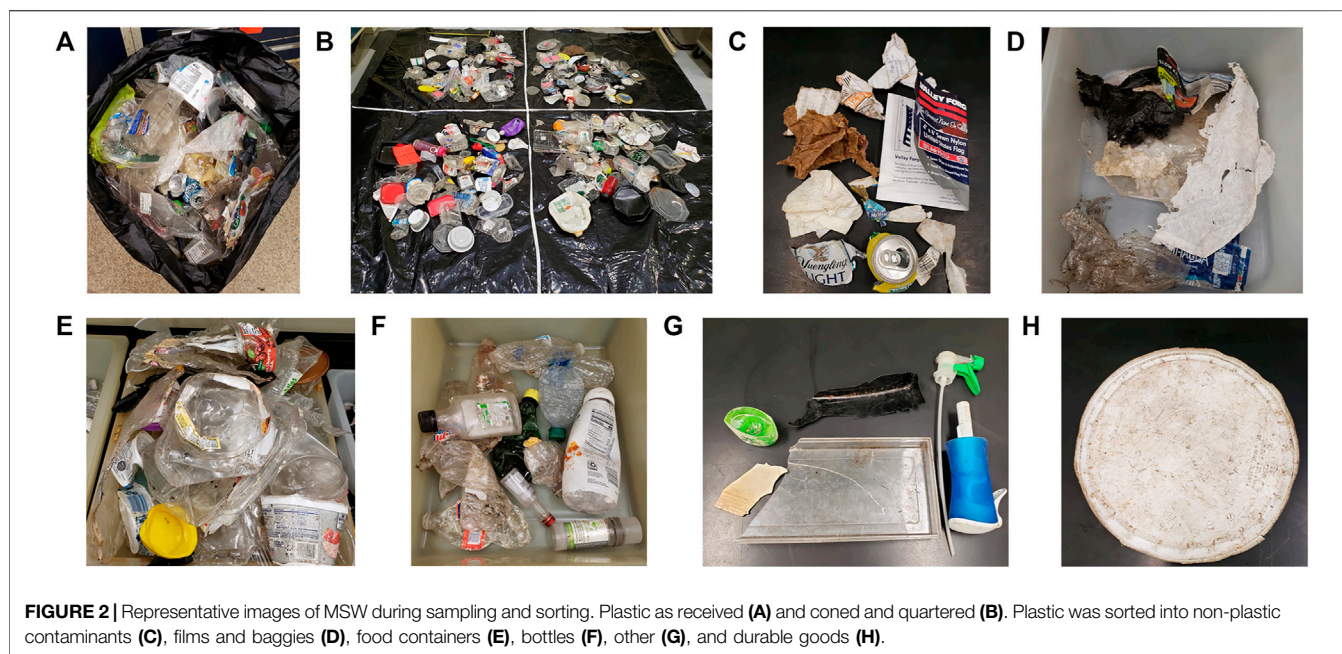
plastic was received. The paper and plastic MSW streams were mixed, coned, and quartered separately on a large plastic tarp. Two quadrants were sampled for characterization and experimentation (8.5 kg mixed paper and 12.2 kg mixed plastic). The remaining two quadrants were reserved for future experimental needs (**Figure 1**). The samples were air dried at room temperature for 24 h in a fume hood prior to sorting. Mass balance characterization of the samples was performed by first sorting into distinct product types (**Figure 2**). Paper samples were sorted into one of six categories: newspaper/office paper, food containers, cardboard, glossy/coated, other paper, and non-paper contaminants (e.g., glass, textiles, aluminum cans). Plastic samples were also sorted into one of six categories: food containers, bottles, durable goods, films, other plastic, and non-plastic contaminants (e.g., glass, aluminum cans, paper products). Plastic waste was further sorted by plastic type using the plastic identification number printed on the product. If no plastic identification number was visible or available, the plastic was sorted into a category based on similar product types. The mass of each plastic type was measured on a standard laboratory balance and used to calculate the mass balance.

During sorting, common contaminants were visually identified in each waste stream for further quantification. Common contaminants in paper and plastic waste fractions were quantified by counting the pieces of waste that contained contamination. Paper contaminants were sorted into the following categories: glossy coatings, food residue, ink, stickies (adhesives or glues), and staples. Plastic contaminants were sorted into the following categories: food residue, "dirt" and labels/thin films. "Dirt" contamination was defined as a coating of particulate that is likely a complex mix of residual container contents (e.g., food, liquids, chemicals) that leaked and had contact transfer from more heavily contaminated materials. Pieces of waste that contained multiple contaminants

simultaneously were quantified separately from waste that contained only a single contamination type.

Size Reduction

Mixed paper and plastic samples were initially shredded to 0.25 inches using a TaskMaster TM8500 industrial shredder (Franklin-Miller, Livingston, NJ, United States). Shredded paper samples were split using a custom rotary splitter and size reduced using a Model 4 Wiley knife mill (Thomas Scientific, Swedesboro, NJ, United States) to pass through a 6 mm screen. The 6 mm paper samples were used for dilute alkaline pretreatment and mechanical refining followed by enzymatic hydrolysis. A portion of the 6 mm samples were re-fed through the Wiley mill to pass through a 2 mm screen. The 2 mm paper samples were fed directly to enzymatic hydrolysis without further pretreatment. The shredded plastic samples were size reduced to pass through a 2 mm screen using an M24M-30e industrial crumbler rotary shear (Forest Concepts, Auburn, WA, United States). Oversized particles were collected and continuously re-fed through the crumbler until they were able to pass through a 2 mm screen.

Plastic, Ink, and Stickies Decontamination

The impact of plastic contamination within the mixed paper stream was investigated by sorting. All non-paper materials were removed from the mixed paper waste prior to size reduction. Plastic contaminants were size reduced separately from paper samples. Based on the mass balance characterization results (**Section 3.1**), 1.42 wt% plastic contaminants were added back to a portion of the size reduced paper.

The impact of ink contamination was investigated using two common paper types found within the mixed paper samples: newspaper and copy paper. Samples without ink contamination were produced by manually cutting out un-printed regions of
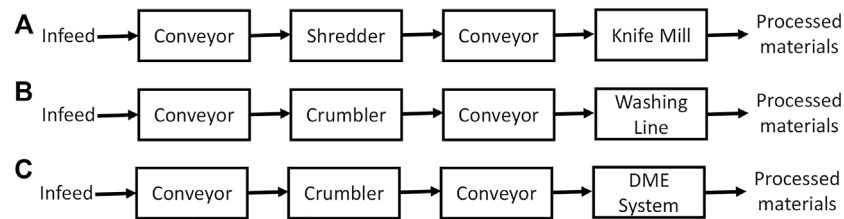
FIGURE 3 | Process flows for feedstock pre-processing unit operations. Paper size reduction **(A)**, plastic size reduction and detergent washing-drying **(B)**, and plastic DME-based washing **(C)**.

MSW copy paper and newspaper. Samples with ink were produced using the same paper sources that were visibly contaminated with ink. As a control, pristine paper samples were produced from brand new copy paper and newspaper that had never been printed on.

The impact of stickies contamination was investigated with cardboard food containers and packaging materials (cereal boxes, six-pack carriers, etc.). Samples with stickies were created by manually cutting out portions of cardboard packaging that contained visible adhesives or glue. Samples without stickies were produced using the same cardboard that did not have visible adhesives or glue. Pristine cardboard samples were produced using brand new cardboard boxes that did not contain visible stickies contamination.

Dilute Alkaline Pre-treatment

30 g of MSW paper samples were dilute alkaline pre-treated in triplicate with 7% (w/w) NaOH at 8% solids loading. The NaOH was diluted with water in a 1-L polypropylene (PP) flask before being inoculated with paper samples. The flasks were incubated at 85°C in a shaking water bath rotating at 100 rpm for 2 h and were manually mixed every 15 min. The flasks were removed from the water bath and allowed to cool at room temperature for 1 h. After cooling, the samples were filtered through a PP fabric filter to remove particles down to 100 microns (McMaster-Carr, Elmhurst, IL, United States) with 4-L vacuum flasks. The paper samples were removed from the PP filter and rinsed twice with 1 L of water for 15 min. The rinsed paper was filtered a second time using the same procedure mentioned above. The pre-treated paper was recovered, and the pH of the material was estimated using pH strips. Replicates were combined into a single composite sample for subsequent analysis. The pre-treated material was dried at 40°C overnight to determine the moisture content. The dilute alkaline pre-treatment liquor was reserved, and sugar concentrations removed during pre-treatment were determined with ion chromatography (IC). Sugars lost during pre-treatment were below the IC limit of detection and were therefore not accounted for in yield calculations. Dilute alkaline pre-treated paper samples were mechanically refined using a Laboratory Beater PFI Mill (Techlab Systems, Itasca, IL, United States) at 4,000 revolutions prior to enzyme hydrolysis.

Low Temperature Conversion

The chemical composition of untreated MSW was measured according to National Renewable Energy Laboratory's (NREL) Laboratory Analytical Procedure for standard biomass analysis (Sluiter et al., 2012). The conversion performance of mixed paper samples was screened using the measurement of sugar yield in enzymatic hydrolysis either with or without dilute alkaline pre-treatment and PFI milling. The percent solids loading of each reaction was decreased to 6% to enable thorough mixing and equal distribution of sodium azide. Enzymatic hydrolysis was performed in triplicate according to the NREL procedure (Selig et al., 2008) using Cellic CTec2 (Novozymes, Franklinton, NC, United States) loaded at 40 mg/g dry weight of biomass and Cellic HTec2 (Novozymes, Franklinton, NC, United States) loaded at 4 mg/g dry weight of biomass. The reactions were incubated at 50°C for 5 days. The hydrolysates were filtered through a 0.22 μm filter plate (MilliporeSigma, Burlington, MA, United States) and sugar concentrations were measured *via* high pressure liquid chromatography (HPLC). Percent yield achieved during enzymatic hydrolysis was calculated with the following equation:

$$\% \ yield = \frac{sugar \ solubilized \ during \ EH}{sugar \ present \ in \ untreated \ MSW} \times 100$$

The presence of fermentation inhibitors was investigated with newspaper, copy paper, and cardboard hydrolysates. HPLC was performed to determine the concentration of acetic acid, levulinic acid, furfural, and 5-hydroxymethylfurfural (HMF).

Detergent and Chemical Washing

10 g of size reduced plastic particles (2 mm) were loaded into a 250 ml Erlenmeyer flask containing 100 ml water. A few drops of dawn dish soap were added, and the flask was placed into a 40°C shaking incubator rotating at 150 rpm for 1 h. The liquid was removed by gravity filtration through filter paper (Whatman, Florham Park, NJ, United States). The washed plastic was rinsed twice by submerging the particles in fresh water and incubating in a 40°C shaking incubator for 1 h. The liquid again was removed by gravity filtration through filter paper. Rinsed plastic was dried overnight in a 40°C oven.

FIGURE 4 | Mass balance of mixed paper product type **(A)**, mixed plastic product type **(B)**, and plastic type **(C)**.
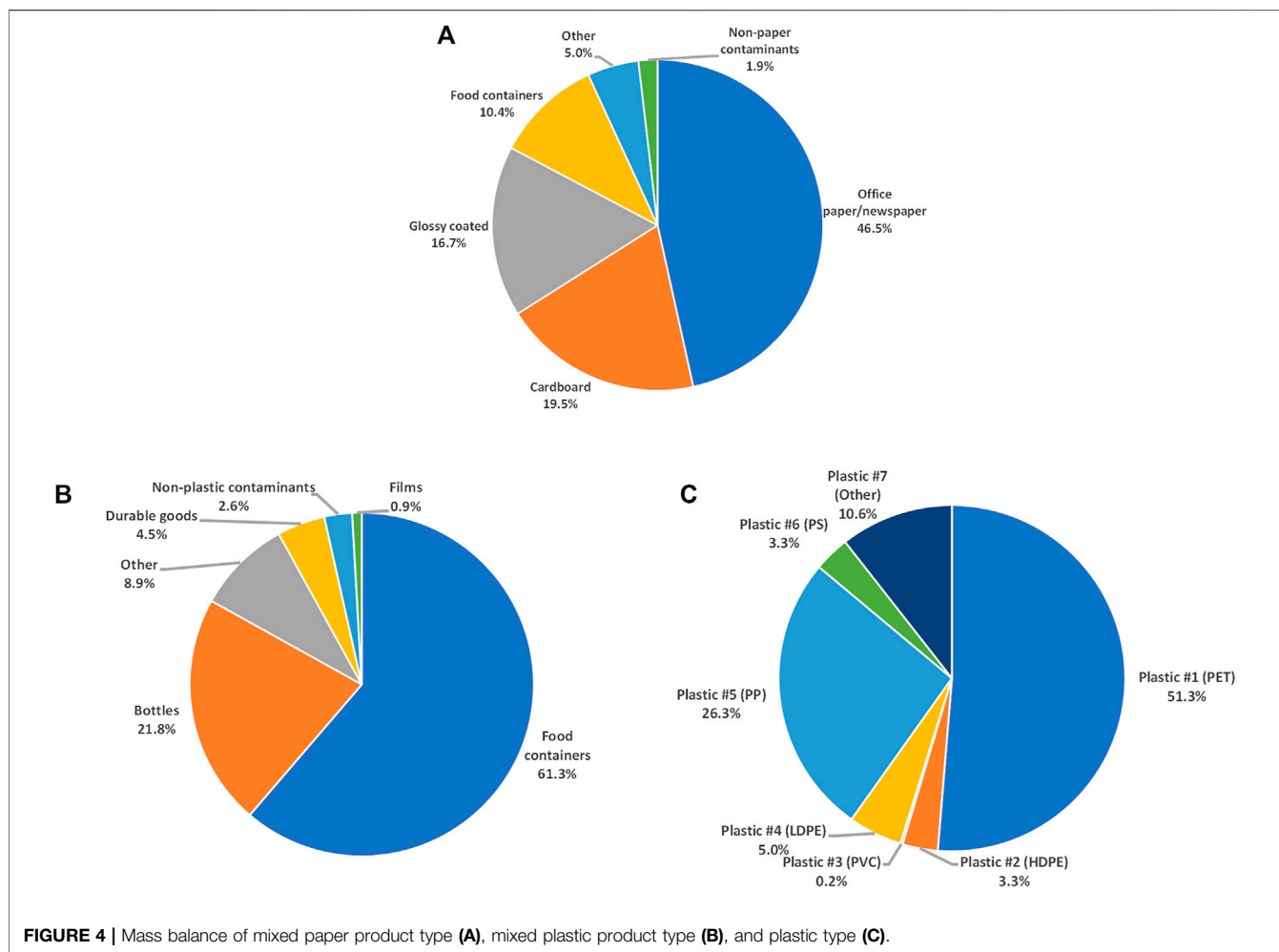
TABLE 1 | Quantification of mixed paper intrinsic contaminants.

Category	Contaminant	Quantity (pieces of MSW)
Single contaminant	Ink	243
	Glossy	24
	Stickies	13
	Other	3
	Food	1
	Staples	0
Multiple contaminants	Ink + stickies	24
	Glossy + stickies	21
	Ink + staples	13
	Glossy + staples	3
	Glossy + food	1
	Glossy + food + stickies	1
	Total	347

A laboratory-scale condensable solvent system has been developed based on a MiniMeP hydrocarbon extraction platform (ExtractionTek Solutions, Wheat Ridge, CO, United States) for use with dimethyl ether (DME) as the working solvent. To prevent seal and gasket failures, the system was modified in accordance with ASTM specification D7901. The DME within this system operates in a closed loop, with liquified DME solvent returned to the operating tank after extraction and decontamination. The solvent transfers through the chilled injection coil to the extraction vessel, where the solvent diffuses into the MSW material. Liquified DME, water, and extracted contaminants is then transferred to the collection vessel and expansion vessel, where heat is supplied to drive the vaporization of solvent, permitting separation and recovery of DME from contaminants. Vaporized solvent is returned to the solvent tank through a recovery pump and discharge coil. This decontamination process operates under 85 psi, and temperature range between min. −4°C (at injection coil) and max. 35°C (at expansion vessel). Approximately 70 g of mixed plastic was washed with DME inside a nylon bag by recirculation for 2 h.

High Temperature Conversion

The conversion performance of mixed plastic samples was screened using microwave assisted fast pyrolysis. One-gram pellets of washed and unwashed plastic were made using a benchtop manual hydraulic press (Carver, Wabash, IN, United States). The plastic was weighed

TABLE 2 | Quantification of mixed plastic contaminants.

Category	Contaminant	Quantity (pieces of MSW)
Single contaminant	Dirt	589
Multiple contaminants	Dirt + labels	286
	Dirt + food + labels	10
	Dirt + food	6
	Total	891

using a laboratory scale and loaded into a pellet die (approximately 16 mm square with 4 mm rounded corners). The die and plastic samples were heated together in an oven at 150°C for 15 min and compressed at 4,000 psi (20,000 lb-f). Two pellets (~2 g) were loaded into a pre-weighed quartz tube (26 mm diameter, 1 m length) assembly and loaded into a microwave assisted pyrolysis instrument that was previously described (Klinger et al., 2015; Klinger et al., 2018). The oxygen was purged from the quartz tube using nitrogen gas. A portion of the quartz tube was packed with dry ice snow to condense vapor to liquid oil. The samples were heated to approximately 500°C and allowed to devolatilize completely. The pyrolysis gas yield was measured by a digital gas flow meter (Omega Engineering, Norwalk, CT, United States) and gas analyzer (Nova Analytical Systems, Hamilton, ON, Canada) equipped with sensors to detect O_2, CO, CO_2, CH_4, and total hydrocarbons. The tube assembly was removed from the instrument, allowed to cool, and weighed. The remaining char present in the quartz tube was removed and weighed using a laboratory balance. The percent yield of gas, char, and liquid oil were calculated gravimetrically.

Unwashed, detergent washed, and DME washed samples were milled using a Retsch ZM200 (Haan, Germany) to pass a 0.2 mm screen and then sent to Huffman Hazen Laboratories (Golden,

CO, United States) for analysis. Samples were dried at 60°C in a forced air oven overnight. Total ash was determined by holding the sample at 750°C in air for 8 h. Inorganic element analysis was completed following ASTMs D3682 and D6349.

Techno-Economic Assessment

Because corn stover can potentially be available at a feedstock cost as low as $30/ton, we targeted this price as an acceptable cost for decontamination to make the material cost competitive with corn stover (Langholtz et al., 2016). A techno-economic assessment (TEA) was conducted to determine the costs of decontamination methods. The TEA examined the complete pre-processing for size reduction and decontamination of non-recyclable plastic and paper residuals from an MRF. A total of four scenarios were evaluated, including: 1) size reduction of paper without old corrugated cardboard (OCC); 2) size reduction of paper including OCC; 3) decontamination of plastic using detergent washing and drying; and 4) decontamination of plastic using the DME process. For each scenario, the total estimated cost included both fixed and operational costs. Fixed costs, that include capital recovery, insurance, and taxes, were estimated following the guidelines published in Turhollow et al. (2009). Operational estimated costs include energy and labor costs to operate equipment.

Figure 3A presents the process flow designed for the size reduction process to reduce particle size of recycled paper to 6 mm. RRS provided the mixed paper tonnage for an appropriately sized MRF (34,125 dry tons/year). It was assumed that processed materials would only include mixed paper recovered from an MRF and would be size reduced and decontaminated on-site prior to shipping to a conversion facility. For both the shredding and knife milling process, it was assumed that there was a dry matter loss of 1%. For scenario four, the process flow and assumptions are identical to scenario three.
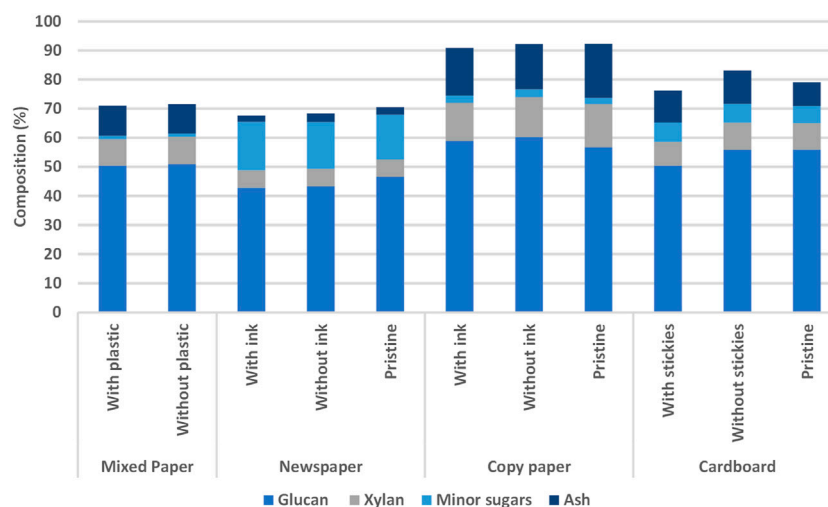
FIGURE 5 | Compositional analysis of MSW paper types. The balance of composition (not shown) consists of glucan, xylan, lignin, extractives, and minor sugars (arabinan, mannan, and galactan).
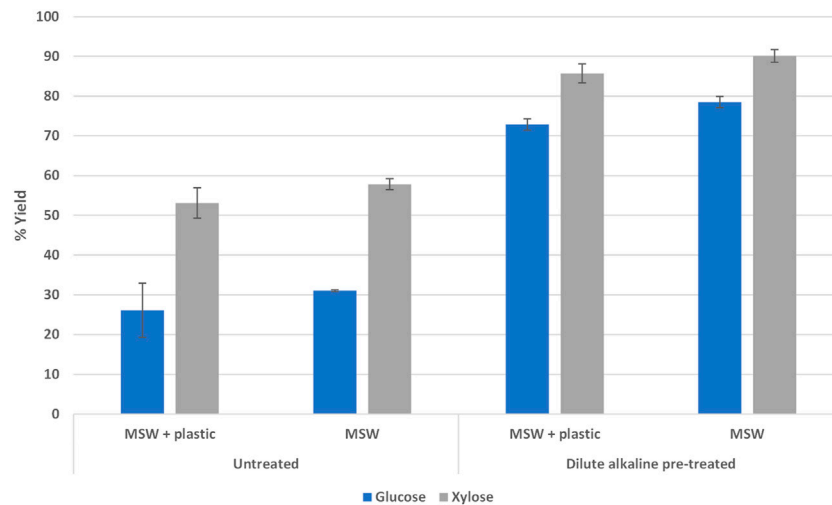
FIGURE 6 | Dilute alkaline pre-treatment and PFI milling increased sugar yields in enzymatic hydrolysis.
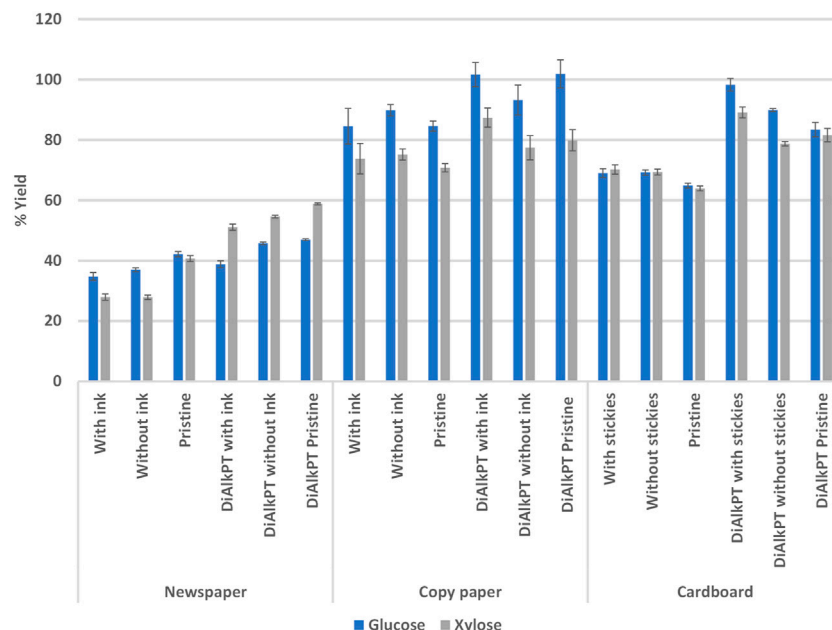
FIGURE 7 | Enzymatic hydrolysis yields were not impacted by the presence of ink and stickies. DiAlkPT, dilute alkaline pre-treated.

However, in this scenario the OCC fraction was included in the infeed.

The design of the system for plastic size reduction and decontamination is presented in **Figure 3B**. This system was designed to process about 3,500 dry tons of plastic annually, assuming 200 operation days a year and 10 h operating time per day. The project collaborators from RRS provided tonnage of plastics produced by a typical MRF that operates with good economics of scale and it was assumed that each MRF would pre-process and decontaminate its own materials prior to sending them to a conversion facility. It was assumed that plastic will be

ground by a M24M-30e industrial crumbler rotary shear (Forest Concepts, Auburn, WA, United States) to 2 mm before going to the decontamination step.

Figure 3C presents the design for a pre-processing system that includes DME-based plastic decontamination with 3,500 dry tons annual capacity. It was assumed that plastic will be ground by a M24M-30e industrial crumbler rotary shear (Forest Concepts, Auburn, WA, United States) to 2 mm before sending to the DME decontamination tank. It also was assumed that about 10% of the DME solution will be used to remove the contaminants and water from the recycled plastic.
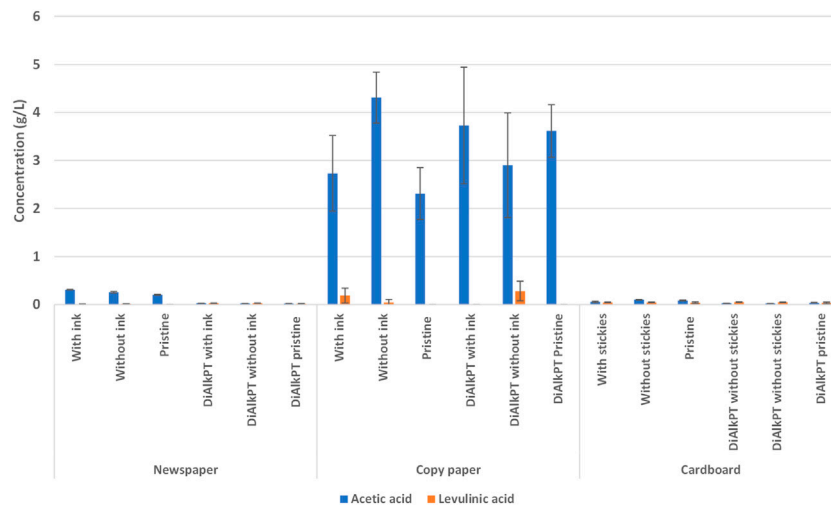
FIGURE 8 | Copy paper had an elevated concentration of the fermentation inhibitor acetic acid during enzymatic hydrolysis. DiAlkPT, dilute alkaline pre-treated.
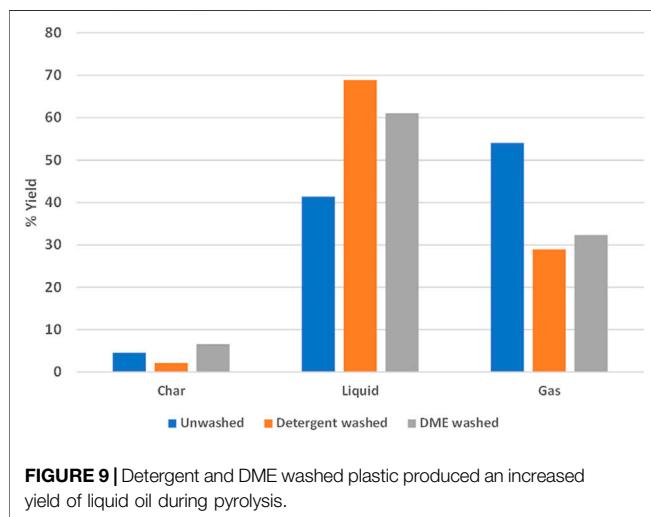
FIGURE 9 | Detergent and DME washed plastic produced an increased yield of liquid oil during pyrolysis.

RESULTS AND DISCUSSION

Mass Balance Characterization

The obtained sample of mixed paper MSW was sorted into product types to characterize mass balance (**Figure 4A**). Office paper and newspaper make up most of the paper fraction (46.5%), followed by cardboard (19.5%), glossy coated (16.7%), food containers (10.4%), and other paper (5.01%).

Non-paper contaminants (plastic, metal, glass, and other) make up 1.9% of the total mass balance of mixed paper MSW. Plastic makes up most (76.4%) of these non-paper contaminants, followed by metal (9.6%), glass (8.9%), and other (5.1%). The presence of glass and metal could be a potential cause of premature wear in process equipment or even damage equipment causing shutdowns for repairs, so they must be removed. The most common intrinsic contaminant present in paper was ink (68.1%), followed by stickies (14.4%), glossy

coatings (12.2%), staples (3.9%), and food (0.7%). Mixed paper contaminant data is summarized in **Table 1**.

The mixed plastic MSW sample was sorted into product types to characterize the composition (**Figure 4B**). Food containers made up most of the plastic fraction (61.3%), followed by bottles (21.8%), other plastic (8.9%), durable goods (4.5%), and films (0.9%). Plastic MSW was further sorted into plastic type using the identification number printed on the product (**Figure 4C**). The most common plastic types identified were polyethylene terephthalate (PET, 51.3%), followed by polypropylene (PP, 26.3%), other (10.6%), low-density polyethylene (LDPE, 5.0%), polystyrene (PS, 3.3%), high-density polyethylene (HDPE, 3.3%), and polyvinyl chloride (PVC, 0.2%).

Non plastic contaminants (paper, metal, glass, and other) made up 2.6% of the total mass balance of mixed plastic MSW. Paper makes up most (51.5%) of these non-plastic contaminants, followed by metal (29.3%), glass (16.1%), and other (3.1%). As described above, glass and metal could have downstream impacts such as equipment wear and trace amounts of metal catalyzing undesirable reactions during pyrolysis.

A contaminant coating labelled as "dirt" was present on 100% of the plastic received. The next most common contaminant was thin film labels, which were present on 33.2% of the plastic products. The least common contaminant was food residue, which was present on only 1.8% of the plastic products. Mixed plastic contaminant data is summarized in **Table 2**.

Low Temperature Conversion

The glucan, xylan, minor sugars (arabinan, mannan, and galactan), and ash contents of MSW paper are shown in **Figure 5**. Enzymatic hydrolysis was carried out to determine the impact of plastic contamination on sugar yields in untreated and dilute alkaline pre-treated mixed paper samples. It was notable that sugar yields for untreated paper were low, which could be indicative of hornification or surface treatments of the paper materials
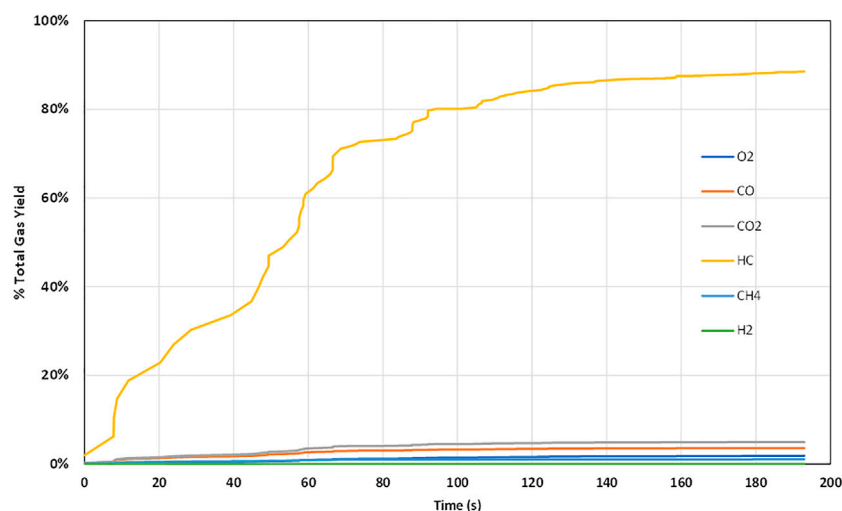
FIGURE 10 | Gaseous products of pyrolysis were mainly composed of hydrocarbons. HC, hydrocarbons.

TABLE 3 | Ash analysis of unwashed, detergent washed, and DME washed MSW plastic. Ash components are % of total ash content.

	Unwashed	Detergent washed	DME washed
Ash % (w/w)	2.59	1.68	1.87
Al as Al_2CO_3% (w/w)	6.02	4.06	4.92
Ca as CaO % (w/w)	15.76	19.24	21.54
Fe as Fe_2O_3% (w/w)	3.24	1.85	3.06
K as K_2O % (w/w)	0.72	0.25	0.44
Mg as MgO % (w/w)	4.81	6.42	3.04
Mn as MnO % (w/w)	0.03	0.02	0.03
Na as Na_2O % (w/w)	8.20	5.29	6.16
P as P_2O_5% (w/w)	0.61	0.85	0.19
Si as SiO_2% (w/w)	52.29	41.00	45.36
Ti as TiO_2% (w/w)	8.45	13.15	14.97
S as SO_3% (w/w)	1.04	1.49	1.33

(Fernandes Diniz et al., 2004). Glucose and xylose yields from EH were not increased when plastic contaminants were removed from mixed paper samples, but yields were increased when samples were dilute alkaline pre-treated and PFI milled.

Dilute alkaline pre-treatment is performed at a relatively low temperature and plastics could be problematic if higher temperatures pre-treatments were used. MSW paper without plastic contamination showed a 31% glucose yield and a 58% xylose yield. When that sample was dilute alkaline pre-treated and PFI milled, the glucose and xylose yields increased to 78% and 90%, respectively. Similarly, MSW paper with plastic contamination showed a 26% glucose yield and a 53% xylose yield. When that sample was dilute alkaline pre-treated and PFI milled, the glucose yield increased to 73% and the xylose yield increased to 86% (**Figure 6**). During the dilute alkaline pre-treatment process, it was noted that ink seemed to be present in the pre-treatment liquor and stickies coated the bottom of the

reaction flask, suggesting that the pre-treatment process could remove these contaminants present in paper.

Enzymatic hydrolysis was used to investigate the effect of ink contamination in newspaper and copy paper. The effect of stickies contamination was investigated with cardboard. Glucose and xylose yield during EH was not increased when ink contaminated paper was removed from the newspaper and copy paper fractions, nor when stickies contamination was removed from the cardboard fractions. The sugar yields of MSW newspaper, copy paper, and cardboard fractions were compared to brand new, pristine samples that did not contain ink and stickies. The results showed that the yield of pristine samples was not different than paper fractions found in MSW. Although no increase in yield was seen when ink or stickies were removed the MSW paper, the sugar yields were increased across all paper fractions when they were dilute alkaline pre-treated and PFI milled (**Figure 7**). Interestingly, higher yields were observed in pre-treated and PFI milled copy paper and cardboard samples that were contaminated with ink and stickies, respectively. Alkaline de-inking causes swelling and peeling of cellulose fibers (Pala et al., 2004). We hypothesize that the removal of ink and stickies observed during dilute alkaline pre-treatment resulted in more extensive fiber damage, resulting in an increased surface area that is vulnerable to enzyme attack. Future research will explore this phenomenon.

It was observed that dilute alkaline pre-treated and mechanically refined newspaper samples had a higher yield of xylose compared to glucose, while the opposite was true for copy paper and cardboard. Production processes used for different paper types result in differing composition and cellulose crystallinity. For example, copy paper has a high cellulose content and low hemicellulose content, while newspaper has a higher hemicellulose content and lower cellulose content (Guerfali et al., 2015). The ratio of newspaper or copy paper within a waste paper stream will impact the corresponding yield of glucose and xylose during EH.

TABLE 4 | Breakdown of costs for size reduction without OCC (scenario 1) and with OCC (scenario 2) pre-processing unit operations.

Scenario 1		Scenario 2	
Equipment	Cost ($/dry ton)	Equipment	Cost ($/dry ton)
Conveyor	$0.23	Conveyor	$0.20
Shredder	$1.61	Shredder	$1.37
Conveyor to storage	$0.24	Conveyor to storage	$0.21
Knife mill	$3.16	Knife mill	$2.64
Total	**$5.25**	**Total**	**$4.41**

The bold values means the total preprocessing costs for the associated scenario

TABLE 5 | Breakdown of costs for detergent washing (scenario 3) and DME-based (scenario 4) pre-processing unit operations.

Scenario 3		Scenario 4	
Equipment	Cost ($/dry ton)	Equipment	Cost ($/dry ton)
Conveyor	$2.09	Conveyor	$2.09
Crumbler	$21.00	Crumbler	$21.00
Conveyor	$2.11	Conveyor	$2.11
Washing tank	$24.81	DME tank	$18.16
Total	**$50.01**	**Total**	**$43.36**

The bold values means the total preprocessing costs for the associated scenario

During initial enzymatic hydrolysis experiments with pristine and MSW copy paper fractions, it was noted that very low sugar yields were achieved. Further investigation revealed that these enzymatic hydrolysis reactions had an elevated pH that was outside the working range of the CTec2 and HTec2 enzymes (pH 5–5.55). Untreated copy paper samples had an average pH of 8.03 and dilute alkaline pre-treated copy paper had an average pH of 7.87. The concentration of citrate buffer was increased from 0.05 to 0.25 M to account for the elevated pH in subsequent EH experiments using copy paper. All newspaper and cardboard samples fell within the working pH range of the enzymes. The variation in these streams and the need to optimize reaction conditions has potential processing implications.

The presence of fermentation inhibitors in newspaper, copy paper, and cardboard hydrolysate samples was used to determine the potential impacts on downstream fermentation. HMF and furfural concentrations were undetectable in all paper fractions. The concentration of acetic acid was notably higher in copy paper samples compared to newspaper and cardboard, while levulinic acid was present in a very low concentration across all samples (**Figure 8**).

The combined pH and fermentation inhibitor data suggests that copy paper has intrinsic qualities that are not ideal for enzymatic hydrolysis and downstream fermentation. A variety of additives and chemicals are used in paper making to increase the brightness and whiteness of copy paper, as well as improving the mechanical and physical properties of the paper. We hypothesize that fillers, bleaching agents, and/or chemical pulping agents present in the copy paper are elevating the pH and concentration of fermentation inhibitors in these samples despite the presence of a 50 mM citrate buffer and 40 mM acetate (**Figure 8**) for buffering. For the copy paper EH, it was necessary to increase the citrate buffer concentration to 250 mM to eliminate the pH shift. Further investigation is needed to determine the potential sources of this phenomenon and to test the impacts of these inhibitor concentrations on fermentation efficiency.

High Temperature Conversion

Liquid oil products obtained from pyrolysis can be upgraded and used as a substitute for conventional fossil fuels (Zaman et al., 2017). Untreated mixed plastic waste produced about 5% char, 42% liquid oil, and 53% gas in microwave fast pyrolysis experiments while mixed plastic washed with detergent reduced char yields to 2%, increased liquid oil yields to 69%, and reduced gas yields to 29%. Mixed plastic washed with DME produced about 7% char, 61% oil, and 32% gas (**Figure 9**). These experiments were intended to quickly screen conversion performance of decontaminated materials. Therefore, the composition of the bio-oil was not determined. In the future, we hope to complete an in-depth investigation of the bio-oil and determine the mechanisms involved in increased oil production. A component of the "dirt" coating in unwashed plastic may have catalyzed cracking reactions that decreased liquid yields. During pyrolysis, it was noted that some types of plastic melted in the transfer tube prior to entry into the pyrolysis chamber and caused feeding problems in the system. Our DME decontamination approach is an effective, novel, and economically feasible method that does not create a wastewater stream.

The composition of gaseous products from pyrolysis of unwashed mixed plastic primarily contained hydrocarbons (**Figure 10**). This suggests that the "dirt" in unwashed plastic is catalyzing cracking reactions that break plastic into lighter hydrocarbons that decrease the liquid oil yields.

Alkali and alkaline earth metals (K, Na, Mg and Ca) are known to catalyze cracking reactions during pyrolysis (Wang et al., 2015). Initial ash analysis indicates that potassium or sodium may be the culprits although further testing is needed to verify this (**Table 3**).

Techno-Economic Assessment

The mixed paper materials that were tested benefitted from a dilute alkaline pre-treatment; however, since this TEA focused on the steps prior to low temperature pre-treatment process, it was not necessary to further decontaminate these materials. The primary contributors to pre-processing costs in paper size reduction without OCC (scenario one) were the knife mill and shredding operations. The overall cost of this pre-processing system (**Table 4**) is estimated at $5.25/dry ton. The inclusion of the OCC fraction (scenario two) into the system increases the annual infeed by 10%. Higher throughput translates in greater economies of scale to reduce the pre-processing costs (**Table 4**) by $0.84/dry ton. The mixed paper materials that were tested benefitted from a dilute alkaline pre-treatment; however, since this is part of the NREL low temperature pre-treatment process, it was not necessary to further decontaminate these materials. Therefore, the decontamination cost was $0/dry ton.

The total cost for the detergent washing system (scenario one) was about $50.01/dry ton (2021$), assuming 1% of dry matter loss in the size reduction step. The washing line combined the washing and drying stages of the pre-processing operation. This unit operation contributed about $24.81/dry ton, nearly 50% of the overall costs (**Table 5**). The crumbler accounted for $21.00/dry ton while the conveyors accounted for $2.09/dry ton. The costs for the system were also influenced by low material throughput of approximately 1.75 tons per hour. The total cost for the DME-based washing system (scenario two) was about $43.36/dry ton, assuming 1% of dry matter loss in the size reduction step (**Table 5**). Compared to the detergent washing-drying process, the DME-based pre-processing costs $6.65 less, mainly due to the lower energy cost in the DME tank as compared to the washing line used in the conventional system. In this system, the crumbler accounts for $21.00/dry ton while the DME system contributes $18.16/dry ton to overall pre-processing costs.

CONCLUSION

In the United States, MSW that is too contaminated or expensive to recycle was exported to China prior to the Green Fence and National Sword policies. The United States lost a destination for much of its contaminated wastes due to these policies. Many cities were forced to discontinue or scale back their recycling programs, resulting in many waste materials being landfilled. Paper and plastic fractions of MSW could potentially be diverted from the landfill and used as feedstocks for conversion to fuels and chemicals. MSW could represent a viable alternative to agricultural residues for biofuel production if low-cost methods for decontamination can be developed.

Although plastic, ink, and stickies contamination within the mixed paper stream did not have a negative impact on enzymatic hydrolysis yield, dilute alkaline pre-treatment and mechanical refining was able to increase yields. When certain paper types within the mixed paper samples were tested, it was observed that copy paper had an elevated pH and increased concentration of fermentation inhibitors. The increased pH had an adverse impact on enzymatic hydrolysis, but it could be compensated for by increasing the reaction buffer concentration. The effect of elevated concentration of fermentation inhibitors was not observed in our experiments but is hypothesized to have an impact in downstream fermentation processes. We hypothesize that additives such as fillers, bleaching agents, and/or pulping agents are causing this phenomenon.

Removal of "dirt" and particulate contamination in mixed plastic MSW with detergent and chemical washing resulted in an increase in liquid oil products during pyrolysis. This is the first study to employ an affordable, non-aqueous decontamination system for MSW that does not create a wastewater problem. DME washing is a promising decontamination technique that can be used for a wide range of waste materials. Further research is needed to determine the impacts of DME decontamination on the conversion of other waste streams (e.g., paper, yard waste).

The major gaseous products produced during pyrolysis were light hydrocarbons, suggesting that "dirt" in unwashed MSW is catalyzing cracking reactions and resulting in lower liquid yields. Initial ash analysis studies suggest that potassium is catalyzing cracking reactions during pyrolysis and decreasing oil yield. The impacts of potassium on pyrolysis are well-known. Future experimentation should focus on determining the composition of bio-oil from washed waste and investigating the mechanism behind increased oil yield.

The washing techniques developed for plastic decontamination ranged from $18.16 to $24.81/dry ton. This fell below the cost target of $30/dry ton, making the material cost competitive with corn stover. Dilute alkaline pre-treated paper did not require further decontamination processes, making the cost $0/dry ton for any decontamination prior to pretreatment. The cost of paper preprocessing ranged from $4.41 to $5.25/dry ton.

Further study is required to determine the culprit behind elevated pH and fermentation inhibitor concentration in copy paper, as well as decreased oil yield in unwashed plastic. In summary, dilute alkaline pre-treatment and washing methods have been shown to be effective decontamination strategies to increase conversion yields of mixed paper and plastic MSW, respectively.

DATA AVAILABILITY STATEMENT

The raw data supporting the conclusion of this article will be made available by the authors, without undue reservation.

AUTHOR CONTRIBUTIONS

FUNDING

ACKNOWLEDGMENTS

REFERENCES

Alcazar-Ruiz, A., Ortiz, M. L., Sanchez-Silva, L., and Dorado, F. (2021). Catalytic Effect of Alkali and Alkaline Earth Metals on Fast Pyrolysis Pre-treatment of Agricultural Waste. *Biofuel Bioprod. Biorefin.* 15 (5), 1473–1484. doi:10.1002/bbb.2253

Ávila-Lara, A. I., Camberos-Flores, J. N., Mendoza-Pérez, J. A., Messina-Fernández, S. R., Saldaña-Duran, C. E., Jimenez-Ruiz, E. I., et al. (2015). Optimization of Alkaline and Dilute Acid Pretreatment of Agave Bagasse by Response Surface Methodology. *Front. Bioeng. Biotechnol.* 3, 146. doi:10.3389/fbioe.2015.00146

Beitsch, R. (2019). A Move by China Puts U.S. Small-Town Recycling Programs in the Dumps. Washington Post. Available at: https://www.washingtonpost.com/national/health-science/a-move-by-china-puts-us-small-town-recycling-programs-in-the-dumps/2019/01/18/6a043642-1825-11e9-8813-cb9dec761e73_story.html.

EPA (2018). National Overview: Facts and Figures on Materials, Wastes, and Recycling. Available at: https://www.epa.gov/facts-and-figures-about-materials-waste-and-recycling/national-overview-facts-and-figures-materials#NationalPicture

Fernandes Diniz, J. M. B., Gil, M. H., and Castro, J. A. A. M. (2004). Hornification? its Origin and Interpretation in wood Pulps. *Wood Sci. Technol.* 37 (6), 489–494. doi:10.1007/s00226-003-0216-2

Guerfali, M., Saidi, A., Gargouri, A., and Belghith, H. (2015). Enhanced Enzymatic Hydrolysis of Waste Paper for Ethanol Production Using Separate Saccharification and Fermentation. *Appl. Biochem. Biotechnol.* 175 (1), 25–42. doi:10.1007/s12010-014-1243-1

Klinger, J., Bar-Ziv, E., Shonnard, D., Westover, T., and Emerson, R. (2015). Predicting Properties of Gas and Solid Streams by Intrinsic Kinetics of Fast Pyrolysis of wood. *Energy Fuels* 30, 318–325. doi:10.1021/acs.energyfuels.5b01877

Klinger, J. L., Westover, T. L., Emerson, R. M., Williams, C. L., Hernandez, S., Monson, G. D., et al. (2018). Effect of Biomass Type, Heating Rate, and Sample Size on Microwave-Enhanced Fast Pyrolysis Product Yields and Qualities. *Appl. Energ.* 228, 535–545. doi:10.1016/j.apenergy.2018.06.107

Langholtz, M. H., Stokes, B. J., and Eaton, L. M. (2016). *2016 Billion-Ton Report: Advancing Domestic Resources for a Thriving Bioeconomy, Volume 1: Economic Availability of Feedstocks.* Oak Ridge, Tennessee: U.S. Department of Energy. doi:10.2172/1271651

Li, C., Liang, L., Sun, N., Thompson, V. S., Xu, F., Narani, A., et al. (2017). Scale-up and Process Integration of Sugar Production by Acidolysis of Municipal Solid Waste/corn stover Blends in Ionic Liquids. *Biotechnol. Biofuels* 10, 13. doi:10.1186/s13068-016-0694-8

Pala, H., Mota, M., and Gama, F. M. (2004). Enzymatic versus Chemical Deinking of Non-impact Ink Printed Paper. *J. Biotechnol.* 108 (1), 79–89. doi:10.1016/j.jbiotec.2003.10.016

Qureshi, M. S., Oasmaa, A., Pihkola, H., Deviatkin, I., Tenhunen, A., Mannila, J., et al. (2020). Pyrolysis of Plastic Waste: Opportunities and Challenges. *J. Anal. Appl. Pyrolysis* 152, 104804. doi:10.1016/j.jaap.2020.104804

Selig, M., Weiss, N., and Ji, Y. (2008). Enzymatic Saccharification of Lignocellulosic Biomass: Laboratory Analytic Procedure. NREL/TP-510-42629.

Shah, A. A., Hasan, F., Hameed, A., and Ahmed, S. (2008). Biological Degradation of Plastics: a Comprehensive Review. *Biotechnol. Adv.* 26 (3), 246–265. doi:10.1016/j.biotechadv.2007.12.005

Sipra, A. T., Gao, N., and Sarwar, H. (2018). Municipal Solid Waste (MSW) Pyrolysis for Bio-Fuel Production: A Review of Effects of MSW Components and Catalysts. *Fuel Process. Technol.* 175, 131–147. doi:10.1016/j.fuproc.2018.02.012

Sluiter, A., Hames, B., Ruiz, R., Scarlata, C., Sluiter, J., Templeton, D., et al. (2012). Determination of Structural Carbohydrates and Lignin in Biomass. Laboratory Analytical Procedure. NREL/TP-510-42618.

Sun, N., Xu, F., Sathitsuksanoh, N., Thompson, V. S., Cafferty, K., Li, C., et al. (2015). Blending Municipal Solid Waste with Corn stover for Sugar Production Using Ionic Liquid Process. *Bioresour. Technol.* 186, 200–206. doi:10.1016/j.biortech.2015.02.087

Thompson, V. S., Ray, A. E., Hoover, A., Emerson, R., Hartley, D., Lacey, J. A., et al. (2019). Assessment of Municipal Solid Waste for Valorization into Biofuels. *Environ. Prog. Sustain. Energ.* 39 (4), e13290. doi:10.1002/ep.13290

Turhollow, A. F., Jr, Webb, E., and Sokhansanj, S. (2009). Cost Methodology for Biomass Feedstocks: Herbaceous Crops and Agricultural Residues. ORNL/TM-2008-105. Oak Ridge National Laboratory.

Wang, L., Sharifzadeh, M., Templer, R., and Murphy, R. J. (2013). Bioethanol Production from Various Waste Papers: Economic Feasibility and Sensitivity Analysis. *Appl. Energ.* 111, 1172–1182. doi:10.1016/j.apenergy.2012.08.048

Wang, K., Zhang, J., Shanks, B. H., and Brown, R. C. (2015). The Deleterious Effect of Inorganic Salts on Hydrocarbon Yields from Catalytic Pyrolysis of Lignocellulosic Biomass and its Mitigation. *Appl. Energ.* 148, 115–120. doi:10.1016/j.apenergy.2015.03.034

Zaman, C. Z., Pal, K., Yehye, W. A., Sagadevan, S., Shah, S. T., Adebisi, G. A., et al. (2017). "Pyrolysis: A Sustainable Way to Generate Energy from Waste," in *Pyrolysis.* Editor M. Samer (London, United Kingdom).

Zhang, S., Yang, X., Zhang, H., Chu, C., Zheng, K., Ju, M., et al. (2019). Liquefaction of Biomass and Upgrading of Bio-Oil: A Review. *Molecules* 24 (12), 2250. doi:10.3390/molecules24122250

Using Incremental Changes to Convert Lignocellulosic Feedstocks to Cellulosic Ethanol

Michael G. Resch[1] and Brandon Emme[2]*

[1]National Renewable Energy Laboratory, Catalytic Carbon Transformation and Scale-Up Center, Golden, CO, United States, [2]ICM Inc., Technology Development, St. Joseph, MO, United States

One billion tons of biomass feedstocks have been identified for the production of renewable biofuels and biochemicals. This is one of the key carbon feedstocks to supply energy to the transportation sector for light duty, heavy duty and aviation fuels. Utilization of lignocellulosic feedstocks supports an improved energy security by reducing demand of petroleum imports, agricultural development, job creation, and reducing greenhouse gas emissions. To date, however, operational challenges have stymied the industrial production of large volumes of lignocellulosic-based fuels and chemicals. As a result, significant research investment has been led by the United States Department of Energy to understand and improve operational reliability at pioneer cellulosic biorefineries. In this perspective article lignocellulosic conversion technologies are described that have been adopted from the starch ethanol process. The developed process culminated in successful demonstration of 1,000-h integrated runs using several feedstocks, including switchgrass, energy sorghum, and two types of corn kernel fiber. This article highlights process development that solved several of the issues that plagued—and continue to plague—many in the cellulosic sugars space such as biomass feeding into equipment, high ash content, diversified co-product value, and others.

Keywords: biomass, biofuels (biodiesel, bioethanol, biogas), biochemicals and bioenergy, biochemical conversions, lignocelllulose saccharification, biorefineries

INTRODUCTION

Process Integration Approaches to Cellulosic Processing Design

The road to commercialization of lignocellulosic biomass to production of biofuels and chemicals has not been as easy as it was sold to investors a decade ago. At that time, [bio] catalyst costs in pretreatment and hydrolysis were considered the critical path to overcome the hurdles to commercialization. Through significant efforts and good science, producers realized dramatic cost reductions in biocatalyst (enzymes and yeast) in the years that followed. Those milestones were followed by a handful of cellulosic plant groundbreakings, largely using engineering and technology originally developed for the pulp and paper industry, where the process design seemed intrinsically obvious, to fill out the rest of the process design around the key technologies.

Unfortunately, these pioneer plants struggled to realize their design capacity. Consequently, policy incentives remain inconsistent and the second round of cellulosic capacity buildout has not occurred. Many potential producers and investors, seeking to "be first to be second," feel the correct first-of-its-kind cellulosic process is still not proven out, noting that significant risks remain in realizing design uptime at full scale.

Processes that break down the fiber structure to low-cost liquid fuels has proven dissimilar to processing pulp and paper where the goal instead is to preserve the fiber structure. These differences are reflected in the significant downtime due to retooling and engineering redesign at pioneer plants, many of whom by 2021 have shuttered operations (Slupska and Bushong, 2019). Producers realized they must cope with broad input variations in moisture, ash content, etc. that were not evaluated at relevant scale during development. These issues have been problematic, with many related to materials transport.

This Perspective article describes process development via incremental changes from the commercial starch ethanol process rather than the pulp and paper process. Herein process design concepts are described that culminated in successful demonstration of 1,000-h integrated runs using several feedstocks, including switchgrass, energy sorghum, and two types of corn kernel fiber. This article highlights a process design approach that solved the issues that plagued—and continue to plague—many processes in the pioneer cellulosic space such as biomass feeding of grasses and grain fibers, high ash content, diversified coproduct value, and others.

MANAGING MATERIAL HANDLING CHALLENGES

Lignocellulosic Feedstocks Systems Are Not Agnostic

The design challenge for an industrial process with poor control of input feedstock quality attributes is exacerbated by the heterogeneous nature of different forms of biomass:

- **Agricultural.** Agricultural feedstock can be subdivided into several subclasses, including grasses, residues, and energy crops. All these agricultural solids have substantive differences in composition, physical characteristics, harvesting methods and storage conditions.
- **Municipal Solid Waste.** MSW can be as varied as the collection and sorting methods used to recover the material post-consumer. MSW cellulose content may include different types of extractives, binders, and inks as part of their previous application.
- **Captive Fibers.** These consist of post-processed food, and are subject to extraction method variations, microbial degradation, and food sources.
- **Woody biomass.** Woody biomass has been used industrially for centuries. Industrial woody feedstocks are almost always subdivided into hardwood and softwood, with variant processing methods applied to exploit each one. Experience has taught the pulp and paper industry that in many cases, blends of hardwood and softwood can improve their flowability and processability (Chauhan et al., 2011; Nugroho, 2012).

Non-Agnosticism: Switchgrass, Energy Sorghum, and Corn Kernel Fiber

In 2015, industry demonstrated ethanol production using lignocellulosic feestocks, including switchgrass, energy sorghum, and corn kernel fibers at a scale of 10 tons per day of continuous production (Javers, 2017). During those runs, process engineers experienced the inherent variation between feedstocks, even those within a lignocellulose sub-category. Special care had been taken to grow, harvest, store and process the feedstocks in such a way as to avoid storage variability from moisture and decomposition (Smith et al., 2013). However, upon grinding the feedstocks and pneumatically transferring to downstream processing, seemingly innocuous steps like tramp washing and wetting of feedstock led to material bridging, rotary airlock plugging, high wear areas, cooling and pumping issues, among others (**Supplementary Figure S1**). Those challenges proved difficult to overcome without equipment and process changes specific for each lignocellulose type.

Agricultural Residues Have Many Ash Sources

Ash content is a significant variant in feedstocks for bioprocessing. In addition to bound ash in the form of dirt and intrinsic ash within the feedstock itself, manufacturing plants must also manage the levels of tramp that comes in with biomass (Zhang et al., 2017). In one of the runs, almost two cubic meters of small rocks were removed from just 10–12 tons of feedstock (Javers, 2017), requiring improved storage design.

Feedstock Variation Impacts the Front End

Ash content, stalk thickness and moisture content can have pronounced impacts on the milling operation. When ash content (often as soil) is high, mechanical wear on milling equipment can significantly reduce equipment lifetime and plant uptime. Stalk thickness directly impacts the load on milling devices to the point where staged milling may be necessary to realize a cost-effective attrition to the desired pretreatment particle size (Zhang et al., 2017). Heterogeneity of feedstock quality also has profound impacts upon the particle size distribution of pre-processing: higher moisture contents in milling tend towards larger particles, while dry biomass produces more fine particles and dust, frequently with a wider particle size distribution (Smith et al., 2013). It is here that the benefits of captive [processed] fibers have distinct advantages, with the cost and consistency burden of grinding already being paid for by the primary product (starch ethanol).

Grinding technology also provides process variability that can cause challenges in hydrolysis. Cutting/chipping, shearing, grinding and crushing modes of attrition can alter the biomass particle morphology and size distribution differently. Cutting and chipping—often used for primary milling of biomass to more homogeneous sizes—are limited by cost at lower particle sizes, yet leave the material still too large to effectively convey and seal into high-pressure reactors (Karinkanta, 2015). Secondary milling is often accomplished by hammermills and similar equipment. While effective, they produce a broad particle size distribution. During the United States Department of Energy's Integrated BioRefinery (DOE IBR) funding of 1,000-h pilot trials at ICM,
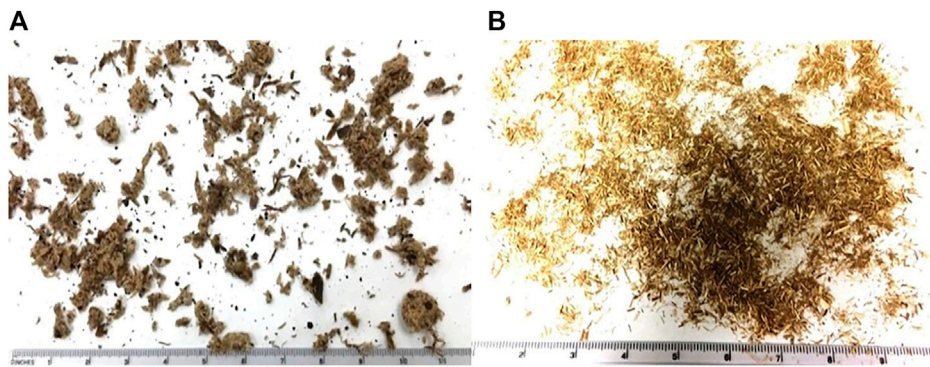
FIGURE 1 | Comparison of woody and herbaceous feedstocks under similar pre-processing particle size reduction. Wood chips **(A)** and switchgrass **(B)** were processed with a hammer mill with screen size #10. The particle and conglomerate material attributes differ substantially using similar processing methods. Thus, the need to tailor handling equipment designs for each feedstock is critical.

a population of unconverted particles persisted even after hydrolysis for both switchgrass and energy sorghum (**Figure 1**). A sugar clarification step was applied to prevent these large pieces from moving forward in the process and causing issues.

Normalizing Storage to Manage Heterogeneity

Storage can play a large role in downtime resulting from some of the above variations. Recently, the national laboratories successfully demonstrated the impact of adaptive controls on reducing downtime of a mill grinding corn stover with variable moisture content (US Department of Energy, 2016). Although uptime was increased, there was a significant loss of rate.

A second approach is to implement a standard feedstock form, such as pellets (Kim et al., 2019). Pellets have the advantages of pre-milled feedstock, reduced moisture variation, improved transportation costs, and ability to use existing infrastructure. Care must be taken with a pelleting approach however to ensure full, rapid and cost effective rehydration at the biorefinery. As of this writing, there are no known uses of pelleting in the biomass process (Tumuluru et al., 2011).

In the end, to process slurries with high solids concentrations (>20% solids to liquid) it may be more pragmatic to control variation by employing bulk averaging to dampen inhomogeneity. This introduces a substantial cost to many biomass feedstocks, and in some cases makes it more expensive than its competitive carbohydrate source: grain starch.

The Biomass Conveying Challenge

The compressibility, cohesivity, plasticity and low bulk density of most biomass sources make it difficult to design, and many pioneer plants are known to have gone through redesigns of the feedstock conveyance systems. Some IBRs found that pre-ground feedstocks pneumatically transported from storage into the plant required a steady feed rate to prevent line plugging (US Department of Energy, 2016).

Mitigating the conveying challenge is not easy or inexpensive for dry solids streams. Narrowing the particle size is often the easiest and most effective mitigation for heterogeneous materials. At smaller particle sizes (50–1,500 micron), most feedstocks act like spheres and flow freely. However, much research has demonstrated that grinding of biomass below 10 mm introduces an unacceptable cost to production (Humbird et al., 2011; Hartley et al., 2021).

To reduce the impact of mechanical cohesivity, dilution of the feedstock with air can help. Making a robust, functioning system involves careful consideration of the feed rate, air velocity and line layout. Overfeeding the conveyance system can result in settling/packing of material. At high air velocity, the biomass stays dilute but wear at piping elbows increases (**Supplementary Figure S1**); too low velocity and material falls out and settles in the line. Too long of a horizontal run—especially one with many elbows—and gravity settles the biomass out in the lines, often requiring human intervention to restore flow.

Hydration—The Floaters and Sinkers Challenge

In order to achieve optimal heating of biomass, fully hydrating the material is not easily achieved for all feedstocks. Switchgrass—presumably due to its stem coating—is easy to wash but problematic to wet, making tempering of the feedstock to constant total solids challenging. Switchgrass formed floating mats on top of IBR slurring vessels; it was difficult to maintain homogeneity, a problem that was solved only after many attempts and equipment modifications (**Figure 2A**).

Conversely, energy sorghum wet too readily. In washing steps, sorghum retained water, resulting in inefficient ash removal and leading to a higher acid requirement and elevated levels of equipment wear. In the slurry vessel, the sorghum would readily dewater and sink. Special controls had to be employed to maintain consistent total solids while continuous feeding into the downstream reactor (**Figure 2B**).
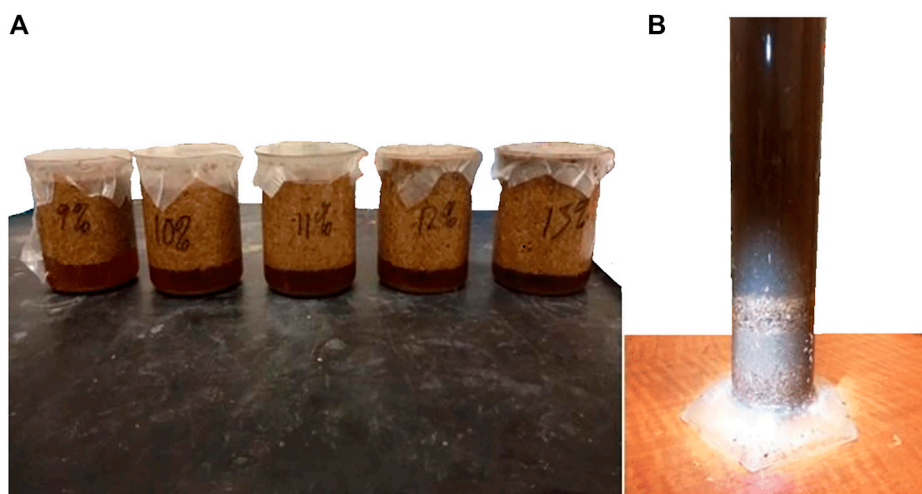
FIGURE 2 | Dilute acid pretreatment switchgrass **(A)** and energy sorghum **(B)** illustrating the floater and sinker characteristic, respectively. Two seemingly similar herbaceous materials pre-processed and thermochemically pre-treated behave quite differently when suspended in liquid. Thus, the equipment design and process for the transport of materials needs is unique for specific feedstock properties throughout the process.

Industry processes used suspended solids instead of wetted solids, thus more aggressive horsepower and thoughtful agitation were adequate to maintain the homogeneity necessary to achieve reliable flow control.

Avoiding Backpressure at the Reactor Throat

Achieving the seal at a high-pressure reactor throat is challenging for solids systems like biomass and can have catastrophic impact on plant uptime and safety if the boundary between high and low pressure fails. If corrosive catalysts are able to blow back in the process, the result can introduce rapid degradation of upstream equipment, especially seals. Backpressure can also cause elevated reaction temperatures that make the area an unsafe work environment.

Many high solids approaches involve mechanically compressing the biomass feed material into a plug, while others attempt to form a seal with the biomass directly. In early designs, one IBR attempted both approaches, neither of which ran successfully for more than a day or two. One key issue was gas permeability in and around the biomass. It was difficult to consistently and sustainably create a seal with material present in the seal; soft seals broke down under the abrasiveness of the biomass, and hard seals would not close completely unless they managed to cut the material or move it from the sealing surface.

The Move to Lower Solids Processing

Due to these challenges during development, one IBR process opted to take a different direction with the reactor design. Whereas making a high-pressure seal with biomass requires complex mechanical sealing systems, making a seal with liquids is relatively simple and reliable. By reducing the total solids target in pretreatment, the demonstration plant achieved a slurry with larger particles yet consistent operation. Additional

benefits included superior heat transfer, mixing, pumping and flash. An artifact of running pretreatment at lower total solids was that hydrolysate sugar concentrations were low, but the costs were effectively mitigated with waste heat evaporators to concentrate the sugars. The approach effectively decoupled the pretreatment and hydrolysis operating conditions from the fermentation such that the pretreatment optima did not limit the fermentation ethanol titer. It was possible to run hydrolysis at only 100 g-sugars/L but still run fermentation at 300 g-sugars/L to realize cost-effective distillation.

Impacts of Lower Solids Front End

A slurry step is often used prior to the pretreatment reactor to condition and temper the biomass for optimal reaction. Removal of buffers, such as ash or proteins, improves the catalyst performance. Additionally, elevating the biomass temperature can improve the heating process by reducing the amount of steam required to reach the reaction temperature. The slurry step also can be utilized to introduce some (or all) of the catalyst where it can be done in a more dilute environment with better mixing.

Pretreatment slurry conditioning depends upon reactor design. Direct steam injection is used in many applications because it is efficient at heating. However, steam injection has the disadvantage of being difficult to distribute evenly due to increased solids, diluted biomass, and requirements on steam quality. Similarly, chemical additions can be problematic (pH adjustment and control) in packed fiber beds where tempering the biomass in a slurry may be limited to avoid over-dilution.

Some process designs utilize slurry to wash and/or transport the biomass to the rector throat, then recover the water and recycle it back to the front of the transport. This approach can mitigate several issues in the process while also saving water, provided considerations are made to reduce build-up of unwanted compounds in the biomass flow that enters the reactor (ex. ash, dirt, and sugars). This must be balanced with

additional capital cost and water balance management. The slurry and/or hydration liquids may not be sent forward with the biomass in the reactor to reduce dilution. When catalyst is applied prior to the reactor where some hydrolysis may occur, it is generally necessary to send the liquid into the reactor with the solids to maintain mass balance control.

A CASE FOR CO-LOCATION

Water balance is arguably the most important consideration with the frontend of a biorefinery. Water provides the heating and cooling, some of the catalyst, and functionally distributes all other chemistry at play. When a biorefinery is designed to be a standalone operation, water and energy must balance. However, when a cellulosic process is co-located with another process, many new and advantageous integrations can be realized.

Consider the biorefinery design where all of the lignin is combusted for energy (Davis et al., 2018). In this case, the lignin volume provides a net electricity export to the grid. However, electricity gets discounted when it goes onto the grid because of unavoidable power transmission losses. If a suitable colocation partner is at-site, all value of the electricity can be utilized by that process at (green) market price.

In some 1.5 generation (captive/corn fiber) processes, sulfuric acid and ammonia used in pretreatment are carried over into the starch based 1st Generation (1G) process at the integrated corn fiber fermentation. The chemicals are still able to perform their normal functions as nitrogen source for yeast growth and pH control for evaporation, effectively cutting the acid/base consumption in half relative to a standalone ethanol plant. Additionally, waste heat from the pretreatment can be used to drive 1G evaporation, and cook water from the 1G ethanol process used for fiber treatment and washing prior to dilute acid pretreatment. Recalcitrant protein on the incoming fiber is partially hydrolyzed during pretreatment, increasing the overall protein efficacy (digestibility) in the feed product (Karinkanta, 2015). Ultimately, all insoluble solids from the 1G process end up in the animal feed stream, providing higher value to a plant than combustion for power.

In a co-located 1st and 2nd generation (cellulosic) biorefinery, the size of the cellulosic site relative to the 1G site next door depends upon integration of the nominal sulfuric acid dose in pretreatment, somewhere between 25–50% of the starch ethanol output. The 1G plant provides inexpensive carbohydrate for the yeast propagation, such that an excess of yeast is produced and can be sold as a high value single cell protein or combined with the rest of the feed ration to boost the overall protein content. The pretreatment provides both steam and waste heat to the 1G process as well.

To date, the process decision to use high dry matter pretreatment for cellulosic processes has been challenging for a large portion of the pioneer cellulosic ethanol plants. The high level of variation in real-world feedstocks has made it difficult to design a robust frontend process to deliver the feedstock to the high-temperature and -pressure reactors with low free water. For biochemical route processes, the lower solids approach of the process will average many of the feedstock quality differences and provide reliable flow into the pretreatment reactor.

IBR process integration allowed for low solids to be done so economically. Colocation afforded many advantages to the water and energy balances of the lignocellulosic facility. As a result, the resulting cellulosic process has a lower capital cost per gallon ethanol than most reported cellulose plants in operation. There may also be other advantages of co-localization such as utilizing the waste CO_2, fertilizer and nutrient separation to take advantage of national and regional incentives to realize low carbon fuels and chemicals.

DISCUSSION

Cellulosic ethanol was validated with over 4,000 h of integrated run at 10 tons per day in the ICM IBR pilot plant, using switchgrass, energy sorghum and two types of corn kernel fiber. The validation process also used a frontend capable of mitigating feedstock variation for more than 400 tons of biomass processed during each trial. It was facilitated by use of incremental engineering changes from the first-generation ethanol process, instead of the more common adaptation of the industrial Pulp and Paper process. There is a foundational truth that feedstock diversity can (and will) resist a "one size fits all" process design for all sources of biomass. The perspectives described in this article are a recognition of the importance of employing demonstrated tools for reducing material flow heterogeneity and variation over time—most notably, use of dilution and benefits of pairing the process with adjacent manufacturing to mitigate water balance and ash limitations. Agricultural feedstock variability is inevitable but leveraging decades of experience with processing cereal grains has demonstrated at scale a cellulosic systems that can be successful in realizing robust operations with low downtime, and as such, should be a consideration of anyone trying to mitigate risk in biorefinery development.

DATA AVAILABILITY STATEMENT

The original contributions presented in the study are included in the article/**Supplementary Material**, further inquiries can be directed to the corresponding author.

AUTHOR CONTRIBUTIONS

BE drafted and created the concept of the article. MR contributed to the writing and editing of the article.

FUNDING

ACKNOWLEDGMENTS

SUPPLEMENTARY MATERIAL

The Supplementary Material for this article can be found online at: https://www.frontiersin.org/articles/10.3389/fenrg.2022.835714/full#supplementary-material

REFERENCES

Chauhan, V., Chakrabarti, S. K., and Thapar, S. K. (2011). Effect of Separate and Mixed Refining of Hardwood and Softwood Pulps on Paper Properties. *Palpu Chongi Gisul/Journal Korea Tech. Assoc. Pulp Paper Industry* 43, 142.

Davis, R. E., Grundl, N., Tao, L., Biddy, M. J., Tan, E. C. D., Beckham, G. T., et al. (2018). *Process Design and Economics for the Conversion of Lignocellulosic Biomass to Hydrocarbon Fuels and Coproducts: 2018 Biochemical Design Case Update; Biochemical Deconstruction and Conversion of Biomass to Fuels and Products via Integrated Biorefinery Pathways*. Golden, CO (United States): National Renewable Energy Lab. NREL.

Hartley, D. S., Thompson, D. N., and Cai, H. (2021). *Woody Feedstocks 2020 State of Technology Report*. United States. Medium: ED.

Humbird, D., Davis, R., Tao, L., Kinchin, C., Hsu, D., Aden, A., et al. (2011). Process Design and Economics for Biochemical Conversion of Lignocellulosic Biomass to Ethanol. *Renew. Energ.* 303 (May), 147.

Javers, J. (2017). *Recovery Act: Pilot Integrated Cellulosic Biorefinery Operations to Fuel Ethanol*. United States, 152. Medium: ED; Size.

Karinkanta, P. (2015). *Dry fine Grinding of Norway spruce (Picea Abies) wood in Impact-Based fine Grinding Mills*.

Kim, S., Dale, B. E., Jin, M., Thelen, K. D., Zhang, X., Meier, P., et al. (2019). Integration in a Depot-based Decentralized Biorefinery System: Corn stover-based Cellulosic Biofuel. *GCB Bioenergy* 11 (7), 871–882. doi:10.1111/gcbb.12613

Nugroho, D. (2012). *Low Consistency Refining of Mixtures of Softwood & Hardwood Bleached Kraft Pulp: Effects of Refining and Power*.

Slupska, M., and Bushong, D. (2019). Lessons from Commercialization of Cellulosic Ethanol - A POET Perspective. *Biofuels, Bioprod. Bioref.* 13, 857–859. doi:10.1002/bbb.2033

Smith, W. A., Bonner, I. J., Kenney, K. L., and Wendt, L. M. (2013). Practical Considerations of Moisture in Baled Biomass Feedstocks. *Biofuels* 4 (1), 95–110. doi:10.4155/bfs.12.74

Tumuluru, J. S., Wright, C. T., Hess, J. R., and Kenney, K. L. (2011). Erratum: A Review of Biomass Densification Systems to Develop Uniform Feedstock Commodities for Bioenergy Application. *Biofuels Bioproducts and Biorefining* 1, 5. doi:10.1002/bbb.324

Us Department of Energy (2016). "US Department of Energy-Office of Energy Efficiency and Renewable Energy–Bioenergy Technologies Office. Summary Report from the October 5-6," in 2016 Biorefinery Optimization Workshop in Chicago, Illinois. DOE/EE-1514 December, Chicago, Illinois, October 5-6.

Zhang, L., Yang, Z., Zhang, Q., Zhu, X., and Hu, H. (2017). Mechanical Behavior of Corn Stalk Pith: an Experimental and Modeling Study. INMATEH Agric. *Eng* 51, 39–48.

Optimizing Chemical-Free Pretreatment for Maximizing Oil/Lipid Recovery From Transgenic Bioenergy Crops and Its Rapid Analysis Using Time Domain-NMR

Shraddha Maitra[1,2], Stephen P. Long[2,3] and Vijay Singh[1,2]*

[1]Department of Agricultural and Biological Engineering, University of Illinois at Urbana-Champaign, Urbana, IL, United States, [2]Center for Advanced Bioenergy and Bioproduct Innovations (CABBI), Department of Energy, Urbana, IL, United States, [3]Carl R. Woese Institute for Genomic Biology, University of Illinois at Urbana-Champaign, Urbana, IL, United States

OPEN ACCESS

Transgenic bioenergy crops have shown the potential to produce vegetative oil by accumulating energy-rich triacylglyceride molecules that can be converted into biofuels (biodiesel and biojet). These transgenic crops cater to improved biofuel yield by providing lipids along with cellulosic sugars. Efficient bioprocessing technologies are needed to utilize these transgenic plants to their maximum potential. To this end, this study investigates a low- and high-severity chemical-free hydrothermal pretreatment of transgenic oilcane 1566 bagasse with *in situ* lipids to maximize the recovery of lipids for biodiesel and fermentable sugars for ethanol with minimal inhibitor generation. Hydrothermal pretreatment at 170°C recovered ~25% of total lipids in the pretreatment liquor, leaving the remainder in bagasse residue for hexane recovery post fermentation . The recovery of lipids in pretreatment liquor remained constant beyond 170°C. Along with lipids, ~35% w/w and ~50% w/w fermentable sugars were recovered post saccharification from bagasse pretreated at 170°C and 210°C for 20 min, respectively. Hydrothermal pretreatment at 170°C for 20 min provided the optimum conditions for maximum recovery of lipids and cellulosic sugars that resulted in enhanced biofuel yield per unit biomass. High severity pretreatment increased the generation of inhibitors beyond the tolerance of fermentation microorganisms. In addition, the application of time-domain proton NMR spectroscopy was extended to bioprocessing. NMR technology facilitated the analysis of total lipids, the composition of fatty acids, and the characterization of free and bound lipids in untreated and pretreated oilcane 1566 bagasse subsequent to each step of biomass to biofuel conversion.

Keywords: biofuels (biodiesel and bioethanol), hydrothermal pretreatment, time-domain 1H NMR spectroscopy, lipid analysis, bioenergy crops

Graphical Abstract |
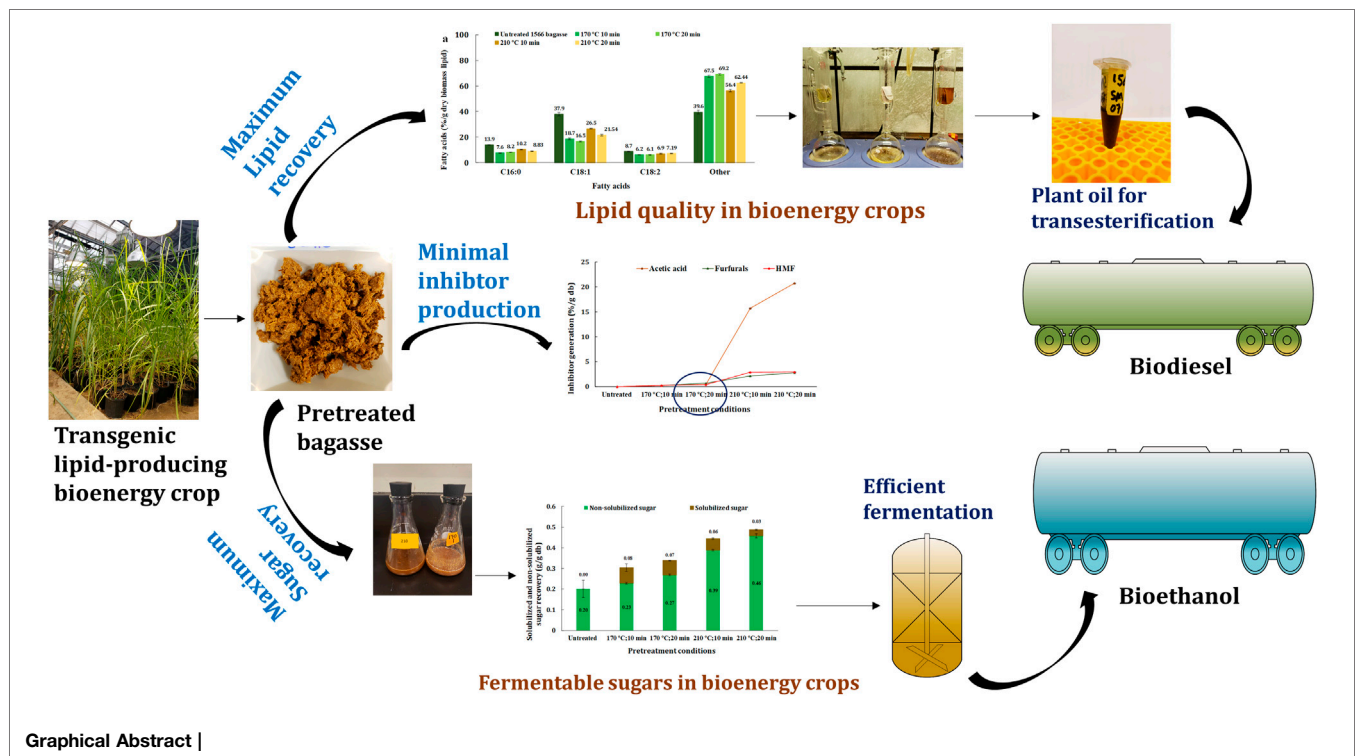
INTRODUCTION

Biofuels are a drop-in, environmentally nontoxic, biodegradable, and less contaminating alternative to conventional fuels with comparable energy efficiency, with strong potential for lowering CO_2 emissions. Cellulosic biomass has immense potential as a renewable feedstock for global energy needs. Bioenergy from traditional biomass such as cereal grains, forestry, and other energy crops constitutes approximately 7% of total global energy consumption (REN21, 2020). Oils from plants are particularly valued since they can be easily converted to biodiesel and bio-jet, serving markets that are unlikely to be electrified. To this end, bioenergy crops such as sugarcane, energycane, sorghum, and miscanthus are being metabolically engineered to shift the carbon flux from sugar to lipid synthesis and accumulation in their vegetative tissues (Zale et al., 2016; Vanhercke et al., 2019; Parajuli et al., 2020).

The accumulation of energy-rich triacylglyceride (TAG) molecules enhances the energy density of these transgenic bioenergy crops as compared to their wild-type varieties. These metabolically engineered transgenic bioenergy crops can be used for the production of both fermentable sugars and lipids/oil. Moreover, the very high productivity of these crops would result in substantially more oil per unit area than conventionally used oilseed crops (Parajuli et al., 2020). For example, sugarcane produces an annual yield of dry biomass of at least 10–20 times more per hectare than soybean; thus, accumulation of ~20% lipids in the vegetative tissues would produce 10–20 times more oil for biodiesel than soybean per unit area (Huang et al., 2016a;

2016b). However, the quality of biodiesel is influenced by the composition of the total lipids of transgenic crops. Genetic engineering to modify the metabolic pathways of transgenic bioenergy crops provides a tool to develop desired feedstock to improve biodiesel quality by having a higher content of short, unbranched, and saturated fatty acids (Knothe, 2008, 2009).

Mechanical pressing and solvent extraction are the two most commonly used procedures for commercial oil extraction from oilseeds for biodiesel production (Atabani et al., 2013; Bhuiya et al., 2016). Although it is anticipated that refinement of bioengineering would eventually raise total oil content in transgenic bioenergy crops to 20%, initial steps have only raised total TAG content to 8 and 4.3% dry weight in the leaf and stem, respectively, along with an increase in total fatty acid content to 13% dry weight in the leaf (Parajuli et al., 2020). Nevertheless, this provides material on which challenges to extraction technologies may be evaluated. Since the total lipid content in transgenic bioenergy crops is lower than that in oilseeds and a considerable percentage of lipids are present in a complex bound form (Zale et al., 2016; Parajuli et al., 2020; Maitra et al., 2021), the conventional methods for oil recovery from oilseeds are not sufficient for effective lipid recovery from transgenic cellulosic biomass. Chemical-free low-severity methods for the extraction are necessary to prevent the decomposition of lipids during pretreatment, followed by saccharification of the residual cellulosic biomass to produce fermentable sugars. Jia et al. (2020) reported an improvement in lipid recovery upon hydrothermal pretreatment of oil-bearing corn germ meal at 180°C for 15 min (Jia et al., 2020).

The time-domain NMR technique provides a faster alternative to the existing lipid characterization and profiling techniques (Berman et al., 2013; Robinson and Cistola, 2014; Nascimento et al., 2017; Nikolskaya and Hiltunen, 2018). Rapid analytical methods for the initial screening of samples are critical in optimizing the extraction technology. Previously, we showed the application of TD-NMR as an effective high-throughput phenotyping method to quantify and characterize *in situ* lipids in transgenic lignocellulosic bagasse (Maitra et al., 2021). TD-NMR facilitates direct analysis of cellulosic biomass for lipid analysis without sample preparation or lipid extraction. Thus, TD-^{1}H NMR provides a convenient and rapid alternative to the tedious wet chemistry technique of fatty acid analysis. The application of TD-NMR for qualitative and quantitative characterization of *in situ* vegetative lipids in cellulosic biomass after each bioprocessing step such as pretreatment, saccharification, simultaneous saccharification, and fermentation (SSF) has not been reported.

The present work investigates low- and high-severity hydrothermal pretreatment for maximizing lipid and sugar recovery with negligible inhibitor generation from the transgenic lipid-producing sugarcane (oilcane 1566) bagasse and extends the application of TD-NMR spectroscopy for the estimation of the total lipid and fatty acid composition in the cellulosic biomass before and after each of the following steps: pretreatment, enzyme hydrolysis, and SSF.

MATERIALS AND METHODS

Transgenic Bioenergy Crop

The transgenic oilcane event 1566 was grown in a greenhouse at the University of Illinois at Urbana-Champaign under controlled environmental conditions. This was a 16-h day in which sunlight was supplemented to ensure a minimum photon flux of 600 μmol m^{-2} s^{-1} light from high-pressure sodium lamps. The temperature was controlled between 28° and 31°C. Whole shoots of wild-type and transgenic plants were harvested at the stage that they would be harvested in the field for processing, that is, before flowering. The leaves were separated from the stem, and juice was extracted using a juicer (Juicematic SC-3 commercial sugarcane juicer). Each stem was passed through the juicer three times to extract maximum juice. The bagasse was dried to constant weight at 50°C. The dried bagasse was cut into smaller pieces of 1–2 inches with pruning shears, followed by shredding in a hammer mill (W-8-H, Schutte-Buffalo Hammermill, Buffalo, NY), with a sieve size of 2 mm. Bagasse was stored at −20°C until it could be used for further processing.

Hydrothermal Pretreatment

The hydrothermal pretreatment at 170 and 210°C for 10 and 20 min was performed in a sand bath (IFB-51 Industrial Fluidized Bath, Techne Inc., Burlington, NJ) attached to an air compressor for even heat distribution. Pretreatment was performed with a 20% w/w biomass solid loading. The transgenic oilcane 1566 bagasse samples were loaded into capped pipe reactors (316 stainless steel reactors: 10.478 cm length × 1.905 cm outer diameter × 0.165 cm wall thickness tubing, SS-T12-S-065–20, Swagelok, Chicago Fluid System Technologies, Chicago, IL; 316 stainless steel caps: SS-1210-C, Swagelok, Chicago Fluid System Technologies, Chicago, IL). A thermocouple [Penetration/Immersion Thermocouple Probe Mini Conn (−418–1652°F), Mc Master-Carr, Robbinsville, NJ] inserted into the reference pipe reactor filled with deionized water was used to monitor the *in situ* temperature. The thermocouple was connected to a data logger (HH306/306A, Datalogger Thermometer, Omega, Stamford, CT). The pretreatment reactions were quenched immediately after 10 and 20 min of pretreatment by submerging the reactors into cold water. The resulting, pretreatment liquor was analyzed for solubilized sugars and inhibitors using HPLC. The pretreated bagasse residue was kept at 4°C for lipid analysis and saccharification.

Saccharification

Enzymatic saccharification was performed on both untreated and pretreated transgenic oilcane 1566 bagasse using standard protocol NREL/TP-5100-63351 (Resch et al., 2015). Enzyme hydrolysis was carried out with 10% (w/w) biomass solid loading for 72 h at 50°C in an incubator shaker at 180 rpm. The working concentrations of the enzyme hydrolysis reaction mixture contained citrate buffer (0.05 M) and sodium azide (0.005%) to inhibit the growth of microorganisms and 16.9 mg protein/g of dry biomass of cellulase and hemicellulose mixture [59.64 FPU/g dry biomass enzyme loading (NS 22257, Novozymes North America, Inc., Franklinton, NC, United States)].

Simultaneous Saccharification and Fermentation (SSF)

Simultaneous saccharification and fermentation were performed on untreated and two differently pretreated transgenic 1566 bagasse [170°C for 20 min and 210°C for 20 min]. The working concentrations of the SSF reaction mixture contained citrate buffer (0.05 M), 16.9 mg protein/g of dry biomass of cellulase and hemicellulase mixture (NS 22257, Novozymes North America, Inc., Franklinton, NC, United States)], and C6/C5 fermenting recombinant *Saccharomyces cerevisiae* (kindly provided by DSM). The yeast was grown on a YPX medium (1% yeast extract, 2% peptone, and 2% xylose) for 48 h at 32°C. Yeast cells were centrifuged and inoculated in the SSF medium to obtain a starting cell O.D$_{600}$ of 0.5. SSF was carried out for 96 h in a shaking incubator (180 rpm) at 32°C with 10% solid loading and sampled after every 24 h. The samples were filtered using 0.2-μm syringe filters and analyzed for sugars and ethanol using HPLC. The bagasse residue obtained post SSF was evaluated for lipid content and composition using TD-NMR.

Sugars and Inhibitor Analysis

The pretreatment liquors and hydrolyzates were centrifuged to separate the solid particles. The supernatants were filtered through 0.2-μm PTFE filters for HPLC analysis. The concentrations of sugars and inhibitors were estimated using an HPLC system (Waters alliance e2695 Separation module, Waters Corporation, MA, United States) equipped with a

refractive index detector and a Bio-Rad Aminex HPX- 87H column (Bio-Rad, Hercules, CA, United States).

Time-Domain 1H-NMR Spectroscopy

Time-domain NMR spectroscopy was used for quantification of total lipids and major fatty acids, that is, palmitic (C16:0), oleic (C18:1), and linoleic (c18:2) acid and characterization of bound and free lipids in the untreated and pretreated transgenic oilcane 1566 bagasse.

Quantification of Total Lipid Using Benchtop Time-Domain- 1H-NMR Spectroscopy

The total *in situ* lipids in untreated and pretreated transgenic oilcane 1566 bagasse were quantified and analyzed for bound and free fractions and major fatty acids (palmitic acid, oleic acid, and linoleic acid) using TD-NMR spectroscopy (Maitra et al., 2021). A low-field benchtop time-domain proton NMR spectroscope (Minispec mq20, Bruker, Massachusetts, United States) was used. The NMR system was equipped with an 18-mm thermostat [1]H-probe operating at 0.47 T/20 MHz and 40°C. For lipid analysis, the bagasse samples were dried (≤2% moisture content) to alleviate the interference of proton signals from water molecules. The time-domain ^{1}H NMR was calibrated with lipids extracted from transgenic bioenergy crops for analyzing *in situ* lipids in transgenic lignocellulosic biomass as reported in previous work (Maitra et al., 2021).

Characterization of Bound and Free Oil Fraction Using TD-NMR

T1T2 relaxation/intensity curves were analyzed for characterization of total lipids into bound and free lipid fractions as reported in the previous work (Maitra et al., 2021). The Carr–Purcell–Meiboom–Gill (CPMG) application was used for acquiring the full exponential decay curves for transverse (*T2*) relaxation times. The longitudinal (*T1*) relaxation time was obtained by the inversion recovery method. A CPMG pulse sequence was applied for the measurement of spin–spin relaxation. The total number of acquired echoes was 800. 90°–180° pulse separation (tau) was 2. The T1 inversion recovery relaxation time had a first and final pulse separation of 2 and 800 ms, respectively. A sampling window of 0.1 ms was used. The recycle sampling delay for the T1 inversion recovery experiment was 2 s. A total of 10 data points were used to fit the curve for each sample. Both *T1* and *T2* relaxation spectra were fitted to a bi-exponential equation of second order as reported previously (Maitra et al., 2021). The CONTIN algorithm software obtained from Bruker provided the continuous distribution of *T1* and *T2* values.

Analyzing Fatty Acid Composition Using TD-NMR

TD-^{1}H NMR was calibrated to quantify palmitic acid (16:0), oleic acid (18:1), and linoleic acid (18:2) in transgenic bagasse samples.

The *minispec Plus,* containing Bruker's *OPUS* software, was used for chemometric processing and storage of TD-NMR data. Chemometric processing included discerning differences between samples, identifying outliers, and obtaining regression models to correlate NMR values with the existing reference data in the software. Separate calibration curves were prepared for each fatty acid. Individual pure fatty acids (≥99% purity) were purchased from Sigma-Aldrich. The fatty acids were stored at −20°C. Palmitic acid (16:0), oleic acid (18:1), and linoleic acid (18:2) used in the study did not show susceptibility to oxidation at the experimental temperature of 40°C on repeated usage.

For non-invasive analysis of fatty acid composition in bagasse samples, pure free fatty acid standards were mixed with the "biomass matrix" as a background for calibration. Since bagasse itself is a complex matrix consisting primarily of lignin, cellulose, and hemicellulose, mixed with a variety of pigments, polyquinones and their oxidation products, membrane-proteins, and phospholipids, it is critical to abate the background signal of proton nuclei because of lipid molecules. The lipid biomolecules were removed from the bagasse by hexane, isopropanol, and ethanol extraction in a Soxhlet extractor. The bagasse obtained after extraction served as a "biomass matrix" for calibration purposes. The lipid-extracted bagasse was mixed with different amounts of pure fatty acid to calibrate the TD-NMR. Palmitic acid (16:0) was heated in a water bath at 65°C to ensure that it was in the oil form and above the crystalline-liquid phase transition before mixing it into the "biomass matrix" for calibration. A combination of FID (free induction decay) and CPMG applications was used to analyze the time decay signal of each fatty acid based on the nanofluidity of hydrocarbon chain packing (Robinson and Cistola, 2014). The decay spectra were evaluated by taking 16 scans with no dummy scans and a receiver gain of 40. Each fatty acid (palmitic acid, oleic acid, and linoleic acid) is expressed as the percentage of the total lipid present per gram of dry biomass.

Organic Solvent Lipid Extraction

Lipids/oils were extracted from the untreated and pretreated bagasse using the organic solvent method as reported by Huang et al. (2017). The organic solvent–extracted samples were analyzed for lipid classes and metabolites using GC/MS and LC/MS/MS. GC/MS and LC/MS/MS were performed at the Metabolomics Lab, Roy J. Carver Biotechnology Center, University of Illinois at Urbana-Champaign, IL, United States. A benchtop Agilent GC/MS (7890A GC with 5975C MS) with commercial Wiley and NIST libraries and a mass range of m/z 2 ~ m/z 800 designed for small metabolite analysis equipped with EI and CI sources were used for targeted metabolite profiling analysis. For LC/MS/MS analysis, a benchtop Sciex LC/MS-5500 QTrap Mass Spectrometer (hybrid triple Quadrupole-linear accelerator trap mass spectrometer) with Turbo V™ Source including ESI and APCI connected to an Agilent 1200 HPLC was used. The scan modes include full scan and selected ion scan for both Q1 and Q3, Product Ion Scan, Precursor Ion Scan, Neutral Loss Scan, Multiple Reaction Monitoring (MRM), Enhanced MS Scan, Enhanced Product Ion Scan, Enhanced Resolution Scan, and MS[3] scan with a mass range of m/z 5 ~ m/z 1,250.

FIGURE 1 | Estimation of total *in situ* lipids in **(A)** the untreated and pretreated transgenic oilcane 1566 bagasse residues and **(B)** untreated and pretreated bagasse residues after saccharification using TD-NMR. Data present the mean of triplicates with a standard deviation of 0.05%.
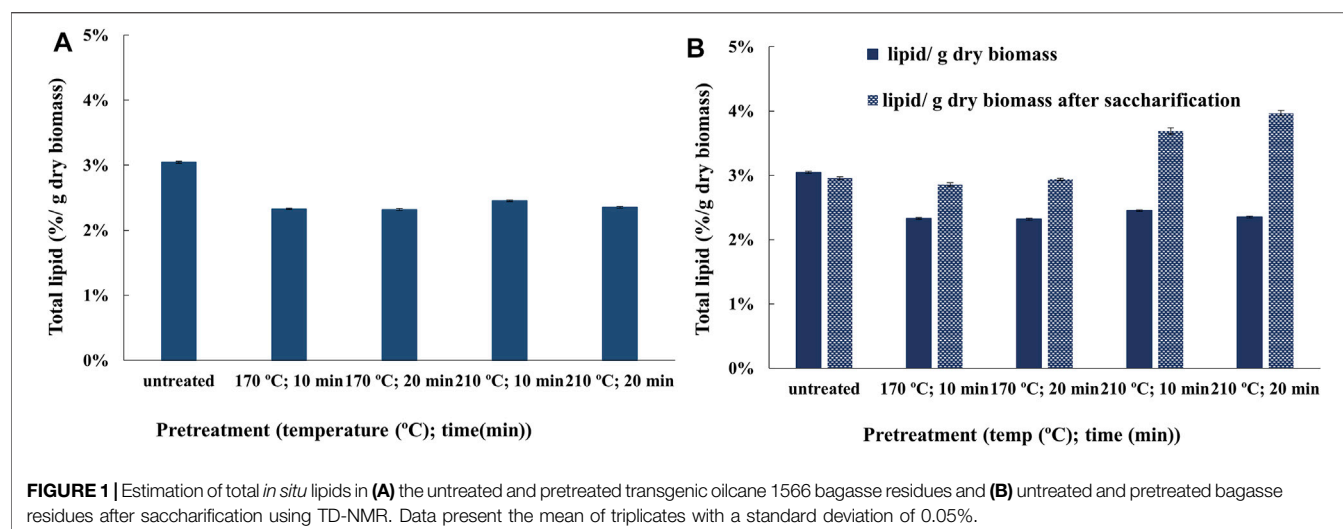
TABLE 1 | Analyzing *T1* relaxation/intensity curves to investigate the fraction of bound and free lipids in the untreated and pretreated bagasse residues after various hydrothermal pretreatment conditions, saccharification, and SSF.

Pretreatment (Temperature, Time)	*T1* ms (bound lipid)	*T1* ms (free lipid)	*T1* ms (free lipid)	*T1* ms (free lipid)	*T1* ms (bound lipid)	*T1* ms (free lipid)
	(after pretreatment)		(after saccharification)		(after SSF)	
Untreated	44 ± 5	190 ± 10	11.2 ± 0.5	75 ± 3	46 ± 5	200 ± 20
170°C, 10 min	37 ± 5	170 ± 10	15 ± 1	72 ± 4	ND[a]	ND[a]
170°C, 20 min	40 ± 4	166 ± 9	16 ± 1	55 ± 4	38 ± 4	140 ± 9
210°C, 10 min	34 ± 2	172 ± 5	13.8 ± 0.5	57 ± 5	ND[a]	ND[a]
210°C, 20 min	35 ± 3	182 ± 6	11.6 ± 0.5	66 ± 5	31 ± 4	99 ± 5

[a]ND- not determined.

RESULTS

Lipid Analysis Using TD-NMR Spectroscopy

The recovery of lipids from transgenic bagasse needs bioprocessing that prevents them from decomposition. To maximize lipid recovery, the transgenic oilcane 1566 bagasse was pretreated with a chemical-free hydrothermal pretreatment at low and high severity. The severity of the pretreatment (R_o) was calculated using the equation (Overend et al., 1987),

$$R_o = t * e^{(T-T_R)/14.75}, \tag{1}$$

where, t, T, and T_R represent the pretreatment time (minutes), pretreatment temperature (°C), and reference temperature, that is, 100°C, respectively. The severity factor of hydrothermal pretreatment at 170°C for 10 and 20 min is 3.06 and 3.36 but 4.23 and 4.54 for pretreatment at 210°C for 10 and 20 min, respectively. The untreated and pretreated bagasse residues were analyzed for total lipids using time-domain ^{1}H-NMR spectroscopy. The untreated transgenic oilcane 1566 bagasse contained 3.05% total lipid per g of dry biomass. Upon hydrothermal pretreatment at 170°C and 210°C for 10 and 20 min, approximately 25% of total lipids were released in the pretreatment liquor (**Figure 1A**). The remaining 75% lipids remained in the bagasse irrespective of the severity of the pretreatment, which was recovered in subsequent steps.

Oil-associated proton relaxation time distributions of untreated and pretreated transgenic oilcane 1566 bagasse were analyzed. The samples exhibited two distinct oil-associated subpopulations of proton nuclei. Shorter and longer relaxation times of proton nuclei correspond to a lesser and higher degree of freedom, which represents the bound and free form of oils/lipids in the cellulosic biomass. In addition, the NMR intensity and magnitude of relaxation times qualitatively correspond to the relative amount of bound and free lipids in the bagasse residue (Maitra et al., 2021). The magnitudes of *T1* relaxation times of untreated and hydrothermally pretreated bagasse are presented in **Table 1**. A decrease in the magnitude of the *T1* relaxation times of pretreated bagasse as compared to untreated bagasse confirmed the release of lipids from the bagasse to the pretreatment liquor. The magnitude of *T2* relaxation times also showed lower oil-associated proton fluidity of bound oil in pretreated biomass residue as compared to the untreated bagasse, while no oil-associated proton fluidity was observed for free oil (**Supplementary Table S1**). The result was mirrored in the total lipid measurement using NMR spectroscopy (**Figure 1A**). The total lipid content of the bagasse residue was reduced from ~3 to 2.3% per g of dry bagasse. The lipid analysis of transgenic oil-containing bagasse using NMR is in agreement with that in our previous study with model biomass (bagasse with externally added crude corn oil) that successfully established the
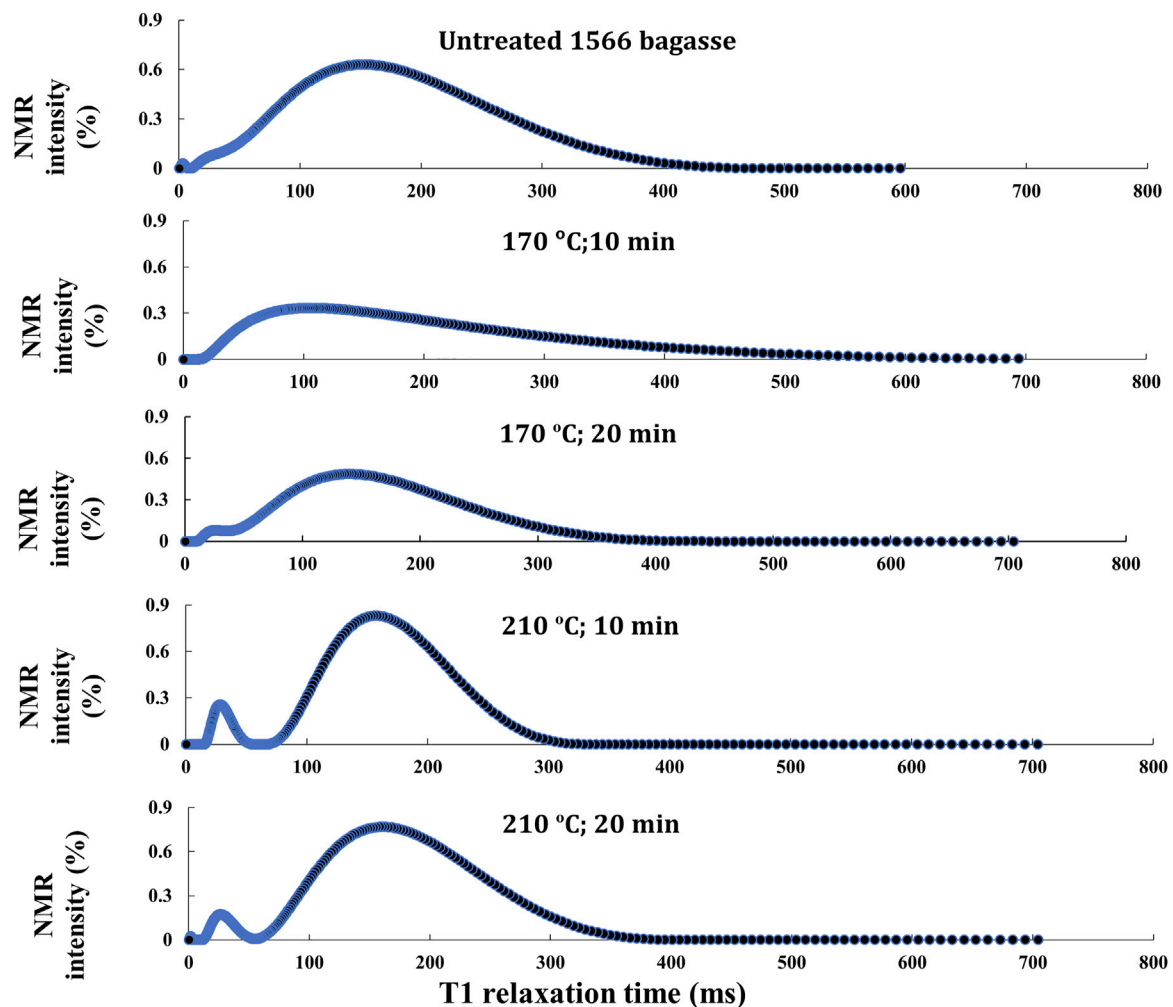
FIGURE 2 | *T1* relaxation/intensity curve analysis of *in situ* lipids in the untreated and pretreated bagasse residue of the transgenic oilcane 1566 bagasse.

application of TD-NMR spectroscopy for precise measurement and characterization of the residual lipids in the biomass fibers after hydrothermal pretreatment (Maitra et al., 2021).

The bagasse residues obtained post saccharification were also analyzed for total lipid content and a change in the magnitude of *T1* relaxation times using TD-^{1}H NMR to investigate the further release of lipids. After saccharification, the total lipid content of bagasse residues increased by 26 and 54% for bagasse pretreated at 170°C (~2.3 to ~2.9% w/w) and 210°C (~2.4 to ~3.9% w/w), respectively (**Figure 1B**). The magnitude of *T1* relaxation times of bagasse residues after saccharification for free oil was found to be lower than their corresponding untreated and pretreated bagasse residues (**Table 1**). The magnitude of *T2* relaxation times for bound oil remained low, and no oil-associated proton fluidity was observed for free oil in biomass residues after saccharification (**Supplementary Table S1**). The magnitude of relaxation times corresponds to the amount of oil-associated proton nuclei, which is directly correlated to the concentration of oil/lipid in the residue (Maitra et al., 2021). Therefore, this observation indicates a further recovery of

45–60% of lipids in the hydrolyzate after saccharification. However, the magnitude of *T1* relaxation time for bound oil showed no significant change in the signals. This suggests that the process of enzyme hydrolysis releases sugars by disrupting the cellulosic and hemicellulosic framework of the bagasse structure, which aids in the further recovery of the free form of lipids. However, the membrane-bound lipids are not recovered.

Analysis of NMR Relaxation/Intensity Curves

The study correlates *T1* relaxation/intensity curves with the recovery of lipid from bagasse residues (**Figure 2**). A reduction in the NMR intensity of the *T1* relaxation/intensity curves of the bagasse pretreated at 170°C for 10 and 20 min as compared to the untreated bagasse suggests reduced oil-associated proton fluidity of the bagasse and, hence, is directly correlated with the release of lipids from cellulosic biomass upon pretreatment (Maitra et al., 2021). The observation is in agreement with the quantitative analysis
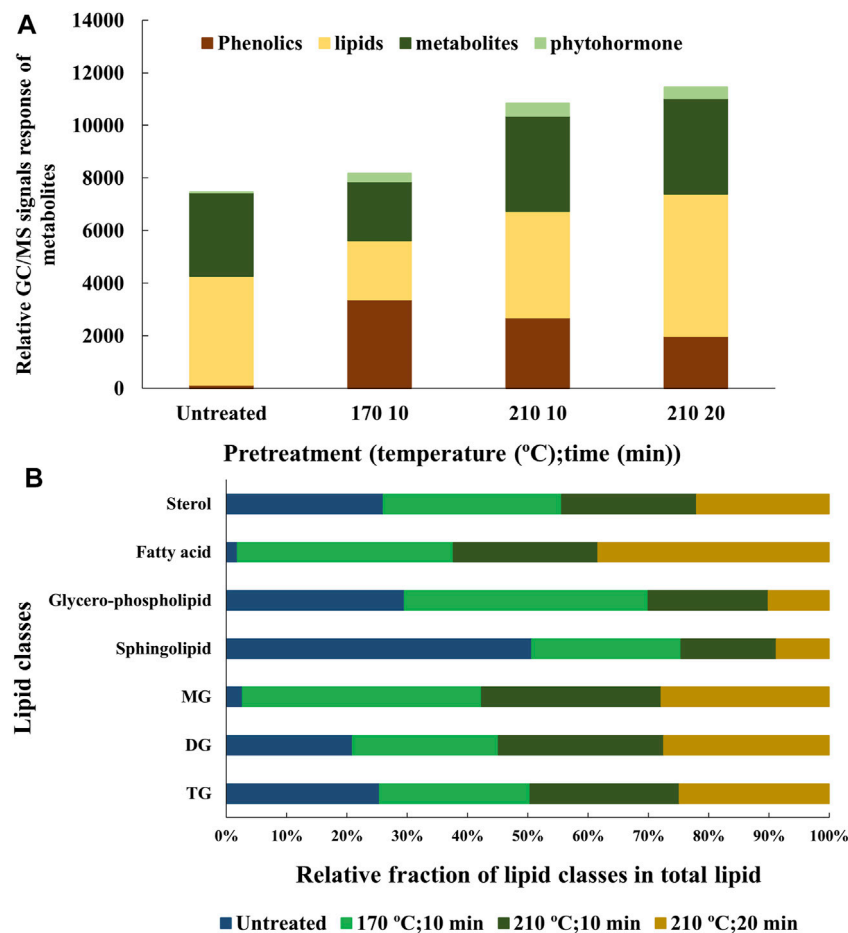
FIGURE 3 | (A) GC/MS analysis of total metabolites and **(B)** LC/MS/MS analysis of various lipid classes of untreated and hydrothermally pretreated transgenic oilcane 1566 bagasse using the organic solvent method. TG, DG, and MG denote triglycerides, diglycerides, and monoglycerides, respectively.

of the lipid content of the biomass residues (**Figure 1A**). $T2$ relaxation/intensity curves mirrored the results of the $T1$ relaxation/intensity curves but displayed lower NMR intensity for each biomass residue (**Supplementary Figure S1**). On the contrary, bagasse pretreated under severe conditions, that is, 210°C for 10 and 20 min exhibited higher NMR intensity. Therefore, the samples were analyzed using GC/MS to investigate the reason for the higher NMR intensity. The GC/MS analysis of the samples showed higher amounts of phenolics and various other metabolites than the untreated bagasse (**Figure 3A**). The proton nucleus metabolites could possibly contribute to the total proton signals, resulting in higher NMR intensity.

Analyzing Changes in Lipid Composition on Pretreatment

A qualitative GC/MS analysis was performed on the hexane-/IPA-extracted samples from untreated and pretreated transgenic oilcane 1566 bagasse (170°C for 10 min and 210°C for 10 and 20 min). The untreated bagasse sample contained >50% lipids; ~

40% plant metabolites such as maleic acid, fumaric acid, salicylic acid, itaconic acid, hydroxyquinone, and their derivatives; and 0.51% of phytohormones like derivatives of phenylacetic acid, indole-acetic acid, and indole-carboxylic acid. Hydrothermal pretreatment significantly increased the generation of phenolic compounds (**Figure 3A**).

LC/MS/MS analysis was performed to investigate the changes in the composition of lipid classes due to low and high severity hydrothermal pretreatment as compared to the untreated bagasse (**Figure 3B**). The untreated bagasse sample showed a higher relative percentage of membrane lipids, that is`, phospholipids and sphingolipids and only 0.02% w/w of free fatty acids. Both low and high severity pretreatment procedures aided in decreasing the membrane lipid content. The levels of mono glycerol (MG) and free fatty acids increased on pretreatment, which can be attributed to the thermal decomposition of membrane lipids during hydrothermal pretreatment (Maher and Bressler, 2007). The relative percentage of triglycerides (TGs), diglycerides (DGs), and sterol remained similar after pretreatment.

FIGURE 4 | Non-invasive analysis of the recovery of three important fatty acids such as palmitic (C16:0), oleic (C18:1), and linoleic (C18:2) acids in the bagasse residues before and after (A) hydrothermal pretreatment and (B) saccharification using TD-NMR.

FIGURE 5 | (A) Total sugar recovered and (B) inhibitors generated during hydrothermal pretreatment of transgenic oilcane 1566 bagasse.
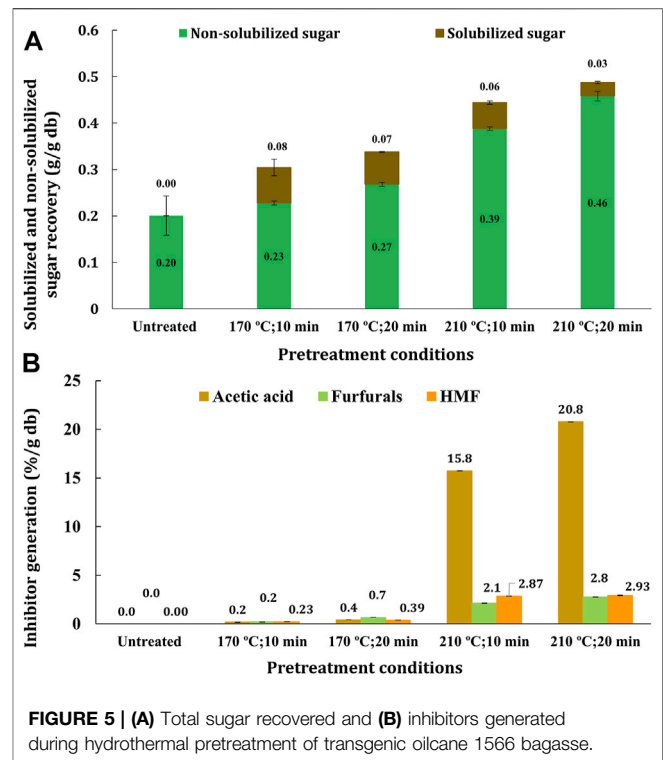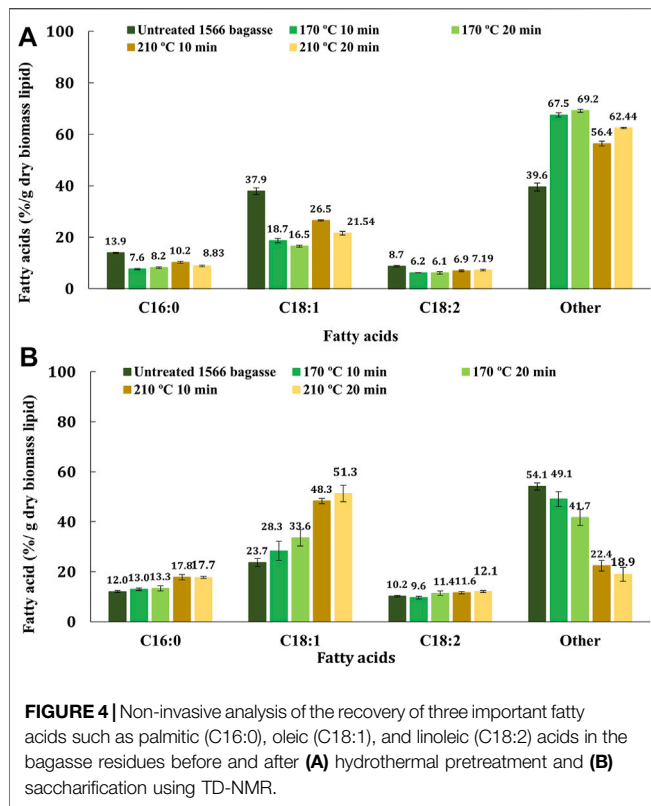
Analysis of Fatty Acid Composition of Transgenic Bagasse Using TD-NMR

The fatty acid profiles of untreated and pretreated bagasse residues are shown in **Figure 4A**. A decrease in the percentage of palmitic acid (C16:0) and oleic acid (C18:1) in the pretreated bagasse residue as compared to untreated bagasse indicates that both low- and high-severity pretreatment release fatty acids in the pretreatment liquor upon pretreatment. Pretreatment at 170°C for 10 and 20 min recovered ~42% palmitic acid (C16:0) (a decrease from 14 to ~8% C16:0 per g dry biomass), ~55% oleic acid (C18:1) (a decrease from 38 to ~17% C18:1 per g dry biomass), and ~30% linoleic acid (C18:2) (~9 to ~6% C18:2 per g dry biomass) in the pretreatment liquor. On the other hand, high-severity pretreatment at 210°C for 10 and 20 min released ~42% palmitic acid (C16:0) (a decrease from 14 to ~8% C16:0 per g dry biomass), 39% of oleic acid (C18:1) (a decrease from 38 to ~23% C18:1 per g dry biomass), and 20% of linoleic acid (C18:2) (a decrease from ~9 to ~7% C18:2 per g dry biomass) in the pretreatment liquor. The other fatty acids and lipid classes were concentrated in the bagasse residue on pretreatment. This observation is in agreement with that of the previously reported study (Jia et al., 2020). Pretreatment temperatures beyond 170°C exhibited no significant improvement in the recovery of fatty acids in pretreatment liquor.

On the other hand, enzyme hydrolysis aided the recovery of fatty acids other than C16:0, C18:1, and C18:2 by ~16% (a decrease from 54 to ~45% per g dry biomass) and ~63% (a decrease from 54 to ~20% C per g dry biomass) from 170°C and

210°C pretreated bagasse, respectively (**Figure 4B**). No further recovery of palmitic (C16:0) or linoleic acids (C18:2) was observed after saccharification. However, bagasse pretreated at 170°C and 210°C showed 1.3 and 2.1 times higher accumulation of oleic acid (C18:1) in the bagasse residue post saccharification, respectively.

Recovery of Fermentable Sugars From Transgenic Oilcane 1566 Bagasse

Besides lipids for biodiesel, fermentable sugars for bioethanol and various value-added bioproducts were recovered from the transgenic oilcane 1566 bagasse. The study categorizes the total sugar yield into solubilized and non-solubilized sugars. The sugars recovered in pretreatment liquor represented the solubilized sugar, while the yield of glucose and xylose obtained post saccharification is denoted as non-solubilized sugar as previously discussed (Maitra and Singh, 2021). Untreated oilcane 1566 bagasse yielded 0.200 ± 0.042 g sugar per g dry biomass on enzyme hydrolysis. Hydrothermal pretreatment at 170°C for 10 and 20 min yielded 0.227 ± 0.004 and 0.268 ± 0.004 g sugar per g dry biomass on saccharification, respectively. Pretreatment at 210°C for 10 and 20 min increased the sugar yield by 1.9 times (0.388 ± 0.003 g/g dry biomass) and 2.3 times (0.457 ± 0.010 g/g dry biomass) post saccharification as compared to the untreated biomass, respectively (**Figure 5A**). The total fermentable sugar (solubilized + non-solubilized sugars) increased from 20% w/w (untreated biomass) to 50% w/w (pretreated at 210°C), demonstrating >80% recovery of total sugar on pretreatment. However, with an increase in sugar
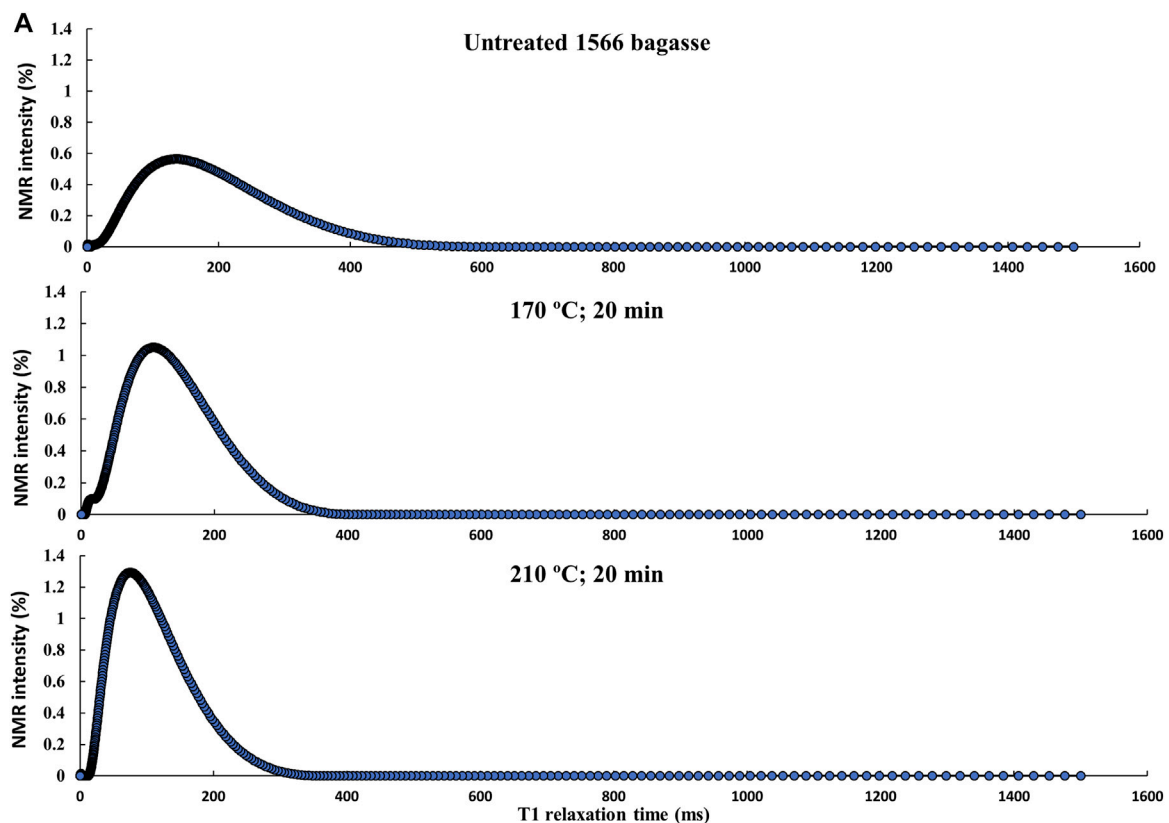
FIGURE 6 | (A) *T1* relaxation/intensity curves analysis of *in situ* lipids, **(B)** amount of total *in situ* lipids, and **(C)** fatty acid profile of lipids in the untreated and pretreated bagasse residues after SSF. Sugar and ethanol profile of **(D)** untreated and hydrothermally pretreated oilcane 1566 bagasse, that is, **(E)** 170°C for 20 min, and **(F)** 210°C for 20 min during SSF.

recovery, the yield of inhibitors, specifically acetic acid, also increased significantly beyond the 170°C pretreatment temperature (**Figure 5B**). The observation is in agreement with that in our previous study that inhibitor generation increases exponentially beyond 170°C in hydrothermal pretreatment (Maitra and Singh, 2021).

Lipid and Ethanol Yield After Simultaneous Saccharification and Fermentation (SSF)

Since ethanol has lipid-solubilizing property, simultaneous saccharification and fermentation (SSF) were performed with untreated and pretreated (170°C and 210°C for 20 min) bagasse to examine the recovery of lipids in the post-fermentation broth as observed in the corn dry–grind process (Moreau et al., 2010; Luangthongkam et al., 2015). The release of lipids from the cellulosic biomass after SSF is evident from the decrease in the magnitude of *T1* relaxation time of pretreated bagasse samples (**Table 1**). A left shift in relaxation/intensity curves of the pretreated bagasse residue after SSF in **Figure 6A** indicates a reduction in the degree of freedom of lipid-associated proton molecules of the pretreated bagasse samples (Maitra et al., 2021). An increase in NMR intensity could be due to the contribution of proton molecules from citrate buffer, yeast, or enzymes used in

SSF. The lipid released during fermentation can be present in different forms, such as oil-in-water emulsion, oil inside unbroken oil bodies, and oil droplets attached to cellulosic biomass (Luangthongkam et al., 2015). However, unlike the dry–grind process, due to the low lipid content in transgenic oilcane 1566 bagasse, most of the lipids remained either attached to or accumulated in the cellulosic biomass. Thus, an increase in the total lipid content of the pretreated bagasse residue after SSF was observed (**Figure 6B**). The fatty acid composition of the bagasse residue after SSF was similar to that of post-saccharification (**Figure 6C**).

The sugar and ethanol profiles of untreated and pretreated bagasse during SSF are presented in **Figures 6D–F**. Oilcane 1566 bagasse pretreated at 170°C for 20 min resulted in the best outcome for enhanced biofuel yield. It yielded a maximum ethanol concentration of 15.3 g/l which is 23.7 and 92.1% higher than ethanol obtained from untreated bagasse (11.6 g/l) and bagasse pretreated at 210°C for 20 min (1.2 g/l), respectively. Glucose and xylose were consumed simultaneously and completely within 48 h of fermentation (**Figure 6E**). A decrease in ethanol concentration after 55 h was observed that could be due to the consumption of ethanol by yeast as a carbon source after complete consumption of sugars (**Figures 6D, E**) (Raamsdonk et al., 2001). It has been observed in several
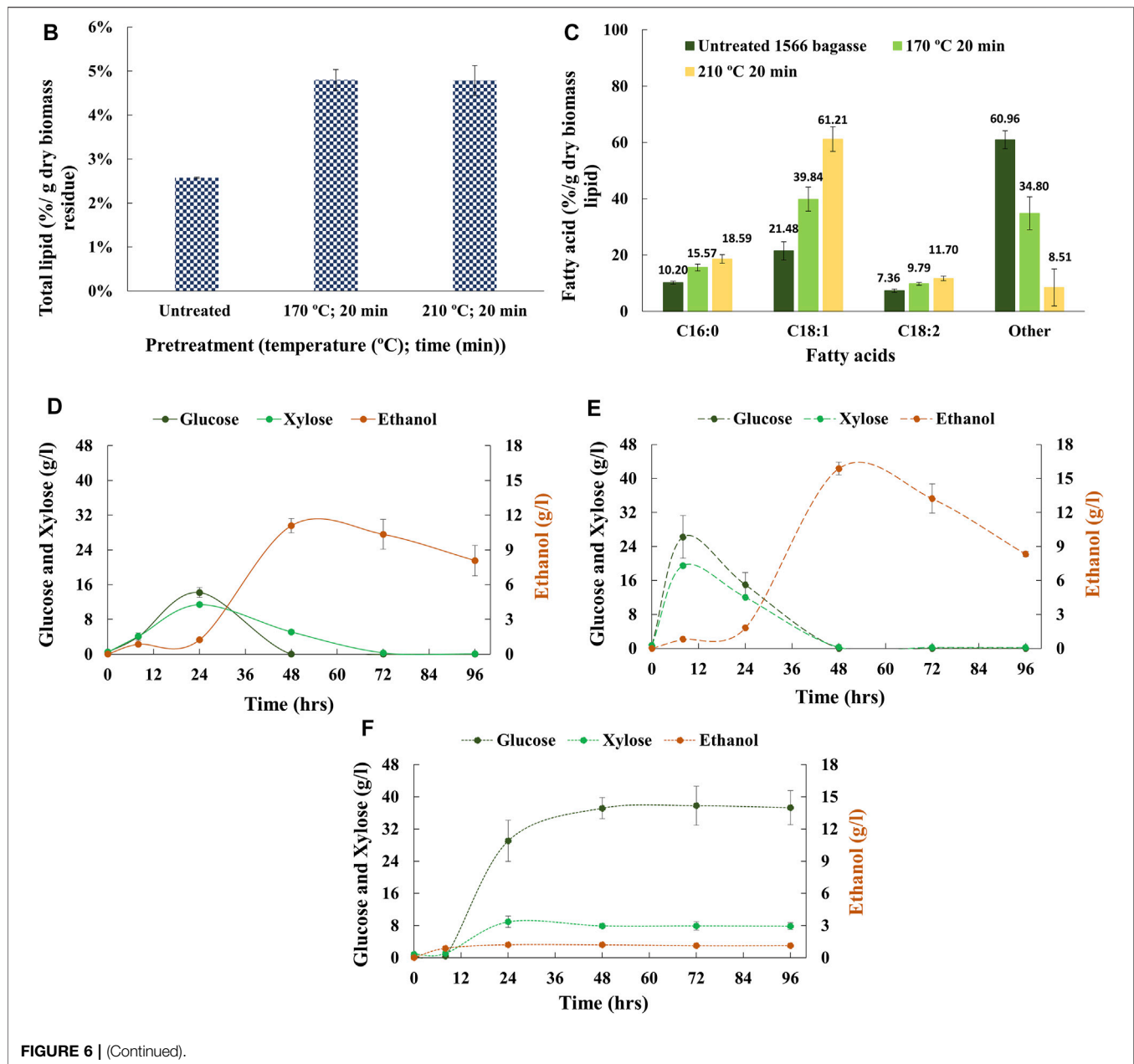
FIGURE 6 | (Continued).

fermentation studies with both Crabtree positive and negative yeasts that once all the sugars in the fermentation medium are consumed, yeasts start to consume sugar metabolism products as a carbon source and proliferate slowly (Polakis and Bartley, 1965; Skoog et al., 1992). Unfortunately, due to high concentration of inhibitors (**Figure 5B**), yeast could not grow well on bagasse pretreated at 210°C for 20 min. No significant change in sugar consumption or ethanol production was observed over 96 h of fermentation (**Figure 6F**). High-severity pretreatment generates inhibitory compounds that restrict the growth of yeast and reduce ethanol yield (**Figures 5B**, **6F**). Removal of inhibitors could improve the fermentation efficiency of high-severity–pretreated bagasse.

DISCUSSION

Recovery and Stability of Lipids During Bioprocess Steps

Plant tissues have a variety of lipid classes present in both bound and free forms. Triacylglyceride (TAG) molecules in the transgenic oilcane 1566 accumulate in the form of droplets inside the vegetative tissues (Parajuli et al., 2020). Recovery of a fraction of these free lipids in the pretreatment liquor decreases the cost of subsequent solvent extraction. The present NMR study showed that hydrothermal pretreatment and saccharification release ~25% of total lipids in pretreatment liquor and

45–60% of the remaining lipids in hydrolyzate, respectively. The remaining bound lipids in the cellulosic biomass can be extracted at the end of the bioprocess using organic solvent extraction (Huang et al., 2017).

Analysis of the stability of *in situ* lipids in the transgenic cellulosic biomass upon pretreatment is critical to optimizing the pretreatment parameters. To this end, time-domain proton NMR spectroscopy can detect minute alterations in the degree of freedom of oil-associated proton nuclei in the bagasse residues after various pretreatment procedures. Changes can be observed in the NMR intensity and the magnitude of relaxation time distribution (Robinson and Cistola, 2014; Nikolskaya and Hiltunen, 2020; Maitra et al., 2021). The *T1* relaxation/intensity curves also provide information on the decomposition of lipids in the pretreated bagasse residue upon pretreatment. In the previous study, the authors demonstrated the effects of hydrothermal, dilute-acid, and alkali pretreatment on model biomass systems (bagasse with externally added crude corn oil). In the alkaline pretreated biomass, alkali caused saponification of the oil in the biomass which resulted in inconsistent relaxation/intensity curves, indicating the decomposition of oil due to the saponification reaction (Maitra et al., 2021). Unlike the NMR relaxation/intensity curves of alkali-pretreated biomass, both low- and high-severity hydrothermal pretreatment retain the stability of *in situ* lipids (**Figure 2**).

The Composition of Lipids Recovered Decides the Quality of Biodiesel

In addition to the stability of lipids, the lipid classes and the fatty acid profile of the lipids in the transgenic bioenergy crops are crucial as they decide the properties of biodiesel such as oxidative stability, freezing point, heating value, lubricity, kinematic viscosity, and cloud point (Knothe and Gerpen, 2005; Knothe, 2008). The approach of hyperaccumulation of lipids in transgenic bioenergy crops also aims to improve the percentage of desirable fatty acids. Therefore, during the development and optimization of the pretreatment protocol for transgenic bioenergy crops, it is necessary to analyze the fatty acid composition of lipids after each step of bioprocessing. TD-NMR provides a rapid and convenient screening method during the initial developmental stages. The TD-NMR technique utilizes the specific *T1T2* relaxometry spectra of saturated (SFA), unsaturated (UFA), and polyunsaturated (PUFA) fatty acids. Each fatty acid exhibits distinct spectra due to the nanofluidity of the hydrocarbon side chains and molecular properties (Robinson and Cistola, 2014; Nikolskaya and Hiltunen, 2018, 2019). The fatty acid composition of seed oils is routinely analyzed using NMR (Ebrahimi et al., 2017; Engelsen and van den Berg, 2017; Gottstein et al., 2019). The present study extends the application of the TD-NMR technique for determining the fatty acid profile of lipids in cellulosic biomass residues subsequent to each bioprocessing step.

TD-NMR analysis of the oil-associated proton fluidity (**Figure 2**) and fatty acid profile (**Figure 4A**) of untreated and pretreated bagasse residues confirmed the release of lipid molecules in the pretreatment liquor upon pretreatment. However, bagasse residues obtained post saccharification showed a relatively higher percentage of C16:0, C18:1, and C18:2 fatty acids (**Figure 4B**). This can be attributed to the deconstruction of the biomass residue to release sugars and the accumulation of membrane-bound lipids in the remaining bagasse residue. An increased fraction of C18:1 (oleic) was observed in the pretreated biomass post saccharification. C18 unsaturated fatty acids are one of the predominant fatty acids in plants. Since both pretreatment and saccharification solubilize the structural carbohydrates, an increase in the percentage of oleic acid (C18:1) in the pretreated bagasse residue after saccharification can be attributed to its higher occurrence as part of membrane-bound lipids (Reszczyńska and Hanaka, 2020). A higher percentage of C18 unsaturated fatty acids, specifically oleic acid in the lipids recovered from transgenic crops, aids the improvement in biodiesel quality by balancing the oxidative stability and cold flow of biodiesel without affecting the cetane number (Knothe, 2009). Interestingly, genetically modification expressed higher average values of oleic fatty acid in the transgenic oilcane bagasse which is best suited for biodiesel.

Enhanced Biofuel Yield From Transgenic Oilcane 1566 Bagasse

Both low- and high-severity chemical-free hydrothermal pretreatment of the transgenic oilcane 1566 bagasse efficiently recover lipids in pretreatment liquor and hydrolyzate, while remaining lipids get concentrated in the bagasse residue that could be recovered post fermentation for biodiesel production. High-severity hydrothermal pretreatment (210°C for 10 and 20 min) improved recovery of various lipid classes as compared to low severity pretreatment (170°C for 10 min) (**Figure 3A**). However, unfortunately, high-severity pretreatment produced >15%, >2.5%, >2% per g dry biomass of acetic acid, HMF, and furfurals, respectively (**Figure 5B**). The high concentration of inhibitory compounds restricted the growth and fermentation process of yeast during SSF, which limited the optimal production of bioethanol (**Figure 6F**), even though the recovery of lipids (**Figure 3A**) and fermentable sugars on saccharification was higher (**Figure 5A**). In hydrothermal pretreatment, the amount of inhibitory compounds generated is a function of biomass type, moisture content during pretreatment, and pretreatment time and temperature (Ximenes et al., 2011; Maitra and Singh, 2021). To this end, the low-severity pretreatment of bagasse recovered comparable lipids, ~35% w/w fermentable sugars, and significantly fewer inhibitory compounds that resulted in enhanced biofuel yield (lipids for biodiesel and bioethanol). Hence, hydrothermal pretreatment of transgenic oilcane 1566 bagasse at 170°C for 20 min provides optimum pretreatment conditions to balance the maximum recovery of lipid and fermentable sugar and minimal generation of inhibitors.

CONCLUSION

The study evaluates and presents chemical-free hydrothermal pretreatment at 170°C for 20 min as an optimized condition that balances the maximum recovery of lipid and fermentable sugars and minimal generation of inhibitors from oilcane 1566 bagasse. The NMR relaxometry spectra revealed that hydrothermal pretreatment prevents the decomposition of *in situ* lipids of transgenic bioenergy crops during the recovery process. Moreover, the study successfully demonstrates the application of time-domain ^{1}H-NMR spectroscopy in the field of bioprocessing for quantification of total lipids in cellulosic biomass, characterization of *in-situ* lipids into bound and free fractions, and determining the fatty acid composition of cellulosic biomass. The use of NMR spectroscopy has significantly sped up the analysis.

DATA AVAILABILITY STATEMENT

The original contributions presented in the study are included in the article/**Supplementary Material**, further inquiries can be directed to the corresponding author.

AUTHOR CONTRIBUTIONS

SM: conceptualization, experiments, data analysis, and manuscript drafting. SL: Development of transgenic plant, supervision, reviewing, and editing the manuscript. VS: conceptualization, supervision, reviewing and editing the manuscript, and funding acquisition.

SUPPLEMENTARY MATERIAL

The Supplementary Material for this article can be found online at: https://www.frontiersin.org/articles/10.3389/fenrg.2022.840418/full#supplementary-material

REFERENCES

Atabani, A. E., Silitonga, A. S., Ong, H. C., Mahlia, T. M. I., Masjuki, H. H., Badruddin, I. A., et al. (2013). Non-edible Vegetable Oils: A Critical Evaluation of Oil Extraction, Fatty Acid Compositions, Biodiesel Production, Characteristics, Engine Performance and Emissions Production. *Renew. Sustain. Energ. Rev.* 18, 211–245. doi:10.1016/j.rser.2012.10.013

Berman, P., Leshem, A., Etziony, O., Levi, O., Parmet, Y., Saunders, M., et al. (2013). Novel 1H Low Field Nuclear Magnetic Resonance Applications for the Field of Biodiesel. *Biotechnol. Biofuels* 6, 55. doi:10.1186/1754-6834-6-55

Bhuiya, M. M. K., Rasul, M. G., Khan, M. M. K., Ashwath, N., and Azad, A. K. (2016). Prospects of 2nd Generation Biodiesel as a Sustainable Fuel-Part: 1 Selection of Feedstocks, Oil Extraction Techniques and Conversion Technologies. *Renew. Sustain. Energ. Rev.* 55, 1109–1128. doi:10.1016/j.rser.2015.04.163

Ebrahimi, P., Viereck, N., Bro, R., and Engelsen, S. B. (2017). Chemometric Analysis of NMR Spectra. *Mod. Magn. Reson.*, 1–20. doi:10.1007/978-3-319-28275-6_20-1

Engelsen, S. B., and van den Berg, F. W. J. (2017). "Quantitative Analysis of Time Domain NMR Relaxation Data," in *Modern Magnetic Resonance.* Editor G. A. Webb (Cham: Springer International Publishing), 1–19. doi:10.1007/978-3-319-28275-6_21-1

Gottstein, V., Müller, M., Günther, J., Kuballa, T., and Vetter, W. (2019). Direct 1H NMR Quantitation of Valuable Furan Fatty Acids in Fish Oils and Fish Oil Fractions. *J. Agric. Food Chem.* 67, 11788–11795. doi:10.1021/acs.jafc.9b04711

Huang, H., Long, S. P., Clemente, T. E., and Singh, V. (2016a). Technoeconomic Analysis of Biodiesel and Ethanol Production from Lipid-Producing Sugarcane and Sweet Sorghum. *Ind. Biotechnol.* 12, 357–365. doi:10.1089/ind.2016.0013

Huang, H., Long, S., and Singh, V. (2016b). Techno-economic Analysis of Biodiesel and Ethanol Co-production from Lipid-producing Sugarcane. *Biofuels, Bioprod. Bioref.* 10, 299–315. doi:10.1002/bbb.1640

Huang, H., Moreau, R. A., Powell, M. J., Wang, Z., Kannan, B., Altpeter, F., et al. (2017). Evaluation of the Quantity and Composition of Sugars and Lipid in the Juice and Bagasse of Lipid Producing Sugarcane. *Biocatal. Agric. Biotechnol.* 10, 148–155. doi:10.1016/j.bcab.2017.03.003

Jia, Y., Kumar, D., Winkler-Moser, J. K., Dien, B., and Singh, V. (2020). Recoveries of Oil and Hydrolyzed Sugars from Corn Germ Meal by Hydrothermal Pretreatment: A Model Feedstock for Lipid-Producing Energy Crops. *Energies* 13, 6022. doi:10.3390/en13226022

Knothe, G., and Gerpen, J. V. (2005). *The Biodiesel Handbook*. Editors G. Knothe, J Van Gerpen, and J. Krahl (AOCS Publishing). Available at: https://www.taylorfrancis.com/books/9781439822357.

Knothe, G. (2008). "Designer" Biodiesel: Optimizing Fatty Ester Composition to Improve Fuel Properties. *Energy Fuels* 22, 1358–1364. doi:10.1021/ef700639e

Knothe, G. (2009). Improving Biodiesel Fuel Properties by Modifying Fatty Ester Composition. *Energy Environ. Sci.* 2, 759–766. doi:10.1039/b903941d

Luangthongkam, P., Fang, L., Noomhorm, A., and Lamsal, B. (2015). Addition of Cellulolytic Enzymes and Phytase for Improving Ethanol Fermentation Performance and Oil Recovery in Corn Dry Grind Process. *Ind. Crops Prod.* 77, 803–808. doi:10.1016/j.indcrop.2015.09.060

Maher, K. D., and Bressler, D. C. (2007). Pyrolysis of Triglyceride Materials for the Production of Renewable Fuels and Chemicals. *Bioresour. Technol.* 98, 2351–2368. doi:10.1016/j.biortech.2006.10.025

Maitra, S., and Singh, V. (2021). Balancing Sugar Recovery and Inhibitor Generation during Energycane Processing: Coupling Cryogenic Grinding with Hydrothermal Pretreatment at Low Temperatures. *Bioresour. Technol.* 321, 124424. doi:10.1016/j.biortech.2020.124424

Maitra, S., Dien, B., Long, S. P., and Singh, V. (2021). Development and Validation of Time-domain 1 H-NMR Relaxometry Correlation for High-throughput Phenotyping Method for Lipid Contents of Lignocellulosic Feedstocks. *GCB Bioenergy* 13, 1179–1190. doi:10.1111/gcbb.12841

Moreau, R. A., Hicks, K. B., Johnston, D. B., and Laun, N. P. (2010). The Composition of Crude Corn Oil Recovered after Fermentation via Centrifugation from a Commercial Dry Grind Ethanol Process. *J. Am. Oil Chem. Soc.* 87, 895–902. doi:10.1007/s11746-010-1568-z

Nascimento, P. A. M., Barsanelli, P. L., Rebellato, A. P., Pallone, J. A. L., Colnago, L. A., and Pereira, F. M. V. (2017). Time-domain Nuclear Magnetic Resonance (TD-NMR) and Chemometrics for Determination of Fat Content in Commercial Products of Milk Powder. *J. AOAC Int.* 100, 330–334. doi:10.5740/jaoacint.16-0408

Nikolskaya, E., and Hiltunen, Y. (2018). Determination of Carbon Chain Lengths of Fatty Acid Mixtures by Time Domain NMR. *Appl. Magn. Reson.* 49, 185–193. doi:10.1007/s00723-017-0953-2

Nikolskaya, E., and Hiltunen, Y. (2019). Molecular Properties of Fatty Acid Mixtures Estimated by Online Time-Domain NMR. *Appl. Magn. Reson.* 50, 159–170. doi:10.1007/s00723-018-1046-6

Nikolskaya, E., and Hiltunen, Y. (2020). Time-Domain NMR in Characterization of Liquid Fuels: A Mini-Review. *Energy Fuels* 34, 7929–7934. doi:10.1021/acs.energyfuels.0c01464

Overend, R. P., Chornet, E., and Gascoigne, J. A. (1987). Fractionation of Lignocellulosics by Steam-Aqueous Pretreatments. *Phil. Trans. R. Soc. Lond. A.* 321, 523–536. doi:10.1098/rsta.1987.0029

Parajuli, S., Kannan, B., Karan, R., Sanahuja, G., Liu, H., Garcia-Ruiz, E., et al. (2020). Towards Oilcane: Engineering Hyperaccumulation of Triacylglycerol into Sugarcane Stems. *GCB Bioenergy* 12, 476–490. doi:10.1111/gcbb.12684

Polakis, E., and Bartley, W. (1965). Changes in the Enzyme Activities of *Saccharomyces cerevisiae* during Aerobic Growth on Different Carbon Sources. *Biochem. J.* 97, 284–297. doi:10.1042/bj0970284

Raamsdonk, L. o. M., Diderich, J. A., Kuiper, A., van Gaalen, M., Kruckberg, A. L., Berden, J. A., et al. (2001). Co-Consumption of Sugars or Ethanol and Glucose in aSaccharomyces Cerevisiae Strain Deleted in theHXK2 Gene. *Yeast* 18, 1023–1033. doi:10.1002/yea.746

REN21 (2020). Renewables 2020 Global Status Report. Available at: https://www.ren21.net/wp-content/uploads/2019/05/GSR_2020_Press_Release_ES.pdf (Accessed September 15, 2021).

Resch, M. G., Baker, J. O., and Decker, S. R. (2015). Low Solids Enzymatic Saccharification of Lignocellulosic Biomass (Laboratory Analytical Procedure). Available at: https://linkinghub.elsevier.com/retrieve/pii/S0925838818308703 (Accessed December 15, 2020).

Reszczyńska, E., and Hanaka, A. (2020). Lipids Composition in Plant Membranes. *Cell Biochem. Biophys.* 78, 401–414. doi:10.1007/s12013-020-00947-w

Robinson, M. D., and Cistola, D. P. (2014). Nanofluidity of Fatty Acid Hydrocarbon Chains as Monitored by Benchtop Time-Domain Nuclear Magnetic Resonance. *Biochemistry* 53, 7515–7522. doi:10.1021/bi5011859

Skoog, K., Hahn-Hägerdal, B., Degn, H., Jacobsen, J. P., and Jacobsen, H. S. (1992). Ethanol Reassimilation and Ethanol Tolerance in Pichia Stipitis CBS 6054 as Studied by 13 C Nuclear Magnetic Resonance Spectroscopy. *Appl. Environ. Microbiol.* 58, 2552–2558. doi:10.1128/AEM.58.8.2552-2558.1992

Vanhercke, T., Belide, S., Taylor, M. C., El Tahchy, A., Okada, S., Rolland, V., et al. (2019). Up-regulation of Lipid Biosynthesis Increases the Oil Content in Leaves ofSorghum Bicolor. *Plant Biotechnol. J.* 17, 220–232. doi:10.1111/pbi.12959

Ximenes, E., Kim, Y., Mosier, N., Dien, B., and Ladisch, M. (2011). Deactivation of Cellulases by Phenols. *Enzyme Microb. Technol.* 48, 54–60. doi:10.1016/j.enzmictec.2010.09.006

Zale, J., Jung, J. H., Kim, J. Y., Pathak, B., Karan, R., Liu, H., et al. (2016). Metabolic Engineering of Sugarcane to Accumulate Energy-dense Triacylglycerols in Vegetative Biomass. *Plant Biotechnol. J.* 14, 661–669. doi:10.1111/pbi.12411

Conflict of Interest: The authors declare that the research was conducted in the absence of any commercial or financial relationships that could be construed as a potential conflict of interest.

Publisher's Note: All claims expressed in this article are solely those of the authors and do not necessarily represent those of their affiliated organizations, or those of the publisher, the editors, and the reviewers. Any product that may be evaluated in this article, or claim that may be made by its manufacturer, is not guaranteed or endorsed by the publisher.

Measurement of Transport Properties of Woody Biomass Feedstock Particles Before and After Pyrolysis by Numerical Analysis of X-Ray Tomographic Reconstructions

Meagan F. Crowley[1], Hariswaran Sitaraman[2], Jordan Klinger[3], Francois Usseglio-Viretta[4], Nicholas E. Thornburg[5], Nicholas Brunhart-Lupo[2], M. Brennan Pecha[1], James H. Dooley[6], Yidong Xia[3] and Peter N. Ciesielski[1]*

[1]National Renewable Energy Laboratory, Renewable Resources and Enabling Sciences Center, Golden, CO, United States, [2]National Renewable Energy Laboratory, Computational Science Center, Golden, CO, United States, [3]Idaho National Laboratory, Energy Environment Science and Technology Directorate, Idaho Falls, ID, United States, [4]National Renewable Energy Laboratory, Center for Energy Conversion and Storage Systems, Golden, CO, United States, [5]National Renewable Energy Laboratory, Center for Integrated Mobility Sciences, Golden, CO, United States, [6]Forest Concepts, LLC, Auburn, WA, United States

Lignocellulosic biomass has a complex, species-specific microstructure that governs heat and mass transport during conversion processes. A quantitative understanding of the evolution of pore size and structure is critical to optimize conversion processes for biofuel and bio-based chemical production. Further, improving our understanding of the microstructure of biochar coproduct will accelerate development of its myriad applications. This work quantitatively compares the microstructural features and the anisotropic permeabilities of two woody feedstocks, red oak and Douglas fir, using X-ray computed tomography (XCT) before and after the feedstocks are subjected to pyrolysis. Quantitative analysis of the three-dimensional (3D) reconstructions allows for direct calculations of void fractions, pore size distributions and tortuosity factors. Next, 3D images are imported into an immersed boundary based finite volume solver to simulate gas flow through the porous structure and to directly calculate the principal permeabilities along longitudinal, radial, and tangential directions. The permeabilities of native biomass are seen to differ by three to four orders of magnitude in the different principal directions, but we find that this anisotropy is substantially reduced in the biochar formed during pyrolysis. The quantitative transport properties reported here enhance the ability of pyrolysis simulations to account for feedstock-specific effects and thereby provide a useful touchstone for the biorefining community.

Keywords: feedstock conversion, x-ray computed tomography, adaptive mesh refinement, pyrolysis, biomass, transport phenomena, characterization, image analysis

INTRODUCTION

Lignocellulosic biomass comprises a species-specific, highly porous, and anisotropic microstructure that originates from its function to transport and store water and nutrients throughout the plant during its lifetime. After harvesting, this microstructure, in tandem with the properties of the cell walls from which it is composed, govern the physical properties of lignocellulosic tissue. These features also influence important phenomena such as intraparticle heat and mass transfer that underlie conversion performance in biofuel and biochemical production processes (Ciesielski et al., 2020). Pyrolysis is a thermochemical method for converting biomass to molecular and oligomeric intermediates (Kan et al., 2016) and is often limited by internal transport of heat and fluid egress within particle pores (Pecha et al., 2019). Another product of pyrolysis is biochar, a carbonaceous material whose porosity is derived partially from the microstructure of the original biomass and partially from the pyrolysis process itself. Biochar has long been used as a soil amendment, (Lehmann, 2007; Verheijen et al., 2010), but has also found utility in advanced applications including catalysis, (Lee et al., 2017), adsorption, (Inyang et al., 2016), and electrochemical devices (Jiang et al., 2013). All of these aforementioned applications rely upon the transport of molecules, ions and/or thermal energy throughout hierarchical porous structures, necessitating a rigorous understanding of the microstructural transport properties of biochar and its parent feedstocks. Indeed, Di Blasi (1997) showed that differences in transport properties including permeability and porosity significantly impact pyrolysis product distributions.

Fundamental physical properties including permeability, tortuosity, and void fraction constrain the diffusive and advective transport that govern applications employing biomass and biochar as substrates. In the context of pyrolysis, intraparticle transport can affect the yield and distribution of products, which highlights the importance of accurately handling microstructural effects to achieve predictive models (Ciesielski et al., 2015; Ciesielski et al., 2020). Direct analysis of the microstructure of biomass feedstocks enables quantification of structural features including permeability, tortuosity, and void fraction to parameterize simulations for transport in porous media (Ciesielski et al., 2021). High-fidelity models of biomass conversion and biochar utilization require accurate transport models to enable scale-up and to mitigate technoeconomic risk of industrial deployment. Combined modeling and experimental works have previously elucidated the importance of directional permeability of biomass during pyrolysis (Di Blasi, 1998; Pecha et al., 2021). Other factors such as density and orientation in a gas stream also impact pyrolysis product quality and yield and have been investigated in studies such as in Kumari et al. (2022) and Pecha et al. (2017), but were not examined in this study as these properties can be measured without detailed information of the 3D microstructure of the material.

Accurate quantitative analysis of the microstructure of biomass by traditional experimental methods is difficult to perform. As discussed by Sun et al. (2021), the fidelity of commonly used techniques for experimentally measuring porosity or specific surface area, such as the density method or physisorption, are negatively impacted by pore structure breakage and undesired off-gassing that occur as functions of the temperature and pressure of the testing environment. Mercury intrusion porosimetry (MIP) is also commonly used, (Plötze and Niemz, 2011), but mercury handling poses significant safety concerns in the laboratory, and it can be difficult to interpret and reproduce results. Furthermore, particle size distributions may lead to misleading readouts of multiple pore sizes that are not necessarily statistically significant. For example, MIP tends to overrepresent the bottlenecks, thus providing an estimation of the minimum radius and not of the desired average radius (Holzer et al., 2013). Both the density method and mercury porosimetry provide limited information regarding geometric features of the microstructure, such as pore connectivity and tortuosity. Biomass tortuosity measurements are scant in the literature, and the techniques employed are difficult and specialized (Törnqvist et al., 2001). In the absence of such information and the inability to assume simplified particle geometries, some of us have previously assumed models of tortuosity as a function of void fraction (Sitaraman et al., 2015; Thornburg et al., 2020), although these assumptions extend beyond the models' intended derivations (Bruggeman, 1935; Millington and Quirk, 1961; Thornburg et al., 2020). In all cases, the sparse information available regarding biomass tortuosity and void fraction applies only to the material's fresh, unconverted state.

Therefore, there is an emergent need to understand partially and fully converted biomass structures to advance physics-based modeling of such conversion processes. X-ray Computed Tomography (XCT)-based techniques and the application of numerical analyses described here provide accessible, direct answers to these knowledge gaps. Refined measurements of tortuosity and void fraction further enable accurate determination of effective diffusivities, which in turn allow for more robust assessments of reaction vs. diffusion limitations in gas–solid (Pecha et al., 2021) and liquid–solid systems (Luterbacher et al., 2013; Thornburg et al., 2020). Mechanical approaches have also been used to measure some microstructural properties. Envelope density analyzers can be used to measure bulk density and thereby estimate particle porosity, also known as the void fraction, defined as the ratio of the volume of void space in a material to its total volume, though this method does not measure pore structure. Directional gas permeabilities can be measured with a Hassler cell and has been performed for various wood samples (Comstock, 1970; Choong et al., 1974; Filomena et al., 2014). However, these experimental approaches have their limitations, and permeability measurement is a time-intensive process that requires specially cut samples. These techniques are likely not applicable to biochar, which is brittle and cannot easily be shaped without damage.

Imaging methods offer a promising approach for characterizing the microstructure of biomass. Confocal scanning laser microscopy (CSLM), scanning electron microscopy (SEM), and transmission electron microscopy
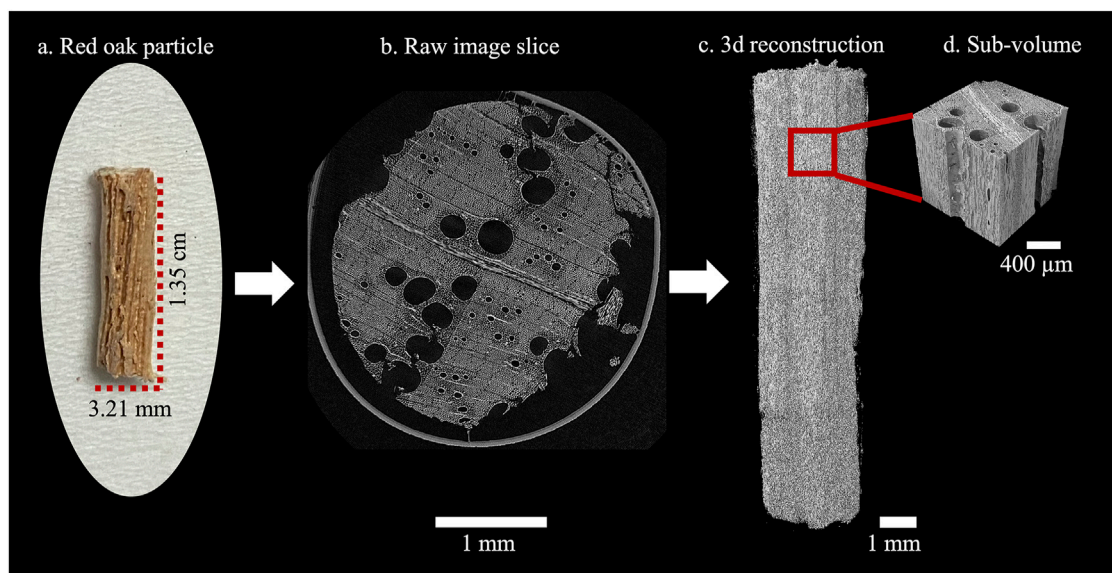
FIGURE 1 | Diagram of XCT workflow. **(A)** Initial particle, native red oak photograph. **(B)** Raw image slice from XCT radiograph. **(C)** 3D Reconstruction of the full particle from the raw images. **(D)** Cropped sub-volume used for numerical analysis and calculation of material properties.

(TEM) are commonly employed to visualize biomass microstructure, yet each have their limitations (Ciesielski et al., 2014). Sample preparation via microtomy for CSLM and TEM can be challenging and may result in artifacts that significantly affect the quality of the images (Boigné et al., 2022). While these methods can be used to produce 3D information about microstructure, by using z-stacking in the case of confocal microscopy, stereo pairs for SEM, and tomography for TEM, the reconstructions often suffer from limited resolution (Shah et al., 2017) and/or missing regions (Bartesaghi et al., 2008) which reduce confidence in measurements of pore geometry. X-ray computed tomography (XCT) is a widely used imaging method to analyze solid samples that produces 3D volumetric images of the microstructure of materials. XCT can provide high spatial resolution while mitigating optical limitations such as beam steering or limited depth of field (Boigné et al., 2022). The 3D reconstructions provided by XCT permit detailed, non-destructive, and direct characterization of the pore microstructure of biomass without the need for any histochemical treatments or intensive sample preparation. Several recent studies have employed XCT to characterize the microstructure of biomass. Sun et al. (2021) calculated the porosity and pore size distribution of loblolly pine samples from XCT reconstructions in a novel study, but important features such as the permeability tensor, tortuosity, or void fraction were not calculated. Boigné et al. (2022) analyzed volume shrinkage within biomass during pyrolysis and oxidation using real-time, *in situ* XCT, but the effects of pyrolysis on transport properties were not quantitatively investigated. Zolghadr et al. (2019) used XCT imaging to characterize the microstructure of crystalline cellulose, switchgrass, and tall fescue microspheres, calculating void fraction and tortuosity but not directional permeabilities.

This study characterizes the microstructure of early wood hardwood (red oak, *Quercus rubra*) and softwood (Douglas fir, *Pseudotsuga menziesii*) samples, before and after pyrolysis, using XCT imaging and quantitative numerical analysis to determine the void fraction, pore size distribution, tortuosity factor, and directional permeability. *MesoFlow*, our in house computational fluid dynamics (CFD) solver, developed using the block structured Cartesian adaptive mesh refinement library AMReX, (Zhang et al., 2019), is used to simulate gas-phase mass transport through the samples by directly importing sub-volumes of the XCT reconstructions. These simulations subsequently provide the principal permeabilities for each sample. Segmented XCT sub-volumes are also imported into the Microstructure Analysis Toolbox (MATBOX), (Cooper et al., 2016; Usseglio-Viretta, 2022), an open-source MATLAB app developed at NREL (available at https://github.com/NREL/MATBOX_Microstructure_analysis_toolbox) to calculate void fraction, pore size distribution, and tortuosity factor by numerical analysis. To the authors' knowledge, this is the first study to import 3D volumetric geometries of biomass before and after pyrolysis from XCT reconstructions into a CFD framework for permeability characterization. A diagram of the XCT workflow is shown in **Figure 1**, illustrating sample renderings from the raw tomographic images to 3D reconstruction, and final reduction to a sub-volume portion used for numerical analysis.

EXPERIMENTAL AND COMPUTATIONAL METHODS

Samples and Experimental Set up

Four total samples were analyzed for this study: a native hardwood red oak particle measuring 13.5 × 3.2 × 3.2 mm, a

pyrolyzed red oak particle measuring 11.7 × 3.0 × 3.0 mm, both provided by Iowa State University, a native softwood Douglas fir particle measuring 2.0 × 2.0 × 2.0 mm provided by Forest Concepts and Idaho National Lab and a pyrolyzed Douglas fir particle of dimensions 4.0 × 2.4 × 4.1 mm provided by Forest Concepts. The red oak and pyrolyzed Douglas fir particles were imaged at the Colorado School of Mines using a Zeiss Xradia 520 Versa sub-micron XCT Scanner, while the native Douglas fir particle was imaged using a General Electric (GE) Phoenix v|tome|x nano X-ray CT at Idaho National Lab.

The red oak dowels were pyrolyzed at 500°C under He in a modified Frontier micropyrolyzer as described in (Pecha et al., 2021) with a char yield of 19% after 90 s. The two Douglas fir samples (25–35 mg) were pyrolyzed in a horizontal spoon reactor under He at 500°C as described by (Christensen et al., 2017) for 5 min with char yields averaging 25%. At least 20 particles were pyrolyzed for each Douglas fir sample and random char particles were chosen for XCT imaging.

For the red oak and pyrolyzed Douglas fir XCT scans, each sample was secured to a mount in the chamber of the scanner using transparent adhesive tape for the larger red oak particles and glue adhesive for the pyrolyzed Douglas fir sample. Tape was not used to secure the Douglas fir sample to the mount because of its smaller size, and the layers of tape negatively impacted the contrast of the images. The X-ray source was tuned to emit with a voltage of 40 kV, 3 W power, and 75 μA current. The X-ray source was positioned 37.1 mm away from the detector, with the sample 20 mm away from the source placed between the source and detector. A ×4 objective magnification was used resulting in a 2 μm resolution for each scan, which was determined by (Sun et al., 2021) to be the minimum resolution to capture sufficient pore structure information.[4] The scanner rotated the sample on the mount from 0 to 360 with an angular step size of 0.22°. X-ray radiographs were captured at each angle with 15 s exposure. The total data acquisition time for each sample ranged from 8 to 32 h, with the larger red oak particles requiring longer acquisition times and the pyrolyzed Douglas fir particle requiring the shortest acquisition time.

The procedure of acquiring the 3D scan of the native Douglas fir sample using a General Electric (GE) Phoenix v|tome|x nano X-ray CT system can be found in (Sun et al., 2021) and is briefly described as follows. First, a sample particle is fixed onto a holder in the system chamber and the holder is programmed to rotate from 0 to 360° with an angular step size of 0.1°. Then radiographs are collected at each angle. Using the phoenix datos|x CT data acquisition software, the projections are then reconstructed to a 3D volume. The raw grey-scale image slices are exported from the software. For the 3D scan in this work, four Douglas fir pine particles are selected from the bulk samples produced by a Forest Concepts Crumbler® rotary shear system. In the imaging stage, several resolution settings, from 0.5 × 0.5 μm² to 4 × 4 μm² were tested, and the 2.2 × 2.2 μm² per voxel is the highest usable resolution to preserve the fine voids in the microstructure. The four 3D scanning processes resulted in four image stacks, each containing 1,419, 1,518, 3,838, and 3,997 images. To avoid the boundary effect in the porosity analysis, in each image stack a

region of interest (ROI) with size of 1.1 × 1.1 × 1.1 mm³ was cropped from the center.

The raw XCT scans of each sample, excluding the native Douglas fir which was imaged at Idaho National Lab, were reconstructed using Zeiss' proprietary software, XMReconstructor, and were subsequently exported as tiff image stacks using DragonFly Pro, (Object Research Systems Inc, 2021), a Graphical User Interface (GUI) application for analyzing and manipulating 3D XCT data. Each data set varies in size due to size variations of the particles. The native red oak data set contains 1,603 total images, where each image is a slice in the z axis with x- and y-dimensions of 1,604 by 6,740 voxels. Each image is 24 MB, resulting in a 34 GB size of the entire dataset. The pyrolyzed red oak data set contains 1,515 total images measuring 1,521 by 5,825 voxels. Each image is 17.8 MB, culminating in a 27 GB dataset. The pyrolyzed Douglas fir data set comprises 1,383 images measuring 1,251 by 977 voxels. The images are 17.8 MB each, for a cumulative size of 3.38 GB. The native Douglas fir data set has 1,520 z-slice images, each with a size of 1,571 by 1,383 voxels and 4.17 MB. The total size of the native Douglas fir dataset is 6.30 GB. All datasets were stored with 16-bit data precision.

Each of the full particle reconstructions were cropped into sub-volumes for direct import into *MesoFlow* and MATBOX using DragonFly Pro. The native and pyrolyzed red oak data were cropped to a cube measuring 642³ voxels, approximately 1.28 mm³. This reduced the size of each data set to 503 MB. The native Douglas fir was binned by a factor of 2 and cropped to a cube measuring 250³ voxels, approximately 1 mm³ reducing the size of the dataset to 30 MB. The pyrolyzed Douglas fir data was smaller and more irregular in size, therefore a rectangular prism measuring 434 × 322 × 424 voxels, approximately 0.87 × 0.64 × 0.85 mm³, was cropped from the data, reducing the size to 237.1 MB.

Gas Flow Simulations and Permeability Calculations

The cropped sub-volumes of each data set are directly imported into a CFD simulation using our in-house solver, *Mesoflow*, which is a compressible finite-volume solver that uses immersed boundary methods and structured Cartesian grids. Our solver is developed on block structured Cartesian adaptive mesh refinement library, AMReX, (Zhang et al., 2019), which has been recently employed for several applications pertaining to combustion, (Sitaraman et al., 2021b), multiphase (Sitaraman et al., 2021a; Musser et al., 2021) and astrophysical (Almgren et al., 2020) flows. Gas-phase transport simulations were run with flow in the longitudinal, radial, or tangential directions using the cropped XCT sub-volumes as the porous media. The National Renewable Energy Laboratory (NREL) High-Performance Computing (HPC) system was used to run all simulations. A total of 12 simulations were run, one with gas flow in each of the three directions for each sub-volume of red oak and Douglas fir before and after pyrolysis. In each simulation, a pressure drop of 1,000 Pa (inlet pressure = 1 E5 Pa, outlet pressure = 1.01E5 Pa) was applied to either end of the sub-volume in the direction of interest, with wall boundaries along the other two

directions. This ensured gas flow only in the direction of interest, and that the three principal components of the permeability could be calculated in isolation. Air was used as the gas in all simulations, with a viscosity of 1e-5 Pa s and a net molecular weight of 0.0289 kg/mol. The native Douglas fir simulations were run with a 4-micron image resolution for each voxel, while the pyrolyzed Douglas fir simulations were run with a resolution of 2 microns. A uniform $512 \times 512 \times 512$ Cartesian grid was used in the native and pyrolyzed Douglas fir simulations. These simulations were run on 128 nodes for a total 4,096 cores for 48 h to ensure the simulation reached steady state with a 4 to 5 order of magnitude drop in momentum residuals. The native and pyrolyzed red oak simulations were run with a 2-micron voxel size, and a uniform $768 \times 768 \times 768$ Cartesian grid. Twelve nodes with 18 cores per node for a total of 216 cores for 240 h were utilized for each of the red oak simulations. The number of nodes used for the red oak simulations was less because the grid size was larger: 128 voxels versus 32 voxels for the Douglas fir simulations. More computational cells were utilized for the red oak simulations because the data sets were larger with a higher resolution than the Douglas fir datasets.

We solve the Navier-Stokes equations in the compressible form on a Cartesian grid framework with an immersed boundary method for resolving complex pore structures, given by:

$$\frac{\partial \rho}{\partial t} + \frac{\partial (\rho U_i)}{\partial x_i} = 0 \qquad (1)$$

$$\frac{\partial (\rho U_i)}{\partial t} + \frac{\partial}{\partial x_j} \left(\rho U_i U_j \right) = -\frac{\partial P}{\partial x_i} + \frac{\partial \tau_{ij}}{\partial x_j} \qquad (2)$$

$$\frac{\partial (\rho e)}{\partial t} + \frac{\partial}{\partial x_i} \left(\rho e + P \right) = \frac{\partial}{\partial x_i} \left(k \frac{\partial T}{\partial x_i} \right) + \frac{\partial \left(\tau_{ij} v_j \right)}{\partial x_i} \qquad (3)$$

where $\rho, U_i, P, e, \tau_{ij}, k, x_i$ represent fluid density, velocity, pressure, total specific energy, viscous stress tensor, thermal conductivity, and spatial coordinate, respectively. The equations are closed using ideal gas law, total energy, and Newtonian fluid assumption, given by **Eqs. 4–6**, respectively:

$$P = \rho R T \qquad (4)$$

$$\rho e = \frac{P}{\gamma - 1} + \frac{1}{2} \rho U_i U_i \qquad (5)$$

$$\tau_{ij} = \mu \left(\frac{\partial U_j}{\partial x_i} + \frac{\partial U_i}{\partial x_j} \right) - \frac{2}{3} \mu \frac{\partial U_k}{\partial x_k} \delta_{ij} \qquad (6)$$

where R, μ, γ are the gas constant, fluid viscosity and isentropic exponent, respectively.

A modified advection upwind splitting method (AUSM) scheme (Liou, 2006) suitable for low Mach number flows along with second-order reconstruction and limiting (Tatsumi et al., 2012) is used for hyperbolic flux discretization and a second order central differencing scheme is used for viscous flux discretization away from the immersed boundary. A second-order explicit Runge-Kutta scheme is used for time advance until a steady-state is achieved.

The XCT geometry, obtained as a voxelated file of intensities, is first read into *Mesoflow*. A threshold intensity value obtained from image processing is used to identify whether a voxel is a solid or a void region. The intensity values were then extrapolated onto the Cartesian grid and all points greater than the threshold are identified as solid regions while the rest are in the fluid region. The Cartesian grids used in this work are kept at a higher resolution than the voxelated files for greater accuracy and grid convergence. The hyperbolic and viscous fluxes were then obtained at each Cartesian face that separates a fluid and solid cell using a simple velocity reflection method which is first order accurate.

Principal permeabilities were extracted from these simulations for application in particle models that utilize a pseudo-homogeneous assumption for internal pore structure (Di Blasi, 1998; Gentile et al., 2017; Pecha et al., 2021). For each particle, three simulations with dominant flow along each axis were set up with a pressure inlet and an outlet along the dominant flow direction and wall boundaries on the transverse boundaries. To the other four boundaries was applied a no flux condition to simulate the Hassler cell type permeability experiments. The simulations were run to steady state as determined by a decrease in calculated momentum residuals of at least four to five orders of magnitude. Permeability was extracted with the simple Darcy's law equation:

$$K_i = \bar{U}_i \mu \left(\frac{\overline{\partial P}}{\partial x_i} \right)^{-1} \qquad (7)$$

where K_i is the permeability, $\bar{U}_i$ is the surface averaged normal fluid velocity and $\frac{\overline{\partial P}}{\partial x_i}$ is the average pressure gradient along flow direction i.

MATBOX Numerical Analysis: Void Fraction, Pore Size Distribution and Tortuosity Calculations

Filtering, segmentation, and calculation of void fraction, pore size distribution, and tortuosity factor were performed with the open source software tool MATBOX (Usseglio-Viretta et al., 2022). The image stacks of the cropped XCT sub-volumes of each sample were loaded in *tiff* format into the MATBOX Filtering and Segmentation module and segmented into 8-bit tiff files with two phases: Phase 0 (void) and Phase 1 (solid) by applying a threshold specific to each sample which was determined by visually analyzing the images. Voxels with intensities below the threshold value are considered void space. An anisotropic diffusion filter developed by (Perona and Malik, 1990) was applied to the full sub-volumes of all of the datasets to smooth the data and reduce noise, except for the native Douglas fir sample which did not require filtering. The pore size distribution, void fraction, and tortuosity factor of each sample were then calculated using the MATBOX Microstructure Characterization module.

The volume fraction is calculated according to **Eq. 8**:

$$\varepsilon_k = \frac{1}{N} \sum_{i=1}^{N} v(i), \text{ with } v(i) = \begin{cases} 1 & if \; v(i) \in \text{phase } k \\ 0 & if \; v(i) \notin \text{phase } k \end{cases} \qquad (8)$$
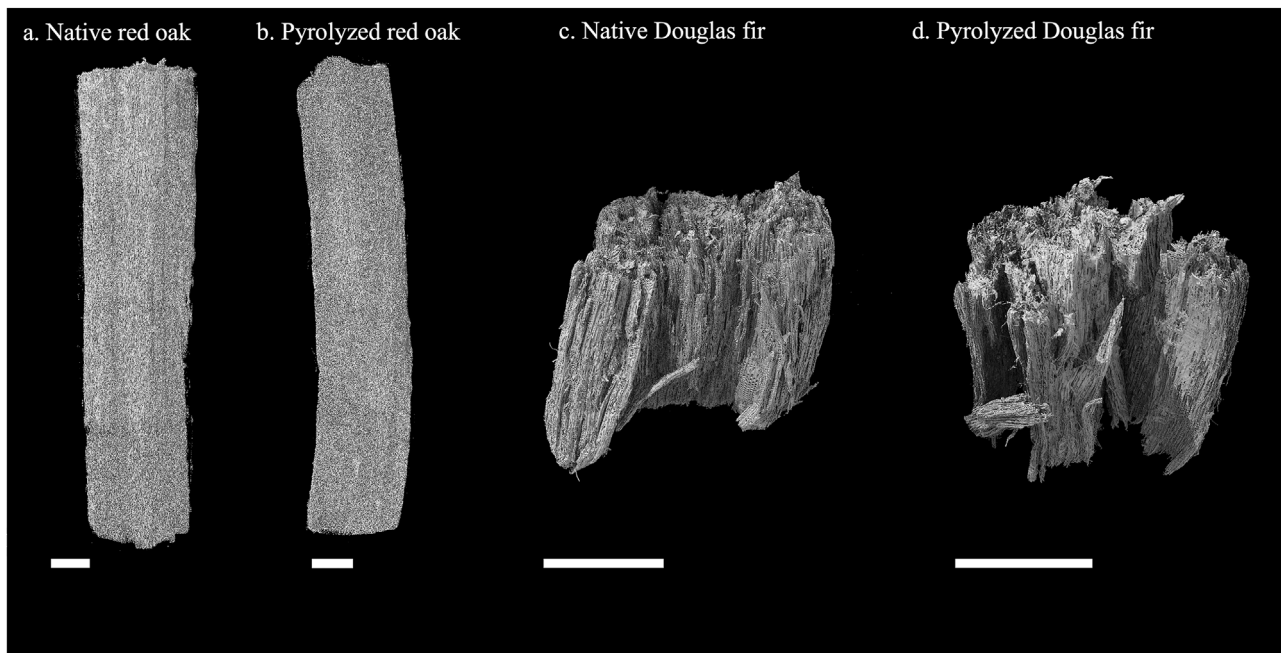
FIGURE 2 | Full particle reconstructions of each sample. **(A)** Native red oak, **(B)** Pyrolyzed red oak, **(C)** Native Douglas fir **(D)** Pyrolyzed Douglas fir. All scale bars indicate 1 mm length.

Where ε_k is the volume fraction of phase k, N is the total number of voxels in the sub-volume, and $v(i)$ is equal to one if it is an element of phase k, and zero otherwise.

The tortuosity factors of the sub-volumes are calculated from the ratio between the effective diffusion coefficient along the longitudinal, radial, or tangential directions and the bulk diffusion coefficient, and the porosity using TauFactor developed by (Cooper et al., 2016). TauFactor calculates tortuosity using a finite-difference based approach and fixed Dirichlet boundary conditions. The algorithm first solves the Laplace equation within the sub-volume in the direction of interest, and the effective diffusion coefficient is obtained by analyzing the concentration field via 1D Fick's first law described in (Laurencin et al., 2012). With these values, the tortuosity, τ, along direction i can be solved for according to **Eq. 9**:

$$\frac{D_{eff,i}}{D_{bulk}} = \frac{\varepsilon}{\tau_i} \tag{9}$$

Where $\frac{D_{eff,i}}{D_{bulk}}$ is the ratio between the effective diffusion coefficient along direction i and the bulk (free fluid) diffusion coefficient, and ε is the porosity (void fraction).

Pore size distributions are calculated using the Euclidean Distance Map Fitting Method (EDMF) described in (Usseglio-Viretta et al., 2020). This method fits the diameter of a sphere such that its Euclidean distance map cumulative function agrees with the one calculated on the sub-volume, providing a distribution of the distance of the void space to the nearest solid surface calculated on the investigated medium. The method provides a characteristic length relevant to be used as a pore diameter to model transport mechanisms. Size

distributions are highly dependent on the numerical method employed to calculate them, as thoroughly investigated in a previous work (Usseglio-Viretta et al., 2020). EDMF exhibits similar results with state of the art discrete particle size algorithms, while being much faster to calculate, and does not suffer from size underestimation of continuum particle size distribution algorithm (Usseglio-Viretta et al., 2020).

RESULTS

3D reconstructions of native and pyrolyzed red oak and Douglas fir particles were obtained via X-Ray computed tomography and reconstruction software. Millimeter-size sub-volumes were extracted from the reconstructions for direct importation into *MesoFlow* gas-phase flow simulations and MATBOX for numerical analysis. **Figure 2** shows the full 3D XCT reconstructions of each sample. The volume shrinkage due to pyrolysis can clearly be seen comparing the native and pyrolyzed samples. **Figure 3** depicts the cropped sub-volumes from each of the full particle reconstructions, along with longitudinal, radial, and tangential slices of each sample. The species-specific microstructures are revealed, as the native red oak exhibits a fine pore (i.e., lumen) structure of fiber cells with large-diameter vessel cell channels characteristic of hardwoods, while the native Douglas fir exemplifies the highly regular pore structure comprising arrays of axial tracheids characteristic of softwoods (Ciesielski et al., 2015). Additionally, the effects of thermal treatment on pore structure are apparent: pyrolysis degrades the pore structure, increases void volume, and reduces
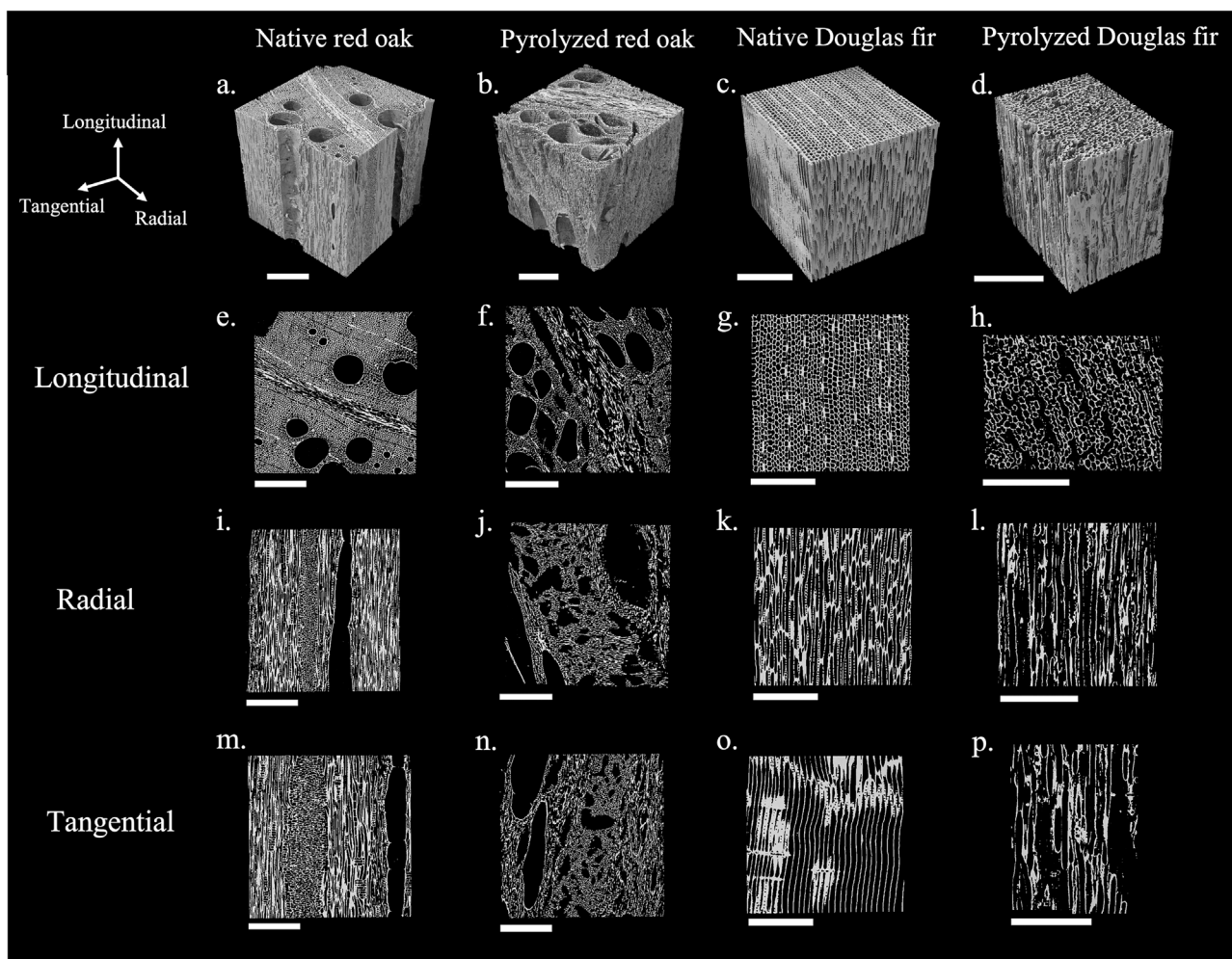
FIGURE 3 | Sub-volumes of each sample with longitudinal, radial, and tangential slices. **(A)** Native red oak sub-volume, **(B)** Pyrolyzed red oak sub-volume, **(C)** Native Douglas fir sub-volume, **(D)** Pyrolyzed Douglas fir sub-volume, Longitudinal slices of **(E)** Native red oak, **(F)** Pyrolyzed red oak, **(G)** Native Douglas fir, **(H)** Pyrolyzed Douglas fir, Radial slices of **(I)** Native red oak, **(J)** Pyrolyzed red oak, **(K)** Native Douglas fir, **(L)** Pyrolyzed Douglas fir, Tangential slices of **(M)** Native red oak, **(N)** Pyrolyzed red oak, **(O)** Native Douglas fir, **(P)** Pyrolyzed Douglas fir. All scale bars indicate 400 µm length.

TABLE 1 | Calculated void fraction, directional tortuosity factors of the void phase, and directional effective diffusivity multipliers [see **Eq. 9**] of each species before and after pyrolysis.

Property	Native red oak	Pyrolyzed red oak	Native Douglas fir	Pyrolyzed Douglas fir
Void Fraction	0.71	0.87	0.66	0.77
Material porosity, % [Literature values from Boigné et al. (2022)]	46.6 ± 0.8	76.6 ± 1.1	51.8 ± 0.8	78.2 ± 1.6
Longitudinal tortuosity factor	1.13	1.16	1.26	1.08
Radial tortuosity factor	2.47	1.29	16.7	1.99
Tangential tortuosity factor	6.00	1.39	38.5	4.02
Longitudinal effective diffusivity multiplier	0.62	0.75	0.52	0.71
Radial effective diffusivity multiplier	0.29	0.67	0.04	0.38
Tangential effective diffusivity multiplier	0.12	0.62	0.02	0.19

directional anisotropy, which is especially obvious in the red oak slices. Despite the stark directional differences inherent to native tissues, thermochemical conversion appears to obscure and even erase several key anatomical features.

To quantify these species- and treatment-specific observations, XCT sub-volumes were next subjected to numerical analysis to estimate microstructural features before and after pyrolysis. The calculated volume fraction and tortuosity

FIGURE 4 | Distance-to-surface map of each sample normal to longitudinal and transverse directions: **(A)** native red oak normal to the longitudinal direction, **(B)** native red oak normal to the tangential direction, **(C)** pyrolyzed red oak normal to the longitudinal direction, **(D)** pyrolyzed red oak normal to the tangential direction, **(E)** native Douglas fir normal to the longitudinal direction, **(F)** native Douglas fir normal to the tangential direction, **(G)** pyrolyzed Douglas fir normal to the longitudinal direction, **(H)** pyrolyzed Douglas fir normal to the tangential direction. Slices shown are taken from the middle of the analyzed XCT reconstruction sub-volumes. Note that the scalebars are unique to each plot.

factors of the void phase of each sample are reported in **Table 1**. The void fractions of the native red oak and the pyrolyzed red oak are overall larger in magnitude compared to those of the native and pyrolyzed Douglas fir. This is likely because of the presence of larger diameter pore channels in the red oak samples, while the Douglas fir samples exhibit smaller pore channels overall. After pyrolysis, a significant increase in void fraction is observed for all samples. The Douglas fir samples show a 15.9% increase in void fraction after pyrolysis, while that of the red oak show a 22.8% increase in void fraction after pyrolysis. Previously reported values of void fraction for Oak and Douglas Fir from Boigné et al. (2022) are also listed in **Table 1**. The calculated values from the current study agree with the previously reported values, with slight variations likely due to variability of the material. Particularly, our calculated value for the void fraction of red oak is significantly higher than that reported by Boigné et al. (2022). We attribute this difference to our sample being taken from early wood red oak, which contains more vessel elements than the bulk material and thus a higher void fraction.

Interesting trends are gleaned from the collection of calculated tortuosity factors and the resultant effective diffusivity multipliers (**Eq. 9**). First, the longitudinal direction of each sample shows the lowest tortuosity factor, consistent with observations of the permeability being highest in the longitudinal directions. This is due to the relatively large vessels present in red oak and the closely packed axial tracheid lumen of Douglas fir species oriented parallel to the longitudinal direction, which promote facile, direct flow (Comstock, 1970). The tortuosity factor in the tangential direction is the highest for all analyzed samples, also in agreement with the calculated values of permeability being lowest

in the tangential direction for all samples, because the tangential direction is perpendicular to both the large longitudinal pore channels and the smaller radial ray cells, therefore there are few if any direct paths for flow in the tangential direction. Second, pyrolysis decreases and nearly unifies all directional tortuosity factors regardless of species by reducing the solid phase volume and increasing void fraction, creating larger pore channels with more direct paths for flow. Remarkably, post-treatment tortuosity values are closely consolidated across all coordinates, as seen by the tight agreement among effective diffusivity multipliers following pyrolysis. Indeed, thermal treatment appears to quantitatively erase many anatomical features, creating less tortuous and more directionally uniform channels for heat and mass transport within partially converted biomass particles.

Figure 4 shows color maps representing the distance to the nearest solid phase surface for each sample normal to the longitudinal and tangential directions. The warmer colors indicate a longer distance to the nearest surface, while cooler colors indicate a shorter distance. The centers of the largest pores are deep red, reflecting that they are furthest from the nearest solid surface, i.e., the cell wall. From these graphs and the results of **Table 2**, one can qualitatively ascertain that pyrolysis increases the size of the void space for both red oak and Douglas fir samples; this finding is visualized by the increase in scale of the colored regions in **Figure 4**. Additionally, the red oak samples show a higher number of warm-colored areas due to the large diameter pore channels characteristic of this species.

Figure 5 shows the fitted Euclidean distance map distribution of the distances to the nearest solid surface for native and pyrolyzed red oak in plot A) as well as native and pyrolyzed

TABLE 2 | Calculated permeability tensors for each sample. All values in units of m^2 (i.e., $m^3 \cdot m/m^2$).

Direction	Native red oak calculated	Literature range red oak (0% moisture)Choong et al. (1974)	Pyrolyzed red oak calculated	Native Douglas fir calculated	Literature range Douglas fir/Pine (5–9% moisture)Choong et al. (1974)	Pyrolyzed Douglas fir calculated
Longitudinal	8.76E-12	9.6E-12 to 6E-11	9.13E-12	1.36E-12	9E-13 to 3E-11	2.81E-12
Radial	3.64E-15	8E-16 to 3.5E-15	3.35E-13	1.81E-14	8E-17 to 2E-15	2.29E-13
Tangential	1.30E-15	4.5E-16 to 1.3E-15	8.98E-13	3.46E-16	1E-17 to 1E-15	1.32E-13

FIGURE 5 | Euclidean distance map probability density distribution of pore to surface distance of each sample. Plot **(A)** shows the distance to surface distribution function of native red oak, shown in black, and pyrolyzed red oak, shown in red. Plot **(B)** shows the distribution function of native Douglas fir, shown in black, and pyrolyzed Douglas fir, shown in red.
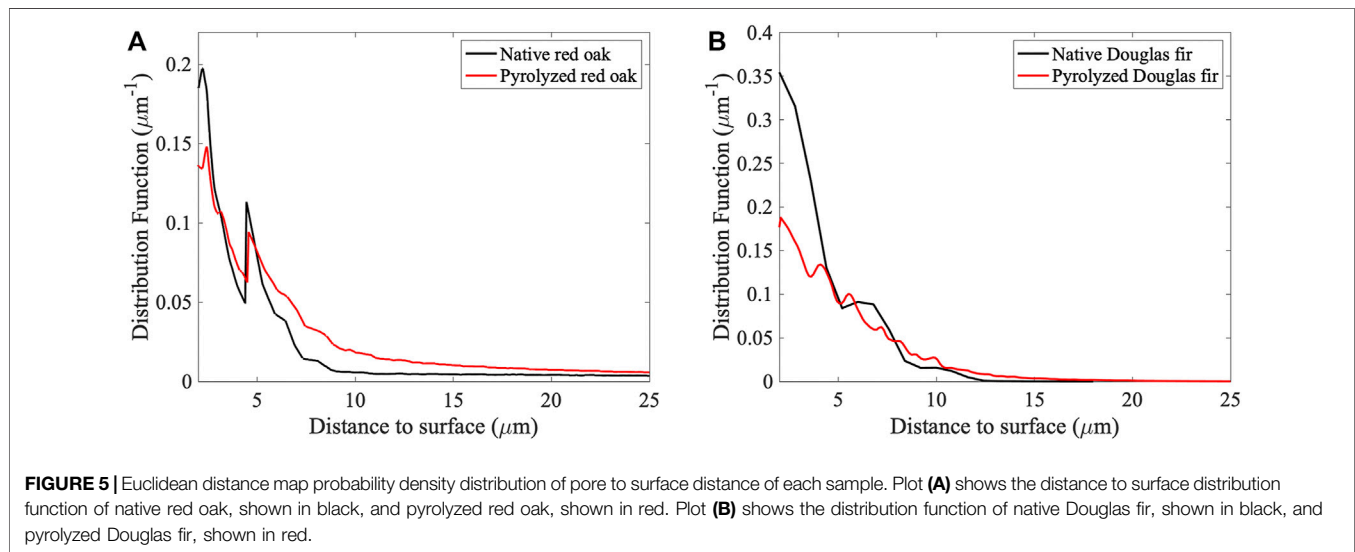
Douglas fir in plot B). We note that these distances roughly correspond to half the pore diameter, since they represent the distance from the center of the pore to the nearest cell wall. The distribution of distances to the nearest surface for native red oak shows two peaks, one at 2.2 μm and the other at 4.5 μm. These distances are characteristic of fiber and vessel cells, respectively, present in the red oak microstructure. While the large vessel elements are clearly visible in the XCT reconstructions and distance maps, their relatively low abundance does not produce a recognizable peak in the distribution function. The pyrolyzed red oak distribution also exhibits these two peaks, although the smaller peaks indicate that less of the void population occupies these distances. Most of the population of pores in the native red oak lies below 10 μm, while the pyrolyzed red oak has a larger population beyond 10 μm. This is due to the increase in void space that occurs during pyrolysis, therefore the pore sizes increase, and their interiors are farther away from the nearest solid surface. Similarly, the native Douglas fir distribution shows peaks at 2 and 6.8 μm, representing the ray cells and tracheid cells, respectively, present in the material. The peaks are noticeably wider for the Douglas fir samples compared to the red oak samples, suggesting that the sizes of the ray and tracheid cells in the Douglas fir samples have more variance. There is a higher population of void spaces beyond 10 μm in the native Douglas fir compared to the red oak, likely due to the more uniformly arrayed pore structures characteristic of the larger

tracheid and ray cells in the softwood tissue compared to the sparser large-diameter vessel cells in red oak. Pyrolysis increases the population of voids beyond 10 μm from the surface in the case of both samples. Interestingly, the pyrolyzed Douglas fir population exhibits a greater number of peaks at different distances, suggesting that there are dominant pore sizes arising from solid phase deterioration upon pyrolysis. The sizes of such voids become more heterogeneous, with fewer populations being concentrated in specific regions characteristic to the large and small cell lumen domains observed for each native species.

The dominant avenues for gas-phase transport in each direction are visualized by the steady-state velocity magnitudes obtained from the permeability simulations plotted in **Figure 6**. For the softwood prior to pyrolysis, fluid transport expectedly occurs primarily in the longitudinal direction, facilitated by axial tracheids, while that in the radial direction traverses ray cell channels. In the tangential direction, pits connecting adjacent tracheid cells serve as the major conduits. Transport follows a similar trend for the red oak samples, apart from the large vessel elements providing the primary avenues in the longitudinal direction. The radial and tangential native oak samples also exhibited the lowest permeability values obtained in this study, with values so low in some regions that they were below the visualization cutoff, giving rise to partially unfilled velocity plots for these two simulations.
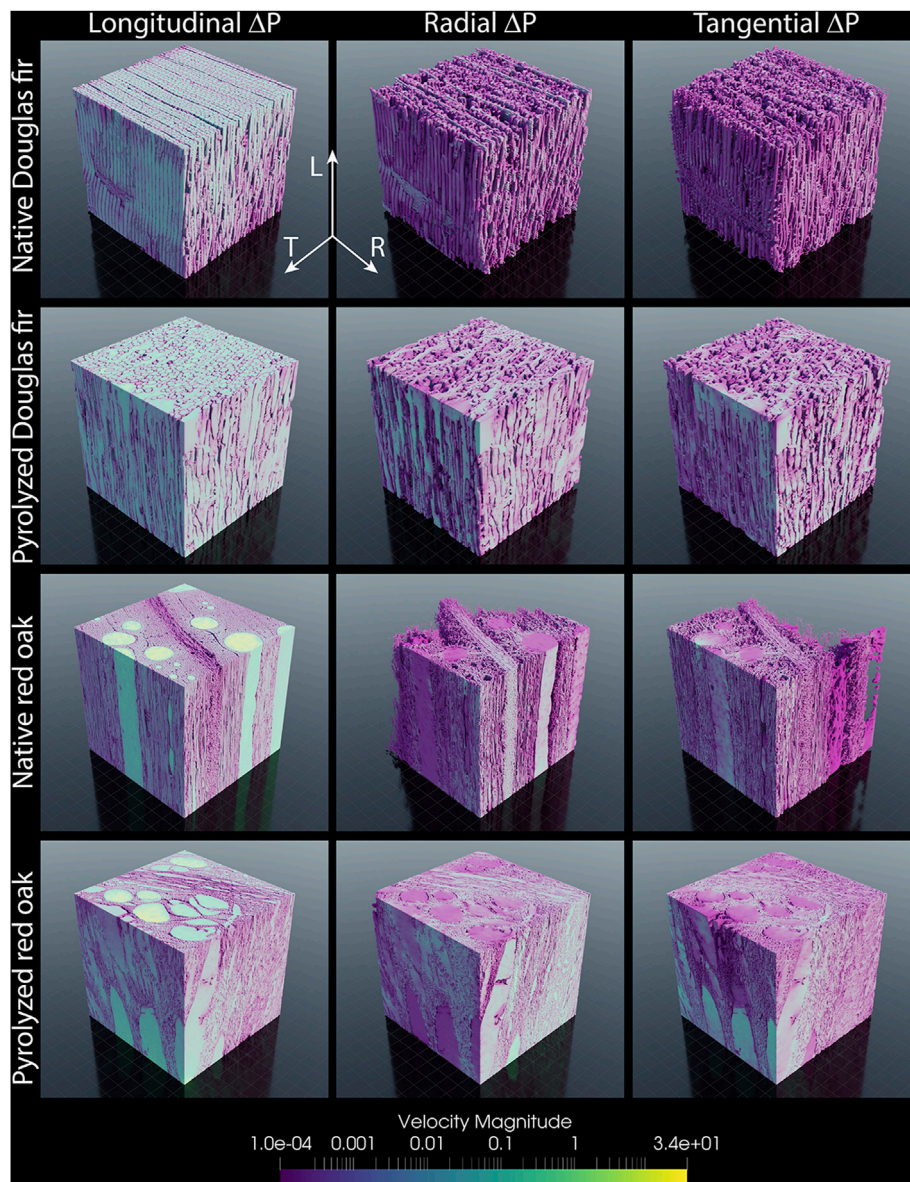
FIGURE 6 | Visualization of permeability simulations at steady state for native and pyrolyzed Douglas fir and red oak XCT sub-volumes. Pressure gradients were applied to only one of the longitudinal, radial, and tangential directions in each case. Velocity magnitudes less than 10^{-4} are below the visualization cutoff, hence the partial renditions for the native red oak simulations in the radial and tangential directions.

The reduction in anisotropy due to pyrolysis is visualized by the velocity magnitude plotted in **Figure 6** and further reflected in the calculated permeability values reported in **Table 2**. In the native samples, the longitudinal direction has the highest permeability by two to four orders of magnitude compared to radial and tangential directions. By contrast, the pyrolyzed samples differ only by roughly one order of magnitude between longitudinal and tangential or radial directions. The permeability of the Douglas fir sample increases in all directions after pyrolysis, whereas the red oak particle exhibits a more significant increase in the tangential and radial directions than in the longitudinal direction after pyrolysis. This is consistent with what can be visually ascertained from the slices in **Figure 3**, and with the consolidation of directional tortuosity factors upon thermal treatment (**Table 1**); the large pore channels in the longitudinal direction of the red oak samples contribute significantly to the permeability, and their growth proportional to their initial size is not as significant as in the tangential and radial directions, or as in the longitudinal direction of the Douglas fir samples. Some of the smaller pores in the red oak sample may also be more prone to plugging by plasticized char material during pyrolysis than in the other directions, an effect which may be further compensated by the creation of new macropores within char domains.

The permeability values computed from the transport simulations shown in **Table 2** yielded results that are nearly within the range of values for red oak and Douglas fir reported in the literature almost 50 years ago. It is interesting to note that for red oak the ratio of longitudinal to axial permeability was calculated as 2,406 and longitudinal to tangential as 6,738; Choong et al. (1974) reported ratios of approximately 2000 and 1,500, respectively. For oak char, the calculated ratio of longitudinal to axial permeability was 27 and the calculated ratio of longitudinal to tangential permeability was 10. Notably, greater macroporosity was evolved in the radial and tangential direction than in the longitudinal direction, which only increases by around 4%. This is consistent with observations that biochar retains its longitudinal pore structure during pyrolysis in part due to the catalytic effects of ash (Montoya et al., 2017). For Douglas fir, the ratio of longitudinal to axial permeability was calculated as 75 and longitudinal to tangential as 3,930; Comstock (1970) reported ratios of approximately 10,000 and 50,000, respectively. Additionally, for nearly all of the native wood samples, the permeabilities calculated in this study fall within the range of the reported values by Choong and Comstock, except for the radial permeability of the native Douglas fir sample which is higher by an order of magnitude. Although the origin of this discrepancy is uncertain, it could potentially be attributed to the specific geometry of the sub-volume investigated here, or to differences in the sensitivity to very small flowrates of our computational method and of the experimental method employed by Comstock. The reported values for permeability from the literature are measured from native biomass samples and not representative of biochar, for which there are no values reported in the literature to the authors knowledge.

DISCUSSION

In biomass pyrolysis, the effects of anisotropic transport phenomena have become increasingly important for sufficiently predictive models. Often, a suitable permeability tensor is not considered due to a lack of viable data, especially to describe its evolution over the course of pyrolytic conversion of biomass. Di Blasi (1998) noted that this permeability *tensor* is important for accurate predictions of conversion times and intraparticle flow patterns with large particles in the conduction-controlled regime. To confront this issue, our team has previously constructed geometric approximations that attempted to capture the dominant features that control transport phenomena at the intraparticle scale, which were assumed to be axial tracheids for softwoods and fiber and vessel cells for hardwoods (Ciesielski et al., 2015). However, the geometric models investigated in the aforementioned study neglected important features such as ray cells and pits, which are revealed by the current work to play a dominant role in facilitating transport in the radial and tangential directions. Additional recent work by some of us has empirically investigated the importance of anisotropic permeability and similarly concluded that large ratios of longitudinal to radial permeabilities must be employed in numerical models in order to

agree with experimental results (Pecha et al., 2021). However, this study did not include dramatic evolution of radial porosity throughout the pyrolytic process that we observe here, due to lack of quantitative microstructural information. The findings in this work suggest that intraparticle transport models may be improved by calculating the permeability tensor as a function of conversion, wherein longitudinal permeability is marginally enhanced, while new macroporosity emerges in the radial and longitudinal dimensions.

Porosity and pore structure also play a role in reactor-scale modeling. Current state-of-the-art reactor-scale models account for changes in particle size and density, as the drag model for particles is a strong function of these parameters. Recently, particle rocketing due to explosive devolatilization along its longitudinal axis has been observed for small particles in benchtop reactor systems with high temperatures (1200°C), which is evidently due to vapors escaping one end of a particle at high velocities (Llamas et al., 2022). Evidently, anisotropic pore structure and porosity evolution play integral roles in the motion of particles inside of a high-temperature fluidized reactor (Ciesielski et al., 2021; Lu et al., 2021; Llamas et al., 2022; Lu et al., 2022).

Despite its advantages, there are still challenges associated with the method of microstructure characterization described in this work. The first is the sheer size of the data acquired and the time required for acquisition: full particle reconstructions range from around 4–35 GB, with up to tens of billions of voxels, requiring an acquisition time exceeding 30 h for the largest samples. The large size of the datasets makes transfer, analysis, simulation, and visualization of the data computationally expensive and arduous. This can be mitigated by downscaling the data by sampling; however, most of the datasets we acquired could not be down-sampled without losing crucial pore resolution. Choosing smaller samples to image is another approach to decreasing the size of the data acquired. Samples with dimensions between 1–5 mm are ideal for reducing data size and acquisition time while still being easy to handle and representative of bulk microstructure. We addressed this issue by cropping regions of the full datasets into smaller sub-volumes, but this could arguably sacrifice the generality of our results as it may not account for natural variations of extended microstructures within the samples. However, the periodicity and scale of the sub-volumes (~1 mm^3) are sufficiently general descriptors of the diversity of pore details, which typically exist on the scale of a few microns (Forest Products Laboratory, 1953). Even after cropping the full datasets into sub-volumes, *Mesoflow* simulations required at least 50,000 CPU core-hours to achieve steady state, using an abundance of high-performance computing resources.

An additional limitation of the present study is the lack of information regarding intra-cell wall transport, phenomena which are expected to strongly depend on biomass speciation. Pyrolysis products originate from the cell wall biopolymers and must navigate out of the nanoporous wall matrix into the macroporosity of the cell lumen prior to exiting the particle (Carpita et al., 1979; Kojiro et al., 2010). Future studies could confront this shortcoming using TEM tomography coupled to

similar computational methods (Hinkle et al., 2015) to develop a dynamic, intra-cell wall transport model that could be coupled to bulk transport in a hierarchical transport simulation. It remains unknown which of these length scales and expected species dependencies may dominate observable pyrolysis performance in laboratory measurements.

While this work provides datapoints regarding the microstructure of biomass before and after pyrolysis, there still exists a knowledge gap regarding the precise physics which underlie microstructural evolution during pyrolysis. A truly game-changing simulation tool would be capable of predicting the dynamic evolution of pore structure as a function of initial pore structure, external heating conditions, intraparticle transport phenomena, and overall extent of pyrolytic conversion. Such a universal tool would enable *a priori* selection of biomass feedstocks and design of pyrolytic processes to achieve specific, optimized porosity for biochar applications, such as soil remediation, adsorption, filtration, and catalysis. However, much work remains to fully parameterize a pyrolysis simulation that accurately predicts pore structure evolution, including quantifying the mechanical properties of lignocellulose at different temperatures and extents of conversion.

CONCLUSION

The current study stands as a proof-of-concept and exposition for capturing particle-scale transport properties of native and thermally treated biomass microstructures using non-destructive XCT imaging paired with numerical analysis and CFD simulations. Detailed characterization of transport properties of red oak and Douglas fir is achieved, including the calculation of directional permeabilities, tortuosity factors, pore size distributions, and void fractions, along with the comparison of these properties before and after pyrolysis. The quantitative microstructural values reported here may be used to parameterize intra-particle transport simulations for these biomass species before and after pyrolysis. A crucial finding of this work is that the anisotropy of the permeability exhibited by native wood tissue is largely attenuated by pyrolysis, which in turn facilitates the creation of unique macroporosity spatially distributed throughout char coproduct domains. While the present findings are specific to the two wood species characterized here, our methods are readily extensible to other feedstocks of interest, such as grasses or genetically modified energy crops, and to alternate conversion strategies where permeability and physical transport properties play governing roles.

REFERENCES

Almgren, A., Sazo, M., Bell, J., Harpole, A., Katz, M., Sexton, J., et al. (2020). CASTRO: A Massively Parallel Compressible Astrophysics Simulation Code. *Joss* 5 (54), 2513. doi:10.21105/joss.02513

Bartesaghi, A., Sprechmann, P., Liu, J., Randall, G., Sapiro, G., and Subramaniam, S. (2008). Classification and 3D Averaging with Missing Wedge Correction in Biological Electron Tomography. *J. Struct. Biol.* 162 (3), 436–450. doi:10.1016/j.jsb.2008.02.008

DATA AVAILABILITY STATEMENT

The raw data supporting the conclusion of this article will be made available by the authors, without undue reservation.

AUTHOR CONTRIBUTIONS

ACKNOWLEDGMENTS

Boigné, E., Bennett, N. R., Wang, A., and Ihme, M. (2022). Structural Analysis of Biomass Pyrolysis and Oxidation Using *In-Situ* X-ray Computed Tomography. *Combustion and Flame* 235, 111737. doi:10.1016/j.combustflame.2021.111737

Bruggeman, D. A. G. (1935). Berechnung verschiedener physikalischer Konstanten von heterogenen Substanzen. I. Dielektrizitätskonstanten und Leitfähigkeiten der Mischkörper aus isotropen Substanzen. *Ann. Phys.* 416 (7), 636–664. doi:10.1002/andp.19354160705

Carpita, N., Sabularse, D., Montezinos, D., and Delmer, D. P. (1979). Determination of the Pore Size of Cell Walls of Living Plant Cells. *Science* 205 (4411), 1144–1147. doi:10.1126/science.205.4411.1144

Choong, E., Tesoro, F., and Manwiller, F. (1974). Permeability of Twenty-Two Small Diameter Hardwoods Growing on Southern pine Sites. *Wood and Fiber* 6 (1), 91–101.

Christensen, E., Evans, R. J., and Carpenter, D. (2017). High-resolution Mass Spectrometric Analysis of Biomass Pyrolysis Vapors. *J. Anal. Appl. pyrolysis* 124, 327–334. doi:10.1016/j.jaap.2017.01.015

Ciesielski, P. N., Wang, W., Chen, X., Vinzant, T. B., Tucker, M. P., Decker, S. R., et al. (2014). Effect of Mechanical Disruption on the Effectiveness of Three Reactors Used for Dilute Acid Pretreatment of Corn stover Part 2: Morphological and Structural Substrate Analysis. *Biotechnol. Biofuels* 7 (1), 47–12. doi:10.1186/1754-6834-7-47

Ciesielski, P. N., Crowley, M. F., Nimlos, M. R., Sanders, A. W., Wiggins, G. M., Robichaud, D., et al. (2015). Biomass Particle Models with Realistic Morphology and Resolved Microstructure for Simulations of Intraparticle Transport Phenomena. *Energy Fuels* 29 (1), 242–254. doi:10.1021/ef502204v

Ciesielski, P. N., Pecha, M. B., Lattanzi, A. M., Bharadwaj, V. S., Crowley, M. F., Bu, L., et al. (2020). Advances in Multiscale Modeling of Lignocellulosic Biomass. *ACS Sust. Chem. Eng.* 8 (9), 3512–3531. doi:10.1021/acssuschemeng.9b07415

Ciesielski, P. N., Pecha, M. B., Thornburg, N. E., Crowley, M. F., Gao, X., Oyedeji, O., et al. (2021). Bridging Scales in Bioenergy and Catalysis: A Review of Mesoscale Modeling Applications, Methods, and Future Directions. *Energy Fuels* 35 (18), 14382–14400. doi:10.1021/acs.energyfuels.1c02163

Comstock, G. L. (1970). Directional Permeability of Softwoods. *Wood Fiber Sci.* 1 (4), 283–289.

Cooper, S. J., Bertei, A., Shearing, P. R., Kilner, J. A., and Brandon, N. P. (2016). TauFactor: An Open-Source Application for Calculating Tortuosity Factors from Tomographic Data. *SoftwareX* 5, 203–210. doi:10.1016/j.softx.2016.09.002

Di Blasi, C. (1997). Influences of Physical Properties on Biomass Devolatilization Characteristics. *Fuel* 76 (10), 957–964. doi:10.1016/S0016-2361(97)00096-3

Di Blasi, C. (1998). Physico-chemical Processes Occurring inside a Degrading Two-Dimensional Anisotropic Porous Medium. *Int. J. Heat mass transfer* 41 (24), 4139–4150. doi:10.1016/s0017-9310(98)00142-2

Filomena, C. M., Hornung, J., and Stollhofen, H. (2014). Assessing Accuracy of Gas-Driven Permeability Measurements: a Comparative Study of Diverse Hassler-Cell and Probe Permeameter Devices. *Solid Earth* 5 (1), 1–11. doi:10.5194/se-5-1-2014

Forest Products Laboratory (1953). *Density, Fiber Length, and Yields of Pulp for Various Species of Wood*. Madison, WI, USA: Forest Products Laboratory.

Gentile, G., Debiagi, P. E. A., Cuoci, A., Frassoldati, A., Ranzi, E., and Faravelli, T. (2017). A Computational Framework for the Pyrolysis of Anisotropic Biomass Particles. *Chem. Eng. J.* 321, 458–473. doi:10.1016/j.cej.2017.03.113

Hinkle, J. D., Ciesielski, P. N., Gruchalla, K., Munch, K. R., and Donohoe, B. S. (2015). Biomass Accessibility Analysis Using Electron Tomography. *Biotechnol. Biofuels* 8 (1), 212–216. doi:10.1186/s13068-015-0395-8

Holzer, L., Wiedenmann, D., Münch, B., Keller, L., Prestat, M., Gasser, P., et al. (2013). The Influence of Constrictivity on the Effective Transport Properties of Porous Layers in Electrolysis and Fuel Cells. *J. Mater. Sci.* 48 (7), 2934–2952. doi:10.1007/s10853-012-6968-z

Inyang, M. I., Gao, B., Yao, Y., Xue, Y., Zimmerman, A., Mosa, A., et al. (2016). A Review of Biochar as a Low-Cost Adsorbent for Aqueous Heavy Metal Removal. *Crit. Rev. Environ. Sci. Tech.* 46 (4), 406–433. doi:10.1080/10643389.2015.1096880

Jiang, J., Zhang, L., Wang, X., Holm, N., Rajagopalan, K., Chen, F., et al. (2013). Highly Ordered Macroporous Woody Biochar with Ultra-high Carbon Content as Supercapacitor Electrodes. *Electrochimica Acta* 113, 481–489. doi:10.1016/j.electacta.2013.09.121

Kan, T., Strezov, V., and Evans, T. J. (2016). Lignocellulosic Biomass Pyrolysis: A Review of Product Properties and Effects of Pyrolysis Parameters. *Renew. Sust. Energ. Rev.* 57, 1126–1140. doi:10.1016/j.rser.2015.12.185

Kojiro, K., Miki, T., Sugimoto, H., Nakajima, M., and Kanayama, K. (2010). Micropores and Mesopores in the Cell wall of Dry wood. *J. Wood Sci.* 56 (2), 107–111. doi:10.1007/s10086-009-1063-z

Kumari, K., Kishore, N., Gupta, S., Aravind, S. V., and Ahmed, G. (2022). Effect of Varying Fraction of Polypropylene Waste on Co-pyrolysis of Delonix Regia and Polyalthia Longifolia Leaves. *Curr. Res. Green Sust. Chem.* 5, 100233. doi:10.1016/j.crgsc.2021.100233

Laurencin, J., Quey, R., Delette, G., Suhonen, H., Cloetens, P., and Bleuet, P. (2012). Characterisation of Solid Oxide Fuel Cell Ni-8YSZ Substrate by Synchrotron X-ray Nano-Tomography: from 3D Reconstruction to Microstructure Quantification. *J. Power Sourc.* 198, 182–189. doi:10.1016/j.jpowsour.2011.09.105

Lee, J., Kim, K.-H., and Kwon, E. E. (2017). Biochar as a Catalyst. *Renew. Sust. Energ. Rev.* 77, 70–79. doi:10.1016/j.rser.2017.04.002

Lehmann, J. (2007). A Handful of Carbon. *Nature* 447 (7141), 143–144. doi:10.1038/447143a

Liou, M.-S. (2006). A Sequel to AUSM, Part II: AUSM+-up for All Speeds. *J. Comput. Phys.* 214 (1), 137–170. doi:10.1016/j.jcp.2005.09.020

Llamas, A. D. G. G., Guo, N., Li, T., Gebart, R., and Umeki, K. (2022). Rapid Change of Particle Velocity Due to Volatile Gas Release during Biomass Devolatilization. *Combustion and Flame* 238, 111898. doi:10.1016/j.combustflame.2021.111898

Lu, L., Gao, X., Dietiker, J.-F., Shahnam, M., and Rogers, W. A. (2022). MFiX Based Multi-Scale CFD Simulations of Biomass Fast Pyrolysis: A Review. *Chem. Eng. Sci.* 248, 117131. doi:10.1016/j.ces.2021.117131

Lu, L., Gao, X., Gel, A., Wiggins, G. M., Crowley, M., Pecha, B., et al. (2021). Investigating Biomass Composition and Size Effects on Fast Pyrolysis Using Global Sensitivity Analysis and CFD Simulations. *Chem. Eng. J.* 421, 127789. doi:10.1016/j.cej.2020.127789

Luterbacher, J. S., Parlange, J.-Y., and Walker, L. P. (2013). A Pore-Hindered Diffusion and Reaction Model Can Help Explain the Importance of Pore Size Distribution in Enzymatic Hydrolysis of Biomass. *Biotechnol. Bioeng.* 110 (1), 127–136. doi:10.1002/bit.24614

Millington, R. J., and Quirk, J. P. (1961). Permeability of Porous Solids. *Trans. Faraday Soc.* 57, 1200–1207. doi:10.1039/tf9615701200

Montoya, J., Pecha, B., Janna, F. C., and Garcia-Perez, M. (2017). Identification of the Fractions Responsible for Morphology Conservation in Lignocellulosic Pyrolysis: Visualization Studies of Sugarcane Bagasse and its Pseudo-components. *J. Anal. Appl. Pyrolysis* 123, 307–318. doi:10.1016/j.jaap.2016.11.015

Musser, J., Almgren, A. S., Fullmer, W. D., Antepara, O., Bell, J. B., Blaschke, J., et al. (2021). MFIX-exa: A Path toward Exascale CFD-DEM Simulations. *Int. J. High Perform. Comput. Appl.* 36, 10943420211009293. doi:10.1177/10943420211009293

Object Research Systems (ORS) Inc (2021). *Dragonfly 2021.3 for [Windows 11]*. Montreal, Canada: Object Research Systems ORS Inc.

Pecha, M. B., Arbelaez, J. I. M., Garcia-Perez, M., Chejne, F., and Ciesielski, P. N. (2019). Progress in Understanding the Four Dominant Intra-particle Phenomena of Lignocellulose Pyrolysis: Chemical Reactions, Heat Transfer, Mass Transfer, and Phase Change. *Green. Chem.* 21 (11), 2868–2898. doi:10.1039/c9gc00585d

Pecha, M. B., Garcia-Perez, M., Foust, T. D., and Ciesielski, P. N. (2017). Estimation of Heat Transfer Coefficients for Biomass Particles by Direct Numerical Simulation Using Microstructured Particle Models in the Laminar Regime. *ACS Sust. Chem. Eng.* 5 (1), 1046–1053. doi:10.1021/acssuschemeng.6b02341

Pecha, M. B., Thornburg, N. E., Peterson, C. A., Crowley, M. F., Gao, X., Lu, L., et al. (2021). Impacts of Anisotropic Porosity on Heat Transfer and Off-Gassing during Biomass Pyrolysis. *Energy & Fuels* 35, 20131. doi:10.1021/acs.energyfuels.1c02679

Perona, P., and Malik, J. (1990). Scale-space and Edge Detection Using Anisotropic Diffusion. *IEEE Trans. Pattern Anal. Machine Intell.* 12 (7), 629–639. doi:10.1109/34.56205

Plötze, M., and Niemz, P. (2011). Porosity and Pore Size Distribution of Different wood Types as Determined by Mercury Intrusion Porosimetry. *Eur. J. Wood Wood Prod.* 69 (4), 649–657. doi:10.1007/s00107-010-0504-0

Shah, S. M., Crawshaw, J. P., and Boek, E. S. (2017). Three-dimensional Imaging of Porous media Using Confocal Laser Scanning Microscopy. *J. Microsc.* 265 (2), 261–271. doi:10.1111/jmi.12496

Sitaraman, H., Kuhn, E. M., Nag, A., Sprague, M. A., Tucker, M. P., and Stickel, J. J. (2015). Multiphysics Modeling and Simulation of High-Solids Dilute-Acid Pretreatment of Corn stover in a Steam-Explosion Reactor. *Chem. Eng. J.* 268, 47–59. doi:10.1016/j.cej.2015.01.020

Sitaraman, H., Vaidhynathan, D., Grout, R., Hauser, T., Hrenya, C. M., and Musser, J. (2021a). An Error-Controlled Adaptive Time-Stepping Method for Particle Advancement in Coupled CFD-DEM Simulations. *Powder Tech.* 379, 203–216. doi:10.1016/j.powtec.2020.10.051

Sitaraman, H., Yellapantula, S., Henry de Frahan, M. T., Perry, B., Rood, J., Grout, R., et al. (2021b). Adaptive Mesh Based Combustion Simulations of Direct Fuel

Injection Effects in a Supersonic Cavity Flame-Holder. *Combustion and Flame* 232, 111531. doi:10.1016/j.combustflame.2021.111531

Sun, Q., Xia, Y., Klinger, J., Seifert, R., Kane, J., Thompson, V., et al. (2021). X-ray Computed Tomography-Based Porosity Analysis: Algorithms and Application for Porous Woody Biomass. *Powder Tech.* 388, 496–504. doi:10.1016/j.powtec.2021.05.006

Tatsumi, S., Martinelli, L., and Jameson, A. (2012). "A New High Resolution Scheme for Compressible Viscous Flows with Shocks," in 33rd Aerospace Sciences Meeting and Exhibit, Reno, NV, January 9–12, 1995, 466.

Thornburg, N. E., Pecha, M. B., Brandner, D. G., Reed, M. L., Vermaas, J. V., Michener, W. E., et al. (2020). Mesoscale Reaction-Diffusion Phenomena Governing Lignin-First Biomass Fractionation. *ChemSusChem* 13 (17), 4495–4509. doi:10.1002/cssc.202000558

Törnqvist, M., Hurme, T., and Rosenholm, J. B. (2001). Drift Speed: a Way of Measuring Diffusion and Tortuosity of Porous Materials. *Colloids Surf. A: Physicochemical Eng. Aspects* 180 (1), 23–31. doi:10.1016/S0927-7757(00)00732-9

Usseglio-Viretta, F. L. E., Finegan, D. P., Colclasure, A., Heenan, T. M. M., Abraham, D., Shearing, P., et al. (2020). Quantitative Relationships between Pore Tortuosity, Pore Topology, and Solid Particle Morphology Using a Novel Discrete Particle Size Algorithm. *J. Electrochem. Soc.* 167 (10), 100513. doi:10.1149/1945-7111/ab913b

Usseglio-Viretta, F. L. E., Patel, P., Bernhardt, E., Mistry, A., Mukherjee, P. P., Allen, J., et al. (2022). MATBOX: An Open-Source Microstructure Analysis Toolbox for Microstructure Generation, Segmentation, Characterization, Visualization, Correlation, and Meshing. *SoftwareX* 17, 100915. doi:10.1016/j.softx.2021.100915

Verheijen, F., Jeffery, S., Bastos, A. C., Van der Velde, M., and Diafas, I. (2010). Biochar Application to Soils. *A. Critical Scientific Review Effects Soil Properties, Processes, Functions. EUR.* 24099, 162.

Zhang, W., Almgren, A., Beckner, V., Bell, J., Blaschke, J., Chan, C., et al. (2019). AMReX: a Framework for Block-Structured Adaptive Mesh Refinement. *Joss* 4 (37), 1370. doi:10.21105/joss.01370

Zolghadr, A., Kelley, M. D., Sokhansefat, G., Moradian, M., Sullins, B., Ley, T., et al. (2019). Biomass Microspheres - A New Method for Characterization of Biomass Pyrolysis and Shrinkage. *Bioresour. Tech.* 273, 16–24. doi:10.1016/j.biortech.2018.09.137

Check for updates

Flowability of Crumbler Rotary Shear Size-Reduced Granular Biomass: An Experiment-Informed Modeling Study on the Angle of Repose

Ahmed Hamed[1], Yidong Xia[1]*, Nepu Saha[1], Jordan Klinger[1], David N. Lanning[2] and Jim Dooley[2]

[1]Energy and Environmental Science and Technology Directorate, Idaho National Laboratory, Idaho Falls, ID, United States, [2]Forest Concepts LLC, Auburn, WA, United States

Biomass has potential as a carbon-neutral alternative to petroleum for chemical and energy products. However, complete replacement of fossil fuel is contingent upon efficient processes to eliminate undesirable characteristics of biomass, e.g., low bulk density, variability, and storage-induced quality problems. Mechanical size reduction via comminution is a processing operation to engineer favorable biomass flowability in handling. Crumbler rotary shear mill has been empirically demonstrated to produce more uniformly shaped particles with higher flowability than hammermilled biomass. This study combines modeling and experimentation to unveil fundamental understandings of the relation between granular particle characteristics and biomass flow behavior, which elucidate underlying mechanisms and guide selection of critical processing parameters. For this purpose, the impact of critical material attributes, including particle size (2–6 mm), particle shape (briquette, chip, clumped-sphere, cube, etc.), and surface roughness, on the angle of repose (AOR) of milled pine chips were investigated using discrete element method (DEM) simulations. Forest Concepts Crumbler rotary shear system is used to produce milled pine particles within the same size range considered in DEM simulations. AOR of different sets of these particles were measured experimentally to benchmark DEM results against experimental data. Specific energy consumption for the comminution of biomass with different particle size and moisture content are measured for technoeconomic analysis. Our results show that the smaller size (2 mm) of pine particle achieves better followability (i.e., smaller AOR) while the energy cost of comminution is significantly higher and bulk density is almost the same as the 6-mm pine particles. For the 2-mm particle size, Crumbles from veneer have better flow properties than Crumbles from chips. Contrarily, no significant difference was observed between the AOR of the two materials for the 6-mm particle size. Furthermore, from DEM simulations, mechanical interlocking between particles was found as a dominant factor in determining AOR of complex-shaped particles such as milled pine, which cannot be accurately captured by using simple particle shapes (e.g., mono-sphere) with a rolling resistance model. Conversely, clumped-sphere model alleviates this limitation without increasing

computational cost significantly and can be used for accurate representation of biomass granular particles when simulating free-flow behavior.

Keywords: angle of repose, discrete element method, mechanical size reduction, biomass feedstocks, Douglas fir

1 INTRODUCTION

The continuing global increase of energy demand dictates exploring more energy resources and expanding the utilization of available options, which should be accompanied by improving the efficiency of the existing technologies. At the same time, the rising concerns about climate change have led to international initiatives that attempt to enforce the decarbonization of energy systems by advocating the transition to clean energy technologies. Accordingly, more stringent constraints on greenhouse gas emission rates to decelerate the global warming effect puts diminishing fossil fuels in a least favorable position in the strategic planning for the future energy roadmap (Renewable Energy Agency, 2018). Bioenergy is a promising technology that can be a crucial player in supplying the energy needs in the years to come (U.S. Department of Energy Bioenergy Technologies Office, 2016). In addition to bioenergy, beneficial bio-based products (e.g., chemicals and materials) are produced during biomass conversion in the biorefinery, analogous to a petroleum refinery. Although biomass is a versatile source of energy with the advantage of being one of the few renewable energy sources that can generate energy on-demand, there are several technical challenges that need to be overcome before policy makers can depend widely on this naturally abundant resource. For example, unlike fossil fuel, the raw form of biomass is not suitable for energy applications due to several reasons including its low bulk density, low calorific value, high moisture and oxygen content, high variability, and hydrophilic nature (Ciesielski et al., 2020; Oyedeji et al., 2020). Consequently, biomass preprocessing is imperative. In this regard, different mechanical (e.g., size reduction and densification), chemical (i.e., washing and leaching), and thermal (e.g., drying and torrefaction) processes can be applied to produce high-quality, uniform feedstock from lignocellulosic biomass (Stelte et al., 2012). This is achieved through changing the biomass physical properties and chemical composition in a way that improves the biofuel conversion performance and efficiency (Gao et al., 2021). Biomass preprocessing techniques are energy intensive processes. Starting from the pretreatment of the raw biomass materials, the energy produced during the feedstock conversion must be much higher than the overall energy consumed in manufacturing the fuel for the biofuel to be economically competitive. In addition, logistics operations (i.e., storage, transport, and reactor feeding) represent another large component of the total cost of generating bioenergy in the biorefinery. Moreover, poor flowability of the biomass feedstocks can lead to process upsets, such as jamming and clogging, during the handling operations (Rackl et al., 2017; Jin et al., 2020; Xia et al., 2020; Lu et al., 2021). This, in turn, can further increase the cost by increasing the downtime. Therefore, optimizing all different processes involved in the production of the biomass feedstock is necessary for this industry to be viable on commercial scale.

Instead of depending on empirical techniques applying univariate trial-and-error methods to reach this goal, Quality by Design (QbD) is a science- and risk-based holistic approach that can be employed to advance the product and process quality in a streamlined, systematic way (Adam et al., 2011). In this approach, the identification of the critical process parameters (CPPs) and critical materials attributes (CMAs) is required to develop a thorough understanding of the relation between the final product quality and the involved materials and processes. In addition, the sensitivity of the end-product quality to the variation in these critical parameters should be determined. Comminution, which comprises several mechanical size reduction techniques such as impact, shear, or compression forces, is an example of an energy consuming unit operation used in the preprocessing of the biomass materials to change the particle size and shape.

Inspired by the QbD approach, the present study investigates the effect of the granular biomass particle characteristics on its flow behavior by combining experimental and computational work. More specifically, the Forest Concepts Crumbler® rotary shear system is used to produce a set of "matched" bulk feedstock samples from conifer veneer and chips that are used to compare the effect of feedstock physical properties, such as particle size and shape, on flowability properties, i.e., angle of repose (AOR). After milling, the feedstocks were dried to less than 10 percent wet-weight basis (%wb) in a low temperature (50°C) downdraft tray dryer. One objective is to compare the attributes and performance of similarly sized particles made from conifer veneer and from Douglas fir chips. The target nominal particle sizes are 6 and 2 mm geometric mean diameter. These represent the most common particle size specifications for gasification and catalytic fast pyrolysis, respectively. Both sizes are also used for biochemical conversion, depending on the pretreatment process, and are in the typical size range for thermochemical conversion of lignocellulosic biomass produced from woody residues. Furthermore, the specific energy consumption for comminution of the biomass with different particle size and moisture content of the feeds and products are measured to facilitate a potential technoeconomic analysis (TEA). Bottomless cylinder test is then used to measure the static AOR experimentally for the different sets of the milled particles to validate the simulation results. For the computational work, the particle-based discrete element method (DEM) is employed to examine the effects of the milled particle morphology models on the granular flow behavior. In details, the impact of particle size (2–6 mm), particle shape (briquette, chips, clumped-sphere, cube, etc.), and surface roughness on the AOR of milled pine are investigated.

AOR, defined as the steepest slope measured from a horizontal plane a heap of unconfined material can maintain without collapsing, is one of the critical parameters used to characterize the mechanical behavior of the granular materials (Cheng and Zhao, 2017; Beakawi Al-Hashemi and Baghabra Al-Amoudi, 2018). It depends on particle contacts and packing arrangements and indicates the self-stability of the materials under certain loading conditions and stress states. Therefore, it is used as a design parameter in applications that depend on slope stability such as bins and hoppers. For example, it is an important index in the design of silos for stockpiling. Moreover, AOR can be used as a quantitative indicator of material flowability. However, several material attributes influence the AOR, which make understanding the micro-behavior of the granular particles essential to reliably predict the macro-behavior, because of the interplay between various underlying mechanisms acting at different length and time scales. Zhou et al. (Zhou et al., 2014) found particle size as well as sliding and rolling frictions to be significant factors controlling the angle of repose in the case of a sand pile, while the bulk density, Young's modulus, Poisson's ratio, and the damping coefficients played negligible roles. The effects of lifting velocity and container shape on the repose angle in a bottomless cylinder test were examined by Liu et al. (Liu et al., 2014). They observed that the repose angle decreases when the lifting velocity or the material height is increased. On the other hand, the increase of the base roughness results in an increase of the AOR. In addition, Nakashima et al. (Nakashima et al., 2011) showed that the sensitivity of AOR to gravity is minimal. Many DEM simulations of AOR considered simplified particle shapes to improve the simulation efficiency and to reduce the computational cost. To examine the validity of this simplification, Chen et al. (Chen et al., 2019, 2020) studied the effect of particle morphology on the angle of repose of ballast materials. They concluded that simple particle shapes can satisfactorily make a good prediction of the AOR in the case of fine particles, where the particle size (rather than the particle morphology) is the predominant factor in determining the mechanical response. However, interlocking effects due to the angularity on the particle surface become more important for larger size aggregates. Liu et al. (Liu et al., 2014, 2020) used ellipsoidal particles to understand the effect of particle shape on flow behavior in cylindrical hoppers and it was found that spherical particles with unity aspect ratio achieves the highest flow rate, and that particle shape has a significant effect on the discharge rate.

From the discussion above, it is evident that DEM is an adept tool to tackle the AOR problem in granular materials. Its significance relies on the fact that emergent dynamics from the interplay between attractive interparticle forces (arising from interatomic and intermolecular interactions) and contact forces (due to friction and resistance to rolling and sliding along the heap surface) are still poorly understood. Thus, without the aid of numerical experiments, it is hard to make a theoretical prediction about which attribute is more important in determining the granular material flowability: particle size or particle shape. This question becomes more important in the case of milled biomass particles with their complex shapes and the high energy consumed in the comminution process. The answer to this question imposes an additional constraint that should be considered in optimizing the system of biomass materials preprocessing, feeding, and handling. The present work sheds light on the impact of particle size and shape on the granular flow behavior and the cost to produce such particle size in terms of the specific energy consumption. The rest of the paper is organized as follows: In the next section, the comminution process for Douglas fir pine is explained, as well as the evaluation of specific energy consumption data for the comminution process. In addition, the bottomless cylinder test is described, and the computational approach is detailed in the same section. In **Section 3**, the DEM simulation results of AOR are presented and compared with the experimental results. Moreover, the implications of the particle size and particle shape are discussed, and the computational cost of the DEM simulations is analyzed. Finally, conclusive remarks are outlined in **Section 4** along with an outlook for future research directions.

2 MATERIALS AND METHODS

2.1 Comminution Process for Douglas Fir Pine

Forest Concepts, LLC produced a set of "matched" bulk feedstock samples from wood veneer and chips that were used to compare the effect of feedstock particle characteristics on flowability properties, i.e., AOR. A single, locally harvested, Douglas fir tree was sectioned into logs and delivered to Forest Concepts in March 2021. The veneer was made by Forest Concepts with its centerless lathe from the Douglas fir logs freshly cut in Edgewood, WA. The log sections were alternately assigned to two lots for the wood veneer processing. The log lots were processed at separate lathe settings to produce veneer with 2 and 6 mm nominal thickness required for downstream processing. The softwood wood chips were supplied at the same time by Shearer Brothers in Shelton, WA for a second preprocessing stream. All materials were comminuted using a Crumbler® rotary shear milling and screening system to produce either the 6-mm or 2-mm nominal particle size feedstocks.

A Forest Concepts Model M24S-30e rotary shear milling system was used for preprocessing to produce Crumbles® from the Douglas fir softwood wood chips and wood veneer, see **Figure 1** for a depiction of the Crumbler® rotary shear system. Particles from wood veneer are observed to be more cubic, have more surface checking, and have a more defined length than particles produced from wood chips. Wood chips, on the other hand, exhibited a needle-like shape. **Figure 2** shows batches from the different samples produced. In the case of veneer, particle thickness is established by the thickness of veneer and particle length is established by the cutter thickness, as the veneer is fed into the rotary shear with the grain parallel to the cutter shaft (i.e., cross-grain). Particle width is less defined as it is created by particle breakage parallel to grain. In contrast, wood chips feed into the rotary shear cutting heads at a random orientation since the chips have nearly equal length and width. Recirculation of the output from one rotary shear unit to another, or recirculation
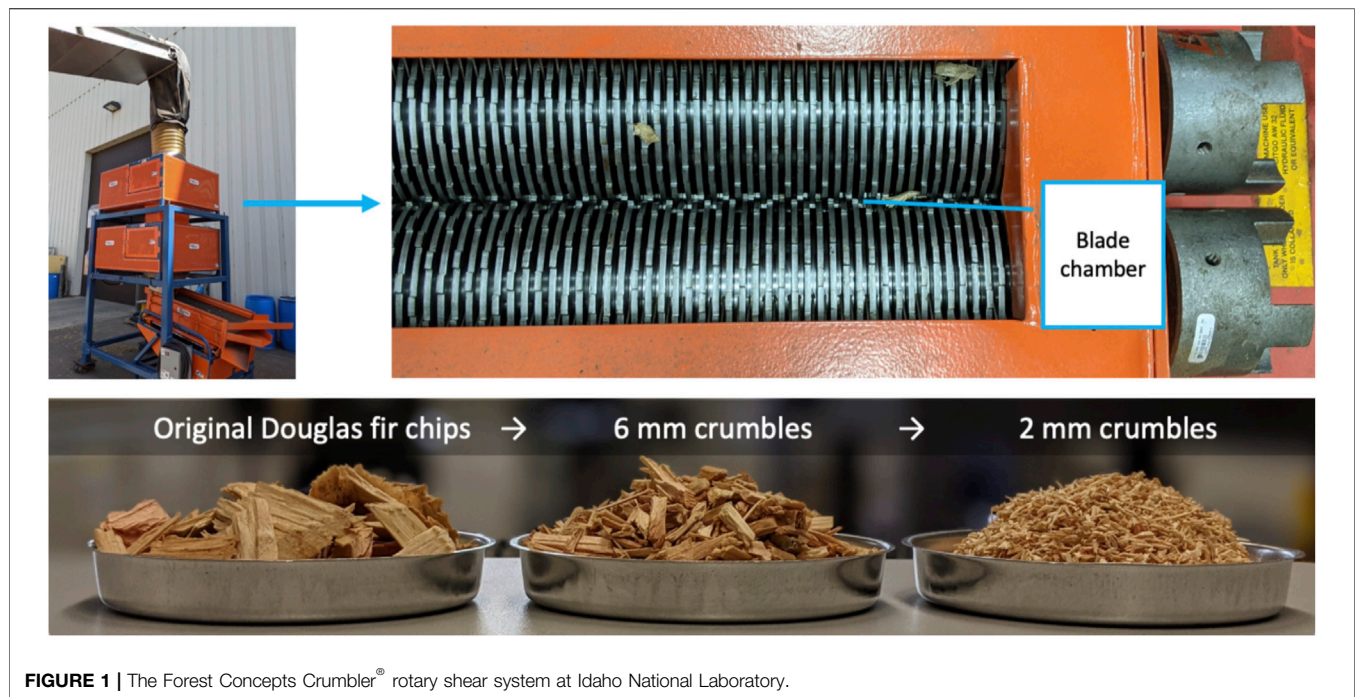
FIGURE 1 | The Forest Concepts Crumbler® rotary shear system at Idaho National Laboratory.

FIGURE 2 | The four types of Crumbler comminuted Douglas fir pine particle samples.

from a screen that has capability to sort by length enables recutting of high-aspect-ratio particles into more cubic shapes. Processing heads with appropriate cutter sets were used during comminution to 6 and 2 mm nominal sizes. The Forest Concepts standard 6-mm nominal size is produced by final screening with a 12.5 mm (1/2-inch) round-hole top screen

and a 2.38 mm (3/32-inch) wire mesh bottom screen using the Forest Concepts Model 2448 orbital screen system. The Forest Concepts standard 2-mm nominal size is produced by final screening with a 3.97 mm (5/32-inch) round-hole top screen and a 0.76 mm wire mesh bottom screen. After milling to size, each material was dried on trays in a Forest Concepts custom cabinet-type downdraft dryer set for 40–50°C. Drying generally took 12–16 h. Low temperature drying is used to avoid loss of volatile organic compounds or otherwise thermally modify the bulk materials. Raw Douglas fir wood veneer and chips had an initial moisture content of 37–44 percent wet-weight basis (wb), well above the fiber saturation level and typical of green wood. After milling, and drying, the final feedstocks had a moisture content between 6 and 10% (wb). Bulk density ranged from 124 to 151 kg/m³ at the final as-shipped moisture contents.

2.2 Comminution Energy Evaluation Procedure

Although the main objective of this study is to quantify the effects of particle characteristics on the flowability of Crumblers, the cost of the comminution process is an equally important aspect that should be always considered side by side with the mechanical performance of feedstocks. To emphasize the importance of the technoeconomic aspect in optimizing feedstocks performance, the present section will be dedicated to cover the method of calculating comminution energy as a mean to include the cost factor in making recommendations about different Crumblers (as will be shown later). Engineering design data for operational biomass milling facilities needs to project the expected total connected power needed to supply a comminution system. The projected total connected power (total energy multiplied

by mass flow rate), or the total power needed at a machine including inefficiencies, is a critical value for scaled plant design. While we can directly scale the specific comminution energy from one feed rate to another, the no-load power must be estimated using engineering judgment or other heuristics. In the following section, the method used to evaluate different parameters needed to calculate the comminution energy will be explained. In addition, implied assumptions will be outlined.

2.2.1 Mass Measurement and Normalization

To determine the as-processed moisture content, Forest Concepts follows a practice of measuring the actual mass at the outfeed from comminution equipment during energy experiments. A sample of the outfeed material is either oven-dried using 50–500-g samples or tested in a rapid moisture analyzer (Arizona Instruments Computrac® Max 4000XL) using 5–10-g samples following standard protocols to determine the oven dry mass of the material processed. The mass flow rate during processing is then stated in terms of oven dry mass per unit time, e.g., oven dry megagrams per hour equivalent (odMg/hour).

2.2.2 Total Energy (Measured)

Total energy is important because it is the most directly measurable energy value from which specific and total connected design energy are calculated. The as-measured total energy is defined as the measured connected electrical load energy input into an actual machine used to conduct an energy consumption experiment. While measuring the electrical feed to a processing device, it is important to be aware that total energy to get the mechanical power output must be adjusted for the power factor. When processing biomass at partial load, total energy will be overstated if voltage and amperage are the only measurements taken. Power measurement must include volts, amps, and phase angle when the machine is powered by an electric motor to account for motor reactive power (power that does not contribute to mechanical work, an artifact of electric motor design). An extensive discussion of power measurement and calculation is included in an American Society of Agricultural and Biological Engineers (ASABE) paper published in 2011 (David N Lanning et al., 2011). The measured total energy, E_T, is given by

$$E_T = \frac{\sum\left[(Ins\,tantaneous\ power) \times \left(\frac{1}{Sampling\ frequency}\right)\right]}{Oven\ dry\ mass\ at\ out feed} \quad (1)$$

Total energy is expressed in terms of energy consumed per unit mass of material processed. A limitation of the total energy method is that the reported energy consumption includes both the specific energy used in actual processing and the drivetrain energy due to friction in the motor, gearboxes, belts, chains, etc. While the actual processing energy is expected to directly relate to biomass feed rates, the drivetrain energy (also called no-load energy) tends to be constant and essentially independent of biomass loading rate. Total energy is thus dependent on machine feed rates and does not scale well from laboratory experiments to commercial-scale well-designed machine

systems. The no-load energy rate must be measured and subtracted from the total energy to obtain the actual comminution energy required for milling the material. This value is called Specific Energy.

2.2.3 Specific Energy (Calculated)

Specific energy can be conceptualized as the amount of energy that is consumed per unit mass of the process beyond what is required to operate the machine with no material. It is the energy that goes into the material to convert infeed particles into smaller outfeed particles. This includes all energy expended in reducing the size of the material, raising the temperature of the material, particle friction, or changing the material moisture content but does not include drivetrain losses, bearing friction, or motor inefficiencies. Specific energy is a critical design value as it is scalable. It can be used to determine the energy requirements for both large and small-scale operations. This value can also be compared to other processes regardless of machine type, quantity, or mass flow rate of material processed. Methods for measurement are detailed in (David N Lanning et al., 2011). Specific energy is often calculated from measurements of the connected electrical load energy prior to processing biomass (no-load energy) and during processing of the biomass (total measured energy, as described above). Subtraction of the no-load from the total during processing yields a reasonable estimate of the specific energy, provided changes in power factor and other drivetrain efficiencies are accounted for. The specific energy, E_s, reads

$$E_S = \frac{\sum\left[(Ins\,tantaneous\ power - Avg.no\ load\ power) \times \left(\frac{1}{Sampling\ frequency}\right)\right]}{Ovendry\ mass\ at\ out feed} \quad (2)$$

2.2.4 Total Connected Design Energy (Calculated)

Specific-to-total energy or "S/T ratio" can be used to estimate total connected design electrical energy load, E_{TCD}, of a well-designed plant from experimentally derived specific energy according to **Eq. 3**. In this equation, design values for commercial-scale processing facilities are calculated by adding estimated drivetrain and motor inefficiencies to the specific energy.

$$E_{TCD} = \frac{E_S}{S/T ratio}. \quad (3)$$

The total connected design power, P_{TCD}, is expressed as

$$P_{TCD} = E_{TCD} * Mass\ Flow\ Rate. \quad (4)$$

The value of the S/T ratio is determined based on experience and is specific to machine configuration and power source (electric, hydraulic, direct-drive, geared, pneumatic, etc.). A specific hammermill may not have the same S/T ratio as a rotary shearing Crumbler machine or a screen. For reference, when fully and continuously loaded, the Crumbler M24 series machines routinely demonstrate an S/T ratio of 70–85%. As such, a reasonable S/T ratio value for the Crumbler machine is

TABLE 1 | Moisture content and comminution energy for crumbles from wood veneer and chips feedstocks.

Nominal size/Raw format	Moisture content (%wb)		Comminution energy (kwh/odt)	
	Initial MC	Final MC	Specific (E_S)	Design (E_{TCD})
6 mm–Veneer	37	7.8	7	9
2 mm–Veneer	42	6.4	44	59
6 mm–Chips	44	8.9	6	9
2 mm–Chips	44	9.1	51	68
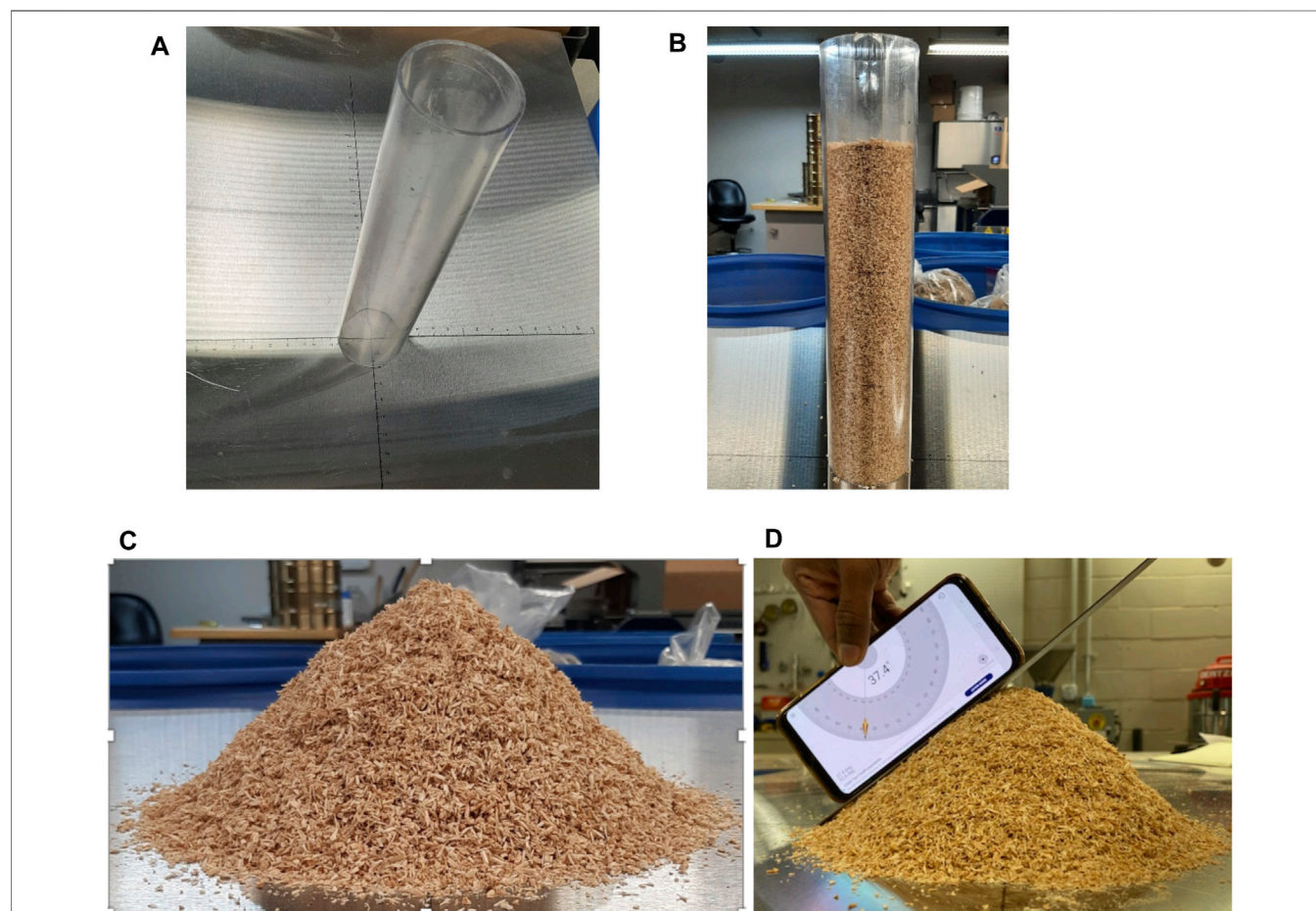
FIGURE 3 | Experimental setup and measurement technique of the static AOR **(A)** empty setup, **(B)** cylinder loaded with sample, **(C)** pile formation, and **(D)** direct AOR measurement using digital protractor.

75% for an at-scale production facility with continuous operation. All total connected design energies and powers reported herein assume an S/T ratio of 75%.

Table 1 provides the values of the specific and design comminution energy for the different particles, along with the initial and final moisture content. As expected, comminution energy was inversely proportional to target particle size. Production of 2-mm nominal size particles consumed approximately 6–8 times as much specific energy as for 6-mm nominal size particle production. In these calculations, design energy values assumed a 75% energy

efficiency for motors and drives powering the comminution equipment. Thus, the comminution energy to produce 6-mm nominal size particles is approximately 9 kwh/odt and the energy to produce 2-mm nominal size particles is in the range of 60–70 kwh/odt, depending on the processing pathway. The energy consumed to produce the raw wood chips is not known. We use the value of 5.5 kwh/odt (19.9 MJ/odt) as reported in the literature (Papworth and Erickson, 1966). The design energy for producing rotary veneer from the logs was 9 kwh/odt for the 6-mm veneer and 14 kwh/odt for the 2-mm veneer.

TABLE 2 | Direct and indirect measurement of static Angle of Repose (AOR).

Sample	Indirect AOR (°)	Direct AOR (°)
2 mm Veneer	28.96 ± 2.99	34.75 ± 3.2
6 mm Veneer	34.55 ± 1.84	40.04 ± 1.33
2 mm Chips	37.54 ± 2.76	39.57 ± 2.12
6 mm Chips	36.7 ± 2.66	40.5 ± 3.18

2.3 Bottomless Cylinder Test and AOR Measurements

The static AOR was measured experimentally at Idaho National Laboratory (INL) for the different samples produced by Forest Concepts. For this purpose, a bottomless (lifting) cylinder test was utilized to contain the sample and generate the pile with little disturbance and equal radial distribution. A hollow polycarbonate cylinder, 7.5 cm in internal diameter and 38 cm long, and a smooth stainless-steel surface (serving as a base) were used for this set of experiments. The distance from the center along the four principal directions was graduated to track the onset and dimension of the pile base. During a typical experiment, the cylinder was placed vertically at the center of the stainless-steel surface shown in **Figure 3A**. The cylinder was filled with a prepared material to a height of 30 cm, see **Figure 3B**. This allowed about 8 cm of empty space to exist between the top of the sample and the cylinder top base to minimize the end effect. The cylinder was lifted manually with caution (slowly with a pull-out velocity around 1.5 m/min). To minimize the human error in the measurement and have a qualitative comparison, only a single operator conducted the whole set of experiments. The material formed a pile while being released from the cylinder as demonstrated in **Figure 3C**. The static AOR was measured from the pile by using two methods: i) direct measurement, and ii) indirect measurement. In the direct measurement a digital protractor was used with a readout to 0.1°, see **Figure 3D**. The device was placed on the hypotenuse of the pile in at least four different locations and the measurements were averaged. For the indirect measurement the height (h) and the radius (r, taken as the average of the four readings along the four principal directions) of the pile were measured and used to calculate the AOR from the relation $\alpha_{AOR} = tan^{-1}(h/r)$. Static AOR was measured at least 10 times for each sample using different batches to minimize the measurement error and material variability. **Table 2** lists the measured angle of repose values for the milled wood veneer and chips feedstocks (2-mm and 6-mm) along with the measurement errors.

2.4 Computational Approach: DEM Model Description

The discrete element methods (DEM) used in the present study refer to a family of computational models that are widely used to simulate the dynamics of particulate materials and predict their behavior. This method is of particular interest to problems pertinent to granular flow, powder mechanics, and rock mechanics (Cleary and Sawley, 2002; Scherer et al., 2016;

Zhong et al., 2016; Rackl et al., 2017). It was originally introduced by Cundall and Strack (Cundall and Strack, 1979). Like molecular dynamics (MD), DEM explores the temporal evolution of its constituents in the phase space by solving the Newton's equation of motion. However, unlike MD, DEM does not resolve the atomic structure. Instead, a DEM particle is a granular or coarse-grained particle representing an ensemble of material atoms and/or molecules at a length scale that typically spans a range between submicron up to a few centimeters. Due to the finite-size nature of DEM particles, rotational degrees of freedom are considered explicitly and stateful contact is trackable. DEM is relatively computationally intensive, and for this reason many DEM studies employ simple shapes (mainly single sphere) for the model particles. This common practice is attributed to the reduction in the computational cost gained from speeding up the force calculation and contact detection, in addition to achieving efficient scaling performance on parallel computers. To capture the actual particle shape effects on the simulated dynamics, a rolling resistance model is usually invoked with an adjustable parameter called the coefficient of rolling friction (Abbaspour-Fard, 2004; Wensrich and Katterfeld, 2012). However, the accuracy of this practice is not clear and requires the recalibration of the model parameters for different particle shapes. To better approximate particles with complex shapes, clumped-sphere model can be employed (Kruggel-Emden et al., 2008). In this model, each particle consists of several rigid base spheres connected by unbreakable bonds and spatially arranged in a way that mimics the targeted shape. Nevertheless, clumped-sphere models are not well suited to model situations where the loading conditions can lead to particle deformation. Another class of DEM simulations make use of bonded-sphere models to account for the deformability of the particles (Xia et al., 2019; Guo et al., 2020, 2021). The main difference between the clumped-sphere and the bonded-sphere models lies in the nature of the bonds connecting the base-spheres comprising individual DEM particles. Unlike the clumped-sphere models, the bonds in the bonded-sphere models can carry forces and moments and allow relative displacements between the base-spheres by the act of external forces. In addition, the bonds between the base-spheres can be broken according to specific criteria, i.e., when the normal or shear stress exceeds the bond strength. A recent review of the state-of-the-art DEM models for the flow of milled biomass can be found in (Xia et al., 2020). More information can also be found in (Coetzee, 2017). In the present work, bonded-sphere models were not considered, as particle deformation is not important in the simulation of the bottomless cylinder test with the granular material heap being unconfined and the gravitational force is the only acting external force.

2.4.1 DEM Fundamental Model Formulation

The system dynamics in DEM is governed by the conservation of linear and angular momentums. So, the translational and rotational motions of particle i are given by, respectively,

$$m_i \ddot{r}_i = \sum_{j=1}^{N} \mathbf{F}_{ij} + m_i g \qquad (5)$$

$$I_i \dot{\omega}_i = \sum_{j=1}^{N} \mathbf{M}_{ij} \tag{6}$$

In the above, the subscripts denote the particle index; m labels the particle mass; r and ω are the position vector and rotational velocity, respectively; $\mathbf{F}$ and $\mathbf{M}$ stand for the pairwise interaction force and torque, respectively, exerted by particle j on particle i; and $\mathbf{g}$ is gravity. In addition, N denotes the total number of particles in the system. It is worth noting that particle self-interaction is excluded, i.e., $i \neq j$.

In the current work, the Hertz-Mindlin contact model (Hertz, 1882; Mindlin and Deresiewicz, 1953) is used to represent the particle-particle interaction forces. In this model, the contact forces have two components, namely, a normal force and a tangential force. Each component is represented by the sum of two terms accounting for elastic and damping forces. In the case of the normal force, it consists of a spring force and a damping force, while for the tangential force a shear force and a damping force are utilized. It is worth noting that the shear force bears a memory effect, as it depends on the history of the relative tangential displacement between the two interacting particles over the time they are in contact. Overall, the pairwise contact force in Hertz-Mindlin model takes the form

$$\mathbf{F}_{ij} = \mathbf{F}_{ij,n} + \mathbf{F}_{ij,t} = \left(k_n \delta_{ij,n} - \gamma_n v_{ij,n} \right) + \left(k_t \delta_{ij,t} - \gamma_t v_{ij,t} \right); \tag{7}$$

with Coulomb friction limit imposed on the magnitude of the tangential force. This yield

$$\left| \mathbf{F}_{ij,t} \right| \leq f_p \left| \mathbf{F}_{ij,n} \right|; \tag{8}$$

where k_n and k_t denote the elastic constants for the normal and tangential contacts; $\delta_{ij,n}$ indicate the overlaps between the two particles in the normal direction; $\delta_{ij,t}$ represents the cumulative relative displacement in tangential direction during the time the two particles being in contact; γ_n and γ_t are the viscoelastic damping constants for the normal and tangential contacts; $v_{ij,n}$ and $v_{ij,t}$ label the relative normal and tangential velocities between the two particles at the point of contact; f_p is the particle friction coefficient; $F_{ij,n}$ and $F_{ij,t}$ are the normal and tangential contact forces, respectively.

The model parameters k_n, k_t, $\delta_{ij,n}$, and $\delta_{ij,t}$ are computed from the material properties through the relations (Guo et al., 2020)

$$k_n = \frac{4}{3} \hat{E} \left(\hat{R} \delta_{ij,n} \right)^{1/2}; \tag{9}$$

$$k_t = 8 \hat{G} \left(\hat{R} \delta_{ij,n} \right)^{1/2}; \tag{10}$$

$$\gamma_n = -2 \sqrt{\frac{5}{3}} \beta \left(\hat{m} \hat{E} \right)^{1/2} \left(\hat{R} \delta_{ij,n} \right)^{1/4}; \tag{11}$$

$$\gamma_t = -4 \sqrt{\frac{5}{3}} \beta \left(\hat{m} \hat{G} \right)^{1/2} \left(\hat{R} \delta_{ij,n} \right)^{1/4}; \tag{12}$$

where the equivalent Young's modulus ($\hat{E}$), radius ($\hat{R}$), shear modulus ($\hat{G}$), mass of two contacting spheres ($\hat{m}$); and the restitutions coefficients (β) are given by (Guo et al., 2020):

$$\frac{1}{\hat{E}} = \frac{1 - v_i^2}{E_i} + \frac{1 - v_j^2}{E_j}; \tag{13}$$

$$\frac{1}{\hat{R}} = \frac{1}{R_i} + \frac{1}{R_j}; \tag{14}$$

$$\frac{1}{\hat{G}} = \frac{2 (2 - v_i)(1 + v_i)}{E_i} + \frac{2 (2 - v_j)(1 + v_j)}{E_j}; \tag{15}$$

$$\frac{1}{\hat{m}} = \frac{1}{m_i} + \frac{1}{m_j}; \tag{16}$$

$$\beta = \frac{ln(e)}{\sqrt{ln^2(e) + \pi^2}}. \tag{17}$$

In the above relations, v is Poisson's ratio; E denotes Young's modulus; R and m label the particle radius and mass, respectively; e stands for the coefficient of the restitution; and again, the subscripts i and j refer to the particle index.

The torque exerted by particle j on particle i can be defined as

$$\mathbf{M}_{ij} = \mathbf{M}_{ij,t} + \mathbf{M}_{ij,r} + \mathbf{M}_{ij,n}. \tag{18}$$

The three torque components on the right-hand-side of **Eq. 14** refer to the torques generated by the tangential contact forces, the rolling friction, and the normal contact forces, respectively. The normal force contribution to the total torque arises when its line of action does not pass through the particle center. Moreover, asymmetric normal forces produce the rolling friction torque, which always acts in the opposite direction of the relative rotation between the two particles to slow it down. Several physical mechanisms can cause rolling friction to be present at the contact between two particles or at the contact between a surface and particle. Micro-slip and friction, plastic deformation, viscous hysteresis, and surface adhesion are all examples of these mechanisms (Ai et al., 2011). In addition, as discussed earlier, the use of idealized spherical shapes in DEM modelling requires considering rolling friction to account for the shape effects due to the non-spherical nature of real particles. A directional constant torque model is used for the rolling friction description in the current work. As the name suggests, in this model the pairwise torque is assumed to be always acting in the opposite direction of the relative rotation between the two interacting particles. Furthermore, the magnitude of the torque depends linearly on the magnitude of the normal contact force. Accordingly, the rolling friction torque acting at the contact between two particles i and j can be expressed as (Ai et al., 2011)

$$\mathbf{M}_{ij,r} = -\frac{\omega_i - \omega_j}{\left| \omega_i - \omega_j \right|} \mu_r \hat{R} \left| \mathbf{F}_{ij,n} \right|; \tag{19}$$

with μ_r being the coefficient of the rolling friction.

2.4.2 AOR Calculation Algorithm From DEM Data

Due to the discrete nature of the granular material with edgy particles and broad range of grain size distribution, the resulting material heap in the bottomless cylinder test is always nonuniform. This deviation from a perfect conical shape is intensified by the initial random packing of the cylinder at rest. The non-ideal heap shape introduces a
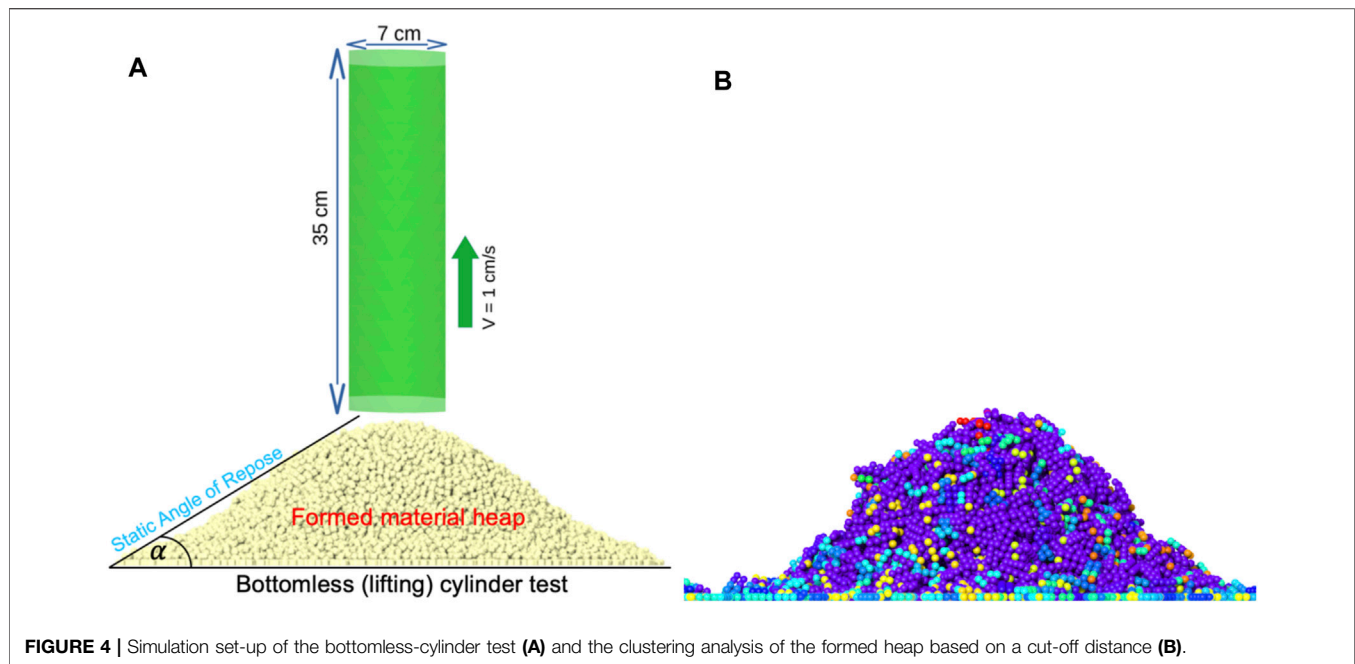
FIGURE 4 | Simulation set-up of the bottomless-cylinder test **(A)** and the clustering analysis of the formed heap based on a cut-off distance **(B)**.
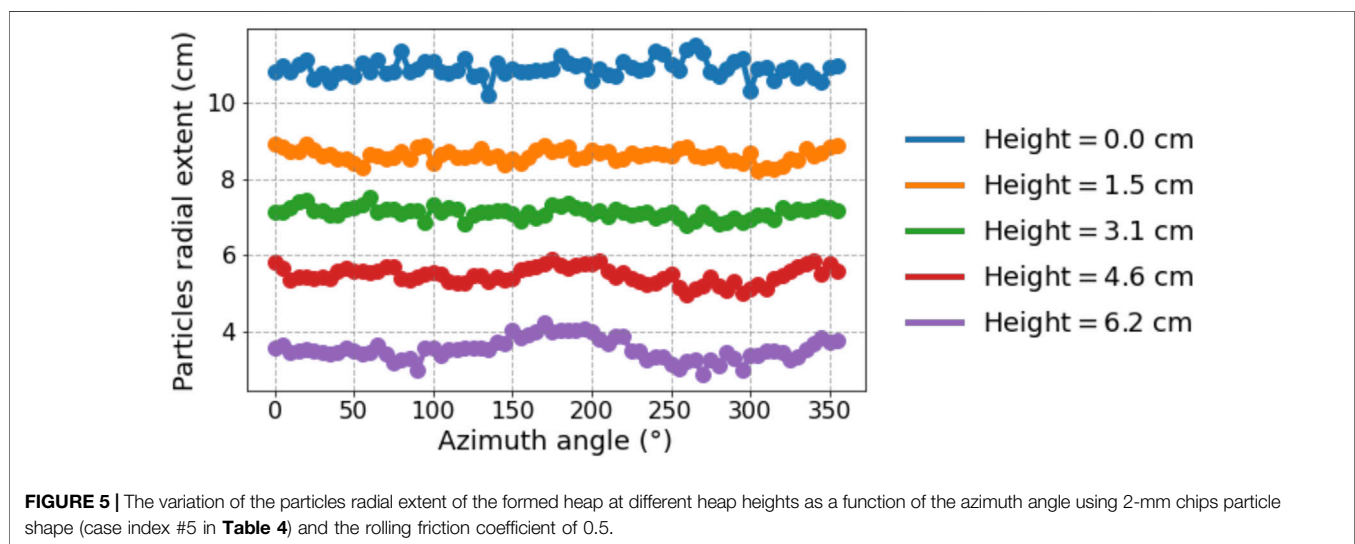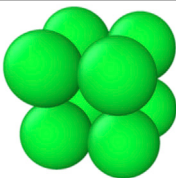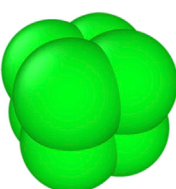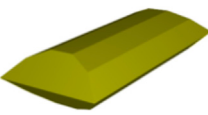
FIGURE 5 | The variation of the particles radial extent of the formed heap at different heap heights as a function of the azimuth angle using 2-mm chips particle shape (case index #5 in **Table 4**) and the rolling friction coefficient of 0.5.

challenge in the analysis of the angle of repose from the DEM simulation results, as the irregular outline curves make the determination of the flank angle difficult, see **Figure 4**. So, for high reproducibility of the analysis and for the evaluated AOR to be reliable, a robust algorithm is needed with numerical errors estimated (Fraczek et al., 2007; Liao et al., 2021; Müller et al., 2021). In this study, an algorithm was developed to achieve this goal. For this purpose, following (Müller et al., 2021), the definition of the angle of repose was modified to be the steepest average slope, measured from the horizontal plane, a distinct volume of the unconfined material heap can maintain without collapsing. The enhanced definition accommodates the local variation of the slope arising from

the nonuniform heap and cohesive materials by avoiding the overestimation of the angle of repose that occurs when the steepest slope is used. It also accounts for the fact that some of the granular particles may settle at locations far from the main heap, which introduces error in the calculations of the slope. Our algorithm consists of three main steps. They can be summarized as follows:

1. Cluster analysis is performed using the centroid coordinates of DEM particles after the end of the simulation, see **Figure 4B**. A cut-off distance is used as the criterion to determine whether a particle belongs to a given cluster. If the distance between the particle and any of the particles

TABLE 3 | List of DEM particle shape models.

Particle shape model	Template shape	Dimensions	Case index
Non-overlapping Clumped-spheres Cube		Multi-sphere inside a cube with a side length of 2 mm (2 × 2 × 2 spheres of D = 1 mm)	1
		Multi-sphere inside a cube with a side length of 6 mm (2 × 2 × 2 spheres of D = 3 mm)	2
Overlapping Clumped-spheres Cube		Multi-sphere inside a cube with a side length of 2 mm (2 × 2 × 2 spheres of D = 2 mm)	3
		Multi-sphere inside a cube with a side length of 6 mm (2 × 2 × 2 spheres of D = 6 mm)	4
Clumped-sphere chip		$1 \times 2 \times 4$ [mm^3] (1 × 2 × 4 spheres of D = 1 mm)	5
		$3 \times 6 \times 12$ [mm^3] (1 × 2 × 4 spheres of D = 3 mm)	6
Briquette		2 mm length	7
		6 mm length	8
Single Cube		2 mm side length	9
		6 mm side length	10
Single Cuboid		$1 \times 2 \times 4$ [mm^3]	11
Single Sphere		3 mm in diameter	12
		6 mm in diameter	13

belonging to the cluster under consideration is found to be less than a factor of 1.1 multiplied by the sum of the two particles radii, then the particle is assigned to that cluster. This procedure is repeated until each individual DEM particle in the system is assigned to a certain cluster. It is worth noting that every DEM particle belongs to one and only one cluster. Afterwards, the clusters are organized in descending order according to their size, and the largest cluster is considered the distinct heap volume and used for further analysis. In this regard, in all simulations, one very

large cluster containing at least 70% of the total number of the particles in the system was always observed, in addition to a much smaller, scattered clusters.

2. To evaluate the average radial extent of the particles within the heap, the volume enclosing the largest cluster is discretized. The discretization scheme employs the cylindrical coordinates. It works by first dividing the total height along the vertical z direction into 20 equally spaced slabs, and then the angular domain within each slab is divided into small bins with an azimuth angle increment of 5°. Within each element of volume, the particle with the farthest radial distance is located, and this radial distance (measured from the heap center) is used as the maximum particle radial extent for that volume element. Next, the average of the collected radial particle extent from different elements of volume at the same height (within the same slab) is calculated and used for further analysis. **Figure 5** shows the variation of the radial particle extent versus the azimuth angle at different heap heights obtained from the analysis of a selected simulation case.

3. The heap slope is finally found by carrying out a linear regression using the data points calculated in the previous step comprising pairs of the average radial particle extent and the associated height. **Figure 6** depicts the angle of repose calculated from the slope of the fitted line along with the raw data and the error in the estimated angle of repose due to the fitting error. The raw data appearing in **Figure 6** was generated from the same simulation case used in **Figure 5**.

3 DEM SIMULATION RESULTS AND DISCUSSION

3.1 Simulation Setup

As was highlighted earlier, several particle shape models were considered in the current DEM simulations. They consist of three

FIGURE 6 | Determination of the static AOR by fitting a linear relation between the heap height and the averaged heap radius using the discretized angular domain scheme shown in **Figure 5**.

clumped-sphere models (i.e., a cube composed of eight overlapping base-spheres; a cube composed of eight non-overlapping base-spheres; a chip composed of eight base-spheres arranged in a two-row by four-column layout), in addition to four individual particle shape models (i.e., briquette, cube, cuboid, and sphere). The overlapping and non-overlapping clumped-sphere cube models share the same shape. However, they differ in the surface roughness. On the other hand, the surface roughness of both the non-overlapping clumped-sphere cube and the clumped-sphere chip models are the same. **Table 3** lists all particle shape models along with their dimensions and schematic diagrams. In addition, all DEM model parameters are listed in **Table 4**. It is worth mentioning that for every case shown in **Table 3** two different sets of simulations were conducted: one with a rolling friction coefficient of 0.5 (as listed in **Table 4**) and the other with no rolling resistance (i.e., $\mu_r = 0$). **Figure 4A** shows the dimensions of the mesh used in the simulations to represent the cylinder surface, which is composed of triangular elements. To be comparable with the physical experiment setup, the diameter was set to 7 cm, while the height was taken as 35 cm. The ratio between the cylinder diameter and the maximum particle size is large enough to minimize the boundary effects. To confirm that, a separate simulation was performed using the particle shape model with the largest size (case index #4) and a larger bottomless cylinder with a diameter as twice large as the original cylinder diameter (14 cm) and the same height (35 cm). No difference in the obtained AOR was observed. To initialize the simulation, a random packing algorithm was used to fill the whole cylinder by DEM particles from one of the considered shape models. The packing stage was controlled by the particle volume fraction with a targeted value of 0.6. This is followed by an equilibration step for 1 s, where the cylinder was kept stationary and resting on an impenetrable horizontal base. During this equilibration stage, the DEM particles move downward inside the cylinder under the influence of gravity causing the top region of the cylinder to become completely empty, while the porosity of the bottom region continues to decrease. The transients induced by the particles rearrangement ends after the system being completely relaxed and all the particles become motionless, which
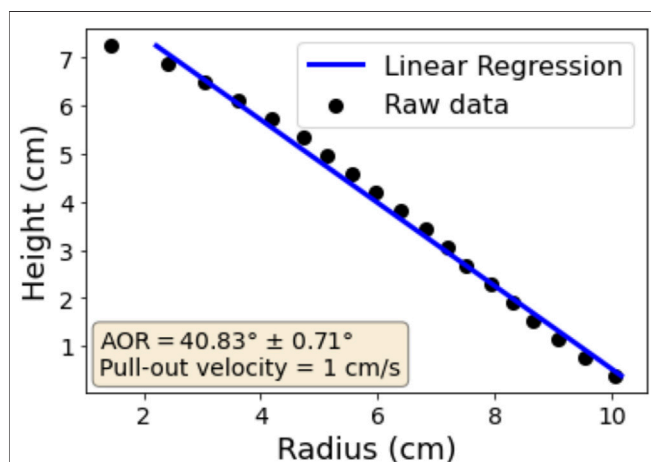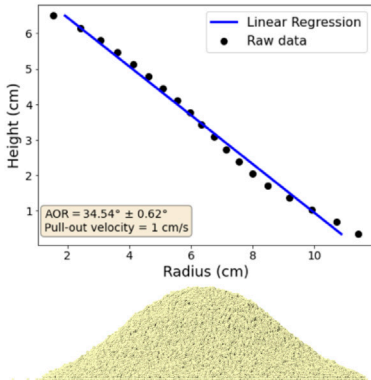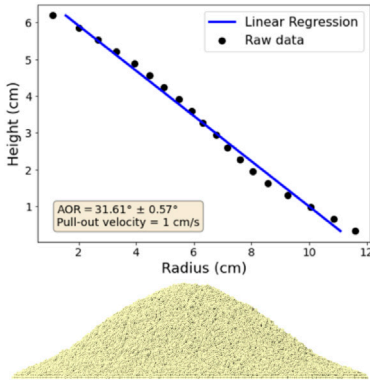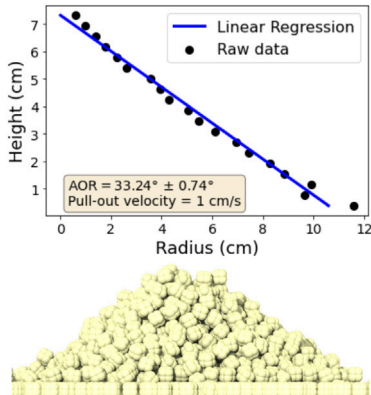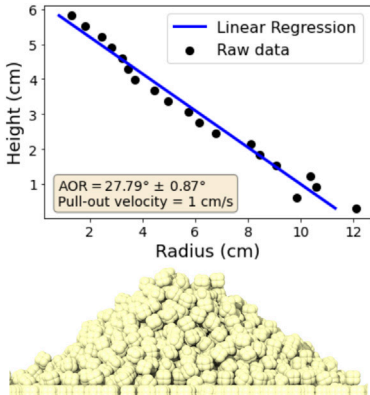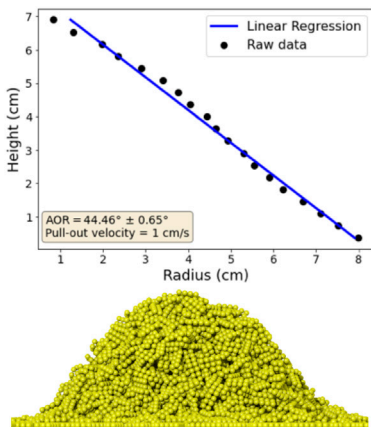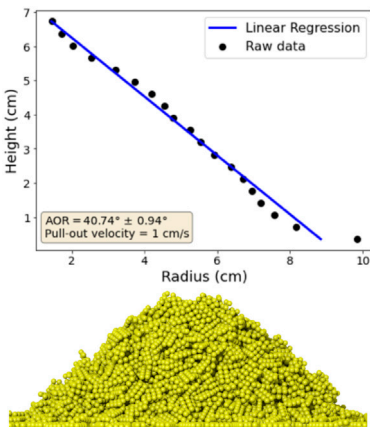
TABLE 4 | Material and contact model parameters used in DEM particle simulations.

Parameter	Value (default)
Particle density [kg/m³]	300
Particle Young's modulus [Pa]	1×10^6
Particle Poisson's ratio	0.3
Boundary density [kg/m³]	7850
Boundary Young's modulus [Pa]	1×10^{11}
Boundary Poisson's ratio	0.3
Rolling friction coefficient	0.5
Particle-particle friction coefficient	0.7
Particle-boundary friction coefficient	0.3
Particle-particle restitution coefficient	0.3
Particle-boundary restitution coefficient	0.3

TABLE 5 | Comparison of the rolling resistance effect on the simulated AOR for different Clumped-spheres particle shape models.
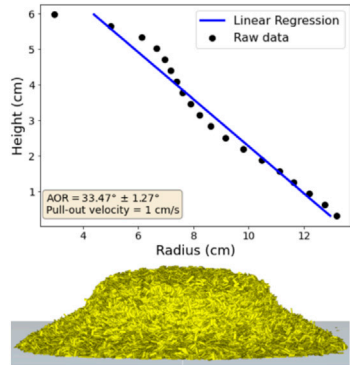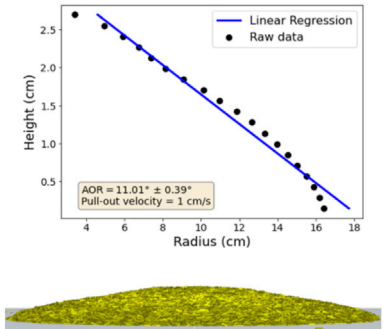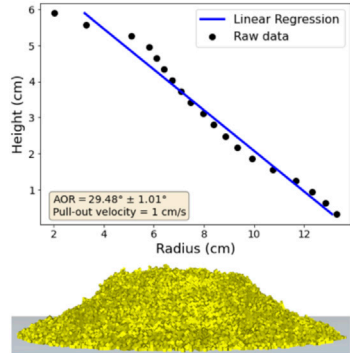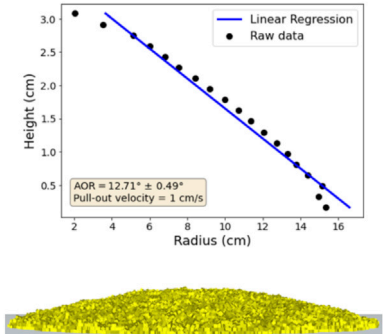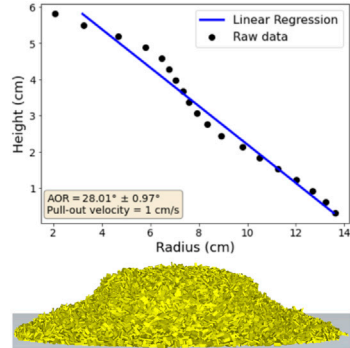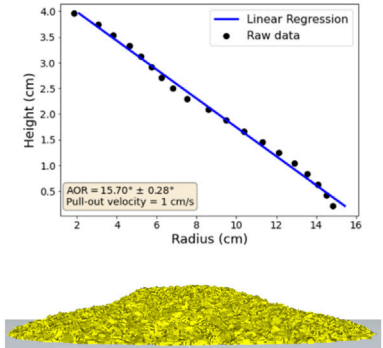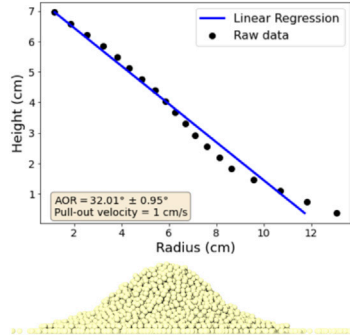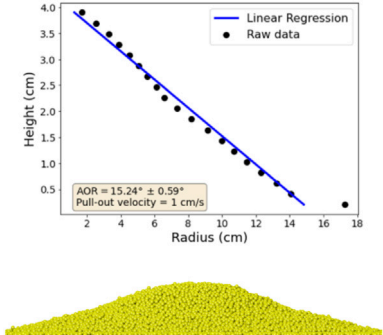
Case index	With rolling resistance $(\mu_r = 0.5)$	No rolling resistance $(\mu_r = 0)$
1		
4		
6		

usually occurs in a fraction of one second. Afterward, the bottomless cylinder test starts by lifting the cylinder upward with a constant velocity of 1 cm/s, which is close to the value reported in the physical experiment. The DEM simulation

continues for an additional period of 10 s. This time was found long enough for all particles in each simulation to reach a complete stop. A timestep size of 1 microsecond was used in all simulations.

TABLE 6 | Effect of rolling resistance on the AOR for different single particle shape models.

Case index	With rolling resistance (μ_r = 0.5)	No rolling resistance (μ_r = 0)
7		
9		
11		
13		

FIGURE 7 | Particle size effect on AOR: the static angle of repose for the different particle shapes considered in the present study versus the effective particle radius using rolling friction coefficients of 0.5 along with the experimentally measured values for Veneer and Chips.

The DEM simulations of the bottomless cylinder test were performed using two different software. LIGGGHTS-INL (Idaho National Laboratory, 2021), which is a capability extension of LIGGGHTS (LAMMPS improved for General Granular and Granular Heat Transfer Simulation) open-source DEM particle simulation software (Kloss et al., 2012), was utilized to simulate the clumped-sphere shape models as well as the single sphere shape model. Rocky DEM (Fonte et al., 2015; Xia et al., 2021) was employed to simulate the rest of the shape models considered in the current work. The main reason for using two different software is because of the difference in the available particle shape features supported by the two software. For example, contrary to Rocky DEM, the briquette shape was not available in LIGGGHTS-INL. Nevertheless, LIGGGHTS-INL efficient parallel computing capabilities make it more suitable for the computationally intensive simulations such as the ones adopting clumped-sphere models, with the total number of elementary particles in the simulation system scaling up by a factor of eight for the same DEM particle size. This remarkable increase in the system size dictates the use of high-performance computer (HPC) for an affordable computational time. To verify that results obtained from the two different software are comparable, the simulation of the particle shape model No. 13 (which adopts a single sphere with a diameter of 6 mm as the DEM particle) was carried out using the two software. In this comparison, the obtained angle of repose (from the set of simulation with the rolling resistance model invoked) was used as the criterion to assess the degree of agreement between the simulation results from the two software. A repose angle of $32.01° \pm 0.95°$ was predicted by LIGGGHTS-INL, while the value obtained from Rocky DEM was $31.75° \pm 0.89°$. The good agreement indicates results obtained from the two different software

packages can be directly compared without affecting our conclusions.

3.2 Particle Shape Impact on AOR and Underlying Mechanisms

One of the main objectives of this study is to understand the effect of particle shape on flow behavior of granular material. **Table 5** presents the formed material heap for the three different clumped-sphere models [visualized with OVITO (Stukowski, 2010)], with and without the rolling resistance model invoked. In addition, the angle of repose analysis for each case is also shown in the same table. By examining the angle of repose obtained from the different clumped-sphere shape models, we find the values range from 28° to 45° with a numerical error that is smaller than 1°. It is evident that the values are high enough to reasonably represent milled biomass materials response. The chip model achieved the highest values for angle of repose, while the overlapping clumped-sphere cube model resulted in the lowest values. This trend was persistent regardless of the particle size. Furthermore, the effect of rolling resistance model on the angle of repose was minimal in all the clumped-sphere models. This was a strong indication that at a given particle size a different mechanism other than the rolling resistance controls the slope of the formed heap. Due to the complex-shape nature of the clumped-sphere models associated with high surface roughness, mechanical interlocking mechanism was considered as the culprit in the degradation of the particulate material flowability in the case of these shape models. This is consistent with our observation that for a particle having a cubic shape of a given size the angle of repose was always higher when non-overlapping base spheres are

Case index	Total no. of base-particles	No. of nodes	No. of CPU cores/node	CPU time (hours)		Total computational time (processor-hours)	
				With rolling friction ($\mu_r = 0.5$)	Without rolling friction ($\mu_r = 0.0$)	With rolling friction ($\mu_r = 0.5$)	Without rolling friction ($\mu_r = 0.0$)
1	752328	8	24	160.5	161.4	30816.0	30988.8
2	34488	1	24	10.1	9.6	242.4	229.9
3	243984	8	24	52.5	49.4	10080.0	9481.6
4	12248	1	24	5.1	5.0	123.3	120.9
5	726320	8	24	200.7	190.6	38529.1	36583.8
6	28592	1	12	12.4	11.9	148.2	142.7
12	54349	4	24	10.2	7.0	977.5	676.1
13	6033	2	24	2.2	1.7	103.1	83.2
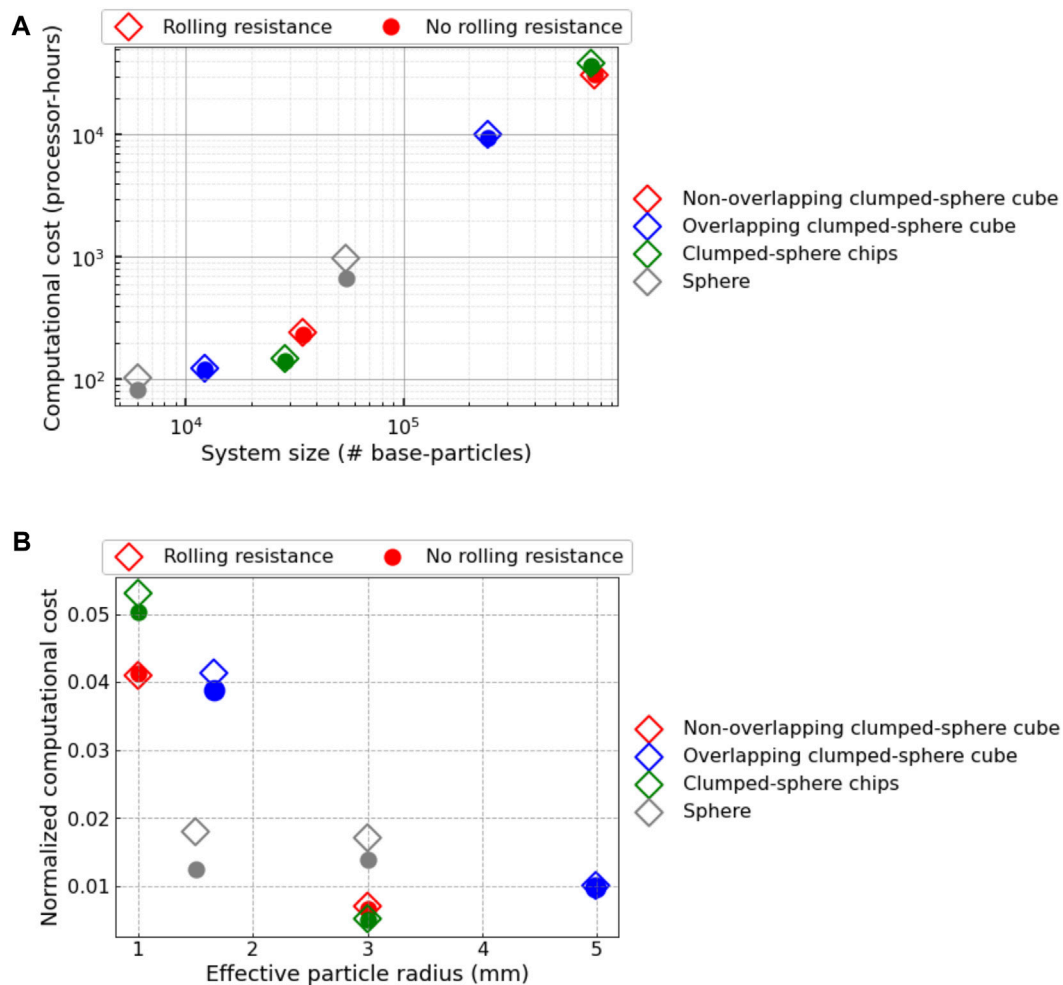
FIGURE 8 | Computational cost of the DEM simulations for different particle shape models **(A)** the total computational cost versus the total number of base-particles (i.e., the total number of particles multiplied by the number of base-sphere for the clumped-sphere shapes), and **(B)** the computational cost normalized by the system size versus the effective particle radius.

used. This is attributed to the high surface roughness achieved in this case when compared with the case of overlapping base spheres.

To confirm the role played by the mechanical interlocking mechanism, **Table 6** shows the effect of the rolling resistance model on the bottomless cylinder test results for the case of single

elementary particle shape models. By looking at the AOR values for the same particle shape with and without rolling resistance, it can be discerned that rolling resistance plays the key role in determining the slope in the case of these shapes. For example, by activating the rolling resistance mechanism, the AOR elevates from values below 15° to above 30°. The absence of any contribution from the mechanical interlocking mechanism in these cases is ascribed to the smoothness of the surface of their particles, which asserts the importance of accounting for the surface roughness of the real granular materials for a reliable prediction of the repose angle. In addition, this behavior emphasizes the importance of adopting rolling resistance model in conjunction with the simple particle shape models, in agreement with the common practice in DEM simulations. Accordingly, in the rest of this study, the comparison between the prediction of the different shape models will focus on the results obtained from the simulations with the rolling resistance activated.

By closely examining the impact of the aspect ratio of the particle dimensions on AOR, we realize that needle-like particle shapes have the highest AOR among all the considered particle shape models. For instance, both the non-overlapping clumped-sphere cube and clumped-sphere chip models consist of eight base spheres of the same size with the only difference being about their layout. However, we see clearly that the chip shape results in a larger angle of repose. The angle of repose for the briquette particle shape asserts the same remark. This is consistent with our experimental measurements showing Crumbles from chips exhibiting slopes larger than the Crumbles from veneer (for which the particles resemble a cubic shape). On the other hand, the smallest AOR obtained in the DEM simulations coincides with the single sphere adopted as the DEM particle shape model. This is related to the features of the spherical shape with its highest symmetry and smoothest surface containing no edges. In agreement with our observation, Zhou et al. (Zhou et al., 2014) analyzed the stress distribution for different particle shapes. They found a significant influence of the particle shape on the magnitude of the pairwise normal contact force. The spherical shapes exhibited the smallest magnitude with normal pressure distribution, showing a relatively constant value in the central region. Unlike spherical particles, a more pronounced stress dip was observed in the case of the non-spherical particles.

3.3 Particle Size Effect on AOR.

Another factor that influences AOR is the particle size. In the present study, we investigated the size effect using both numerical and physical experiments. **Figure 7** combines all AORs obtained from the simulation of different particle shape models along with the experimental data for veneer and chips particles. In this regard, for the sake of comparison with the simulated AOR, experimental results obtained from the direct measurement method was used, see **Section 2.3**. The reason behind the choice of this method is its compatibility with the developed algorithm used in the slope analysis of the simulation results. For each DEM particle shape model, two different particle sizes were simulated. The results are plotted versus the effective particle radius. For the clumped-sphere models and particle shapes with

aspect ratio different from one, the effective size was taken to be the radius of the sphere with equivalent volume. The effective particle radius lies in the range between 1 and 5 mm, with the overlapping clumped-sphere shape model having the largest effective size. For all the modeled shapes, the static AOR increases with increasing the particle size.

It is apparent that the values of simulated AOR obtained using the non-overlapping clumped-sphere cube shape model is in a good agreement with the experimentally measured values for Crumbles from veneer, while the clumped-sphere chip model achieves the best agreement with the Crumbles from chips. However, we would like to emphasize that the assessment of which particle shape models agrees better with experiment based solely on the value of AOR can be sometimes misleading. For example, recalibrating the rolling friction coefficient can render other shape models (i.e., the briquette, cube, and cuboid shapes) good candidates to reproduce the experimental data for a given particle size. Nevertheless, the significant difference between these different shape models belongs to the variation in the sensitivity of the AOR to the change in the particle size. This serves as strong evidence that particle size should not be regarded as a completely independent parameter in the description of AOR. It is correlated with other factors such as particle shape and surface roughness. So, the dependence of AOR on the particle size is implicit but not explicit. Thus, using simpler shape models along with the right particle size and calibrated rolling resistance coefficient does not guaranty reliable prediction of the flow behavior of the granular materials when the particle size is changed. In this regard, our experimental results indicate that Crumbles from chips have minimal sensitivity to the size effects, which is unlike the case of Crumbles from veneer. This suggests that as far as the mechanical characteristic are concerned, accurate estimation of the particle size is more important in the case of Crumbles from veneer. In addition, Crumbles from chips can tolerate a wider range of particle size distribution without affecting its flow properties.

In agreement with our findings, anecdotal results from various labs and researchers suggest a preference for using feedstocks from veneer over feedstocks from chips. The most-stated benefit is that veneer-derived feedstocks flow very easily through hoppers and screw feeders. The uniform particle length of veneer-based particles and high surface checking are believed to enable more precise tuning of reactors, resulting in higher yields and higher quality products. However, the cost of producing veneer-derived feedstocks is perceived to be higher than for particles from chips. Also, chips are widely available and can be made from branches, small diameter stems, and short rotation trees; however, veneer can only be made from bole wood of sufficient diameter to be economical (typically 125 mm or greater for centerless lathes and 250 mm or greater for spindle-type lathes).

Before we conclude this discussion, it should be noted that our DEM contact model assumes cohesionless particles, which should be deemed appropriate given the fact that the Crumbles used in the experiment were dried to small values of moisture content. Nevertheless, in other scenarios where cohesion is not negligible, additional attractive forces should be added to the DEM contact model. For those scenarios, the relation between the angle of

repose and the particle size could show the opposite trend using the same simulation setup. For example, Elekes and Parteli (Elekes and Parteli, 2021) constructed a semi-empirical formula for such scenarios, which predicts the static AOR as a function of the particle size over a large span of length scale. They used experimental data as well as DEM simulations for this purpose. Given the varieties of particle shape models considered in the present study and the persistent trend exhibiting larger AOR for bigger particle size, capturing the opposite behavior should be mainly attributed to the incorporation of attractive forces in the contact model itself. This type of force can arise due to particle cohesion induced by moisture content, for example, or because of the Van der Waals forces originating from intermolecular interactions. The contribution of the Van der Waals forces to the particle-particle interactions is mainly important at a much lower length scale with particle sizes less than a few microns (Elekes and Parteli, 2021). This reported opposite trend serves as additional evidence that the dependence of AOR on the particle size is implicit. Furthermore, the relation between the particle size and AOR can alternate trend by changing the values of other influential parameters.

3.4 Analysis of the DEM Simulations Computational Cost on HPC.

As noted earlier in **Section 3.1**, HPCs were used to perform the clumped-sphere shape models simulations via LIGGGHTS-INL. In this regard, Sawtooth, the latest INL supercomputer, was utilized for these sets of simulations. Sawtooth uses CentOS platform and consists of 2079 compute nodes with each compute node having two Intel Xeon 8268 CPUs (each CPU comprises 24 HPE SGI 8600 cores) and 192 GB of RAM. In this part, HPC computational resources for the different simulated cases is furnished. For the sake of comparison, mono-sphere shape model simulations were also performed on HPC to establish a reference case. **Table 7** provides a detailed information about the computational resources used for each simulation, which includes the number of compute nodes, the CPU cores count per node, and the CPU time. In addition, the computational system size in terms of the total number of base spheres is also reported in the same table. Moreover, the computational cost, taken as the total computational time in the unit of Processors-hours, is listed. Total computational time was evaluated by calculating the multiplication product of the total number of CPU cores used and the CPU time.

Figure 8A depicts the relation between the computational cost and the system size for the different particle shape models, with and without the rolling resistance model invoked. As would be expected, higher computational cost is needed to simulate larger systems. However, invoking the rolling resistance model does not introduce any remarkable computational cost except for the case of the mono-sphere shape model. This indicates the additional cost needed to calculate the extra term in the contact model accounting for the rolling resistance is minimal. Moreover, it suggests the relatively higher cost in the case of mono-sphere model is attributed to the communication time overhead and the

populous neighbor lists associated with activating the rolling resistance model. This overhead originates from the denser material heap formed in that case, remember that the AOR for a mono-sphere model with a rolling resistance is higher than the case without a rolling resistance by a factor of two. It is worth noting that the absence of the rolling resistance in the case of mono-base DEM particles with smooth surface causes some of these particles to roll away from the main material pile and form isolated small clusters, which introduces computing load imbalance among the CPU cores. Nevertheless, the load balance feature available in LIGGGHTS-INL adjusts the size of the processor subdomain to balance the number of particles and thus the computational loads continue to be evenly distributed across the computational resources. Apparently, the dynamic load balance successfully minimized the impact of the scattered particles on the computational cost.

To facilitate the comparison between the computational cost of different particle shape models, a normalized metric was utilized. The normalized computational cost was plotted versus the effective particle radius, as shown in **Figure 8B**. For the vertical axis, the computational cost was normalized by the system size and has the unit of processor-hours per base-sphere A careful examination reveals all clumped-sphere models exhibit an increase in the normalized computational cost regardless of the state of the rolling resistance model. However, the rate of increase of this computational cost is different. Moreover, the clumped-sphere models outperform the mono-sphere model for the larger effective DEM particle size (smaller system size). Nevertheless, this behavior changes for the smaller particle size with the mono-sphere model having a cost lower by a factor in the range of 2–3. This suggests the major component contributing to the overall computational cost differs for the larger particle sizes from the smaller ones. For the larger particle size, particle shape models that produced higher repose angle incurred lower normalized computational cost. To the contrary, the situation is quite the opposite for the smaller particle size, with the clumped-sphere chip model possessing the highest normalized computational cost. This could be attributed to the nonlinear increase in the coordination number by increasing the system size and the associated increase in the computing time spent in calculating the pairwise interactions between particles in direct contact. This is augmented by the increase in the communication time across compute nodes, since a higher number of compute nodes is needed to simulate a larger system size. This effect is expected to be more prominent in the case of heaps with higher density, i.e., larger AOR. On the other hand, for a smaller system size, the temporal evolution of system dynamics with particles exploring larger region in the spatial domain makes neighbor list updates more frequent, and it turns out this contribution to the overall computational workload becomes more significant. This is accompanied by the decrease in the workload required to compute particle-particle interaction forces. Hence, the computational cost under such circumstances will be higher for systems with smaller AOR.

The analysis of the used computational resources presented herein demonstrates the computational efficiency of clumped-

sphere models for force calculations and contact detection. Even for simulation cases of the clumped-sphere models that are more expensive than the corresponding mono-sphere case, the increase in the computational cost is moderate. Furthermore, this comparison does not account for one more aspect that pertains to the minimum feature size resolved by each model. Although different shape models used similar effective particle sizes, clumped-sphere particle shape models possess higher resolution, as the base-sphere size is much smaller. Accordingly, the moderate increase in the computational cost associated with the use of some of these shape models is still affordable for the length scale under consideration and is completely justified by the more accurate physical behaviors captured through these particle shape models.

4 SUMMARY AND FUTURE OUTLOOK

Angle of repose (AOR) is an important macroscopic parameter that can be used to characterize the free-flow behavior of granular materials. The AOR is not an intrinsic material property, as it depends on several extrinsic factors including particle characteristics, which can be engineered to control the flowability of these particulate materials. In the case of lignocellulosic biomass, identifying the underlying mechanisms controlling its mechanical behavior and determining influential parameters is crucial for the optimization of preprocessing and handling unit operations without compromising feedstocks performance or conversion efficiency. Promoting fundamental understandings of the impact of the critical material attributes on the biomass feedstocks response can guide the selection of the critical processing parameters. This progress will render bioenergy technologies economically competitive and enable their deployment at the commercial scale. Thus, advances in bioenergy research will allow this energy source to play a vital role in shaping the clean energy portfolio to meet increasing global energy demands while satisfying the proposed measures to mitigate climate changes. Comminution is one of the costliest and energy-intensive operations in the preprocessing of biomass feedstocks. So, the present study employed an integrated experimental and computational approach to investigate the effects of particle shape and size on the AOR using Forest Concepts Crumbler[®] rotary shear system to produce two reduced particle sizes of conifer veneer and Douglas fir, i.e., 2 and 6 mm. The bottomless cylinder test was conducted in the laboratory and simulated using discrete element method (DEM) to evaluate AOR. Simulated AOR for different particles shapes and sizes were compared and benchmarked against experiment. In addition, the specific energy consumption for the comminution of produced Crumbles and moisture content for different particle sizes were also measured and reported. Moreover, the impact of additional factors on AOR, e.g., surface roughness and rolling resistance were investigated.

Our experimental results showed that while the smaller size (2 mm) of pine particles achieves better followability

(i.e., smaller AOR), the energy cost of comminution is significantly higher, and the bulk density is almost the same as the 6-mm pine particles. In addition, 2-mm Crumbles from veneer have better flow properties than 2-mm Crumbles from chips, which was ascribed to the difference in particle shape. To the contrary, no significant difference was observed between the AOR of the two geometries when the 6-mm particle size was utilized. In addition, Crumbles from chips exhibited minimal sensitivity to variation in particles size. Furthermore, the DEM results identified the mechanical interlocking between contacting particles as the dominant factor in determining the AOR in the case of complex-shaped particles such as milled pine, which cannot be accurately captured by using simple particle shapes (e.g., mono-sphere) in conjunction with a rolling resistance model. This is attributed to the correlation between the sensitivity of AOR to the variation in particle size and particle shape. Hence, the use of simple particle shapes along with a rolling friction coefficient calibrated with experimental data for a given particle size will not be adequate to predict the AOR for a different particle size. To the contrary, the clumped-sphere model alleviates this limitation without significant increase in the computational cost and can be used for accurate simulations of biomass granular flow. This was evidenced by the better agreement achieved with the experiment by using clumped-sphere particle model with a layout mimicking the shape of the corresponding Crumble. In addition, the minimal dependency of clumped-sphere models prediction on the contribution of rolling resistance mechanism to the particle-particle interaction asserts the adequacy of these models to predict AOR. This observation indicated the role played by other underlying mechanisms arising from particle morphology and motivated the investigation of surface roughness and aspect ratio effects on AOR. The DEM results confirmed that for the same particle shape, higher surface roughness leads to larger AOR. Similarly, using different configurations having the same composition of base spheres within clumped-sphere shape models indicated that the deviation of the aspect ratio from one gives rise to a larger repose angle. This is found consistent with the observed trend highlighting the increase of repose angle with the particle size. All remarks concluded from the DEM simulation results were found in good agreement with our experimental findings.

In conclusion, the present study investigated quantitatively the impact of particle characteristics of dry milled pine on its flow behavior and illustrated the importance of adopting experimentally validated computational models to explore regions in topological space that could be inaccessible to experimentation. In addition, the coupling of the computational approach to the experimental work elucidated the underlying mechanisms and their individual contributions to the mechanical behavior of this granular material. However, developing reliable predictive models to this multivariate problem dictates accounting for many factors. Several future directions can be considered to achieve this goal, which can be summarized as follows.

- As noted, AOR is not an intrinsic material property, so the influence of other factors such as moisture content, porosity, and temperature need to be examined.
- Regardless of the shape model used in the present study, a persistent trend was observed regarding the relation between particle size and predicted AOR for the same amount of material: the larger the particle size the larger AOR. Capturing scenarios under which this trend is reversed requires incorporation of the attractive forces (for example Van der Waals force) in the description of the contact model in DEM simulations. This is expected to be more important for small particle sizes at or below the microscale and/or for wet particles.
- AOR could be an effective indicator of the flow behavior of granular particles. However, the prediction from this indicator should be limited to stress-free circumstances. For applications where external stresses are expected to be affecting the behavior of the material, a more reliable indicator is needed. This requires extending the scope of the study to probe the viscoplastic response of the materials under consideration to account for inelastic deformation processes. DEM models that account for these effects are available, e.g., (Chen et al., 2022), and will be considered in future studies.
- The selection of the set of optimal process parameters can be performed through a comprehensive technoeconomic analysis. This, in turn, requires a thorough quantification of the impact of critical material properties on different aspects of the feedstock, from the time of harvesting the raw biomass all the way up to its service-time in the conversion reactor. This includes optimizing for material handling, transportation, and preprocessing operations in conjunction with the feedstock performance and thermochemical conversion efficiency in the biorefinery. Accordingly, engineering particle characteristics for favorable flowability is only one criterion in a multi-objective optimization problem that should include other characteristics such as the chemical and thermal behavior.

DATA AVAILABILITY STATEMENT

The original contributions presented in the study are included in the article, further inquiries can be directed to the corresponding author.

AUTHOR CONTRIBUTIONS

AH conceptualized the article, performed the part of DEM simulations on HPC *via* LIGGGHTS-INL, and drafted/edited the full manuscript. YX conceptualized the article, supervised the work, performed the part of DEM simulations using Rocky DEM, and edited the full manuscript. NS and JK performed the bottomless cylinder test experiment and measured the AOR, contributed to the drafting of the relevant section (**Section 2.3**), and edited the manuscript. DL and JD supplied the comminuted wood veneer and chips feedstock, performed the characterization of the supplied particles physical properties and the evaluation of comminution energy, contributed to the drafting of the relevant sections (**Sections 2.1**, **2.2**), and edited the manuscript.

FUNDING

ACKNOWLEDGMENTS

REFERENCES

Abbaspour-Fard, M. H. (2004). Theoretical Validation of a Multi-Sphere, Discrete Element Model Suitable for Biomaterials Handling Simulation. *Biosyst. Eng.* 88, 153–161. doi:10.1016/j.biosystemseng.2004.03.010

Adam, S., Suzzi, D., Radeke, C., and Khinast, J. G. (2011). An Integrated Quality by Design (QbD) Approach towards Design Space Definition of a Blending Unit Operation by Discrete Element Method (DEM) Simulation. *Eur. J. Pharm. Sci.* 42, 106–115. doi:10.1016/j.ejps.2010.10.013

Ai, J., Chen, J.-F., Rotter, J. M., and Ooi, J. Y. (2011). Assessment of Rolling Resistance Models in Discrete Element Simulations. *Powder Techn.* 206, 269–282. doi:10.1016/j.powtec.2010.09.030

Beakawi Al-Hashemi, H. M., and Baghabra Al-Amoudi, O. S. (2018). A Review on the Angle of Repose of Granular Materials. *Powder Techn.* 330, 397–417. doi:10.1016/j.powtec.2018.02.003

Chen, F., Xia, Y., Klinger, J. L., and Chen, Q. (2022). A Set of Hysteretic Nonlinear Contact Models for DEM: Theory, Formulation, and Application for Lignocellulosic Biomass. *Powder Techn.* 399, 117100. doi:10.1016/j.powtec.2021.117100

Chen, H., Zhao, S., and Zhou, X. (2020). DEM Investigation of Angle of Repose for Super-ellipsoidal Particles. *Particuology* 50, 53–66. doi:10.1016/j.partic.2019.05.005

Chen, J., Gao, R., and Liu, Y. (20192019). Numerical Study of Particle Morphology Effect on the Angle of Repose for Coarse Assemblies Using DEM. *Adv. Mater. Sci. Eng.* 2019, 1–15. doi:10.1155/2019/8095267

Cheng, N.-S., and Zhao, K. (2017). Difference between Static and Dynamic Angle of Repose of Uniform Sediment Grains. *Int. J. Sediment Res.* 32, 149–154. doi:10.1016/j.ijsrc.2016.09.001

Ciesielski, P. N., Pecha, M. B., Lattanzi, A. M., Bharadwaj, V. S., Crowley, M. F., Bu, L., et al. (2020). Advances in Multiscale Modeling of Lignocellulosic Biomass. *ACS Sust. Chem. Eng.* 8, 3512–3531. doi:10.1021/acssuschemeng.9b07415

Cleary, P. W., and Sawley, M. L. (2002). DEM Modelling of Industrial Granular Flows: 3D Case Studies and the Effect of Particle Shape on Hopper Discharge. *Appl. Math. Model.* 26, 89–111. doi:10.1016/S0307-904X(01)00050-6

Coetzee, C. J. (2017). Review: Calibration of the Discrete Element Method. *Powder Techn.* 310, 104–142. doi:10.1016/j.powtec.2017.01.015

Cundall, P. A., and Strack, O. D. L. (1979). A Discrete Numerical Model for Granular Assemblies. *Géotechnique* 29, 47–65. doi:10.1680/geot.1979.29.1.47

Elekes, F., and Parteli, E. J. R. (2021). An Expression for the Angle of Repose of Dry Cohesive Granular Materials on Earth and in Planetary Environments. *Proc. Natl. Acad. Sci. USA* 118, e2107965118. doi:10.1073/pnas.2107965118

Fonte, C. B., Oliveira, J. A. A., and Almeida, L. C. de. (2015). DEM-CFD COUPLING: MATHEMATICAL MODELLING AND CASE STUDIES USING ROCKY-DEM® AND ANSYS FLUENT®. in *Elev. Int. Conf. CFD Miner. Process Ind*, CSIRO Organization, Melbourne, Australia, 1–7.

Frączek, J., Złobecki, A., and Zemanek, J. (2007). Assessment of Angle of Repose of Granular Plant Material Using Computer Image Analysis. *J. Food Eng.* 83, 17–22. doi:10.1016/j.jfoodeng.2006.11.028

Gao, X., Lu, L., Shahnam, M., Rogers, W. A., Smith, K., Gaston, K., et al. (2021). Assessment of a Detailed Biomass Pyrolysis Kinetic Scheme in Multiscale Simulations of a Single-Particle Pyrolyzer and a Pilot-Scale Entrained Flow Pyrolyzer. *Chem. Eng. J.* 418, 129347. doi:10.1016/j.cej.2021.129347

Guo, Y., Chen, Q., Xia, Y., Klinger, J., and Thompson, V. (2021). A Nonlinear Elasto-Plastic Bond Model for the Discrete Element Modeling of Woody Biomass Particles. *Powder Techn.* 385, 557–571. doi:10.1016/j.powtec.2021.03.008

Guo, Y., Chen, Q., Xia, Y., Westover, T., Eksioglu, S., and Roni, M. (2020). Discrete Element Modeling of Switchgrass Particles under Compression and Rotational Shear. *Biomass and Bioenergy* 141, 105649. doi:10.1016/j.biombioe.2020.105649

Hertz, H. (1882). Ueber die Berührung fester elastischer Körper. *J. für die reine Angew. Mathematik (Crelles Journal)* 1882, 156–171. doi:10.1515/crll.1882.92. 15610.1515/9783112342404-004

Idaho National Laboratory. (2021). LIGGGHTS-INL: A Capability-Extended Adaptation of the LIGGGHTS Open Source Discrete Element Method (DEM) Particle Simulation Software based on LIGGGHTS release version 4.0.0. Available at: *https://github.com/idaholab/LIGGGHTS-INL*.

Jin, W., Stickel, J. J., Xia, Y., and Klinger, J. (2020). A Review of Computational Models for the Flow of Milled Biomass Part II: Continuum-Mechanics Models. *ACS Sust. Chem. Eng.* 8, 6157–6172. doi:10.1021/acssuschemeng.0c00412

Kloss, C., Goniva, C., Hager, A., Amberger, S., and Pirker, S. (2012). Models, Algorithms and Validation for Opensource DEM and CFD-DEM. *Pcfd* 12, 140–152. doi:10.1504/PCFD.2012.047457

Kruggel-Emden, H., Rickelt, S., Wirtz, S., and Scherer, V. (2008). A Study on the Validity of the Multi-Sphere Discrete Element Method. *Powder Techn.* 188, 153–165. doi:10.1016/j.powtec.2008.04.037

Lanning, David. N., DooleyDooley, H., and Lanning, Christopher. J. (2011). *Torque-arm Method to Measure Specific Energy in Laboratory Scale Biomass Preprocessing Equipment*. St. Joseph, MI: American Society of Agricultural and Biological Engineers. doi:10.13031/2013.38988

Liao, Z., Yang, Y., Sun, C., Wu, R., Duan, Z., Wang, Y., et al. (2021). Image-based Prediction of Granular Flow Behaviors in a Wedge-Shaped Hopper by Combing DEM and Deep Learning Methods. *Powder Techn.* 383, 159–166. doi:10.1016/j.powtec.2021.01.041

Liu, S. D., Gan, J. Q., Zou, R. P., Yu, A. B., and Zhou, Z. Y. (2020). Wall Stress Analysis in an Unsteady Hopper Flow with Ellipsoidal Particles. *Powder Techn.* 361, 1–9. doi:10.1016/j.powtec.2019.11.053

Liu, S. D., Zhou, Z. Y., Zou, R. P., Pinson, D., and Yu, A. B. (2014). Flow Characteristics and Discharge Rate of Ellipsoidal Particles in a Flat Bottom Hopper. *Powder Techn.* 253, 70–79. doi:10.1016/j.powtec.2013.11.001

Lu, Y., Jin, W., Klinger, J., and Dai, S. (2021). Flow and Arching of Biomass Particles in Wedge-Shaped Hoppers. *ACS Sust. Chem. Eng.* 9, 15303–15314. doi:10.1021/acssuschemeng.1c05628

Mindlin, R. D., and Deresiewicz, H. (1953). Elastic Spheres in Contact under Varying Oblique Forces. *J. Appl. Mech.* 20, 327–344. doi:10.1115/1.4010702

Müller, D., Fimbinger, E., and Brand, C. (2021). Algorithm for the Determination of the Angle of Repose in Bulk Material Analysis. *Powder Techn.* 383, 598–605. doi:10.1016/j.powtec.2021.01.010

Nakashima, H., Shioji, Y., Kobayashi, T., Aoki, S., Shimizu, H., Miyasaka, J., et al. (2011). Determining the Angle of Repose of Sand under Low-Gravity Conditions Using Discrete Element Method. *J. Terramechanics* 48, 17–26. doi:10.1016/j.jterra.2010.09.002

Oyedeji, O., Gitman, P., Qu, J., and Webb, E. (2020). Understanding the Impact of Lignocellulosic Biomass Variability on the Size Reduction Process: A Review. *ACS Sust. Chem. Eng.* 8, 2327–2343. doi:10.1021/acssuschemeng.9b06698

Papworth, R. L., and Erickson, J. R. (1966). Power Requirements for Producing Wood Chips. *For. Prod. J.* 16, 31–36.

Rackl, M., Top, F., Molhoek, C. P., and Schott, D. L. (2017). Feeding System for wood Chips: A DEM Study to Improve Equipment Performance. *Biomass and Bioenergy* 98, 43–52. doi:10.1016/j.biombioe.2017.01.003

Renewable Energy Agency (2018). *Global Energy Transformation: A Roadmap to 2050*. Available at: www.irena.org.

Scherer, V., Mönnigmann, M., Berner, M. O., and Sudbrock, F. (2016). Coupled DEM-CFD Simulation of Drying wood Chips in a Rotary Drum - Baffle Design and Model Reduction. *Fuel* 184, 896–904. doi:10.1016/j.fuel.2016. 05.054

Stelte, W., Sanadi, A. R., Shang, L., Holm, J. K., Ahrenfeldt, J., and Henriksen, U. B. (2012). Recent Developments in Biomass Pelletization - A Review. *BioRes* 7, 4451–4490. doi:10.15376/biores.7.3.4451-4490

Stukowski, A. (2010). Visualization and Analysis of Atomistic Simulation Data with OVITO-The Open Visualization Tool. *Model. Simul. Mater. Sci. Eng.* 18, 015012. doi:10.1088/0965-0393/18/1/015012

U.S. Department of Energy Bioenergy Technologies Office (2016). *Biorefinery Optimization Workshop Summary Report*, (Chicago, IL: U.S. Department of Energy).

Wensrich, C. M., and Katterfeld, A. (2012). Rolling Friction as a Technique for Modelling Particle Shape in DEM. *Powder Techn.* 217, 409–417. doi:10.1016/j. powtec.2011.10.057

Xia, Y., Chen, F., Klinger, J. L., Kane, J. J., Bhattacharjee, T., Seifert, R., et al. (2021). Assessment of a Tomography-Informed Polyhedral Discrete Element Modelling Approach for Complex-Shaped Granular Woody Biomass in Stress Consolidation. *Biosyst. Eng.* 205, 187–211. doi:10.1016/j.biosystemseng.2021.03.007

Xia, Y., Lai, Z., Westover, T., Klinger, J., Huang, H., and Chen, Q. (2019). Discrete Element Modeling of Deformable Pinewood Chips in Cyclic Loading Test. *Powder Techn.* 345, 1–14. doi:10.1016/j.powtec.2018.12.072

Xia, Y., Stickel, J. J., Jin, W., and Klinger, J. (2020). A Review of Computational Models for the Flow of Milled Biomass Part I: Discrete-Particle Models. *ACS Sust. Chem. Eng.* 8, 6142–6156. doi:10.1021/acssuschemeng.0c00402

Zhong, W., Yu, A., Liu, X., Tong, Z., and Zhang, H. (2016). DEM/CFD-DEM Modelling of Non-spherical Particulate Systems: Theoretical Developments and Applications. *Powder Techn.* 302, 108–152. doi:10.1016/j.powtec.2016.07.010

Zhou, Z. Y., Zou, R. P., Pinson, D., and Yu, A. B. (2014). Angle of Repose and Stress Distribution of Sandpiles Formed with Ellipsoidal Particles. *Granular Matter* 16, 695–709. doi:10.1007/s10035-014-0522-4

Conflict of Interest: Authors DL and JD were employed by the company Forest Concepts LLC.

The remaining authors declare that the research was conducted in the absence of any commercial or financial relationships that could be construed as a potential conflict of interest.

The handling editor AR declared a shared affiliation with the author(s) AH, YX, NS, JK at the time of review.

Publisher's Note: All claims expressed in this article are solely those of the authors and do not necessarily represent those of their affiliated organizations, or those of the publisher, the editors and the reviewers. Any product that may be evaluated in this article, or claim that may be made by its manufacturer, is not guaranteed or endorsed by the publisher.

Comparing Calibration Algorithms for the Rapid Characterization of Pretreated Corn Stover Using Near-Infrared Spectroscopy

Zofia Tillman and Edward J. Wolfrum*

Renewable Resources and Enabling Sciences Center, National Renewable Energy Laboratory, Golden, CO, United States

Rapid characterization of biomass composition is a key enabling technology for biorefineries—the ability to measure the chemical composition of biomass materials entering the biorefinery as well as the composition of key process intermediate streams would allow real-time process control and the development of robust models to predict process performance. The utility of near-infrared (NIR) spectroscopy for rapid characterization requires multivariate algorithms for building calibration models. The most prevalent algorithm used for building calibration models using NIR spectra is the linear modeling algorithm Partial Least Squares Regression (PLS). Nonlinear regression algorithms (which are typically more computationally intensive than linear modeling approaches) have gained popularity in recent years due to their ability to solve a wide variety of classification and regression problems and the dramatic increase in available computational resources. In this work, we demonstrate that a calibration model can predict the composition of corn stover process intermediate samples pretreated with three different treatments—hot water (HW), dilute acid (DA), and deacetylation followed by dilute acid (DDA). We quantitatively compare three different algorithms for building prediction models based on near-infrared spectroscopy—partial least squares (PLS), support vector machines (SVM), and random forests (RF). We demonstrate the utility of improving model performance by accounting for instrument performance variability using repeated measurements of standard materials (e.g., the "repeatability file" strategy) and investigate its performance with nonlinear regression techniques, and we discuss methods for quantifying the uncertainties of specific predictions among the three methods.

Keywords: NIR, rapid analysis, corn stover, pretreatment, chemometrics, biomass

1 INTRODUCTION

Rapid characterization of biomass composition is a key enabling technology for biorefineries—the ability to measure the chemical composition of biomass materials entering the biorefinery as well as the composition of key process intermediate streams would allow real-time process control and the development of robust models to predict process performance. There is substantial literature on the use of spectroscopic methods such as near-infrared (NIR) spectroscopy for rapid biomass characterization going back several decades (Abrams et al., 1987; Sanderson et al., 1996; Kelley

et al., 2002; Tsuchikawa, 2007; Labbe et al., 2008; Tsuchikawa and Kobori, 2015) and including some comprehensive reviews (Xiao et al., 2014; Skvaril et al., 2017).

The use of NIR spectroscopy for rapid characterization requires multivariate algorithms for building calibration models (Höskuldsson, 1988; Beebe et al., 1998; Pasquini, 2018). The most prevalent algorithm used for building calibration models using NIR spectra is Partial Least Squares Regression (PLS). PLS is an extension of multiple linear regression and uses feature extraction to produce new latent variables (principal components) composed of linear combinations of the original variables that describe the majority of the variance correlated with the outcome of interest (Höskuldsson, 1988). While originally developed for the field of econometrics, PLS has been used in chemometrics since the 1970s, and is currently a standard method for NIRS regression (Geladi and Kowalski, 1986).

Nonlinear regression techniques have demonstrated utility in solving a wide variety of classification and prediction problems. In recent years their usage has increased due to a combination of dramatically increased availability of high-performance computing (HPC) tools and access to open-source implementation of these algorithms in computing languages such as R and Python. Support Vector Machines (SVM) (Awad and Khanna, 2015) and Random Forest (RF) (Breiman, 2001; Fawagreh et al., 2014) are two such nonlinear machine learning techniques. SVM regression expands upon the support vector machine classification technique (Cristianini and Shawe-Taylor, 2000) to fit a hyperplane that minimizes the residuals outside a defined error margin (ε-margin). In the training process, a cost parameter, C, is chosen, which defines the penalty for residuals above a certain value. SVM can be used to explain linear and nonlinear relationships through the use of kernel functions (Cristianini and Shawe-Taylor, 2000; Awad and Khanna, 2015). Radial bias functions (RBF) are often used with training sets having nonlinear relationships between dependent and independent variables. RBF functions require the additional tuning of the parameter σ, which controls for the level of nonlinearity in the model. Random Forest Modeling develops individual decision trees based on a randomly chosen selection of predictors and then aggregates tree results to determine the outcome of interest. The user must decide upon the number of predictors to use in each model, and the number of models (the number of trees) to include in the forest (Breiman, 2001).

There have been direct comparisons of the performance of these regression techniques with NIR spectral data. RBF-SVM was found to be statistically significantly better than PLS at predicting soil quality parameters in spectral data sets greater than 1,000 samples, as evidenced by reductions in RMSEP of 14%–29% (de Santana et al., 2021). A study using NIR to quantify caffeine content in tea samples found a 9% improvement in RMSEP from SVM as compared to PLS (Chanda et al., 2019). RF was found to be statistically significantly better than PLS at predicting soil quality parameters from a regionally diverse soil spectra database, with improvements ranging from 8%–16% RMSEP (de Santana et al., 2018). RF led to improvements in the

predictive modeling of petroleum products (paraffin, naphthene, and total aromatic wt%) in naphtha and gasoline samples of up to 18% SEP compared to PLS, and RF was more robust against overfitting than PLS for outcomes with narrow ranges (Lee et al., 2013). It may be that the success of these nonlinear approaches may be related to the presence of nonlinear relationships between NIR spectra and the primary analytical measurements.

The strategy of using a "repeatability file" to reduce the impact of instrument and environmental changes on spectral variability over the long term was introduced over 30 years ago (Shenk and Westerhaus, 1991). It has been demonstrated to decrease the effect of spectral variance associated with instrument and environmental (e.g., temperature, humidity) variability in partial least squares regression. These variabilities are more prominent and important to account for in samples that inherently contain water, such as biomass (Near-Infrared Spectroscopy in Agriculture, 2004). This approach uses repeated measurements of external materials to create a collection of spectra. The difference of each spectrum in the collection from the collection mean value are then calculated. These difference spectra are appended to the mean-centered calibration or training set (with appropriate weighting factors) and assigned the mean composition values for the training set. These "repeatability" spectra thus capture any spectral variation that is not correlated with compositional changes because the composition of these external materials does not change over time. The difference spectra represent uncontrolled environmental or instrumental variability. Including these spectra in the calibration set explicitly quantifies measured spectral variation not associated with sample composition variability.

To our knowledge, a comparison of how the nonlinear regression algorithms SVM and RF perform at predicting key biomass compositional attributes (structural carbohydrate, lignin, and ash content) in pretreated corn stover samples across a variety of pretreatments has not been demonstrated previously. Furthermore, the effect of the "repeatability file" strategy to control for instrument and environmental variance using nonlinear regression algorithms (rather than PLS) has not been demonstrated. In this work, we thus extend the existing literature in the following ways –

- We demonstrate that a single calibration model can predict the composition of corn stover samples subjected to three different pretreatments—hot water (HW), dilute acid (DA), and deacetylation followed by dilute acid (DDA)
- We quantitatively compare three different algorithms for building prediction models based on near-infrared spectroscopy—partial least squares (PLS), support vector machines (SVM), and random forests (RF)
- We demonstrate the utility of improving model performance by accounting for instrument performance and environmental variability using repeated measurements of standard materials (e.g., the "repeatability file" algorithm) and its performance with nonlinear regression techniques.

- We discuss methods for quantifying the uncertainties of specific predictions from the three methods

2 MATERIALS AND METHODS

2.1 Sample Set

The dataset used in this work consisted of 151 corn stover samples which were subject to different pretreatments– hot water (HT), dilute acid (DA), and deacetylation followed by dilute acid (DDA). All pretreatment experiments were performed using a horizontal pretreatment reactor operated at multiple temperatures (150°C–200°C) and two different mean residence times (12 and 20 min). The reactor systems used have been described previously (Shekiro et al., 2014). In brief, the corn stover was impregnated with either hot water (HW) or dilute acid (DA, DDA) prior to entering the pretreatment reactor. DDA samples were subjected to a batch deacetylation step using a separate reaction system. Samples were taken immediately before or immediately after the horizontal pretreatment reactor once steady-state conditions were reached in the reactor and were refrigerated until compositional analysis.

The corn stover feedstock used in this work was harvested in Trumbull County Iowa in September 2020 using single-pass harvesting. The corn stover was milled to pass through a 19.05 mm (¾ inch) screen using a knife mill and stored in flexible supersacks until use.

2.2 Analytical Methods

To prepare the corn stover samples for analytical chemistry, stored samples were removed from refrigeration, washed with deionized water to remove any soluble material, air-dried to less than 10% moisture, knife-milled to pass through a 2 mm screen, and stored in plastic bags until further analysis.

Primary analytical data were generated using NREL Laboratory Analytical Procedures (LAPs, https://www.nrel.gov/bioenergy/biomass-compositional-analysis.html). In brief, the biomass samples underwent a 2-stage acid hydrolysis to solubilize structural carbohydrates which were measured *via* high-pressure liquid chromatography. Lignin was measured as the acid-insoluble residue after hydrolysis, and total ash was determined using a combustion assay. Because all samples in this work had undergone pretreatment, the samples were not extracted prior to analytical hydrolysis. The primary analytical chemical data (wet chemistry) were produced between August 2020 and January 2021.

2.3 Near Infrared Spectroscopy Methods

Near-infrared (NIR) spectra used in the training set were collected using a Metrohm NIRS XDS Multivial Analyzer (Metrohm AG Switzerland). Samples were removed from their plastic bags and stored under house vacuum for at least 24 h before scanning to eliminate variability due to moisture content. Relative humidity readings in the lab on all days of scanning ranged from 13%–44%. Temperature readings in the lab on all days of scanning ranged from 21.8°C to 25.2°C. Samples were placed in quartz optical glass sample cups and scanned in

reflectance mode between April and June 2021. Spectra were collected over the range of 400.0–2499.5 nm (0.5 nm resolution). Spectra were the average of 32 unique scans, which were reference standardized to Certified Reflectance standards (Metrohm AG Switzerland). Spectra were collected using NIRS Vision 4.1 (Metrohm AG Switzerland). The entire sample population was scanned a second time between October 2021 and January 2022. None of the spectra created during this second scanning period were included in the calibration set, but instead used to evaluate the robustness of the models. The duplicate scans will be referred to later as the "late training" set.

2.4 Modeling

The open-source programming language R (http://www.r-project.org) was used for all model building. The following packages were used: *prospectr* for spectral transformation and selection of calibration and independent validation populations, *tidymodels* recipes for dimensionality reduction techniques, the *pls* package for PLS models, *kernlab* for SVM models, *randomForest* for RF models, *caret* for model tuning and cross-validation, and the *tidyverse* collection of packages for data cleaning and wrangling. All model training was performed on individual laptops or a local HPC cluster. Unique models were created for four analytes—glucan, xylan, lignin, and ash—using each modeling algorithm (PLS, SVM, RF).

Supervised (PLS) and unsupervised (PCA) dimensionality reduction were evaluated as additional preprocessing techniques for both SVM and RF models. No additional preprocessing was used for the PLS model building.

The R scripts used to for spectral transformation, developing the repeatability file, and regression modeling can be found in the **Supplementary Material**.

2.4.1 Spectral Transformation

Spectra were normalized using the Standard Normal Variate (SNV) transformation and smoothed using the Savitzky-Golay algorithm (second order polynomial, first derivative, and window size of 7). Spectra were then truncated to remove the visible region below 600 nm, which corresponded with a low signal to noise ratio, and the region between 1,075 and 1,125 nm, which corresponded with a detector change that causes an abrupt shift in absorbance. Centering was performed on the training-set prior to model fitting.

The Kennard Stone algorithm (*prospectr* package) was used to select an independent validation set that was spectrally representative of the population, and therefore could evaluate how well each model acted at predicting samples within the observed spectral variance. This method resulted in 120 samples for calibration and 31 for validation.

2.4.2 Managing Instrumental Variability

To minimize the effect(s) of instrument variability on spectra collection and therefore regression model performance, we implemented the "repeatability file" strategy using stable biomass check cell spectra (Near-Infrared Spectroscopy in Agriculture, 2004). A total of 15 spectra were collected from each of two corn stover samples over the course of the scanning

campaign. The two samples were selected to be representative of the calibration population.

The spectra were normalized, smoothed, and truncated using the same procedure used on the training spectra. The spectra were then grouped by sample and recentered to a mean value of zero. The centered, transformed spectra were weighted using the technique suggested by Acharya (Acharya et al., 2014), which corresponded to a weight (W) of 2. The spectra were paired with the mean wet chemistry values for the entire calibration set and added to the calibration set used for modeling. All models were created and evaluated with and without the addition of these spectra to the calibration data set to determine how the "repeatability file" strategy affected model performance.

2.4.3 Model Validation

Ten repeated-10-fold cross validation was used to tune each model to the appropriate hyperparameter selection. For the PLS model, the only hyperparameter was the number of principal components (PCs) in the model. The optimal number of PCs was chosen based on the RMSECV value. For the SVM model, two hyperparameters required tuning—cost (C) and the radial kernel scaling parameter sigma (σ). For the RF model, two hyperparameters required tuning—the number of randomly selected predictors chosen at each split (mtry) and the number of trees used in the model (ntree). For the SVM and RF models, hyperparameter tuning was performed using a grid search across an initially wide set of hyperparameters, and selection was based on the combination of hyperparameters that resulted in the lowest RMSECV. The initial grids for each model are shown in the **Supplemental Material** model building scripts. If the hyperparameter combination chosen by this technique resulted in an edge case (at least one of the parameters was one of the minimum or maximum options in the grid), the grid was expanded iteratively until the resulting hyperparameter combination did not include an edge case.

Model performance was evaluated by comparing the root mean squared errors (RMSE) associated with different predictions—predictions of the calibration or training population (RMSEC), the repeated 10-fold cross validation results (RMSECV), and the prediction of the independent validation set (RMSEP). In addition to these three standard measures of model performance, we also calculated the RMSE of the prediction of the second set of calibration set spectra, the "late training" set—the calibration set re-scanned several months after the original scans (RMSE-late). Models were also evaluated *via* the correlation coefficients (R^2) for the same scenarios (e.g., training, cross-validation, independent validation, late training). We used a Student's t-test (after applying the Fisher z-transform) to compare correlation coefficients, and an F-test to compare RMSE values (Roggo et al., 2003).

3 RESULTS AND DISCUSSION

3.1 Compositional and Spectral Variability

The compositional analysis data for the pretreated corn stover samples (organized by pretreatment chemistry and sampling location) are shown in **Table 1** and **Figure 1**. The compositional analysis results show several consistent trends that are attributed to the both the pretreatment used and the sampling location.

3.1.1 Compositional Variability

The overall composition of the HW and DA samples taken at the reactor inlet are very similar for all four analytes, while the DDA samples taken at the reactor inlet are consistently higher in glucan content and lower in both lignin and ash content. The xylan content for inlet samples with all pretreatments is similar. Because the HW and DA samples from the reactor inlet had not yet been subject to elevated temperatures, and all samples were washed prior to analysis, these samples should be quite similar in glucan, xylan, and lignin content. The mean ash content of the DA samples is slightly lower than for the HW samples, since dilute acid is more aggressive in removing inorganic materials than water even at ambient temperature. The DDA samples at the reactor inlet had been subjected to deacetylation, which removes acetate side chains from hemicellulose, extractives, and a portion of lignin, xylan, and ash. Thus, this results in increased glucan content and reduced lignin and ash content. The loss in extractives, lignin, and ash, which collectively increases the remaining glucan content, is offset by the loss in hemicellulose during deacetylation, keeping the xylan content approximately constant.

Thermochemical pretreatment increases the glucan and lignin content and decreases the xylan content. Again, this is consistent with the chemistry of pretreatment, where elevated temperature and the presence of a catalyst (for DA and DDA) result in the solubilization of a large portion of the hemicellulose fraction, a small portion of the lignin fraction, but virtually none of the glucan fraction. This results in pretreated samples with substantially higher glucan, lower xylan, and higher lignin contents. The HW chemistry does not use a catalyst, and so is less effective in removing xylan and therefore enriching the sample in glucan and lignin. The larger variability in the post-pretreatment HW samples is due to the impact of reactor temperature and residence time—higher temperatures and longer residence times increase xylan removal and therefore increase the residual glucan and lignin contents (full data presented in **Supplementary Material**).

3.1.2 Spectral Variability

Figure 2 shows the mean values of the collected (A and B) and mathematically-transformed (C and D) NIR spectra both before (A and C) and after (column and D) thermochemical pretreatment for the three different pretreatments used in this work. As described previously, all collected spectra were mathematically transformed (normalization and derivatization) prior to use in model building.

The collected spectra of samples taken before pretreatment (**Figure 2A**) have lower maximum absorbance at 500 nm in comparison to corresponding samples taken after pretreatment (**Figure 2B**) but have higher absorbance in the NIR range. The spectra of DDA samples show higher absorbance in the NIR range prior to pretreatment, while HW treated samples show the

TABLE 1 | Summary of compositional analysis data for population. Summary statistics for glucan, xylan, lignin and ash (%DW) content in the sample population used in this work. Summary statistics are shown for each of the pretreatments, with samples taken from catalyst-impregnated samples prior to (before) and after thermochemical pretreatment (after).

		ALL	Pretreatment					
			Hot water (HW)		Dilute acid (DA)		Deacetylated dilute acid (DDA)	
			Before	After	Before	After	Before	After
N		151	17	10	41	27	28	28
Mean (%)	Glucan	48.0	39.0	49.9	39.2	54.4	47.2	60.1
	Xylan	18.5	23.2	16.0	24.1	9.2	24.5	11.4
	Lignin	23.2	20.8	23.4	22.0	29.1	19.4	24.5
	Ash	1.6	2.3	1.8	1.7	2.3	1.0	1.1
Min (%)	Glucan	35.6	37.5	42.8	35.6	50.1	44.1	56.9
	Xylan	4.2	22.1	4.2	22.0	5.5	20.1	6.8
	Lignin	17.5	19.8	20.7	19.7	25.8	17.5	22.8
	Ash	0.6	1.8	1.5	0.7	1.6	0.6	1.0
Max (%)	Glucan	64.5	40.4	58.9	41.6	57.9	51.4	64.5
	Xylan	29.5	25.6	22.8	29.5	14.4	27.3	15.0
	Lignin	31.3	22.1	29.2	23.1	31.3	21.6	26.2
	Ash	3.0	3.0	2.2	2.8	2.8	1.3	1.4
SD (%)	Glucan	8.4	0.9	6.1	1.0	2.1	2.1	2.1
	Xylan	7.0	1.0	7.1	1.9	2.3	1.9	2.4
	Lignin	3.4	0.7	3.1	0.7	1.3	1.1	0.8
	Ash	0.6	0.4	0.2	0.4	0.3	0.2	0.1

DA, dilute acid; DDA, deacetylated/dilute acid; HW, hot water; DW, dry weight.

highest absorbance in the visible range after treatment. The transformed spectra of the samples collected prior to pretreatment are substantially different from the corresponding spectra collected after pretreatment. Close inspection of the transformed spectra shows that the HW and DA sample spectra are more similar to each other than to the DDA sample spectra, both before and after pretreatment. This is consistent with the differences in primary analytical chemistry—spectral variability follows compositional variability.

To investigate the spectral variability in more detail, we used Principal Component Analysis (PCA) to reduce the dimensionality of the transformed NIR spectra of the corn stover samples. **Figure 3A** shows a key result of this PCA in a score plot of the first two principal components. Sample points are colored by sampling location, and sample point symbols denote different pretreatment chemistries. The NIR spectra of the reactor inlet and reactor outlet samples are substantially different from each other (PC1), and the NIR spectra of the DDA samples are substantially different from the DA and HW samples (PC2). The DA and HW samples show substantial overlap. Note also that the NIR spectra of the independent validation samples held out of the model building (solid symbols) overlap the NIR spectra of the calibration samples (open symbols)—they are representative of the overall sample population and therefore a good indicator of model performance for spectra within the variance described by the calibration set. In **Figure 3B** we plot the glucan content vs. PC1 values. Glucan content correlates strongly and

inversely with sampling location ($r = -0.87$)—samples taken from the reactor outlet have higher glucan content and lower PC1 values than reactor inlet samples. The separation of the population by chemistry seen in **Figure 3A** is still evident—DDA samples are consistently higher in glucan content than either HW or DA samples.

3.2 Construction of Quantitative Models

Supervised (PLS) and unsupervised (PCA) dimensionality reduction techniques were evaluated as additional spectral transformation techniques prior to SVM and RF. No additional spectral preprocessing was used for PLS. Dimensionality reduction using PLS resulted in better SVM models compared to either no dimensionality reduction or dimensionality reduction using PCA. No dimensionality reduction led to the best performing RF model. Details of these models are provided in the **Supplementary Material**—for the balance of this work we compare PLS, SVM with dimensionality reduction using PLS, and RF with no dimensionality reduction.

Figure 4A shows the variability in raw spectra observed in the biomass external reference check cells. Regions of high variability in check cell spectra occur at 1,400 and 1,900 nm, which correspond to the first overtone of the O-H stretch and the combination mode H-O-H bend and O-H stretch in water, respectively (Near-Infrared Spectroscopy in Agriculture, 2004). Ambient building sensor data showed fluctuations in both the relative humidity and temperature of the laboratory over that

FIGURE 1 | Dot plot depicting the distribution of primary analytical data (separated by pretreatment chemistry) of the combined calibration and independent validation sample set for glucan **(A)**, xylan **(B)**, lignin **(C)**, and ash **(D)** content (%DW). Samples are prior to (before) and after thermochemical pretreatment (after), which is represented by color. Average measured glucan and lignin contents (%DW) increase and average measured xylan content (%DW) decreases after thermochemical pretreatment for all pretreatments. DDA treated samples show higher glucan and lower lignin and ash content than DA or HW. DA, dilute acid; DDA, deacetylated/dilute acid; Water, hot water; DW, dry weight.

time. It is likely that these fluctuations are the root cause of this variability. **Figure 4B** compares the variability observed in the transformed check cell spectra to that observed in the training set. The variability observed at 1,900 nm in the check cells has a similar in range to that observed across the entire training set, suggesting that little useful compositional information can be obtained from this region of the spectra.

Figure 5 compares the performance results (measured as RMSE) for cross validation (**Figures 5A–D**), independent validation **Figures 5E–H**, and late training validation (**Figures 5I–L**) for PLS, RF, and SVM models made with and without the addition of the check cell spectra variability to the calibration set through implementation of the "repeatability file" strategy. The tabulated results are presented in the **Supplementary Material**. SVM and PLS models showed statistically significant improvements in glucan, xylan, and ash performance across the independent validation and late training sets with the inclusion of a repeatability file ($\alpha = 0.05$). These results support the idea that the repeatability file improves NIR model performance for outcomes that are highly influenced by water when PLS is used

for dimensionality reduction. All models predicting lignin showed no statistically significant improvement with the addition of a repeatability file, indicating that the prediction of lignin from pretreated biomass *via* NIR is more robust to the environmental variability encountered during this work than the structural carbohydrates.

RF models showed no significant difference in performance with the use of the "repeatability file" strategy. Random forest models are known to be robust against the inclusion of unimportant predictors and outliers (Breiman, 2001; Lee et al., 2013). Because of the algorithm's robustness against unimportant variables, inclusion of the NIR regions with high check cell variability had no substantial impact on the model performance, regardless of whether a repeatability file is added. Furthermore, the decision tree algorithm used in RF models treats the repeatability file check cell variance like outliers to the calibration set rather than variance to ignore. The nonlinear nature of the individual decision trees is robust against such outliers, making the addition of the check cell spectra in the repeatability file algorithm superfluous—it neither improves the model by decreasing the effect of this
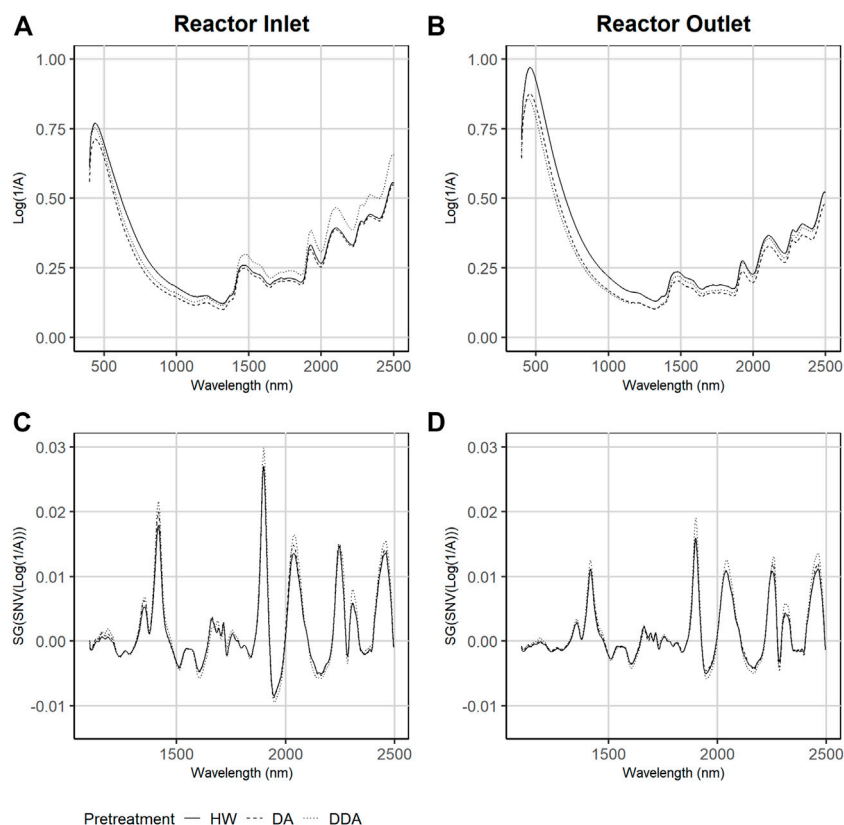
FIGURE 2 | Average Near-infrared (NIR) and Visible (Vis) diffuse reflectance spectra collected across the three different pretreatments. Samples are taken from catalyst-impregnated samples prior to pretreatment (before) and after thermochemical pretreatment (after). Plots **(A)** and **(B)**—raw NIR spectra as collected. Plots **(C)** and **(D)**—NIR spectra after spectral transforming *via* Standard Normal Variate and Savitsky-Golay smoothing. DA, dilute acid; DDA, deacetylated/dilute acid; Water, hot water; DW, dry weight.
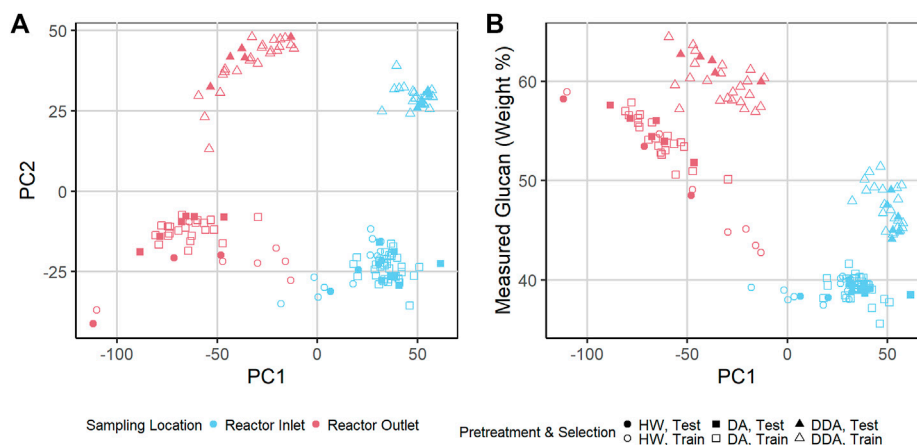
FIGURE 3 | **(A)** Scatter plot of Principal Component 2 (PC 2) vs. PC 1 of transformed near-infrared (NIR) spectra of pretreated corn stover samples. The samples represent three different pretreatments. Samples are taken from catalyst-impregnated samples prior to (before) and after thermochemical pretreatment (after). The DA and HW samples appear more similar to each other than to the DDA samples. **(B)** Scatter plot of measured glucan content (%DW) vs. PC 1 of transformed NIR spectra of pretreated corn stover samples. PC 1 is highly correlated with the glucan content—variability in chemical composition strongly affects PC 1 variance, demonstrating that spectral variance follows composition variance. DDA samples have consistently higher glucan content than DA and HW samples (see text). DA, dilute acid; DDA, deacetylated/dilute acid; Water, hot water; DW, dry weight.
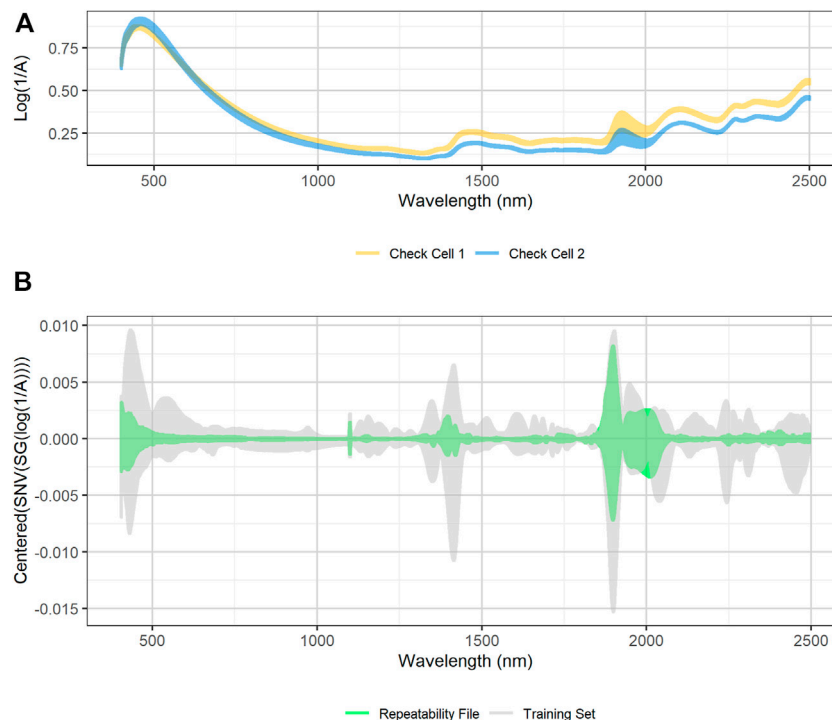
FIGURE 4 | (A) Plot of raw diffuse reflectance spectra of external standard materials check cells. The two external standard material check cells were created at the beginning of the project from two unique pretreated corn stover feedstocks. The check cells were scanned 15 times over the course of 6 months. High variability in the reflectance spectra exists at 1,900 nm, which corresponds to a known water overtone **(B)** SNV/SG/centered spectra of calibration spectra (grey) overlaid with SNV/SG/centered difference spectra of the external standard material check cells (green). The variability of the calibration spectral between 1,900 and 2,050 nm is similar in magnitude to the variability observed in the external standard material check cells. The ratio of calibration spectra variability to repeatability file variability is low in the visible region below 500 nm, at the 1,100 nm detector change, and at 1,400 nm, which corresponds to another water peak.

variability nor decreases model performance by including this variability. A comparison of the variable importance predictor scores between the RF models with and without the inclusion of the repeatability file (**Supplementary Material**) shows little change in which predictors are used in modeling.

3.3 Modeling Algorithm Comparisons

In **Table 2** we show the R^2 and RMSE values for all four analytes of interest (glucan, xylan, lignin, ash) for all three modeling approaches (PLS, SVM, RF) for calibration, cross-validation, independent validation, and late training. For these models, the calibration data set was augmented with repeated check cell spectra using the "repeatability file" strategy.

The SVM algorithm resulted in the statistically significantly better cross validation performance compared to both PLS and RF across all constituents. The best SVM models had an RMSECV of 0.89 for glucan content, 0.71 for xylan content, 0.49 for lignin content, and 0.23 for ash content. No statistically significant differences were found between the RF and PLS model RMSECV results for any analyte.

Prediction performance with an independent validation set is a more stringent test of model performance than cross-validation. The performance results for the independent validation predictions (RMSEP) were mixed between the different model types. The SVM algorithm predicted glucan, xylan, and lignin content from the independent validation set with greater accuracy than the PLS algorithm. The residual plots included in the **Supplementary Material** graphically demonstrate the reduced scatter in the prediction residuals and reduced bias in samples with high glucan content with the SVM algorithm. The RF algorithm predicted glucan and xylan content with greater accuracy than the PLS algorithm, while the SVM algorithm resulted in better accuracy at predicting lignin content and reduced bias in samples with high glucan content than RF, but similar overall performance at predicting xylan content. All modeling techniques resulted in similar prediction performance at predicting ash content for the independent validation set.

Finally, the prediction performance of the rescanned calibration set (the "late-training" set described above) is another test of model performance which includes the model's ability to differentiate instrumental or environmental variance from variance associated with wet chemistry. The SVM algorithm showed better performance at predicting all constituents using the late training set as compared to PLS, and better performance at predicting xylan and lignin content than RF. SVM and RF had similar performance for predicting ash and glucan content. RF models predicted all constituents with higher accuracy than PLS.
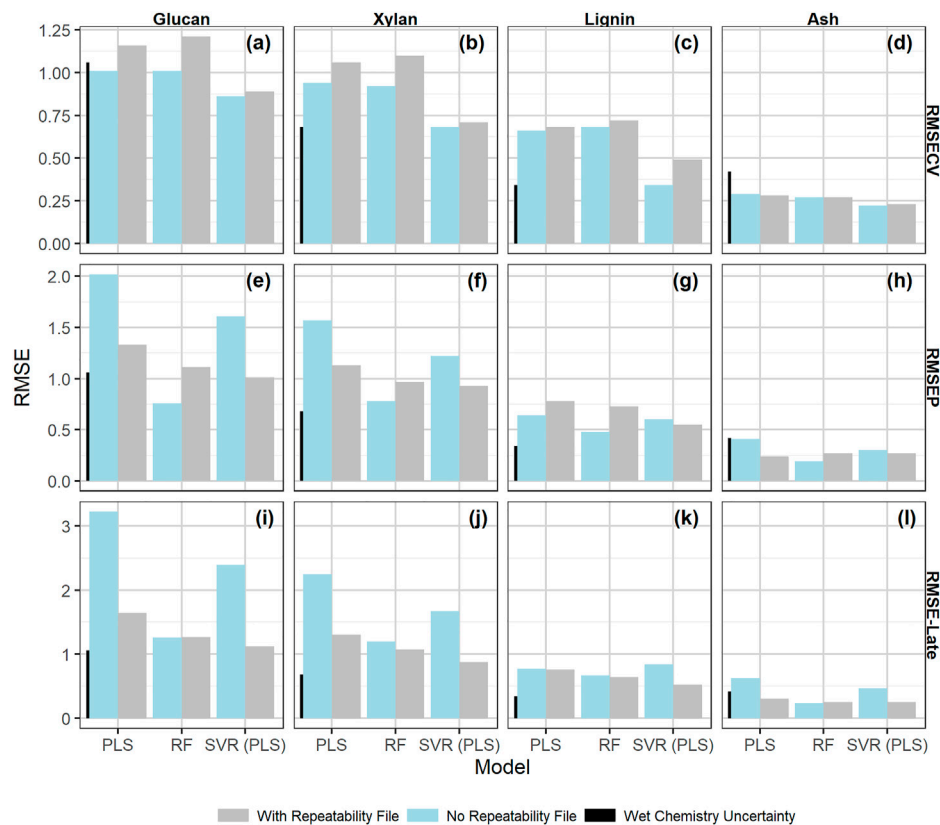
FIGURE 5 | Bar chart of the model performance measured by RMSE values by constituent with the calibration data set alone or augmented by the check cell difference spectra, the "repeatability file" strategy. The measures of performance shown are as follows: **(A–D)** : RMSECV (root mean square error of 10 × 10-fold cross validation); **(E–H)**: the RMSEP root mean square error of prediction; **(I–L)**: the RMSE-late (root mean square error of late scan predictions). The measurement uncertainty associated with the primary analytical method, (Templeton et al., 2010) which is two times the standard deviation from the primary analytical method, is shown for scale as the leftmost black bar on each graph. The "repeatability file" algorithm improves the performance of the SVM and PLS models as measured by RMSEP and RMSE-late but has little effect on the RF model (see text).

TABLE 2 | Summary of model performance results by constituent. Performance results for each model build for each constituent of interest.

Performance parameter		%Glucan			%Xylan			%Lignin			%Ash		
		PLS	SVM (PLS)	RF	PLS	SVM (PLS)	RF	PLS	SVM (PLS)	RF	PLS	SVM (PLS)	RF
Training	RMSEC	1.04	0.73	0.46	0.91	0.58	0.41	0.60	0.43	0.28	0.24	0.17	0.11
	R^2	0.98	0.99	1.00	0.98	0.99	1.00	0.97	0.98	0.99	0.83	0.92	0.97
Cross validation	RMSECV	1.16	0.89	1.21	1.06	0.71	1.10	0.68	0.49	0.72	0.28	0.23	0.27
	R^2	0.98	0.99	0.98	0.98	0.99	0.97	0.96	0.98	0.95	0.77	0.85	0.79
Independent validation	RMSEP	1.33	1.01	1.11	1.13	0.93	0.97	0.78	0.55	0.73	0.24	0.27	0.27
	R^2	0.98	0.99	0.99	0.98	0.99	0.99	0.96	0.98	0.97	0.83	0.80	0.81
Late training	RMSE-late	1.64	1.12	1.27	1.30	0.88	1.07	0.76	0.52	0.64	0.31	0.25	0.25
	R^2	0.97	0.99	0.98	0.97	0.99	0.98	0.96	0.98	0.97	0.77	0.83	0.88

RMSEC, root mean squared error of calibration; R^2, coefficient of determination, the square of correlation coefficient R; RMSECV, root mean square error of cross validation; RMSEP, root mean square error of prediction; RMSE-late, root mean square error of late scan predictions.

While all three algorithms provided acceptable models, the RF algorithm required more computational resources—approximately 10–20 times longer than either the PLS or SVM algorithms. Final versions of the RF models were trained using a local HPC cluster, while the final PLS and SVM models were trained on a standard laptop computer.

Figures 6, **7** show the predicted versus measured cross validation and independent validation results across the three
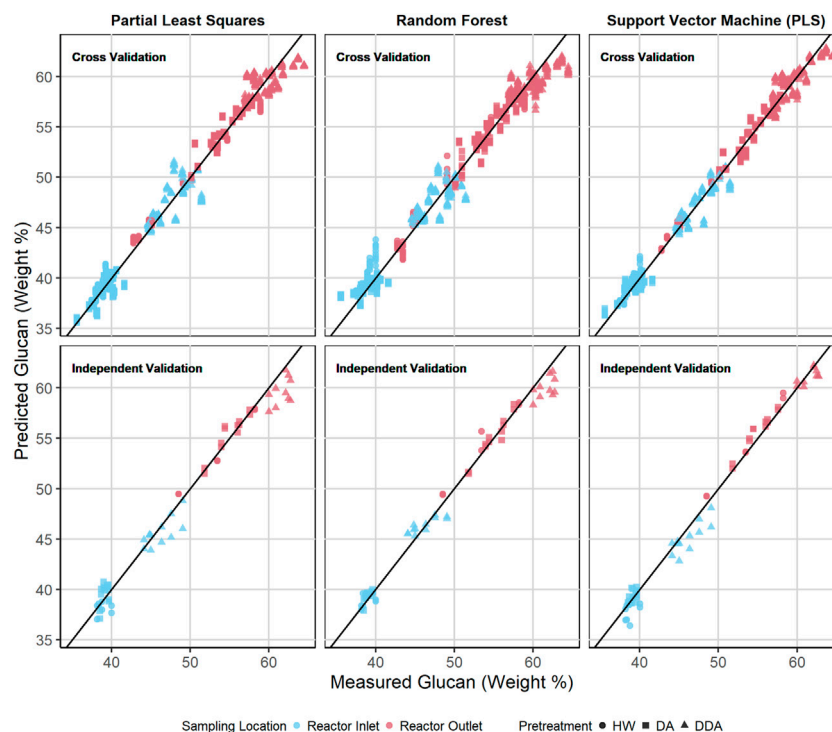
FIGURE 6 | Predicted vs. measured glucan content (%DW) for PLS, RF, and SVM models. The symbol shape represents the different pretreatment used, while the color represents the sampling location—before or after thermochemical pretreatment. The upper row depicts the repeated 10-fold cross validation results for each model. The lower row depicts the independent validation results for each model. DA, dilute acid; DDA, deacetylated/dilute acid; Water, hot water; DW, dry weight.

modeling techniques for measured glucan and lignin content (%DW). Similar plots for measured xylan and ash, as well as residual plots for all four constituents, are provided in the **Supplementary Material**. In agreement with the statistics presented in **Table 2** and discussed above, graphical displays of model performance show all three algorithms provide acceptable prediction results for all constituents, with the SVM modeling results appearing slightly superior to PLS and RF for both the cross-validation and independent validation predictions. In particular, we observe that the SVM modeling algorithm appears to provide better glucan predictions for the samples with the highest glucan content (as measured by prediction residuals).

Moreover, a single model can accurately predict the composition of corn stover samples undergoing three different pretreatment chemistries (HW, DA, DDA) and at multiple locations within the process (before and after the thermochemical pretreatment reactor). We believe this has substantial implications on the feasibility of real-time characterization using on-line NIR spectroscopy—a single model could be built and maintained for implementation at multiple points in the process.

Discussions about the relative performance of different modeling approaches or different modeling algorithms should take the uncertainty of the primary analytical data used as the dependent variables into account. Differences in RMSE values smaller than the primary analytical uncertainties are not practically significant. In **Figure 5** we include a small vertical

bar in all plots corresponding to the uncertainty of the primary analytical chemistry (Templeton et al., 2010) estimated as two times the standard deviation of multiple replicate measurements by analysts. Thus, the improvements in both glucan and xylan RMSE-late values for the PLS and SVM models by using the "repeatability file" strategy are both statistically and practically significant, while the improvements in the ash predictions for these models are statistically significant but not practically significant.

RMSE values like those presented for the PLS, SVM, and RF models developed in this work provide an estimate of the average uncertainty for samples in the model population (e.g., training, independent validation). However, they do not provide an estimate of uncertainty of a specific prediction. Like in primary analytical chemistry measurements, some estimation of the uncertainty of a specific prediction from a rapid characterization model is important to provide a quantitative estimate of the confidence the user should have in that specific prediction.

Linear modelling approaches like PLS have a robust literature discussing this issue (Faber, 2005; Olivieri et al., 2006; Zhang and Garcia-Munoz, 2009; Garrido-Varo et al., 2019; Emil Eskildsen and Næs, 2020). Some measures of uncertainty calculate a confidence interval for the prediction similarly to that of a linear model where the confidence interval increases with the distance in multivariate space from the spectra to be predicted to the center of the calibration population and decreases as the
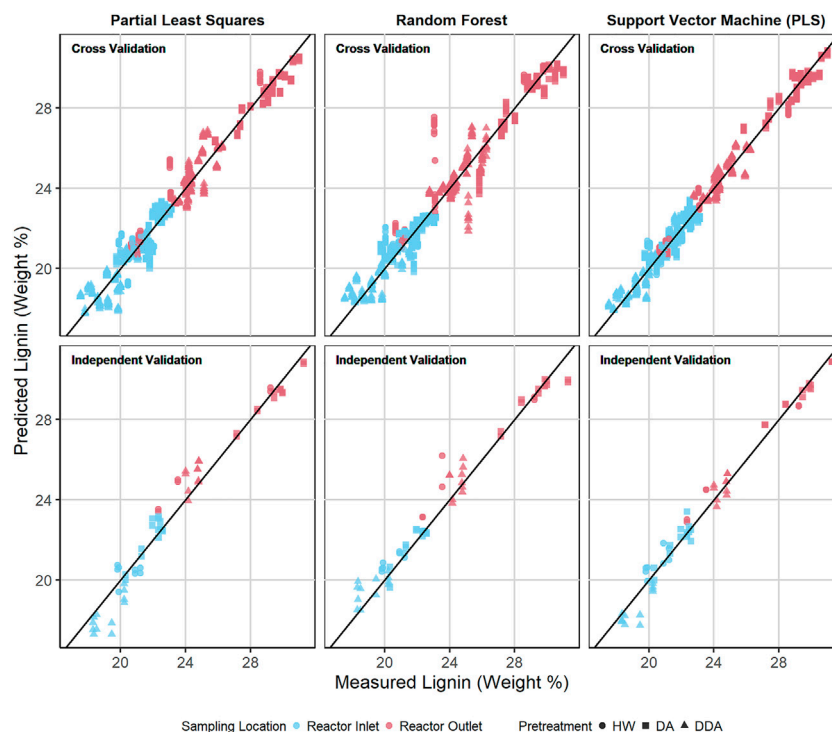
FIGURE 7 | Predicted vs. measured lignin content (%DW) for PLS, RF, and SVM models. The symbol shape represents the different pretreatment used, while the color represents the sampling location—before or after thermochemical pretreatment. The upper row depicts the repeated 10-fold cross validation results for each model. The lower row depicts the independent validation results for each model.

quality of the calibration model increases. Other uncertainty measures calculate a population membership region based on the Mahalanobis distance of a sample to the center of the calibration population. This is the basis of the well-known global-H, neighborhood-H (GH, NH) statistic (Westerhaus, 2014).

While a detailed comparison of these different uncertainty measures is beyond the scope of this work, we wish to point out that these measures are based on an evaluation of spectral similarity in a linear modeling framework (e.g., PLS, PCA, PCR). Thus, such uncertainty estimates may be appropriate for use with Support Vector Regression even with nonlinear kernels if a linear dimensionality reduction technique (like PCA or PLS) is used. However, Random Forest Regression is a nonlinear technique, and use of uncertainty estimations using such assumptions are inappropriate. There has been some research into uncertainty measures for RF (McAlexander and Mentch, 2020; Tavazza et al., 2021), but consensus on the best approach has not been reached, nor has the application of any specific approach to RF models based on spectroscopy been demonstrated. In the absence of such consensus, a concern with using an RF model is the inability to estimate a confidence interval for individual predictions.

3.4 Selecting a Model
In this work we have compared the performance of three different modelling approaches (PLS, SVM, and RF) for

developing a rapid characterization model for a population of pretreated corn stover samples using three different pretreatment chemistries. All three approaches resulted in acceptable models as measured by multiple RMSE assessments (training, cross-validation, independent validation, late-training) when compared to the uncertainty in the primary analytical chemistry methods. The use of repeated check cell spectra *via* the "repeatability file" strategy improved the performance of both the PLS and SVM algorithms. The RF algorithm performed equivalently with or without a "repeatability file". The use of dimensionality reduction *via* PLS improved the performance of the SVM algorithm. The RF algorithm performed best without any dimensionality reduction. While all three algorithms provided acceptable models, the RF algorithm required more computational resources—RF models took approximately 10–20 times longer to solve than the either PLS or SVM models. Multiple robust estimations of prediction uncertainty exist for the PLS algorithm, and these uncertainty algorithms can also be used for SVM algorithms when dimensionality reduction is used as an additional spectral preprocessing step. No such robust estimates of uncertainty exist for the RF algorithm.

Based on these results, we believe the SVM algorithm is the method of choice for this dataset when used with both the "repeatability file" strategy and dimensionality reduction using PLS. The SVM algorithm presents a good compromise between

computational efficiency and prediction performance and permits the use of multiple robust estimations of individual prediction uncertainties.

DATA AVAILABILITY STATEMENT

The raw data supporting the conclusion of this article will be made available by the authors, without undue reservation.

AUTHOR CONTRIBUTIONS

EW conceived of the study and supervised its execution. ZT contributed to the model selection, performed all spectral acquisition, data organization and reduction, all modelling, statistical analysis of modelling results, and prepared all figures and tables. ZT and EW jointly drafted and edited the manuscript.

FUNDING

ACKNOWLEDGMENTS

SUPPLEMENTARY MATERIAL

The Supplementary Material for this article can be found online at: https://www.frontiersin.org/articles/10.3389/fenrg.2022.878973/full#supplementary-material

REFERENCES

Abrams, S. M., Shenk, J. S., Westerhaus, M. O., Barton, F. E., and Barton, F. E., II (1987). Determination of Forage Quality by Near Infrared Reflectance Spectroscopy: Efficacy of Broad-Based Calibration Equations. *J. Dairy Sci.* 70, 806–813. Available at: http://jds.fass.org/cgi/content/abstract/70/4/806. doi:10.3168/jds.s0022-0302(87)80077-2

Acharya, U. K., Walsh, K. B., and Subedi, P. P. (2014). Robustness of Partial Least-Squares Models to Change in Sample Temperature: I. A Comparison of Methods for Sucrose in Aqueous Solution. *J. Near Infrared Spectrosc.* 22, 279–286. doi:10.1255/jnirs.1113

Awad, M., and Khanna, R. (2015). "Support Vector Regression," in *Efficient Learning Machines: Theories, Concepts, and Applications for Engineers and System Designers*. Editors M. Awad and R. Khanna (Berkeley, CA: Apress), 67–80. doi:10.1007/978-1-4302-5990-9_4

Beebe, K. R., Pell, R. J., and Seasholtz, M. B. (1998). *Chemometrics: A Practical Guide*. New York: Wiley and Sons.

Breiman, L. (2001). Random Forests. *Mach. Learn.* 45, 5–32. doi:10.1023/A:1010933404324

Chanda, S., Hazarika, A. K., Choudhury, N., Islam, S. A., Manna, R., Sabhapondit, S., et al. (2019). Support Vector Machine Regression on Selected Wavelength Regions for Quantitative Analysis of Caffeine in Tea Leaves by Near Infrared Spectroscopy. *J. Chemom.* 33, e3172. doi:10.1002/cem.3172

Cristianini, N., and Shawe-Taylor, J. (2000). *An Introduction to Support Vector Machines and Other Kernel-Based Learning Methods*. Cambridge: Cambridge University Press. doi:10.1017/CBO9780511801389

de Santana, F. B., de Souza, A. M., and Poppi, R. J. (2018). Visible and Near Infrared Spectroscopy Coupled to Random Forest to Quantify Some Soil Quality Parameters. *Spectrochimica Acta Part A Mol. Biomol. Spectrosc.* 191, 454–462. doi:10.1016/j.saa.2017.10.052

de Santana, F. B., Otani, S. K., de Souza, A. M., and Poppi, R. J. (2021). Comparison of PLS and SVM Models for Soil Organic Matter and Particle Size Using Vis-NIR Spectral Libraries. *Geoderma Reg.* 27, e00436. doi:10.1016/j.geodrs.2021.e00436

Emil Eskildsen, C., and Næs, T. (2020). Sample-Specific Prediction Error Measures in Spectroscopy. *Appl. Spectrosc.* 74, 791–798. doi:10.1177/0003702820913562

Faber, K. (2005). Multivariate Prediction Uncertainty. Available at: www.chemometrics.com (Accessed February 2, 2022).

Fawagreh, K., Gaber, M. M., and Elyan, E. (2014). Random Forests: From Early Developments to Recent Advancements. *Syst. Sci. Control Eng.* 2, 602–609. doi:10.1080/21642583.2014.956265

Garrido-Varo, A., Garcia-Olmo, J., and Fearn, T. (2019). A Note on Mahalanobis and Related Distance Measures in WinISI and the Unscrambler. *J. Near Infrared Spectrosc.* 27, 253–258. doi:10.1177/0967033519848296

Geladi, P., and Kowalski, B. R. (1986). Partial Least-Squares Regression: A Tutorial. *Anal. Chim. Acta* 185, 1–17. doi:10.1016/0003-2670(86)80028-9

Höskuldsson, A. (1988). PLS Regression Methods. *J. Chemom.* 2, 211–228. doi:10.1002/cem.1180020306

Kelley, S. S., Jellison, J., and Goodell, B. (2002). Use of NIR and Pyrolysis-MBMS Coupled with Multivariate Analysis for Detecting the Chemical Changes Associated with Brown-Rot Biodegradation of Spruce Wood. *FEMS Microbiol. Lett.* 209 (02), 107–111. doi:10.1111/j.1574-6968.2002.tb11117.x

Labbé, N., Lee, S.-H., Cho, H.-W., Jeong, M. K., and André, N. (2008). Enhanced Discrimination and Calibration of Biomass NIR Spectral Data Using Non-Linear Kernel Methods. *Bioresour. Technol.* 99, 8445–8452. doi:10.1016/j.biortech.2008.02.052

Lee, S., Choi, H., Cha, K., and Chung, H. (2013). Random Forest as a Potential Multivariate Method for Near-Infrared (NIR) Spectroscopic Analysis of Complex Mixture Samples: Gasoline and Naphtha. *Microchem. J.* 110, 739–748. doi:10.1016/j.microc.2013.08.007

McAlexander, R. J., and Mentch, L. (2020). Predictive Inference with Random Forests: A New Perspective on Classical Analyses. *Res. Polit.* 7, 205316802090548. doi:10.1177/2053168020905487

Near-Infrared Spectroscopy in Agriculture (2004). Near-Infrared Spectroscopy in Agriculture. 1st ed. Madison, WI: John Wiley & Sons. doi:10.2134/agronmonogr44

Olivieri, A. C., Faber, N. M., Ferré, J., Boqué, R., Kalivas, J. H., and Mark, H. (2006). Uncertainty Estimation and Figures of Merit for Multivariate Calibration (IUPAC Technical Report). *Pure Appl. Chem.* 78, 633–661. doi:10.1351/pac200678030633

Pasquini, C. (2018). Near Infrared Spectroscopy: A Mature Analytical Technique with New Perspectives - A Review. *Anal. Chim. Acta* 1026, 8–36. doi:10.1016/j.aca.2018.04.004

Roggo, Y., Duponchel, L., Ruckebusch, C., and Huvenne, J.-P. (2003). Statistical Tests for Comparison of Quantitative and Qualitative Models Developed with Near Infrared Spectral Data. *J. Mol. Struct.* 654, 253–262. doi:10.1016/S0022-2860(03)00248-5

Sanderson, M. A., Agblevor, F., Collins, M., and Johnson, D. K. (1996). Compositional Analysis of Biomass Feedstocks by Near Infrared Reflectance Spectroscopy. *Biomass Bioenergy* 11, 365–370. doi:10.1016/S0961-9534(96)00039-6

Shekiro, J., III, Kuhn, E. M., Nagle, N. J., Tucker, M. P., Elander, R. T., and Schell, D. J. (2014). Characterization of Pilot-Scale Dilute Acid Pretreatment Performance Using Deacetylated Corn Stover. *Biotechnol. Biofuels* 7, 23. doi:10.1186/1754-6834-7-23

Shenk, J. S., and Westerhaus, M. O. (1991). New Standardization and Calibration Procedures for Nirs Analytical Systems. *Crop Sci.* 31, 1694–1696. doi:10.2135/cropsci1991.0011183X003100060064x

Skvaril, J., Kyprianidis, K. G., and Dahlquist, E. (2017). Applications of Near-Infrared Spectroscopy (NIRS) in Biomass Energy Conversion Processes: A Review. *Appl. Spectrosc. Rev.* 52, 675–728. doi:10.1080/05704928.2017.1289471

Tavazza, F., DeCost, B., and Choudhary, K. (2021). Uncertainty Prediction for Machine Learning Models of Material Properties. *ACS Omega* 6, 32431–32440. doi:10.1021/acsomega.1c03752

Templeton, D. W., Scarlata, C. J., Sluiter, J. B., and Wolfrum, E. J. (2010). Compositional Analysis of Lignocellulosic Feedstocks. 2. Method Uncertainties. *J. Agric. Food Chem.* 58, 9054–9062. doi:10.1021/jf100807b

Tsuchikawa, S. (2007). A Review of Recent Near Infrared Research for Wood and Paper. *Appl. Spectrosc. Rev.* 42, 43–71. doi:10.1080/05704920601036707

Tsuchikawa, S., and Kobori, H. (2015). A Review of Recent Application of Near Infrared Spectroscopy to Wood Science and Technology. *J. Wood Sci.* 61, 213–220. doi:10.1007/s10086-015-1467-x

Westerhaus, M. (2014). Eastern Analytical Symposium Award for Outstanding Achievements in Near Infrared Spectroscopy: My Contributions to Near Infrared Spectroscopy. *NIR News* 25, 16–20. doi:10.1255/nirn.1492

Xiao, L., Wei, H., Himmel, M. E., Jameel, H., and Kelley, S. S. (2014). NIR and Py-Mbms Coupled with Multivariate Data Analysis as a High-Throughput Biomass Characterization Technique: A Review. *Front. Plant Sci.* 5, 388. doi:10.3389/fpls.2014.00388

Zhang, L., and Garcia-Munoz, S. (2009). A Comparison of Different Methods to Estimate Prediction Uncertainty Using Partial Least Squares (PLS): A Practitioner's Perspective. *Chemom. Intell. Lab. Syst.* 97, 152–158. doi:10.1016/j.chemolab.2009.03.007

Arthrospira Cell Residues for Lactic Acid Fermentation as Bioproducts From Waste Utilization

Wanida Pan-utai[1]*, Sitanan Thitiprasert[2] and Soisuda Pornpukdeewattana[3]

[1]Department of Applied Microbiology, Institute of Food Research and Product Development, Kasetsart University, Bangkok, Thailand, [2]Research Unit in Bioconversion and Bioseparation for Value-Added Chemical Production, Institute of Biotechnology and Genetic Engineering, Chulalongkorn University, Bangkok, Thailand, [3]Division of Fermentation Technology, School of Food Industry, King Mongkut's Institute of Technology Ladkrabang, Bangkok, Thailand

Arthrospira (*Spirulina*) *platensis* is a freshwater cyanobacterium that is commercially produced as a food source on a global scale and considered safe for human consumption. After C-phycocyanin (C-PC) extraction, the waste cell residue (WCR) is composed of nutrients with 30% protein content. Here, the potential of WCR as a nitrogen source for *Bacillus coagulans* cultivation and bioproducts was evaluated. Nitrogen substitute from WCR under different conditions of $20-100 \, g \, L^{-1}$ was performed. *B. coagulans* cultivation was achieved with maximal viable cells at 7.6–9.5 log CFU mL^{-1}. Increasing WCR gave decreasing lactate production. The highest lactate production at $27 \, g \, L^{-1}$ was achieved from WCR $20 \, g \, L^{-1}$, highlighting the potential use of *A. platensis* waste biomass residue as a nitrogen source for the growth of lactic acid bacteria and zero-waste biotechnology methodology. The utilization of renewable resources is a crucial step toward developing a sustainable industrial society.

Keywords: *Arthrospira*, waste cell residue, *Bacillus coagulans*, bioproduct, zero-waste

INTRODUCTION

Arthrospira (*Spirulina*) *platensis* cyanobacteria have attracted increased commercial interest due to their high protein content, essential amino acids, fatty acids, and pigments (De la Jara et al., 2018). The rich source of biochemical composition has become an interest in the food and health industry, and *Arthrospira* has shown value from the medical point of view (Furmaniak et al., 2017). Microalgal biomass is a valuable natural source of bioactive compounds that can be used in a variety of applications including the food sector (Ferreira et al., 2021), pharmaceuticals and nutraceuticals (Jha et al., 2017; Mehariya et al., 2021), therapeutic potentials (Khavari et al., 2021), cosmetics (Yarkent et al., 2020), biodiesel and biogas (González-González et al., 2018), and wastewater bioremediation (De Souza et al., 2022). *Arthrospira*, also known as *Spirulina*, is a well-known microalgal strain that has been globally cultured on a large commercial scale (Mostafa and El-Gendy, 2017). *A. platensis* biomass showed high potential as a source of various value-added product applications including bioethanol from carbohydrate and feed supplements because of its high protein and fatty acid contents (Raja et al., 2016). Previous studies demonstrated bioethanol production from *A. platensis*

Abbreviations: X_m, maximal cell growth (Log CFU mL^{-1}); C_P, maximal lactate concentration (g L^{-1}); Q_P, volumetric productivity of lactate production (g L^{-1} h^{-1}); $Y_{P/S}$, lactate yield coefficient (g g^{-1}); *Yield*, conversion of glucose into lactate with a theoretical yield of 1.0 g lactate g^{-1} glucose.

biomass and biomethane production from waste cell residue (WCR) (Rempel et al., 2019). Chng et al. (2016) studied the production of bioethanol using lipid-extracted biomass from *Scenedesmus dimorphus* microalgae. Bioproducts from microalgae or waste cell residues are directly produced by fermentation or hydrolysis of the fraction before fermentation. Recent studies have shown the effectiveness of *Arthrospira* in the prevention of diabetes as an antiviral, immune-stimulator, and anticancer agent, with digestive improvement as well as growth of *Lactobacilli* (Christaki et al., 2011; Nicoletti, 2016). Several products from microalgal and cyanobacterial biorefineries with minimal waste outputs have been approved for the powerful valorization of biomass (Prabha et al., 2022).

Lactic acid fermentation as a food preservative method significantly improves the safety, shelf life, and nutritional properties of foods (De Marco Castro et al., 2019; Thompson et al., 2020) and is utilized in around 70% of food industry products (Eş et al., 2018). Fermentative biorefineries have wide-ranging product potential including fermented vegetables, fermented milk, meat industries, bio-preservatives, probiotics chemicals, biofuels, and pharmaceuticals (Raj et al., 2022).

Moreover, lactic acid fermentation has the potential for green production, biodegradation, and biocompatible polylactic acid (PLA) substitution for petroleum-based plastic (Nduko and Taguchi, 2021). Lactic acid fermentation can produce three forms of lactic acid, namely, L-lactate, D-lactate, or both D- and L-lactates depending on the microorganism used (Prasirtsak et al., 2019). *Bacillus coagulans* is a lactic acid-producing, spore-forming, catalase-positive bacterium with an optimal growth temperature of 35–50°C. These bacteria can utilize glucose, sucrose, lactose, and mannitol to produce L-lactic acid (Cao et al., 2020). Moreover, *B. coagulans* has also been accorded the Generally Recognized as Safe (GRAS) status by the US Food and Drug Administration (FDA) (Endres et al., 2009; Hazards, 2013). *B. coagulans* has significant benefits to the host immune system (Cao et al., 2020). Currently, *B. coagulans* is used as a functional food in chocolate, ice cream, and pasta. The spore-forming nature of *B. coagulans* is comparable to other probiotic bacterial strains, with high stability in functional food products (Majeed et al., 2016). Previous studies reported that lactic acid bacteria (LAB) have the ability to degrade the cell walls of plants and cyanobacteria through hydrolysis, resulting in the conversion of complex organic compounds such as polysaccharides, lipids, and proteins within the cells into smaller molecules with enhanced properties (De Marco Castro et al., 2019).

Algae and cyanobacteria have high nutritional values as suitable substrates for fermented food production. Fermented products from seaweed, microalgae, and *Arthrospira* were obtained as plant-derived substrates using various fermentation processes of lactic acid bacteria, yeast, or mixed cultures of microorganisms. These products are highly desired in the market with bioproduct applications (Gupta and Abu-Ghannam, 2011; Uchida and Miyoshi, 2013; Niccolai et al., 2019). Most previous reports studied microalgae as feedstock for lactic acid production using lactobacilli as the lactic acid bacteria. The hydrolysate of microalgae *Chlorella vulgaris* ESP-31

was used as feedstock for lactate production from *Lactobacillus plantarum* 23 (Chen et al., 2020) and *L. brevis* (Ścieszka and Klewicka, 2020), while whole freeze-dried *Arthrospira* biomass was used as the substrate for lactate production by *L. plantarum* ATCC 8014 (Niccolai et al., 2019; Niccolai et al., 2020) and wet *Arthrospira* biomass was used as the substrate in fermentation by *L. plantarum* ATCC 8014 for nutraceutical properties (De Marco Castro et al., 2019). However, large-scale lactate production from microorganisms involves the high cost of fermentation media as one of the most critical bottlenecks in industrial lactate production (Cubas-Cano et al., 2018). Lactic acid bacteria (LAB) require complex nutrition that consists of high carbon sources, amino acids, vitamins, and nucleotides (Mokoena, 2017). Nitrogen, vitamins, and other nitrogenous growth-stimulating elements are abundant in yeast extract and peptone (Abbasiliasi et al., 2017). Organic nitrogen sources such as yeast extract, peptone, and other proteinous substrates must be added to LAB culture media, increasing the cost of medium formulation. As a result, it is important to discover low-cost alternatives for these expensive ingredients. *Bacillus* strains can grow and produce L-lactic acid under minimal nutritional requirements (Poudel et al., 2016).

Few studies have focused on producing lactate from waste cells of microalgal biomass in a biorefinery as a zero-waste process, while lactate production from *Bacillus coagulans* has never been reported. Waste microalgae and cyanobacteria can be used as an alternative nitrogen source for lactic acid production, representing bioproducts as a renewable resource with reduced production cost. Therefore, this study was conducted to investigate the potential of novelty waste *A. platensis* cell residues after C-phycocyanin extraction in a culture medium by *B. coagulans* ATCC 7050 for lactate production as a renewable resource.

MATERIALS AND METHODS

Materials
Analytical grade Zarrouk medium composed of sodium bicarbonate, sodium nitrate, dipotassium phosphate, potassium sulfate, sodium chloride, magnesium sulfate, calcium chloride, iron sulfate, ethylenediaminetetraacetic acid, and other reagents was purchased from Ajax Finechem Pty Ltd. (Auckland, New Zealand). GYP medium composed of glucose monohydrate, granulated yeast extract, peptone from meat, and other reagents was purchased from EMD Millipore Corporation (Burlington, United States). *Bacillus coagulans* ATCC 7050 was purchased from the American Type Culture Collection (ATCC, United States).

Microalgae Cultivation and Preparation
Microalgae Preparation
Arthrospira (Spirulina) *platensis* IFRPD 1182 was obtained from the Algae Laboratory at the Institute of Food Research and Product Development, Kasetsart University, Thailand. *A. platensis* was maintained and cultivated in a modified Zarrouk medium (Pan-utai et al., 2020) in photobioreactors and then

scaled up to a 200-L outdoor open raceway pond. The biomass of *A. platensis* was grown to log phase and then harvested by nylon membrane filtration. The harvested cells were cleaned with fresh water to remove any residual culture medium. *A. platensis* biomass preparation was dried in a hot air oven (Thermo Scientific, Germany) at 60°C for 6 h and then milled to 0.5 mm particle size.

Waste Cell Residue Preparation

C-phycocyanin (C-PC) was extracted from *A. platensis* biomass under optimal conditions (Pan-utai et al., 2018) of biomass solvent ratio 1:15 (w/v) with 10 mM phosphate buffer at pH 7.0 and incubated under a controlled extraction temperature of 25°C for 24 h. The C-phycocyanin (C-PC) supernatant was then separated by centrifugation at 10,000 $x\,g$ for 30 min (Model 6000, High-Speed Refrigerated Centrifuge, KUBOTA, Japan) at 25°C. After C-PC extraction, the cell pellet remained as the waste cell residue (WCR). This residue was dried in a hot air oven at 60°C for 6 h and then milled to 0.5 mm particle size for further analysis as a substrate for lactic acid fermentation.

Biochemical Composition

The prepared *A. platensis* biomass and waste cell residue (WCR) were analyzed to determine their biochemical compositions following NREL methods. Moisture content was determined by oven-drying at 105°C to constant weight (Sluiter et al., 2008a). Ash content was determined by ignition of the dried samples in an electric furnace at 550°C (Sluiter et al., 2008b). Protein content was determined by the Kjeldahl method (Hames et al., 2008), and lipid content was determined using a modified Bligh and Dyer method (Pan-utai et al., 2019). Briefly, the samples were suspended in distilled water, methanol, and chloroform at a ratio of 0.8:2.0:1.0 and mixed well. The mixture was ultrasonically homogenized for 15 min and then separated by centrifuging at 6,153 $x\,g$ for 15 min. The lipid phase was collected, and the cell debris was extracted until the cells had no color. The lipid extract was filtered to remove contaminated cell debris and dried to constant weight at 80°C. After extraction of C-PC, the supernatant was collected, and the absorbance was determined at 615 and 652 nm using a UV-vis spectrophotometer (SP-8001, UV/Vis Spectrophotometer, Metertech, Taiwan) (Pan-utai and Iamtham, 2019). C-phycocyanin content (C-PC) is calculated by **Eq. 1** as follows:

$$C - PC\ (mg\,mL^{-1}) = \frac{OD_{615} - 0.474OD_{652}}{5.34} \quad (1)$$

Pigment Determination

Chlorophyll was extracted from the samples with methanol and stored at 4°C for 24 h. The optical density of the supernatant was measured at 662 and 645 nm. The chlorophyll content is calculated from the combination of chlorophyll a and b using the following **Eqs. 2, 3** (Pan-utai et al., 2021):

$$Chlorophyll\ a\ (mg\,mL^{-1}) = 11.75OD_{662} - 2.35OD_{645} \quad (2)$$

$$Chlorophyll\ b\ (mg\,mL^{-1}) = 18.61OD_{645} - 3.96OD_{662} \quad (3)$$

Glucose Analysis

Glucose in waste cell residues was determined by analysis of the carbohydrate in the biomass following Yuan et al. (2016). WCR *A. platensis* biomass was hydrolyzed by 72% (w/w) sulfuric acid at 30°C for 1 h. The acid concentration of the samples was then adjusted to 4% (w/w), and the samples were sterilized at 121°C for 1 h. The glucose concentration in the supernatant hydrolysate was determined on a Hewlett-Packard HP 1100 Series HPLC system with a refractive index detector (Agilent Technologies, United States), using a cross-linked resin hydrogen ionic 300 × 7.8 mm Aminex HPX-87H (9 μm) column (Bio-Rad). The column oven was set at 50°C, and the mobile phase was 5 mM sulfuric acid. The flow rate was set at 0.5 ml min^{-1} using a refractive index detector at 40°C. Glucose contents in the samples are calculated according to **Eq. 4**:

$$Glu\cos e\ content\ (\%) = \frac{Glu\cos e\ produced\ (g)}{Dry\ weight\ of\ sample} \times 100. \quad (4)$$

FERMENTATION

Inoculum Preparation

Lactate production was performed by *B. coagulans* ATCC 7050 maintained in GYP medium and 10% skim milk and stored at −20°C. The GYP medium had the following composition (g L^{-1}): glucose 10 g, yeast extract 5 g, peptone 5 g, KH_2PO_4 0.25 g, K_2HPO_4 0.25 g, and salt solution 10 ml consisting of (L^{-1}) $MgSO_4.7H_2O$ 40 g, $MnSO_4.5H_2O$ 2 g, $FeSO_4.7H_2O$ 2 g, and NaCl 2 g. The pH value of the GYP medium was adjusted to 6.8 (Thitiprasert et al., 2017). Primary inoculum preparation of *B. coagulans* ATCC 7050 was cultured in GY medium consisting of (g L^{-1}): glucose 10 g, yeast extract 15 g, NH_4Cl 4 g, KH_2PO_4 0.5 g, K_2HPO_4 0.5 g, and salt solution 20 ml. The pH value of the GY medium was adjusted to 6.8 (Jaiaue et al., 2021). The inoculum culture was placed in an incubator shaker at 200 rpm, with temperature controlled at 37°C for 18 h. Then, 10% (v v^{-1}) of *B. coagulans* ATCC 7050 cells were transferred to secondary inoculum preparation, cultured at 37°C, 200 rpm for 6 h, and used as the starter for *B. coagulans* cultivation.

Lactate Production by *B. coagulans*

WCR was used as the supplemented feedstock for lactate production under different concentrations of 20, 40, 60, 80, and 100 g L^{-1} in the culture medium. The control experiment was conducted without WCR. The medium formulation was modified by the culture medium corresponding to lactate fermentation from 120 g L^{-1} of initial glucose concentration (Tolieng et al., 2018). WCR was used to replace yeast extract in the culture medium, consisting of (g L^{-1}): glucose 120 g, NH_4Cl 2 g, KH_2PO_4 0.25 g K_2HPO_4 0.25 g, and salt solution 10 ml. Then, the culture medium was sterilized at 121°C for 15 min. *B. coagulans* ATCC 7050 inoculum at 10% (v v^{-1}) was transferred into the culture medium for growth and lactate

production. The cultivation was performed at a working volume of 50 ml medium in a 250-ml Erlenmeyer flask. The culture was incubated at 37°C in a shaker at 200 rpm. Fermented samples were collected at the start of fermentation and every 12 h for viable cell growth, glucose, and lactic acid determination. The pH was measured using a pH meter (Lab 850, Schott, Germany).

Viable Cell Determination

B. coagulans ATCC 7050 was collected during the fermentation process for viable cell determination. Colony-forming units (CFU) were counted in 1 ml sample collected from the fermentation broth. The fermentation broth was diluted to an appropriate multiple with sterile water, and then 100 μL sample was spread on a nutrient agar (NA) plate and cultured at 37°C for 48 h.

Glucose and Lactate Determination

Fermentation samples were collected and centrifuged at 6,153 $\boldsymbol{x}\,\boldsymbol{g}$ for 20 min, with the supernatant stored at −20°C until analysis. Glucose, lactate, acetate, and ethanol were analyzed using high-performance liquid chromatography (HPLC). Cell-free fermentation broth samples were filtered through a nylon membrane, while the remaining glucose and lactate products were determined using a Hewlett-Packard HP 1100 Series HPLC system with a reflective index detector (Agilent Technologies, United States) and a 300 mm × 7.8 mm Aminex HPX-87H organic acid column (9 μm particle size and 8% cross-linkage) (Bio-Rad). The column was maintained at 50°C in a column oven. The sample was injected and eluted with 5 mM H_2SO_4 at a flow rate of 0.5 ml min^{-1}. Glucose anhydrous (CAS-No. 108337, Merck, Germany), L-lactic acid (CAS-No. 46937, Sigma-Aldrich, Singapore), acetic acid (Glacial, AR grade, Ajax Finechem Pty Ltd., Auckland, New Zealand), and absolute ethanol (99.5%, GR grade, DUKSAN, South Korea) were used as external standards to calculate the concentration from the peak area.

Kinetic Parameters

Viable cells of *B. coagulans* ATCC 7050 were assessed for growth and lactate production, and the kinetic parameters were calculated. The maximal value of viable cell growth was X_m. Lactate productivity (Q_P) was calculated as the ratio of variation in lactate concentration ($P_m - P_0$) to fermentation time, as shown in **Eq. 5**:

$$Q_P \left(g\,L^{-1}\,h^{-1}\right) = \frac{P_m - P_0}{dt}. \tag{5}$$

The lactate yield coefficient is calculated using **Eq. 6**:

$$Y_{P/S} \left(g\,g^{-1}\right) = \frac{\Delta P}{\Delta S} \tag{6}$$

where $Y_{P/S}$ is the lactate yield coefficient in g g^{-1} unit. Abbreviations of ΔP and ΔS represent differences in lactate and glucose production, respectively.

RESULTS

Biochemical Composition of the Microalgae

A. platensis IFRPD 1182 was used as the initial substrate, which was prepared as both microalgal biomass and waste cell residue (WCR) from C-PC extraction and also used as the substrate for fermentation as of renewable resource. Biochemical compositions of *Arthrospira platensis* IFRPD 1182 microalgal biomass and WCR are shown in **Supplementary Table S1**. The initial *A. platensis* biomass had the highest protein and C-PC contents. C-PC is a blue pigment composed of proteins. After C-PC extraction, the C-PC remaining contained 8.33% (mg g^{-1}) as around 12.6% of C-PC in the initial biomass. However, 30% (DW) protein content and more than 63% of the initial biomass, including other compositions, remained in the WCR. Therefore, the potential of the remaining WCR nutrition was studied as an alternative nitrogen source for lactate production.

Potential of *B. coagulans* ATCC 7050 Cultivation

The potential of WCR substitution for nitrogen sources in the fermentation of lactic acid bacteria was studied as a low-cost medium and renewable resource. Lactate fermentation by *B. coagulans* ATCC 7050 with different WCR concentrations at 20–100 g L^{-1} substituted for yeast extract as the alternative nitrogen source was studied in the culture broth. Parameters of cell growth, glucose consumed, and lactate produced are shown in **Figure 1**. Various WCR concentrations were studied to substitute nitrogen sources in the fermentation medium of *B. coagulans* ATCC 7050. The fermentation medium without WCR and yeast extract was used as the control (**Figure 1A**). *B. coagulans* ATCC 7050 cells grown at different WCR concentrations and constant glucose of 120 g L^{-1} reached exponential values within 12 h of fermentation, while glucose concentration slightly reduced at 48 h of fermentation. A maximal lactate concentration was obtained after 12 h of fermentation at 4.5 g L^{-1}. The results from the control experiments without a nitrogen source in the fermentation medium showed that *B. coagulans* was not appropriate for cell growth and lactate production. Fermentation in all experiments produced by-products, shown in **Figure 2**. At longer fermentation time, acetate and ethanol production increased with also large amounts of by-products.

Viable *B. coagulans* ATCC 7050 growth at different WCR concentrations during fermentation are shown in **Figures 1B–F**. The results indicated that higher WCR concentration led to higher viable cell growth, while glucose as the carbon source in the culture media was almost completely consumed by *B. coagulans* at the end of fermentation. Lactate production at different treatments increased with cell growth and fermentation time. **Supplementary Table S2** shows the pH values during fermentation at various treatments. *B. coagulans* ATCC 7050 growth and lactate production led to an increase in acidity from 6 to 4.6. Maximal *B. coagulans* ATCC 7050 viable growth at various WCR concentrations without a nitrogen source

FIGURE 1 | Time course of *B. coagulans* ATCC 7050 growth and lactate production under various conditions as **(A)** control, **(B)** WCR 20 g L^{-1}, **(C)** WCR 40 g L^{-1}, **(D)** WCR 60 g L^{-1}, **(E)** WCR 80 g L^{-1}, and **(F)** 100 g L^{-1}. All values are represented as means (±SD).
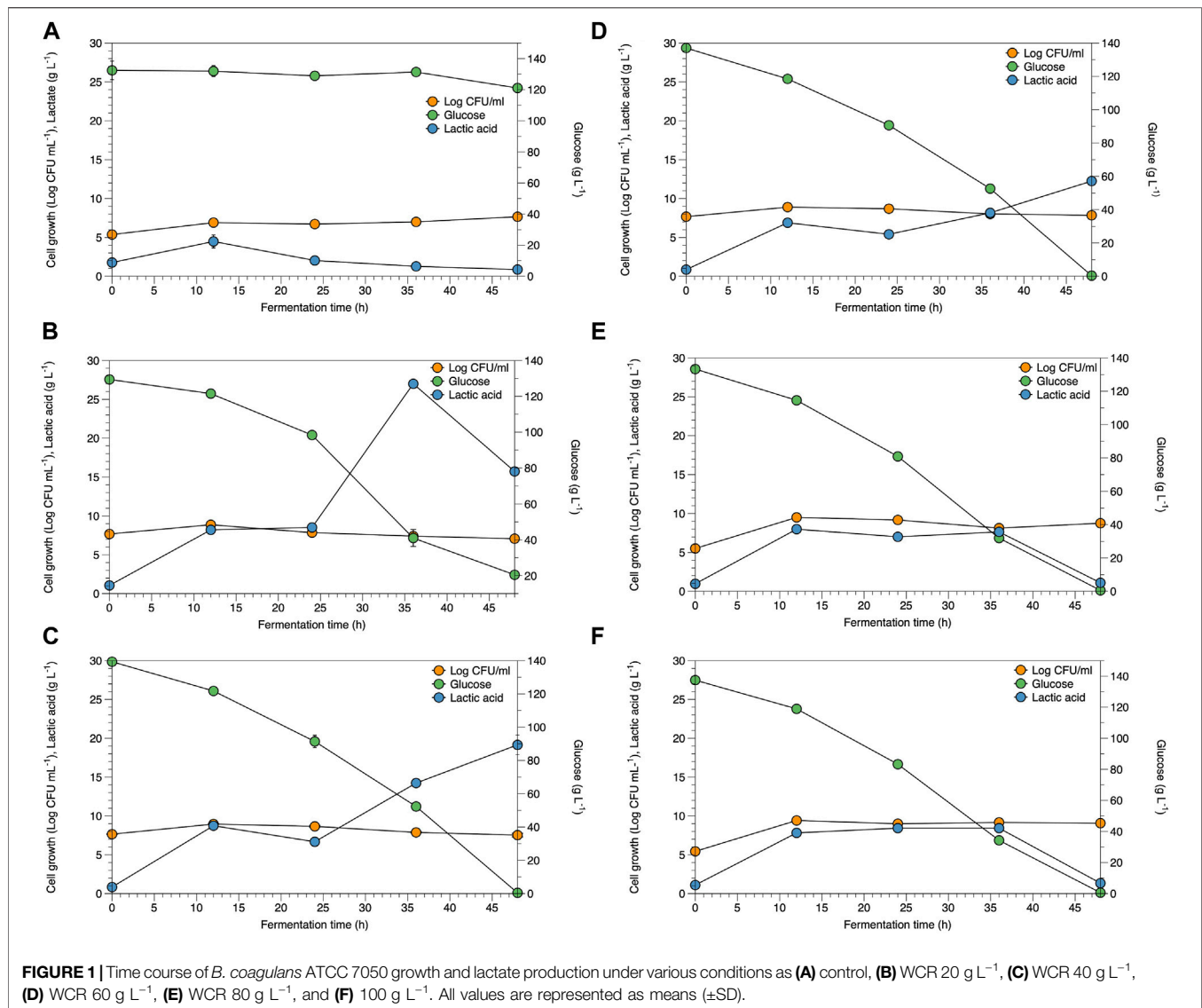
is shown in **Figure 2**. *B. coagulans* ATCC 7050 grew and increased during fermentation. Maximal cell growth at various WCR concentrations ranged from 7.6 to 9.5 log CFU mL^{-1} (**Figure 3**). Increasing WCR concentration in the fermentation media gave viable cell growth, whereas viable *B. coagulans* ATCC 7050 decreased in the treatment without WCR and other nitrogen sources (control experiment).

Parameters of *B. coagulans* ATCC 7050 fermentation at different WCR conditions for potential lactate production are shown in **Supplementary Table S3**. Maximal lactate concentration (C_P) under various WCR concentrations ranged from 8 to 27 g L^{-1}, with the highest recorded at 20 g L^{-1}. Higher WCR concentration in the fermentation broth decreased lactate production. Lactate productivity (Q_P) ranged from 0.23 to 0.75 g L^{-1} h^{-1} under different WCR concentrations in the fermentation process. Maximal lactate concentration and productivity were recorded at 20 g L^{-1} WCR and not significantly different from 80 g L^{-1}. The maximal lactate yield coefficient ($Y_{P/S}$) and

theoretical yield of lactate ($Yield$) were obtained from *B. coagulans* ATCC 7050 fermentation using 20 and 80 g L^{-1} WCR concentration, with a nonsignificant difference compared to the control. The optimal condition for *B. coagulans* ATCC 7050 fermentation, giving a maximal yield of lactate, was 80 g L^{-1} WCR.

DISCUSSION

Arthrospira is well known as a rich protein source with high nutritional value. The nutritional composition of WCR showed useful protein, carbohydrate, and lipid content, with C-phycocyanin and chlorophyll contents of 8.33 ± 0.54 and 13.43 ± 0.17 mg g^{-1} DW, respectively. Previous reports recorded that wet biomass of *Arthrospira* gave enhanced nutraceutical properties by fermentation with *Lactobacillus plantarum* (De Marco Castro et al., 2019). Microalgal biomass

FIGURE 2 | Time course of *B. coagulans* ATCC 7050 growth and acetate and ethanol production under various conditions as **(A)** control, **(B)** WCR 20 g L^{-1}, **(C)** WCR 40 g L^{-1}, **(D)** WCR 60 g L^{-1}, **(E)** WCR 80 g L^{-1}, and **(F)** 100 g L^{-1}. All values are represented as means (±SD).

FIGURE 3 | Maximal *B. coagulans* ATCC 7050 growth using waste *Arthrospira* cell residues at various concentrations. All values are represented as mean (±SD).

of *A. platensis* was used as feedstock for biogas production (Dębowski et al., 2020), while *A. platensis* solid-state fermentation with LAB was performed for aromatic profile evaluation (Martelli et al., 2021). Generally, simple sugars such as glucose and sucrose are used as carbon sources for lactate fermentation (Olszewska-Widdrat et al., 2020). Most previous reports focused on *Arthrospira* with complete nutritional enrichment of microalgae. Carbohydrates from microalgae can be converted to fermentable sugars by hydrolytic processes. However, the fermentation requires large amounts of carbohydrate at up to more than 70% DW of the microalgal biomass, limiting control in large-scale cultivation of carbohydrate-enriched *Arthrospira* (Liu et al., 2019). Our results showed glucose content from WCR biomass using acid hydrolysis followed by HPLC determination as 35.50 ± 0.13%

DW. Various WCR concentrations were used as feedstock addition fermentation at 20, 40, 60, 80, and 100 g L^{-1}, with hydrolyzed glucose contents of 7.10, 14.20, 21.30, 28.40, and 35.50 g L^{-1}, respectively. WCR was sterilized at 121°C for 15 min without pretreatment with acid hydrolysis and performed the same as culture broth giving glucose content at only 0.3% DW. Thus, the addition of WCR substitute in culture media at 0.06–0.30 g L^{-1} gave reduced glucose with increasing media formulation. Our results showed mainly protein content in the biochemical composition of nutrition values from WCR. Yeast extract is a nutrient source of vitamins and amino acids for microorganism growth, with high cost at approximately 38% of the total medium cost in lactate production (Meng et al., 2012; Ma et al., 2014). Therefore, WCR shows significant potential as a source of nitrogen feedstock to produce bioproducts. In our study, fermentation of WCR as the nitrogen source was evaluated for *B. coagulans* growth and lactate production.

B. coagulans cultivation from WCR addition in culture media at different loadings showed variable cell growth and lactate production. Increasing WCR gave higher maximal viable cell growth because the biomolecules of WCR containing amino acids, vitamins, and proteins supported cell growth. The control experiments without WCR and nitrogen source addition found that *B. coagulans* could use glucose as the carbon source. However, cell growth limitation was stimulated by other nutrients necessary for complete cell growth. Oh et al. (2003) confirmed that yeast extract was the most effective nitrogen source for cell growth and lactate production. Amino acids are important molecules that serve as the fundamental components or building blocks of proteins (Moini, 2019). They play a significant role in facilitating microbial cell growth (Idrees et al., 2020). Moreover, amino acids including glycine, serine, and tyrosine in yeast extract play a central role in promoting cell growth (Li et al., 2011). The protein content of *Arthrospira* is high and contains all the essential amino acids with good digestibility (Bernaerts et al., 2019; Niccolai et al., 2019). Khandual et al. (2021) found large amounts of each amino acid in the total biomass after C-phycocyanin extraction. Therefore, WCR addition in *B. coagulans* culture media stimulated microbial cell growth.

Viable cell growth increased when WCR feedstock loading increased, while lactate production increased with fermentation time. WCR loading in the culture medium stimulated cell growth and lactate production, as confirmed by the control experiments. The results showed glucose consumption to produce lactate. Moreover, during *B. coagulans* ATCC 7050 fermentation supplemented with WCR, various LAB fermentation metabolites such as lactate, acetate, ethanol, aroma compounds, and enzymes were produced (Raj et al., 2022). *B. coagulans* produces homofermentative lactic acid under anaerobic conditions (Okada et al., 1979). However, this homofermentation reaction also produces by-products including acetate kinase and alcohol dehydrogenase in the acetate and ethanol conversion process. Our results showed that both lactate and by-products were produced under unsuitable fermentation conditions. Su and Xu (2014) also determined ethanol and acetate as the primary fermentation

products under aerobic conditions. The acetate kinase-encoding gene present in the *B. coagulans* genome prefers an energy-generating pathway, with acetic acid synthesis to metabolize accumulated NADH following the loss of the lactate dehydrogenase function (Sun et al., 2016). These reasons support our results. Moreover, lactate production by glucose fermentation of *B. coagulans* was inhibited by glucose concentrations higher than 100 g L^{-1} (Michelson et al., 2006), leading to decreased growth rate and underfermentation (Glaser and Venus, 2018). Lactic acid-producing bacteria are metabolized by the phosphogluconase pathway that produces various co-products such as acetate, CO$_2$, and ethanol, with low lactate yield as the end product of fermentation (Bintsis, 2018; Abedi and Hashemi, 2020). Pyruvate molecules can be reduced to lactate, with acetate to ethanol and CO$_2$ (Mendes Ferreira and Mendes-Faia, 2020). These were used as a carbon source for lactate and bioproducts in this study. Therefore, the relationship between the quantities of acetate and ethanol that decreased the theoretical yield to 0.50 g g^{-1} depends on the capacity of bacteria to reoxidize NADH created in the initial procedure, as well as its energy demands (Yu et al., 2020).

Kinetic parameters of *B. coagulans* ATCC 7050 cultivation using WCR substituted by yeast extract were calculated in terms of fermentation time for maximal lactate production at 12 h. WCR addition achieved higher lactate production, with increased nutrients in the culture media associated with cell growth. Maximal lactate yield was achieved at WCR addition of 20 g L^{-1}, indicating sufficient nitrogen and other nutrients for direct utilization of cell growth. When WCR loading increased, the pigments of C-PC and chlorophyll also increased, promoting the nutraceutical properties of *Arthrospira* fermentation (De Marco Castro et al., 2019). However, higher pigments and total phenolic compounds may inhibit bacteria cultivation (Takó et al., 2020) as well as have a positive effect on microorganisms (Adebo and Gabriela Medina-Meza, 2020). *Arthrospira* biomass can also serve as a nutrient source during the fermentation process (Luiza Astolfi et al., 2020). Moreover, *B. coagulans* is catalase-positive and produces energy from glucose via glycolysis, the citric acid cycle (TCA), and the electron transport chain, resulting in high growth rates. Lactate was produced with high productivity at higher cell growth (Thitiprasert et al., 2017). Therefore, WCR was utilized as a renewable resource to replace expensive yeast extract for lactate production by *B. coagulans*.

Supplementary Table S4 compares previous fermentation studies of bioproducts produced from various substances. Lactate production from lyophilized biomass cyanobacterium *Arthrospira platensis* F&M-C256 by *Lactobacillus plantarum* ATCC 8014 reached 3.7 g L^{-1} lactate concentration (Niccolai et al., 2019). *A. platensis* F&M-C256 was also successfully evaluated in a vegetal soybean drink and in water by probiotic *L. plantarum* ATCC 8014 at 1.7 g L^{-1} (Niccolai et al., 2020). Our results showed the highest lactate production due to different bacterial strains and substrate consumed. Using WCR as the nitrogen source reduced the cost of the culture medium with direct utilization without pretreatment. Werlang et al. (2020) studied *A. platensis* as a raw material for D-lactic acid production via saccharification and fermentation enzymatic processes using the lactogenic *Escherichia coli* strain JU15, giving D-lactate at

$25.5 \, g \, L^{-1}$, as an alternative option for renewable resources as the carbon source for bacterial cultivation. *B. coagulans* can produce L-lactate by fermentation generally in a synthetic medium. L-Lactate production by *B. coagulans* has been studied using different fermentation medium compositions and processes (Fan et al., 2016; Tolieng et al., 2018). Here, alternative nitrogen sources to replace yeast extract in the fermentation medium realized higher L-lactate concentrations. Other substrates as the fermentation medium and processes for lactate production were applied to cassava starch hydrolysates and sludge hydrolysates (Ma et al., 2014; Ooi and Wu, 2015). The complete GY culture medium obtained high lactate production (Tolieng et al., 2018). Our results gave lower lactate but still reduced medium cost and used WCR as a renewable resource for nutraceutical ingredients for health. Using *Arthrospira* biomass as the substrate for lactate production by the probiotic bacterium significantly increased essential amino acid contents and the bioactive profile through probiotic growth and pre- and probiotic bio-active substance production (De Marco Castro et al., 2019; Yu et al., 2020). Therefore, waste *Arthrospira* cell residue from C-PC extraction can act as an alternative substrate for probiotic *B. coagulans* cultivation and produce lactate as renewable bioproducts.

CONCLUSION

Waste cell residue of *Arthrospira* IFRPD 1182 biomass from C-PC extraction showed feasibility as an alternative substrate for *B. coagulans* ATCC 7050 cultivation. WCR acted as a nitrogen source that replaced yeast extract in culture media, resulting in reduced production cost. *B. coagulans* ATCC 7050 cultivation gave maximal lactate yield at $20 \, g \, L^{-1}$ WCR. However, the fermentation process should be further studied to give high lactate production in a shorter time, with *Arthrospira* saccharification and fermentation also investigated to enhance production efficiency. Our results demonstrated the feasibility of utilizing waste resources from the cyanobacterium *Arthrospira* to produce valuable products. WCR was proven as a significant

alternative resource for *Bacillus coagulans* growth, bioproduct production, and also reducing waste in food systems.

DATA AVAILABILITY STATEMENT

The original contributions presented in the study are included in the article/**Supplementary Material**; further inquiries can be directed to the corresponding author.

AUTHOR CONTRIBUTIONS

WP-u: conceptualization, formal analysis, writing—review and editing, and visualization. ST: conceptualization and validation. SP: validation.

FUNDING

ACKNOWLEDGMENTS

SUPPLEMENTARY MATERIAL

The Supplementary Material for this article can be found online at: https://www.frontiersin.org/articles/10.3389/fenrg.2022.878597/full#supplementary-material

REFERENCES

Abbasiliasi, S., Tan, J. S., Tengku Ibrahim, T. A., Bashokouh, F., Ramakrishnan, N. R., Mustafa, S., et al. (2017). Fermentation Factors Influencing the Production of Bacteriocins by Lactic Acid Bacteria: a Review. *RSC Adv.* 7, 29395–29420. doi:10.1039/c6ra24579j

Abedi, E., and Hashemi, S. M. B. (2020). Lactic Acid Production - Producing Microorganisms and Substrates Sources-State of Art. *Heliyon* 6, e04974. doi:10.1016/j.heliyon.2020.e04974

Adebo, O. A., and Gabriela Medina-Meza, I. (2020). Impact of Fermentation on the Phenolic Compounds and Antioxidant Activity of Whole Cereal Grains: A Mini Review. *Molecules* 25, 927. doi:10.3390/molecules25040927

Bernaerts, T. M. M., Gheysen, L., Foubert, I., Hendrickx, M. E., and Van Loey, A. M. (2019). The Potential of Microalgae and Their Biopolymers as Structuring Ingredients in Food: A Review. *Biotechnol. Adv.* 37, 107419. doi:10.1016/j.biotechadv.2019.107419

Bintsis, T. (2018). Lactic Acid Bacteria as Starter Cultures: An Update in Their Metabolism and Genetics. *AIMS Microbiol.* 4, 665–684. doi:10.3934/microbiol.2018.4.665

Cao, J., Yu, Z., Liu, W., Zhao, J., Zhang, H., Zhai, Q., et al. (2020). Probiotic Characteristics of Bacillus Coagulans and Associated Implications for Human Health and Diseases. *J. Funct. Foods* 64, 103643. doi:10.1016/j.jff.2019.103643

Chen, P.-T., Hong, Z.-S., Cheng, C.-L., Ng, I.-S., Lo, Y.-C., Nagarajan, D., et al. (2020). Exploring Fermentation Strategies for Enhanced Lactic Acid Production with Polyvinyl Alcohol-Immobilized Lactobacillus Plantarum 23 Using Microalgae as Feedstock. *Bioresour. Technol.* 308, 123266. doi:10.1016/j.biortech.2020.123266

Chng, L. M., Chan, D. J. C., and Lee, K. T. (2016). Sustainable Production of Bioethanol Using Lipid-Extracted Biomass from Scenedesmus Dimorphus. *J. Clean. Prod.* 130, 68–73. doi:10.1016/j.jclepro.2016.02.016

Christaki, E., Florou-Paneri, P., and Bonos, E. (2011). Microalgae: a Novel Ingredient in Nutrition. *Int. J. Food Sci. Nutr.* 62, 794–799. doi:10.3109/09637486.2011.582460

Cubas-Cano, E., González-Fernández, C., Ballesteros, M., and Tomás-Pejó, E. (2018). Biotechnological Advances in Lactic Acid Production by Lactic Acid Bacteria: Lignocellulose as Novel Substrate. *Biofuels, Bioprod. Bioref ining* 12, 290–303. doi:10.1002/bbb.1852

De La Jara, A., Ruano-Rodriguez, C., Polifrone, M., Assunção, P., Brito-Casillas, Y., Wägner, A. M., et al. (2018). Impact of Dietary Arthrospira (Spirulina) Biomass

Consumption on Human Health: Main Health Targets and Systematic Review. *J. Appl. Phycol.* 30, 2403–2423. doi:10.1007/s10811-018-1468-4

De Marco Castro, E., Shannon, E., and Abu-Ghannam, N. (2019). Effect of Fermentation on Enhancing the Nutaceutical Properties of *Arthrospira Platensis* (Spirulina). *Fermentation* 5, 28. doi:10.3390/fermentation5010028

De Souza, D. S., Valadão, R. C., De Souza, E. R. P., Barbosa, M. I. M. J., and de Mendonça, H. V. (2022). Enhanced Arthrospira Platensis Biomass Production Combined with Anaerobic Cattle Wastewater Bioremediation. *Bioenerg. Res.* 15, 412–425. doi:10.1007/s12155-021-10258-4

Dębowski, M., Kisielewska, M., Kazimierowicz, J., Rudnicka, A., Dudek, M., Romanowska-Duda, Z., et al. (2020). The Effects of Microalgae Biomass Co-substrate on Biogas Production from the Common Agricultural Biogas Plants Feedstock. *Energies* 13, 2186. doi:10.3390/en13092186

Endres, J. R., Clewell, A., Jade, K. A., Farber, T., Hauswirth, J., and Schauss, A. G. (2009). Safety Assessment of a Proprietary Preparation of a Novel Probiotic, Bacillus Coagulans, as a Food Ingredient. *Food Chem. Toxicol.* 47, 1231–1238. doi:10.1016/j.fct.2009.02.018

Eş, I., Mousavi Khaneghah, A., Barba, F. J., Saraiva, J. A., Sant'ana, A. S., and Hashemi, S. M. B. (2018). Recent Advancements in Lactic Acid Production - a Review. *Food Res. Int.* 107, 763–770. doi:10.1016/j.foodres.2018.01.001

Fan, M., Ebrahimi, M., Quitmann, H., Aden, M., and Czermak, P. (2016). An Innovative Optical Sensor for the Online Monitoring and Control of Biomass Concentration in a Membrane Bioreactor System for Lactic Acid Production. *Sensors* 16, 411. doi:10.3390/s16030411

Ferreira, A., Guerra, I., Costa, M., Silva, J., and Gouveia, L. (2021). "Future Perspectives of Microalgae in the Food Industry," in *Cultured Microalgae for the Food Industry.* Editors T. Lafarga and G. Acién (Academic Press), 387–433. doi:10.1016/b978-0-12-821080-2.00008-3

Furmaniak, M. A., Misztak, A. E., Franczuk, M. D., Wilmotte, A., Waleron, M., and Waleron, K. F. (2017). Edible Cyanobacterial Genus Arthrospira: Actual State of the Art in Cultivation Methods, Genetics, and Application in Medicine. *Front. Microbiol.* 8, 2541. doi:10.3389/fmicb.2017.02541

Glaser, R., and Venus, J. (2018). Co-fermentation of the Main Sugar Types from a Beechwood Organosolv Hydrolysate by Several Strains of *Bacillus Coagulans* Results in Effective Lactic Acid Production. *Biotechnol. Rep.* 18, e00245. doi:10.1016/j.btre.2018.e00245

González-González, L. M., Correa, D. F., Ryan, S., Jensen, P. D., Pratt, S., and Schenk, P. M. (2018). Integrated Biodiesel and Biogas Production from Microalgae: Towards a Sustainable Closed Loop through Nutrient Recycling. *Renew. Sustain. Energy Rev.* 82, 1137–1148. doi:10.1016/j.rser.2017.09.091

Gupta, S., and Abu-Ghannam, N. (2011). Bioactive Potential and Possible Health Effects of Edible Brown Seaweeds. *Trends Food Sci. Technol.* 22, 315–326. doi:10.1016/j.tifs.2011.03.011

Hames, B., Scarlata, C., and Sluiter, A. (2008). Determination of Protein Content in Biomass. Technical Report NREL/TP-510-42625. Golden, CO, USA: National Renewable Energy Laboratory.

Hazards, E. P. O. B. (2013). Scientific Opinion on the Maintenance of the List of QPS Biological Agents Intentionally Added to Food and Feed (2013 Update). *EFSA J.* 11, 3449. doi:10.2903/j.efsa.2013.3449

Idrees, M., Mohammad, A. R., Karodia, N., and Rahman, A. (2020). Multimodal Role of Amino Acids in Microbial Control and Drug Development. *Antibiotics* 9, 330. doi:10.3390/antibiotics9060330

Jaiaue, P., Srimongkol, P., Thitiprasert, S., Tanasupawat, S., Cheirsilp, B., Assabumrungrat, S., et al. (2021). A Modified Approach for High-Quality RNA Extraction of Spore-Forming *Bacillus Subtilis* at Varied Physiological Stages. *Mol. Biol. Rep.* 48, 6757–6768. doi:10.1007/s11033-021-06673-7

Jha, D., Jain, V., Sharma, B., Kant, A., and Garlapati, V. K. (2017). Microalgae-based Pharmaceuticals and Nutraceuticals: An Emerging Field with Immense Market Potential. *ChemBioEng Rev.* 4, 257–272. doi:10.1002/cben.201600023

Khandual, S., Sanchez, E. O. L., Andrews, H. E., and de la Rosa, J. D. P. (2021). Phycocyanin Content and Nutritional Profile of Arthrospira Platensis from Mexico: Efficient Extraction Process and Stability Evaluation of Phycocyanin. *BMC Chemistry.* 15, 24.

Khavari, F., Saidijam, M., Taheri, M., and Nouri, F. (2021). Microalgae: Therapeutic Potentials and Applications. *Mol. Biol. Rep.* 48, 4757–4765. doi:10.1007/s11033-021-06422-w

Li, M., Liao, X., Zhang, D., Du, G., and Chen, J. (2011). Yeast Extract Promotes Cell Growth and Induces Production of Polyvinyl Alcohol-Degrading Enzymes. *Enzyme Res.* 2011, 179819. doi:10.4061/2011/179819

Liu, Q., Yao, C., Sun, Y., Chen, W., Tan, H., Cao, X., et al. (2019). Production and Structural Characterization of a New Type of Polysaccharide from Nitrogen-Limited Arthrospira Platensis Cultivated in Outdoor Industrial-Scale Open Raceway Ponds. *Biotechnol. Biofuels* 12, 131. doi:10.1186/s13068-019-1470-3

Luiza Astolfi, A., Rempel, A., Cavanhi, V. A. F., Alves, M., Deamici, K. M., Colla, L. M., et al. (2020). Simultaneous Saccharification and Fermentation of *Spirulina* Sp. And Corn Starch for the Production of Bioethanol and Obtaining Biopeptides with High Antioxidant Activity. *Bioresour. Technol.* 301, 122698. doi:10.1016/j.biortech.2019.122698

Ma, K., Maeda, T., You, H., and Shirai, Y. (2014). Open Fermentative Production of L-Lactic Acid with High Optical Purity by Thermophilic *Bacillus Coagulans* Using Excess Sludge as Nutrient. *Bioresour. Technol.* 151, 28–35. doi:10.1016/j.biortech.2013.10.022

Majeed, M., Majeed, S., Nagabhushanam, K., Natarajan, S., Sivakumar, A., and Ali, F. (2016). Evaluation of the Stability of *Bacillus Coagulans* MTCC 5856 during Processing and Storage of Functional Foods. *Int. J. Food Sci. Technol.* 51, 894–901. doi:10.1111/ijfs.13044

Martelli, F., Cirlini, M., Lazzi, C., Neviani, E., and Bernini, V. (2021). Solid-State Fermentation of Arthrospira Platensis to Implement New Food Products: Evaluation of Stabilization Treatments and Bacterial Growth on the Volatile Fraction. *Foods* 10, 67. doi:10.3390/foods10010067

Mehariya, S., Goswami, R. K., Karthikeysan, O. P., and Verma, P. (2021). Microalgae for High-Value Products: A Way towards Green Nutraceutical and Pharmaceutical Compounds. *Chemosphere* 280, 130553. doi:10.1016/j.chemosphere.2021.130553

Mendes Ferreira, A., and Mendes-Faia, A. (2020). The Role of Yeasts and Lactic Acid Bacteria on the Metabolism of Organic Acids during Winemaking. *Foods* 9, 1231. doi:10.3390/foods9091231

Meng, Y., Xue, Y., Yu, B., Gao, C., and Ma, Y. (2012). Efficient Production of L-Lactic Acid with High Optical Purity by Alkaliphilic Bacillus Sp. WL-S20. *Bioresour. Technol.* 116, 334–339. doi:10.1016/j.biortech.2012.03.103

Michelson, T., Kask, K., Jõgi, E., Talpsep, E., Suitso, I., and Nurk, A. (2006). l(+)-Lactic Acid Producer Bacillus Coagulans SIM-7 DSM 14043 and its Comparison with Lactobacillus Delbrueckii Ssp. Lactis DSM 20073. *lactis DSMEnzyme Microb. Technol.* 39, 861–867. doi:10.1016/j.enzmictec.2006.01.015

Moini, J. (2019). *Epidemiology of Diabetes.* Palm Bay, FL, United States: Elsevier.

Mokoena, M. P. (2017). Lactic Acid Bacteria and Their Bacteriocins: Classification, Biosynthesis and Applications against Uropathogens: A Mini-Review. *Molecules* 22, 1255. doi:10.3390/molecules22081255

Mostafa, S. S. M., and El-Gendy, N. S. (2017). Evaluation of Fuel Properties for Microalgae *Spirulina Platensis* Bio-Diesel and its Blends with Egyptian Petro-Diesel. *Arabian J. Chem.* 10, S2040–S2050. doi:10.1016/j.arabjc.2013.07.034

Nduko, J. M., and Taguchi, S. (2020). Microbial Production of Biodegradable Lactate-Based Polymers and Oligomeric Building Blocks from Renewable and Waste Resources. *Front. Bioeng. Biotechnol.* 8, 618077. doi:10.3389/fbioe.2020.618077

Niccolai, A., Bažec, K., Rodolfi, L., Biondi, N., Zlatić, E., Jamnik, P., et al. (2020). Lactic Acid Fermentation of *Arthrospira Platensis* (Spirulina) in a Vegetal Soybean Drink for Developing New Functional Lactose-free Beverages. *Front. Microbiol.* 11, 560684. doi:10.3389/fmicb.2020.560684

Niccolai, A., Shannon, E., Abu-Ghannam, N., Biondi, N., Rodolfi, L., and Tredici, M. R. (2019). Lactic Acid Fermentation of *Arthrospira Platensis* (Spirulina) Biomass for Probiotic-Based Products. *J. Appl. Phycol.* 31, 1077–1083. doi:10.1007/s10811-018-1602-3

Nicoletti, M. (2016). Microalgae Nutraceuticals. *Foods* 5, 54. doi:10.3390/foods5030054

Oh, H., Wee, Y. H., Yun, J. S., and Ryu, H. W. (2003). Lactic Acid Production Through Cell-Recycle Repeated-Batch Bioreactor. *Appl Biochem Biotechnol.* 105–108, 603–613.

Okada, S., Suzuki, Y., and Kozaki, M. (1979). A New Heterofermentative Lactobacillus Species with Meso-Diaminopimelic Acid in Peptidoglycan, Lactobacillus Vaccinostercus Kozaki and Okada Sp. Nov. *J. Gen. Appl. Microbiol.* 25, 215–221. doi:10.2323/jgam.25.215

Olszewska-Widdrat, A., Alexandri, M., López-Gómez, J. P., Schneider, R., and Venus, J. (2020). Batch and Continuous Lactic Acid Fermentation Based on A Multi-Substrate Approach. *Microorganisms* 8, 1084. doi:10.3390/microorganisms8071084

Ooi, K. Y., and Wu, J. C. (2015). Use of Dry Yeast Cells as a Cheap Nitrogen Source for Lactic Acid Production by Thermophilic *Bacillus Coagulans* WCP10-4. *Front. Chem. Sci. Eng.* 9, 381–385. doi:10.1007/s11705-015-1534-2

Pan-Utai, W., Boonpok, S., and Pornpukdeewattana, S. (2021). Combination of Mechanical and Chemical Extraction of Astaxanthin from *Haematococcus pluvialis* and its Properties of Microencapsulation. *Biocatal. Agric. Biotechnol.* 33, 101979. doi:10.1016/j.bcab.2021.101979

Pan-Utai, W., and Iamtham, S. (2019). Extraction, Purification and Antioxidant Activity of Phycobiliprotein from *Arthrospira Platensis*. *Process Biochem.* 82, 189–198. doi:10.1016/j.procbio.2019.04.014

Pan-Utai, W., Kahapana, W., and Iamtham, S. (2018). Extraction of C-Phycocyanin from Arthrospira (Spirulina) and its Thermal Stability with Citric Acid. *J. Appl. Phycol.* 30, 231–242. doi:10.1007/s10811-017-1155-x

Pan-Utai, W., Poopat, N., Parakulsuksatid, P., and Pan-Utai, W. (2020). Photoautotrophic Cultivation of Arthrospira Maxima for Protein Accumulation under Minimum Nutrient Availability. *Appl. Food Biotechnol.* 7, 225–233. doi:10.22037/afb.v7i4.30353

Pan-Utai, W., Srinophakun, P., and Inrung, W. (2019). Nutrients Formulation to Maximize Ankistrodesmus Sp. Microalgal Cell Biomass and Lipid Productivities. *J. Biol. Res. (Italy)* 92, 95–100. doi:10.4081/jbr.2019.8547

Poudel, P., Tashiro, Y., and Sakai, K. (2016). New Application of Bacillus Strains for Optically Pure L-Lactic Acid Production: General Overview and Future Prospects. *Biosci. Biotechnol. Biochem.* 80, 642–654. doi:10.1080/09168451.2015.1095069

Prabha, S., Vijay, A. K., Paul, R. R., and George, B. (2022). Cyanobacterial Biorefinery: Towards Economic Feasibility through the Maximum Valorization of Biomass. *Sci. Total Environ.* 814, 152795. doi:10.1016/j.scitotenv.2021.152795

Prasirtsak, B., Thitiprasert, S., Tolieng, V., Assabumrungrat, S., Tanasupawat, S., and Thongchul, N. (2019). D-lactic Acid Fermentation Performance and the Enzyme Activity of a Novel Bacterium Terrilactibacillus Laevilacticus SK5-6. *Ann. Microbiol.* 69, 1537–1546. doi:10.1007/s13213-019-01538-8

Raj, T., Chandrasekhar, K., Kumar, A. N., and Kim, S.-H. (2022). Recent Biotechnological Trends in Lactic Acid Bacterial Fermentation for Food Processing Industries. *Syst Microbiol Biomanuf* 2, 14–40. doi:10.1007/s43393-021-00044-w

Raja, R., Hemaiswarya, S., Ganesan, V., and Carvalho, I. S. (2016). Recent Developments in Therapeutic Applications of Cyanobacteria. *Crit. Rev. Microbiol.* 42, 394–405. doi:10.3109/1040841X.2014.957640

Rempel, A., De Souza Sossella, F., Margarites, A. C., Astolfi, A. L., Steinmetz, R. L. R., Kunz, A., et al. (2019). Bioethanol from *Spirulina Platensis* Biomass and the Use of Residuals to Produce Biomethane: An Energy Efficient Approach. *Bioresour. Technol.* 288, 121588. doi:10.1016/j.biortech.2019.121588

Ścieszka, S., and Klewicka, E. (2020). Influence of the Microalga *Chlorella Vulgaris* on the Growth and Metabolic Activity of *Lactobacillus* Spp. Bacteria. *Foods (Basel, Switz.* 9, 959. doi:10.3390/foods9070959

Sluiter, A., Hames, B., Hyman, D., Payne, C., Ruiz, R., Scarlata, C., et al. (2008a). Determination of Total Solids in Biomass and Total Dissolved Solids in Liquid Process Samples. Technical Report NREL/TP-510-42621. Golden, CO, USA: Laboratory Analytical Procedure (LAP)National Renewable Energy Laboratory.

Sluiter, A., Hames, B., Ruiz, R., Scarlata, C., Sluiter, J., and Templeton, D. (2008b). Determination of Ash in Biomass. Laboratory Analytical Procedure (LAP). Technical Report NREL/TP-510-42622. Golden, CO, USA: National Renewable Energy Laboratory.

Su, F., and Xu, P. (2014). Genomic Analysis of Thermophilic *Bacillus Coagulans* Strains: Efficient Producers for Platform Bio-Chemicals. *Sci. Rep.* 4, 3926. doi:10.1038/srep03926

Sun, L., Zhang, C., Lyu, P., Wang, Y., Wang, L., and Yu, B. (2016). Contributory Roles of Two L-Lactate Dehydrogenases for L-Lactic Acid Production in Thermotolerant *Bacillus Coagulans*. *Sci. Rep.* 6, 37916. doi:10.1038/srep37916

Takó, M., Kerekes, E. B., Zambrano, C., Kotogán, A., Papp, T., Krisch, J., et al. (2020). Plant Phenolics and Phenolic-Enriched Extracts as Antimicrobial Agents against Food-Contaminating Microorganisms. *Antioxidants* 9, 165. doi:10.3390/antiox9020165

Thitiprasert, S., Kodama, K., Tanasupawat, S., Prasitchoke, P., Rampai, T., Prasirtsak, B., et al. (2017). A Homofermentative *Bacillus* Sp. BC-001 and its Performance as a Potential L-Lactate Industrial Strain. *Bioprocess Biosyst. Eng.* 40, 1787–1799. doi:10.1007/s00449-017-1833-8

Thompson, H. O., Önning, G., Holmgren, K., Strandler, H. S., and Hultberg, M. (2020). Fermentation of Cauliflower and White Beans with Lactobacillus Plantarum - Impact on Levels of Riboflavin, Folate, Vitamin B12, and Amino Acid Composition. *Plant Foods Hum. Nutr.* 75, 236–242. doi:10.1007/s11130-020-00806-2

Tolieng, V., Nuhwa, R., Thongchul, N., and Tanasupawat, S. (2018). Characterization of Lactic Acid-Producing *Bacillus Coagulans* Strains with Their Antibacterial Activity and L-Lactic Acid Production. *Thai J. Pharm. Sci.* 42, 138–145.

Uchida, M., and Miyoshi, T. (2013). Algal Fermentation†mdash;The Seed for a New Fermentation Industry of Foods and Related Products. *Jarq* 47, 53–63. doi:10.6090/jarq.47.53

Werlang, E. B., Ibarra, E. S., Neves, F. d. F., Julich, J., Martinez, A., and Schneider, R. d. C. d. S. (2020). D-Lactate Production from Spirulina (*Arthrospira Platensis*) Biomass Using Lactogenic *Escherichia coli*. *Bioresour. Technol. Rep.* 12, 100598. doi:10.1016/j.biteb.2020.100598

Yarkent, Ç., Gürlek, C., and Oncel, S. S. (2020). Potential of Microalgal Compounds in Trending Natural Cosmetics: A Review. *Sustain. Chem. Pharm.* 17, 100304. doi:10.1016/j.scp.2020.100304

Yu, J., Ma, D., Qu, S., Liu, Y., Xia, H., Bian, F., et al. (2020). Effects of Different Probiotic Combinations on the Components and Bioactivity of Spirulina. *J. Basic Microbiol.* 60, 543–557. doi:10.1002/jobm.201900699

Yuan, T., Li, X., Xiao, S., Guo, Y., Zhou, W., Xu, J., et al. (2016). Microalgae Pretreatment with Liquid Hot Water to Enhance Enzymatic Hydrolysis Efficiency. *Bioresour. Technol.* 220, 530–536. doi:10.1016/j.biortech.2016.08.117

Effect of Moisture and Feedstock Variability on the Rheological Behavior of Corn Stover Particles

Ziwei Cheng[1]*, David W. Gao[1,2], Fiona M. Powers[1,3], Ricardo Navar[1], Juan H. Leal[1], Oyelayo O. Ajayi[4] and Troy A. Semelsberger[1]*

[1]Material Physics Applications Division, Los Alamos National Laboratory, Los Alamos, NM, United States, [2]Department of Chemical and Biomolecular Engineering, University of California, Los Angeles, United States, [3]Department of Mechanical Engineering, Montana State University, Bozeman, MT, United States, [4]Applied Materials Division, Argonne National Laboratory, Argonne, IL, United States

Continuous feeding, processing, and handling of biomass powders is pivotal to the economic viability of integrated biorefineries. However, current challenges associated with the operational reliability of bulk solids handling and transport greatly impact the process economics and ultimately the widespread commercialization of integrated biorefineries. In this work, we examine the effect of moisture and feedstock variability on the flow behavior of corn stover biomass particles. The total flow energy, compressibility, shear properties, and wall friction angles were measured for corn stover samples A and B containing 0%, 15%, 25%, 50%, and 75% (mass fraction) moisture contents using a FT4 powder rheometer. In general, the flowability of both A and B was reduced when moisture was present as indicated by the stability and variable flow rate, compressibility, and shear tests. The 15% moisture sample had the highest flow energy, revealing the interplay between the increased surface tension and looser packing both of which were caused by liquid bridging. The 75% moisture sample had the highest compressibility and the lowest flowability factor (ff_c). The trend in wall friction angle was found to be dependent upon the surface hydrophobicity of the wall material. The wall friction angle on the hydrophilic, stainless-steel surface increased with moisture and therefore poses additional handling challenges. On the other hand, the wall friction angle on the hydrophobic polymer surfaces were the lowest for samples with intermediate moisture contents. Sample B had greater bulk density, smaller compressibility, and greater flowability than the sample A, as suggested by the compressibility and shear tests. The wall friction angle of sample B was higher than or equal to that of sample A depending on both the type and the surface roughness of the wall material.

Keywords: corn stover, moisture, wettability, feedstock variability, powder rheology, FT4, surface energy, cohesion

1 INTRODUCTION

As global fossil fuel resources continue to diminish and awareness on greenhouse gas emissions and national energy security grow, the industrial and research communities have been seeking alternative renewable sources to produce fuels and chemicals. Non-edible biomass such as forestry and agricultural wastes has become an attractive option because it is renewable, abundant, and does not compete with the global food supply. Biorefineries are processing facilities that convert biomass

into value-added products such as biofuels, biochemicals, bioenergy, and other biomaterials (Ng et al., 2017). An integrated biorefinery (IBR) employs various combinations of feedstock and conversion technologies to produce a variety of products. Despite decades of research and development, IBRs have still not been commercialized due to challenges in their economic viability. Achieving the economic viability of IBRs calls for the continuous, reliable operation of biomass processing and handling equipment. However, existing bulk solids handling equipment was often designed for the continuous flow of coal, and it is common for biomass-sourced bulk solids to clog, jam, and form arches and ratholes in them. These flow stoppages result in down times and increased operational costs associated with shutting down, unclogging, cleaning, and restarting the equipment, hampering the process economics. It is therefore crucial to understand the flow behavior of biomass so that processing and handling equipment can be redesigned to ensure continuous flow.

The flow behavior of biomass is based upon many intrinsic and extrinsic factors, such as particle size, shape, chemical composition, degree of self-heating, ash content, and moisture. Among these properties, moisture in general negatively impacts the flow of biomass bulk solids and therefore has been extensively researched. Prior literature works on the flow behavior of biomass-sourced bulk solids have demonstrated that the indicators for flowability can be either sensitive or insensitive to moisture depending on the type of biomass and the moisture content being studied. Mattsson et al. (Mattsson and Kofman, 2003) determined the bridging tendency of willow shoot particles with different particle sizes and moisture contents using an in-house built bridging apparatus. Two moisture levels from each particle size group were studied, ranging from 15.7 wt% to 58.1 wt%. The critical diameter to avoid bridging was always higher for the high moisture sample. In a follow-up work from the same group, Jensen et al. (2004) determined the bridging tendency of whole trees, logging residues, and roundwood fuels processed by different chippers with various moisture contents. When the type of wood, processing equipment, and particle size distribution were kept constant, while sample moisture was adjusted through drying, a decrease in the tendency to bridge was observed in most samples. For a few samples, drying did not affect the tendency to bridge. Thompson and Ross (1983) reported that the coefficient of friction (μ) of wheat grain on a steel surface increased with increasing moisture content from 8 to 20%, but at 24% moisture content, it decreased.[5] Afzalinia and Roberge (2007) studied the wall friction coefficient of alfalfa and barley straw on a stainless steel surface. Both materials had increased wall friction angles with moisture. For alfalfa, μ showed a quadratic relationship within the range of 12.0–42.2 wt% moisture content. For barley straw, however, μ showed a linear relationship within the range of 12.2–45.7 wt% moisture content. Ileleji and Zhou (2008) measured the angle of repose of high moisture (63.2 wt% water) and low moisture (7.2 wt% water) bulk corn stover particles; they found the high moisture sample has much higher angle of repose than the low moisture sample. Littlefield et al. (2011) studied the effect of moisture on the compression, angle of repose, and shear properties of pecan shells. Five samples, ranging from 4.2 to 24.6 wt% moisture were used. It was discovered that the bulk density, particle density and tap density linearly decreased with increase in moisture. Both the compressibility and angle of repose increased with the increase in moisture. As for the shear properties, the cohesion significantly increased with the increase in moisture, and the flowability factor dropped from free-flowing regime ($ff_c > 10$) to the cohesive regime ($2 < ff_c < 4$) with the increase in moisture. The angle of internal friction, however, was not affected by the change in moisture. Gil et al. (2013) investigated the effect of moisture on the shear properties and wall friction angles of poplar and corn stover powders using a Jenike shear cell tester. Again, only a low moisture (7–9 wt% water) and a high moisture (28–33 wt% water) sample were used. The cohesion, unconfined yield stress, major principal stress, and static and effective angles of internal friction were all higher in the high moisture poplar and corn stover samples than the low moisture samples. The wall friction angle on the stainless steel surface was higher for the high moisture poplar and corn stover sample, while the wall friction angle on the high molecular polyethylene (HMPE) surface was lower for the high moisture poplar and corn stover samples. Crawford et al. (2016) studied the effect of moisture on the compression, shear, and wall friction properties of corn stover using a Freeman FT4 powder rheometer. Only one stainless steel surface was used for the wall friction test. Only a 50 wt% (water) and a dry sample were used for comparison. The corn stover sample had greater compressibility, static and effective angles of internal friction, cohesion, unconfined yield stress, major principal stress and wall friction angle than the dry corn stover sample. These conclusions were in good agreement with the work of Gil et al. (2013), Stasiak et al. (2019) used a Jenike shear tester and a Schulze ring shear tester to measure the shear properties of pine sawdust, shavings and pellets as a function of moisture. Six wet samples (10, 20, 30, 40, 50 and 60 wt% water) were used. They have also constructed a vane shear tester (VST) to measure the torque exerted by the sample. It was observed that the torque measured by the VST increases monotonically with moisture for all three types of pine samples on both testers. However, the moisture did not significantly affect the cohesion, apparent shear stress or the flowability factor.

Although the aforementioned studies have investigated the effect of moisture on the flow properties of corn stover and other biomass feedstocks, most studies focused on shear properties and dynamics data were lacking. In addition, only a few moisture levels within a narrow moisture range of no more than 50 wt% was covered in these studies, and flowability data on biomass powders with high moisture contents are very limited. Little studies were focused on the difference in flow properties of agricultural biomass materials harvested from different bales. Surface property measurements, such as surface energy and surface area, have been not used alongside rheological measurements to correlate flow to surface properties. To bridge these gaps, the effect of moisture and feedstock variability on the rheological properties of corn stover powders was investigated. The objective of this study is to measure the dynamics, bulk, shear, and surface properties of dry and wet corn stover samples harvested from different bales and evaluate how these properties are affected by moisture in these different bales. A wide range of moisture contents will be covered, ranging from 0 wt% to 75 wt%, to obtain a complete moisture profile.

SCHEME 1 | The wetting and drying protocol for corn stover *A*.
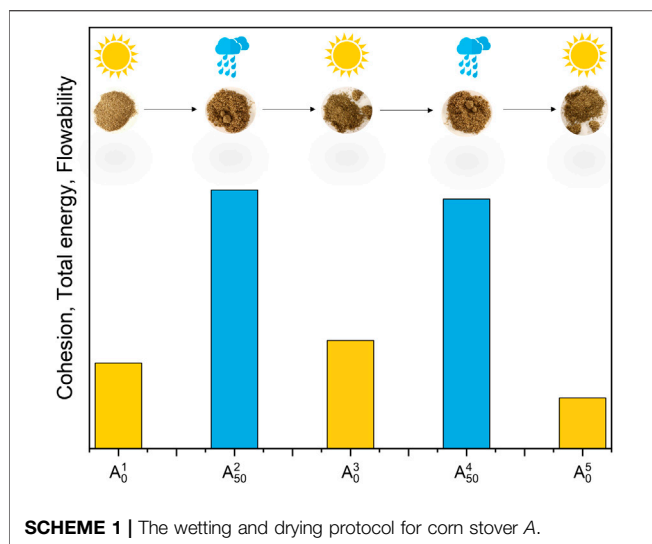
2 MATERIALS AND METHODS

2.1 Corn Stover Samples

Corn stover refers to non-edible portions of the plant—including the stem, leaves, stalk and cob. Corn stover is the largest single agricultural resource with an estimated production of 154–232 million dry metric tons per annum (Leal et al., 2019). The abundance of corn stover therefore makes it a desirable biomass feedstock. The corn stover samples referred to as *A* and *B* used in this work were from two different bales that were both harvested from Poweshiek County in Iowa, United States. Both were baled using a Heston 2270XD square baler in October 2018. The ash contents of *A* and *B* were very similar - 7% and 6%, respectively. The grinding and milling were carried out at Idaho National Laboratory (INL, Idaho Falls, Idaho, USA). The bales were processed through a Vermeer BG480 bale processer with a 75 mm screen then a Bliss Hammermill with a 25 mm screen at the Biomass Feedstock National User Facility (BFNUF) located at INL. Select samples were collected after the second mill, then milled to pass a 2 mm screen (Ray et al., 2020). Particle size distributions were provided by Idaho National Laboratory and are presented in the **Supplementary Tables S1, S2**.

2.2 Sample Preparation

The subsequent drying and wetting for the as-received *A* and *B* was carried out at Los Alamos National Laboratory (Los Alamos, New Mexico, United States). Samples were placed through various drying and wetting steps, indicated by A_x^y, where x is the wt% moisture used in the sample, and y is the step in the procedure. Y is comprised of f total steps, as can be seen in **Scheme 1** (*vide infra*), which are:

(1) Drying of the as-received sample
(2) Wetting at x wt% moisture
(3) Drying of the wet sample
(4) Re-wetting of the sample using x wt% moisture
(5) Re-drying of the sample

The as-received *A* and *B* samples were placed in an oven kept at 45°C for 24 h to remove any existing moisture. The dried *A* and

B were referred to as A_0^1 and B_0^1, respectively. To prepare the wet samples, A_0^1 and B_0^1 samples were placed in a plastic bag; the moisture was then introduced by manually adding deionized (DI) water to the respective samples. The bag containing the corn stover-water mixture was then manually shaken to ensure homogeneous mixing. The wet sample was left in the sealed bag for at least 12 h before testing to allow moisture equilibration. The moisture content (MC, **Eq. 1**) of the sample is defined as the mass percentage of water over the total weight of the sample, as follows:

$$MC = \frac{m_{water}}{m_{water} + m_{DCS}} \times 100\% \tag{1}$$

where m_{water} is the mass of water added, and m_{DCS} is the mass of the dry corn stover.

Four mixtures containing 15%, 25%, 50% and 75% moisture content were prepared for each corn stover sample (**Figure 1**). Samples were labelled as A_X and B_X, where $_X$ is the moisture wt% Photos of dry and wet *A* samples are shown in **Supplementary Figure S1**. These wet *A* and *B* samples, together with A_0 and B_0, were analyzed using a powder rheometer with details provided in **Section 2.3**. Additionally, all dried samples were analyzed with Inverse Gas Chromatography (IGC) to study the changes in the surface of the biomass.

For the wetting-redrying study, a separate batch of as-received corn stover *A* was first dried to remove any existing moisture (*i.e.*, A_0^1), and then mixed with equal mass of DI water to reach 50% moisture (named the "wet" sample), to create A_{50}^2, as outlined in **Scheme 1**. Subsequently, A_{50}^2 was transferred from the bag into a beaker to be placed in the oven kept at 45°C for 24 h (**Scheme 1**, A_0^3). Lastly, an additional wetting (A_{50}^4) and redrying (A_0^5) step was performed on the same sample and was subsequently analyzed.

2.3 Powder Rheometer

The rheological properties of the dry and wet samples *A* and *B* were analyzed using a Freeman FT4 powder rheometer (Freeman Technology Ltd., UK). The instrument can run shear, bulk, and dynamics properties testing. Because powders can be subject to shear, stirring and compression forces during processing and handling, all three types of testing need to be conducted to understand the flow behavior of powders when they are subject to different types of forces. Shear properties testing measures the flow properties of a powdered sample when its top surface is subject to shear. These include shear and wall friction tests. Bulk property testing measures the properties of the powder as a bulk, such as bulk density and % compressibility under different consolidation pressures. Dynamics properties testing measures the flow properties of the powder under constant stirring, such as the flow energy. In this work, we conduct all three types of tests to access the flow behavior of corn stover in different powder handling processes. The details in the test methods are provided in **Section 2.3.1** through **Section 2.3.4**.

Four types of fixtures—a 48 mm diameter blade, a 48 mm diameter vented piston, a 48 mm diameter shear cell, and a
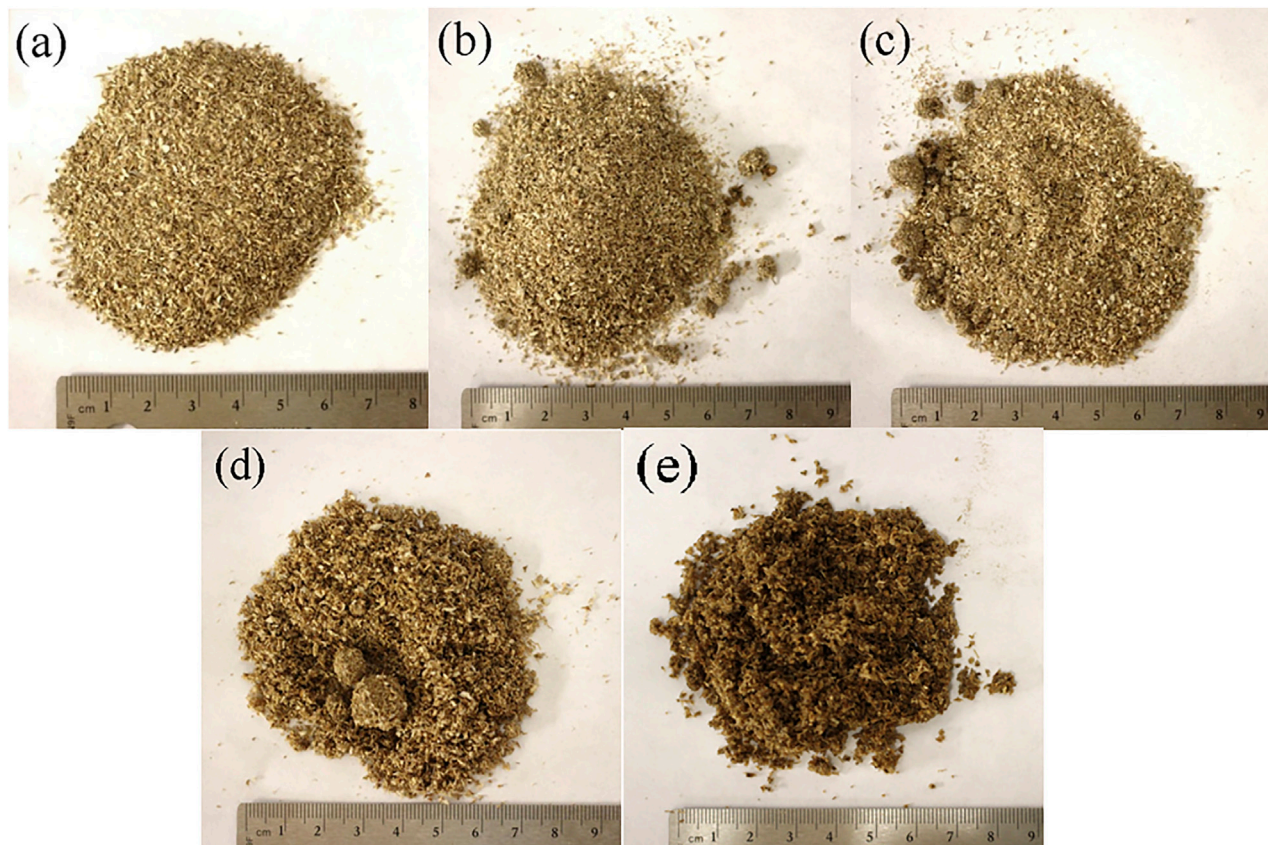
FIGURE 1 | Images of the **(A)** dry, **(B)** 15% moisture, **(C)** 25% moisture, **(D)** 50% moisture, and **(E)** 75% moisture A samples. The ruler is included in each image for scale.

48 mm diameter wall friction disk assembly were used. Different fixtures were attached to the instrument depending on the type of test performed. For the stability and variable flow rate test, a sample holder 160 ml in volume and 50 mm in inner diameter was used. For the other tests, a sample holder 85 ml in volume and 50 mm in inner diameter was used. Each testing program starts with one or more conditioning cycles where the blade rotates into the bottom of the powder bed and rotates back up to the initial position. This blade action eliminates any prior stress history of the sample. Next, the top portion of sample was manually split off using the splitting mechanism on the sample holder shown in **Figure 2**, so that the amount and height of the sample was always consistent before the start of testing steps. Each test was run repeatedly for at least five times to ensure reproducibility. The error bars were calculated as the standard deviation of these five runs.

2.3.1 Shear Test

Shear testing yields rich information about the strength of the bulk solid and the interaction among the particles themselves. During shear testing, the sample was first conditioned once using the 48 mm diameter blade to remove any previous stress history. Next, a vented piston 48 mm in diameter was used to compress the sample to 9 kPa of normal stress. Then the top portion of the sample was split off, the vented piston was removed and a shear cell 48 mm in diameter was attached. The shear cell has 18 blades. The shear cell was first lowered into the powder bed to be in contact with the sample to reach 9 kPa normal stress. This is also referred to as "pre-shear" stress. Then the shear cell started rotating at an angular velocity of 18°/min. The sample was sheared at 9 kPa until the shear stress reaches a steady state as defined by the measured shear stresses having less than 1% difference. Subsequently, the normal stress was reduced, allowing room for the particles to distend and move past one another. At that point, a yield stress could be measured (Crawford et al., 2016). The sample was again pre-sheared at 9 kPa and then sheared at a smaller normal stress of 7 kPa. The pre-shear/shear cycles were repeated at decreasing normal stresses of 6, 5, 4, 3, 2, and 1 kPa. The shear stress vs. normal stress plot was referred to as the yield locus. The yield locus was then analyzed using the FT4 data analysis software. Mohr's stress circle analysis was carried out to find the cohesion, unconfined yield strength (UYS), major principal stress (MPS), static angle of internal friction (ϕ_i), and effective angle of internal friction (ϕ_e). The flowability factor, ff_c, is defined as the ratio between the major principal stress to the unconfined yield strength and is used to compare the flowability of the samples.

FIGURE 2 | Splitting mechanism on all the sample holders used in this work. Adapted with permission from Freeman et al. (2015).
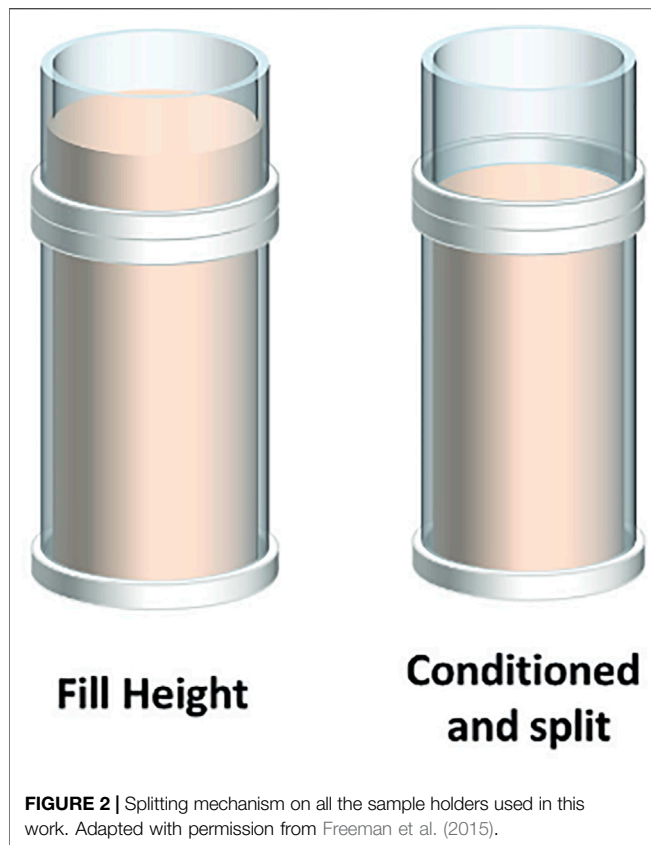
2.3.2 Compressibility Test

The compressibility test measures changes in sample volume (%) as a function of a series of mechanical forces (normal pressures) applied downward on the vertical axis via a vented piston. Initially, an accurate estimation of the sample volume was problematic as the loading of the wet sample produced poor consolidation resulting in large voids within the bulk. To overcome this, the initial conditioning step was replaced with the following steps:

(1) Load 1/6 (volume) of the sample into the sample holder
(2) Place a flat 50 g weight over sample
(3) Tap weight 3 times, elevating the weight at *ca.* 2 inches from the sample
(4) Split off portion above split level
(5) Attach 48 mm vented piston

Steps 1–3 were repeated 3 times, until the final volume was 2/3 full (over the sample split-level). The piston started compressing the sample at a range of increasing applied normal stresses between 0.5 and 15 kPa. The compressibility of the sample (C), as can be seen in **Eq. 2**, is calculated as follows:

$$C = \frac{V_0 - V}{V_0} \times 100\% \qquad (2)$$

where V_0 is the volume of the sample before compression and V is the volume of the sample at a given applied normal stress. Aside from compressibility, this test also outputs the initial bulk density of the sample before compression. Photos of the dry and wet samples before and after compression are given in **Supplementary Figure S1**.

2.3.3 Stability and Variable Flow Rate Test

The stability and variable flow rate test measures the amount of work a blade exerts to move through a bed containing the powdered sample. First, the sample was conditioned once using the 48 mm diameter blade, and the top portion was then split off. The testing procedure involves 11 alternating conditioning and testing cycles. In each conditioning cycle, the blade rotates down clockwise into the sample holder to 35 mm above the bottom of the powder bed; then, it travels up clockwise to the initial height. In each testing cycle, the blade rotates clockwise as it travels to 35 mm above the bottom of the sample holder. The 35 mm minimum height was chosen to avoid force and torque overloads when running the wet samples with high flow energies. Photos of sample *A* with 75% moisture (A_{75}^2) before, during and after the test was given in **Supplementary Figures S2A,C**, respectively. When the blade rotates in the sample bed, it forms a rat-hole behind it (**Supplementary Figure S2B**). When the blade comes around, the rat-hole is eliminated as a new one forms. As a result, the powders become loosened (**Supplementary Figure S2C**).

The work the blade has done during each test cycle was calculated from force and torque recordings and referred to as the total energy (E), as shown in **Eq. 3**:

$$E = \int_0^H \left(\frac{T}{R\tan\alpha} + F \right) dH \qquad (3)$$

where H is the instantaneous penetration depth, T is the measured torque, R is the radius of the blade, α is the blade helix angle, and F is the measured axial force. A helix angle of 5° was used for all the tests.

The linear velocity of the blade was 100 mm/s for the first eight testing cycles, and decreases to 70, 40, and 10 mm/s for the ninth, tenth and eleventh testing cycles, respectively. An illustration of the test setup and calculation of the total energy is shown in **Figure 3**.

The total energy (TE) of the seventh test is defined as the basic flowability energy (BFE).

The stability of the sample was evaluated by calculating the stability index (SI). SI (**Eq. 4**) is used as an indicator for the change in flow energy during repeated testing:

$$SI = \frac{BFE}{TE, test\,1} \qquad (4)$$

The sensitivity of flow energy to blade rotation speed was evaluated by calculating the Flow rate Index (FRI) (**Eq. 5**):

$$FRI = \frac{TE, test\,11}{TE, test\,8} \qquad (5)$$

FIGURE 3 | Stability and variable flow rate test setup. The graph on the right depicts the calculation of the total energy of a test cycle. Adapted with permission from Freeman et al. (2015).
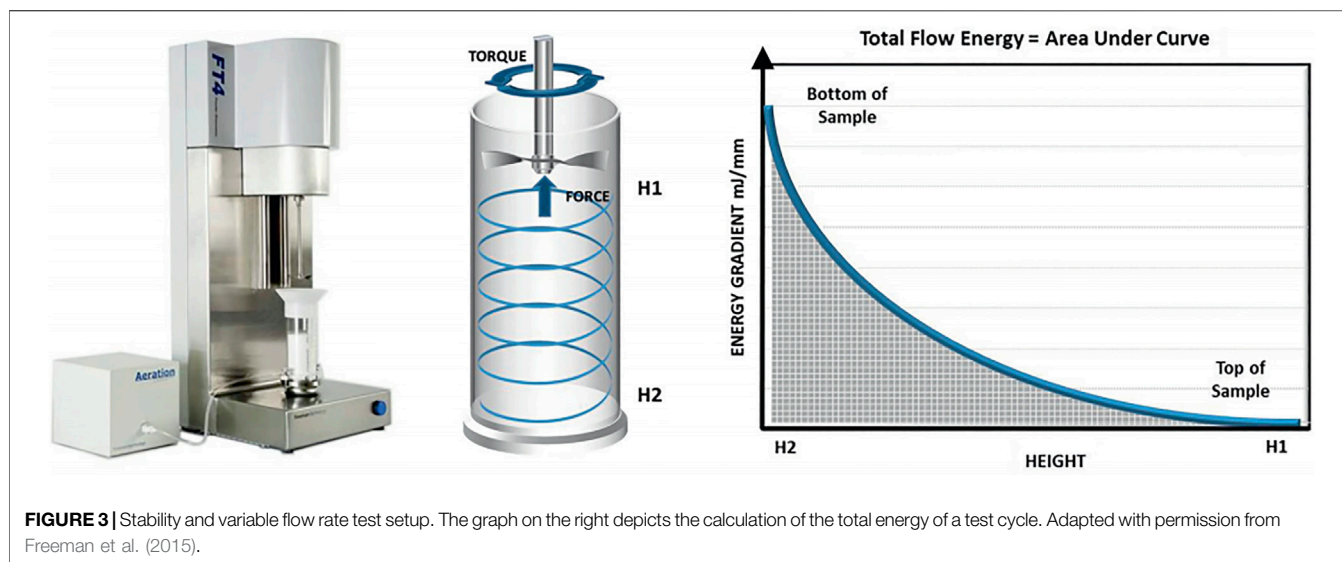
2.3.4 Wall Friction Test

The wall friction test measures the amount of wall shear stress between the bulk solid and the wall material of the storage or processing equipment given a series of wall normal stresses. In this test, the sample was first conditioned once using the 48 mm diameter blade, and then consolidated to 9 kPa normal stress using the 48 mm diameter vented piston. Next, the wall friction disk assembly was attached to the instrument. The wall friction disk assembly consists of a rod, a 48 mm diameter disk, and a screw that holds the rod and the disk together. The assembly was lowered to get in contact with the top surface of the sample until the normal stress reaches 9 kPa. Then the disk started rotating at an angular velocity of 18°/min, creating a shear stress on the surface of the powder bed. The sample underwent one pre-shear step where the normal stress used for the pre-shear cycle was kept at 9 kPa, followed by five successive shear steps where the normal stress used started out at 7 kPa and went down to 6, 5, 4, and 3 kPa. The measured wall shear stress vs. the wall normal stress was called the wall yield locus. The wall yield locus was fitted using linear regression with a coefficient of determinization (R^2) greater than 0.99, and the wall friction angle (**Eq. 6**) was calculated as the inverse tangent of the slope of the best-fit line:

$$\Phi_w = \arctan\left(\frac{\tau_w}{\sigma_w}\right) \quad (6)$$

where ϕ_w denotes wall friction angle, τ_w and σ_w are the wall shear and normal stresses, respectively.

Three wall friction disks were used in this study:

(1) Stainless-steel disk (manufacturer supplied); average roughness factor (R_a) 1.2 μm
(2) In-house manufactured polytetrafluoroethylene (PTFE) disk; average R_a 0.480 μm
(3) In-house manufactured high-density polyethylene (HDPE) disk; average R_a 0.094 μm

The stainless-steel disks were cut out from a large sheet with the grain being lateral across the face of the disk. The R_a value represents the average surface roughness of the entire sheet. The R_a of the PTFE and HDPE disks were measured using a Bruker Contour GT optical profilometer, as can be seen in **Supplementary Figures S3, S4**. The R_a of the PTFE disk is 0.48 μm in the X direction and 0.48 μm in the Y-direction. The R_a of the HDPE disk is 0.094 μm in the X direction and 0.107 μm in the Y-direction. At the pre-shear step, it was found that each wall material required a different amount of time for the shear stress to reach equilibrium. Therefore, different disks were made to rotate over different angles at the same angular velocity. The stainless-steel disk was made to rotate for 60°, while the PTFE and HDPE disks were made to rotate for 240° and 180°, respectively.

In the wetting-drying study, to preserve any structure within the wetted-and-dried A samples (A_0^3) they were analyzed on the FT4 using shear, compressibility, stability and variable flow rate, and wall friction testing programs that were the same as described in **Section 2.3** except that there were no conditioning steps at the beginning of each program. The error bars were also calculated as the standard deviation of five repeat runs.

2.4 BET Surface Area

Multipoint BET specific surface area (SSA) was collected using a Micromeritics 3Flex instrument. All BET analyses data were obtained using nitrogen as the adsorbate gas. The secondary drying step and outgassing consisted of samples with masses ranging from 1.3 to 1.6 g; these were further conditioned with low pressure at 45°C until isobaric conditions were reached ($\leq 1 \times 10^{-5}$ mmHg). This step was crucial in obtaining reproducible and reliable results. The typical masses lost during this final drying step for all samples was less than 0.5 mg. BET range was determined from a linear fit of the BET plot. The linear fit was selected using seven increasing points (1-p/p°) up to the maximum on the Rouquerol transform plot. All experiments performed produced positive BET "C" constants.

2.5 Surface Energy *via* Inverse Gas Chromatograph

The impact of wetting and drying on at the microscale was investigated by tracking surface chemistry changes with surface energy measurements. These measurements were performed *via* Inverse Gas Chromatography (IGC) using a Surface Energy Analyzer (SEA) from Surface Measurement Systems (SMS). After surface area data collection, samples A_0^1, A_0^3, and A_0^5 were loaded and packed into silanized glass columns sourced from SMS with the following dimensions: 4 mm ID x 6 mm OD x 300 mm L. Each sample was loaded into a new silanized column resulting in a solid (no gaps) packed column of densities between 0.13 and 0.64 g/cm^3. Dispersive surface energy (γ_s^d) was estimated using HPLC grade *n*-alkanes (C$_7$–C$_{10}$) from Sigma-Aldrich. A monopolar Lewis acid (trichloromethane) and base (ethyl acetate) of HPLC grade from Sigma-Aldrich were used for the specific surface energy (γ_s^{ab}) portion of the experiments. Probe to probe interactions were avoided by conducting experiments at infinite dilution (0.005 n/n$_m$ or 0.5% mono-layer coverage). Analysis conditions such as carrier gas type (He), flow rate (10 sccm) and column temperature of 30°C were maintained throughout all analyses. A 60 min conditioning step was selected before each run with identical conditions to allow for equilibration. The dispersive surface energy component was calculated using the Dorris-Gray method, and the acid-base (or specific) surface energy components were calculated using the Della Volpe scale and the polarization method (Hargreaves et al., 2013). In the SEA Analysis software, the center of mass option was used to determine retention time due to the asymmetrical peaks produced as a result of the polar probe-surface interactions. Instrument reproducibility was within 0.5% deviation using the mannitol reference standard provided by Surface Measurement Systems.

3 RESULTS AND DISCUSSION

3.1 Effect of Moisture and Feedstock Variability on Corn Stover Flow Behavior

3.1.1 Shear Testing

The shear properties of dry and wet samples *A* and *B* obtained by performing Mohr's stress circle analysis on the yield locus are presented in **Figure 4**. As depicted in **Figure 4A**, the flowability factors (ff$_c$) of both *A* and *B* sharply decrease with the increase in moisture from 0% to 25%, and then slowly decrease with the increase in moisture to 50%. The ff$_c$ of the samples with 50% and 75% moisture contents are very similar. Both A_0^1 and B_0^1 samples fell into the "free-flowing" regime while all the wet *A* and *B* samples fell into the "cohesive" regime. Based on the ff$_c$ value, the B_0^1 has greater flowability than A_0^1. The cohesion (**Figure 4B**) of *A* first increased as moisture content increases from 0% to 25%, and then reached a plateau at higher moisture levels. The cohesion of *B* first increased as moisture content increases from 0% to 50%, and then reaches a plateau at 75% moisture. The increase in cohesion with moisture has been commonly observed in literature works focusing

on the flow behavior of wet food (Rennie et al., 1999; Teunou and Fitzpatrick, 1999) and biomass (Hargreaves et al., 2013; Littlefield et al., 2011; Gil et al., 2013; Crawford et al., 2016) particles. However, the plateauing cohesion at high moisture contents has not been observed possibly due to such high moisture contents (above 50%) were not investigated by other researchers. The static and effective angles of internal friction for both *A* and *B* first increase with moisture from 0% to 25% (**Figures 3C,D**) and then stops increasing when the moisture becomes higher. The UYS and MPS values for dry and wet *A* and *B* samples are given in **Supplementary Figure S5**.

3.1.2 Compressibility and Bulk Density

As shown in **Figures 5A,B**, the compressibility of both *A* and *B* increase monotonically with the moisture content at each applied normal stress level. At lower moistures (0%–15%), the liquid bridges loosen the packing of the particles, therefore increasing the amount of void space between the particles thus increasing the compressibility. As shown in **Figures 5C,D**, there is a slight decrease in bulk density from 0% to 15% moisture. At higher moistures (25%, 50%, and 75%), larger agglomerates form and the packing becomes even looser. The bulk density, however, reaches a minimum at 25% moisture and starts to increase rapidly at higher moistures (**Figures 5C,D**). This sharp increase is expected due to the density of water being much higher than the bulk density of the dry corn stover.

3.1.3 Stability and Variable Flow Rate Test

The full total energy profile of the dry and wet *A* and *B* samples, obtained by the stability and variable flow rate test, is depicted in **Figure 6**. By comparing **Figures 6A,B**, one can see the total energy of dry sample *B* is higher than that of the dry sample *A*. Taken together with the bulk density data in **Figures 5C,D**, the higher total energy of dry sample *B* can be attributed by the greater number of particles impinging upon the blade. To better observe the effect of repeated testing and blade speed on the total energy, the stability index (SI) and flow rate index (FRI) were calculated, with the results given in **Supplementary Figure S6**. Due to the inhomogeneous and polydisperse nature of the samples, large relative standard deviations (>10%) in both SI and FRI were observed. The SI for samples *A* and *B* with 0% through 50% moisture contents are similar and close to 1, suggesting that the flow energy measured at each testing cycle was relatively stable. The SI values for the 75% moisture samples are smaller than that of the other samples. The smaller SI is most likely due to the deagglomeration of the large clusters within the highly wet sample as it was being made to flow. The FRI for all the dry and wet samples *A* and *B* were similar and close to 0.8, which suggests that all the samples are sensitive to the blade speed and exhibits a pseudoplastic behavior.

The BFE values for *A* and *B* with different moisture contents (**Supplementary Figure S7**) were examined. Interestingly, the BFE values of *A* samples increase as the moisture content rises from 0 to 15% and goes through a maximum at 15% moisture (**Supplementary Figure S7A**). As the moisture further increase, the BFE starts to decrease. However, the BFE at 75% moisture is still slightly higher compared to the BFE of the dry sample. This non-monotonic trend, when taken together with the previously observed trends in cohesion and compressibility, can be attributed to the

FIGURE 4 | Shear test results for *A* and *B*. **(A)** Flowability factor for *A* and *B* at 0, 15, 25, 50, and 75% moisture contents. **(B)** Cohesion for *A* and *B* at 0, 15, 25, 50, and 75% moisture contents. **(C)** Static and effective angles of internal friction of *A* with 0, 15, 25, 50, and 75% moisture contents. **(D)** Static and effective angles of internal friction of *B* with 0, 15, 25, 50, and 75% moisture contents. Data points were obtained from steps A_0^1, A_x^2, B_0^1, and B_x^2.

formation of liquid bridges between the particles. On one hand, liquid bridges increase the cohesive forces between the particles, therefore leading to greater resistance to the blade and causing increased flow energy. On the other hand, the liquid bridges can result in looser packing in the bulk structure which decreases the resistance to the blade by decreasing the interaction between the blade and the more loosely packed particles. When the moisture content is less than or equal to 15%, the effect of the cohesive forces dominates, so that the BFE increases with the moisture content and reaches a maximum at 15%. However, as moisture further increases to 25% and the packing of the powder becomes looser due to the formation of more and larger liquid bridges, the effect of the looser packing becomes dominant, so that the BFE starts to decrease. As

moisture increases to 50%, the cohesion stops increasing (**Figure 4B**) while the compressibility continues to increase as the packing becomes even looser. The BFE continues to decrease but the BFE at 75% moisture is still higher than that of the dry sample. At this point, it is unclear whether water has completely saturated some of the particles and formed liquid films around them. However, since the BFE at 75% is still higher than that of the dry sample, the flow-resisting effect of liquid bridges outweighs the flow-enhancing effect that the liquid films have. For the *B* samples, the BFE still peaks at 15% moisture and decreases as the moisture further increases (**Supplementary Figure S5B**). However, different from Sample *A*, the BFE of sample *B* at 75% moisture content is lower than that of the dry sample *B*.
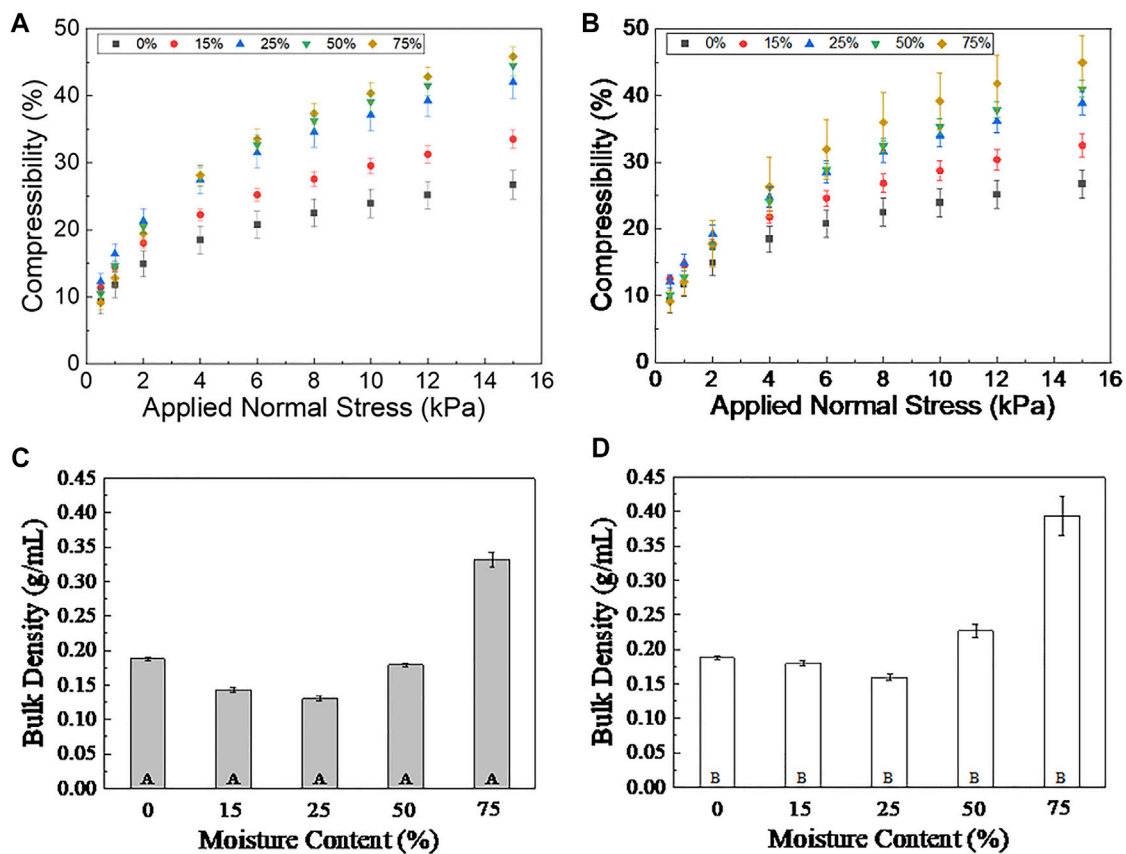
FIGURE 5 | (A) The % compressibility as a function of applied normal stress for **(A)** *A* samples and **(B)** *B* samples, and the bulk density for **(C)** *A* samples and **(D)** *B* samples with 0, 15, 25, 50, and 75% moisture contents. Data points were obtained from steps A_0^1, A_x^2, B_0^1, and B_x^2.
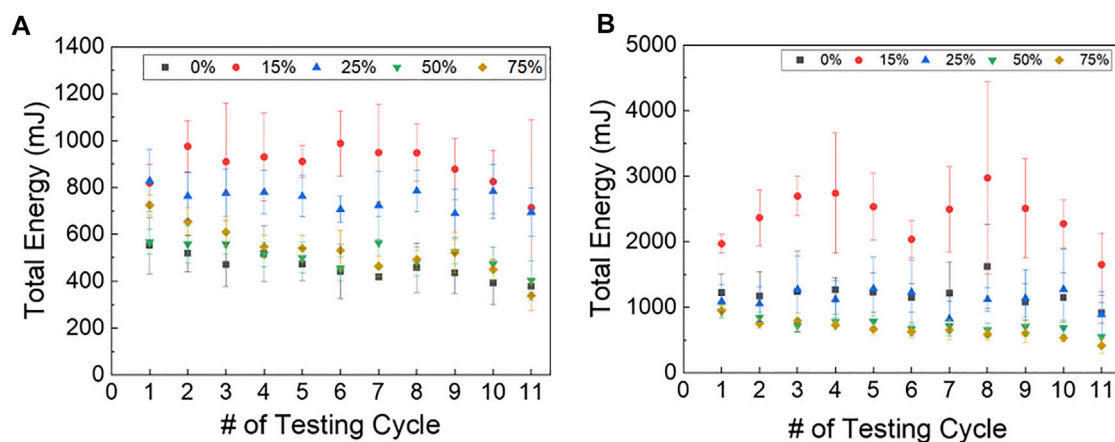
FIGURE 6 | The total energy of the 11 test cycles for **(A)** *A* samples and **(B)** *B* samples, with 0, 15, 25, 50, and 75% moisture contents. Data points were obtained from steps A_0^1, A_x^2, B_0^1, and B_x^2.

The role of water on the flow behavior on non-biomass powders, such as coal, has been more thoroughly studied. For example, Lu et al. (Lu et al., 2018) studied the effect of moisture on the flowability of pulverized coal. A shear test and a stability and variable flow rate test were conducted using an FT4 powder rheometer. As expected, the ff$_c$ kept decreasing with moisture in the 1.6 to 29 wt% moisture range. The cohesion first increased at a slow rate and then started increasing more rapidly when the moisture went above 15 wt%. Surprisingly, the
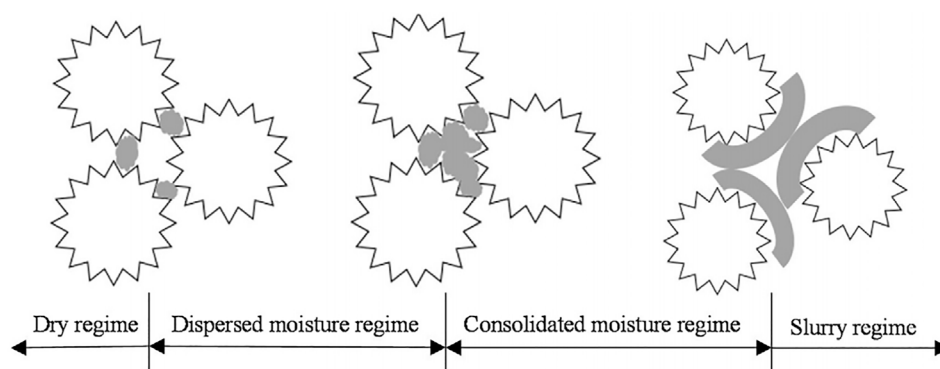
FIGURE 7 | Schematic of contacting particles with increasing moisture content. The white shapes with coarse edges represent particles and the gray dots and lines represent water droplets. Adapted with permission from Lu et al. (2018).

BFE of coal first decreased as moisture increased from 1.6 to 15 wt%, and then increased as moisture further increased to 29 wt%. The authors then predicted the interparticle forces using a microscale approach with the Rumpf equation combined with the shear testing data as well as using a theoretical approach by combining the Kelvin equation and the Laplace–Young equation. Based on the cohesion and BFE data, and visual observations of the wet coal samples, the authors categorized their samples into four different regimes—the dry regime, the dispersed moisture regime, the consolidated moisture regime and the slurry regime (**Figure 7**). In the dry regime, there is little to no water between the coal particles and the bulk appears powdery. As the moisture content increased, the powder entered the dispersed moisture regime where coal particles started to agglomerate as water starts to form liquid bridges between the particles and driving up the interparticle capillary forces. As the moisture content keeps increasing, small liquid bridges merge and form large ones which leads to faster increase in the capillary forces, hence the consolidated moisture regime. Adding moisture beyond the consolidated moisture regime resulted in the slurry regime—defined as the point where all particles are completely surrounded by water.

Pictures of the dry (A_0) and wet (A_{15}, A_{25}, A_{50}, A_{75}) A samples are shown in **Supplementary Figure S1**. It can be seen in **Supplementary Figure S1A** that the dry sample appears powdery and free of lumps. As the moisture continued to increase, the color of the sample gradually darkened (**Supplementary Figures S1C,D**). Uponreaching 75% moisture content (**Supplementary Figure S1E**), the samples became darker in color and clumping was observed. The formation of liquid bridges is supported by data from the shear, compressibility, and stability and variable flow rate tests. Nevertheless, no consolidated moisture regime could be observed, as the cohesion value first increased at 0–50% moisture and then plateaued at 75% moisture.

3.1.4 Wall Friction

Three commonly used materials for constructing powder handling and storage units are chosen for the wall friction test. Among them, stainless steel represents a hydrophilic surface while PTFE and HDPE both represent hydrophobic surfaces.

The wall friction angles of A and B samples as a function of moisture content on all three surfaces is given in **Figure 8**. The dry sample B has a slightly higher ϕ_w than the dry sample A. The ϕ_w for both A and B on the stainless-steel surface first increases when the moisture content increases from 0% to 50%. This can be attributed to the increasing number of liquid bridges between the particles which increases the adhesive forces between the stainless steel surface and the sample. ϕ_w stops increasing as the moisture reaches 50% and above, indicating that liquid bridges have taken up all the available spaces between the particles.

The ϕ_w values of A and B on both PTFE and HDPE surfaces first decreased when the moisture content increases (0%–50% for PTFE and 0%–25% for HDPE). This trend aligned with the change in wall friction angle on the HMWPE surface with moisture for poplar and corn stover observed by Gil et al.[8] In another study conducted by Schulze (Schulze, 2008), it was found that the wall friction angle of flue gas desulfurization (FGD) gypsum powders on a mild steel surface increased with moisture content, but the wall friction angle of the same powder on the ultra-high molecular weight polyethylene (UHWM-PE) surface decreased with moisture content. According to Schulze (Schulze, 2008), on poorly wetted, hydrophobic materials such as PTFE, no liquid bridges can form. Instead, liquid films form between the PTFE and the particles, creating lubrication which lowers the ϕ_w of the particles. Nevertheless, the wall friction angles go through a minimum at intermediate moisture levels (50% for PTFE and 25% for HDPE), and then starts to increase at higher moisture levels (75% for PTFE and 50% for HDPE). This increase is likely due to the presence of free water in the sample holder which makes the powder to slightly float, enabling a greater amount of powders to be in contact with the hydrophobic disks and exerting greater resistance on them.

In general, a ϕ_w equal to or greater than 30° signifies a high potential for material binding to vessel walls during discharge (Crawford et al., 2016). The wall friction data given in **Figure 8** suggested that vessels constructed with stainless steel walls of $R_a = 1.2$ μm will pose greater challenges when processing corn stover compared to with PTFE and HDPE walls.
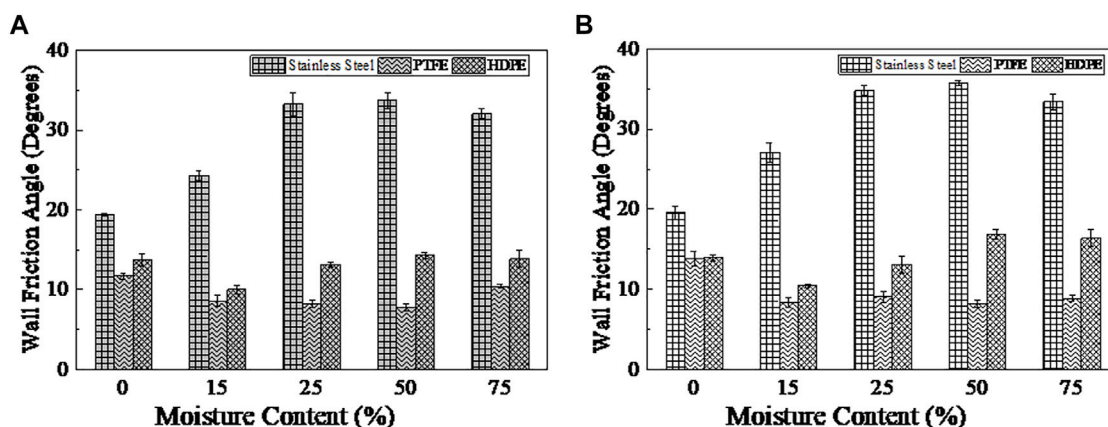
FIGURE 8 | The wall friction angles of the **(A)** A and **(B)** B samples, with 0, 15, 25, 50, and 75% moisture contents on stainless steel, PTFE and HDPE surfaces. The R_a value of the stainless-steel surface is 1.2 µm. The R_a of the PTFE disk is 0.48 µm in the X direction and 0.48 µm in the Y-direction. The R_a of the HDPE disk is 0.094 µm in the X direction and 0.107 µm in the Y-direction.

3.2 Re-Drying the Wet Sample

To further elucidate the effect of moisture addition to the dried corn stover sample, A_{50}^2 was prepared and subsequently dried (A_0^3) following the procedure described in **Scheme 1**, so that the effect of water on the corn stover particles can be analyzed without the liquid bridges. Images of these wetting and drying steps can be seen in **Figures 7A–C**, respectively. Furthermore, an additional rewetting (A_{50}^4) and redrying step (A_0^5)) was carried out to the same sample to observe if any effects or changes with respect to its rheological properties have undergone in the first wetting-drying step. It can be observed in **Supplementary Figure S8C** that after the 50% moisture sample was dried, the lumps were still present, and in addition, some new, large, loose clusters formed. The flow properties of these wetting-and-drying steps were then compared to the initial dried sample with the results given in **Figure 9**.

As illustrated in **Figure 9A**, A_0^3 and A_0^5 demonstrated lower flow energies than A_0^1. But the compressibility, given in **Figure 9B**, was very similar to that of the dry, initial sample. It is possible that after the wetting and drying, some residual moisture is still bound to the surfaces of the particles, causing greater electric potential between the particles. Furthermore, when comparing the dry samples, an increase in the ff_c along with a decrease in cohesion can be observed from A_0^1 to A_0^5. Using unpaired student's t-test for the data in **Figures 9C–F** revealed that A_0^3 sample has greater cohesion, smaller ff_c, angles of internal friction and wall friction angle compared to A_0^1. These all point to the greater cohesive strength, adhesive strength and difficulty to flow in step A_0^3. A_0^5 interestingly showed a lower cohesion and higher ff_c, which may indicate possible changes of the biomass in the macroscale, improving overall handling.

3.3 Surface Area, Brunauer–Emmett–Teller Approach

Sample mass and surface area values are required input during method development for IGC experiments—the targeted surface coverage relies on an accurate estimate of surface area in the column. The resulting surface areas for samples A_0^1, A_0^3, and A_0^5 were 1.29 m²/g, 0.61 m²/g, and 0.99 m²/g, respectively. The differences in surface area values can be attributed to structural changes as well as the inherent variability that biomass is associated with. Wetting, drying, and mechanical stirring may affect the pore structure, ultimately closing or opening pores, thus causing variations in surface area measurements.

3.4 Surface Energy *via* Inverse Gas Chromatography

In certain situations, the forces governing particle-particle interactions at the microscale can often be significant enough to influence bulk solid flow through cohesive mechanisms such as caking, ratholing, or adhesive methods such as gumming up equipment. The effect of wetting and drying on surface energy with sample A was investigated. **Figure 10** illustrates the percent changes of surface energy in sample A relative to the native sample, A_0^1 (initial starting condition for comparison). The surfaces of sample A were sensitive to wetting and drying, demonstrated by the increases in all components with the exception of the work of adhesion. For example, the "Dispersive SE" category in **Figure 10** illustrates the increase in dispersive surface energy (~20%) of the second wetting and drying cycle (A_0^5) from the initial sample (A_0^1). The work of adhesion (sample A to liquid water) was calculated using the Della Volpe scale and Della Volpe surface energy values of water.

The process of wetting and drying may have facilitated the removal of water-soluble extracts or surface contaminants as well as migration of bulk (internal) moieties towards the surface (external) through a leaching process, thus exposing a new surface. These modified surfaces appeared as a result of continued cycling which exhibited a decreased adhesion to liquid water. The data suggested that internal moieties favorable towards the adhesion of water migrate towards the surface in the first cycle and remain on the corn stover surface
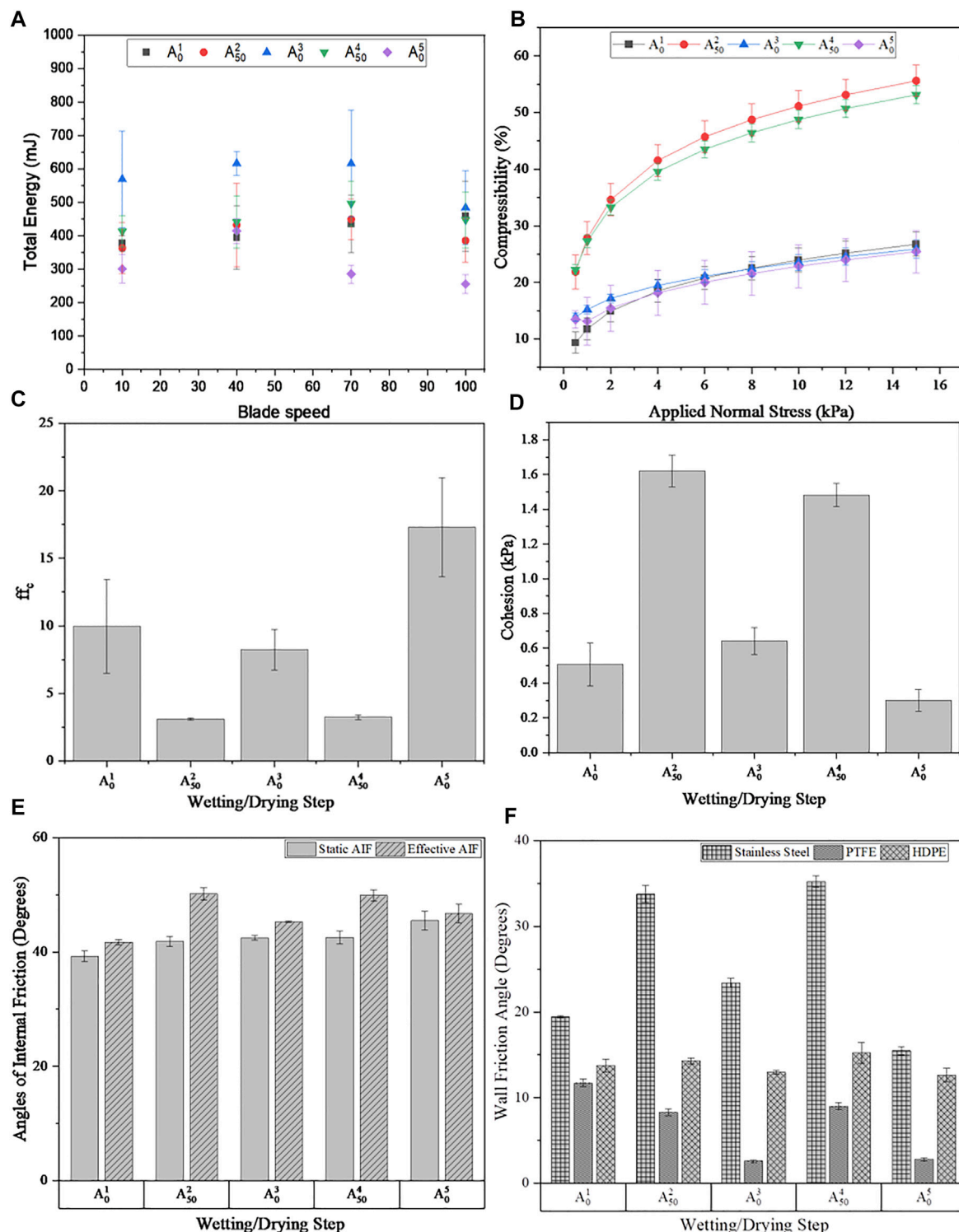
FIGURE 9 | The **(A)** total energy, **(B)** compressibility, **(C)** flowability factor, **(D)** cohesion, **(E)** static and effective angles of internal friction and **(F)** wall friction angles as a function of repeated wetting/drying of sample A.

throughout the drying (A_0^1 to A_0^3). Results after the second cycle suggest a stronger dispersive surface energy influence due to possible surface changes. Consequently, the measured increases

in dispersive surface energy from A_0^3 to A_0^5 resulted in a more hydrophobic surface, which had a negative impact on the calculated adhesion to water.
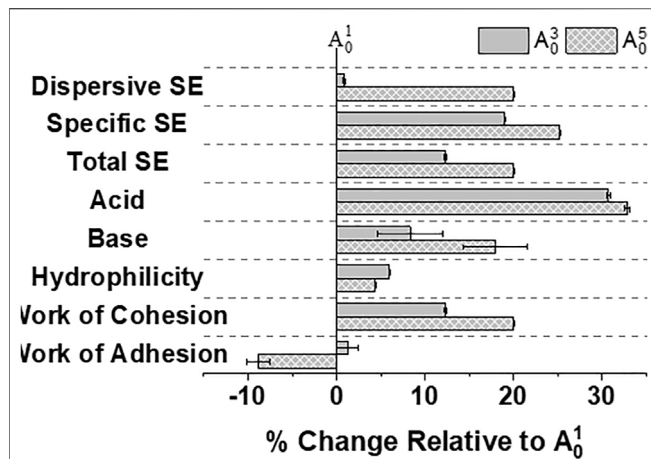
FIGURE 10 | Percentage changes in surface energy as a function of wetting and drying cycles for Sample *A*. Note: all quantified changes are relative to the initial corn stover sample.

The approximate surface energies of the wall materials under study can be found throughout the literature. Although the values may differ slightly from article to article, the general trend for total surface energy follows that stainless steel > HDPE > PTFE. In addition, the chemical nature of stainless steel surface has a profound effect as well, *i.e.*, oxidized or reduced. The low specific surface energy of PTFE is responsible for the degree of hydrophobicity and decreased interactions with hydrophilic surfaces, *i.e.* water and corn stover.

4 CONCLUSION

The flow energy, compressibility, shear properties and wall friction angles were measured for corn stover samples from two different bales—*A* and *B*, with 0% (dry), 15%, 25%, 50% and 75% moisture contents. All the wet samples showed greater basic flowability energy, compressibility, cohesion, unconfined yield strength, angles of internal friction and lower flowability factor (ff$_c$) than the dried samples. Of all the dry and wet *A* and *B* samples, the *A* and *B* samples with 15% moisture had the highest basic flowability energy. The *A* and *B* samples with 75% moisture was the most compressible and had the smallest ff$_c$. Among all the wall materials tested, the wall friction angle on the stainless-steel surface were in general greater than those on the PTFE and HDPE surfaces. Although samples *A* and *B* showed slight variations in their rheological properties, these values do not significantly differ to hinder the overall processing of these samples; both samples were similarly affected by the different moisture content, where they both exhibited the same trends at different wt%. In general, the feedstock variability observed among two disparate samples, originating from two different bales typically lead to significant changes in critical material attributes such as (but not limited to) ash content, crystallinity, surface energy, composition, and surface area; however, our study showed that the rheological properties were not impacted by feedstock variability. Wetting and then drying the corn stover leads to lower flow energies, higher compressibility, higher unconfined yield strength, and higher angles of internal friction compared to the initial, dry sample, pointing to the looser packing and formation of new clusters during wetting. However, when repeating the process, some changes could be observed, particularly in the cohesion, ff$_c$, and UYS. Rheological data indicated that the sample was more free-flowing when applying more wetting and subsequent drying steps, possibly modifying how the particles are interacting with one another, as evidenced by surface energy analysis carried out in the IGC. Such changes can be crucial when it comes to the handling of the feedstock along with potentially showing that undergoing wetting-drying steps can be considered as a pre-treatment to attain a better-flowing feed, aiding in the overall discharging and handling operation.

DATA AVAILABILITY STATEMENT

The original contributions presented in the study are included in the article/**Supplementary Material**, further inquiries can be directed to the corresponding authors.

AUTHOR CONTRIBUTIONS

DG assisted in revising the manuscript. FP assisted in data collection. RN assisted in data collection and revision. JL assisted in data collection and revision. OA assisted in profilometry. TS assisted in final revision.

SUPPLEMENTARY MATERIAL

The Supplementary Material for this article can be found online at: https://www.frontiersin.org/articles/10.3389/fenrg.2022.868050/full#supplementary-material

REFERENCES

Afzalinia, S., and Roberge, M. (2007). Physical and Mechanical Properties of Selected Forage Materials. *Canadian Biosystems Engineering* 49.

Crawford, N. C., Nagle, N., Sievers, D. A., and Stickel, J. J. (2016). The Effects of Physical and Chemical Preprocessing on the Flowability of Corn Stover. *Biomass Bioenergy* 85, 126–134. doi:10.1016/j.biombioe.2015.12.015

Freeman, T., Brockbank, K., and Armstrong, B. (2015). Measurement and Quantification of Caking in Powders. *Procedia Eng.* 102, 35–44. doi:10.1016/j.proeng.2015.01.104

Gil, M., Schott, D., Arauzo, I., and Teruel, E. (2013). Handling Behavior of Two Milled Biomass: SRF Poplar and Corn Stover. *Fuel Process. Technol.* 112, 76–85. doi:10.1016/j.fuproc.2013.02.024

Hargreaves, K. K., Zielińska, M., and Cenkowski, S. (2013). "Flowability of Distiller's Spent Grains Processed with Air and Superheated Steam Drying," in 2010 North Central ASABE/CSBE Conference. doi:10.13031/2013.36289

Ileleji, K. E., and Zhou, B. (2008). The Angle of Repose of Bulk Corn Stover Particles. *Powder Technol.* 187 (2), 110–118. doi:10.1016/j.powtec.2008.01.029

Jensen, P. D., Mattsson, J. E., Kofman, P. D., and Klausner, A. (2004). Tendency of Wood Fuels from Whole Trees, Logging Residues and Roundwood to Bridge over Openings. *Biomass Bioenergy* 26 (2), 107–113. doi:10.1016/S0961-9534(03)00101-6

Leal, J. H., Moore, C. M., Sutton, A. D., and Semelsberger, T. A. (2019). Surface Energy of Air Fractionated Corn Stover. *Industrial Crops Prod.* 137, 628–635. doi:10.1016/j.indcrop.2019.05.046

Littlefield, B., Fasina, O. O., Shaw, J., Adhikari, S., and Via, B. (2011). Physical and Flow Properties of Pecan Shells-Particle Size and Moisture Effects. *Powder Technol.* 212 (1), 173–180. doi:10.1016/j.powtec.2011.05.011

Lu, H., Guo, X., Jin, Y., and Gong, X. (2018). Effect of Moisture on Flowability of Pulverized Coal. *Chem. Eng. Res. Des.* 133, 326–334. doi:10.1016/j.cherd.2018.03.023

Mattsson, J. E., and Kofman, P. D. (2003). Influence of Particle Size and Moisture Content on Tendency to Bridge in Biofuels Made from Willow Shoots. *Biomass Bioenergy* 24 (6), 429–435. doi:10.1016/S0961-9534(02)00178-2

Ng, D. K. S., Ng, K. S., and Ng, R. T. L. (2017). "Integrated Biorefineries," in *Encyclopedia of Sustainable Technologies*, 299–314. doi:10.1016/B978-0-12-409548-9.10138-1

Ray, A. E., Williams, C. L., Hoover, A. N., Li, C., Sale, K. L., Emerson, R. M., et al. (2020). Multiscale Characterization of Lignocellulosic Biomass Variability and its Implications to Preprocessing and Conversion: A Case Study for Corn Stover. *ACS Sustain. Chem. Eng.* 8 (8), 3218–3230. doi:10.1021/acssuschemeng.9b06763

Rennie, P. R., Chen, X. D., Hargreaves, C., and MacKereth, A. R. (1999). Study of the Cohesion of Dairy Powders. *J. Food Eng.* 39 (3), 277–284. doi:10.1016/S0260-8774(98)00158-7

Schulze, D. (2008). *Powders and Bulk Solids: Behaviour, Characterization, Storage and Flow*, 22. Springer.

Stasiak, M., Molenda, M., Bańda, M., Wiącek, J., Parafiniuk, P., Lisowski, A., et al. (2019). Mechanical Characteristics of Pine Biomass of Different Sizes and Shapes. *Eur. J. Wood Prod.* 77 (4), 593–608. doi:10.1007/s00107-019-01415-w

Teunou, E., and Fitzpatrick, J. J. (1999). Effect of Relative Humidity and Temperature on Food Powder Flowability. *J. Food Eng.* 42 (2), 109–116. doi:10.1016/S0260-8774(99)00087-4

Thompson, S. A., and Ross, I. J. (1983). Compressibility and Frictional Coefficients of Wheat. *Trans. ASAE* 26 (4), 1171–1176. doi:10.13031/2013.34099

On the Fidelity of Computational Models for the Flow of Milled Loblolly Pine: A Benchmark Study on Continuum-Mechanics Models and Discrete-Particle Models

Wencheng Jin[1]*, Yimin Lu[1,2], Feiyang Chen[1,3], Ahmed Hamed[1], Nepu Saha[1], Jordan Klinger[1], Sheng Dai[2], Qiushi Chen[3] and Yidong Xia[1]*

[1]Energy and Environment Science and Technology Directorate, Idaho National Laboratory, Idaho Falls, ID, United States, [2]School of Civil and Environmental Engineering, Georgia Institute of Technology, Atlanta, GA, United States, [3]The Glenn Department of Civil Engineering, Clemson University, Clemson, SC, United States

The upstream of bioenergy industry has suffered from unreliable operations of granular biomass feedstocks in handling equipment. Computational modeling, including continuum-mechanics models and discrete-particle models, offers insightful understandings and predictive capabilities on the flow of milled biomass and can assist equipment design and optimization. This paper presents a benchmark study on the fidelity of the continuum and discrete modeling approaches for predicting granular biomass flow. We first introduce the constitutive law of the continuum-mechanics model and the contact law of the coarse-grained discrete-particle model, with model parameters calibrated against laboratory characterization tests of the milled loblolly pine. Three classical granular material flow systems (i.e., a lab-scale rotating drum, a pilot-scale hopper, and a full-scale inclined plane) are then simulated using the two models with the same initial and boundary conditions as the physical experiments. The close agreement of the numerical predictions with the experimental measurements on the hopper mass flow rate, the hopper critical outlet width, the material stopping thickness on the inclined plane, and the dynamic angle of repose, clearly indicates that the two methods can capture the critical flow behavior of granular biomass. The qualitative comparison shows that the continuum-mechanics model outperforms in parameterization of materials and wall friction, and large-scale systems, while the discrete-particle model is more preferred for discontinuous flow systems at smaller scales. Industry stakeholders can use these findings as guidance for choosing appropriate numerical tools to model biomass material flow in part of the optimization of material handling equipment in biorefineries.

Keywords: granular materials, discrete-element, finite-element, lignocellulose biomass, hopper flow, flow regime

1 INTRODUCTION

Biorefineries can convert sustainable biomass into bio-energy (directly *via* combustion through intermediate fuels such as ethanol) and bio-chemicals (e.g., succinic acid). Over the past decade, bio-energy has achieved a steady increase in the U.S. renewable energy portfolio and is a vital contributor

for supporting the U.S. to accomplish the carbon-neutral goal (DOE-BETO, 2016). However, biorefineries suffer from unreliable operations in transportation, storage, and handling of granular biomass feedstocks. These process upsets, manifested in various occasions such as hopper arching, screw jamming, and particle segregation, can cause significant downtime of operations resulting in non-competitive market values of bio-products (Hess et al., 2007; Ramírez-Gómez, 2016; Dale, 2017; Ilic et al., 2018; Cheng et al., 2021). All these issues result from the poor flowability of the granular biomass feedstocks. Both experimental characterization (Hernandez et al., 2017; Salehi et al., 2019; Stasiak et al., 2019) and numerical modeling (Jin et al., 2020b; Xia et al., 2020) have been used to address the flowability issue with the objectives of optimizing equipment geometry/operation and optimizing the granular feedstock characteristics. However, experiments cannot measure all the critical state parameters constraint by sensors (e.g., shear testers only quantify two stress components of a full stress tensor), which are crucial to elucidate the flow physics. In addition, experiments are not economically viable to conduct at the industrial scale with a comprehensive test plan. Numerical modeling validated by experimental data is expected to address the experimental limitations and achieve the above objectives. Both the continuum-mechanics models and the discrete-particle models have been continuously developed, improved, and used to predict the flow behavior of the granular biomass feedstocks.

The continuum-mechanics models assume that the granular material can be treated as a continuum, for which the constitutive laws can describe the mechanical flow behavior. The variation of biomass species, particle size, and particle morphology are realized by using different constitutive laws or different values of the constitutive material parameters. For example, the authors previously applied the modified Drucker-Prager/Cap model (Jin et al., 2020a), the NorSand model (Jin et al., 2020b), and the hypoplastic model (Lu et al., 2021a,b) to predict the flow behavior of the milled loblolly pine with different particle size distributions. Yi et al. (2020a,b) used the modified Cam-Clay model and the Drucker-Prager/Cap model to simulate the milled corn stover and Douglas fir.

The discrete-particle models track individual particles and predict particle trajectories from the collisions with neighboring particles. The variation of particle size, morphology, and mechanical properties resulting from biomass species and pre-processing are explicitly described and simulated in discrete-particle modeling. For example, Xia et al. (2019) and Guo et al. (2020) used flexible clumped spheres to approximate different particle shapes for milled loblolly pine and switch grass. Xia et al. (2021) explicitly modeled the complex-shaped pine chips using the polyhedral discrete element model. Guo et al. (2021) developed an experiment-informed, semi-empirical, elasto-plastic bond model for discrete element modeling of woody biomass particles. A recent effort by Chen et al. (2022) proposed a set of complex particle contact laws to describe particle interactions using monospheres.

The continuum-mechanics and discrete-particle models have been used to simulate the granular biomass flow in various characterization tests, including uniaxial compression, axial

shear, Schulz ring shear, and pilot-scale hopper with considerable success so far. In general, the continuum-mechanics models are found to be efficient in predicting large flow systems with reduced-order accuracy. In contrast, the discrete-particle models are more computationally expensive with higher precision and are more suitable for investigating the fundamental physics of granular flow at smaller scales. However, a quantitative comparison on capturing the in-depth flow physics at different scales and the associated computational cost of the two modeling approaches has been an untouched area in the literature.

This paper attempts to address this issue by benchmarking the numerical predictions of flow systems from a continuum model and a particle model against physical experiments. In **Section 2**, we briefly introduce the solution algorithms and the constitutive/contact laws of the two modeling approaches, followed by the targeted granular material (i.e., milled loblolly pine) and its material parameters for the two models. In **Section 3**, we detail the experimental and numerical setup of a lab-scale rotary drum test, a pilot-scale hopper test, and a full-scale inclined plate test. The qualitative and quantitative comparison among the experimental measurements and the numerical predictions from the two modeling methods are presented for each test. We then discuss the apparent advantages and disadvantages of the two modeling approaches based on the benchmark cases in **Section 4**. Lastly, the conclusion is provided in **Section 5**.

2 METHODS AND MATERIALS

2.1 Continuum-Mechanics Model
2.1.1 Solution Algorithm
The principles of continuum-mechanics are the conservation of mass and momentum, which are the governing equations to describe the motion at any point, $\vec{x}$, in the granular flow system:

$$\frac{1}{\rho}\frac{\mathrm{D}\rho}{\mathrm{D}t} + \nabla \cdot \vec{v} = 0, \tag{1}$$

$$\rho\frac{\mathrm{D}\vec{v}}{\mathrm{D}t} = \rho\vec{g} + \nabla \cdot \boldsymbol{\sigma}, \tag{2}$$

where ρ is the bulk density of the granular material, $\vec{v}$ is the velocity vector, $\boldsymbol{\sigma}$ is the Cauchy stress tensor, and $\vec{g}$ is the body-force vector due to gravity. We also use $\mathrm{D}a/\mathrm{D}t = \partial a/\partial t + \vec{v}\cdot\nabla a$ to represent the material derivative. A constitutive model that relates the stress tensor to the motion is required to close the above governing equations. The hypoplastic model developed by Gudehus (1996) and Bauer (1996) (termed as G-B model hereafter) is adopted and briefly outlined in **Section 2.1.2**.

The above governing equations can be solved by many numerical methods, such as the mesh-based finite-element method (FEM) and finite-volume method (FVM), and the meshless smoothed-particle hydrodynamic (Jin et al., 2020b). We adopt the FEM with the coupled Lagrangian-Eulerian (CEL) approach as the resolution algorithm in this paper. The CEL approach solves the governing equations using two steps: 1) The granular material domain is discretized using Lagrangian

mesh, and the deformable mesh tracks the movement of material; 2) the deformed mesh is returned to its initial position, and the deformed material properties are then interpolated back to the "fixed" mesh. This scheme enables CEL to model large deformation without the mesh-tangling issue.

2.1.2 Constitutive Model

The G-B hypoplastic model was formulated to model the soil behavior with the critical state concept, defined as the state of stress and void ratio upon which granular material can flow infinitely without volumetric changes. This constitutive model has been applied to effectively model various types of soil (Bauer, 1996; Gudehus, 1996; Herle and Gudehus, 1999; Mašín, 2005; Wójcik and Tejchman, 2009; Liao and Yang, 2021) and biomass materials (Lu et al., 2021b,a). The stress-motion relation and the void ratio e evolution of the G-B model are expressed in rate form as:

$$\dot{\sigma} = f_s \left(\mathbb{L} : \dot{\gamma} + f_d \mathbf{N} \sqrt{\dot{\gamma} : \dot{\gamma}} \right) \tag{3a}$$

$$\dot{e} = (1 + e) \operatorname{Tr}(\dot{\gamma}) \tag{3b}$$

where $\dot{\sigma} = \dot{\sigma} - \dot{\omega} \cdot \sigma + \sigma \cdot \dot{\omega}$ is the objective (Jaumann) stress-rate tensor. $\dot{\gamma}$ and $\dot{\omega}$ are the symmetrical strain rate tensor and the anti-symmetrical spin rate tensor, and they can be obtained as:

$$\dot{\gamma} = \frac{1}{2} \left(\nabla \vec{v} + \nabla \vec{v}^T \right), \tag{4a}$$

$$\dot{\omega} = \frac{1}{2} \left(\nabla \vec{v} - \nabla \vec{v}^T \right). \tag{4b}$$

The forth order tensor $\mathbb{L}$ and the second order tensor $\mathbf{N}$ in **Eq. 3a** are the linear and nonlinear modulus, they are expressed in terms of the current state (i.e., stress tensor σ and void ratio e) and the material friction angle at the critical state ϕ_c. The coefficients f_s and f_d in **Eq. 3a** take the influence of density and pressure on the stress into account. Their detailed expression are described in Gudehus (1996), Bauer (1996), and Lu et al. (2021b). We implemented the G-B hypoplastic model in the Abaqus User Material Subroutine (VUMAT) and open-sourced the code in GitHub (https://github.com/idaholab/GranularFlowModels). We also validated the model for various lab-scale shear tests and pilot-scale hopper tests (Lu et al., 2021a,b).

2.2 Discrete-Particle Model

2.2.1 Solution Algorithm

The discrete-particle models are generally referred as models solved by the discrete element method (DEM). With the theory initially established by Cundall and Strack (1979) and Chung (2006), DEM simulates the bulk flow behavior of granular materials by explicitly tracking the motion of each single particle of an assembly. The particle motion, expressed in terms of translation and rotation, is governed by the Newton-Euler equations:

$$m \frac{\mathrm{d}^2 \vec{x}}{\mathrm{d} t^2} = \vec{F} \tag{5}$$

$$I \frac{\mathrm{d}^2 \vec{\psi}}{\mathrm{d} t^2} = \vec{M} \tag{6}$$

where m and I are the particle's mass and moment of inertia, $\vec{x}$ and $\vec{\psi}$ are the particle's translational and rotational vectors, $\vec{F}$ and $\vec{M}$ are the internal and external force and moment experienced by the particle. The force and moment are evaluated and summed through the contact forces from the interaction with its neighbours, the gravity and prescribed body forces, and the damping due to particle movement. The governing equations automatically satisfy the mass conservation, and they are explicitly solved in each time increment for all particles. A contact model that relates motion and force between two particles is required to complete the above governing equations in **Eqs 5**, **6**. We adopt the contact model proposed by Chen et al. (2022) in this paper, and we briefly introduce it in the following section.

2.2.2 Contact Model

For granular material with complex particle shapes and sizes, one can explicitly model the complex shapes and sizes in DEM. However, such an approach is computationally expensive because of the mathematical complexity involved in describing particle shapes and in detecting and resolving particle contacts. Alternatively, the influence of particle-scale characteristics (e.g., shapes, sizes, deformability) on bulk behavior can be indirectly modeled with advanced contact laws with spherical particles. This latter approach is appealing for simulating larger-scale problems due to its computational efficiency and is therefore adopted in this study. Specifically, we adopt a recently proposed nonlinear hysteretic model to calculate the interaction forces (Chen et al.,2022). This model is capable of capturing the sophisticated bulk behavior of granular biomass that yield strain hardening, interlocking, and cohesion, when subjected to variable compressive and repeated loading conditions. It is mathematically expressed as:

$$F_{hys} = \begin{cases} \bar{F}_{nl}^{(m)} = \alpha k_1^{(m)} \left(\delta - \delta_0^{(m-1)} \right)^{\chi} + f_1^{(m)} & \text{loading/reloading} \\[2mm] \bar{F}_{nu}^{(m)} = C k_2^{(m)} \left(e^{\frac{\beta^{(m)}}{r^*} \left(\delta - \delta_0^{(m)} \right)} - 1 \right) + f_2^{(m)} & \text{unloading} \\[2mm] F_{nc}^{(m)} = -K_{nc} \delta & \text{cohesion} \end{cases} \tag{7}$$

where F_{nl} and F_{nu} denote the normal force component in compressive loading and unloading, respectively. F_{nc} is the cohesion force. The superscripts (m) and $(m-1)$ indicate the current and previous loading cycles, respectively. δ and δ_0 are the total and plastic overlap distances. k_1, k_2, K_{nc}, α, and C are the material parameters to represent particle stiffness. The exponent χ is the loading displacement power function index, f_1 and f_2 are two numerical correction terms to avoid the discontinuity in force calculation. Note that this model tracks the contact history of two contacting particles since the detection of their contact. The storage of history (e.g., plastic deformation δ_0, loading cycle m) requires large computing memory and enables to model history-dependent flow behavior. The above contact model only accounts for normal interaction forces. We

adopt the classical Mindlin theory (Mindlin, 1953; Kruggel-Emden et al., 2008) to calculate the tangential interaction forces.

2.3 Granular Material

The granular material used in this study is milled loblolly pine chips. The loblolly pine trees from a southeastern Georgia plantation in the U.S. were first processed in a flail chain to remove the bark, limbs, and needles. The main bole of the tree was chipped at the plantation to a nominal 50 mm size, then hammer milled in the Biomass Feedstock National User Facility at Idaho National Laboratory until the particles pass a retention screen of 6 mm. We further dried the granular pine chips in a rotary drum and stored with a moisture content of approximately 6%. The sieve analysis of the material sample shows that the cumulative passing particle size distribution has characteristic (10, 50, and 90% respectively) parameters of $d_{10} = 0.38$ mm, $d_{50} = 0.82$ mm, $d_{90} = 1.79$ mm. A more detailed description of sample preparation has been reported in an earlier work (Jin et al., 2020a).

We conducted extensive characterization on the mechanical behavior of the loblolly pine chips using the cyclic axial compression, the Schulze ring shear test, and the vibration test (Jin et al., 2020a). A workflow to calibrate the G-B hypoplastic model parameters for the loblolly pine chips using the characterization data was established by Lu et al. (2021b). **Table 1** lists the calibrated material parameters, in which the internal friction angle at critical state ϕ_c and the exponent α determine the critical and the peak stress values. The granulate hardness h_s, the exponent n and β control the elastic behavior of the material. The minimum, the critical and the maximum void ratios at zero pressure e_{d0}, e_{c0} and e_{i0} provide the void ratio (density) boundaries that the granular material can achieve.

For the discrete-particle model, we calibrated both the contact model parameters and the DEM spherical particle parameters (i.e., particle radius, particle density, Young's modulus, Poisson's ratio) for the targeted loblolly pine chips. **Table 2** summarizes the calibrated DEM particle-particle (P-P) contact model parameters against the cyclic axial compression tests on loblolly pine chips. The calibration procedure is detailed in Chen et al. (2022) for the hysteretic contact model parameters (for normal contact force component) and in Xia et al. (2019) for the Mindlin model (for tangential contact force component). Note the parameters (A_1, A_2, A_3) listed in the table are correlated with k_1 and k_2 in **Eq. 7**. Also, the "coarse-grained" DEM adopted in this study allows the spherical particles not equivalent to physical particles in shape and size. The bulks of spheres with radius of 1.5 mm were calibrated to render the equivalent bulk behavior of the biomass samples and used for all the following simulations. In addition to the hysteretic and the Mindlin contact models, we also adopt the rolling resistance model to account for the interlocking effect

of the complex-shaped pine particles by applying the constant torque (Zhou et al., 1999). The typical range of the parameter associated with this model (i.e., rolling resistance μ_r) is 0.6–1.0, and we calibrated this parameter through trial-and-error in hopper simulation detailed in the following section.

For the particle-wall (P-W) contact, we adopted the same set of contact models as for the particle-particle (P-P) contact. All the model parameters are the same except the friction coefficient μ_f and rolling friction coefficient μ_r, which are the two dominant parameters controlling frictional behavior. We chose the initial values of the two parameters by balancing a single sphere particle on an inclined plane with an inclination angle of 8.5° (Chen, 2022) from the experimental measurement for milled loblolly pine. The influence of varying these parameters on the flow behavior will be demonstrated in the case studies. The P-W column in **Table 2** lists all parameters for the particle-wall contact.

3 BENCHMARK CASES

3.1 Hopper Flow and Arching

Hoppers are one of the most widely used equipment to handle granular materials across several industries including the bioenergy sector. Inconsistent hopper flow, such as hopper arching (Horabik and Molenda, 2014), rathole, surging flow, poses a significant challenge in biorefineries. Robust and high-fidelity numerical models can help to address this challenge by directly simulating hopper flow at various scales. In this section, we used the calibrated FEM and DEM models to simulate a hopper flow of the milled loblolly pine at the pilot-scale, and compared the predictions against experimental measurements to show the capabilities of the two models.

3.1.1 Experimental and Model Setup

The experimental tests to characterize the flow of milled loblolly pine in a wedge-shaped hopper are detailed in Lu et al. (2021a). **Figures 1A,B** show the front, side, and top views of the hopper and the size of the hopper, respectively. The hopper is customized with motors that can rotate its sidewalls to form any given semi-inclination angle θ. During the experiments, the hopper is first charged with the milled pine feedstock to a targeted height $H = 0.68$ m. Then the hopper opens its outlet by gradually sliding the two sidewalls in the upward-directions, holding the semi-angle constant. We measured the critical outlet width as the maximum orifice size at which the feedstock cannot continuously flow out of the hopper. We also logged the accumulated mass during the flow test to quantify the mass flow rate for any combination of outlet opening width W and semi-inclination angle θ.

A full 3D hopper discharge simulation is neither computationally viable for DEM nor necessary, as the experiments observed flow pattern is in plane strain condition. As shown in **Figures 1A,B** thin cross-section of the hopper is considered with a depth of 3 mm in the out-of-plane direction (i.e, one layer of mono-spheres). The hopper walls are meshed with triangular elements. The charging process was simulated

TABLE 1 | Calibrated G-B hypoplastic model parameters for the loblolly pine chips.

ϕ_c [°]	h_s (kPa)	n (-)	e_{d0} (-)	e_{c0} (-)	e_{i0} (-)	α (-)	β (-)
47.3	187.6	0.30	0.50	1.06	1.38	0.3	1.0

TABLE 2 | Calibrated DEM model parameters for loblolly pine chips.

Parameter	Symbol	Value (P-P)	Value (P-W)	Unit
Loading force scaling coefficient	α'	20	20	—
Loading power function index	χ	2	2	—
Loading stiffness coefficient	A_1	6×10^8	6×10^8	—
Initial loading stiffness coefficient	A_2	5×10^4	5×10^4	—
Unloading stiffness coefficient	A_3	5	5	—
Cohesion force coefficient	K_{nc}	1×10^{-4}	1×10^{-4}	—
Unloading force scaling coefficient	C	1×10^{-7}	1×10^{-7}	—
Particle radius	r	1.5	—	mm
Density	ρ	390	—	kg/m^3
Young's modulus	E	1×10^6	1×10^6	Pa
Poisson's ratio	ν	0.3	0.3	—
Restitution coefficient	e	0.3	0.3	—
Friction coefficient	μ_f	0.5	0.2	—
Rolling friction coefficient	μ_r	0.8	0.6	—

using the rainfall method (Härtl and Ooi, 2008; Xia et al., 2019), with which the particles were inserted into the computational domain and allowed to deposit in the hopper under gravity. The insertion zone is located at the top of the bin (1.2 m above the bottom of hopper) with a width of 0.6 m and height of 0.2 m. We adopted the rainfall method because it resembles the physical hopper charging procedure in experiments. Once the hopper was charged up to the same height H as the experiments, we stopped the insertion and let the particles sit in the hopper for a period to reach force equilibrium. The equilibrium was achieved when the maximum velocity of all the inserted particles was less than 1 mm/s. The charging and equilibrium process took about

FIGURE 1 | Overview of the hopper flow problem: **(A)** The top, side and front views of the customized hopper; **(B)** The geometry of the numerical models with simplified hopper thickness; **(C)** The comparison of flow pattern and arching from the DEM and FEM models; **(D)** The comparison of the stress distributions for the consistent flow and arching cases from the DEM and FEM models.
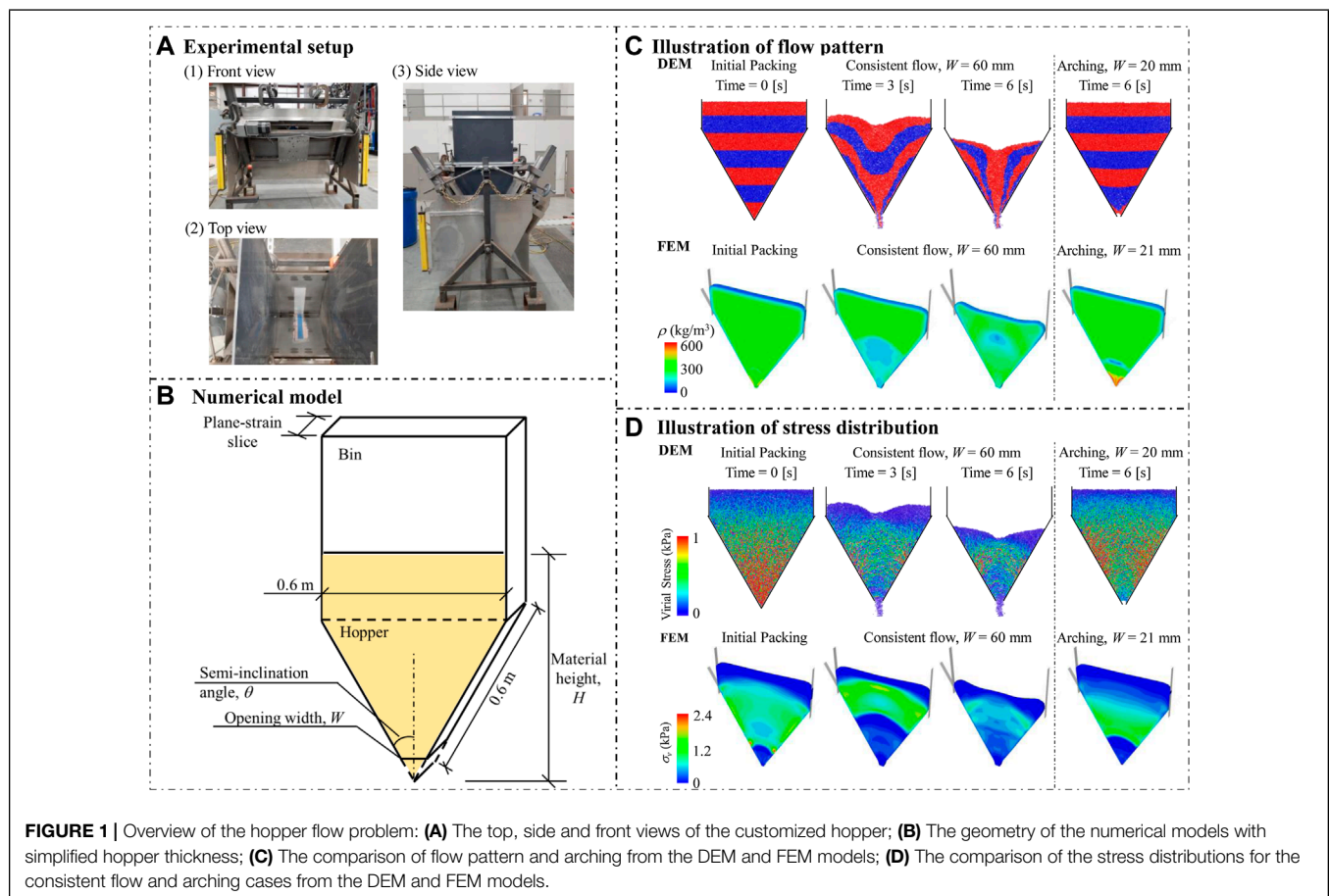
1.5 s of physical time to finish. We trimmed the extra particles that are above the target height after the equilibrium. Different from the experimental procedure, we removed the lower sections of the hopper walls to create an opening with target width to initiate the discharging process. This simplification prevents additional disturbance of the particle packing. To obtain the critical outlet width, we run multiple simulations with gradually smaller opening widths until clogging happens. The mean value of the width of the clogging case and the width of the last case with smooth flow is defined as the critical outlet width, which has an accuracy of ±1.25 mm as we use 2.5 mm step size for hopper opening. The cumulative discharged mass was calculated by multiplying the discharge particle number with the particle mass.

The hopper flow simulation using the continuum FEM model has been described in our previous studies Lu et al. (2021b,a). Briefly, a half slice of the hopper with a thickness of 25 mm is modeled given its plane strain condition and its symmetrical flow pattern. The hopper walls are modeled as rigid bodies, and their interaction with the material is directly simulated through the Coulomb friction model with a wall friction angle of 8.5°. We simulated the charging step by applying gravity on the material and letting it rest until the stress equilibrium is achieved. Note that we assigned initial bulk density and void ratio according to the physical measurement. The following discharging step was realized by sliding sidewalls upwards following the experimental procedure and the material began flowing until the hopper is fully discharged. The mass flow rate q_m is evaluated by extracting and integrating the nodal velocity and the elemental density of all elements at the outlet. The critical outlet width W_{cr} is obtained by the Dichotomy method, in which we simulated two different outlet widths W of flowing and arching situations and then gradually narrow the range of W until a dramatic change of flow responses occurs with two close outlet widths in 1 mm.

3.1.2 Results
Comparing the DEM results with experimental results of hopper discharge, we found that when the rolling friction coefficient μ_r is

in the range of 0.6–1.0, the DEM model provides predictions with a good agreement with the FEM predictions and the experimental measurements. Accordingly, we used $\mu_r = 0.8$ for all the following hopper flow simulations.

Figure 1C presents a qualitative comparison of the flow patterns predicted by the DEM and FEM models, with a hopper semi-inclination angle of 30° and a hopper opening $W = 60$ mm. Note the original distribution of the particles is colored by horizontal bands in the DEM case, while the FEM case shows the bulk density. While both the models predict a smooth discharge, the DEM model shows a funnel flow pattern (i.e., first-in last-out) and the FEM model predicts a mass flow pattern (i.e., first-in first-out). As the corresponding physical experiment of the same hopper configuration tended to yield pattern toward mass flow from our laboratory observation, we surmise that the particle-wall friction coefficient assigned in the DEM simulations might be higher than needed. Normally, lower wall friction tends to yield mass flow patterns in hopper discharge. Nevertheless, the particle-wall interaction parameters chosen in the DEM simulations have negligible influence on the mass flow rate and the critical arching distance reported in the following. When the hopper opening reduces to 20 mm, both models predict hopper arching phenomenon with arch-shaped virial stress distribution (Subramaniyan and Sun, 2008) from the DEM model and the arch-shaped vertical stress distribution from the FEM model in **Figure 1D**. **Figure 1D** also shows the stress distribution for case of $W = 60$ mm. The stress pattern of the two models match each other in general except in the hopper outlet area.

To examine whether the two numerical models can quantitatively capture the effect of outlet width on the discharging flow response, a suite of simulations with different outlet widths are performed. The results of the accumulative discharged mass against time are plotted in **Figure 2A**. For the same hopper opening width W, the DEM model prediction (solid lines) and the FEM model results (dashed line with markers) agree well with each other, especially for the openings W larger than 40 mm. Note that we scaled both the DEM and FEM predictions, because the DEM model has less total material for flow due to its model set-up (trim and hopper opening) and FEM model post-processing assumes the same velocity and density at a node within a time
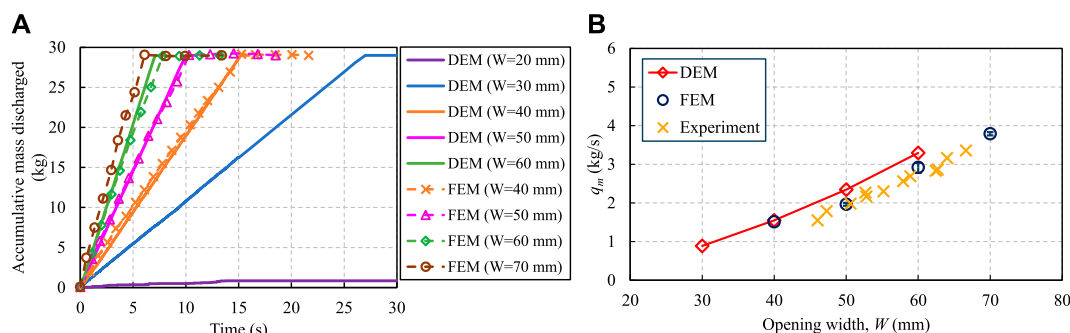
FIGURE 2 | Quantitative comparison of **(A)** the cumulative mass discharged where the case with $W = 20$ mm is clogged, and **(B)** the mass flow rate q_m against hopper opening width W among the DEM and FEM model predictions, and the experimental measurements, where the error bar in FEM results represents the numerical variation caused by different time step size.

increment. **Figure 2B** compares the calculated mass flow rate q_m between the DEM and FEM results, with reference to the experimental measurements for different hopper opening widths. The FEM model predicts a close agreement with the experimental data, whereas the DEM model slightly over-predicts the mass flow rate. The slight over-prediction is primarily due to larger particle-particle porosity of the bulk (and consequently lower total solid fraction of the bulk) than the physical materials in the initial packing. In the DEM simulation, the total mass of the material is nevertheless guaranteed by using a large sphere density, so the bulk density of the packed DEM spheres is comparable to the FEM simulation and the physical material. The coarse-grained spheres in the DEM simulations, without considering any cohesive force between the spheres in this case study, tend to deplete slightly faster from the hopper than the continuum description of the same process.

Moreover, we obtained the critical outlet widths for different semi-inclination angles from the DEM and FEM results, and compared them against the experimental measurements in **Figure 3**. The error bar of the experimental data represents the variation of multiple measurements except the case of inclination angle $\theta = 30°$. Both the FEM and DEM models predicted values of the W_{cr} agree well with the experimental data for different inclination angles. The slight difference between the model predictions and the experimental data for $32^o < \theta < 34^o$ is primarily due to the local effect of pine samples near the outlet area with a non-representative particle size distribution (Lu et al., 2021a). This localization effect is often observed in biorefineries as a variation of critical outlet size (error bar) is observed for the same feeding material.

The quantitative comparison in **Figure 2** and in **Figure 3** demonstrates that both the FEM model and DEM model can reasonably capture the critical flow behavior of milled loblolly pine inside the hopper. If we neglect the required computational cost and modeling effort, we recommend that both models are suitable to inform the operation and design of wedge-shaped hoppers for the flowing of milled biomass.

FIGURE 3 | The variation of the critical outlet width with increasing hopper semi-inclination angle, predicted by the DEM and FEM models along with the experimental measurements. The error bar of the experimental data represents the min-max range of multiple measurements.

3.2 Inclined Plane Flow

Granular flow on an inclined plane is a widely adopted benchmark test to decipher flow physics given it is a well-controlled granular flow system. It can also physically model engineering applications, such as landslides in geohazard mitigation. One of the most 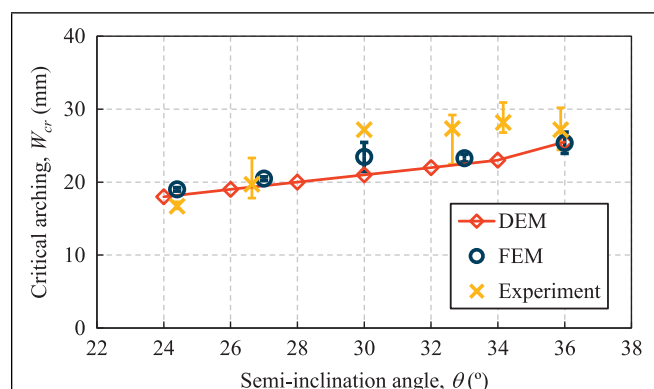intriguing features is its inclusion of flows in both quasi-static and dense flow regimes, which are distinguished by their shear rate and realized simply with a variation of the inclination angle (Pouliquen, 1999; Pouliquen and Forterre, 2002; Jop et al., 2005, 2006; Forterre and Pouliquen, 2008). In this work, we focus on investigating the in-flow velocity and the after-flow material stopping thickness on the plane, by performing FEM and DEM simulations as well as physical inclined plane experiments.

3.2.1 Experimental and Model Setup
Figure 4A presents the customized experimental setup of pine chips flowing on an inclined plane with adjustable inclined angle η, along with its front view sketched in **Figure 4B**. An inclined ramp with a width of 760 mm is fixed on an aluminum frame. A cuboid-shaped material storage bin is installed at the upper end of the ramp with a length of 570 mm, a height of 915 mm, and the same width of 760 mm as the ramp. The sidewall facing the ramp can slide upwards in its plane to initiate material flow at a targeted gate opening. The plane's inclination angle η can be adjusted by changing the height of the two supporting legs near the storage bin. A layer of pine chips is glued on the ramp to form a no-slip boundary condition.

The physical tests started with filling the storage bin with the milled loblolly pine, followed by flow initiation through sliding the gate to a preset height. After the flow stopped, we measured the thickness h_{stop} of the material remained on the ramp using laser displacement sensors. h_{stop} was only characterized at the middle of the ramp along the length of the plane.

Given the symmetrical feature with respect to the middle surface (shown as red plane in **Figure 5A**) of the experiment setup and the observed flow pattern, we constructed a 3D symmetrical FEM model with the same geometry as the physical experiment. For the boundary conditions, the inclined plane was considered as a no-slip boundary with all degrees of freedom been constrained, and the surfaces inside the storage box were considered as full-slip boundaries with no movements at the normal direction and no constraints at the tangential direction. We performed the FEM simulation using the calibrated G-B hypoplastic model (**Section 2.1**) following the same steps as the experiments. Each simulation began with a consolidation step until the stress equilibrium was achieved in the storage bin. The flow was then initiated by releasing the constraints of the nodes at the gate surface within a preset height. We stopped the simulation until material stops flowing, and we quantified the stopping thickness by extracting the material volume fraction in each element above the plane and summing up the heights of the elements occupied by the material.

Constrained by the computational cost, the DEM model for the inclined plane assumed the flow follows plane strain condition. A thin cross-section with a thickness of 15 mm (5 times of the mono-sphere size) in the out-of-plane direction
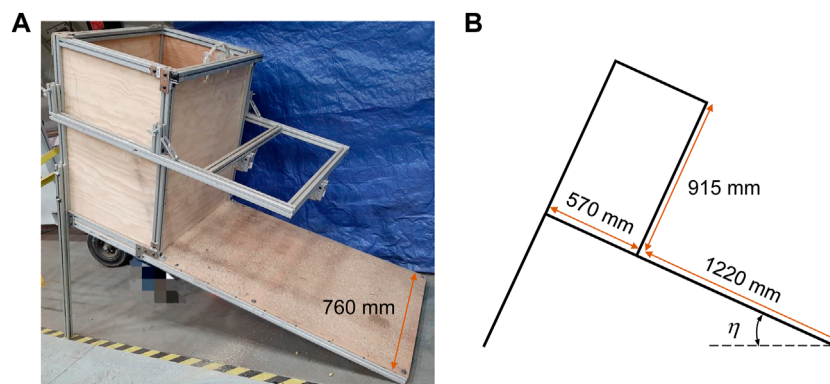
FIGURE 4 | Experimental setup and geometry of the inclined plane tests. **(A)** A plane with a material storage bin at the top is hold by an aluminum frame. The height of the frame below the bin can be adjusted to vary the inclined angle of the plane. **(B)** The front view of the experimental setup.

was modeled with a periodic boundary condition for the two surfaces. The rest of the DEM model geometry was kept the same as the experiments. The plane and storage bin walls were explicitly modeled as rigid walls composed by triangular elements. The initial particle packing inside the storage box was created following the same rainfall procedure as described in **Section 3.1**. Once the storage box was filled up to the target height (i.e., 0.5 m in this study), we stopped the insertion and consolidated the particles until they reached equilibrium. The flow was initiated by raising the right wall of the storage box to a certain height. After the modeled flow stopped, the thickness of the material remained on the ramp was measured by capturing the maximum heights of particles along the ramp.

3.2.2 Results

Figure 5A presents a qualitative comparison of FEM- and DEM-simulated material profiles with the colors denoting the magnitude of flow velocity during a steady-flow state. The "steady-flow state" is defined as the state at which the material height on the ramp stays the same with negligible variance in velocity distribution. The FEM and DEM results generally agree with each other on both the velocity magnitude and the material profile for the inclined angle η = 29.5° and 37°. However, the DEM model cannot capture material flow outside along the ramp side boundaries, as the DEM simulation domain used periodic condition (plane strain assumption) at these boundaries.

Figure 5B quantitatively compares the material stopping thickness h_{stop} along the length of the ramp obtained from
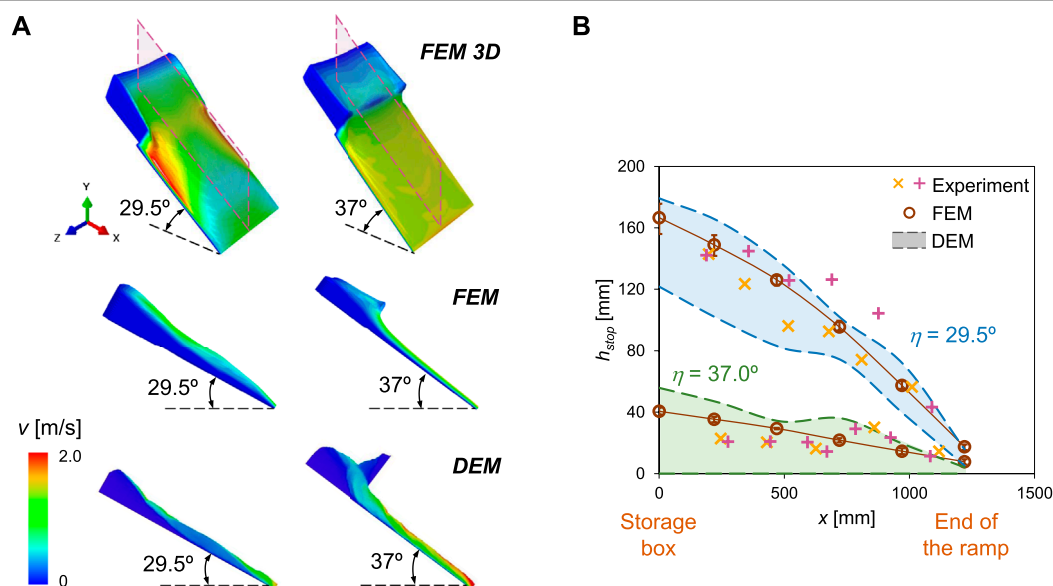
FIGURE 5 | (A) Qualitative comparison of the predicted material profile overlapped with velocity distribution at a steady-flow state for two inclination angles. **(B)** Quantitative comparison of the stopping thickness h_{stop} of the material among the FEM and DEM model predictions and physical measurements.

physical experiments and numerical simulations, in which "×"s and "+"s stand for two experimental measurements with the same plane inclination angle and gate opening height, "○"s represent the FEM results, where the error bars mean the prediction variation from different gate opening heights (22–48 cm for 29.5° ramp and 8–19 cm for 37° ramp); the colored bands between dashed lines are the DEM predicted h_{stop} range with the rolling resistance between 0.6 and 1.0 (as discussed in **Section 3.1.2**). It was found that, at both the inclination angles 29.5° and 37°, the DEM model with the calibrated material parameters can successfully cover the range of experimental measurements using different rolling resistance coefficients. The FEM model results render a smooth material profile and agree with the experimental measurements. Moreover, the small error bars on the FEM data points indicate that the gate opening height, equivalent to the initial flow velocity, has a minor influence on the material stopping thickness, as proved by the experimental observation (note the two experimental measurements of each inclination angle η were measured with the same gate opening, the variation is due to particle packing difference.). Both the quantitative and qualitative comparisons demonstrate the FEM and DEM models with proper material calibration can capture the quasi-static and dense flow regimes.

3.3 Rotating Drum

Angle of Repose (AoR) is an effective macroscopic property that is often used to characterize the mechanical behavior of granular materials. AoR has been widely used as a quantitative measure of granular materials flowability under stress-free condition. For example, AoR is one of the parameters utilized in the design of hoppers and storage bins (Frankowski and Morgeneyer, 2013; Beakawi Al-Hashemi and Baghabra Al-Amoudi, 2018; Hamed et al., 2022). Two types of AoR can be identified, namely, the static and the dynamic one. They differ by a few degrees with the smaller one being the dynamic AoR. The dynamic AoR is defined as the inclination angle of the free surface with respect to the horizontal of the formed material heap, and it is linked to the segregation phenomena of the particulate materials (Beakawi Al-Hashemi and Baghabra Al-Amoudi, 2018). In this work, the dynamic AoR of loblolly pine chips was studied using the rotating drum test. Both DEM and FEM were used to simulate the test. In addition, the dynamic AoR of the *as-ground* pine chips was physically measured

in the laboratory as a benchmark value for the numerical models.

3.3.1 Experimental and Model Setup

A sealed polycarbonate drum is used to measure the dynamic AoR as shown in **Figure 6A**. The drum is 14.5 cm in internal diameter and 20.2 cm long. The cylinder was loaded up to 50% of its height with the milled loblolly pine (around 303.8 +/− 0.2 g) following the standard testing procedure. We closed the drum with a transparent polycarbonate sheet and placed it on the revolver. The revolver was rotated at a fixed speed of 20 revolutions per minute (rpm) until the free plane surface was formed with a constant slope, see **Figure 6A**. The inclination angle between the free surface and the horizon is the dynamic AoR and was measured manually from outside of the transparent side of the cylinder using a digital protractor (with readout to 0.1°). Dynamic AoR was measured 10 times using different batches to minimize the measurement error and the sample variability.

Different rotational speeds were attempted in the simulations of the rotating drum test using DEM and FEM. **Figure 6B** shows the full 3D DEM model with the same geometry as the experiments. The calibrated contact model parameters with 3 mm mono-sphere particles reported in the previous section were used for the drum simulation. We start the simulation by filling the stationary drum up to 50% of the drum volume using a random packing algorithm. This is followed by an equilibrium step, where the particles rearrange themselves under the influence of gravity. Afterwards, we rotate the drum with a preset constant rotational speed. Once the steady-state is achieved, we extract the slope of the free surface as the dynamic AoR. We used 1 μs as the step size and simulated 10 s of rotating.

The configuration of the FEM model is presented in **Figure 6C**, where the cross-section geometry is exactly same as the experiment and a reduced thickness of 25 mm along the axial direction is utilized to save the computational cost. This plane-strain consideration was validated by a full 3D modeling study, in which the predicted dynamic AoR is uniform along the axial direction and equals to the value predicted from the plane-strain case. A symmetrical boundary condition along the thickness direction is applied on the front and the back surfaces of the FEM model, while the contact between the drum and the material is explicitly modeled using the Coulomb friction law. We

FIGURE 6 | Rotating drum test configuration: the experimental set-up **(A)**; the DEM model set-up with the same dimension as the experiment **(B)**; and the geometrical configuration of the FEM model **(C)**.

FIGURE 7 | Three particle flow patterns observed at different rotational speeds. The top row are snapshots obtained from FEM simulations, while the DEM snapshots are displayed at the bottom row.

analyzed the influence of wall friction on the modeling results and we found that a wall friction angle greater than 20° results in a stable dynamic AoR with negligible variation. Therefore, friction angle of 20° is used for all rotating drum simulations. The simulation domain was meshed with element size of 5 mm and a time step of 10–20 μs was used for all simulation cases.

3.3.2 Results

The flow pattern in the rotating drum differs due to differences in rotational speeds, the wall friction angle between the drum surface and the material, and the filling degree (Frankowski and Morgeneyer, 2013; Zheng and Yu, 2015; Beakawi Al-Hashemi and Baghabra Al-Amoudi, 2018). **Figure 7** depicts three different particle flow patterns (i.e., rolling, cascading, and centrifuging) observed in the FEM and DEM simulations of the rotating drum at different rotational speeds. The FEM snapshots display a color-coded bulk density, while the DEM snapshots show the particles configuration and the outline of the free surface at a cross-section. The rolling pattern occurs at a low rotational speed of 10 rpm and is characterized by a flat free surface that arises due to the continuous circulation of the particles in the drum. When the drum rotates at an intermediate rotational speed of 50 rpm, particles undergo cascading pattern at which the free surface fails to maintain a flat shape. The exhibited curvature in the free surface and expanded volume of material are associated with the spatial heterogeneity of porosity with denser interior region and higher porosity near the surface. Fast rotational speeds (300 rpm) give rise to the centrifuging regime because the centrifugal force outweighs gravity. In this regime, the particles adhere to the drum and form a ring-like shape.

The effect of the rotational speed on the dynamic AoR within the rolling regime was investigated. **Figure 8** illustrates the change of the dynamic AoR with the increasing rotational

speed. The experimentally measured value of AoR at the rotational speed of 20 rpm is overlapped in the same figure. The error bar represents the standard deviation of multiple measurements. The quantitative comparison shows the DEM model predicted value has an excellent agreement with the experimental data while the FEM model slightly over-predicts the dynamic AoR about 1.5° for the rotation speed of 20 rpm. In addition, the two models correctly capture the increase of the dynamic AoR with the increasing rotational speeds, which is consistent with the observations and findings in (Frankowski and Morgeneyer, 2013). We also observe the slight difference in the predicted rate of increase with FEM showing a faster rate. This flow characteristic will be investigated using experiments in a future study.

FIGURE 8 | Dynamic angle of repose (AoR) versus the rotational speed from the FEM and DEM model predictions and the experimental measurement.
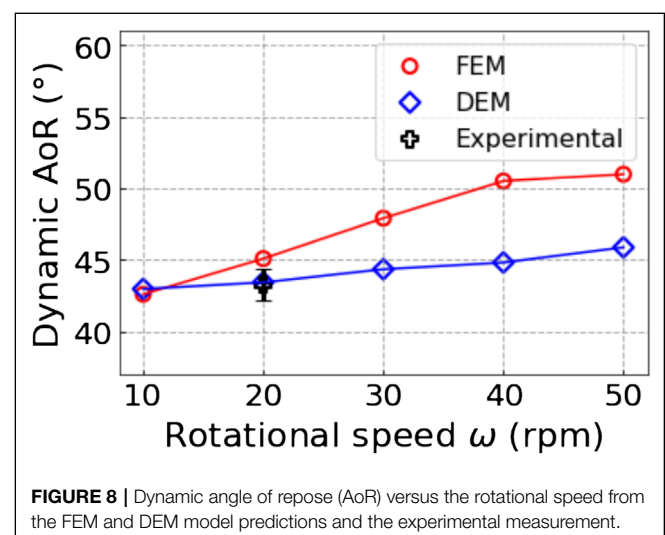
4 DISCUSSION

Generally, continuum-mechanics models are more efficient and effective for modeling bulk granular flow problems at large scales, while the discrete-particle models are more often applied to understand the interactions of particles at smaller scales. The three flow cases presented in this work have demonstrated that both the continuum-mechanics model with a classic constitutive law and the discrete-particle model with a group of sophisticated contact laws can quantitatively simulate the biomass granular flow behavior at different scales. Nevertheless, the two modeling approaches are found to apparently have distinctive advantages and disadvantages given their fundamental differences described in **Section 2**.

- The constitutive law of the continuum-mechanics FEM model only requires eight material parameters to describe the flow behavior of the milled loblolly pine, whereas the contact laws and mono-sphere particles of the discrete-particle DEM model require 14 parameters. In addition, most of the material parameters of the FEM model (**Table 1**) have physical meaning and can be directly obtained from the lab characterization data (Lu et al., 2021b). In contrast, the particle-scale contact parameters (**Table 2**) were all fitted through a single set of cyclic axial compression data (Xia et al., 2019; Chen et al., 2022), though more sets of data can be used. The risk is that, if the objective fitting function has multiple saddle points, the calibration process may result in a local set of optimal values instead of their true global optimal.
- The Coulomb friction between the wall and the granular material is directly realized in the continuum FEM model. The wall friction angle is an independent parameter that can be assigned for any given wall materials and granular materials. In contrast, the particle-based DEM model indirectly captures wall friction by adjusting contact model parameters (e.g., frictional coefficient and rolling friction coefficient in this study). This disadvantage makes the DEM model double the effort in parameterization.
- Limited by the continuum assumption, the FEM model cannot accurately simulate the sharp boundaries between the moving material and the void (i.e., void in this paper). In contrast, the particle-based DEM model can easily handle these boundaries. For example, the FEM model predicts a extremely small mass flow rate for hopper arching shown in **Figures 1C,D**, while the DEM can predict a complete stop of material flow. Another example is the centrifuging pattern of rotary drum shown in **Figure 7**. The continuum FEM model represents the void space with an extremely-low density material, while the particle DEM model can physically simulate the centrifuging pattern with the void at the center.
- The initial void ratio/porosity of a granular system plays a significant role in its flow pattern (surge flow v. s. mass flow, see Lu et al. (2021a)). The initial value of the void ratio/porosity can be assigned directly in the continuum FEM model given its constitutive model is formulated in the framework of the critical state particle mechanics (i.e., the state of a granular assembly is determined by the stress tensor and the void

ratio, and the assembly can shear/flow infinitely under a critical state without volumetric strain variation). The coarse-grained DEM model describes bulk solids using spheres, which limits its theoretical min-max void ratio/porosity range. To overcome this limit, dilation of DEM particle volume can be used to reduce the initial void volume fraction (Lattanzi and Stickel, 2020), which yet requires additional force equilibrium afterwards. Also, the initial particle packing (i.e., void ratio/porosity) prepared using the rain fall method of the DEM model results in the inter-particle void ratio in a bulk that is often larger than the physical material. Particle shape-resolved DEM model is another way to realistically realize any initial porosity of materials; yet, its computational cost is not affordable for large systems Xia et al. (2021).

In addition to the capability differences in capturing physics between the continuum model and the particle model, the computational cost of the two models is also distinctive. **Figure 9** shows the comparison of computational cost between the continuum FEM model and the DEM model for typical cases of the three simulated flow problems. Note we used the CPU core hours—the computational time multiplied by the number of cores, to quantify the computational cost. **Figure 9** shows that the DEM model took more core hours for all three cases, which is though expected. However, regarding the computational cost, the degree of advantage of the continuum FEM model over the DEM model varies in each case. For the hopper simulation, the computational cost of the case with semi-inclination angle 30° and outlet opening width 60 mm is presented with modeled physical flow time 11 s for both the FEM model and the DEM model. Because only a single layer of spheres (3 mm) in the out-of-plane direction for hopper were simulated by the particle DEM model, the computational efficiency of DEM is close to the continuum model. However, for the inclined plate simulation with inclination angle 29.5^o modeling 18.8 s physical time, the
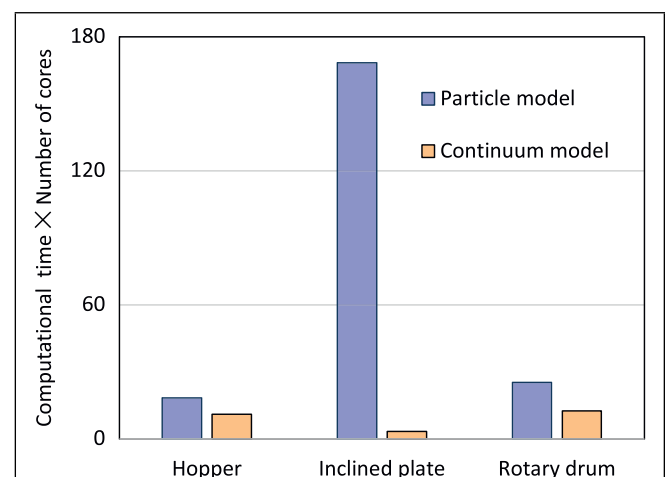
FIGURE 9 | Comparison on the computational cost between the continuum FEM model and the particle DEM model for the hopper flow simulation ($\theta = 30^O, W = 60mm$ and physical time $t = 11s$), the inclined plate simulation ($\eta = 29.5^O, t = 18.8\ s$), and the rotary drum simulation ($\omega = 20$ rpm, $t = 10\ s$).

FEM model outperforms the particle model with about 40 times the computational time advantage. This is because the high dimension ratio between a typical size of the experimental set-up and the size of the DEM spheres (3 mm in diameter) requires a huge amount of DEM spheres to represent the material, while the FEM model can mesh the 3D domain using relative coarse meshes and takes advantage of the non-slip boundary condition between the material and inclined plate wall. However, this huge amount of computational cost advantage of the continuum model does not hold for the lab-scale rotary drum. Only two times of computational cost is gained by the continuum model over the particle model for the case with 20 rpm rotation modeling 10 s physical time.

The above comparison of physics capturing and computational cost shows that the FEM model is preferred when the targeted problems are at pilot- or industry-scales and its continuum assumption is satisfied. In contrast, the DEM model is better at simulating lab-scale granular systems with discontinuities. A more sophisticated strategy is to couple the advantages of the continuum and particle models and simulate the granular flow problems using the multi-scale concurrent framework (Liang and Zhao, 2019). Take the hopper as an example, the bulk hopper material, as well as the interaction between the material and hopper wall, can be modeled using the efficient continuum FEM model. While the domain in the vicinity of the hopper outlet, including the particle flow into the downstream feeder/reactor, can be better handled by the particle DEM model. Nevertheless, a coupled FEM-DEM modeling approach will require significant further development and validation, before it can be reliably introduced for engineering applications that involve complex geometries.

5 CONCLUSION

This study reports the detailed comparison of a continuum-mechanics model and a coarse-grained discrete-particle model on the predictive fidelity and computational cost for simulating biomass granular flow. After briefly introducing the two models, we benchmarked their predictions against physical measurements for a lab-scale rotating drum flow test, a pilot-scale hopper flow test, and a full-scale inclined plate flow test. The predicted bulk flow behavior from the two models, i.e., the dynamic angle of repose of the rotary drum, the mass flow rate and the critical outlet width of hopper, and the stopping thickness of the inclined plate flow, all matched well with the experimental measurements. However, their fundamental differences in theories and solution algorithms resulted in distinctive apparent advantages and disadvantages of capturing

granular flow physics. The continuum-mechanics model has the apparent advantages of parameterization in material and wall friction, direct initial state assignment, and computational efficiency for large-scale flow systems. In contrast, the discrete-particle model is more robust for handling discontinuous flow problems and decipher particle interaction during flow for smaller-scale systems. This comparative study has provided insights that industry stakeholders may find helpful when choosing suitable and experiment-informed/validated numerical models and packages as advanced design tools to assist the design and optimization of biomass granular flow systems.

DATA AVAILABILITY STATEMENT

The original contributions presented in the study are included in the article, further inquiries can be directed to the corresponding authors.

AUTHOR CONTRIBUTIONS

WJ conceptualized the article, drafted the introduction, methods and discussion sections, supervised the FEM modeling and edited full manuscript. YL performed all FEM analysis and drafted the inclined plate section; FC performed DEM analysis of the hopper and the inclined plate and drafted the hopper section; AH performed DEM modeling of the rotary drum and drafted the rotary drum section; NS and JK performed all the experimental characterization and edited full manuscript; YX supervised the DEM modeling and edited full manuscript. SD and QC edited full manuscript.

FUNDING

ACKNOWLEDGMENTS

REFERENCES

Bauer, E. (1996). Calibration of a Comprehensive Hypoplastic Model for Granular Materials. *Soils Found.* 36, 13–26. doi:10.3208/sandf.36.13

Beakawi Al-Hashemi, H. M., and Baghabra Al-Amoudi, O. S. (2018). A Review on the Angle of Repose of Granular Materials.

Powder Technol. 330, 397–417. doi:10.1016/j.powtec.2018.02.003

Chen, F. (2022). *Discrete Element Modeling of the Shape- and History-dependent Behavior of Granular Materials.* Ph.D. thesis (Clemson, SC, USA: Clemson University).

Chen, F., Xia, Y., Klinger, J. L., and Chen, Q. (2022). A Set of Hysteretic Nonlinear Contact Models for DEM:Theory, Formulation, and

Application for Lignocellulosic Biomass. *Powder Technol.* 399, 117100. doi:10.1016/j.powtec.2021.117100

Cheng, Z., Leal, J. H., Hartford, C. E., Carson, J. W., Donohoe, B. S., Craig, D. A., et al. (2021). Flow Behavior Characterization of Biomass Feedstocks. *Powder Technol.* 387, 156–180. doi:10.1016/j.powtec.2021.04.004

Chung, Y. (2006). *Discrete Element Modelling and Experimental Validation of a Granular Solid Subject to Different Loading Conditions*. Ph.D. thesis (Edinburgh, Scotland: University of Edinburgh).

Cundall, P. A., and Strack, O. D. L. (1979). A Discrete Numerical Model for Granular Assemblies. *Géotechnique* 29, 47–65. doi:10.1680/geot.1979.29.1.47

Dale, B. (2017). A Sober View of the Difficulties in Scaling Cellulosic Biofuels. *Biofuels, Bioprod. Bioref.* 11, 5–7. doi:10.1002/bbb.1745

DOE-BETO (2016). "Biorefinery Optimization Workshop Summary Report," in *Tech. Rep.* (Chicago, IL, United States: Bioenergy Technologies Office, Office of Energy Efficiency and Renewable Energy, U.S. Department of Energy).

Forterre, Y., and Pouliquen, O. (2008). Flows of Dense Granular Media. *Annu. Rev. Fluid Mech.* 40, 1–24. doi:10.1146/annurev.fluid.40.111406.102142

Frankowski, P., and Morgeneyer, M. (2013). Calibration and Validation of Dem Rolling and Sliding Friction Coefficients in Angle of Repose and Shear Measurements. *AIP Conf. Proc.* 1542, 851–854. doi:10.1063/1.4812065

Gudehus, G. (1996). A Comprehensive Constitutive Equation for Granular Materials. *Soils Found.* 36, 1–12. doi:10.3208/sandf.36.1

Guo, Y., Chen, Q., Xia, Y., Klinger, J., and Thompson, V. (2021). A Nonlinear Elasto-Plastic Bond Model for the Discrete Element Modeling of Woody Biomass Particles. *Powder Technol.* 385, 557–571. doi:10.1016/j.powtec.2021.03.008

Guo, Y., Chen, Q., Xia, Y., Westover, T., Eksioglu, S., and Roni, M. (2020). Discrete Element Modeling of Switchgrass Particles under Compression and Rotational Shear. *Biomass Bioenergy* 141, 105649. doi:10.1016/j.biombioe.2020.105649

Hamed, A., Xia, Y., Saha, N., Klinger, J., Lanning, D. N., and Dooley, J. (2022). Flowability of Crumbler Rotary Shear Size-Reduced Granular Biomass: An Experiment-Informed Modeling Study on the Angle of Repose. *Front. Energy Res.* 10, 859248. doi:10.3389/fenrg.2022.859248

Härtl, J., and Ooi, J. Y. (2008). Experiments and Simulations of Direct Shear Tests: Porosity, Contact Friction and Bulk Friction. *Granul. Matter* 10, 263–271. doi:10.1007/s10035-008-0085-3

Herle, I., and Gudehus, G. (1999). Determination of Parameters of a Hypoplastic Constitutive Model from Properties of Grain Assemblies. *Mech. Cohes.-Frict. Mat.* 4, 461–486. doi:10.1002/(SICI)1099-1484(199909)4:5<461::AID-CFM71>3.0.CO;2-P

Hernandez, S., Westover, T. L., Matthews, A. C., Ryan, J. C. B., and Williams, C. L. (2017). Feeding Properties and Behavior of Hammer- and Knife-Milled Pine. *Powder Technol.* 320, 191–201. doi:10.1016/j.powtec.2017.07.002

Hess, J. R., Wright, C. T., and Kenney, K. L. (2007). Cellulosic Biomass Feedstocks and Logistics for Ethanol Production. *Biofuels, Bioprod. Bioref.* 1, 181–190. doi:10.1002/bbb.26

Horabik, J., and Molenda, M. (2014). Mechanical Properties of Granular Materials and Their Impact on Load Distribution in Silo: a Review. *Sci. Agric. Bohem.* 45, 203–211. doi:10.1515/sab-2015-0001

Ilic, D., Williams, K., Farnish, R., Webb, E., and Liu, G. (2018). On the Challenges Facing the Handling of Solid Biomass Feedstocks. *Biofuels, Bioprod. Bioref.* 12, 187–202. doi:10.1002/bbb.1851

Jin, W., Klinger, J. L., Westover, T. L., and Huang, H. (2020a). A Density Dependent Drucker-Prager/cap Model for Ring Shear Simulation of Ground Loblolly Pine. *Powder Technol.* 368, 45–58. doi:10.1016/j.powtec.2020.04.038

Jin, W., Stickel, J. J., Xia, Y., and Klinger, J. (2020b). A Review of Computational Models for the Flow of Milled Biomass Part Ii: Continuum-Mechanics Models. *ACS Sustain. Chem. Eng.* 8, 6157–6172. doi:10.1021/acssuschemeng.0c00412

Jop, P., Forterre, Y., and Pouliquen, O. (2006). A Constitutive Law for Dense Granular Flows. *Nature* 441, 727–730. doi:10.1038/nature04801

Jop, P., Forterre, Y., and Pouliquen, O. (2005). Crucial Role of Sidewalls in Granular Surface Flows: Consequences for the Rheology. *J. Fluid Mech.* 541, 167–192. doi:10.1017/S0022112005005987

Kruggel-Emden, H., Wirtz, S., and Scherer, V. (2008). A Study on Tangential Force Laws Applicable to the Discrete Element Method (Dem) for Materials with Viscoelastic or Plastic Behavior. *Chem. Eng. Sci.* 63, 1523–1541. doi:10.1016/j.ces.2007.11.025

Lattanzi, A. M., and Stickel, J. J. (2020). Hopper Flows of Mixtures of Spherical and Rod-like Particles via the Multisphere Method. *AIChE J.* 66, e16882. doi:10.1002/aic.16882

Liang, W., and Zhao, J. (2019). Multiscale Modeling of Large Deformation in Geomechanics. *Int. J. Numer. Anal. Methods Geomech.* 43, 1080–1114. doi:10.1002/nag.2921

Liao, D., and Yang, Z. (2021). Non-coaxial Hypoplastic Model for Sand with Evolving Fabric Anisotropy Including Non-proportional Loading. *Int. J. Numer. Anal. Methods Geomechanics* 45, 2433–2463. doi:10.1002/nag.3272

Lu, Y., Jin, W., Klinger, J., and Dai, S. (2021a). Flow and Arching of Biomass Particles in Wedge-Shaped Hoppers. *ACS Sustain. Chem. Eng.* 9, 15303–15314. doi:10.1021/acssuschemeng.1c05628

Lu, Y., Jin, W., Klinger, J., Westover, T. L., and Dai, S. (2021b). Flow Characterization of Compressible Biomass Particles Using Multiscale Experiments and a Hypoplastic Model. *Powder Technol.* 383, 396–409. doi:10.1016/j.powtec.2021.01.027

Mašín, D. (2005). A Hypoplastic Constitutive Model for Clays. *Int. J. Numer. Anal. Meth. Geomech.* 29, 311–336. doi:10.1002/nag.416

Mindlin, R. D., and Deresiewicz, H. (1953). Elastic Spheres in Contact under Varying Oblique Forces. *J. Appl. Mech.* 20, 327–344. doi:10.1115/1.4010702

Pouliquen, O., and Forterre, Y. (2002). Friction Law for Dense Granular Flows: Application to the Motion of a Mass Down a Rough Inclined Plane. *J. Fluid Mech.* 453, 133–151. doi:10.1017/S0022112001006796

Pouliquen, O. (1999). Scaling Laws in Granular Flows Down Rough Inclined Planes. *Phys. fluids* 11, 542–548. doi:10.1063/1.869928

Ramírez-Gómez, Á. (2016). Research Needs on Biomass Characterization to Prevent Handling Problems and Hazards in Industry. *Part. Sci. Technol.* 34, 432–441. doi:10.1080/02726351.2016.1138262

Salehi, H., Poletto, M., Barletta, D., and Larsson, S. H. (2019). Predicting the Silo Discharge Behavior of Wood Chips - A Choice of Method. *Biomass bioenergy* 120, 211–218. doi:10.1016/j.biombioe.2018.11.023

Stasiak, M., Molenda, M., Bańda, M., Wiącek, J., Parafiniuk, P., Lisowski, A., et al. (2019). Mechanical Characteristics of Pine Biomass of Different Sizes and Shapes. *Eur. J. Wood Prod.* 77, 593–608. doi:10.1007/s00107-019-01415-w

Subramaniyan, A. K., and Sun, C. T. (2008). Continuum Interpretation of Virial Stress in Molecular Simulations. *Int. J. Solids Struct.* 45, 4340–4346. doi:10.1016/j.ijsolstr.2008.03.016

Wójcik, M., and Tejchman, J. (2009). Modeling of Shear Localization during Confined Granular Flow in Silos within Non-local Hypoplasticity. *Powder Technol.* 192, 298–310. doi:10.1016/j.powtec.2009.01.021

Xia, Y., Chen, F., Klinger, J. L., Kane, J. J., Bhattacharjee, T., Seifert, R., et al. (2021). Assessment of a Tomography-Informed Polyhedral Discrete Element Modelling Approach for Complex-Shaped Granular Woody Biomass in Stress Consolidation. *Biosyst. Eng.* 205, 187–211. doi:10.1016/j.biosystemseng.2021.03.007

Xia, Y., Lai, Z., Westover, T., Klinger, J., Huang, H., and Chen, Q. (2019). Discrete Element Modeling of Deformable Pinewood Chips in Cyclic Loading Test. *Powder Technol.* 345, 1–14. doi:10.1016/j.powtec.2018.12.072

Xia, Y., Stickel, J. J., Jin, W., and Klinger, J. (2020). A Review of Computational Models for the Flow of Milled Biomass Part I: Discrete-Particle Models. *ACS Sustain. Chem. Eng.* 8, 6142–6156. doi:10.1021/acssuschemeng.0c00402

Yi, H., Puri, V. M., Lanning, C. J., and Dooley, J. H. (2020a). "*Determination of Fundamental Mechanical Properties of Biomass Using the Cubical Triaxial Tester to Model Biomass Flow*," in *2020 ASABE Annual International Virtual Meeting* (St. Joseph, Michigan, USA: American Society of Agricultural and Biological Engineers), 1. doi:10.13031/aim.202000058

Yi, H., Puri, V. M., Lanning, C. J., and Dooley, J. H. (2020b). "*Finite Element Modeling of Biomass Hopper Flow*," in *2020 ASABE Annual International Virtual Meeting* (St. Joseph, Michigan, USA: American Society of Agricultural and Biological Engineers), 1. doi:10.13031/aim.202000059

Zheng, Q. J., and Yu, A. B. (2015). Modelling the Granular Flow in a Rotating Drum by the Eulerian Finite Element Method.

Powder Technol. 286, 361–370. doi:10.1016/j.powtec.2015.08.025

Zhou, Y. C., Wright, B. D., Yang, R. Y., Xu, B. H., and Yu, A. B. (1999). Rolling Friction in the Dynamic Simulation of Sandpile Formation. *Phys. A Stat. Mech. its Appl.* 269, 536–553. doi:10.1016/S0378-4371(99)00183-1

Impacts of Biologically Induced Degradation on Surface Energy, Wettability, and Cohesion of Corn Stover

Juan H. Leal[1]*, Eric J. Meierdierks[1], Ricardo Navar[1], Cameron M. Moore[2], Allison E. Ray[3] and Troy A. Semelsberger[1]*

[1]Material Physics Applications Division, Los Alamos National Laboratory, Los Alamos, NM, United States, [2]Chemistry Division, Los Alamos National Laboratory, Los Alamos, NM, United States, [3]Science and Technology, Idaho National Laboratory, Idaho Falls, ID, United States

The impacts of biological degradation on surface area, surface energy, wettability, and cohesion of anatomically fractionated (i.e., leaf, stalk, and cob) and bulk corn stover are presented in this study. The physical, thermal and chemical properties of corn stover are critical material attributes that not only influence the mechanical processing and chemical conversion of corn stover, but also the bulk solids handling and transport. The measured surface areas were observed to be dependent on the degree of biological degradation (mild vs. moderate vs. severe) and on the anatomical fraction. The surface area of the bulk corn stover samples increased with the degree of biological degradation. The leaf fraction was the most sensitive to biological degradation, resulting in an increase in surface area from $0.5 \, m^2/g$ (mildly degraded) to $1.2 \, m^2/g$ (severely degraded). In contrast, the surface area of the cob fraction remained relatively unaffected by the degree of biological degradation (i.e., mildly degraded–$0.55 \, m^2/g$, severely degraded–$0.40 \, m^2/g$. All biologically degraded samples resulted in significant changes to the surface chemistry (evidenced by an increase in surface energy. As a general trend, the surface energy of bulk corn stover increased with the degree of biological degradation—the same trend was observed for the leaf and stalk anatomical fractions; however, the surface energy for the cob fraction remained unchanged. Wettability, calculated from surface energy, for bulk corn stover samples did not reveal any discernable trend with the degree of biological degradation. However, trends in wettability were observed for the anatomical fractions, with wettability increasing for the stalk and leaf fractions, and decreasing for the cob fraction. Excluding the cob fraction, the work of cohesion increased with the degree of biological degradation. Understanding the impacts of biological degradation on the physical, chemical and thermal properties of corn stover offers insights to improve the overall operational reliability, efficiency and economics of integrated biorefineries.

Keywords: surface energy, biological heating, degradation, corn stover, cohesion, wettability

1 INTRODUCTION

Global energy consumption continues to increase steadily as predicted by the United States. Energy Information Administration (EIA), with renewables slated to be the fastest growing energy source by 2040 (EIA, 2019). As energy demands increase, so does the importance of securing our nation's energy supplies, and with global climate change as a serious concern, the motivation for the United States and others in the global community to work towards replacing petroleum with renewable energy sources is gaining momentum. Currently, almost half (45%) of renewable energy used in the United States is biomass sourced, making up 5% of total energy usage—*which has more than doubled in the past 20 years* (Renewable Energy Sources, 2019). After the 3 Billion Ton study, the UnitedStates Department of Energy (DOE) has determined that there is a sustainable supply of biomass to potentially replace 30% of petroleum production with biofuel by 2030 (Perlack, 2005; Perlack et al., 2011; Langholtz et al., 20162016).

Biomass is a renewable, low cost, and abundant feedstock with established conversion methods to biofuels and platform chemicals; however, the commercialization of Integrated Biorefineries (IBR) is still not achievable. The challenges facing IBRs are associated with the lack of throughput and operational reliability of bulk solids and handling; thus preventing IBRs from achieving the DOE technical cost target of ethanol at $3.00 per gallon of gasoline (gge) (Harmon et al., 2017). In order to achieve the cost target, the operational reliability (i.e., time on stream) of a bio-refinery must exceed 90% (currently estimated around 30%) (Biorefinery Optimization Workshop Summary, 2016). Critical material attributes and feedstock variability are largely responsible for the inconsistent and unreliable operations of bulk solids handling and transport. Critical material attributes include (but not limited to): moisture content, surface area, particle size, aspect ratios, wettability, cohesion and anatomical fraction. The critical material attributes investigated in this paper are anatomical fraction, wettability, surface area, and ash.

Biomass storage conditions (time, temperature, environment) is a major source of feedstock variability that directly impacts the quality of feedstock through changes in the critical material attributes (Searcy et al., 2015; Nagle et al., 2020). Biomass storage is a necessary process because the harvest window is much shorter than the required year-long processing window. A known challenge with biomass storage is biologically induced degradation, which occurs in piles or bales of organic material such as corn stover (Smith et al., 2020). Biological degradation is complex process resulting from respiration of plant tissues, abiotic oxidation and microbial degradation—resulting in the loss of valuable sugars, and dry-matter (Bose et al., 2020).

The biological degradation of biomass directly affects the quality of the feedstock, which in turn influences the overall conversion, yield and economics of IBRs (Smith et al., 2014; Ray et al., 2020). Biological degradation is analogous to composting which involves three types of bacteria, psychrophilic, mesophilic, and thermophilic. (Hanson-Harding, 2013) Biological degradation can be broadly grouped into microbial-induced degradation, thermal degradation and partial/complete oxidation. Microbial-induced degradation is the result of bacteria breaking down the biomass. Thermal degradation is the temperature dependent degradation (i.e., decomposition) of biomass in the presence or absence of oxygen. Under adiabatic conditions, the bale temperature continues to rise to the point where partial oxidative degradation starts. Complete oxidation only proceeds when the oxygen concentration is high enough to support combustion. Prior to complete combustion, partial oxidation is the dominate reaction because oxygen is the limiting reactant. The products from biological heating is a function of time, temperature, and oxygen concentration. A deeper understanding how biological heating contributes to feedstock variability offers opportunities for engineering improvements to handle the range of feedstock properties while still maintaining continuous operation.

The objective of this research is to investigate the effects that biological heating has on corn stover properties such as surface area, surface energy, cohesion, and wettability. This paper presents the characterization of 21 samples (bulk and anatomical fractions) among five bales that were visually identified as being exposed to varying degrees of biologically degradation.

2 MATERIALS AND METHODS

2.1 Corn Stover Samples

Corn stover, the residue left after corn (*Zea mays*) has been harvested, is the greatest source of agricultural residue in the United States (Turhollow et al., 2014; Bradley et al., 2019). Corn stover consists of stalks, leaves, cobs and is a low-cost material for the production and supply of biofuel and platform chemicals (Kumar et al., 2008; Liu et al., 2014; Woźniak et al., 2021). Samples of corn stover were provided by Idaho National Laboratory (INL) for surface energy analysis and were stored in sealed plastic bags at room temperature. All samples were sourced from five bales (bale 1, 2, 3, 5, and 6) collected within a single field in Iowa and dissected into three categories based on visual identification of biologically induced heating or degradation. **Figure 1A** shows a segmented bale affected by biological degradation. There is a visual difference between the mildly heated (**Figure 1B**), which are light in color, and the severely heated, (**Figure 1C**) darker and almost black, samples. The stalk, leaf, and cob (anatomical fractions) were separated from part of bale 5 by visual inspection into 3 degrees of heating—mild 1), moderate 2), and severely 3) heated corn stover (**Figure 2**). All samples were then processed through three stages of milling. First through a Vermeer BG480 bale processer fitted with a 75 mm screen, followed by a Bliss Hammermill with a 25 mm screen. Samples were further milled using a Thomas Model 4 Wiley knife mill (Thomas Scientific, Swedesboro, NJ) fitted with a 2 mm screen producing 21 samples (**Table 1**) and were placed in plastic grab bags (25 g).

FIGURE 1 | (A) A dissected bale showing various degrees of biological degradation, **(B)** a closer look at the mildly degraded section showing little to no browning, and **(C)** severely degraded corn stover appearing very dark, nearly black (images provided by staff at Idaho National Laboratory*).
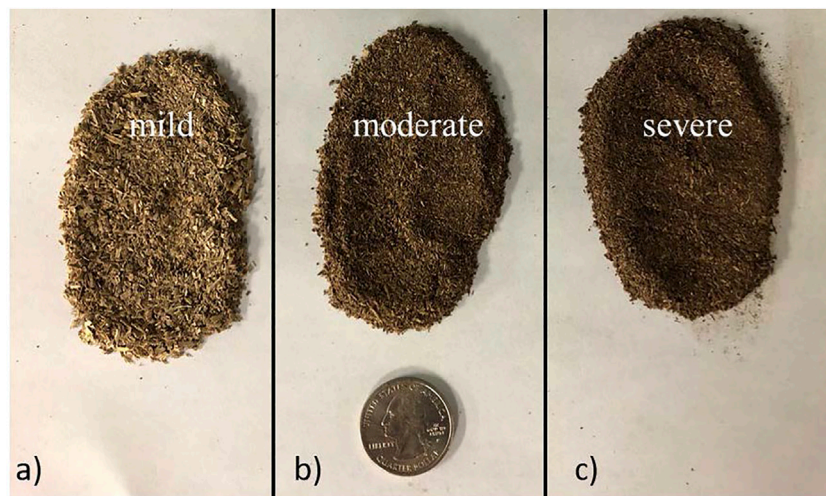
FIGURE 2 | (A) 2 mm grind of mildly heated corn stover (leaf), **(B)** moderately heated, **(C)** severely heated.

2.2 Sample Drying

The as-received moisture content of the corn stover samples were measured using our TGA (thermal gravimetric analyzer). The as-received moisture contents ranged from 7–15 wt%. All samples were dried to moisture contents less than 2 wt% in a custom built in-house drying station consisting of a packed-bed, convection oven and argon purge gas. Sample drying was necessary to obtaining surface area measurements using the nitrogen adsorption technique (residual moisture would produce a virtual leak). The samples were weighed and loaded into a stainless steel tube (O.D. = 1 inch, Length = 8 inches) which was then placed into the convection oven and connected to the

UHP argon purge gas. The isothermal drying temperature was maintained at 45°C during the 10 h drying cycle. The argon flow rate through the packed-bed was maintained at 150 sccm for all samples. Three to 4 g of corn stover were typical bed loadings. A final sample conditioning step was performed on the surface area analyzer (see § 2.3) prior to surface area analysis.

2.3 Specific Surface Areas

Multipoint specific surface area (SSA) was collected using a Micromeritics 3Flex instrument and the Brunauer–Emmett–Teller (BET) theory. All adsorption data were obtained using nitrogen as the adsorbate gas. The

	Control	Mildly biologically heated	Moderately biologically heated	Severely biologically heated
Bale 1	B	B		
Bale 2		B	B	
Bale 3		B	B	B
Bale 5	B,C,S,L	B,C,S,L	B,C,S,L	C,S,L
Bale 6	B		B	B

secondary drying step and outgassing consisted of samples with masses ranging from 1.3 to 1.6 g. BET range was determined from a linear fit of the BET plot. The linear fit was selected using seven increasing points (1-p/p°) up to the maximum on the Rouquerol transform plot. All experiments performed produced positive BET "C" constants.

2.4 Ash Content Measurement

Corn stover reportedly contains about 5-7 wt% of intrinsic ash (Bonner et al., 2014)—*which is inorganic material that is taken up naturally within plant tissue during the growth process.* Conversely, extrinsic ash is inorganic material introduced to the plant exterior by the external surroundings during harvest, collection, and storage (Lizotte et al., 2015; Lacey et al., 2016). In order to track and correlate the impacts of ash, all ash data were collected after completing the surface energy measurements. Note: surface energy measurements are non-destructive which allowed us to use the same sample for ash quantification.

Ash content was determined using a Netzsch 449 Jupiter simultaneous thermal analyzer (STA). The corn stover recovered after surface energy analysis was weighed and placed in three 500 μl alumina crucibles (~333 mg corn stover per crucible) for ash analyses. The temperature program consisted of an initial 30 min isotherm at 25°C, followed by a 6°C/min ramp to 107°C in an argon environment (40 sccm), where the temperature was held isothermally until no further mass loss could be observed (approximately 2 h). Afterwards, the purge gas was switched from argon to air (40 sccm) with a temperature ramp of 10°C/min to 750°C. Temperature was held isothermally at 750°C for 1 h to verify the complete oxidation of the material—*indicated by no additional mass loss*. The remaining mass represented the weight percent of total ash (extrinsic plus intrinsic) relative to moisture-free corn stover.

2.5 Surface Energy, Inverse Gas Chromatography

Surface energy measurements were carried out at via inverse gas chromatography at infinite dilution using a Surface Energy Analyzer (SEA) from Surface Measurement Systems (SMS), outfitted with a flame ionization detector (FID). After drying and collecting surface area measurements the corn stover samples were packed in silanized glass columns. Vapor probe properties used for the calculations in this study are tabulated in **Table 2**. The silanized glass columns used for all analyses were sourced from SMS with the following

dimensions; 4 mm ID, 6 mm OD × 300 mm L. Each sample was loaded into a new silanized column resulting in a solid (no gaps) packed column of densities between 0.13 and 0.64 g/cm³. To avoid probe to probe interactions, all surface energy measurements were performed at infinite dilution (0.005 n/n_m or 0.5% mono-layer coverage). For each analysis (1 column per sample run in triplicate), the carrier gas used was helium (10 sccm), and the column temperature was maintained at 30°C with a 60 min conditioning step (identical conditions). In the SEA Analysis software, the center of mass option was used to determine retention time due to the asymmetrical peaks produced as a result of the polar probe-surface interactions. Instrument reproducibility was within 0.5% deviation using the mannitol reference standard provided by Surface Measurement Systems.

2.5.1 Total Surface Energy

The free total surface energy (γ_s^t) is the sum of the dispersive (γ_s^d) and specific (γ_s^{sp}) surface energy components. The subscripts in the equations presented represent either corn stover surface using an s (solid) or the vapor probe using an l (liquid), while the superscripts denote the surface energy component (t = total, d = dispersive, sp = specific).

$$\gamma_s^t = \gamma_s^d + \gamma_s^{sp} \tag{1}$$

2.5.2 Dispersive Surface Energy

Dispersive surface energy (γ_s^d) was estimated using HPLC (High Performance Liquid Chromatography) grade n-alkanes (C_7–C_{10}) from Sigma-Aldrich. The dispersive surface energy component was calculated using the Dorris-Gray method. The adsorption dispersive free energy of a methylene group ΔG^{CH_2}, is calculated from the slope of the line, $RT\Delta\ln\left(\frac{V_{N,n+1}}{V_{N,n}}\right)$ from plotting $RT\Delta\ln V$ against n, the number of carbons in the alkane. Retention volume, V is measured directly from the surface energy analyzer. The dead volume (obtained from the methane injections) was subtracted to provide net retention volume, V_N. **Eq. 2** was used to therefore calculate the dispersive surface energy where R is the gas constant, T is temperature, V_N is net retention volume, N_A is Avogadro's number, a_{CH_2} is the cross sectional area of a methylene group, γ_{CH_2} is the dispersive surface energy of a methylene group, and n is the number of carbons in the alkane.

$$\gamma_s^d = \frac{1}{4\gamma_{CH_2}}\left(\frac{RT\cdot\ln\left(\frac{V_{N,n+1}}{V_{N,n}}\right)}{N_A\cdot a_{CH_2}}\right)^2 \tag{2}$$

TABLE 2 | Characteristics of the Dispersive and Acid-Base IGC probes used in this study.

Solvent	a (Å²)	γ^d (mJ/m²)	γ^+ (mJ/m²)	γ^- (mJ/m²)
Water	1.1	21.8	25.5	25.5
n-heptane	57.0	20.3	0.0	0.0
n-octane	63.0	21.3	0.0	0.0
n-nonane	69.0	22.7	0.0	0.0
n-decane	75.0	23.4	0.0	0.0
Trichloromethane	44.0	25.0	3.8	0.0
Ethyl acetate	33.0	19.6	0.0	19.2

2.5.3 Specific Surface Energy

A monopolar Lewis acid (trichloromethane) and base (ethyl acetate), of HPLC grade from Sigma-Aldrich were used for the specific surface energy (γ_s^{sp}) portion of the experiments. The acid-base (or specific) surface energy components were calculated using the van Oss-Chaudhury-Good (vOCG) scale and the polarization method (Leal et al., 2019). The product of RT and the natural log of the net retention volumes of the polar probes were plotted against their deformation polarizability, P_D. The vertical distance from the alkane trend line to the plotted polar probe determines the specific free energy of adsorption:

$$-\Delta G^{sp} = -\left(\Delta G - \Delta G^d\right) = RT \cdot \ln V_N \qquad (3)$$

Determining the specific contributions was applied using the following approach:

$$-\Delta G^{sp} = 2N_A a\left(\sqrt{\gamma_l^+ \gamma_s^-} + \sqrt{\gamma_l^- \gamma_s^+}\right) \qquad (4)$$

where γ_l^+ and γ_l^- represent the electron acceptor (acid) and electron donor (base) parameters (vOCG scale) of the probe molecule (**Table 2**), γ_s^+ and γ_s^- are the acid and base parameters of the corn stover surface. Values of γ_s^+ and γ_s^- were calculated using the measured $-\Delta G^{sp}$ values of trichloromethane (TCM) and ethyl acetate (EtOAc). Monopolar probes such as TCM are assigned a zero value for either the acidic or basic component (whether Lewis acid or base), e.g., $\gamma_s^- = 0.0$ mJ/m^2, and was reduced to:

$$-\Delta G_{TCM} = 2N_A a_{TCM}\sqrt{\gamma_{TCM}^+ \gamma_S^-} \qquad (5)$$

Then Rearranged Into:

$$\gamma_S^- = \left(\frac{-\Delta G_{TCM}}{2N_A a_{TCM}}\right)^2 \left(\frac{1}{\gamma_{TCM}^+}\right) \qquad (6)$$

This same process was followed using ethyl acetate's measured free enthalpy of adsorption ($-\Delta G_{EtOAc}$), electron donor value and cross-sectional to obtain the acidic component of the corn stover surface, γ_s^+. With both γ_s^+ and γ_s^-, the specific surface energy (γ_s^{ab}) was obtained using:

$$\gamma_s^{ab} = 2\sqrt{\gamma_s^+ \gamma_s^-} \qquad (7)$$

2.5.4 Wettability

The ratio of specific over total surface energy, known as hydrophilicity, is a useful tool in the prediction of changes in wettability. These values can be used to track changes in sample sets as a result of storage conditions, and physical or chemical treatments.

$$Wettability = \frac{\gamma_s^{sp}}{\gamma_s^t} \qquad (8)$$

2.5.5 Work of Cohesion and Work of Adhesion

The work of cohesion is defined as the intermolecular attractive force acting between two adjacent portions of a substance, the force that holds a piece of matter together
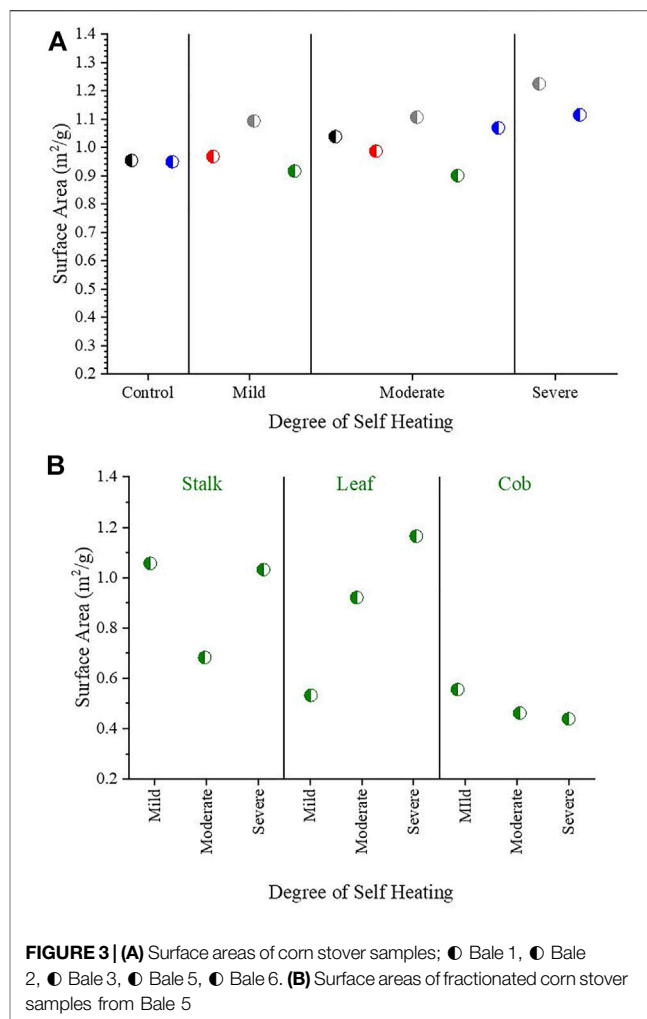
FIGURE 3 | (A) Surface areas of corn stover samples; ◐ Bale 1, ◐ Bale 2, ◐ Bale 3, ◐ Bale 5, ◐ Bale 6. **(B)** Surface areas of fractionated corn stover samples from Bale 5

(Li et al., 2020). The work of cohesion for both corn stover and water was calculated using **Eq. 9**. The variable x may be substituted for either s to denote a solid or l, when referring to liquid (water in this case).

$$\text{Work of Cohesion}\left(W_{coh}^x\right) = 2\left(\sqrt{\gamma_x^d \gamma_x^d} + \sqrt{\gamma_x^+ \gamma_x^-} + \sqrt{\gamma_x^- \gamma_x^+}\right) \qquad (9)$$

The work of adhesion (calculated with **Eq. 10** measures the sum of interfacial forces between the corn stover surface (s) and the surface of liquid water (l) in a multicomponent approach. All calculations involving water surface energy used the physical properties of water presented in **Table 2**.

$$\text{Work of Adhesion}\left(W_{adh}^{sl}\right) = 2\left(\sqrt{\gamma_s^d \gamma_l^d} + \sqrt{\gamma_s^+ \gamma_l^-} + \sqrt{\gamma_s^- \gamma_l^+}\right) \qquad (10)$$

The ratio (Φ, phi) of the work of adhesion (W_{adh}^{sl}) to the work of cohesion of water (W_{coh}^l) is represented by **Eq. 11**.

$$\phi = W_{adh}^{sl} \big/ W_{coh}^l \qquad (11)$$

3 RESULTS AND DISCUSSION

3.1 Bet Surface Areas

Surface area and porosity changes may affect downstream processes such as enzymatic conversion. Enhanced enzyme accessibility is a limiting factor and pretreatments aim to increase this by creating or increasing voids, slits and generally increasing surface area (Ishizawa et al., 2007). In addition to surface energy, surface texture, area, and porosity plays an important role in wetting behavior of biomass. Understanding and controlling the parameters that affect biomass wetting characteristics may prove to be useful to biorefinery operators seeking to reduce wetting times during pretreatment or enzymatic digestion. **Figure 3A** shows the measured surface areas for the 12 non-fractionated bulk corn stover samples. The average surface area for the bulk corn stover samples was 1.03 m^2/g, with a standard deviation of 0.09 m^2/g and a range of 0.90–1.22 m^2/g. The overall trend in surface area of the bulk corn stover samples increased with extent of biological degradation. The surface areas for the fractionated samples (stalk, leaf, and cob) are shown in **Figure 3B** as a function of the degree of self-heating. The average ($\bar{x}$) surface area for the anatomical fractions was 0.76 m^2/g which is lower than the average surface area of the bulk corn stover samples. The surface areas among the fractionated samples ranged from 0.44–1.16 m^2/g, with the highest surface areas observed for the severely degraded leaf and stalk fractions. The lowest surface areas were observed for the cob fraction with surface area ranging from 0.55 m^2/g for the mildly degraded sample, to 0.44 m^2/g for the severely degraded sample. The surface area of the cob fraction remained relatively unchanged with respect to degree of degradation—*demonstrating a resistance to thermal degradation, perhaps attributed to properties unique to the cob such as structure and density*. The leaf fraction was observed to be the most sensitive to the degree of biological degradation. A two-fold increase in the leaf surface area was measured, with the surface area increasing from 0.53 m^2/g for the mildly degraded sample, to 1.12 m^2/g for the severely degraded sample. The surface areas of the stalk fraction are unique in that the surface areas are uncorrelated to the degree of biological degradation. Given the relative size of the sample to the size of the bale for which the samples came from, the mildly degraded stalk sample may not be a representative sample of these conditions. The authors fully recognize that the most challenging aspect in correlating our characterization data to the degree of biological degradation lies in the fact that the degraded samples were visually identified as being mildly, moderately, or severely degraded; unfortunately, there are no quantitative metrics to differentiate the degree of biological degradation at this point. Until then the characterization trends provided are based on visual markers.

3.2 Total Ash Content Measurement

High level of inorganic material in corn stover can cause accelerated wear in hammer-mills, knife-mills, and screw feeders (Lacey et al., 2018). This soil-borne contamination has deleterious effects in downstream operations such as acid pretreatment, enzymatic hydrolysis and the fermentation

FIGURE 4 | (A) Total ash measurements of bulk bale samples; □ Bale 1, □ Bale 2, □ Bale 3, □ Bale 5, □ Bale 6. **(B)** Total ash measurements of fractionated corn stover samples from Bale 5 [box upper and lower limit = data max. and min., whiskers = sample standard deviation (Coeff. 1.5), solid horizontal line = median, hollow internal box = mean].
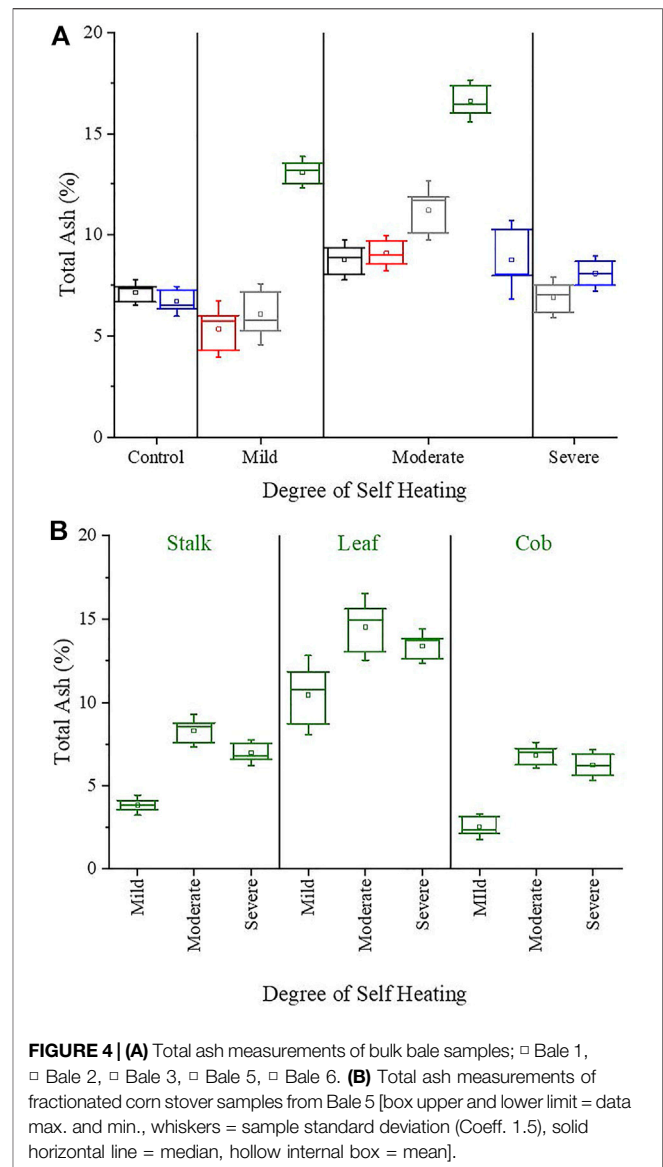
processes (Weiss et al., 2010; Fang and Jia, 2012). Ash measurements were congruent with data collected previously in house and by collaborators from Idaho National Laboratory (Leal et al., 2020; Li et al., 2020). Ash data are plotted for the bulk bale samples in **Figure 4A** as a function of biological self-heating. The percent ash is the mass ratio of remaining ash to the mass of dried corn stover (× 100). The data set has an average ash content of 8.9% with a standard deviation (σ) and variance (σ^2) of 3.2%, and 10.3, respectively. The range of total ash measured was 4–17%. The ash data for the fractionated samples are presented in **Figure 4B** as a function of biological self-heating. The average ash content of this data set is 8.2% with a standard deviation (σ) and variance (σ^2) of 3.9%, and 15.2, respectively. The range of measured ash among the fractionated corn stover data set was 2%–16%. The variability in ash content observed here and in the literature (Xiong et al., 2008; Agblevor et al., 1995; K. J. Shinners et al., 2009; Shinners et al., 2011; Xiong et al., 2010;

Fang and Jia, 2012; Werther et al., 2000) are most likely due to the variations in the collecting, storage, handling, and analytical technique.

3.3 Inverse Gas Chromatography Surface Energy

The intermolecular forces related to van der Waals (non-polar) interactions and Coulombic (polar) interactions are studied using surface energy characterization with inverse gas chromatography (IGC). The non-polar or van der Waals interactions are termed the dispersive surface energy component. The polar, or Coulombic interactions are referred to as the specific surface energy portion of the surface energy. These measurements offer fundamental thermodynamic insights that lead to predictions in surface compatibility, solubility, adhesion, cohesion, wettability (hydrophilicity/hydrophobicity), and adsorption capacity (Lloyd, 1994; Colorado and Lee, 2000; Etzler, 2003; Gérardin et al., 2007; Lee et al., 2008; Winandy and Shupe, 2010; Hubbe et al., 2015). Increased cohesion in corn stover is suspected to cause poor flow and agglomeration in bulk solids handling through rat-holing and arching in hoppers during conveyance operations (Leal et al., 2020; Ray et al., 2020).

Measured surface energies of a material are representative of the chemical composition of the surface exposed to the vapor probes. Inorganic material (ash content) on the surface of corn stover may result in higher values of surface energy as they generally present higher values (often greater than 1,000 mJ/m^2) (Vitos et al., 1998). Another influence on surface energy that has been reported is particle size (Amara et al., 2012). However, that dependency can be misleading. Articles suggesting a dependency of surface energy on particle size are strictly measuring sub-micron particles (nano) composed of inorganic material. The corn stover particles measured in this study are of sizes ranging from 0.18 to 2.00 mm (50% greater than 0.5 mm) and carbonaceous. Surface energy dependency from particle size does not apply to these larger particles.

Surface energy units are energy per unit area of surface (i.e. mJ/m^2). Therefore, if the chemical composition of the surface does not change there should be zero difference in surface energy between large and small particles. However, smaller particles often have different surface energy values compared to larger particles. There are a few explanations for this. During size reduction, particles often undergo energetic processes such as milling or grinding (Ho et al., 2012). These processes can create surface disorder, reduce crystallinity, expose preciously inaccessible interfaces, or cleave material in ways that favor one crystal plane over others (Heng et al., 2006; Jaffari et al., 2014; Shah et al., 2015). Nanoparticles may have different surface energy values as they may be composed of fewer crystal planes, or a dominant plane may be exposed compared to surfaces of larger particles (Heng et al., 2006; Ho et al., 2009; Smith et al., 2017).

3.3.1 Total Surface Energy

The bulk ground samples in **Figure 3C**, (bales 1, 2, 3, 5, and 6) show increases in total surface energy as the degree of self-heating increases. The average value was 108.07 mJ/m^2 for this set of samples, and the range was 92.68–128.12 mJ/m^2; $\bar{\sigma}$ = 0.86 mJ/m^2. In **Figure 5C**, the total surface energy for the fractionated samples is displayed as a function of the degree of self-heating. The average total surface energy for all nine fractionated samples was 97.68 mJ/m^2, and the range was 85.89–124.37 mJ/m^2; $\bar{\sigma}$ = 0.46 mJ/m^2. The greatest changes in total surface energy were evidenced in the leaf fraction, an increase from 91.10 mJ/m^2 in the mildly self-heated sample to 123.65 mJ/m^2 in the severely self-heated sample. There was no observable change in the total surface energy of the cob with varied degrees of self-heating. The total surface energy of the stalk was observed to increase from the mildly self-heated to the moderately self-heated sample, 86.13 and 89.25 mJ/m^2, respectively.

3.3.2 Dispersive Surface Energy

The dispersive surface energy of the bulk ground samples of bales 1, 2, 3, 5, and 6 are displayed in **Figure 5A**. There is an observed increase in dispersive surface energy in all bales with increased degrees of self-heating. A measurable change in dispersive energy is an indicator of chemical changes to the surface, a change in the amount of apolar chemical species exposed per area. The self-heating may have caused migration of or movement of apolar portions to the surface resulting in an observed increase in dispersive surface energy. Bale 6, for example, shows an increase from 39.10 mJ/m^2 (mild) to 45.40 mJ/m^2 (severe), demonstrating the greatest change among the bales. Student t-tests reveal the changes in dispersive energy from self-heating to be significant among all bale samples (non-fractionated). The fractionated samples, with the exception of the cob (**Figure 6A**), increase monotonically as a function of self-heating. According to student t-tests all samples showed to be different from one another with the exception of the moderate ($\bar{x}$ = 39.87, σ = 0.08) to severe ($\bar{x}$ = 39.82, σ = 0.125) cob samples; t (Perlack, 2005) = 0.50, p = 0.65. The effects of self-heating had the most impact on the leaf fraction, evidenced in **Figure 6A**. The leaf dispersive surface energy increased from 40.24 mJ/m^2 to 46.96 mJ/m^2, mild to moderately self-heated, respectively. The dispersive energies of the stalk and cob were not impacted as strongly as in the leaf fraction. One possible explanation for this can be explored among the differences in composition, structure, or even the position in the self-heated bale. For example, the leaf is much thinner than the stalk or cob, possibly resulting in a more efficient transfer of heat. There are also compositional differences between the fractions, varying concentrations of cellulose, hemicellulose, and lignin, which could possibly influence the selection process of the organisms responsible for the self-heating. The authors believe that without better control over the experimental parameters and sample selection, it is not possible to determine the exact reasons behind the discrepancies.

3.3.3 Specific Surface Energy

Specific surface energy for bales 1, 2, 3, 5, and 6 are plotted against the degrees of self-heating in **Figure 5B**. Bales 3 and 6 severe samples measured at higher specific surface energies than those samples self-heated to a lesser degree. Student t-tests suggest self-heating significantly changes the specific surface energy of the samples in **Figure 5B**, with the exception of bale 2 mild ($\bar{x}$ = 65.1,

FIGURE 5 | (A) Dispersive, **(B)** specific, **(C)** total surface energy and **(D)** hydrophilicity of bulk bale samples; □ Bale 1, □ Bale 2, □ Bale 3, □ Bale 5, □ Bale 6 [box upper and lower limit = data max. and min., whiskers = sample standard deviation (Coeff. 1.5), solid horizontal line = median, hollow internal box = mean].
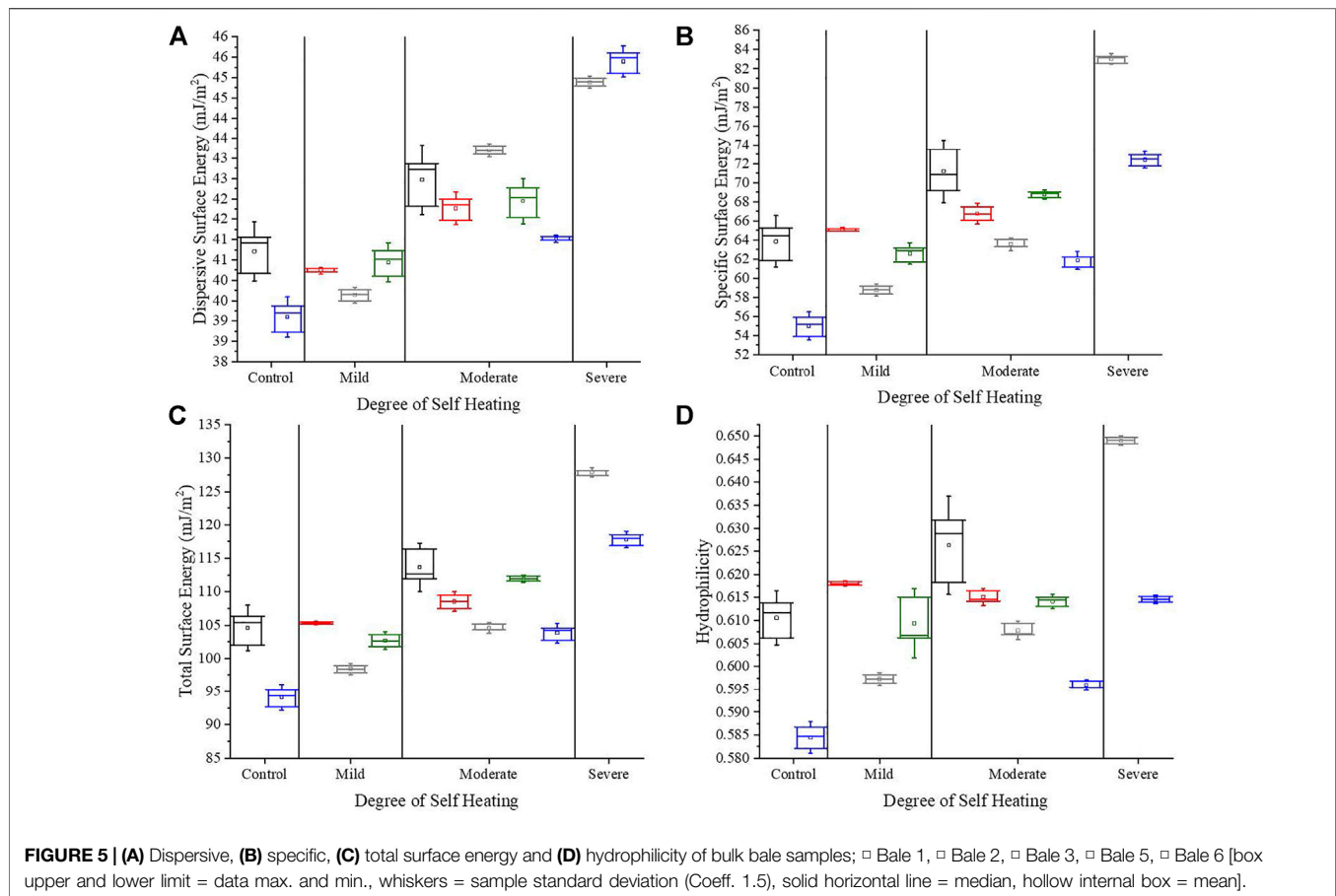
$\sigma = 0.12$) to moderate ($\bar{x} = 66.75$, $\sigma = 0.74$); t (Renewable Energy Sources, 2019) = 3.83, $p = 0.06$. A look at the specific surface energies of the three fractions on **Figure 6B** shows the leaf to be more sensitive to self-heating than the stalk or the cob. The leaf experienced an increase of ~26 mJ/m^2 from mild (50.86 mJ/m^2) to severe (76.69 mJ/m^2), however, the stalk increased ~10 mJ/m^2 from mild (47.18 mJ/m^2) to moderate (~57.83 mJ/m^2) and then decreased by ~4 mJ/m^2 to 53.60 mJ/m^2. *t*-tests revealed no significant changes in the cobs specific surface energy (~50 mJ/m^2). The measured changes of specific surface energy in these samples are indicators of chemical changes to the exposed surfaces of the corn stover. The data suggests heating influences the surface chemistry of the leaf, by way of either creating new surfaces, or exposing new surfaces through migration of inner positioned, polar moieties to the surface. Corn stover has a varied composition; the lignin, cellulose, inorganics, and extractives that make up the plant have very different chemical structures. For example, lignin is an aromatic alcohol, its migration (Ray et al., 2020), or exposure to the surface would be expected to cause an increase in the specific surface energy, via acidic contributions.

3.3.3.1 Effects of Self-Heating on Acid/Base Values
Figures 7A,B display the acid and base surface energy values, respectively, which comprise the specific surface energy.

Self-heating increased the acid sites (electron acceptors) on the surface except for bale 2, which experienced a decrease in acid sites from the mild to moderate self-heating. The basic sites (electron donors) were also observed to increase with self-heating, although the changes in bale 1 control ($\bar{x} = 53.41$, $\sigma = 2.16$) to moderate ($\bar{x} = 52.54$, $\sigma = 2.88$); t (Perlack et al., 2011) = 0.42, $p = 0.70$ and bale 3 moderate ($\bar{x} = 53.24$, $\sigma = 0.39$) to severe ($\bar{x} = 52.69$, $\sigma = 0.25$); t (Perlack, 2005) = 2.06, $p = 0.13$ were not determined to be significant. In Figures **Figures 7C,D**, the leaf is measured to increase in both the acid and base contributions of specific surface energy. The surface of the stalk tends to increase in acid sites when heated from mild to moderate. However, the increases observed here may also be contributed to ash content (inorganics) present in all corn stover samples.

3.3.3.2 Ash Influence on Specific Surface Energy
The amounts of inorganic matter in biomass feedstocks can range widely based on harvesting practices, plant type, and storage. Plants naturally contain a physiological amount of inorganics that are vital to biological functions; these amounts can vary among plant types and are referred to as intrinsic ash content. Proximate analysis provides values of this physiological mineral content as a wt% of the dry biomass matter and are reported to be less than 10 wt. % on the average. High ash content (above 10%) in biomass feedstock is often attributed to practices and techniques in
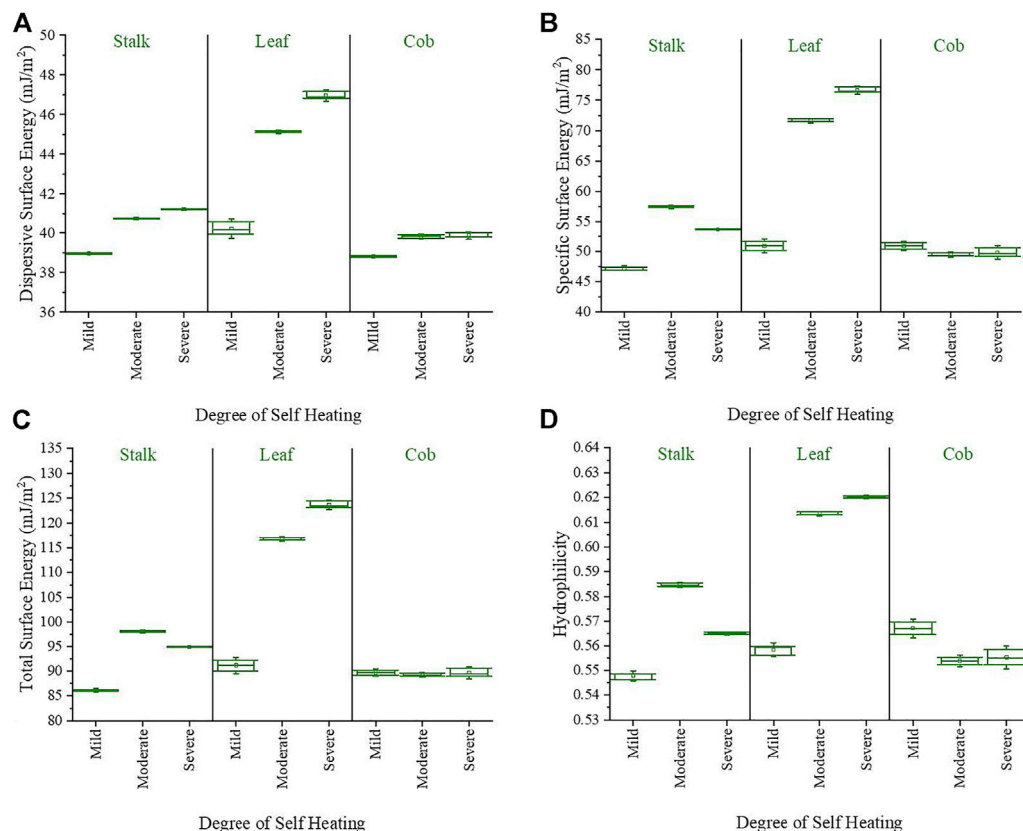
FIGURE 6 | (A) Dispersive, **(B)** specific, **(C)** total surface energy, and **(D)** hydrophilicity of corn stover anatomically fractionated samples from Bale 5 [box upper and lower limit = data max. and min., whiskers = sample standard deviation (Coeff. 1.5), solid horizontal line = median, hollow internal box = mean].

harvesting, handling and storage—*these methods allow for the accumulation of extrinsic mineral/inorganic content such as dirt.* The impacts of ash on the surface energy of corn stover has been found to significantly increase specific surface energy values in ash concentrations above 10% w/w (Leal et al., 2020). It was demonstrated that it is possible to wash out most of the ash over 10% w/w, suggesting that those inorganics were extrinsic, not intrinsic. Increases in surface energy translate into increased values of calculated hydrophilicity (**section 3.3.4**)—*changes that may negatively affect material flowability properties.* **Figure 4A** shows the variability of ash content in the bulk bale samples. Ash contents over 10% were observed only in the bale five mild, moderate and bale 3 moderate samples. These samples are a ground mix of stalk, leaf, and cob fractions and the mass distribution of each is uncertain. Amounts of ash increase in samples from control to mild or mild to moderate but decrease in bale 3 moderate to severe sample. The increase in ash may contribute to increases in surface energy, but in the case of bale 3 the ash content decreases from the moderate to severe self-heating, however the specific surface energy increases from ~63 mJ/m^2 to ~84 mJ/m^2. The increase in ash as a result of heating from mild to moderate is unclear and may be a result of a loss in organic mass during the heating or as a result of biological organismal consumption. **Figure 4B** illustrates the amount of ash measured in the mild, moderate and severely

heated fractionated samples. Previously observed trends in non-degraded corn stover indicated a monotonic increase in surface energy with increasing ash content (mostly in increases of the acidic component of the surface) (Leal et al., 2020). The effects of self-heating have convoluted the interpretation of the aforementioned trend of surface energy and ash.

3.3.4 Wettability

Figure 5D shows self-heating did not affect the wettability of samples in bales 2 and 5. However, according to the calculated hydrophilicity, bales 1, 3, and 6 are predicted to have increased in wetting ability. Severe degradation of corn stover results in an increase in water extractive content, likely due to a disruption of the cell wall structural integrity (Li et al., 2020). Changes in the surface chemistry of the degraded corn stover, in addition to the disrupted cell wall integrity, may also contribute to the increase in water extracted content observed by Li et al. (2020). Functional groups on the right side in **Table 3** are conducive to a hydrophobic surface, whereas the groups on the left side contribute to its hydrophilic nature. Without more information, it is unclear to whether an increase in oxygen to carbon ratio has occurred. **Figure 6D** shows a monotonic increase in calculated wettability of the leaf. The stalk fraction increased wettability with moderate self-heating, but further exposure to self-heating reversed the trend. Of all three fractions, the cob was the least affected by

FIGURE 7 | (A) Acid (bulk corn stover), **(B)** Base (bulk corn stover); □ Bale 1, □ Bale 2, □ Bale 3, □ Bale 5, □ Bale 6. **(C)** Acid (anatomical fractions), and **(D)** Base (anatomical fractions) contributions of surface energy with respect to degree of biological heating [box upper and lower limit = data max. and min., whiskers = sample standard deviation (Coeff. 1.5), solid horizontal line = median, hollow internal box = mean].

TABLE 3 | Common functional groups contributing to wettability.

More wettable	Less wettable
R-OH	R-CH$_3$
R-COO$^-$	R-CH$_2$-CH$_2$-R′
R-Al$_n$(OH)$_m$	R-CF$_3$

self-heating with respect to wettability. The cylindrical solid structure of the cob may have prevented the effects of degradation from reaching internal parts of the cob, restricting the changes to the surface, thus leaving the bulk of the cobs mass relatively unaffected. The overall implications on downstream processing may manifest themselves in slower drying times for fractions with higher wettability, or decreased moisture uptake rates for fractions with decreased wettability. The differences in wettability among the fractions and degrees of degradation can result in segregation, or clumping of the bulk material, causing issues with handling operations through biorefinery equipment (e.g., hoppers and screw feeders).

3.3.5 Work of Cohesion and Work of Adhesion

The calculated work of cohesion for bulk and fractionated corn stover samples can be observed in **Figures 8A,C**, respectively. Increases in cohesive forces were observed from the control to the severely heated bulk corn stover samples. Self-heating had the greatest effect on the leaf fraction of corn stover, and least on the cob.

Figures 8B,D display the work of adhesion (corn stover sample to liquid water) of both the bulk and fractionated corn stover samples. Using the vOCG scale, the trend in adhesion is similar to the work of cohesion (corn stover), but the values are overall lower. The average percent difference from work of cohesion to adhesion of the bulk samples increases with degrees of self-heating. Work of adhesion is 13.00% lower than work of cohesion in the control, 14.68% in the mild, 16.99% in the moderate, and 22.01% in the severe group. This indicates that self-heating produces a compounding effect on biomass feedstock via increases in water adsorption and particle cohesion, potentially resulting in rat-holing, arching, and poor flow in hoppers or jamming of screw feeders of biorefineries.

Eq. 11 implies that when comparing the two competing forces acting on a drop of water, if Φ is greater than one, the drop will spread easier because the net forces are in favor of adhesion. **Figure 9** illustrates an observable monotonic increase in Φ with respect to biological self-heating. The authors understand this to be an oversimplified estimation of real-world phenomena where there are other factors to consider, e.g., surface roughness, hierarchal structures, heterogeneity, etc., which may positively or negatively affect the magnitude of IGC measured cohesion or adhesion. The simplicity of Φ offers a less abstract view of wettability and provides another method of evaluation for discussion.

FIGURE 8 | (A) Work of Cohesion, **(B)** Work of Adhesion, of bulk bale samples; □ Bale 1, □ Bale 2, □ Bale 3, □ Bale 5, □ Bale 6. **(C)** Work of Cohesion (anatomical fractions), and **(D)** Work of Adhesion (anatomical fractions) with respect to degree of biological heating [box upper and lower limit = data max. and min., whiskers = sample standard deviation (Coeff. 1.5), solid horizontal line = median, hollow internal box = mean].
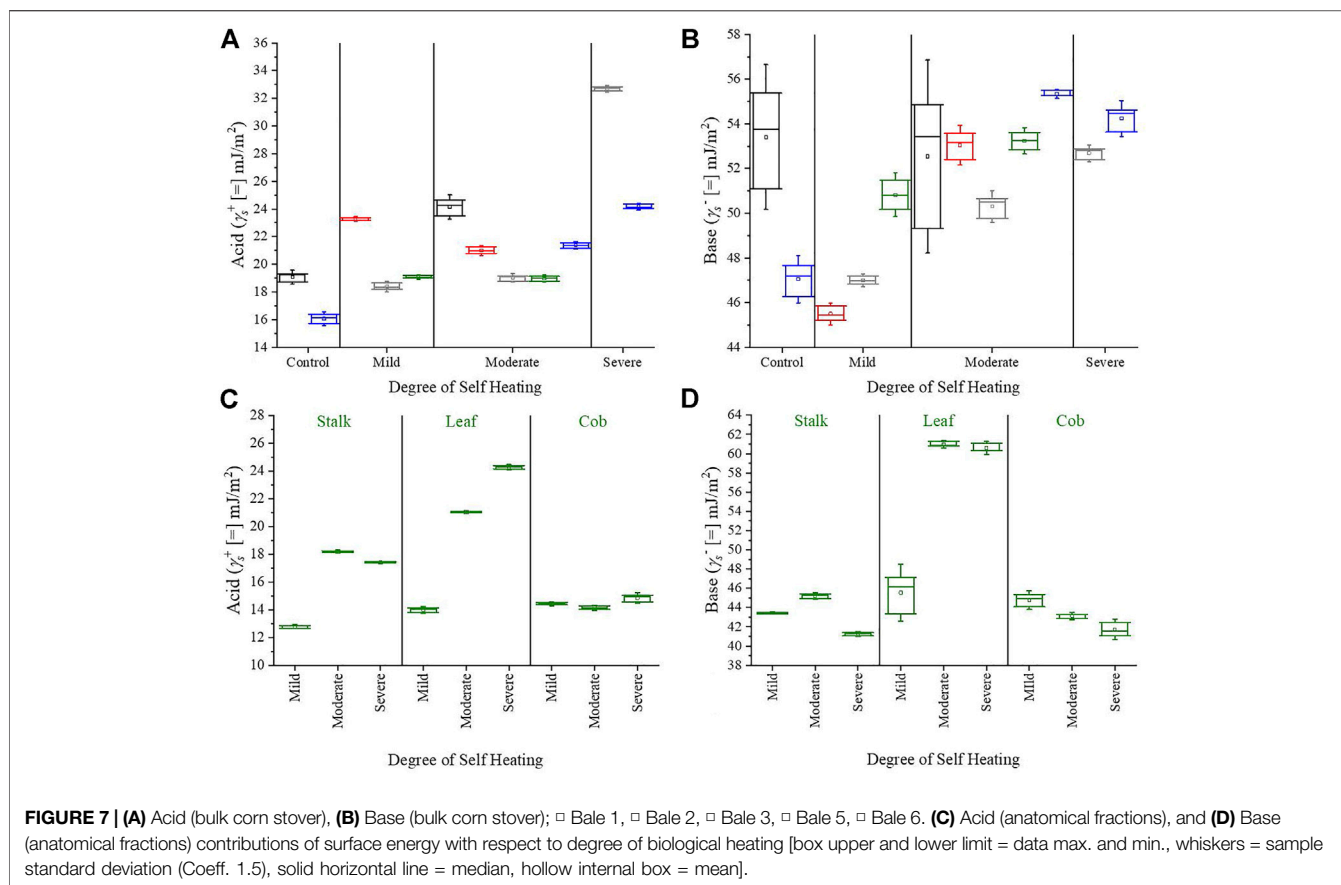

FIGURE 9 | The ratio of the work of adhesion, W_{adh}^{sl}, and work of cohesion of water, W_{coh}^{l}, is plotted as a dimensionless value denoted by "Φ." Dotted lines have been added to assist the reader in comparing samples of the same bale; ▣ Bale 1, ▣ Bale 2, ▣ Bale 3, ▣ Bale 5, ▣ Bale 6.

Further utility in the works of adhesion can be explored in the measurements of solid-solid interfaces involving biomass feedstock, for instance the surface of a hopper, or surface of a screw feeder where lower works of adhesion could prove optimal. Future work aims to couple flow behavior of biomass feedstock (rheological measurements) with surface energy for a direct evaluation of impacts (Cheng et al., 2021).

4 CONCLUSION

Biological degradation (a known source of feedstock variability) was shown to have pronounced impacts on the surface area, surface energy, wettability and cohesion of corn stover. The implications of biological degradation negatively impact not only the overall efficiency, conversion, and yields of integrated biorefineries; but also the operational reliability of bulk solids handling and transport of corn stover. Surface area is a critical material attribute that can be used as a proxy for the pretreatment reactivity; an increase in the corn stover surface area corresponds to an increase in the pretreatment conversion/reactivity. The surface area of the bulk corn stover samples increased with the degree of biological degradation. The leaf fraction was the most sensitive to biological degradation, resulting in an increase in surface area from 0.5 m^2/g (mildly degraded) to 1.2 m^2/g (severely degraded). In contrast, the surface area of the cob fraction remained relatively unaffected by the degree of biological degradation (i.e., mildly degraded–0.55 m^2/g, severely degraded–0.40 m^2/g).

All biologically degraded samples in this study resulted in significant changes to the surface chemistry (evidenced by an

increase in surface energy). As a general trend, the surface energy of bulk corn stover increased with the degree of biological degradation—the same trend was observed for the leaf and stalk anatomical fractions; however, the surface energy for the cob fraction remained unchanged. Wettability (calculated from surface energy) is a characteristic property that impacts the overall efficiency and conversion of pretreatment processes—hydrophilic (i.e., wettable) materials lead to higher water-uptake rates (correlating to higher conversion rates) as compared to hydrophobic, or non-wettable materials. The wettability for bulk corn stover samples did not reveal any discernable trend with the degree of biological degradation. However, trends in wettability were observed for the anatomical fractions, with wettability increasing for the stalk and leaf fractions, and decreasing for the cob fraction. Excluding the cob fraction, the work of cohesion increased with the degree of biological degradation. The quantified impacts of biological degradation on the physiochemical and thermodynamic properties of corn stover presented in this study offer fundamental insights to improve the overall conversion, economics, and operational reliability of Integrated Biorefineries.

DATA AVAILABILITY STATEMENT

The raw data supporting the conclusions of this article will be made available by the authors, without undue reservation.

REFERENCES

AUTHOR CONTRIBUTIONS

JL performed most of the experiments, EM assisted with a few surface area measurements, TS assisted JL with writing, RN and CM assisted in editing content. AR helped process and supply samples from INL.

Agblevor, F. A., Besler, S., and Wiselogel, A. E. (1995). Fast Pyrolysis of Stored Biomass Feedstocks. *Energy fuels.* 9 (4), 635–640. doi:10.1021/ef00052a010

Amara, H., Nelayah, J., Creuze, J., Chmielewski, A., Alloyeau, D., Ricolleau, C., et al. (2012). *Is There Really a Size Effect on the Surface Energy of Nanoparticles.* [Internet]. Available from: https://hal.archives-ouvertes.fr/hal-03310351.

Biorefinery Optimization Workshop Summary (2016). *Biorefinery Optimization Workshop Summary Report.* [Internet]. Chicago. [cited 2019 Mar 28]. Available from: https://www.energy.gov/sites/prod/files/2017/02/f34/biorefinery_optimization_workshop_summary_report.pdf.

Bonner, I. J., Smith, W. A., Einerson, J. J., and Kenney, K. L. (2014). Impact of Harvest Equipment on Ash Variability of Baled Corn Stover Biomass for Bioenergy. *Bioenerg. Res.* 7 (3), 845–855. doi:10.1007/s12155-014-9432-x

Bose, E., Leal, J. H., Hoover, A. N., Zeng, Y., Li, C., Ray, A. E., et al. (2020). Impacts of Biological Heating and Degradation during Bale Storage on the Surface Properties of Corn Stover. *ACS Sustain. Chem. Eng.* 8 (37). doi:10.1021/acssuschemeng.0c03356

Bradley, T. H., Baral, N. R., Davis, R., Baral, N. R., Davis, R., and Bradley, T. H. (2019). Supply and Value Chain Analysis of Mixed Biomass Feedstock Supply System for Lignocellulosic Sugar Production. *Biofuels, Bioprod. Biorefining.* 13 (3), 635–659.

Cheng, Z., Leal, J. H., Hartford, C. E., Carson, J. W., Donohoe, B. S., Craig, D. A., et al. (2021). Flow Behavior Characterization of Biomass Feedstocks. *Powder Technol.,* 156–180. doi:10.1016/j.powtec.2021.04.004

Colorado, R., and Lee, T. R. (2000). Physical Organic Probes of Interfacial Wettability Reveal the Importance of Surface Dipole Effects. *J. Phys. Org. Chem.* 13 (12), 796–807. doi:10.1002/1099-1395(200012)13:12<796::aid-poc317>3.0.co;2-#

Eia (2019). EIA Projects 28% Increase in World Energy Use by 2040 - Today in Energy. *U.S. Energy Inf. Adm.* [Internet]. [cited 2019 Mar 28]. Available from: https://www.eia.gov/todayinenergy/detail.php?id=32912.

Etzler, F. M. (2003). Characterisation of Surface Free Energies and Surface Chemistry of Solids. *Contact angle, wettability adhesion* 3, 219–263.

Fang, X., and Jia, L. (2012). Experimental Study on Ash Fusion Characteristics of Biomass. *Bioresour. Technol.* 104, 769–774. doi:10.1016/j.biortech.2011.11.055

Gérardin, P., Petrič, M., Petrissans, M., Lambert, J., and Ehrhrardt, J. J. (2007). Evolution of Wood Surface Free Energy after Heat Treatment. *Polym. Degrad. Stab.* 92 (4), 653–657.

Hanson-Harding, B. (2013). *Composting.* New York, NY: The Rosen Publishing Group, Inc.

Harmon, L., Hallen, R., Lilga, M., Heijstra, B., Palou-Rivera, I., and Handler, R. (2017). *A Hybrid Catalytic Route to Fuels from Biomass Syngas.* Golden, CO (United States).

Heng, J. Y. Y., Bismarck, A., Lee, A. F., Wilson, K., and Williams, D. R. (2006). Anisotropic Surface Energetics and Wettability of Macroscopic Form I Paracetamol Crystals. *Langmuir* 22 (6), 2760–2769. doi:10.1021/la0532407

Ho, R., Naderi, M., Heng, J. Y. Y., Williams, D. R., Thielmann, F., Bouza, P., et al. (2012). Effect of Milling on Particle Shape and Surface Energy Heterogeneity of Needle-Shaped Crystals. *Pharm. Res.* 29 (10), 2806–2816. doi:10.1007/s11095-012-0842-1

Ho, R., Wilson, D. A., and Heng, J. Y. Y. (2009). Crystal Habits and the Variation in Surface Energy Heterogeneity. *Cryst. Growth & Des.* 9 (11), 4907–4911. doi:10.1021/cg900696f

Hubbe, M. A., Gardner, D. J., and Shen, W. (2015). Contact Angles and Wettability of Cellulosic Surfaces: A Review of Proposed Mechanisms and Test Strategies. *BioResources* 10 (4), 8657–8749. doi:10.15376/biores.10.4.hubbe_gardner_shen

Ishizawa, C. I., Davis, M. F., Schell, D. F., and Johnson, D. K. (2007). Porosity and its Effect on the Digestibility of Dilute Sulfuric Acid Pretreated Corn Stover. *J. Agric. Food Chem.* 55 (7), 2575–2581. doi:10.1021/jf062131a

Jaffari, S., Forbes, B., Collins, E., Khoo, J., Martin, G. P., and Murnane, D. (2014). Evidence for the Existence of Powder Sub-populations in Micronized Materials: Aerodynamic Size-Fractions of Aerosolized Powders Possess Distinct Physicochemical Properties. *Pharm. Res.* 31 (12), 3251–3264. doi:10.1007/s11095-014-1414-3

K. J. Shinners, K. J. K. J., G. C. Boettcher, G. C., D. S. Hoffman, D. S. D. S., J. T. Munk, J. T., R. E. Muck, R. E., and P. J. Weimer, P. J. (2009). Single-Pass Harvest

of Corn Grain and Stover: Performance of Three Harvester Configurations. *Trans. ASABE* 52 (1), 51–60. doi:10.13031/2013.25940

Kumar, A., Wang, L., Dzenis, Y. A., Jones, D. D., and Hanna, M. A. (2008). Thermogravimetric Characterization of Corn Stover as Gasification and Pyrolysis Feedstock. *Biomass Bioenergy* 32 (5), 460–467. doi:10.1016/j.biombioe.2007.11.004

Lacey, J. A., Aston, J. E., and Thompson, V. S. (2018). Wear Properties of Ash Minerals in Biomass. *Front. Energy Res.* 6, 119. doi:10.3389/fenrg.2018.00119

Lacey, J. A., Emerson, R. M., Thompson, D. N., and Westover, T. L. (2016). Ash Reduction Strategies in Corn Stover Facilitated by Anatomical and Size Fractionation. *Biomass Bioenergy* 90, 173–180. doi:10.1016/j.biombioe.2016.04.006

Langholtz, M., Stokes, B., and Eaton, L. (20162016). 2016 Billion-Ton Report: Advancing Domestic Resources for a Thriving Bioeconomy (Executive Summary). *Ind. Biotechnol.* 12 (5), 282–289. doi:10.1089/ind.2016.29051.doe

Leal, J. H., Torres, E. L., Rouse, W. T., Moore, C. M., Sutton, A. D., Hoover, A. N., et al. (2020). *Impacts of Inorganic Material (Total Ash) on Surface Energy, Wettability, and Cohesion of Corn Stover.*

Leal, J. H., Moore, C. M., Sutton, A. D., and Semelsberger, T. A. (2019). Surface Energy of Air Fractionated Corn Stover. *Industrial Crops Prod.* 137, 628–635. doi:10.1016/j.indcrop.2019.05.046

Lee, S., Park, J.-S., and Lee, T. R. (2008). The Wettability of Fluoropolymer Surfaces: Influence of Surface Dipoles. *Langmuir* 24 (9), 4817–4826. doi:10.1021/la700902h

Li, C., Kerner, P., Williams, C. L., Hoover, A., and Ray, A. E. (2020). Characterization and Localization of Dynamic Cell Wall Structure and Inorganic Species Variability in Harvested and Stored Corn Stover Fractions as Functions of Biological Degradation. *ACS Sustain. Chem. Eng.* 8 (18), 6924–6934. doi:10.1021/acssuschemeng.9b06977

Liu, Z.-H., Qin, L., Li, B.-Z., and Yuan, Y.-J. (2014). Physical and Chemical Characterizations of Corn Stover from Leading Pretreatment Methods and Effects on Enzymatic Hydrolysis. *ACS Sustain. Chem. Eng.* 3 (1), 140–146. doi:10.1021/sc500637c

Lizotte, P.-L., Savoie, P., and De Champlain, A. (2015). Ash Content and Calorific Energy of Corn Stover Components in Eastern Canada. *Energies* 88 (6), 48274827–48483838. doi:10.3390/en8064827

Lloyd, T. B. (1994). Experimental Procedures to Characterize Acid-Base and Dispersion Force Contributions to Solid Wettability A Review. *Colloids Surfaces A Physicochem. Eng. Aspects* 93 (C), 25–37. doi:10.1016/0927-7757(94)02907-5

Nagle, N. J., Donohoe, B. S., Wolfrum, E. J., Kuhn, E. M., Haas, T. J., Ray, A. E., et al. (2020). Chemical and Structural Changes in Corn Stover after Ensiling: Influence on Bioconversion. *Front. Bioeng. Biotechnol.* 8, 739. doi:10.3389/fbioe.2020.00739

Perlack, R. D. (2005). *Biomass as Feedstock for a Bioenergy and Bioproducts Industry: The Technical Feasability of a Billion-Ton Annual Supply*. Oak Ridge, TN: Oak Ridge National Laboratory.

Perlack, R. D., Eaton, L. M., and Langholtz, M. H. (2011). US Billion Ton Update: Biomass Supply for a Bioenergy and Bioproducts Industry (Executive Summary). *Ind. Biotechnol.* 7 (5), 375–380.

Ray, A. E., Williams, C. L., Hoover, A. N., Li, C., Sale, K. L., Emerson, R. M., et al. (2020). Multiscale Characterization of Lignocellulosic Biomass Variability and its Implications to Preprocessing and Conversion: A Case Study for Corn Stover. *ACS Sustain. Chem. Eng.* 8 (8), 3218–3230. doi:10.1021/acssuschemeng.9b06763

Renewable Energy Sources (2019). Energy Explained, Your Guide to Understanding Energy. *Energy Inf. Adm.* [Internet]. [cited 2019 Mar 28]. Available from: https://www.eia.gov/energyexplained/?page=renewable_home.

Searcy, E., Lamers, P., Hansen, J., Jacobson, J., Hess, R., and Webb, E. (2015). *Advanced Feedstock Supply System Validation Workshop*. United States: Golden, CO.

Shah, U. V., Olusanmi, D., Narang, A. S., Hussain, M. A., Tobyn, M. J., Hinder, S. J., et al. (2015). Decoupling the Contribution of Surface Energy and Surface Area on the Cohesion of Pharmaceutical Powders. *Pharm. Res.* 32 (1), 248–259. doi:10.1007/s11095-014-1459-3

Shinners, K. J., Wepner, A. D., Muck, R. E., and Weimer, P. J. (2011). Aerobic and Anaerobic Storage of Single-Pass, Chopped Corn Stover. *Bioenerg. Res.* 4 (1), 61–75. doi:10.1007/s12155-010-9101-7

Smith, R. R., Shah, U. V., Parambil, J. V., Burnett, D. J., Thielmann, F., and Heng, J. Y. Y. (2017). The Effect of Polymorphism on Surface Energetics of D-Mannitol Polymorphs. *Aaps J.* 19 (1), 103–109. doi:10.1208/s12248-016-9978-y

Smith, W. A., Bonner, I. J., Kenney, K. L., Wendt, L. M., Smith, W. A., Bonner, I. J., et al. (2014). *Practical Considerations of Moisture in Baled Biomass Feedstocks Practical Considerations of Moisture in Baled Biomass Feedstocks*, 7269.

Smith, W. A., Wendt, L. M., Bonner, I. J., and Murphy, J. A. (2020). Effects of Storage Moisture Content on Corn Stover Biomass Stability, Composition, and Conversion Efficacy. *Front. Bioeng. Biotechnol.* 8, 716. doi:10.3389/fbioe.2020.00716

Turhollow, A., Perlack, R., Eaton, L., Langholtz, M., Brandt, C., Downing, M., et al. (2014). The Updated Billion-Ton Resource Assessment. *Biomass Bioenergy* 70,149–164. doi:10.1016/j.biombioe.2014.09.007

Vitos, L., Ruban, A. v., Skriver, H. L., and Kollár, J. (1998). The Surface Energy of Metals. *Surf. Sci.*, 411 (1–2), 186–202. doi:10.1016/s0039-6028(98)00363-x

Weiss, N. D., Farmer, J. D., and Schell, D. J. (2010). Impact of Corn Stover Composition on Hemicellulose Conversion during Dilute Acid Pretreatment and Enzymatic Cellulose Digestibility of the Pretreated Solids. *Bioresour. Technol.* 101 (2), 674–678. doi:10.1016/j.biortech.2009.08.082

Werther, J., Saenger, M., Hartge, E.-U., Ogada, T., and Siagi, Z. (2000). Combustion of Agricultural Residues. *Prog. Energy Combust. Sci.* 26 (1), 1–27. doi:10.1016/s0360-1285(99)00005-2

Winandy, J. E., and Shupe, T. F. (2010). FROM HYDROPHILICITY to HYDROPHOBICITY : A CRITICAL REVIEW : PART I . WETTABILITY and SURFACE BEHAVIOR Cheng Piao. *Wood Fiber* 42 (4), 490–510.

Woźniak, M., Ratajczak, I., Wojcieszak, D., Waśkiewicz, A., Szentner, K., Przybył, J., et al. (2021). Chemical and Structural Characterization of Maize Stover Fractions in Aspect of its Possible Applications. *Materials* 14 (6).

Xiong, S., Burvall, J., Örberg, H., Kalen, G., Thyrel, M., Öhman, M., et al. (2008). Slagging Characteristics during Combustion of Corn Stovers with and without Kaolin and Calcite. *Energy fuels.* 22 (5), 3465–3470. doi:10.1021/ef700718j

Xiong, S., Öhman, M., Zhang, Y., and Lestander, T. (2010). Corn Stalk Ash Composition and its Melting (Slagging) Behavior during Combustion. *Energy fuels.* 24 (9), 4866–4871. doi:10.1021/ef1005995

Revisiting Theoretical Tools and Approaches for the Valorization of Recalcitrant Lignocellulosic Biomass to Value-Added Chemicals

Le Thanh Mai Pham[1,2†], Hemant Choudhary[1,2†], Rahul Gauttam[1,3†], Steven W. Singer[1,3], John M. Gladden[1,4], Blake A. Simmons[1,3], Seema Singh[1,2]* and Kenneth L. Sale[1,5]*

[1]Deconstruction Division, Joint BioEnergy Institute, Emeryville, CA, United States, [2]Department of Bioresource and Environmental Security, Sandia National Laboratories, Livermore, CA, United States, [3]Biological Systems and Engineering Division, Lawrence Berkeley National Laboratory, Berkeley, CA, United States, [4]Department of Biomaterials and Biomanufacturing, Sandia National Laboratories, Livermore, CA, United States, [5]Department of Computational Biology and Biophysics, Sandia National Laboratories, Livermore, CA, United States

Biorefinery processes for converting lignocellulosic biomass to fuels and chemicals proceed *via* an integrated series of steps. Biomass is first pretreated and deconstructed using chemical catalysts and/or enzymes to liberate sugar monomers and lignin fragments. Deconstruction is followed by a conversion step in which engineered host organisms assimilate the released sugar monomers and lignin fragments, and produce value-added fuels and chemicals. Over the past couple of decades, a significant amount of work has been done to develop innovative biomass deconstruction and conversion processes that efficiently solubilize biomass, separate lignin from the biomass, maximize yields of bioavailable sugars and lignin fragments and convert the majority of these carbon sources into fuels, commodity chemicals, and materials. Herein, we advocate that advanced *in silico* approaches provide a theoretical framework for developing efficient processes for lignocellulosic biomass valorization and maximizing yields of sugars and lignin fragments during deconstruction and fuel and chemical titers during conversion. This manuscript surveys the latest developments in lignocellulosic biomass valorization with special attention given to highlighting computational approaches used in process optimization for lignocellulose pretreatment; enzyme engineering for enhanced saccharification and delignification; and prediction of the genome modification necessary for desired pathway fine-tuning to upgrade products from biomass deconstruction into value-added products. Physics-

Abbreviations: ABTS, 2,2′-azino-bis(3-ethylbenzothiazoline-6-sulfonic acid; BLAST, Basic Local Alignment Search Tool; [C₂mim][OAc], 1-ethyl-3-methyl-imidazolium acetate; [C₄mim]Cl, 1-butyl-3-methylimidazolium chloride; CBD, carbohydrate-binding domain; CBHs, Cellobiohydrolases; CD, catalytic domain; CEs, carbohydrate esterases; COSMO-RS, Conductor like Screening Model for Real Solvents; DFT, Density Functional Theory; DP, degree of polymerization; EFMs, elementary flux modes; EGs, Endoglucanases; GROMOS, GROningen MOlecular Simulation; HMMs, hidden Markov models; HSP, Hansen solubility parameters; IL, inonic liquid; LiP, lignin peroxidase; LMEs, Lignin-modifying enzymes; LODE, long-distance equivariant; LPMO, lytic polysaccharide monooxygenases; MD, molecular dynamics; ML, Machine learning; MnP, manganese peroxidase; NBO, natural bond orbital; NGS, next-generation sequencing; PCFF, Polymer Consistent Force Field; QC, quantum chemical; QM/MM-FEP, free-energy perturbation based quantum mechanics/molecular mechanics; QTAIM, quantum theory of atoms in molecules; SBS, secondary binding site; SIP, stable isotope probing; VP, versatile peroxidase.

based modeling approaches such as density functional theory calculations and molecular dynamics simulations have been most impactful in studies aimed at exploring the molecular level details of solvent-biomass interactions, reaction mechanisms occurring in biomass-solvent systems, and the catalytic mechanisms and engineering of enzymes involved in biomass degradation. More recently, with ever increasing amounts of data from, for example, advanced mutli-omics experiments, machine learning approaches have begun to make important contributions in synthetic biology and optimization of metabolic pathways for production of biofuels and chemicals.

INTRODUCTION

Plant biomass is the most abundant renewable source of carbon accessible to humanity. Lignocellulosic biomass is primarily comprised of three natural polymers: cellulose, hemicellulose, and lignin (Higuchi, 1997) (**Figure 1**). Cellulose is a linear, homologous polymer consisting of β-D-glucose units bonded together by β-1-4-glycosidic bonds. The degree of polymerization (DP) of cellulose is variable in different types of biomass (Hallac and Ragauskas, 2011). For example, the DP of cellulose chains ranges from 10,000 to 15,000 for native wood and cotton, respectively. The glucose polymers of cellulose are held together by van der Waals bonds and networks of strong H-bonds, enforcing crystalline regions and leading to the great strength and recalcitrance of cellulose (Shen and Gnanakaran, 2009). These cellulose microfibrils are entangled with hemicellulose and lignin within the plant cell wall. Hemicellulose is a heteropolysaccharide composed of pentose

polymers (xylose and arabinose) and hexose polymers (glucose, galactose, and mannose) with DP ranging from 50 to 200 monosaccharides (Farhat et al., 2017; You et al., 2019) and sugar (uronic) acids (Huffman, 2003). Lignin is the third component and comprises 15 – 35 wt% of lignocellulose. Lignin is a three-dimensional amorphous polymer composed of three phenylpropanoid monolignols: ρ-coumaryl, coniferyl, and sinapyl alcohols, which in the lignin polymer are the ρ-hydroxyphenyl (H), guaicyl (G), and syringyl (S) units, respectively. The ratio of the three monolignols varies among plant phenotypes, resulting in many different lignin forms. The creation of a variety of linkages among these monolignols during lignin polymerization in the cell wall makes lignin a highly branched complex heterologous polymer. These linkages between H, G and S subunits are β-O-4′, β-5, α-O-4, 4-O-5′, β-β in primary and β-1′, and 5-5′ in minor content (Yoo et al., 2016). The predominant linkages in lignin are beta-aryl ether bonds, typically 50% in softwood and 60% in
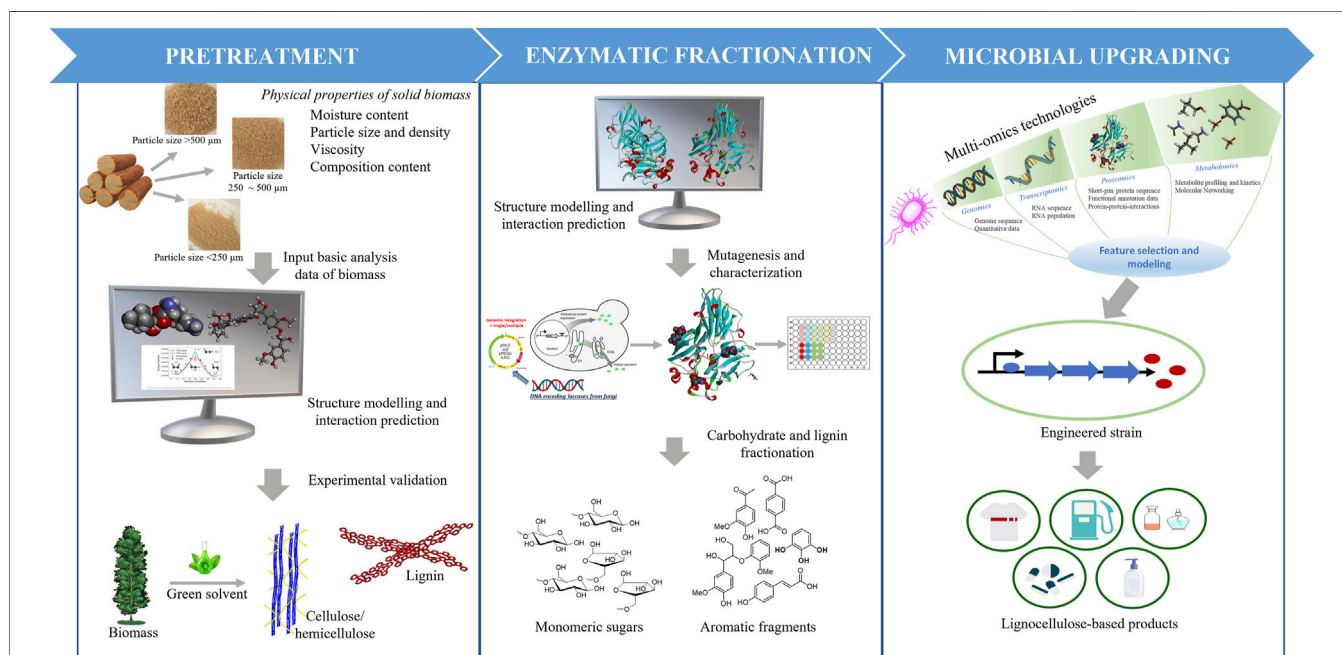
FIGURE 1 | Computational strategies used in process optimization for lignocellulose biomass deconstruction and upgrading to valuable fuels and chemicals.

hardwood (Yoo et al., 2016). Several parameters affect the structure of lignocellulose, including the DP of cellulose fibers, the degree of crystallinity, how well the hemicellulose coats cellulose, the amount of lignin, and how the lignin protects the cellulose fibers. Therefore, the information on lignocellulose structure and composition will govern and direct strategies for deconstructing lignocellulose and converting it into value-added products.

Due to the complex nature of biomass and variation in its composition and structure, there is no universally optimized process for physical-chemical pretreatment and conversion of lignocellulosic biomass to valuable products (Ray et al., 2020). The recalcitrance of biomass to deconstruction and conversion is created in part by the crystallinity of cellulose, the complex interactions among cellulose, hemicellulose, and lignin, and the heterogeneity of lignin. This limits biomass deconstruction and escalates the pretreatment and enzymatic saccharification costs. To help optimize the processing steps, computational approaches have been used to develop a fundamental understanding of the interactions among biomass components and solvents for improving the accessibility to carbohydrate fibers before enzyme-catalyzed saccharification, the structure and function of biomass-degrading enzymes for engineering improved stability and activity under harsh pretreatment conditions, and the engineering of metabolic pathways in production hosts for improved titers and metabolic rates. The use of advanced computational techniques to optimize integrated pretreatment technologies (**Figure 1**, left panel) is discussed in **Section 2**. Computational methods, including quantum mechanical and molecular mechanical calculations, have been employed to help develop novel strategies for enzyme preparation, enzyme engineering, and enzyme mixture formulations to improve saccharification and lignolysis. Some of the latest studies on protein engineering approaches are discussed in **Section 3** (**Figure 1**, middle panel). Finally, in **Section 4** (**Figure 1**, right panel) of this review, we survey computational tools applied to system biology studies, including advanced technologies, multi-omics, and additional tools necessary for desired pathway engineering and fine-tuning to maximize yields from upgrading products produced during biomass deconstruction into value-added fuels, chemicals, and other products.

HIGHLIGHTS IN THE APPLICATION OF COMPUTATIONAL METHODS IN LIGNOCELLULOSE PRETREATMENT

Lignocellulosic biomass, including human-inedible agricultural, forest, and herbaceous residues, stands out as a sustainable alternative for renewable, carbon-neutral production of fuels, chemicals, materials, and energy (Castilla-Archilla et al., 2019). However, the direct use of lignocellulosic biomass is restricted due to its recalcitrance to degradation, which is due to the strong covalent and hydrogen bond interactions among the complex chemical structure of its constituents, namely, cellulose, hemicellulose, and lignin, and thus, pretreatment is necessary

(Gibson, 2012; Haghighi Mood et al., 2013). Existing approaches include biological, abiotic (physical, chemical, and physicochemical), and hybrid technologies (**Figure 2**) (Tu and Hallett, 2019). An ideal pretreatment technology would successfully disrupt the strong interactions among biopolymers, leading to their selective fractionation, minimize by-product formation, and be economically viable. Nevertheless, optimizing these objectives alone or in combination is essential to benefit the overall process, as each pretreatment technology, owing to its unique characteristics, is applicable to a specific biomass type and source. For example, physical pretreatment approaches are the most conventional methods for lignocellulosic biomass pretreatment. However, their limited scalability, high energy requirements, and multiple feedstock non-viability narrow their applicability. Chemical pretreatment methods involving hot water, dilute acid, ionic liquids, alkali, organic solvents (organosolv), and ammonia fiber expansion have been widely studied (Haghighi Mood et al., 2013; Bhardwaj et al., 2019). While requiring less energy and being generally non-toxic, biological pretreatments typically require longer retention times for effective pretreatment, hindering their commercial feasibility.

Pretreatment of lignocellulosic biomass facilitates the production of biologically available intermediates such as glucose, cellulose, and lignin fragments that can be converted to final products such as biohydrogen, biomethane, bioethanol, biomethanol, biobutanol, and bio-diesel. The efficiency of a given pretreatment process is a function of the constituents of the biomass and how they interact with the pretreatment process. Rigorous efforts to optimize a single biomass pretreatment technology or combinations of technologies have improved economic viability and environmental sustainability. However, the mission is still not accomplished, given the vast number of variables involved in optimizing pretreatment technologies. In this regard, computational tools that leverage experimental datasets have become essential in identifying sustainable and robust multi-product biorefinery methodologies. The field of computational chemistry and biology has become increasingly predictive in the twenty-first century, and active applications have been extended to studies, predictions, and optimization of biomass pretreatment technologies. These simulation approaches predict desired outputs based on existing experimental datasets in which pretreatment efficacy has been measured for a diverse set of feedstocks under a variety of pretreatment conditions. Computational methods used to understand and predict pretreatment efficacy have predominantly used atomistic physics-based modeling, but atomic scale machine learning methods are also being developed that have the potential to speed up pretreatment optimization.

Atomic-scale modeling techniques, including density functional theory (DFT) and molecular dynamics (MD), have been instrumental in advancing the understanding of experimental pretreatment results and predicting the properties of biomass-solvent systems at the level of atom-by-atom interactions among biomass, water, and solvent. DFT is a powerful tool for obtaining static properties such as local energy minima, reaction pathways, and transition states and calculating

FIGURE 2 | Pivotal pretreatment approaches for the valorization of lignocellulosic biomass.
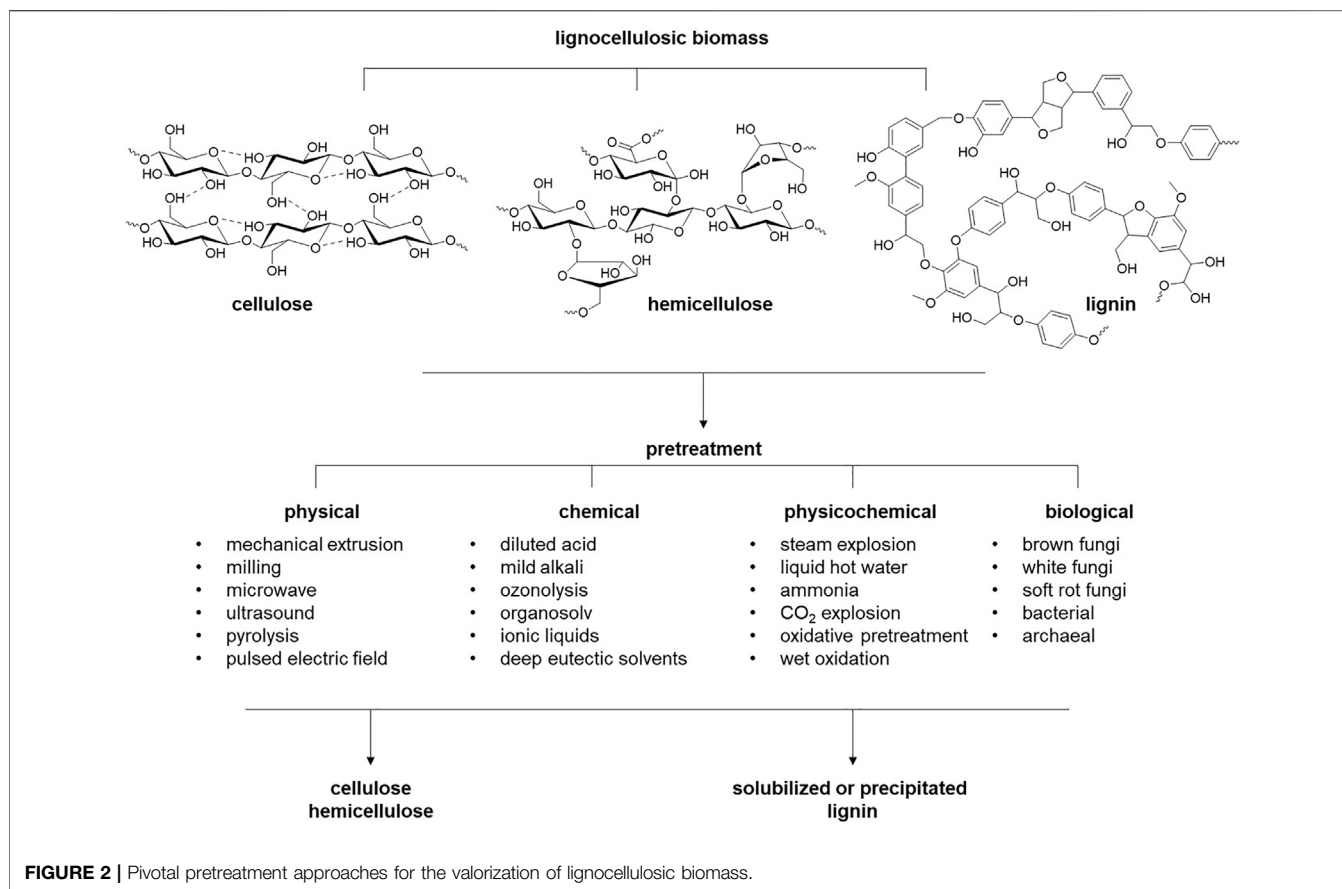
other thermodynamic properties for a relatively small system (tens to hundreds of atoms) (Cohen et al., 2012). For evaluation of larger systems (thousands to millions of atoms), MD simulations are critical in calculating equilibrium thermodynamic and physical properties (as a function of hydrogen bonds), sampling conformational states, and evaluating femtosecond to millisecond dynamics and the role of long-range forces (Rapaport et al., 1996; Frenkel and Smit, 2002). It is to be noted that classical MD simulations are limited to studying equilibrium states and properties of the system, and quantum chemistries such as bond-breaking and bond-forming are not considered. However, accurate force fields for calculating non-bonded interactions, including van der Waals and Coulombic interactions, are essential to understanding interactions between lignocellulosic biomass components and pretreatment solvents to design an efficient process. The total potential energy of the given lignocellulosic biomass system is calculated using empirical force fields such as GROningen MOlecular Simulation (GROMOS), Polymer Consistent Force Field (PCFF), and Chemistry at Harvard Macromolecular Mechanics (CHARMM). The MD methods using these force fields to study biomass–solvent interactions are discussed in the upcoming sections.

Machine learning (ML) approaches have the potential to generate predictive models of biomass pretreatment efficacy and would provide potentially much faster ways to evaluate

and optimize pretreatment technologies. However, ML approaches require either very large databases from which to learn how to predict pretreatment outcomes from inputs and/or the ability to account for and features the atomic scale forces governing biomass–solvent interactions. Recently, neural networks have been developed that provide insights into the atomistic properties of molecules and are trained to look for a specific "structure" or "moiety" with a defined interaction or activity (Grisafi and Ceriotti, 2019). They computed the atom-global information on the structure and composition utilizing Smooth Overlap of Atomic Properties (SOAP), long-distance equivariant (LODE), and similar ideas to improve the accuracy and efficiency of long-range information. This ML approach provides a representation of the system that accounts for both short-range atomistic interactions and long-range interactions, giving it the potential to help design and optimize an efficient pretreatment method.

Modeling Cellulose and Lignin Structures

The structures of cellulose, hemicellulose, and lignin and their interactions play an essential role in accurately predicting the pretreatment efficacies, i.e., creating the initial coordinates in terms of biopolymer structure is vital for investigating their properties and their interactions with solvents (Ciesielski et al., 2020). Typical tools for building structures of sugar polymers include "**Cellulose Builder**" (Gomes and Skaf, 2012) and

"**doGlycans**" (Danne et al., 2017). While the former facilitates the construction of any length of various cellulose crystalline forms such as I_α, I_β, II, and III, the latter enables a structural topology for cellulose and hemicellulose. In 2003, amorphous and crystalline cellulose models were compared using MD simulations for the first time. The study also analyzed various properties and showed that their conformational states, density, and hydrogen bonding networks were consistent with available experimental data (Mazeau and Heux, 2003). Since then, significant progress has been made in modeling cellulose crystal structures and their hydrogen-bonding networks (Ciesielski et al., 2020). MD simulations have also been employed to study twisted conformations of cellulose around their glycosidic linkages, as was observed in atomic force and transmission electron microscopy studies (Hanley et al., 1997; Bowling et al., 2001). The deviation of glycosidic linkages from 180° was suggested using MD simulations; however, the twisted microfibril was unstable and reverted to the original untwisted structure independent of the temperature (Matthews et al., 2011; Matthews et al., 2012). In another interesting study, the anti- and syn-conformations of four different glucan decasaccharides were evaluated using the CHARMM36 force field and compared with small-angle X-ray scattering to unveil the glycosidic linkage flexibility (Kameda et al., 2018). MD simulation of branched hemicelluloses revealed the higher stiffness of the glucomannan backbone compared to the xylan backbone (Martínez-Abad et al., 2017), stability of various conformers (Berglund et al., 2019), and impact of acetylation on cellulosic interactions (Busse-Wicher et al., 2014).

Similarly, "**Lignin Builder**" (Vermaas et al., 2018) enables the design of representative lignin linkages into models of lignin polymers (hardwood, softwood, and grass) for simulation studies. Several other approaches based on kinetic Monte Carlo and DFT have also been reported to generate lignin structures (Zhang et al., 2011; Dellon et al., 2017; Orella et al., 2019). Based on the structures developed, quantum chemical calculations using AM1, HF, and DFT/B3LYP levels of theory were employed to examine the interaction characteristics such as hydrogen bonding between cellulose-hemicellulose and covalent bond linkages for hemicellulose-lignin systems (Zhang et al., 2011). These studies predicted the potential to disrupt or dissociate C_1-O bonds in xylan-lignin complexes and β-O bonds in lignin-glucomannan complexes during pretreatment. In addition, an exciting study highlighted the variability of interaction energy based on the orientation of these biopolymers, i.e., a stacked configuration between polymers affords higher interactions (Yang et al., 2019). As discussed in the next section, these builder tools have facilitated the building of various lignocellulosic models and the understanding of interactions between biomass and various solvents.

Understanding the Interactions of Biomass With Pretreatment Solvents

In this section, we will limit our discussions to molecular and ionic solvent-based pretreatment technologies. The limitless possibilities of molecular and ionic solvents limit the full exploration of every unique combination within the context of experimental methodologies. Computational methods have been used to help understand the dominant factors governing the efficacy of solvent-based pretreatment of lignocellulosic biomass. Typically, in biomass pretreatment, quantum chemical (QC) and MD simulations have been adapted to understand the interactions of the various biomass components with the pretreatment solvent, which in turn helps to understand and predict the fractionation abilities of the solvent (or solvent class) under consideration (**Table 1**). Also, pre-existing solubility parameters such as Hildebrand (Quesada-Medina et al., 2010), Hansen solubility parameters (HSP) (Hansen, 2007; Cheng et al., 2018), and Conductor like Screening Model for Real Solvents (COSMO-RS) models have been extensively studied for several chemical pretreatment technologies employing organic solvents, deep eutectic solvents, and ionic liquids (Balaji et al., 2012; Casas et al., 2013; Achinivu et al., 2021). Recently, ionic liquids (salts possessing organic cations with a melting point below 100°C) have attracted significant attention as a promising pretreatment solvent. Several modeling methods have been developed to understand how these solvents fractionate or solubilize lignocellulosic biomass. For instance, the solubility of lignin in a given solvent was determined based on the Hildebrand solubility and thermodynamic parameters such as activity coefficients and excess enthalpy (Casas et al., 2012). These studies concluded that more robust exothermic behavior and lower activity coefficient values are required for enhanced interaction/solubility for any given solute-solvent pair. In another instance, density functional theory (DFT) studies were employed to calculate the hydrogen bonding interaction between solvent (ionic liquid) and biopolymer (lignin) to determine the pretreatment efficacies of these solvents (Rashid et al., 2016; Zhang et al., 2017). Dispersion-corrected DFT models established the role of cations in regulating the solubilities of lignocellulosic components as a function π-stacking (Janesko, 2011). Ji and Lv suggested that both C-H···π and strong hydrogen bonding are critical to enhanced delignification performance using three solvent systems, namely para-toluenesulfonic acid, choline chloride-lactic acid eutectic, and 1-allyl-3-methylimidazolium chloride (Ji and Lv, 2020). Singh et al. have extensively studied the dissolution of cellulose in pure 1-ethyl-3-methylimidazolium acetate ([C_2mim][OAc]) and mixtures of [C_2mim][OAc] and water systems (Liu H. et al., 2010; Shi et al., 2014; Parthasarathi et al., 2015). The role of water as cosolvent was established in these studies, identifying the "ideal" IL-water ratio (4:1 for [C_2mim][OAc] and water system) for maximum disruption of intermolecular hydrogen bonding within cellulose.

Interestingly, the simulation studies suggested repacking de-crystallized cellulose into an amorphous form with high water content in pure [C_2mim][OAc]. A recent study by Achinivu et al. and team has screened various structurally and functionally distinct amines and developed a toolset to provide rapid identification of effective pretreatment solvents (Achinivu et al., 2021). This study employed a theoretical analysis (validated by an experimental dataset) to develop a predictive model for a given class of solvent. In the first step, the

TABLE 1 | Molecular simulation techniques used for understanding interactions between biomass-solvent.

Method [Basis set/Force Field]	Substrate	Solvent	Reference
DFT [6-31G(d)]	Cellobiose	[C$_4$mim]Cl	Novoselov et al. (2007)
	Dimethoxyglucose	[C$_2$mim][OAc]	Ding et al. (2012)
DFT [6-311+G(d,p)]	Cellobiose	[C$_4$mim]Cl	Li et al. (2015b)
	Lignin	[C$_4$mim]-anion	Zhang et al. (2017)
DFT-D [6-311++G(2d,2p)]	Glucose	[C$_1$mim]Cl	Janesko, (2011)
DFT [6-311+G(d,p)]/MD [GLYCAM]	2,4,6-mer oligomers	[C$_4$mim]Cl	Xu et al. (2012)
	10-mer oligomer	[C$_4$mim][OAc]	Zhao et al. (2013b)
MD [COMPASS]	Glucose derivatives	[C$_n$mim]Cl	Derecskei and Derecskei-Kovacs, (2006)
MD [CHARMM]	Microfibril	[C$_4$mim]Cl	(Cho et al. 2011; Gross et al., 2011; 2012)
MD [AMBER]	Cellulose Iβ	[C$_4$mim][OAc]	Gupta et al. (2011)
MD [OPLS]	Cellobiose	[C$_4$mim]Cl	Zhang et al. (2012)
	Cellulose bunch	[C$_4$mim]Cl	(Rabideau et al. 2013; Rabideau et al. 2014; Rabideau and Ismail, 2015)
MD [OPLS-AA]	Glucose	[C$_1$mim]Cl	Youngs et al. (2006)
	Glucose	[C$_2$mim][OAc]	Felczak et al. (2011)
	Glucose	[C$_2$mim][OAc]	Andanson et al. (2014)
	Cellulose Iβ	[C$_n$mim]Cl	Huo et al. (2013)
	Lignin	9 ILs	Hu et al. (2020)
MD [GLYCAM]	Glucose	[C$_4$mim]Cl	Jarin and Pfaendtner, (2014)
	Glucose and Cellobiose	[C$_2$mim][OAc]	Bharadwaj et al. (2015)
	5,10,20-mer oligomers	[C$_2$mim][OAc]	Liu et al. (2010a)
	10-mer oligomer	[C$_2$mim]-anions	Zhao et al. (2013a)
	10-mer oligomer	[C$_4$mim]Cl	Mostofian et al. (2014a)
	Microfibril	[C$_4$mim]Cl	(Mostofian et al. 2011; Mostofian et al. 2014b)
	Microfibril	[C$_2$mim][OAc]	Liu et al. (2012)
	Cellulose bunch	[C$_2$mim][OAc]	Li et al. (2015b)
COSMO-RS	Glucose	320 ILs	Casas et al. (2012)
	Cellotriose	>2000 ILs	Kahlen et al. (2010)
	3*3 structure	750 ILs	Casas et al. (2013)
	1,3,4-mer oligomers	357 ILs	Liu et al. (2016)
	Lignin	Cholinium-Anions	Yao et al. (2021)
	Lignocellulosic biomass	Ethanolamine and Acetic acid	Huang et al. (2021)
	Lignin	Cholinium-Anions	Mohan et al. (2021)

interaction of biomass with organic solvents with various functional groups was studied using HSP and COSMO-RS toolsets to reveal amines as better solvents for lignocellulosic pretreatment. Then, the differences in the interactions of various amines were studied using the quantum theory of atoms in molecules (QTAIM) and QC calculations (interaction energies and natural bond orbital (NBO) analysis) to suggest the importance of electrostatic interactions and hydrogen bonding between amines and lignin for enhanced solubility. Various computational studies of ionic liquid solvent systems in the pretreatment of biomass have heavily relied on COSMO-RS predictions and hydrogen bond basicity to predict the biopolymer solubilities in the ionic liquid (Chu and He, 2019; Iqbal et al., 2019). Yao et al. extended the application of COSMO-RS prediction to demonstrate the synergistic advantages of multiple ions in a cholinium-based ionic liquid system for the pretreatment of sorghum biomass (Yao et al., 2021). Mood et al. showed that solubility parameters of ionic liquids and deep eutectic solvents calculated using COSMO-RS are predictive of lignin solubility under the like-dissolves-like principal and developed a new method to calculate solubility parameters from MD simulation trajectories, allowing predictions to be made for much larger lignin polymers (Mohan et al., 2021; Mohan et al., 2022).

In summary, molecular simulations are necessary to support experiments and provide critical missing links that experiments cannot access, considering the complexity of the lignocellulosic biomass structure. MD simulations are used to account for the dynamical behavior of molecular systems and understand solvent–biomass interactions during pretreatment. In contrast, reactive force fields, which rely on the bond order, bond distance, and bond energy, provide a detailed explanation of bond breaking and bond-forming reactions during simulations. Multiscale modeling has been used to successfully investigate physical and chemical properties, reaction mechanisms, and overall system dynamics. These tools and approaches also help understand the structure-activity relationships and assist in developing novel solvents and maximizing yields or selectivity in multi-product biorefinery settings. These computational toolsets have the potential to speed up the design, development, and deployment of novel solvents for a robust biorefinery and, when eventually combined with machine learning, will provide tools for rapidly evaluating potential new solvents and deconstruction processes. Despite all these developments in both computational and experimental techniques, a knowledge gap still exists in developing a robust multi-product biorefinery, namely: *1*) complete insights into the whole molecular structure of biomass; *2*) efficient and robust

processes for the conversion of biomass to chemicals; *3)* mechanistic understanding of the role of solvents during pretreatment; and *4)* key interactions and orientations of polymer components. In addition, some of these simulations are fundamentally expensive as they may take several days depending on the complexity of the molecule involved. The combination of experiments including imaging and spectroscopy, computational modeling, and/or machine learning is expected to contribute to the future design of stratified structures of lignocellulosics and generate a large number of structured materials and chemicals in the future. Furthermore, the understanding developed through the optimization of biomass pretreatment using these simulation tools will promote overall process yields while reducing energy requirements and carbon footprints.

COMPUTATIONAL MODELING METHODS FOR UNDERSTANDING CATALYTIC MECHANISMS AND ENGINEERING ENZYMES

A variety of computational methods utilize new advances in computing to understand the underlying mechanisms of the biocatalysts used to promote efficient biotransformation of substrates into value-added products. These computational methods, which differ in computational cost and accuracy, can simulate biocatalytic processes at different molecular levels. For instance, protein-ligand or enzyme-substrate docking is a molecular modeling technique that can predict a ligand's position and orientation (substrate, a small molecule) when it is bound to a protein/enzyme (Kearsley et al., 1994; Friesner et al., 2004; Wang and Pang, 2007; Zsoldos et al., 2007). Modeled interactions between an enzyme and its substrate(s) provide insights into predicting the activation or inhibition of an enzyme and providing information for rational enzyme design. In this method, dealing with receptor flexibility in docking methodologies is still challenging due to the large number of degrees of freedom of the enzyme the calculation needs to consider (Totrov and Abagyan, 2008; Cerqueira et al., 2009; Antunes et al., 2015). The enzyme-ligand complex is often the starting point for molecular dynamics (MD) simulations, which are used to analyze the physical movements of atoms and molecules and the time evolution of enzyme-substrate interactions (Levitt and Warshel, 1975; Warshel, 1976). MD simulations explore the time evolution of a particular interacting system for a fixed period of time on nano to microsecond time scales, and the trajectories of atoms and molecules are determined by numerically solving Newton's equations of motion. Theoretical studies utilizing MD simulation provide insights into the intricate dynamics of biological macromolecules (protein or protein-ligand complex) through observing crucial interactions (e.g., hydrophobic interactions, van der Waals, hydrogen bonds), thus understanding protein folding and unfolding, protein stability, and conformational changes (Levitt, 1982; Moal and Bates, 2012;

Khan et al., 2016). However, simulation accuracy is strongly dependent on the quality of ligand parameterization, which can be improved by using high-accuracy quantum mechanics/ molecular mechanics (QM/MM) methods (Warshel and Levitt, 1976; Brunk and Rothlisberger, 2015). This method combines the strengths of *ab initio* QM calculation (accuracy) and MM (speed) methods. However, it demands the high computational cost of conformational searching and the limitations of implicit solvation effects. In the last two decades, hybrid QM/MM calculations have become a powerful approach to studying enzymatic reactions (Martí et al., 2004; Mulholland, 2005; Riccardi et al., 2006; Senn and Thiel, 2009; Warshel, 2014).

There has been exhaustive research to improve individual enzyme characteristics through either rational design or directed evolution strategies. The rational approach to protein engineering *via* computational methods facilitates development in this field. Simulation of an enzyme structure, substrate, or complex cam provides molecular and structural mechanisms of enzymatic action. This section highlights the increasing evidence of computational modeling methods as a powerful tool in the study and engineering of hydrolases and oxidoreductases, especially for their application as biocatalysts in lignocellulose deconstruction. We compiled and tabulated the computational methods in the studies cited below in **Table 2**.

Cellulases and Hemicellulases

Cellulases are divided into three groups: endoglucanases (EC 3.2.1.4), cellobiohydrolases (EC 3.2.1.91), and β-glycosidases (3. 2. 1. 21), that work synergistically to catalyze the conversion of cellulose to glucose in a process known as saccharification. Endoglucanases (EGs) catalyze the breaking of internal glycosidic bonds of the amorphous part of the cellulose chain, producing new ends of glucose polymers (Medve et al., 1998). Cellobiohydrolases (CBHs), also called exoglucanases, bind to these newly created ends and catalyze hydrolysis of glycosidic bonds in glucose polymers, producing cellobiose (Teeri, 1997). Finally, β-glycosidases catalyze the break of glycosidic bonds in cellobiose, producing glucose monomers (Riou et al., 1998; Decker et al., 2001) and are typically the rate-limiting step in the full conversion of cellulose to glucose. Due to the recalcitrant nature of lignocellulosic, saccharification of cellulose to glucose is slow, and in the second generation of conversion of lignocellulose to ethanol requires several-fold more active hydrolytic enzymes than for saccharification from starch (Balan, 2014). Low activity and high costs of cellulases are the bottlenecks for their industrial use in the valorization of lignocellulosic biomass. Some endoglucanases and cellobiohydrolases are composed of a catalytic domain (CD) and a carbohydrate-binding domain (CBD). The CBD increases enzymatic activity on specific and solid substrates and helps disrupt the crystalline structure of cellulose. Several MD simulation studies have been conducted to understand cellulase adsorption to cellulose and the role of CBDs. A hundred nanosecond timescale MD simulations of Cel7A from *Geotrichum candidum* strain 3C (GcaCel7A) were studied in three different forms: free form, in complex with a cellononaose substrate, and in complex with microfibrils of cellulose. These simulations revealed a significant difference in

TABLE 2 | List of hydrolases and lignin-modifying enzymes engineered by protein engineering.

Enzyme	Organism	Techniques	Improvement/understanding	References
Cellulase	*Geotrichum candidum Heterobasidion irregulare Heterobasidion jecorina Phanerocheate chrysosporium Penicillium funiculosum*	MD simulation	Interaction between cellulase and cellononaose, microfibril of cellulose	(Borisova et al. 2015; Momeni et al. 2013; Ogunmolu et al. 2017)
	Trichoderma reesei	MD simulation	Glycosylated linkers of CBM serve as the rate-limiting step in cellulose degradation	(Payne et al. 2013; Knott et al. 2014)
	Trichoderma reesei Phanerodontia chrysosporium	QM/MM	Hydrolysis mechanism *via* stabilization of acyclic oxocarbenium-like transition state, leading to the opening of the glucopyranose ring and formation of an unstable acyclic hemiacetal	(Li et al. 2010; Liu et al. 2010; Wang et al. 2011; Wang et al. 2016; Iglesias-Fernández et al. 2017; Zong et al. 2019; Bharadwaj et al. 2020; Pereira et al. 2021)
Xylanase	*Bacillus subtilis Talaromyces thermophilus*	MD simulation	The hydrophobic site at N-terminal and C-terminal plays a vital role in contact with the reducing end of xylooligosaccharides	(Li et al. 2017; Ngenyoung et al. 2021)
	Paenibacillus xylanivorans	MD simulation	Unveiling secondary binding site on the surface of xylanases	
Lignin peroxidase	*Phanerocheate chrysosporium Trametopsis cervine Pleurotus eryngii Klebsiella pneumoniae*	QM/MM calculation	Unveiling role of the surface-active site in the oxidation of high redox potential substrates	(Smith et al. 2009; Bernini et al. 2012; Romero et al. 2019; Miki et al. 2013; Acebes et al. 2017; Nys et al. 2021)
	Phanerocheate chrysosporium	QM/MM calculation	Identifying specific amino acids which influence the oxidative power	(Castro et al. 2016; Pham et al. 2016; Singh et al. 2021; Pham et al. 2021)
Manganese peroxidase	*Ceriporiopsis subvermispora*	Docking and MD simulation	Two histidines, H220 and H142, interacted, forming hydrogen bonds with ABTS's negatively charged ABTS sulfonates	
Laccase	*Trametes versicolor*	QM/MM-FEP	The oxidation state of the surrounding residues affected the T1 copper site redox potential	Götze and Bühl, (2016)

the dynamics of substrate-bound enzymes compared with free enzymes (Borisova et al., 2015). Similar studies on substrate-bound enzymes revealed the cellulose-binding site was highly conserved in other cellulases, Cel7A from *Heterobasidion irregulare* (HirCel7A), *Heterobasidion jecorina* (HjeCel7A), and Cel7D from *Phanerochaete chrysosporium* (PchCel7D), and PfCBH1 from *Penicillium funiculosum* when bound with cellononaose and microcrystalline cellulose (Momeni et al., 2013; Ogunmolu et al., 2017). Forty nanosecond MD simulations of *Trichoderma reesei* Cel6A and Cel7A showed the flexible glycosylated linkers of CBD bind nonspecifically to cellulose and can serve as the rate-limiting step in cellulose degradation (Payne et al., 2013; Knott et al., 2014). While MD simulations have been used to study the interaction between cellulases and cellulose and cellulase CBDs and cellulose, QM/MM simulations have been used to reveal the transition state of oligosaccharide hydrolysis (Liu J. et al., 2010; Li et al., 2010; Wang et al., 2011; Wang et al., 2016; Iglesias-Fernández et al., 2017; Zong et al., 2019; Bharadwaj et al., 2020; Pereira et al., 2021). Li et al. elucidated the mechanism of enzymatic catalysis of cellulase Cel7A from *Trichoderma reesei* (Li et al., 2010). At the level of accuracy of the applied theory, detailed structural and energetic information revealed an S(N)2-type-like mechanism *via* loose transition state structures. In similar work using QM/MM, an endocyclic mechanism for PcCel45A was revealed in which an acyclic oxocarbenium-like transition state is stabilized, leading to the opening of the glucopyranose ring and the formation of an unstable acyclic hemiacetal that can be readily decomposed into hydrolysis products (Pereira et al., 2021).

Hemicellulases are a group of enzymes that catalyze the hydrolysis of galactans, xylans, and mannans. The primary enzyme is endoxylanase (EC 3.2.1.8), which hydrolyzes β-d xylano pyranosyl linkages of xylan to form xylooligosaccharides. Secondly, β-D xylosidase (EC 3.2.1.3, xylobiase) catalyzes the hydrolysis of xylobiose or xylooligosaccharides from the nonreducing end, producing D-xylose sugar in the hydrolysates. Control of the desired xylooligosaccharide size range is one of the most challenging studies in xylose degradation, and several endoxylanase engineering attempts have been aimed at changing the range of xylooligosaccharides produced. For example, Pollet et al. engineered the BsXynA xylanase from *Bacillus subtilis* by replacing a Tyr at the binding site with an Ala and improved the variety of xylooligosaccharides produced by the enzyme (Pollet et al., 2010). A similar catalytic pattern in T-Xyn xylanase from *Talaromyces thermophilus* F1208 was revealed by double mutations at a region near the N-terminal and the C-terminal, which resulted in the absence of xylose monomer product (Li et al., 2017). Atomistic MD simulations were used to understand the mechanisms underlying these efficiency losses. The MD trajectory analysis suggested that the mutation-induced binding pocket tilting resulted in an additional hydrophobic contact between the reducing end of xylooligosaccharides and Trp128 (Ngenyoung et al., 2021).

A secondary binding site (SBS) on the surface of the GH11 xylanases has been discovered in a few endoxylanases from *Bacillus subtilis* (PDB ID: 2QZ3) (Cuyvers et al., 2011), *Aspergillus niger* (PDB ID: 2QZ2) (Vandermarliere et al., 2008),

and *Bacillus circulans* (BcX) (PDB ID: 1XNB) (Ludwiczek et al., 2007). Recently, MD simulations of *Px*Xyn11B from *Paenibacillus xylanivorans* A57 revealed an essential role of SBS in the activity and conformational mobility of the enzyme, demonstrating that the SBS stabilizes ligand binding, allowing it to be bound within the active site for a longer time period and resulting in more controlled enzymatic breakdown to products (Briganti et al., 2021). These findings explain the observed enzyme kinetics and shed light on the product control of the xylanase enzymes by protein engineering.

Lignin-Modifying Enzymes

Lignin-modifying enzymes (LMEs) are enzymes produced by fungi and bacteria that catalyze bond breaking of a variety of bonds in lignin polymers to degrade lignin to bioavailable substrates. In nature, these lignin fragments are consumed by microbes, and in synthetic biology applications they are fed to organisms engineered to convert them into biofuels and bioproducts. LMEs include peroxidases, such as lignin peroxidase (LiP, EC 1.11.1.14), manganese peroxidase (MnP, EC 1.11.1.13), versatile peroxidase (VP, EC 1.11.1.16), and many phenol oxidases of the laccase type (EC 1.10.3.2). LiP and MnP contain a heme-iron in their active sites that participates as a reducing agent in the general peroxidase catalytic mechanism. The heme-iron is first oxidized by hydrogen peroxide, and electrons are then shuttled from lignin through soluble mediators such as phenolic veratryl alcohol or, in the case of MnP, Mn(II). VP shares the structural and catalytic properties of both LiP and MnP (Ruiz-Dueñas and Martínez, 2009). Laccases are multi-copper oxidases that catalyze one-electron oxidation of a wide range of phenolic compounds (Hamid and Khalil ur, 2009; Pollegioni et al., 2015). Various computation-aided studies have attempted to improve the catalytic efficiency of LDEs through understanding lignin-aromatic compound binding modes, critical structures that impact oxidative power, and electron transfer pathways, using the approaches elaborated in the following paragraphs.

Molecular docking studies have been carried out to predict the binding modes of aromatic substrates and lignin model compounds to LiP, MnP, and laccase, and MD simulations were performed to study the resulting enzyme-substrate complexes (Borrelli et al., 2005; Chen et al., 2011; Fernández-Fueyo et al., 2014; Singh et al., 2021). Rational enzyme engineering of MnP6 from *C. subvermispora* has also been carried out with the help of computational methods (Acebes et al., 2016). Acebes et al. started by using the protein energy landscape exploration (PELE) algorithm to inspect the active sites of both systems, ABTS-MnP6 and ABTS-MnP4. These explorations showed that in the energetically minimum structure of MnP4 located at the main heme channel, two histidines, H220 and H142, interacted, forming hydrogen bonds with the negatively charged sulfonates of ABTS. Furthermore, the high-performance molecular dynamics simulations-DESMOND were recently used to perform deep, rigorous structural and functional fluctuation analyses of docked complexes between lignin model compounds and LiP. The findings demonstrated that LiP interacts with chlorinated

compounds through ionic interaction, while hydrophobic and H-bond contacts have been observed in all lignin-model compounds (Singh et al., 2021).

The oxidative power (redox potential) of LDE is a critical factor in the successful degradation of bulky and recalcitrant lignin substrates. QM/MM simulations have been used to identify specific amino acids that influence the oxidative power of LiP, which suggested mutations with higher oxidative abilities or with the capacity to function under different pH conditions (Castro et al., 2016; Pham et al., 2016; Kohler et al., 2018; Singh et al., 2021). Recently, using *ab initio* molecular dynamic simulations and climbing-image Nudge Elastic Band-based transition state searches, Pham et al. suggested the effect of lower pH on LiP activity is *via* protonation of aliphatic hydroxyl groups, which resulted in lower energetic barriers for bond-cleavages, particularly β-O-4′ bonds (Pham et al., 2021). Molecular mechanical free-energy perturbation (QM/MM-FEP) methods in combination with explicit solvent simulations have been used to study the redox potentials (RP), acidity constants, and isomerization reactions of the laccases (Hong et al., 2011; Vázquez-Lima et al., 2012; Li J. et al., 2015; Götze and Bühl, 2016). More recently, the pH dependence and effect of mutants on the laccase redox potentials at the T1 site were studied with QM/MM approaches. The authors found that the oxidation state of the surrounding residues affected the T1 copper site redox potential by about 0.2–0.3 V and was changed to −1.37 V when the replacement of a protonation state corresponded to a neutral environment. The predicted change in the redox potential of the F463M mutant (−0.1 V) was consistent with observations for a related laccase (Götze and Bühl, 2016).

The extant peroxidases (LiP and VP), which have high redox potentials, proved their ability to degrade non-phenolic lignin by using a tryptophanyl radical interacting with the bulky polymer at the surface of the enzyme (Ayuso-Fernández et al., 2018). LiP oxidizes different non-phenolic lignin model compounds, including β-O-4 linkage-type arylglycerol-aryl ethers, forming a radical cation through one-electron oxidation. Radical cation formation leads to side-chain cleavage, demethylation, intramolecular addition, and rearrangements (Kirk et al., 1986; Miki et al., 1986; Wong, 2009). Oxidation of non-phenolic aromatic substrates of high redox potential such as veratryl alcohol (VA) was mediated through the tryptophan radical (Trp171) present in LiP from *Phanerocheate chrysosporium,* which has been elucidated through QM/MM calculations at the B3LYP/CHARMM level of theory (Bernini et al., 2012; Romero et al., 2019). The experimental work was performed to validate these calculations through the catalytic engineering activity of *Coprinus cinereus* peroxidase (CiP) (Smith et al., 2009). By mimicking the surroundings of Trp171 in *Phanerocheate chrysosporium* LiP, some specific acid residues were introduced to the catalytic Trp178 in CiP to create variant D178W/R257E/R271D. The EPR characterization crucially showed that [Fe(IV) = O Trp-179(*)] in engineered CiP was the reactive intermediate with veratryl alcohol (Smith et al., 2009). Similar works reported the electron transfer mechanism of VA at Tyr181 in *Trametopsis cervina* LiP (Miki et al., 2013), at Trp164 in VP from *Pleurotus eryngii* (Pogni et al., 2006; Bernini et al., 2014; Acebes et al., 2017)

and ABTS oxidation at Y247 in *Klebsiella pneumoniae* dye-decolorizing peroxidase (*Kp*DyP) (Nys et al., 2021).

The MD, QM, and QM/MM simulations were mainly presented as auxiliary tools to explain the experimental evidence in aspects like cellulose and lignin fractionation reported for these enzymes. A broad set of molecular and computational tools allowed the creation of models and more efficient screening methods. We believe that, during subsequent years and advances in hardware, software, and algorithms, more accurate and predictive computational tools will greatly benefit studies aimed at rational protein design to improve the catalytic activity of a given hydrolase and oxidoreductase for a specific substrate. The conjunction of these experimental and computational techniques will help design more efficient biocatalysts for lignocellulosic bioconversion.

Auxiliary Enzymes

In addition to the three classes of synergistic cellulolytic enzymes and the various lignin modifying enzymes described above, additional auxiliary enzymes have been implicated as being required for maximum bioconversion of lignocellulosic biomass to compounds amenable to biological uptake and conversion. Besides cellulolytic enzymes that cleave off various monosaccharide side chains, other enzymes are required for the deprotection of the polysaccharide backbone. Polysaccharide sulfatases remove sulfate ester groups (Bäumgen et al., 2021), while carbohydrate esterases catalyze the cleavage of *O*- and *N*-acetyl groups from carbohydrates (Davies et al., 2005). In contrast to the carbohydrate esterases (CEs), the sulfatases are not included in the Crazy database but are listed in the SulfAtlas database instead (Barbeyron et al., 2016).

Lignin-degrading auxiliary enzymes enable lignin degradation through the sequential action of several proteins that may include oxidative H2O2 (Kumar and Chandra, 2020). This group includes cellobiose dehydrogenase, aryl alcohol oxidases, glyoxal oxidase, glucose oxidase, and pyranose 2-oxidase (Kumar and Chandra, 2020). Lignin-degrading auxiliary enzymes cannot alone catalyze complete depolymerization of lignin and typically work synergistically with additional enzymes. The auxiliary enzyme classes, such as redox enzymes, act in conjunction with other CAZymes, including lytic polysaccharide monooxygenases (LPMOs), lignin peroxidases and laccases. LPMO activity has been described as crucial during cellulose hydrolysis and is currently present in commercial cellulase preparations. These enzymes have also been studied by molecular dynamics simulations to understand binding properties and to design rational engineering approaches (Liu et al., 2018; Guo et al., 2020). In particular, MD simulations suggest roles for both aromatic and acidic residues in the substrate-binding of LPMO from the white-rot fungus *Heterobasidion irregulare* (Liu et al., 2018). This study provided additional insight into cellulose binding by C1-specific LPMOs, giving a molecular-level picture of active site substrate interactions. Furthermore, a combination of information from calculations run on the HotSpot Wizard 3.0, dezyme web server, and MD simulations in the study of LPMO from *Myceliophthora thermophila C1*, was used to rationally design a mutant (R17L)

LPMO with a 1.8-fold increase in specific activity and a 1.92-fold increase in catalytic efficiency (k_{cat}/K_m). The increased degree of the reducing sugar yield from microcrystalline cellulose and three plant biomass materials during hydrolysis using cellulase in combination with the R17L LPMO mutant was approximately two times higher than with the WT LPMO (Guo et al., 2020).

COMPUTATIONAL APPROACHES USED IN HARNESSING MICROBIAL POTENTIAL FOR LIGNOCELLULOSE VALORIZATION

Systems biology follows a holistic approach to analyzing cell biology from subcellular levels to the entire organism using computer-aided tools and mathematical models (Kitano, 2002). System biology tools include the following advanced omics technologies: *Genomics* – the set of studies on the structure, function, evolution, mapping, and editing of genomes (Khoury et al., 2009); *Transcriptomics* - the complete set of RNA transcripts (Piétu et al., 1999); *Proteomics* – investigation of protein production, degradation, modification, and their interactions (Dupree et al., 2020); and *Metabolomics* - chemical processes involving small molecule substrates, intermediates, and products of cell metabolism (Clish, 2015). Each omics platform requires data handling, annotation of biomolecules, design and analytic assumptions, statistical power analysis, and data archiving and sharing. However, a single omics analysis can't fully solve the complexities of microbial biology. Multi-omics techniques have opened new avenues for exploring microbial diversity by contributing to available databases (metabolite, RNA, DNA, and protein databases) at a scale not imagined previously. Integrating such diverse data types requires data normalization, statistical power analysis, and big-data machine-learning tools for a multi-omics analysis (Libbrecht and Noble, 2015; Min et al., 2016). Available computational tools for interpretation and analysis of analysis of omics data and integration of genomics and metabolomics data include MapMan (Thimm et al., 2004), Pathway Studio (Yuryev et al., 2009); for transcriptomics and proteomics data include iCluster (Shen et al., 2009), SteinerNet (Tuncbag et al., 2012), Paintomics (Hernández-de-Diego et al., 2018); for transcriptomics and metabolomics data include Paintomics (Hernández-de-Diego et al., 2018), PRIMe (Akiyama et al., 2008), MEtaboAnalyst 5.0 (Pang et al., 2021) and for multi-omics data include IntegrOmics (Lê Cao et al., 2009), 3Omics (Kuo et al., 2013), Qiagen Ingenuity Pathway Analysis (Krämer et al., 2014). Multi-omics approaches have been applied in several research areas, from bio-based fuel production to biopharmaceutical development to studies of diseases. This section will highlight some multi-omics-aided studies for lignocellulose valorization.

High-Throughput Genome Sequencing

The massive development in next-generation sequencing (NGS) technologies has led to extensive publicly available genomics databases. However, genome mining is dependent solely on computational methods and bioinformatics tools to

interconnect the complex biological networks within a single species and across microbial species. The recent development in genome mining tools such as antiSMASH, ClustScan, BAGEL, SMURF, NP.searcher, and PRISM has untapped the metabolic potential of microorganisms for biomass degradation (Lee N. et al., 2020). These tools can be used to scan the genomes of multiple organisms simultaneously to predict homologous genes based on highly conserved sequences. In their review, Ren et al. have covered the progress of genome-mining tools for predicting natural products of pharmaceutical importance (Ren et al., 2020). The majority of them are used for pathway prediction by identifying essential genes involved in metabolite synthesis and utilizing Basic Local Alignment Search Tool (BLAST) or hidden Markov models (HMMs) for genome mining (Ren et al., 2020). In one metagenomic study, stable isotope probing (SIP) was used to identify and characterize the microbiome in different soil layers for lignocellulose degradation (Wilhelm et al., 2019). The identification and genomic content of bacterial consortia were assessed using 16S rRNA gene amplicon and shotgun metagenomics. In another study, the comparative genomic analysis of *C. subvermispora* and *P. chrysosporium* revealed the presence of more than seven genes encoding laccases in *C. subvermispora*. In contrast, there was no gene encoding for laccase for lignin degradation in *P. chrysosporium*. The same study identified that the *C. subvermispora* genome contains as many as three times more genes for MnP than *P. chrysosporium* (Fernandez-Fueyo et al., 2012).

From Protein Chemistry to Proteomics

Proteomic analysis is used to identify enzymes present and to quantify the expression of enzymes and has proved helpful for identifying the CAZymes in microbes involved in biomass deconstruction. LC-MS/MS-based secretome profiling from several microorganisms grown on different substrates revealed the presence of laccases, auxiliary proteins, and hydrolases (Sethupathy et al., 2021). Proteomic analysis of the ligninolytic bacterium *Arthrobacter phenanthrenivorans* Sphe3 on a medium containing three different carbon sources identified several enzymes involved in catalysis of aromatic degradation, including phenanthrene (Vandera et al., 2015). The study also identified genes involved in catabolite repression in the presence of glucose. When exposed to three xenobiotics, a similar study performed in *Sphingobium chungbukense* DJ77 identified major proteins to map catabolic pathways for naphthalene, phenanthrene, and biphenyl (Lee et al., 2016). The proteomic analysis of the secretomes and enzymes from different microorganisms can be used to begin to understand the full complement of enzymes involved in lignin depolymerization and facilitate increasing the ligninolytic activity of commercially used enzyme cocktails.

Multi-Omics and Genome Engineering Tools–Game-Changers for Systems Biology

Synthetic biology involves engineering new biological systems for the practical purposes of providing them with new and/or improved metabolic abilities. Synthetic biology exploits both traditional metabolic engineering tools (such as plasmid-mediated) and more sophisticated modern genome engineering tools (such as CRISPR/Cas9 and CRAGE) for combinatorial strain development for the industrial production of compounds (Wang et al., 2019; Gauttam et al., 2021). Then, the genome editing era and multi-omics technology led to new synthetic biology, metabolic engineering, and systems biology tools for metabolic pathway analysis and engineering. These tools contributed to the discovery of novel native metabolic pathways to degrade lignin and assimilate its aromatic products (Brown and Chang, 2014). For example, the combinatorial genomic and proteomic analysis of *Pandoraea* sp. ISTKB grown in the presence of vanillic acid and kraft lignin has revealed a unique aerobic pathway for lignin degradation (Kumar and Kim, 2018). This "-CoA" mediated degradation pathway for phenylacetate and benzoate has been reported in merely 4–5% of sequenced bacterial genomes. The comparative analysis also revealed the presence of ligninolytic enzymes such as peroxidases, oxidases, oxidoreductases, laccases, oxygenases, and etherizes in *Pandoraea* sp (Kumar and Kim, 2018). The information accumulated through multi-omics approaches can be integrated to rebuild models for novel lignin-degrading pathways in novel microorganisms with ligninolytic potential.

Besides revealing novel ligninolytic microbes and enzymes, several studies have been performed using synthetic biology to produce high-value end products from lignin using engineered microorganisms. Most microorganisms utilize glucose; however, deconstructed lignocellulosics also consist of alternative sugars such as xylose and arabinose that are also economically attractive sources of fermentable and upgradable sugars. For example, an *Escherichia coli* MS04 strain was engineered to assimilate xylose anaerobically and tolerate high acetate concentrations (Fernández-Sandoval et al., 2012). This strain was used to produce ethanol from corn stover hydrolysate (Parra-Ramírez et al., 2018). Among eukaryotes, oleaginous yeasts such as *Rhodosporidium toruloides, Cutaneotrichosporon oleaginosus,* and *Lipomyces starkeyi* can readily metabolize many substrates, including xylose and aromatics, and show excellent tolerance against a wide range of potentially toxic intermediates (Yaegashi et al., 2017; Valdés et al., 2020). Naturally, very few microbes can decompose lignin into vanillin; nevertheless, there are reports for microbial production of vanillin from lignin (Nguyen et al., 2021). For example, the deletion of the *vdh* gene resulted in the conversion of ferulic acid to vanillin in *Pycnoporus cinnabarinus* (Tilay et al., 2010), *Amycolatopsis sp.* (Fleige et al., 2013), and *Pseudomonas fluorescens* (Di Gioia et al., 2011). Similarly, *vdh* deletion in *R. jostii* RHA1 resulted in 96 mg/L vanillin from wheat straw lignocellulose (Sainsbury et al., 2013). On the other hand, *Pseudomonas putida* KT2440 strain is well known for its tolerance against xenobiotics compounds, aromatic metabolism (e.g., *p*-coumarate and ferrulate), and the availability of a wide range of advanced genetic factors tools for pathway engineering (Martínez-García and de Lorenzo, 2019; Lee S. et al., 2020). *P. putida* KT2440 was engineered to enhance the conversion of non-preferred substrates such as *p*-coumarate and ferrulate in the presence of preferred substrate glucose (Johnson et al., 2017). Through metabolic modeling and genome editing, *Pseudomonas* not only can grow in harsh environments but can also co-utilize

multiple substrates, which suggests the potential of this organism to convert most of the carbon present in lignocellulosic biomass into advanced bioproducts.

The compounds *cis, cis*-muconic acid (*cis, cis*-MA) recently drew significant attention because they are an intermediate for adipic acid production, a captive feedstock in the production of nylon fibers and plastics. Recently, Crc regulation of metabolic pathways for the production of muconate in the engineered strain *P. putida* KT2440-CJ102 was predicted and confirmed using mass spectrometry (MS)-based proteomics and gene editing (Johnson et al., 2017a). It was demonstrated that deletion of the gene encoding Crc enhances metabolism of both 4-HBA and vanillate, leading to enhanced muconate production from *p*-coumarate or ferulate when either glucose or acetate are supplied as a source of carbon and energy. In similar work, an engineered *Sphingobium sp.* SYK6 strain produced muconic acid in the absence of glucose from lignin extracts of Japanese cedar and birch (Sonoki et al., 2018). The deletion of muconate cycloisomerase, combined with further engineering, improved muconic acid production in *Amycolatopsis sp., Corynebacterium glutamicum,* and *P. putida* (Barton et al., 2018; Becker et al., 2018; Kohlstedt et al., 2018). Notably, NExT-EMA used a tool that channels elementary flux modes (EFMs) into network-embedded thermodynamic (NET) analysis to analyze *E. coli* and *Saccharomyces cerevisiae* metabolic networks. Stoichiometric analysis of 32–99% on glucose and/or palmitate can contribute to the maximum theoretical product carbon yield in routes to adipic acid production. This work highlights the importance of pathway and organism choice to maximize the potential of a biobased process, leading the metabolic engineering community toward highly efficient biotechnical production of adipic acid (Averesch et al., 2018).

Developing synthetic microbial constructs for bioconversion of lignocellulose-based products into industrial chemicals often requires extensive pathway engineering involving designing artificial pathways and optimizing rate-limiting enzymes. While integrating multi-omics data and genome editing tools has opened new metabolic engineering avenues to speed up the combinatorial strain development for lignocellulosic biomass conversion using microbes, engineering a host organism to produce new products still has long development times due to the need for a detailed understanding of the host organism's metabolic pathways. Recently, researchers have begun to apply machine learning and probabilistic modeling algorithms to predict how cells respond to changes in their DNA and biochemistry and to make recommendations for the next engineering cycle without the need for a detailed understanding of the host organism's metabolism (Radivojević et al., 2020; Lawson et al., 2021). The development and application of machine learning approaches to systems biology and metabolic engineering promises to greatly reduce development times.

CONCLUDING REMARKS

Computational tools and methods are becoming essential to optimizing the various processes involved in converting lignocellulosic biomass to valuable fuels and chemicals, from data-driven optimization of deconstruction to molecular-level

understanding and rational engineering of enzymes to discovery and building metabolic pathways for synthesis of final products. The tremendous amount of complex chemical and biological data available for analysis and generated by computational biology and chemistry highlights the considerable power and usefulness of computational sciences to develop lignocellulosic biofuels and products. This review highlights and emphasizes the power of synergistic computational and experimental studies aimed at the full-scale optimization of the conversion of lignocellulosic biomass into valuable products. Through valid approximations to the physical laws, modern algorithms, and supercomputers, computational biology and chemistry tools can simulate systems containing hundreds of millions of atoms, required to study the interactions of solvent systems with biomass components and simulate the interactions of solvent systems and engineer enzymes. Recent developments in machine learning and big data analytics have enabled the discovery of new enzyme systems, microbes for biomass conversion, and the engineering of metabolic pathways to produce desired fuels and chemicals. Continued development and growth in applications of computational approaches to optimize pretreatment of lignocellulosic biomass, rational design of enzymes, and next-generation paradigms of predictive approaches in synthetic and system biology are essential for the fundamental science required for development and optimization of viable lignocellulosic biomass conversion processes.

AUTHOR CONTRIBUTIONS

LTMP, HC, and RG wrote the manuscript. All authors read and approved the final manuscript.

FUNDING

REFERENCES

Acebes, S., Fernandez-Fueyo, E., Monza, E., Lucas, M. F., Almendral, D., Ruiz-Dueñas, F. J., et al. (2016). Rational Enzyme Engineering through Biophysical and Biochemical Modeling. *ACS Catal.* 6 (3), 1624–1629. doi:10.1021/acscatal.6b00028

Acebes, S., Ruiz-Dueñas, F. J., Toubes, M., Sáez-Jiménez, V., Pérez-Boada, M., Lucas, M. F., et al. (2017). Mapping the Long-Range Electron Transfer Route in Ligninolytic Peroxidases. *J. Phys. Chem. B* 121 (16), 3946–3954. doi:10.1021/acs.jpcb.7b00835

Achinivu, E. C., Mohan, M., Choudhary, H., Das, L., Huang, K., Magurudeniya, H. D., et al. (2021). A Predictive Toolset for the Identification of Effective Lignocellulosic Pretreatment Solvents: a Case Study of Solvents Tailored for Lignin Extraction. *Green Chem.* 23 (18), 7269–7289. doi:10.1039/D1GC01186C

Akiyama, K., Chikayama, E., Yuasa, H., Shimada, Y., Tohge, T., Shinozaki, K., et al. (2008). PRIMe: a Web Site that Assembles Tools for Metabolomics and Transcriptomics. *Silico Biol* 8 (3-4), 339–345.

Andanson, J.-M., Bordes, E., Devémy, J., Leroux, F., Pádua, A. A. H., and Gomes, M. F. C. (2014). Understanding the Role of Co-solvents in the Dissolution of Cellulose in Ionic Liquids. *Green Chem.* 16 (5), 2528–2538. doi:10.1039/C3GC42244E

Antunes, D. A., Devaurs, D., and Kavraki, L. E. (2015). Understanding the Challenges of Protein Flexibility in Drug Design. *Expert Opin. Drug Discov.* 10 (12), 1301–1313. doi:10.1517/17460441.2015.1094458

Averesch, N. J. H., Martínez, V. S., Nielsen, L. K., and Krömer, J. O. (2018). Toward Synthetic Biology Strategies for Adipic Acid Production: An In Silico Tool for Combined Thermodynamics and Stoichiometric Analysis of Metabolic Networks. *ACS Synth. Biol.* 7 (2), 490–509. doi:10.1021/acssynbio.7b00304

Ayuso-Fernández, I., Ruiz-Dueñas, F. J., and Martínez, A. T. (2018). Evolutionary Convergence in Lignin-Degrading Enzymes. *Proc. Natl. Acad. Sci. U.S.A.* 115 (25), 6428–6433. doi:10.1073/pnas.1802555115

Balaji, C., Banerjee, T., and Goud, V. V. (2012). COSMO-RS Based Predictions for the Extraction of Lignin from Lignocellulosic Biomass Using Ionic Liquids: Effect of Cation and Anion Combination. *J. Solut. Chem.* 41 (9), 1610–1630. doi:10.1007/s10953-012-9887-3

Balan, V. (2014). Current Challenges in Commercially Producing Biofuels from Lignocellulosic Biomass. *ISRN Biotechnol.* 2014, 1–31. doi:10.1155/2014/463074

Barbeyron, T., Brillet-Guéguen, L., Carré, W., Carrière, C., Caron, C., Czjzek, M., et al. (2016). Matching the Diversity of Sulfated Biomolecules: Creation of a Classification Database for Sulfatases Reflecting Their Substrate Specificity. *PLOS ONE* 11 (10), e0164846. doi:10.1371/journal.pone.0164846

Barton, N., Horbal, L., Starck, S., Kohlstedt, M., Luzhetskyy, A., and Wittmann, C. (201839116). Enabling the Valorization of Guaiacol-Based Lignin: Integrated Chemical and Biochemical Production of Cis,cis-Muconic Acid Using Metabolically Engineered Amycolatopsis Sp ATCC 39116. *Metab. Eng.* 45, 200–210. doi:10.1016/j.ymben.2017.12.001

Bäumgen, M., Dutschei, T., and Bornscheuer, U. T. (2021). Marine Polysaccharides: Occurrence, Enzymatic Degradation and Utilization. *ChemBioChem* 22 (13), 2247–2256. doi:10.1002/cbic.202100078

Becker, J., Kuhl, M., Kohlstedt, M., Starck, S., and Wittmann, C. (2018). Metabolic Engineering of Corynebacterium Glutamicum for the Production of Cis, Cis-Muconic Acid from Lignin. *Microb. Cell. Fact.* 17 (1), 115–129. doi:10.1186/s12934-018-0963-2

Berglund, J., Azhar, S., Lawoko, M., Lindström, M., Vilaplana, F., Wohlert, J., et al. (2019). The Structure of Galactoglucomannan Impacts the Degradation under Alkaline Conditions. *Cellulose* 26 (3), 2155–2175. doi:10.1007/s10570-018-1737-z

Bernini, C., Pogni, R., Basosi, R., and Sinicropi, A. (2014). Prediction of Hydrogen-Bonding Networks Around Tyrosyl Radical inP. Eryngiiversatile Peroxidase W164Y Variants: a QM/MM MD Study. *Mol. Simul.* 40 (6), 485–490. doi:10.1080/08927022.2013.822967

Bernini, C., Pogni, R., Basosi, R., and Sinicropi, A. (2012). The Nature of Tryptophan Radicals Involved in the Long-Range Electron Transfer of Lignin Peroxidase and Lignin Peroxidase-like Systems: Insights from Quantum Mechanical/molecular Mechanics Simulations. *Proteins* 80 (5), 1476–1483. doi:10.1002/prot.24046

Bharadwaj, V. S., Knott, B. C., Ståhlberg, J., Beckham, G. T., and Crowley, M. F. (2020). The Hydrolysis Mechanism of a GH45 Cellulase and its Potential Relation to Lytic Transglycosylase and Expansin Function. *J. Biol. Chem.* 295 (14), 4477–4487. doi:10.1074/jbc.RA119.011406

Bharadwaj, V. S., Schutt, T. C., Ashurst, T. C., and Maupin, C. M. (2015). Elucidating the Conformational Energetics of Glucose and Cellobiose in Ionic Liquids. *Phys. Chem. Chem. Phys.* 17 (16), 10668–10678. doi:10.1039/c5cp00118h

Bhardwaj, N., Kumar, B., and Verma, P. (2019). A Detailed Overview of Xylanases: an Emerging Biomolecule for Current and Future Prospective. *Bioresour. Bioprocess.* 6 (1), 40. doi:10.1186/s40643-019-0276-2

Borisova, A. S., Eneyskaya, E. V., Bobrov, K. S., Jana, S., Logachev, A., Polev, D. E., et al. (2015). Sequencing, Biochemical Characterization, Crystal Structure and Molecular Dynamics of Cellobiohydrolase Cel7A from Geotrichum Candidum 3C. *Febs J.* 282 (23), 4515–4537. doi:10.1111/febs.13509

Borrelli, K. W., Vitalis, A., Alcantara, R., and Guallar, V. (2005). PELE: Protein Energy Landscape Exploration. A Novel Monte Carlo Based Technique. *J. Chem. Theory Comput.* 1 (6), 1304–1311. doi:10.1021/ct0501811

Bowling, A. J., Amano, Y., Lindstrom, R., and Brown, Jr, R. M. (2001). Rotation of Cellulose Ribbons During Degradation with Fungal Cellulase. *Cellulose* 8 (1), 91–97. doi:10.1023/A:1016660621440

Briganti, L., Capetti, C., Pellegrini, V. O. A., Ghio, S., Campos, E., Nascimento, A. S., et al. (2021). Structural and molecular dynamics investigations of ligand stabilization via secondary binding site interactions in Paenibacillus xylanivorans GH11 xylanase. *Comput. Struct. Biotechnol. J.* 19, 1557–1566. doi:10.1016/j.csbj.2021.03.002

Brown, M. E., and Chang, M. C. (2014). Exploring bacterial lignin degradation. *Curr. Opin. Chem. Biol.* 19, 1–7. doi:10.1016/j.cbpa.2013.11.015

Brunk, E., and Rothlisberger, U. (2015). Mixed Quantum Mechanical/Molecular Mechanical Molecular Dynamics Simulations of Biological Systems in Ground and Electronically Excited States. *Chem. Rev.* 115 (12), 6217–6263. doi:10.1021/cr500628b

Busse-Wicher, M., Gomes, T. C. F., Tryfona, T., Nikolovski, N., Stott, K., Grantham, N. J., et al. (2014). The pattern of xylan acetylation suggests xylan may interact with cellulose microfibrils as a twofold helical screw in the secondary plant cell wall of *Arabidopsis thaliana*. *Plant J.* 79 (3), 492–506. doi:10.1111/tpj.12575

Casas, A., Omar, S., Palomar, J., Oliet, M., Alonso, M. V., and Rodriguez, F. (2013). Relation between differential solubility of cellulose and lignin in ionic liquids and activity coefficients. *RSC Adv.* 3 (10), 3453–3460. doi:10.1039/C2RA22800A

Casas, A., Palomar, J., Alonso, M. V., Oliet, M., Omar, S., and Rodriguez, F. (2012). Comparison of lignin and cellulose solubilities in ionic liquids by COSMO-RS analysis and experimental validation. *Industrial Crops Prod.* 37 (1), 155–163. doi:10.1016/j.indcrop.2011.11.032

Castilla-Archilla, J., O'Flaherty, V., and Lens, P. N. L. (2019). "Biorefineries: Industrial Innovation and Tendencies," in *Biorefinery: Integrated Sustainable Processes for Biomass Conversion to Biomaterials, Biofuels, and Fertilizers*. Editors J.-R. Bastidas-Oyanedel and J. E. Schmidt (Cham: Springer International Publishing), 3–35. doi:10.1007/978-3-030-10961-5_1

Castro, L., Crawford, L. E., Mutengwa, A., Götze, J. P., and Bühl, M. (2016). Insights into structure and redox potential of lignin peroxidase from QM/MM calculations. *Org. Biomol. Chem.* 14 (8), 2385–2389. doi:10.1039/c6ob00037a

Cerqueira, N. M. F. S. A., Bras, N. F., Fernandes, P. A., and Ramos, M. J. (2009). MADAMM: a multistaged docking with an automated molecular modeling protocol. *Proteins* 74 (1), 192–206. doi:10.1002/prot.22146

Chen, M., Zeng, G., Tan, Z., Jiang, M., Li, H., Liu, L., et al. (2011). Understanding lignin-degrading reactions of ligninolytic enzymes: binding affinity and interactional profile. *PLoS One* 6 (9), e25647. doi:10.1371/journal.pone.0025647

Cheng, F., Ouyang, T., Sun, J., Jiang, T., and Luo, J. (2018). Using solubility parameter analysis to understand delignification of poplar and rice straw with catalyzed organosolv fractionation processes. *BioRes* 14 (1), 486–499. doi:10.15376/biores.14.1.486-499

Cho, H. M., Gross, A. S., and Chu, J.-W. (2011). Dissecting force interactions in cellulose deconstruction reveals the required solvent versatility for overcoming biomass recalcitrance. *J. Am. Chem. Soc.* 133 (35), 14033–14041. doi:10.1021/ja2046155

Chu, Y., and He, X. (2019). MoDoop: An Automated Computational Approach for COSMO-RS Prediction of Biopolymer Solubilities in Ionic Liquids. *ACS Omega* 4 (1), 2337–2343. doi:10.1021/acsomega.8b03255

Ciesielski, P. N., Pecha, M. B., Lattanzi, A. M., Bharadwaj, V. S., Crowley, M. F., Bu, L., et al. (2020). Advances in Multiscale Modeling of Lignocellulosic Biomass. *ACS Sustain. Chem. Eng.* 8 (9), 3512–3531. doi:10.1021/acssuschemeng.9b07415

Clish, C. B. (2015). Metabolomics: an emerging but powerful tool for precision medicine. *Cold Spring Harb. Mol. Case Stud.* 1 (1), a000588. doi:10.1101/mcs.a000588

Cohen, A. J., Mori-Sánchez, P., and Yang, W. (2012). Challenges for Density Functional Theory. *Chem. Rev.* 112 (1), 289–320. doi:10.1021/cr200107z

Cuyvers, S., Dornez, E., Rezaei, M. N., Pollet, A., Delcour, J. A., and Courtin, C. M. (2011). Secondary substrate binding strongly affects activity and binding affinity ofBacillus subtilisandAspergillus nigerGH11 xylanases. *Febs J.* 278 (7), 1098–1111. doi:10.1111/j.1742-4658.2011.08023.x

Danne, R., Poojari, C., Martinez-Seara, H., Rissanen, S., Lolicato, F., Róg, T., et al. (2017). doGlycans-Tools for Preparing Carbohydrate Structures for Atomistic Simulations of Glycoproteins, Glycolipids, and Carbohydrate Polymers for GROMACS. *J. Chem. Inf. Model.* 57 (10), 2401–2406. doi:10.1021/acs.jcim.7b00237

Davies, G. J., Gloster, T. M., and Henrissat, B. (2005). Recent structural insights into the expanding world of carbohydrate-active enzymes. *Curr. Opin. Struct. Biol.* 15 (6), 637–645. doi:10.1016/j.sbi.2005.10.008

Decker, C. H., Visser, J., and Schreier, P. (2001). β-Glucosidase multiplicity from Aspergillus tubingensis CBS 643.92: purification and characterization of four β-glucosidases and their differentiation with respect to substrate specificity, glucose inhibition and acid tolerance. *Appl. Microbiol. Biotechnol.* 55 (2), 157–163. doi:10.1007/s002530000462

Dellon, L. D., Yanez, A. J., Li, W., Mabon, R., and Broadbelt, L. J. (2017). Computational Generation of Lignin Libraries from Diverse Biomass Sources. *Energy fuels.* 31 (8), 8263–8274. doi:10.1021/acs.energyfuels.7b01150

Derecskei, B., and Derecskei-Kovacs, A. (2006). Molecular dynamic studies of the compatibility of some cellulose derivatives with selected ionic liquids. *Mol. Simul.* 32 (2), 109–115. doi:10.1080/08927020600669627

Di Gioia, D., Luziatelli, F., Negroni, A., Ficca, A. G., Fava, F., and Ruzzi, M. (2011). Metabolic engineering of Pseudomonas fluorescens for the production of vanillin from ferulic acid. *J. Biotechnol.* 156 (4), 309–316. doi:10.1016/j.jbiotec.2011.08.014

Ding, Z.-D., Chi, Z., Gu, W.-X., Gu, S.-M., Liu, J.-H., and Wang, H.-J. (2012). Theoretical and experimental investigation on dissolution and regeneration of cellulose in ionic liquid. *Carbohydr. Polym.* 89 (1), 7–16. doi:10.1016/j.carbpol.2012.01.080

Dupree, E. J., Jayathirtha, M., Yorkey, H., Mihasan, M., Petre, B. A., and Darie, C. C. (2020). A Critical Review of Bottom-Up Proteomics: The Good, the Bad, and the Future of this Field. *Proteomes* 8 (3), 14. doi:10.3390/proteomes8030014

Farhat, W., Venditti, R. A., Hubbe, M., Taha, M., Becquart, F., and Ayoub, A. (2017). A Review of Water-Resistant Hemicellulose-Based Materials: Processing and Applications. *ChemSusChem* 10 (2), 305–323. doi:10.1002/cssc.201601047

Felczak, K., Chen, L., Wilson, D., Williams, J., Vince, R., Petrelli, R., et al. (2011). Cofactor-type inhibitors of inosine monophosphate dehydrogenase via modular approach: targeting the pyrophosphate binding sub-domain. *Bioorg. Med. Chem.* 19 (5), 1594–1605. doi:10.1016/j.bmc.2011.01.042

Fernández-Fueyo, E., Acebes, S., Ruiz-Dueñas, F. J., Martínez, M. J., Romero, A., Medrano, F. J., et al. (2014). Structural implications of the C-terminal tail in the catalytic and stability properties of manganese peroxidases from ligninolytic fungi. *Acta Cryst. D. Biol. Crystallogr.* 70 (Pt 12), 3253–3265. doi:10.1107/s1399004714022755

Fernandez-Fueyo, E., Ruiz-Dueñas, F. J., Ferreira, P., Floudas, D., Hibbett, D. S., Canessa, P., et al. (2012). Comparative genomics of Ceriporiopsis subvermispora and Phanerochaete chrysosporium provide insight into selective ligninolysis. *Proc. Natl. Acad. Sci. U.S.A.* 109 (14), 5458–5463. doi:10.1073/pnas.1119912109

Fernández-Sandoval, M. T., Huerta-Beristain, G., Trujillo-Martinez, B., Bustos, P., González, V., Bolivar, F., et al. (2012). Laboratory metabolic evolution improves acetate tolerance and growth on acetate of ethanologenic *Escherichia coli* under non-aerated conditions in glucose-mineral medium. *Appl. Microbiol. Biotechnol.* 96 (5), 1291–1300. doi:10.1007/s00253-012-4177-y

Fleige, C., Hansen, G., Kroll, J., Steinbüchel, A., and microbiology, e. (2013). Investigation of the Amycolatopsis sp. strain ATCC 39116 vanillin dehydrogenase and its impact on the biotechnical production of vanillin. *Appl. Environ. Microbiol.* 79 (1), 81–90. doi:10.1128/AEM.02358-12

Frenkel, D., and Smit, B. (2002). "Introduction," in *Understanding Molecular Simulation*. Editors D. Frenkel and B. Smit. Second Edition (San Diego: Academic Press), 1–6. doi:10.1016/b978-012267351-1/50003-1

Friesner, R. A., Banks, J. L., Murphy, R. B., Halgren, T. A., Klicic, J. J., Mainz, D. T., et al. (2004). Glide: a new approach for rapid, accurate docking and scoring. 1. Method and assessment of docking accuracy. *J. Med. Chem.* 47 (7), 1739–1749. doi:10.1021/jm0306430

Gauttam, R., Mukhopadhyay, A., Simmons, B. A., and Singer, S. W. (2021). Development of dual-inducible duet-expression vectors for tunable gene expression control and CRISPR interference-based gene repression in Pseudomonas putida KT2440. *Microb. Biotechnol.* 14 (6), 2659–2678. doi:10.1111/1751-7915.13832

Gibson, L. J. (2012). The hierarchical structure and mechanics of plant materials. *J. R. Soc. Interface.* 9 (76), 2749–2766. doi:10.1098/rsif.2012.0341

Gomes, T. C. F., and Skaf, M. S. (2012). Cellulose-builder: a toolkit for building crystalline structures of cellulose. *J. Comput. Chem.* 33 (14), 1338–1346. doi:10.1002/jcc.22959

Götze, J. P., and Bühl, M. (2016). Laccase Redox Potentials: pH Dependence and Mutants, a QM/MM Study. *J. Phys. Chem. B* 120 (35), 9265–9276. doi:10.1021/acs.jpcb.6b04978

Grisafi, A., and Ceriotti, M. (2019). Incorporating long-range physics in atomic-scale machine learning. *J. Chem. Phys.* 151 (20), 204105. doi:10.1063/1.5128375

Gross, A. S., Bell, A. T., and Chu, J.-W. (2012). Entropy of cellulose dissolution in water and in the ionic liquid 1-butyl-3-methylimidazolim chloride. *Phys. Chem. Chem. Phys.* 14 (23), 8425–8430. doi:10.1039/c2cp40417f

Gross, A. S., Bell, A. T., and Chu, J.-W. (2011). Thermodynamics of cellulose solvation in water and the ionic liquid 1-butyl-3-methylimidazolim chloride. *J. Phys. Chem. B* 115 (46), 13433–13440. doi:10.1021/jp202415v

Guo, X., An, Y., Chai, C., Sang, J., Jiang, L., Lu, F., et al. (2020). Construction of the R17L mutant of MtC1LPMO for improved lignocellulosic biomass conversion by rational point mutation and investigation of the mechanism by molecular dynamics simulations. *Bioresour. Technol.* 317, 124024. doi:10.1016/j.biortech.2020.124024

Gupta, K. M., Hu, Z., and Jiang, J. (2011). Mechanistic understanding of interactions between cellulose and ionic liquids: A molecular simulation study. *Polymer* 52 (25), 5904–5911. doi:10.1016/j.polymer.2011.10.035

Haghighi Mood, S., Hossein Golfeshan, A., Tabatabaei, M., Salehi Jouzani, G., Najafi, G. H., Gholami, M., et al. (2013). Lignocellulosic biomass to bioethanol, a comprehensive review with a focus on pretreatment. *Renew. Sustain. Energy Rev.* 27 (C), 77–93. doi:10.1016/j.rser.2013.06.033

Hallac, B. B., and Ragauskas, A. J. (2011). Analyzing cellulose degree of polymerization and its relevancy to cellulosic ethanol. *Biofuels, Bioprod. Bioref.* 5 (2), 215–225. doi:10.1002/bbb.269

Hamid, M., and Khalil-ur-Rehman, R. (2009). Potential applications of peroxidases. *Food Chem.* 115 (4), 1177–1186. doi:10.1016/j.foodchem.2009.02.035

Hanley, S. J., Revol, J.-F., Godbout, L., and Gray, D. G. (1997). Atomic force microscopy and transmission electron microscopy of cellulose from Micrasterias denticulata; evidence for a chiral helical microfibril twist. *Cellulose* 4 (3), 209–220. doi:10.1023/A:1018483722417

Hansen, C. M. (2007). "Hansen Solubility Parameters," in *Hansen Solubility Parameters: A User's Handbook*. 2nd Edn (Boca Raton, FL: CRC Press). doi:10.1201/9781420006834

Hernández-de-Diego, R., Tarazona, S., Martínez-Mira, C., Balzano-Nogueira, L., Furió-Tarí, P., Pappas, G. J., Jr., et al. (2018). PaintOmics 3: a web resource for the pathway analysis and visualization of multi-omics data. *Nucleic Acids Res.* 46 (W1), W503–w509. doi:10.1093/nar/gky466

Higuchi, T. (1997). "Structure and Functions of Wood," in *Biochemistry and Molecular Biology of Wood*. Editor T. Higuchi (Berlin, Heidelberg: Springer Berlin Heidelberg), 1–42. doi:10.1007/978-3-642-60469-0_1

Hong, G., Ivnitski, D. M., Johnson, G. R., Atanassov, P., and Pachter, R. (2011). Design parameters for tuning the type 1 Cu multicopper oxidase redox

potential: insight from a combination of first principles and empirical molecular dynamics simulations. *J. Am. Chem. Soc.* 133 (13), 4802–4809. doi:10.1021/ja105586q

Hu, N., Xu, D., Fang, J., Li, H., Mo, J., Zhou, M., et al. (2020). Intracellular recording of cardiomyocyte action potentials by nanobranched microelectrode array. *Biosens. Bioelectron.* 169, 112588. doi:10.1016/j.bios.2020.112588

Huang, K., Mohan, M., George, A., Simmons, B. A., Xu, Y., and Gladden, J. M. (2021). Integration of acetic acid catalysis with one-pot protic ionic liquid configuration to achieve high-efficient biorefinery of poplar biomass. *Green Chem.* 23 (16), 6036–6049. doi:10.1039/D1GC01727F

Huffman, F. G. (2003). "URONIC ACIDS," in *Encyclopedia of Food Sciences and Nutrition*. Editor B. Caballero. Second Edition (Oxford: Academic Press), 5890–5896. doi:10.1016/b0-12-227055-x/01221-9

Huo, F., Liu, Z., and Wang, W. (2013). Cosolvent or antisolvent? A molecular view of the interface between ionic liquids and cellulose upon addition of another molecular solvent. *J. Phys. Chem. B* 117 (39), 11780–11792. doi:10.1021/jp407480b

Iglesias-Fernández, J., Hancock, S. M., Lee, S. S., Khan, M., Kirkpatrick, J., Oldham, N. J., et al. (2017). A front-face 'SNi synthase' engineered from a retaining 'double-SN2' hydrolase. *Nat. Chem. Biol.* 13 (8), 874–881. doi:10.1038/nchembio.2394

Iqbal, J., Muhammad, N., Rahim, A., Khan, A. S., Ullah, Z., Gonfa, G., et al. (2019). COSMO-RS predictions, hydrogen bond basicity values and experimental evaluation of amino acid-based ionic liquids for lignocellulosic biomass dissolution. *J. Mol. Liq.* 273, 215–221. doi:10.1016/j.molliq.2018.10.044

Janesko, B. G. (2011). Modeling interactions between lignocellulose and ionic liquids using DFT-D. *Phys. Chem. Chem. Phys.* 13 (23), 11393–11401. doi:10.1039/C1CP20072K

Jarin, Z., and Pfaendtner, J. (2014). Ionic Liquids Can Selectively Change the Conformational Free-Energy Landscape of Sugar Rings. *J. Chem. Theory Comput.* 10 (2), 507–510. doi:10.1021/ct4010036

Ji, H., and Lv, P. (2020). Mechanistic insights into the lignin dissolution behaviors of a recyclable acid hydrotrope, deep eutectic solvent (DES), and ionic liquid (IL). *Green Chem.* 22 (4), 1378–1387. doi:10.1039/C9GC02760B

Johnson, C. W., Abraham, P. E., Linger, J. G., Khanna, P., Hettich, R. L., and Beckham, G. T. (2017a). Eliminating a global regulator of carbon catabolite repression enhances the conversion of aromatic lignin monomers to muconate in Pseudomonas putida KT2440. *Metab. Eng. Commun.* 5, 19–25. doi:10.1016/j.meteno.2017.05.002

Kahlen, J., Masuch, K., and Leonhard, K. (2010). Modelling cellulose solubilities in ionic liquids using COSMO-RS. *Green Chem.* 12 (12), 2172–2181. doi:10.1039/C0GC00200C

Kameda, Y., Maeda, S., Amo, Y., Usuki, T., Ikeda, K., and Otomo, T. (2018). Neutron Diffraction Study on the Structure of Hydrated Li+ in Dilute Aqueous Solutions. *J. Phys. Chem. B* 122 (5), 1695–1701. doi:10.1021/acs.jpcb.7b12218

Kearsley, S. K., Underwood, D. J., Sheridan, R. P., and Miller, M. D. (1994). Flexibases: A way to enhance the use of molecular docking methods. *J. Computer-Aided Mol. Des.* 8 (5), 565–582. doi:10.1007/BF00123666

Khan, S., Farooq, U., and Kurnikova, M. (2016). Exploring Protein Stability by Comparative Molecular Dynamics Simulations of Homologous Hyperthermophilic, Mesophilic, and Psychrophilic Proteins. *J. Chem. Inf. Model.* 56 (11), 2129–2139. doi:10.1021/acs.jcim.6b00305

Khoury, M. J., Feero, W. G., Reyes, M., Citrin, T., Freedman, A., Leonard, D., et al. (2009). The genomic applications in practice and prevention network. *Genet. Med.* 11 (7), 488–494. doi:10.1097/GIM.0b013e3181a551cc

Kirk, T. K., Tien, M., Kersten, P. J., Mozuch, M. D., and Kalyanaraman, B. (1986). Ligninase of Phanerochaete chrysosporium. Mechanism of its degradation of the non-phenolic arylglycerol β-aryl ether substructure of lignin. *Biochem. J.* 236 (1), 279–287. doi:10.1042/bj2360279

Kitano, H. (2002). Systems biology: a brief overview. *Science* 295 (5560), 1662–1664. doi:10.1126/science.1069492

Knott, B. C., Crowley, M. F., Himmel, M. E., Ståhlberg, J., and Beckham, G. T. (2014). Carbohydrate-protein interactions that drive processive polysaccharide translocation in enzymes revealed from a computational study of cellobiohydrolase processivity. *J. Am. Chem. Soc.* 136 (24), 8810–8819. doi:10.1021/ja504074g

Kohler, A. C., Simmons, B. A., and Sale, K. L. (2018). Structure-based Engineering of a Plant-Fungal Hybrid Peroxidase for Enhanced Temperature and pH Tolerance. *Cell. Chem. Biol.* 25 (8), 974–983. e973. doi:10.1016/j.chembiol.2018.04.014

Kohlstedt, M., Starck, S., Barton, N., Stolzenberger, J., Selzer, M., Mehlmann, K., et al. (2018). From lignin to nylon: cascaded chemical and biochemical conversion using metabolically engineered Pseudomonas putida. *Metab. Eng.* 47, 279–293. doi:10.1016/j.ymben.2018.03.003

Krämer, A., Green, J., Pollard, J., Jr., and Tugendreich, S. (2014). Causal analysis approaches in Ingenuity Pathway Analysis. *Bioinformatics* 30 (4), 523–530. doi:10.1093/bioinformatics/btt703

Kumar, A., and Chandra, R. (2020). Ligninolytic enzymes and its mechanisms for degradation of lignocellulosic waste in environment. *Heliyon* 6 (2), e03170. doi:10.1016/j.heliyon.2020.e03170

Kumar, P., and Kim, B. S. (2018). Valorization of polyhydroxyalkanoates production process by co-synthesis of value-added products. *Bioresour. Technol.* 269, 544–556. doi:10.1016/j.biortech.2018.08.120

Kuo, T.-C., Tian, T.-F., and Tseng, Y. J. (2013). 3Omics: a web-based systems biology tool for analysis, integration and visualization of human transcriptomic, proteomic and metabolomic data. *BMC Syst. Biol.* 7 (1), 64. doi:10.1186/1752-0509-7-64

Lawson, C. E., Martí, J. M., Radivojevic, T., Jonnalagadda, S. V. R., Gentz, R., Hillson, N. J., et al. (2021). Machine learning for metabolic engineering: A review. *Metab. Eng.* 63, 34–60. doi:10.1016/j.ymben.2020.10.005

Lê Cao, K.-A., González, I., and Déjean, S. (2009). integrOmics: an R package to unravel relationships between two omics datasets. *Bioinformatics* 25 (21), 2855–2856. doi:10.1093/bioinformatics/btp515

Lee, N., Hwang, S., Kim, J., Cho, S., Palsson, B., Cho, B.-K., et al. (2020a). Mini review: genome mining approaches for the identification of secondary metabolite biosynthetic gene clusters in Streptomyces. *Comput. Struct. Biotechnol. J.* 18, 1548–1556. doi:10.1016/j.csbj.2020.06.024

Lee, S., Sohn, J.-H., Bae, J.-H., Kim, S. C., Sung, B. H. J. B., and Engineering, B. (2020b). *Current Status of Pseudomonas Putida Engineering for Lignin Valorization*, 1–10.

Lee, S. Y., Sekhon, S. S., Ban, Y.-H., Ahn, J.-Y., Ko, J. H., Lee, L., et al. (2016). Proteomic analysis of polycyclic aromatic hydrocarbons (PAHs) degradation and detoxification in Sphingobium chungbukense DJ77. *J. Microbiol. Biotechnol.* 26 (11), 1943–1950. doi:10.4014/jmb.1606.06005

Levitt, M. (1982). Protein conformation, dynamics, and folding by computer simulation. *Annu. Rev. Biophys. Bioeng.* 11, 251–271. doi:10.1146/annurev.bb.11.060182.001343

Levitt, M., and Warshel, A. (1975). Computer simulation of protein folding. *Nature* 253 (5494), 694–698. doi:10.1038/253694a0

Li, J., Du, L., and Wang, L. (2010). Glycosidic-bond hydrolysis mechanism catalyzed by cellulase Cel7A from Trichoderma reesei: a comprehensive theoretical study by performing MD, QM, and QM/MM calculations. *J. Phys. Chem. B* 114 (46), 15261–15268. doi:10.1021/jp1064177

Li, J., Farrokhnia, M., Rulíšek, L., and Ryde, U. (2015a). Catalytic Cycle of Multicopper Oxidases Studied by Combined Quantum- and Molecular-Mechanical Free-Energy Perturbation Methods. *J. Phys. Chem. B* 119 (26), 8268–8284. doi:10.1021/acs.jpcb.5b02864

Li, Q., Sun, B., Xiong, K., Teng, C., Xu, Y., Li, L., et al. (2017). Improving special hydrolysis characterization into Talaromyces thermophilus F1208 xylanase by engineering of N-terminal extension and site-directed mutagenesis in C-terminal. *Int. J. Biol. Macromol.* 96, 451–458. doi:10.1016/10.1016/j.ijbiomac.2016.12.050

Li, Y., Liu, X., Zhang, S., Yao, Y., Yao, X., Xu, J., et al. (2015b). Dissolving process of a cellulose bunch in ionic liquids: a molecular dynamics study. *Phys. Chem. Chem. Phys.* 17 (27), 17894–17905. doi:10.1039/C5CP02009C

Libbrecht, M. W., and Noble, W. S. (2015). Machine learning applications in genetics and genomics. *Nat. Rev. Genet.* 16, 321–332. doi:10.1038/nrg3920

Liu, B., Kognole, A. A., Wu, M., Westereng, B., Crowley, M. F., Kim, S., et al. (2018). Structural and molecular dynamics studies of a C1-oxidizing lytic polysaccharide monooxygenase from Heterobasidion irregulare reveal amino acids important for substrate recognition. *Febs J.* 285 (12), 2225–2242. doi:10.1111/febs.14472

Liu, H., Cheng, G., Kent, M., Stavila, V., Simmons, B. A., Sale, K. L., et al. (2012). Simulations Reveal Conformational Changes of Methylhydroxyl Groups during Dissolution of Cellulose Iβ in Ionic Liquid 1-Ethyl-3-methylimidazolium Acetate. *J. Phys. Chem. B* 116 (28), 8131–8138. doi:10.1021/jp301673h

Liu, H., Sale, K. L., Holmes, B. M., Simmons, B. A., and Singh, S. (2010a). Understanding the Interactions of Cellulose with Ionic Liquids: A Molecular Dynamics Study. *J. Phys. Chem. B* 114 (12), 4293–4301. doi:10.1021/jp9117437

Liu, J., Wang, X., and Xu, D. (2010b). QM/MM study on the catalytic mechanism of cellulose hydrolysis catalyzed by cellulase Cel5A from Acidothermus cellulolyticus. *J. Phys. Chem. B* 114 (3), 1462–1470. doi:10.1021/jp909177e

Liu, Y.-R., Thomsen, K., Nie, Y., Zhang, S.-J., and Meyer, A. S. (2016). Predictive screening of ionic liquids for dissolving cellulose and experimental verification. *Green Chem.* 18 (23), 6246–6254. doi:10.1039/C6GC01827K

Ludwiczek, M. L., Heller, M., Kantner, T., and McIntosh, L. P. (2007). A secondary xylan-binding site enhances the catalytic activity of a single-domain family 11 glycoside hydrolase. *J. Mol. Biol.* 373 (2), 337–354. doi:10.1016/j.jmb.2007.07.057

Martí, S., Roca, M., Andrés, J., Moliner, V., Silla, E., Tuñón, I., et al. (2004). Theoretical insights in enzyme catalysis. *Chem. Soc. Rev.* 33 (2), 98–107. doi:10.1039/B301875J

Martínez-Abad, A., Berglund, J., Toriz, G., Gatenholm, P., Henriksson, G., Lindström, M., et al. (2017). Regular Motifs in Xylan Modulate Molecular Flexibility and Interactions with Cellulose Surfaces. *Plant Physiol.* 175 (4), 1579–1592. doi:10.1104/pp.17.01184

Martínez-García, E., and de Lorenzo, V. (2019). Pseudomonas putida in the quest of programmable chemistry. *Curr. Opin. Biotechnol.* 59, 111–121. doi:10.1016/j.copbio.2019.03.012

Matthews, J. F., Beckham, G. T., Bergenstråhle-Wohlert, M., Brady, J. W., Himmel, M. E., and Crowley, M. F. (2012). Comparison of Cellulose Iβ Simulations with Three Carbohydrate Force Fields. *J. Chem. Theory Comput.* 8 (2), 735–748. doi:10.1021/ct2007692

Matthews, J. F., Bergenstråhle, M., Beckham, G. T., Himmel, M. E., Nimlos, M. R., Brady, J. W., et al. (2011). High-Temperature Behavior of Cellulose I. *J. Phys. Chem. B* 115 (10), 2155–2166. doi:10.1021/jp1106839

Mazeau, K., and Heux, L. (2003). Molecular Dynamics Simulations of Bulk Native Crystalline and Amorphous Structures of Cellulose. *J. Phys. Chem. B* 107 (10), 2394–2403. doi:10.1021/jp0219395

Medve, J., Karlsson, J., Lee, D., and Tjerneld, F. (1998). Hydrolysis of microcrystalline cellulose by cellobiohydrolase I and endoglucanase II fromTrichoderma reesei: Adsorption, sugar production pattern, and synergism of the enzymes. *Biotechnol. Bioeng.* 59 (5), 621–634. doi:10.1002/(sici)1097-0290(19980905)59:5<621::aid-bit13>3.0.co;2-c

Miki, K., Renganathan, V., and Gold, M. H. (1986). Mechanism of .beta.-aryl ether dimeric lignin model compound oxidation by lignin peroxidase by Phanerochaete chrysosporium. *Biochemistry* 25 (17), 4790–4796. doi:10.1021/bi00365a011

Miki, Y., Pogni, R., Acebes, S., Lucas, F., Fernández-Fueyo, E., Baratto, M. C., et al. (2013). Formation of a tyrosine adduct involved in lignin degradation by Trametopsis cervina lignin peroxidase: a novel peroxidase activation mechanism. *Biochem. J.* 452 (3), 575–584. doi:10.1042/bj20130251

Min, S., Lee, B., and Yoon, S. (2016). Deep learning in bioinformatics. *Brief. Bioinform* 18, 851–869. doi:10.1093/bib/bbw068

Moal, I. H., and Bates, P. A. (2012). Kinetic rate constant prediction supports the conformational selection mechanism of protein binding. *PLoS Comput. Biol.* 8 (1), e1002351. doi:10.1371/journal.pcbi.1002351

Mohan, M., Choudhary, H., George, A., Simmons, B. A., Sale, K., and Gladden, J. M. (2021). Towards understanding of delignification of grassy and woody biomass in cholinium-based ionic liquids. *Green Chem.* 23 (16), 6020–6035. doi:10.1039/D1GC01622A

Mohan, M., Huang, K., Pidatala, V. R., Simmons, B. A., Singh, S., Sale, K. L., et al. (2022). Prediction of solubility parameters of lignin and ionic liquids using multi-resolution simulation approaches. *Green Chem.* 24 (3), 1165–1176. doi:10.1039/D1GC03798F

Momeni, M. H., Payne, C. M., Hansson, H., Mikkelsen, N. E., Svedberg, J., Engström, Å., et al. (2013). Structural, Biochemical, and Computational Characterization of the Glycoside Hydrolase Family 7 Cellobiohydrolase of the Tree-killing Fungus Heterobasidion irregulare*. *J. Biol. Chem.* 288 (8), 5861–5872. doi:10.1074/jbc.M112.440891

Mostofian, B., Cheng, X., and Smith, J. C. (2014a). Replica-exchange molecular dynamics simulations of cellulose solvated in water and in the ionic liquid 1-butyl-3-methylimidazolium chloride. *J. Phys. Chem. B* 118 (38), 11037–11049. doi:10.1021/jp502889c

Mostofian, B., Smith, J. C., and Cheng, X. (2014b). Simulation of a cellulose fiber in ionic liquid suggests a synergistic approach to dissolution. *Cellulose* 21 (2), 983–997. doi:10.1007/s10570-013-0018-0

Mostofian, B., Smith, J. C., and Cheng, X. (2011). The solvation structures of cellulose microfibrils in ionic liquids. *Interdisc. Sci. Comput. Life Sci.* 3 (4), 308–320. doi:10.1007/s12539-011-0111-8

Mulholland, A. J. (2005). Modelling enzyme reaction mechanisms, specificity and catalysis. *Drug Discov. Today* 10 (20), 1393–1402. doi:10.1016/s1359-6446(05)03611-1

Ngenyoung, A., Muhammad, A., Rattanarojpong, T., Sutthibutpong, T., and Khunrae, P. (2021). Effect of N-terminal modification on the mode of action between the Xyn11A and Xylotetraose. *Int. J. Biol. Macromol.* 170, 240–247. doi:10.1016/10.1016/j.ijbiomac.2020.12.154

Nguyen, L. T., Phan, D.-P., Sarwar, A., Tran, M. H., Lee, O. K., Lee, E. Y., et al. (2021). Valorization of industrial lignin to value-added chemicals by chemical depolymerization and biological conversion. *Industrial Crops Prod.* 161, 113219. doi:10.1016/j.indcrop.2020.113219

Novoselov, N. P., Sashina, E. S., Petrenko, V. E., and Zaborsky, M. (2007). Study of dissolution of cellulose in ionic liquids by computer modeling. *Fibre Chem.* 39 (2), 153–158. doi:10.1007/s10692-007-0030-y

Nys, K., Furtmüller, P. G., Obinger, C., Van Doorslaer, S., and Pfanzagl, V. (2021). On the Track of Long-Range Electron Transfer in B-Type Dye-Decolorizing Peroxidases: Identification of a Tyrosyl Radical by Computational Prediction and Electron Paramagnetic Resonance Spectroscopy. *Biochemistry* 60 (15), 1226–1241. doi:10.1021/acs.biochem.1c00129

Ogunmolu, F. E., Jagadeesha, N. B. K., Kumar, R., Kumar, P., Gupta, D., and Yazdani, S. S. (2017). Comparative insights into the saccharification potentials of a relatively unexplored but robust Penicillium funiculosum glycoside hydrolase 7 cellobiohydrolase. *Biotechnol. Biofuels* 10 (1), 71. doi:10.1186/s13068-017-0752-x

Orella, M. J., Gani, T. Z. H., Vermaas, J. V., Stone, M. L., Anderson, E. M., Beckham, G. T., et al. (2019). Lignin-KMC: A Toolkit for Simulating Lignin Biosynthesis. *ACS Sustain. Chem. Eng.* 7 (22), 18313–18322. doi:10.1021/acssuschemeng.9b03534

Pang, Z., Chong, J., Zhou, G., de Lima Morais, D. A., Chang, L., Barrette, M., et al. (2021). MetaboAnalyst 5.0: narrowing the gap between raw spectra and functional insights. *Nucleic Acids Res.* 49 (W1), W388–W396. doi:10.1093/nar/gkab382

Parra-Ramírez, D., Martinez, A., and Cardona, C. A. (2018). Technical and economic potential evaluation of the strain *Escherichia coli* MS04 in the ethanol production from glucose and xylose. *Biochem. Eng. J.* 140, 123–129. doi:10.1016/j.bej.2018.09.015

Parthasarathi, R., Balamurugan, K., Shi, J., Subramanian, V., Simmons, B. A., and Singh, S. (2015). Theoretical Insights into the Role of Water in the Dissolution of Cellulose Using IL/Water Mixed Solvent Systems. *J. Phys. Chem. B* 119 (45), 14339–14349. doi:10.1021/acs.jpcb.5b02680

Payne, C. M., Resch, M. G., Chen, L., Crowley, M. F., Himmel, M. E., Taylor, L. E., 2nd, et al. (2013). Glycosylated linkers in multimodular lignocellulose-degrading enzymes dynamically bind to cellulose. *Proc. Natl. Acad. Sci. U.S.A.* 110 (36), 14646–14651. doi:10.1073/pnas.1309106110

Pereira, C. S., Silveira, R. L., and Skaf, M. S. (2021). QM/MM Simulations of Enzymatic Hydrolysis of Cellulose: Probing the Viability of an Endocyclic Mechanism for an Inverting Cellulase. *J. Chem. Inf. Model.* 61 (4), 1902–1912. doi:10.1021/acs.jcim.0c01380

Pham, L. T. M., Deng, K., Northen, T. R., Singer, S. W., Adams, P. D., Simmons, B. A., et al. (2021). Experimental and theoretical insights into the effects of pH on catalysis of bond-cleavage by the lignin peroxidase isozyme H8 from Phanerochaete chrysosporium. *Biotechnol. Biofuels* 14 (1), 108. doi:10.1186/s13068-021-01953-7

Pham, L. T. M., Kim, S. J., and Kim, Y. H. (2016). Improvement of catalytic performance of lignin peroxidase for the enhanced degradation of lignocellulose biomass based on the imbedded electron-relay in long-range electron transfer route. *Biotechnol. Biofuels* 9 (1), 247. doi:10.1186/s13068-016-0664-1

Piétu, G., Mariage-Samson, R., Fayein, N.-A., Matingou, C., Eveno, E., Houlgatte, R., et al. (1999). The Genexpress IMAGE knowledge base of the human brain transcriptome: a prototype integrated resource for functional and computational genomics. *Genome Res.* 9 (2), 195–209. doi:10.1101/gr.9.2.195

Pogni, R., Baratto, M. C., Teutloff, C., Giansanti, S., Ruiz-Dueñas, F. J., Choinowski, T., et al. (2006). A Tryptophan Neutral Radical in the Oxidized State of Versatile Peroxidase from Pleurotus eryngii. *J. Biol. Chem.* 281 (14), 9517–9526. doi:10.1074/jbc.M510424200

Pollegioni, L., Tonin, F., and Rosini, E. (2015). Lignin-degrading enzymes. *Febs J.* 282 (7), 1190–1213. doi:10.1111/febs.13224

Pollet, A., Lagaert, S., Eneyskaya, E., Kulminskaya, A., Delcour, J. A., and Courtin, C. M. (2010). Mutagenesis and subsite mapping underpin the importance for substrate specificity of the aglycon subsites of glycoside hydrolase family 11 xylanases. *Biochimica Biophysica Acta (BBA) - Proteins Proteomics* 1804 (4), 977–985. doi:10.1016/j.bbapap.2010.01.009

Quesada-Medina, J., López-Cremades, F. J., and Olivares-Carrillo, P. (2010). Organosolv extraction of lignin from hydrolyzed almond shells and application of the δ-value theory. *Bioresour. Technol.* 101 (21), 8252–8260. doi:10.1016/j.biortech.2010.06.011

Rabideau, B. D., Agarwal, A., and Ismail, A. E. (2013). Observed Mechanism for the Breakup of Small Bundles of Cellulose Iα and Iβ in Ionic Liquids from Molecular Dynamics Simulations. *J. Phys. Chem. B* 117 (13), 3469–3479. doi:10.1021/jp310225t

Rabideau, B. D., Agarwal, A., and Ismail, A. E. (2014). The role of the cation in the solvation of cellulose by imidazolium-based ionic liquids. *J. Phys. Chem. B* 118 (6), 1621–1629. doi:10.1021/jp4115755

Rabideau, B. D., and Ismail, A. E. (2015). Mechanisms of hydrogen bond formation between ionic liquids and cellulose and the influence of water content. *Phys. Chem. Chem. Phys.* 17 (8), 5767–5775. doi:10.1039/C4CP04060K

Radivojević, T., Costello, Z., Workman, K., and Garcia Martin, H. (2020). A machine learning Automated Recommendation Tool for synthetic biology. *Nat. Commun.* 11 (1), 4879. doi:10.1038/s41467-020-18008-4

Rapaport, D. C., Blumberg, R. L., McKay, S. R., and Christian, W. (1996). The Art of Molecular Dynamics Simulation. *Comput. Phys.* 10 (5), 456. doi:10.1063/1.4822471

Rashid, T., Kait, C. F., and Murugesan, T. (2016). A "Fourier Transformed Infrared" Compound Study of Lignin Recovered from a Formic Acid Process. *Procedia Eng.* 148, 1312–1319. doi:10.1016/j10.1016/j.proeng.2016.06.547

Ray, A. E., Williams, C. L., Hoover, A. N., Li, C., Sale, K. L., Emerson, R. M., et al. (2020). Multiscale Characterization of Lignocellulosic Biomass Variability and Its Implications to Preprocessing and Conversion: a Case Study for Corn Stover. *ACS Sustain. Chem. Eng.* 8 (8), 3218–3230. doi:10.1021/acssuschemeng.9b06763

Ren, H., Shi, C., and Zhao, H. (2020). Computational tools for discovering and engineering natural product biosynthetic pathways. *iScience* 23 (1), 100795. doi:10.1016/j.isci.2019.100795

Riccardi, D., Schaefer, P., YangYu, H., Yu, H., Ghosh, N., Prat-Resina, X., et al. (2006). Development of Effective Quantum Mechanical/Molecular Mechanical (QM/MM) Methods for Complex Biological Processes. *J. Phys. Chem. B* 110 (13), 6458–6469. doi:10.1021/jp056361o

Riou, C., Salmon, J.-M., Vallier, M.-J., Günata, Z., and Barre, P. (1998). Purification, Characterization, and Substrate Specificity of a Novel Highly Glucose-Tolerant β-Glucosidase from Aspergillus oryzae. *Appl. Environ. Microbiol.* 64 (10), 3607–3614. doi:10.1128/aem.64.10.3607-3614.1998

Romero, J. O., Fernández-Fueyo, E., Avila-Salas, F., Recabarren, R., Alzate-Morales, J., and Martínez, A. T. (2019). Binding and Catalytic Mechanisms of Veratryl Alcohol Oxidation by Lignin Peroxidase: A Theoretical and Experimental Study. *Comput. Struct. Biotechnol. J.* 17, 1066–1074. doi:10.1016/j.csbj.2019.07.002

Ruiz-Dueñas, F. J., and Martínez, Á. T. (2009). Microbial degradation of lignin: how a bulky recalcitrant polymer is efficiently recycled in nature and how we can take advantage of this. *Microb. Biotechnol.* 2 (2), 164–177. doi:10.1111/j.1751-7915.2008.00078.x

Sainsbury, P. D., Hardiman, E. M., Ahmad, M., Otani, H., Seghezzi, N., Eltis, L. D., et al. (2013). Breaking Down Lignin to High-Value Chemicals: The Conversion of Lignocellulose to Vanillin in a Gene Deletion Mutant of Rhodococcus jostii RHA1. *ACS Chem. Biol.* 8 (10), 2151–2156. doi:10.1021/cb400505a

Senn, H. M., and Thiel, W. (2009). QM/MM methods for biomolecular systems. *Angew. Chem. Int. Ed.* 48 (7), 1198–1229. doi:10.1002/anie.200802019

Sethupathy, S., Morales, G. M., Li, Y., Wang, Y., Jiang, J., Sun, J., et al. (2021). Harnessing microbial wealth for lignocellulose biomass valorization through

secretomics: a review. *Biotechnol. Biofuels Bioproducts* 14 (1), 1–31. doi:10.1186/s13068-021-02006-9

Shen, R., Olshen, A. B., and Ladanyi, M. (2009). Integrative clustering of multiple genomic data types using a joint latent variable model with application to breast and lung cancer subtype analysis. *Bioinformatics* 25 (22), 2906–2912. doi:10.1093/bioinformatics/btp543

Shen, T., and Gnanakaran, S. (2009). The stability of cellulose: a statistical perspective from a coarse-grained model of hydrogen-bond networks. *Biophysical J.* 96 (8), 3032–3040. doi:10.1016/j.bpj.2008.12.3953

Shi, J., Balamurugan, K., Parthasarathi, R., Sathitsuksanoh, N., Zhang, S., Stavila, V., et al. (2014). Understanding the role of water during ionic liquid pretreatment of lignocellulose: co-solvent or anti-solvent? *Green Chem.* 16 (8), 3830–3840. doi:10.1039/C4GC00373J

Singh, A. K., Katari, S. K., Umamaheswari, A., and Raj, A. (2021). In Silico exploration of lignin peroxidase for unraveling the degradation mechanism employing lignin model compounds. *RSC Adv.* 11 (24), 14632–14653. doi:10.1039/D0RA10840E

Smith, A. T., Doyle, W. A., Dorlet, P., and Ivancich, A. (2009). Spectroscopic evidence for an engineered, catalytically active Trp radical that creates the unique reactivity of lignin peroxidase. *Proc. Natl. Acad. Sci. U.S.A.* 106 (38), 16084–16089. doi:10.1073/pnas.0904535106

Sonoki, T., Takahashi, K., Sugita, H., Hatamura, M., Azuma, Y., Sato, T., et al. (2018). Glucose-Free cis,cis-Muconic Acid Production via New Metabolic Designs Corresponding to the Heterogeneity of Lignin. *ACS Sustain. Chem. Eng.* 6 (1), 1256–1264. doi:10.1021/acssuschemeng.7b03597

Teeri, T. T. (1997). Crystalline cellulose degradation: new insight into the function of cellobiohydrolases. *Trends Biotechnol.* 15 (5), 160–167. doi:10.1016/S0167-7799(97)01032-9

Thimm, O., Bläsing, O., Gibon, Y., Nagel, A., Meyer, S., Krüger, P., et al. (2004). MAPMAN: a user-driven tool to display genomics data sets onto diagrams of metabolic pathways and other biological processes. *Plant J.* 37 (6), 914–939. doi:10.1111/j.1365-313x.2004.02016.x

Tilay, A., Bule, M., Annapure, U., and chemistry, f. (2010). Production of Biovanillin by One-Step Biotransformation Using Fungus Pycnoporous cinnabarinus. *J. Agric. Food Chem.* 58 (7), 4401–4405. doi:10.1021/jf904141u

Totrov, M., and Abagyan, R. (2008). Flexible ligand docking to multiple receptor conformations: a practical alternative. *Curr. Opin. Struct. Biol.* 18 (2), 178–184. doi:10.1016/j.sbi.2008.01.004

Tu, W.-C., and Hallett, J. P. (2019). Recent advances in the pretreatment of lignocellulosic biomass. *Curr. Opin. Green Sustain. Chem.* 20, 11–17. doi:10.1016/j.cogsc.2019.07.004

Tuncbag, N., McCallum, A., Huang, S.-s. C., and Fraenkel, E. (2012). SteinerNet: a web server for integrating 'omic' data to discover hidden components of response pathways. *Nucleic Acids Res.* 40, W505–W509. Web Server issue). doi:10.1093/nar/gks445

Valdés, G., Mendonça, R. T., and Aggelis, G. (2020). Lignocellulosic biomass as a substrate for oleaginous microorganisms: a review. *Appl. Sci.* 10 (21), 7698. doi:10.3390/app10217698

Vandera, E., Samiotaki, M., Parapouli, M., Panayotou, G., and Koukkou, A. I. (2015). Comparative proteomic analysis of Arthrobacter phenanthrenivorans Sphe3 on phenanthrene, phthalate and glucose. *J. Proteomics* 113, 73–89. doi:10.1016/j.jprot.2014.08.018

Vandermarliere, E., Bourgois, T. M., Rombouts, S., van Campenhout, S., Volckaert, G., Strelkov, S. V., et al. (2008). Crystallographic analysis shows substrate binding at the −3 to +1 active-site subsites and at the surface of glycoside hydrolase family 11 endo-1,4-β-xylanases. *Biochem. J.* 410 (1), 71–79. doi:10.1042/bj20071128

Vázquez-Lima, H., Guadarrama, P., and Martínez-Anaya, C. (2012). Geometric distortions on a three-coordinated T1 Cu site model as a potential strategy to modulate redox potential. A theoretical study. *J. Mol. Model.* 18 (2), 455–466. doi:10.1007/s00894-011-1063-y

Vermaas, J. V., Dellon, L. D., Broadbelt, L. J., Beckham, G. T., and Crowley, M. F. (2018). Automated Transformation of Lignin Topologies into Atomic Structures with LigninBuilder. *ACS Sustain. Chem. Eng.* 7 (3), 3443–3453. doi:10.1021/acssuschemeng.8b05665

Wang, G., Zhao, Z., Ke, J., Engel, Y., Shi, Y.-M., Robinson, D., et al. (2019). CRAGE enables rapid activation of biosynthetic gene clusters in undomesticated bacteria. *Nat. Microbiol.* 4 (12), 2498–2510. doi:10.1038/s41564-019-0573-8

Wang, J., Hou, Q., Dong, L., Liu, Y., and Liu, C. (2011). QM/MM studies on the glycosylation mechanism of rice BGlu1 β-glucosidase. *J. Mol. Graph. Model.* 30, 148–152. doi:10.1016/j.jmgm.2011.06.012

Wang, Q., and Pang, Y.-P. (2007). Preference of small molecules for local minimum conformations when binding to proteins. *PLoS One* 2 (9), e820. doi:10.1371/journal.pone.0000820

Wang, Y., Song, X., Zhang, S., Li, J., Shu, Z., He, C., et al. (2016). Improving the activity ofTrichoderma reeseicel7B through stabilizing the transition state. *Biotechnol. Bioeng.* 113 (6), 1171–1177. doi:10.1002/bit.25887

Warshel, A. (1976). Bicycle-pedal model for the first step in the vision process. *Nature* 260 (5553), 679–683. doi:10.1038/260679a0

Warshel, A., and Levitt, M. (1976). Theoretical studies of enzymic reactions: dielectric, electrostatic and steric stabilization of the carbonium ion in the reaction of lysozyme. *J. Mol. Biol.* 103 (2), 227–249. doi:10.1016/0022-2836(76)90311-9

Warshel, A. (2014). Multiscale Modeling of Biological Functions: From Enzymes to Molecular Machines (Nobel Lecture). *Angew. Chem. Int. Ed.* 53 (38), 10020–10031. doi:10.1002/anie.201403689

Wilhelm, R. C., Singh, R., Eltis, L. D., and Mohn, W. W. (2019). Bacterial contributions to delignification and lignocellulose degradation in forest soils with metagenomic and quantitative stable isotope probing. *Isme J.* 13 (2), 413–429. doi:10.1038/s41396-018-0279-6

Wong, D. W. S. (2009). Structure and action mechanism of ligninolytic enzymes. *Appl. Biochem. Biotechnol.* 157 (2), 174–209. doi:10.1007/s12010-008-8279-z

Xu, H., Pan, W., Wang, R., Zhang, D., and Liu, C. (2012). Understanding the mechanism of cellulose dissolution in 1-butyl-3-methylimidazolium chloride ionic liquid via quantum chemistry calculations and molecular dynamics simulations. *J. Comput. Aided Mol. Des.* 26 (3), 329–337. doi:10.1007/s10822-012-9559-9

Yaegashi, J., Kirby, J., Ito, M., Sun, J., Dutta, T., Mirsiaghi, M., et al. (2017). Rhodosporidium toruloides: a new platform organism for conversion of lignocellulose into terpene biofuels and bioproducts. *Biotechnol. Biofuels* 10 (1), 241. doi:10.1186/s13068-017-0927-5

Yang, H., Watts, H. D., Gibilterra, V., Weiss, T. B., Petridis, L., Cosgrove, D. J., et al. (2019). Quantum Calculations on Plant Cell Wall Component Interactions. *Interdiscip. Sci. Comput. Life Sci.* 11 (3), 485–495. doi:10.1007/s12539-018-0293-4

Yao, A., Choudhary, H., Mohan, M., Rodriguez, A., Magurudeniya, H., Pelton, J. G., et al. (2021). Can Multiple Ions in an Ionic Liquid Improve the Biomass Pretreatment Efficacy? *ACS Sustain. Chem. Eng.* 9 (12), 4371–4376. doi:10.1021/acssuschemeng.0c09330

Yoo, C. G., Pu, Y., Li, M., and Ragauskas, A. J. (2016). Elucidating Structural Characteristics of Biomass using Solution-State 2 D NMR with a Mixture of Deuterated Dimethylsulfoxide and Hexamethylphosphoramide. *ChemSusChem* 9 (10), 1090–1095. doi:10.1002/cssc.201600135

You, X., Wang, X., Liang, C., Liu, X., and Wang, S. (2019). Purification of hemicellulose from sugarcane bagasse alkaline hydrolysate using an aromatic-selective adsorption resin. *Carbohydr. Polym.* 225, 115216. doi:10.1016/j.carbpol.2019.115216

Youngs, T. G. A., Holbrey, J. D., Deetlefs, M., Nieuwenhuyzen, M., Costa Gomes, M. F., and Hardacre, C. (2006). A molecular dynamics study of glucose solvation in the ionic liquid 1,3-dimethylimidazolium chloride. *Chemphyschem* 7 (11), 2279–2281. doi:10.1002/cphc.200600569

Yuryev, A., Kotelnikova, E., and Daraselia, N. (2009). Ariadne's ChemEffect and Pathway Studio knowledge base. *Expert Opin. Drug Discov.* 4 (12), 1307–1318. doi:10.1517/17460440903413488

Zhang, X., Yang, W., and Blasiak, W. (2011). Modeling Study of Woody Biomass: Interactions of Cellulose, Hemicellulose, and Lignin. *Energy fuels.* 25 (10), 4786–4795. doi:10.1021/ef201097d

Zhang, Y., He, H., Dong, K., Fan, M., and Zhang, S. (2017). A DFT study on lignin dissolution in imidazolium-based ionic liquids. *RSC Adv.* 7 (21), 12670–12681. doi:10.1039/C6RA27059J

Zhang, Z., Liu, B., and Zhao, Z. (2012). Efficient acid-catalyzed hydrolysis of cellulose in organic electrolyte solutions. *Polym. Degrad. Stab.* 97 (4), 573–577. doi:10.1016/j.polymdegradstab.2012.01.010

Zhao, Y., Liu, X., Wang, J., and Zhang, S. (2013a). Effects of anionic structure on the dissolution of cellulose in ionic liquids revealed by molecular simulation. *Carbohydr. Polym.* 94 (2), 723–730. doi:10.1016/j.carbpol.2013.02.011

Zhao, Y., Liu, X., Wang, J., and Zhang, S. (2013b). Insight into the cosolvent effect of cellulose dissolution in imidazolium-based ionic liquid systems. *J. Phys. Chem. B* 117 (30), 9042–9049. doi:10.1021/jp4038039

Zong, Z., Li, Q., Hong, Z., Fu, H., Cai, W., Chipot, C., et al. (2019). Lysine Mutation of the Claw-Arm-Like Loop Accelerates Catalysis by Cellobiohydrolases. *J. Am. Chem. Soc.* 141 (36), 14451–14459. doi:10.1021/jacs.9b08477

Zsoldos, Z., Reid, D., Simon, A., Sadjad, S. B., and Johnson, A. P. (2007). eHiTS: a new fast, exhaustive flexible ligand docking system. *J. Mol. Graph. Model.* 26 (1), 198–212. doi:10.1016/j.jmgm.2006.06.002

Multiscale Shear Properties and Flow Performance of Milled Woody Biomass

Jordan Klinger[1]*, Nepu Saha[1], Tiasha Bhattacharjee[1], Susan Carilli[1], Wencheng Jin[1], Yidong Xia[1], Richard Daniel[2], Carolyn Burns[2], Oyelayo Ajayi[3], Ziwei Cheng[4], Ricardo Navar[4] and Troy Semelsberger[4]

[1]Energy and Environment Science and Technology Directorate, Idaho National Laboratory, Idaho Falls, ID, United States, [2]Energy and Environment Directorate, Pacific Northwest National Laboratory, Richland, WA, United States, [3]Applied Materials Division, Argonne National Laboratory, Lemont, IL, United States, [4]Material Physics Applications Division, Los Alamos National Laboratory, Los Alamos, NM, United States

One dominant challenge facing the development of biorefineries is achieving consistent system throughput with highly variant biomass feedstock quality and handling performance. Current handling unit operations are adapted from other sectors (primarily agriculture), where some simplifying assumptions about granular mechanics and flow performance do not translate well to a highly compressible and anisotropic material with nonlinear time- and stress-dependent properties. This work explores the shear and frictional properties of loblolly pine at multiple experimental test apparatus and particle scales to elucidate a property window that defines the shear behavior over a range of material attributes (particle size, size distribution, moisture content, etc.). In general, it was observed that the bulk internal friction and apparent cohesion depend strongly on both the stress state of the sample in granular shear testers and the overall particle size and distribution span. For equipment designed to characterize the quasi-static shear stress failure of bulk materials ranging from 50 to 1,000 ml in test volume, similar test results were observed for finely milled particles (50% passing size of 1.4 mm) with a narrow size distribution (span between 10 and 90% passing size of 0.9 mm), while stress chaining and over-torque issues persisted for the bench-scale test apparatus for larger particle sizes or widely dispersed sample sizes. Measurement of the anisotropic particle–particle friction ranged from coefficients of approximately 0.20 to 0.45 and resulted in significantly higher and more variable friction measurements for larger particle sizes and in perpendicular alignment orientations. To supplement these laboratory-scale properties, this work explores the flow of loblolly pine and Douglas fir through a pilot-scale wedge-shaped hopper and a screw feeder. For the gravity-driven hopper flow, the critical arching distance and mass discharge rate ranged from approximately 10 to 30 mm and 2 to 16 tons/hour, respectively, for both materials, where the arching distance depends strongly on the overall particle size and depends less on the hopper inclination angle. Comparatively, the auger feeder was found to be much more impacted by the size of the particles, where smaller particles had a more consistent and stable flow while consuming less power.

Keywords: biomass, shear, granular flow, flow friction, hopper flow

1 INTRODUCTION

Due to the limited resource of fossil fuel and growing sentiment toward global warming, alternative sources of energy are today's demand. Biomass is considered one of the most abundant and easy-to-access alternative renewable resources of energy and chemicals (Binder and Raines, 2009; Bilgili et al., 2017). However, handling of biomass feedstock is one of the key challenges to the commercialization of biomass as an energy source. Poor understanding of biomass handling, especially with regard to biomass flowability during feedstock conversion process design, may result in excessive process downtime due to common granular material interactions such as unanticipated feed silo ratholing, screw feeder jamming, etc. (Ramírez-Gómez, 2016; Dale, 2017; Ilic et al., 2018; Cheng et al., 2021). Many factors influence the flow properties of biomass materials, such as particle size, particle shape, moisture content, and surface roughness (Liu et al., 2015; Lu et al., 2018). A complete understanding of the flow behavior of biomass as functions of their intrinsic material properties is required to minimize the downtime and improve the commercialization feasibility of feedstock conversion processes.

Until the mid-20th century, the bulk solid flow mainly focused on pharmaceutical ingredients and food powders with relatively regular particle shape and size and little if any moisture content (Fitzpatrick et al., 2004; Faqih et al., 2007; Hou and Sun, 2008; Zhou et al., 2010). The traditional methods used for the powder flowability characterization include the angle of repose test, packing property test, gravity discharge test, and shear test (Krantz et al., 2009; Leturia et al., 2014; Rezaei et al., 2018). Typical properties of biomass particles, which include high moisture content, hygroscopic nature, low bulk density, heterogeneous shapes, and fibrous nature, make them different from the conventional granular particles (e.g., pharmaceutical ingredients). Since the powder flow is multidimensional (Prescott and Barnum, 2000), these unique characteristics of biomass make it more difficult to experimentally measure the characteristic properties. For example, the standard characterization tests suffer from either an inadequate measurement of full stress state (e.g., ring shear test) or limited strain range to reach the critical shear state (e.g., triaxial shear test) for granular biomass feedstocks (Barletta et al., 2015; Hernandez et al., 2017; Lu et al., 2021b).

A variety of shear characterization techniques exist on the market. These range in complexity from rotating plates common in commercial rheometers (or linear stages) to textured cups and customized devices/cells, with a variety of shear mechanisms/zones to accommodate non-idealities in large or non-uniform samples. It is of scientific and commercial interest to evaluate the performance of the range of available commercial and custom shear testers to gain confidence in their ability to accurately characterize the flowability of complex biomass feedstocks and enable a broader range of material characterization techniques to academia and industry. In general, these devices measure the resistance to dynamic or quasi-static (dependent on the rate) shearing with varying applied stresses. These devices usually measure either a continuous shear response (more typical to rheometer-style devices) or create discretized test conditions

where the bulk is either re-tested or exchanged between test zones (more typical of "granular testers"). Typically, granular tests preformat the granular solids to yield a given internal stress and particle packing (void volume) configuration. By preformatting the material over a range of internal stresses and measuring the force required to initiate motion, one can characterize apparent internal friction, bulk cohesion, and the unconfined yield strength and major principal stresses through a Mohr's circle analysis (Comanici and Barsanescu, 2018; Westover and Hartley, 2018; Pachón-Morales et al., 2020). Compared to granular testers, rheometers are more common due to their ease of use and ability to quantify the shear behavior of both viscous fluids and semi-solid materials (such as yield stress fluids). However, for granular materials, they are known to have torque and particle size limitations stemming from the tendency of granular materials to develop stress chains between test geometry surfaces and resulting in bias, noisy, or stochastic measurements because of convoluted impacting factors from particle size and morphology-induced complex packing, interlocking, etc. (Senff et al., 2009; Leturia et al., 2014). While the physical properties of low-moisture, granular biomass feedstocks drive the use of specialized test instruments (e.g., the shear cells developed by Jenike, Schulze, and Peschl) for granular materials, the ubiquity of rheometers in industrial and research laboratory settings facilitates their potential use as opportunistic replacements for specialized granular testing equipment. However, several factors, such as specialized geometries and test apparatuses, limit the use of rheometers for testing granular materials. Regardless of the instrument used to carry out material shear characterization, the main thrust of any characterization effort is to enable 1) predictive assessment of material feeding and handling behaviors and 2) evaluation of the prime impacts of material attributes on handling operation performance. As a first step in meeting this goal for biomass feedstock materials, it is critical to benchmark the effectiveness and impact of these characterization techniques and measurement scales on shear properties while working with biomass particles of various sizes.

To this end, we investigated the bulk shear failure of softwoods resulting in an apparent internal friction angle and bulk cohesion as well as contributing factors of particle–particle and particle–surface frictions using various testers, including a Schulze ring shear tester, a high precision air bearing rheometer, and a Freeman FT4 powder rheometer. These shear characterizations are performed at different scales, in addition to a range of particle scales to collectively contribute to this multiscale analysis. In particulate systems, as in the present study of pine particles, the complex kinematics of micromechanics of the particles' motion and rearrangement also contribute to the measured friction. Nevertheless, the examination of the particle surface features and structures provides some insight into the strong anisotropic friction behavior of the pine particles. This study also explored the impact of the material attributes on the flow performance by gravity-driven flow in a variable wedge hopper and mechanically assisted flow in a screw feeder. Finally, the applicability and limitations of the characterization techniques were discussed.

TABLE 1 | Size distribution and bulk density of the feedstocks.

Feedstock	Label	Comminution method	Nominal separatory sieve size (mm)	Size distribution			Bulk density (kg/m³)
				D_{10} (mm)	D_{50} (mm)	D_{90} (mm)	
Loblolly pine	S1	Hammer mill, ½"	0.00–0.85	0.46 ± 0.01	0.69 ± 0.01	0.82 ± 0.00	237.9
Loblolly pine	S2	Hammer mill, ½"	0.85–2.00	0.96 ± 0.00	1.36 ± 0.01	1.84 ± 0.00	242.2
Loblolly pine	S3	Hammer mill, ½"	2.00–3.35	2.08 ± 0.00	2.45 ± 0.00	3.08 ± 0.00	236.4
Loblolly pine	S4	Hammer mill, ½"	3.35–4.75	3.43 ± 0.00	3.80 ± 0.01	4.47 ± 0.01	242.5
Loblolly pine	S5	Hammer mill, ½"	4.75–6.35	4.84 ± 0.00	5.26 ± 0.01	6.02 ± 0.01	240.7
Loblolly pine	S6	Hammer mill, ½"	0.85–6.35	0.76 ± 0.02	1.52 ± 0.01	3.01 ± 0.03	258.0
Loblolly pine	S7	Hammer mill, ¼"	N/A	0.34 ± 0.01	0.84 ± 0.02	1.64 ± 0.04	248.4
Loblolly pine	S8	Hammer mill, ½"	0.85–6.35	1.14 ± 0.05	2.36 ± 0.09	4.24 ± 0.17	184.2
Douglas fir	S9	Rotary shear 1 mm	0.40–1.70	0.51 ± 0.01	0.99 ± 0.02	1.5 ± 0.02	174.0
Douglas fir	S10	Rotary shear 2 mm	0.80–4.00	0.83 ± 0.02	1.51 ± 0.03	2.14 ± 0.02	177.8
Douglas fir	S11	Rotary shear 4 mm	2.40–9.50	1.95 ± 0.1	3.27 ± 0.17	4.67 ± 0.12	176.5

2 MATERIALS AND METHODS

2.1 Materials
This study on the multiscale shear properties focuses on loblolly pine grown on plantations (Edgefield, South Carolina, approximately 25 years of maturity) and collected using relevant industrial methods. Whole trees were cut (Tigercat 724G feller buncher) and pulled by a grapple skidder (Tigercat 630E grapple skidder) to loading decks. The whole trees passed through a flail chain system to remove most of the bark, limbs, and needles on the way to the infeed of the chipper (Peterson Pacific 5000H disc knife chipper) by knuckle boom. The remaining chipped and de-barked stem/bole was loaded into primary transportation and stored outdoors at Idaho National Laboratory (INL). The pine samples were then further size-reduced using a Schutte Buffalo (18 7,300) hammer mill with a 12 mm screen. The wood chips were air-dried over 24 h at 105°C to an approximate moisture content of 10%. The samples then went through particle size exclusion performed with a continuous sieve system (SWECO-ZS24C4444INP3WC) to make sample volumes needed for testing. Sample nomenclature is by the sieve screen size obtained from this separation, and the actual size distribution is noted in the respective analysis. The continuous and imperfect nature of this separator yields an actual size distribution that is slightly more dispersed than the nominal size class suggests but still has >85% of particles, by mass, within the stated class.

The Douglas fir samples used in this study were obtained and preprocessed by Forest Concepts (Auburn, WA) with their rotary sheer size reduction technique. Clean, debarked logs were sourced from the Pacific northwest and chipped prior to arriving at Forest Concepts. These chips were processed as-received (green moisture, ~35%–40%) through a nominal 4-mm crumbling rotor set and sieved between 9.5 mm (3/8 inch) and 2.4 mm (3/32 inch). Particles over the sieve top size were recirculated until all material passed through to the smaller sizes, and the fines below the bottom screen were not used in this study. A portion of the material between these screen sizes was set aside and dried (nominally labeled 4 mm), while the rest was carried to produce the smaller sample sizes. The nominal 2- and 1-mm samples were produced in a similar manner, with sieve screening between 4.0 mm (5/32 in)–0.8 mm (20 mesh) and 1.7 mm (10 mesh)–0.4 mm (40 mesh) for the samples, respectively. After the 2-mm nominal reduction, the sample was dried prior to producing the 1-mm nominal sample.

The size distribution and bulk density, along with the nomenclature (used in the later sections) of the feedstocks, are shown in **Table 1**. The particle size distributions (approximately 100 g samples) were measured in a stack of analytical sieves (RX-30 W.S. Tyler Rotap). The sieve stack was agitated for 15 min to achieve size separation, and the recovered mass on each screen was measured on a balance with readability to 0.01 g. Particle size distribution measurements were performed in triplicate. In the case of the incremental particle classes (S1–S5), the whole material distribution was used to estimate the size distribution parameters with a log–normal distribution fitted through least-squares regression. As listed in **Table 1**, the particle size and size distribution of the investigated samples span multiple classes. Quantitatively, there is up to approximately an order of magnitude (D_{50} ranging from 0.69 to 5.26) change in particle scales studied.

2.2 Methods
2.2.1 Shear Test
Shear test of the studied feedstock (denoted "S1"–"S6" in **Table 1**) was conducted using three different testing instruments, including a Schulze ring shear tester, a high precision air bearing rheometer, and a Freeman FT4 powder rheometer, to understand the limitations of the characterization techniques. An automated Schulze ring shear tester (Dietmar Schulze Schüttgutmesstechnik, Wolfenbüttel, Germany) was used to measure the shear strength of the materials using a size M shear cell (outer diameter of 20 cm and inner diameter of 10 cm) as per ASTM D6773-08. The comparison tests were performed at 1, 5, and 10 kPa pre-shear consolidation stresses, followed by four varying levels of normal stress to develop the yield criterion. For reference, the ring shear tester has a large annular cross-section with an outer diameter of approximately 200 mm and a material depth of 40 mm with a test volume of 900 ml and a rotational speed of 0.02 rad/min, resulting in a quasi-static yielding measurement.

An AR 2000 high-precision air-bearing rheometer (TA Instruments, New Castle, DE) was used to characterize the stress response of sized fractions of a loblolly pine biomass feedstock as a function of normal force loads spanning 0.2–5 N (nominally 0.1–2.5 kPa) and at an angular velocity of 0.03 rad/s. To maintain normal force targets during testing, the rheometer was allowed to adjust its own gap (between −2 and +5 mm deeper into the material as needed). The test was conducted in a test cup with an irregular finned baseplate and baffled fins on the wall. For the majority of measurements, the diameter of the base was 64.0 mm, while the base asperities were 2 mm tall and 1 mm width. The radial fins were 1 mm high and ran the length of the wall (20 mm). For select measurements, 55.0 and 59.5 mm bases were used to evaluate the impact of base radius on the measurement. For all tests, a 50-mm plate rotor with matching irregular fins was used. All tests employed approximately 10 mm of fill material. In general, loblolly pine samples were tested in their as-received condition. However, a limited set of tests were conducted with loblolly pines that had been soaked in room-temperature ($20 \pm 2°C$) deionized water for 24 h and free-drained (resulting in loblolly pine with approximately 70% moisture by mass). In total, 14 separate "shear vs. normal force response" curves were characterized to characterize the impact of loblolly pine size fraction and moisture content as well as the impact of test geometry size on measurements made by the standard laboratory rheometer.

This study also examined the rheological properties measured *via* a Freeman FT4 powder rheometer (Norcross, GA). The primary use of the instrument is to characterize the flow properties of solid particles, while offering the ability to quantify the flow properties under dynamic conditions. External variables influencing the flow properties include consolidation, composition, wall friction, particle size, aeration, moisture, shear rate, and storage time. Critical material attributes focused on including particle size and distribution and moisture content. For these tests, a 50-mm diameter cup was used. The rotational rates were varied from 10 to 100 mm/s, and the applied normal stress ranged from 5 to 15 kPa in a similar range to those studied in the Schulze tester.

2.2.2 Multiscale Friction

A test method to directly measure the instantaneous particle–particle and particle–wall friction of biomass materials was developed to probe how friction changed under different conditions. The method is based on the adaptation of a high-precision reciprocating sliding tribometer shown in **Supplementary Figure S1**. Tribometers are devices designed specifically to measure friction and can measure normal and tangential forces at a contact interface at a very high sampling rate (>1,000 Hz) and hence can provide fine details of instantaneous friction behavior at contact interface. The setup for biomass friction measurement consists of a stationary top rectangular ($12 \times 10 \times 6.5$ mm) plate made of the wall material and a moving lower rectangular ($45 \times 40 \times 6.5$ mm) plate in reciprocating motion (see **Supplementary Figure S1B**). The contact kinematics of the Jenike shear tester and the reciprocating tribometer are indeed very similar; there are some salient differences between the two measurement techniques. The

Jenike shear tester measures the shear strength of confined and consolidated bulk granular materials, while the tribometer measures instantaneous frictional interactions between ensembles of unconfined particles. Comparison of the average friction or shear forces (shear stress) from tribometer and the shear strength from Jenike tester could be instructive and provide potential connection between the two test methods. The tribometer data provide fine details that enable a better understanding of contact dynamics and physics governing particle interaction during shear, such as the anisotropy of friction in irregular shaped particles. Furthermore, the tribometer requires relatively small quantity of materials for testing, while the Jenike shear cell could require a considerable amount of material, depending on the cell size.

For the biomass material friction measurement, a copious amount of biomass material was attached to the lower plate. A second layer of loose biomass material is placed on top of the attached layer to accommodate the shear during testing. For particle–particle friction measurements, the biomass material is attached to the top plate as well. For particle–wall friction measurement, the top plate (made of the wall material of interest) without biomass material is slid over the loss biomass layer. Both the normal and tangential forces are measured during sliding. The test parameters for friction measurement in the tribometer include pressure (normal force), shear rate (sliding speed), stroke length, and temperature. The normal loads of 5, 10, 15, and 25 N impose a nominal pressure of about 42 kPa (6 Psi), 83 kPa (12 Psi), 125 kPa (18 Psi), and 208 kPa (30 Psi), respectively. It should be noted that the interparticle pressures were considerably higher, as indicated by the pressure map. For each load, friction measurements were conducted at sliding speeds of 1.67, 3.33, 5.0, and 6.67 mm/sec. Five replicate measurements were made under each test condition to test the range of variability in the frictional behavior of the tested biomass materials. All the tests were conducted under ambient conditions.

Scanning electron microscopy (SEM) examination of the pine particle surfaces was also conducted to enable better understanding of the frictional behavior. An FEI Quanta 400F environmental SEM system was used for the examination in a secondary electron imaging (SEI) mode. A relatively low accelerating voltage of 1.0 kV was used for the SEM examination in order to minimize the charging effect because the particles of pine biomass material are not electrically conducting. The characteristic features on the surfaces of the pine particles in different orientations were examined.

2.2.3 Flow Performance

To understand and demonstrate how variable material attributes impact the flow performance in real flow systems, five samples (denoted "S7"–"S11" in **Table 1**) were tested in the wedge hopper and the Acrison® screw feeder. A custom hopper with an adjustable outlet and sidewalls was used to measure the critical arching distance and flow rate of the studied feedstocks. The hopper consists of two side walls and two vertical end walls. For the critical arching distance and flow tests, around 15 kg of sample was loaded in the adjustable hopper for each batch test. The inclination angle of the side walls was varied between 28 and 36° at 4° intervals, where the end walls remained 400 mm
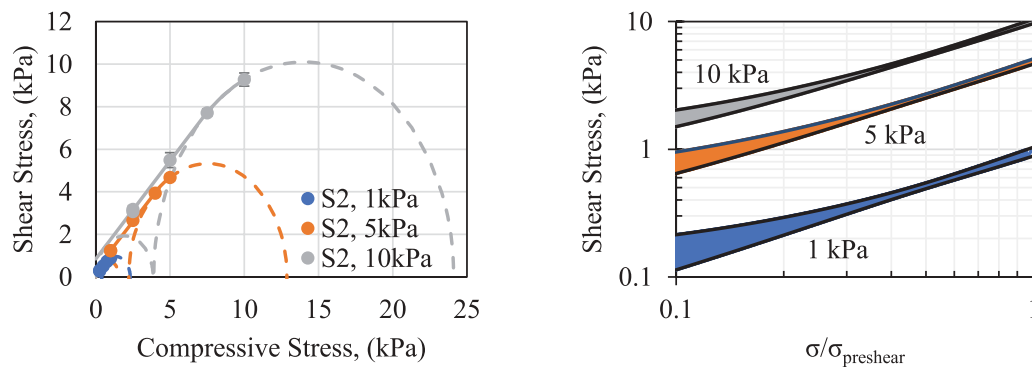
FIGURE 1 | (Left) Ring shear test for sample S2 at pre-shear conditions of 1, 5, and 10 kPa. The error bars represent the standard deviation between 10 measurements. (Right) Log–log scale plot of the 95% confidence interval bands for the yield loci at the three conditions with the compressive stress condition normalized by the applied pre-shear stress as labeled.

apart during all tests. The hopper opening was increased step-wise using 2-step motors attached with the two side walls. The minimum opening at which all the loaded material smoothly flows out from the hopper is defined as the critical arching distance of the material. The critical arching distance was determined for each sample at each inclination angle. The flow test was conducted at nine random openings (> critical arching) of the hopper. The time required to pass all the material through the hopper opening was recorded, which was ultimately used for the flow rate calculation. All these tests were conducted at least twice.

The feeding behavior of each sample was further tested using the Acrison® Bin Weight Screw Feeder (model 402X-250-75-BDF1.5-E/2). This unit consists of a large feed bin atop an interchangeable feed screw auger and several conditioning augers slightly above the feed screw to mix the material and ensure reliable flow. These tests used a 63-mm diameter solid shaft screw with a pitch of equal dimension. The entire unit is mounted on load cells to measure the system mass and connected to a power meter, allowing for measurements of the feed rate and power consumption.

During the feeder tests, the unit was operated under two different modes: 1) controlled auger rotational frequency and 2) controlled loss-in-mass feed rate with active control. In mode (1), the rotational speeds of the auger were set at 10, 20, 30, 40, and 50% of its full capacity. In mode (2), the tests were conducted at set feed rates of 20, 40, 60, 80, and 100 pounds per hour (LBH). For all tests, the mass feed rate was recorded by the feeder controller and archived in a laptop computer *via* a custom LabView VI. These data were further used to calculate the specific power consumption of each sample under both operational modes. All tests were performed in duplicate for each sample.

3 RESULTS AND DISCUSSION

3.1 Effect of Measurement Techniques on Shear Properties

3.1.1 Schulze Ring Shear Tester
Figure 1 shows the shear stress of feedstock S2 under three different pre-shear stresses (1, 5, and 10 kPa) using the RST

technique. The apparent internal friction is relatively consistent ($41.6 \pm 2.0°$, $42.2 \pm 0.8°$, and $42.6 \pm 1.0°$) among the three pre-shear stress conditions, and their standard deviation is within experimental variability. The results also show a slight increase in the average value with increasing pre-shear stress. The bulk cohesion shows an increase with increasing pre-shear conditions and is approximately 0.08 ± 0.01, 0.35 ± 0.04, and 0.85 ± 0.25 kPa for initial pre-shear of 1, 5, and 10 kPa, respectively. The values for the analysis are tabulated in **Table 2**. As the shear condition approached the pre-shear condition, the yield surface has a slightly sub-linear decrease that is accounted for the prediction of the principal stresses. **Figure 1** also shows the 95% confidence interval bands for the respective yield loci. For presentation and clarity, the compressive stress, σ, is normalized with the relevant pre-shear condition, $\sigma_{preshear}$, to place the data on similar scales. The results show that the loci depend significantly on the applied pre-shear event and that the material's bulk yielding behavior is dependent on both the stress state of the material and the stress history. Materials with higher magnitude stress history require a greater force to reach flow inception. As a result, this implies that rapidly fluctuating stress environments can cause inconsistent flow patterns and performance in larger-scale equipment.

These testing procedures were extended to two additional samples, S6 and S4, to compare a relatively broad particle size distribution and an overall larger particle size distribution. These overall results from the RST are summarized in **Table 2**, where σ_1 is the major principal stress, FC is the unconfined yield stress, δ is the apparent internal friction assuming zero cohesion, ϕ_i is the internal friction, and flowability is a relative index calculated as the ratio of σ_1 and FC. On average, the RST resulted in a statistically similar internal friction for all three samples ($42.4°$ on average), with a slightly increasing friction angle for increasing pre-shear stress with an exception for the S4 sample. Similarly, the apparent cohesion increases for all samples with increasing pre-shear stress. For all the pre-shear levels, the highest cohesion was measured in the smallest particle size sample, while the larger size sample (S4) had the lowest cohesion. For all three materials, there is a systematic bias when comparing to a linear trend, and the measured cohesion appears to have a power law or

TABLE 2 | Shear properties of loblolly pine (S2, S4, and S6) from the RST.

Sample	Pre-shear (kPa)	σ_1 (kPa)	FC (kPa)	δ (°)	ϕ_i (°)	Cohesion (kPa)	Flowability
S2	10	24.1	3.9	46.1	42.6	0.85	6.3
	5	12.9	1.6	44.8	42.2	0.35	8.2
	1	2.3	0.3	44.7	41.6	0.08	6.9
S4	10	25.0	3.3	45.0	42.2	0.73	7.6
	5	11.4	0.8	41.4	39.9	0.18	15.0
	1	2.4	0.1	45.8	44.8	0.03	19.7
S6	10	25.3	3.2	46.1	43.4	0.70	7.9
	7.5	18.7	1.9	45.0	42.8	0.42	9.7
	5	12.0	1.0	43.1	41.3	0.22	12.2
	2.5	5.9	0.5	45.4	43.7	0.10	12.4
	1	2.3	0.3	44.7	41.6	0.07	7.2

exponential-type growth with increasing pre-shear stress. The flowability of the powder is qualitatively interpreted through the ratio of the major principal stress to the unconfined yield strength, where higher values indicate more free-flowing solids (Dietmar, 2008; Miccio et al., 2011; Pachón-Morales et al., 2020). The highest flowability was measured in the largest particle size, while the lowest was in the small particles, while the distribution has a value closer to the smaller particles than the large (i.e., the sample flowability is given by S4 > S6 >~ S2). The largest particles showed a decreasing flowability with increasing stress, while the other samples showed a more complex result with higher stress values. Here, the intermediate stresses (2.5 and 5.0 kPa) appeared to make the bulk easier to shear followed by a more resilient bulk solid with further increase in the stress state.

The range in the unconfined yield strength measured here for pine samples S2, S4, and S6 are similar to those reported by Falk et al. (2015), which ranged from approximately 0.3 to 3.0 kPa over the similar pre-shear stress region. In the testing of mixed pine chips at a 15 kPa normal pressure in a Jenike shear cell, Stasiak et al. (2018) reported lower values of internal friction (31.3°) and higher values of cohesion (2.5 kPa). This could be due to the difference in the test method as well as testing at higher normal pressure conditions. Miccio et al. (2013) measured the shear properties of several sawdust samples at relatively low pre-shear conditions in an RST and found similar values for cohesion (0.12 and 0.16 kPa) and internal friction (43.3 and 45.6°) at ~0.79 kPa pre-shear. Their testing of olive husks at higher normal stress conditions also resulted in similar values to the wood reported here (42.8° internal friction and 0.27 kPa cohesion at 4.4 kPa pre-shear).

When examining the internal friction and cohesion, there can be some shift or translation due to different levels of pre-shear compression stress. This is related to the stress-memory of the material and can be significant for biomass. Between different levels of pre-shear stress, changes in the cohesion and in some cases the internal friction were observed (Chen et al., 2018; Fanesi et al., 2021). As a result, the magnitude of the measured shear properties, as well as the changes in the stress memory to the generalized size and shape parameters, was further studied to understand their effect on biomass rotational shear. The bulk cohesion of additional loblolly pine samples, shown in **Figure 2**, is well-described by a power-law-type relation with increasing stress
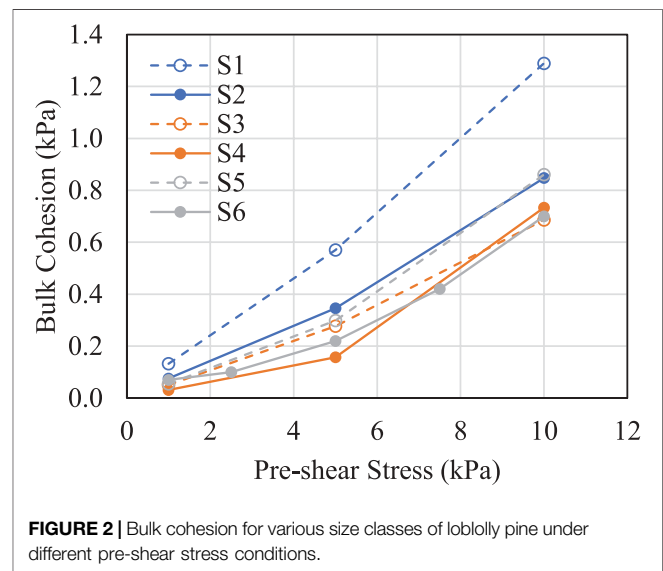
FIGURE 2 | Bulk cohesion for various size classes of loblolly pine under different pre-shear stress conditions.

(for example, see the sample trend for S6 in the **Supplementary Figure S2** with $R^2 > 0.99$ and standard error in a cohesion prediction of 0.001 kPa or 0.2%–2%). As shown in **Figure 2**, the smaller particle size fractions (e.g., S1 and S2) appear to have higher cohesion, and the bulk cohesion decreases with an increase in particle size. It is apparent that the particle size/distribution is a material attribute that impacts the apparent cohesion and the flow behavior of the materials. Materials with smaller particle sizes or more fine contents tend to have higher cohesion and lower flowability than those with larger particle sizes and fewer fines. This is because smaller particles or more distributed particles led to more contact points, thereby increasing apparent cohesion (Shi et al., 2018). A more comprehensive statistical investigation of how particle size and size distribution quantitatively track with these shear properties is planned for future work.
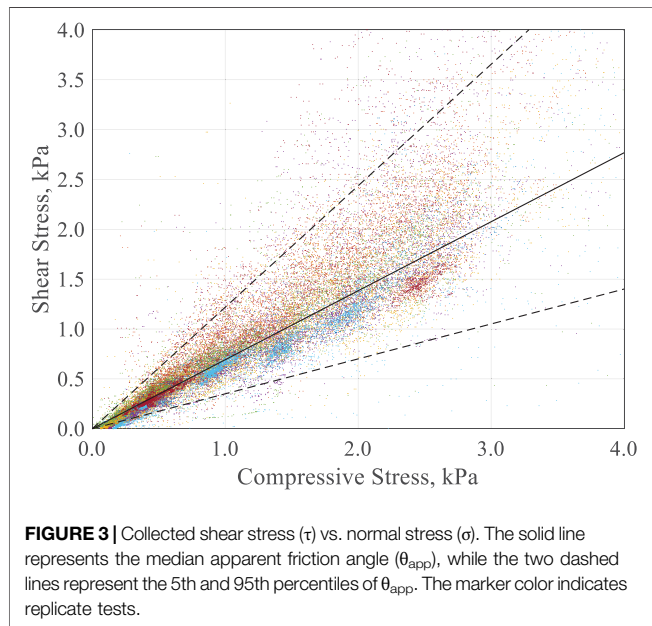
3.1.2 High Precision Air Bearing Rheometer

A select subset of results collected in the TA rheometer system using different size loblolly pin biomass samples (S2, S4, and S6) and tested under the same nominal measuring conditions (cup

TABLE 3 | Best-fit constitutive parameters (μ and c) and dynamic friction angle (θ) as determined by the linear regression analysis of source measurements for loblolly pine along with the apparent dynamic (θ_{app}) angle at three selected percentiles.

Sample	Cup size (mm)	μ	θ (°)	Cohesion (kPa)	r^2	θ_{app} (°)			θ_{app} span (°)
						D_{10}	D_{50}	D_{90}	
S2	64.0	0.759 ± 0.002	43.5 ± 0.1	−0.110 ± 0.006	0.969	22.9	37.2	46.4	23.5
S4	64.0	0.633 ± 0.004	36.2 ± 0.2	0.018 ± 0.010	0.964	21.5	37.2	51.5	30.0
S6	64.0	0.747 ± 0.012	42.8 ± 0.7	−0.075 ± 0.044	0.736	20.2	39.7	54.0	33.8

The span listed in the right-most column represents the difference between the θ_{app} for the 10th and 90th percentiles. The uncertainties provided for each set of μ, θ, and c represent twice the standard error of the fitting parameter. All measurements were carried out using the 64-mm base.

FIGURE 3 | Collected shear stress (τ) vs. normal stress (σ). The solid line represents the median apparent friction angle (θ_{app}), while the two dashed lines represent the 5th and 95th percentiles of θ_{app}. The marker color indicates replicate tests.
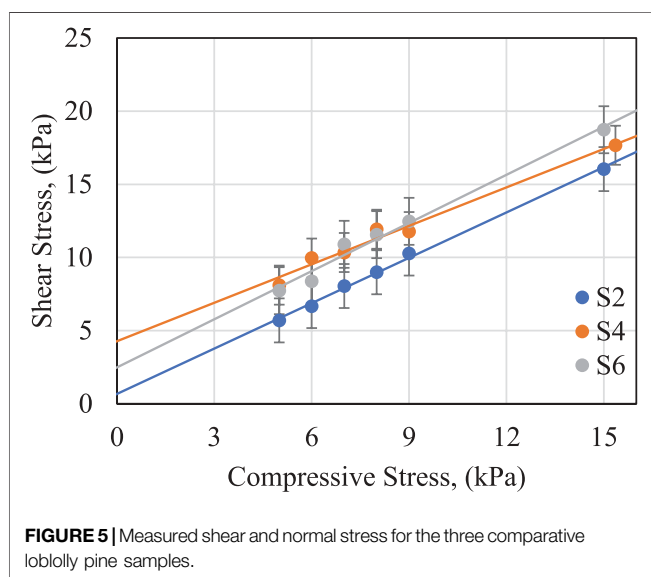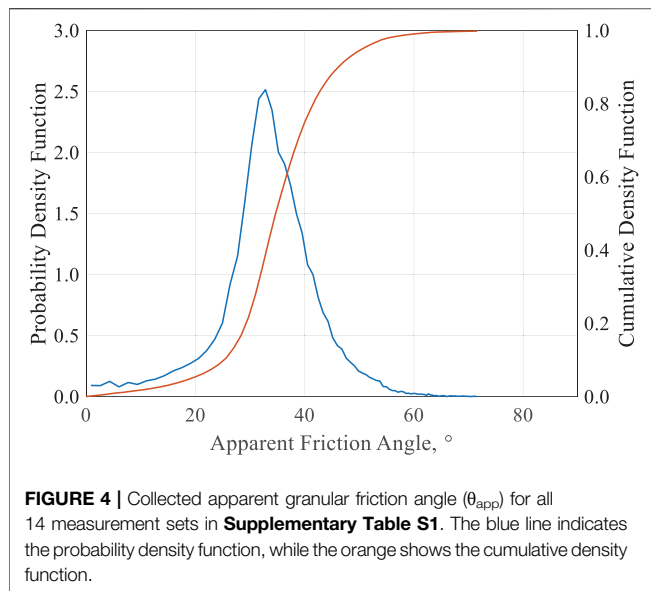
size and moisture content) are summarized in **Table 3**. In general, the measured values of the internal friction are close to those measured in the RST, however with the exception of the larger particle sizes (S4) where a significantly lower internal friction was recorded. Here, direct comparison of μ for S4 and the other two materials reported in **Table 3** finds S4 to be approximately 15% smaller, whereas S2 and S6 agree with the RST measurement within ~3%. These measurements with larger particles also show the most variable or widest distributions of recorded values. This phenomenon is likely due to a coupled interaction of equipment limitations along with material impacts (e.g., limited shear region gap relative to measured particle dimension). In general, the apparent cohesion for all materials and trials trended toward 0 kPa, likely due to the comparatively low applied normal stress achievable by this commercial unit (typically 3.5 kPa or less).

The measured normal force (σ) and torque (τ) data depend on how the time series measurements at each normal force condition are interpreted, and for this study, the values were taken each 0.3 s. Because these tests are performed dynamically, many points are captured during a test. Through replication, the tests were composited into a single data series where linear regression was used to fit the data series. For sample S2, the fit parameters for friction angle and cohesion were 43.5 ± 0.1° and −0.110 ±

0.006 kPa, respectively. Compared to the granular tester discussed earlier, the friction angle was biased slightly low but very close in the overall magnitude. The predicted cohesion (essentially zero) is closer to the lower end of the applied normal force (~1 kPa) of the granular tester. Distributions of the apparent dynamic friction angle were also generated to describe the range of commonly observed values with the 10th, 50th, and 90th percentile values presented in **Table 3**.

Parametric studies on the TA rheometer data were also distilled through statistical analysis to determine the most impactful material attributes and test conditions. **Figure 3** shows the aggregated shear stress (τ) measured as a function of the applied normal stress (σ) for all 14 loblolly pine measurement sets presented in **Supplementary Table S1**. Each point in **Figure 3** represents a single 3.3 Hz measurement. The data presented in **Figure 3** suggest that, as expected, normal and shear stresses are correlated. However, the correlation is broadly distributed (i.e., it is not characterized by a singular or narrowly distributed apparent friction angle). Rather, the combination of system parameters (wood moisture content, feedstock size, test cup diameter, etc.), coupled with the evolution of the particle configuration in the test geometry itself, leads to the variation in the stress required to maintain parallel plate rotation. That is, variation in the apparent dynamic friction arises from both natural variation in the orientation of the wood particles (which allows sliding in some configurations or leads to stress chaining in others) and variation associated with the system configuration itself (cup size and wood moisture content).

Different from the analysis and conclusions from the RST above, data gathered on this rheometer in **Figure 3** suggest that the aggregate granular response of loblolly pine, at least as characterized by the TA rheometer, was approximately Columbic with no apparent stress of cohesion over the range of normal forces tested (roughly 0–3 kPa). The loblolly pine, appearing to be a cohesionless Columbic material in this stress range, means that the apparent dynamic friction angle (θ_{app}) should be independent of the applied normal force under the tested conditions. **Figure 4** shows the probability and cumulative density functions for all θ_{app} measured. The distribution is approximately Gaussian with a median and average friction angle of 34.7 and 36.3°, respectively. The configurational variation of the friction angle manifests by a relatively broad distribution; here, the 2-sigma (i.e., the 5th and 95th percentiles) are 19.3 and 50.6° and represent a roughly ±15° confidence bound.

FIGURE 4 | Collected apparent granular friction angle (θ_{app}) for all 14 measurement sets in **Supplementary Table S1**. The blue line indicates the probability density function, while the orange shows the cumulative density function.

FIGURE 5 | Measured shear and normal stress for the three comparative loblolly pine samples.

3.1.3 FT4 Rheometer

Results obtained in an FT4 rheometer are shown in **Figure 5** (and tabulated in **Supplementary Table S2**), again, for the same three loblolly pine samples (S2, S4, and S6). Overall, the translation between the normal and measured shear stresses is similar in magnitude between the feedstocks. The largest particle size among those three samples, 3.35–4.75 mm (S4) sample, has the lowest resultant friction (~15% lower), while the smallest (S2) and the broad (S6) samples have similar (within 6%) and slightly higher friction angles, respectively. Like the common RST analysis, the apparent bulk cohesion is extracted by extrapolating the yield surface back to a zero applied compressive stress. Comparatively to the lower particle size discussed above, these data are the highest in the largest particle size (S4) and are

significantly higher in magnitude (5.9 kPa), as compared to what was measured in the RST. As a result, the effective internal friction for this sample was lower with an unexpectedly high unconfined yield strength (22.7 kPa). Note that there were limitations in measuring at very low normal stresses in the FT4, which, in turn, impacts the accuracy of this prediction. Furthermore, additional work in the future would be needed to better understand the impact of the comparative loading material depth and rotor design that is embedded in the material.

Comparatively, the shear stresses measured with the FT4 rheometer for the smallest sample (S2), as shown in **Figure 5**, resulted in a very similar extrapolated apparent cohesion (1.01 kPa) to that measured at 10 kPa pre-shear stress in the RST and slightly higher measured shear stress per unit of applied normal stress (51.7° internal friction). The respective internal frictions for S4 and S6 are closer to the RST magnitude at 43.5° and 48.0°, respectively. Qualitatively, S2 and S6 have statistically similar internal frictions and S4 has a lower average measured friction. This agrees with the observations on the TA rheometer system and could be an artifact of the comparatively large particles. To that effect, there was also the greatest observed variability for these larger particles in the TA rheometer system. This indicates that the measurement was perhaps strongly coupled to the loading method, particular orientation of particles, packing, etc., that accumulated to larger uncertainty as well as incompatibility with this scale of particle. The results presented here, however, are also consistent with measurements of other sawdust (43.8–48.2 kPa) and rice straw (42.4–46.3 kPa) measured in the literature with the same commercial device (Guo et al., 2015). Additional information from these testing routines (compressibility and rotation energy) is presented in **Supplementary Figure S3** and **Supplementary Figure S4**. In general, it was found that the materials were similar in compressibility from 4.2 to 8.3% at 2 kPa and 11.3–13.3% at 12 kPa, and the flow energies were similar for S6 and S4, while S2 was significantly lower.

3.2 Particle–Particle and Particle–Surface Interactions

The tribometry measurements were made for sample S4 with the particles aligned in such a way that the sliding direction is either parallel or perpendicular to the wood grain of the particles. **Figure 6** shows the variation of the instantaneous friction coefficient during one reciprocating particle–particle sliding cycle. In general, the particle–particle instantaneous friction coefficient is relatively higher and rather noisy when sliding in the perpendicular direction. For parallel direction sliding, the instantaneous friction is smaller and less noisy. The average friction coefficients for particles sliding in the parallel and perpendicular directions are 0.26 and 0.34, respectively, as shown in **Figure 6**. However, the standard deviation of friction in the perpendicular direction is substantially high, reflective of the noisy behavior of instantaneous friction behavior in that direction. In simple flow systems such as hoppers and bins, particles tend to align as they are discharged. These differences in friction coefficients could suggest that as materials are charged or loaded into intermediate vessels or batch/semi-batch systems,
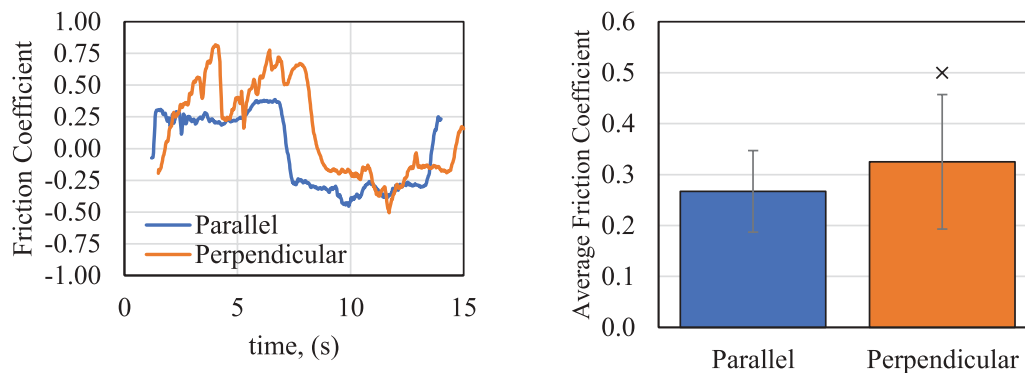
FIGURE 6 | (Left) Instantaneous friction coefficient for pine particle (S4) sliding in parallel direction and perpendicular direction and (right) average friction coefficient.

the flow friction of random particle orientation could directly contribute to problems during flow inception, such as that presented later in this work.

The friction coefficient is defined as the ratio of the tangential or frictional force to the normal force. Traditional definition of the friction coefficient ignores the direction of the forces. In **Figure 6**, as well as later figures, the direction of the frictional forces is considered when calculating the friction coefficient. Thus, frictional force reversal during reciprocation is reflected as negative values for friction coefficient. The figures can be viewed as the friction force vector normalized by the normal force. This approach enables the assessment of the symmetry for friction behavior during reciprocal sliding as well as the evaluation of frictional energy dissipation. As can be seen in **Figure 6**, the forward motion (~1–6 s) of the tribometer results in an average parallel friction coefficient near 0.25, while a similar value near −0.25 is observed during the period (~8–14 s) when the stage is moving in the opposite direction.

In the tribometry measurement of friction of pine particles, clear anisotropy was observed in terms of friction behavior and magnitude of the friction coefficient. This was further confirmed by the SEM images of pine particles. **Figure 7** shows the SEM micrograph of the sides and cross-sectional views of a pine particle. The image scales are shown in the bottom-right corner, and panels 1) and 2) are at 200 μm, while 3) is 100 μm. The distinctive structures of the pine surfaces were expected, which contributed to the frictional anisotropy. Differences in the particle surface features are not the only reason for the frictional variation. The particle scale frictional anisotropy may have a significant impact on the biomass material flow at the macroscale in a unit operating system. Alignment in some direction may be more conducive to easy flow, while other particle arrangements may be detrimental to flow.

In the particle scale measurement of particle–particle and particle–wall, the results are highly repeatable, as shown in three repeat tests of **Figures 8A–C** for the three studied loblolly pine samples, respectively. For the three materials (S2, S4, and S6), the size scale of the particles was less of an impact on the measurement, and the larger impact was the variation and inconsistency in measurement that increased with the

concentration of large particles. One major observation in the friction result is the effect of particle size on the frictional behavior. For sample S2, the friction (**Figure 8A**) exhibits relatively minimal noise which should translate to more consistent shear and flow. Interestingly, although this also resulted in a lower friction coefficient compared to the other samples, this sample has the highest apparent bulk cohesion measured from the shear tests above. The friction in the larger particles (S4) was higher and rather noisy (**Figure 8B**), which can result in uneven shear and flow. The friction behavior of broad particle sieve (S3) was also noisy but not to the same extent as the large ones.

The relative frictional energy dissipation during the tribometry particle scale friction measurement can be estimated by plotting the friction coefficient as a function of position, as shown in **Figure 9**. The smaller the area of the friction–distance plot, the smaller the amount of frictional energy dissipation. This frictional energy assessment from lab-scale measurement may provide an indication of the energy or power required for bulk shear and flow of biomass materials.

It is clear from the abovementioned discussion that both the physical properties of feedstock and the measuring techniques have a great impact on the shear properties. In the study, we further investigated the interaction of the particle–surface friction using RST and FT4. In both systems, a range of material surface finishes were used and characterized for the areal roughness texture. This is a measure of the average deviation in height changes about a mean plane (Sa) or line scan (Ra). To determine the wall friction angle, a similar set of conditions were used to measure the resultant shear stress at stable flow, as particles are forced across a surface coupon with a vaned lid/bob. **Figure 10** shows a summary of the measured (RST) wall friction angle for S2 and the areal surface roughness as measured by a laser scanning confocal microscope. In this test setup, a variety of potential equipment surface materials were selected to bound potential equipment wall frictions, including steel (304 stainless brushed and mirror finish, carbon steel, AR500 ultra wear-resistant steel), aluminum (two different brushed finished and a mirror finish), and a polymer surface (texture and ultra-slippery). In general, it is observed that a greater surface texture translates to a higher measured wall friction in the test setup. Interestingly, the measurement increases
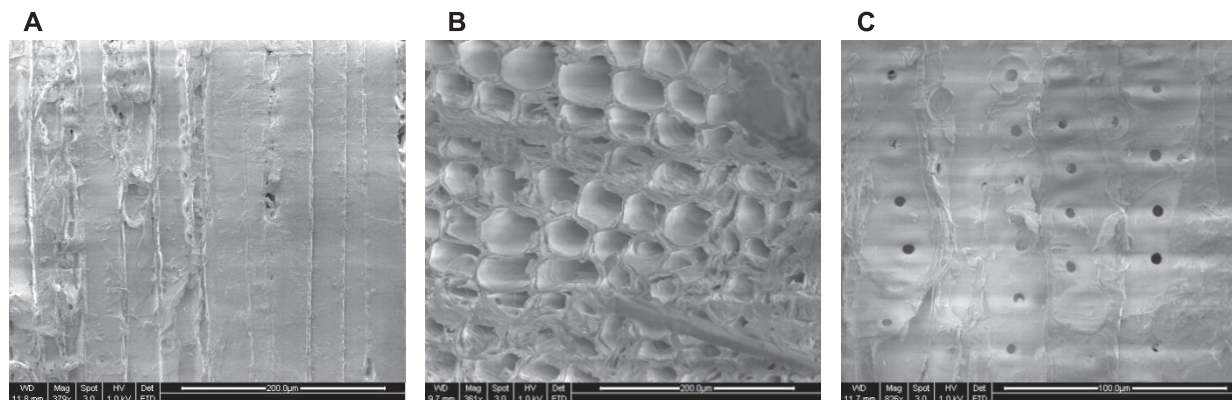
FIGURE 7 | SEM micrograph of a pine particle: **(A)** side view, **(B)** cross-sectional view, and **(C)** angular side.
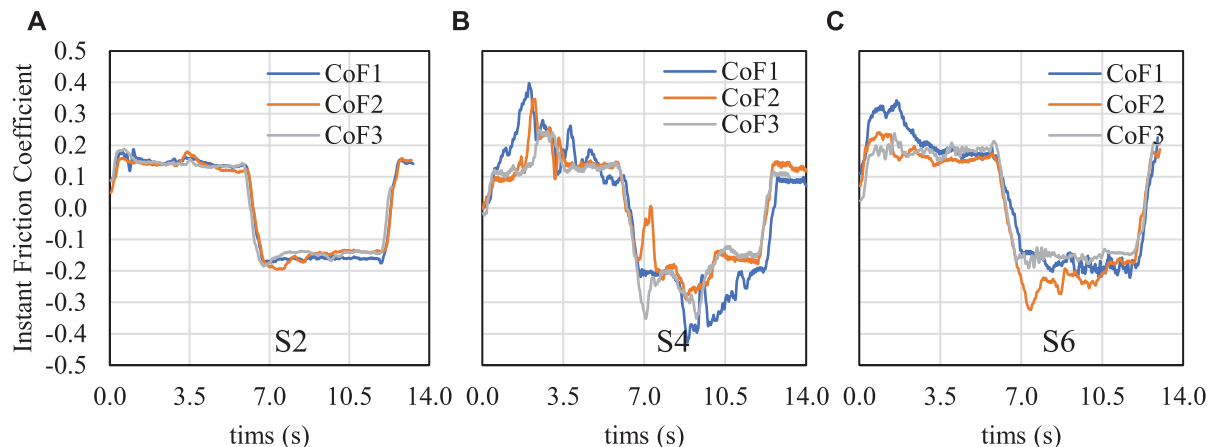
FIGURE 8 | Particle–wall friction for samples **(A)** S2, **(B)** S4, and **(C)** S6.
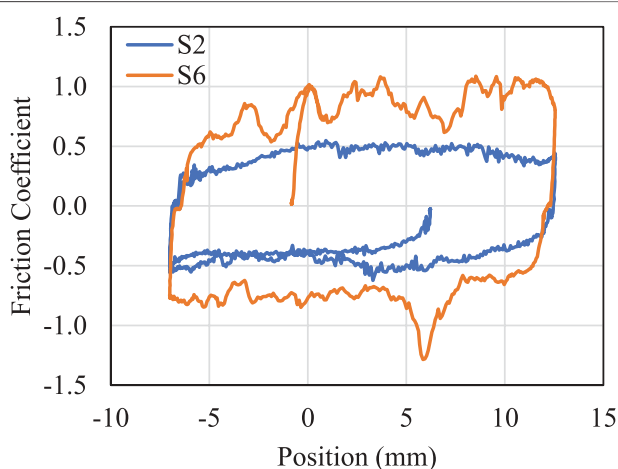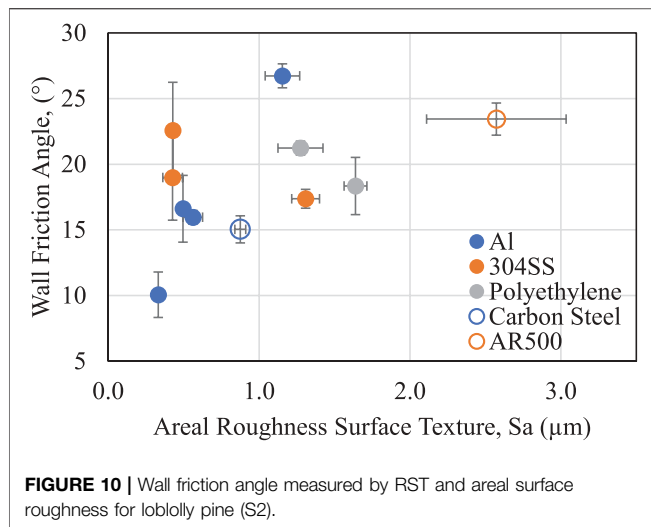

FIGURE 9 | Friction energy dissipation during the particle–particle friction measurement for samples S2 and S6.

more than 15° across the (aluminum) samples and indicates a strong potential for changes in surface frictions from what might be intuited as modest changes in surface finish (<1.0 μm difference in Sa). This sample (S2) was observed to have a particle–surface friction angle between 15 and 23° (excluding the high/low data point) depending on the surface finish.

Similar tests (discussed above) were performed in the FT4 with the three materials, and the findings are shown in **Table 4** and **Supplementary Figure S5**. In these tests, the wall coupons studied included a stainless steel (SS), as well as a Teflon (PTFE) and high-density polyethylene (HDPE) surface. The measured friction for the SS has the highest value and has the highest roughness. The polymer surfaces have more complex relationships but result in overall lower friction angles. The impact of the particle size on the measured friction angle is likewise difficult to discern a direct relationship. For the SS disc coupon, S2 and S6 samples have similar stress relationships. For the PTFE sample, the magnitude of the resulting wall stresses is statistically distinct, although the apparent friction angle given

FIGURE 10 | Wall friction angle measured by RST and areal surface roughness for loblolly pine (S2).

FIGURE 11 | Critical arching distance in a wedge hopper.

TABLE 4 | Effective friction angles in the FT4 for loblolly pine for different wall coupons.

Sample	Friction angle (°)		
	SS, Ra = 1.2	PTFE, Ra = 0.48	HDPE, Ra = 0.10
S2	24.0	4.4	3.5
S4	20.3	3.3	10.9
S6	23.3	3.4	9.6

the standard error in the slope regression suggests they are similar. For the HPDE surface, S4 and S6 samples have similar friction angles and magnitudes, while the smallest particle size (S2) results in a drastically lower friction angle. Although the same material surfaces were not shared for this comparison, both show that the surface texture had an influence on the overall friction angle. Compared to the measurements made between the devices, the SS coupons have similar magnitudes (17–23° in RST, while 20–24° in FT4 for the common, smallest sample size), where the values measured here are slightly higher. The polymer surfaces characterized in the FT4 have significantly lower measured friction angles compared to those in the RST.

The abovementioned discussion and characterization clearly suggest that the physical properties of both biomass and particle–surface interaction have a significant influence on the shear properties, which ultimately affect the material flowability at bulk. Thus, the following section will discuss the flow properties of loblolly pine (S7–S8), and as a comparison, Douglass fir (S9–S11).
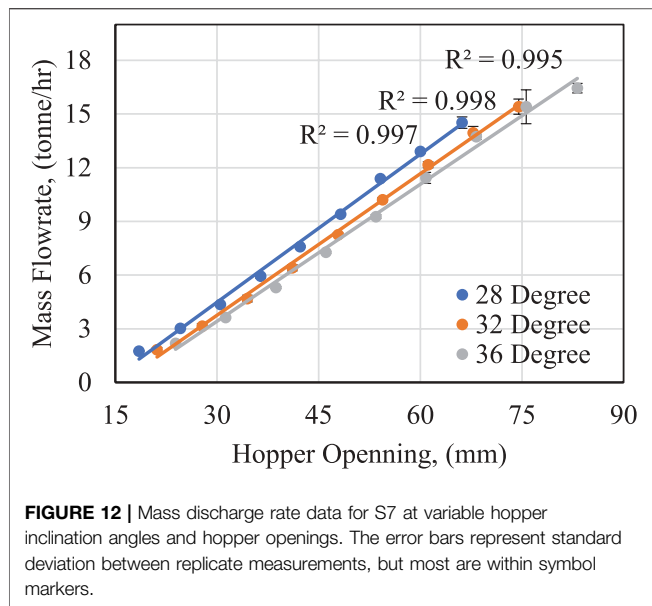
3.3 Flow Performance
One of the critical design criteria for a feed bin or hopper is the discharge opening gap. While this is chiefly linked to the discharge rate through the cross-sectional opening, this is also critical to ensuring that the material is consistently discharged, and the feedstock is not able to establish stress bridges that support the bulk solid from the gravitational driving force. As a result, this critical arching distance is a minimum design criterion and should be regarded as a loose design parameter,
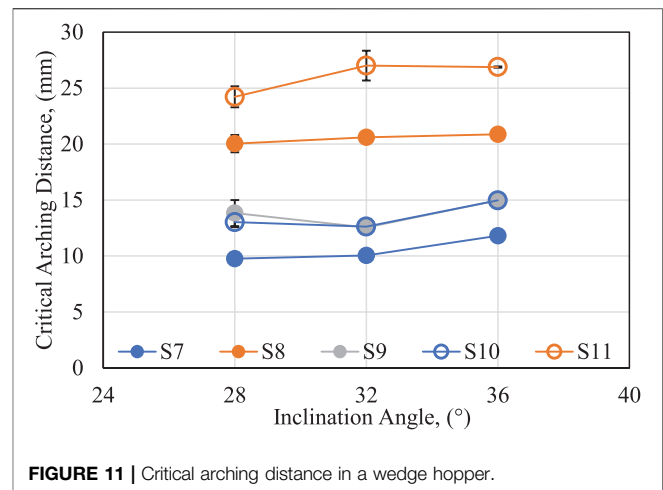
where conservative design practices would consider a design factor that is able to incorporate material variability and process upset conditions as much as possible (Lu et al., 2021a). **Figure 11** shows the data collected from the critical arching distance testing for the five samples (S7–S11), as shown in **Table 1**, where S11 has the largest measured arching distance (followed by S8), while S7 is the lowest (followed by S10). Here, these data correlate well with the overall particle sizes noted in the samples; S7 had the smallest particle sizes, while S11 had the largest. Interestingly, S9 and S10 had very similar performance, where the mean size of S10 was much closer to that of S8 rather than S9. This suggests that the performance is rather sensitive to the mean particle sizes, or the various preprocessing strategies used in sample generation had a direct influence as well. Note that the disparate differences between S7 and S8 compared to S9 and S10 (similar jumps in particle sizes for different comminution methods) support the later. One hypothesis for the observation of these flow performance arises from differences in the particle aspect ratios. The S9–S11 samples were produced from a shear-based comminution process (Forest Concepts Crumbler®), which uses particle recycle to more readily control the fiber length and size distribution compared to a once-through high-velocity hammer mill impact. These resulting particle geometries and sizes could play into the bulk properties through the cohesion and internal friction, for example, as discussed above. These materials show arching distances from 10 to 27 mm. While prior work has indicated generally higher values and a positive relationship between arching distance and inclination angle (Lu et al., 2021a), here there was only a modest positive trend with no clear description for all samples. However, in this situation where there was minimal material surcharge above the arching test, it can be concluded that the arching distance results are much less sensitive to the inclination angle compared to even the relatively modest changes in material type/format/size presented here. As a result, we recommend that the style and consistency of biomass comminution should be critically considered when designing or adapting flow systems for biomass samples.

When the hopper gap is opened sufficiently beyond the arching distance to achieve mass flow, the discharge rate for

FIGURE 12 | Mass discharge rate data for S7 at variable hopper inclination angles and hopper openings. The error bars represent standard deviation between replicate measurements, but most are within symbol markers.

each material and inclination angle was measured for nine variable opening distances (cross-sectional area). Sample traces of this are shown in **Figure 12** and in **Supplementary Figure S6** for S7 and S8–S11, respectively. The incremental change in flow rate with opening and inclination angle for all five samples is summarized in **Table 5**. Similar qualitative trends (inverse) are observed in the flow rate compared to the arching distance. For example, S7 has the lowest arching distance and the greatest specific discharge rate, while S11 has the greatest arching distance and the lowest specific discharge rate. S8–S10 were recorded at similar discharge rates with incremental opening. These trends are also qualitatively like that of the material bulk density in **Table 1**. Due to the linearity of these specific rates, a provisional mass flow rate, or flow envelope, could be designed for using such flow data. While the relative deviation in specific flow rates between the materials had a 13%–22% relative standard deviation, when these were normalized with the bulk density, this decreases to 3%–6%, indicating that a significant variance in the discharge rate with opening is explainable with the bulk density. Additionally, this suggests that the overall volumetric discharge rate is similar between the materials. Given the variable, but fixed outlet geometry, this might also suggest that the particle packing at the discharge is similar on a gross volumetric basis.

In comparison to these gravity-driven flow tests, these test samples were also characterized in a screw feeder. To convey material through a conveyor (i.e., screw), the central shaft imparts a forward motion to the material contained in the feeder barrel. Typically for dry solid feeders with non-powder materials, the flights are partially filled and lead to a periodic or short-time "slugging" feeding behavior due to the nature of the device. In general, as particles approach smaller, more uniform geometries, this behavior will dampen and similar reduction in rate variability is expected, as the rotation frequency is increased (although the flights become more difficult to fill completely or consistently). This is similarly observed through the reaction torque (power

consumption measured and used as a proxy here) exerted on the feed screw. Typical power consumption traces from S7 and S8 are shown in **Figure 13** (see **Supplementary Figure S7** for S9–S11) and are illustrative to how different the results can be from the same material with a slightly different size/distribution. Falk et al. (2015) noted similar slugging behaviors in their study of screw feeders and related this to a measured dynamic angle of repose. They concluded that on a small timescale (10 Hz), there was no relationship to the feeding variability or behavior. On a comparatively larger timescale (0.5 Hz), however, they noted that this pulsating flow variability was correlated with the dynamic angle of repose. With lower angles, the buildup of material piles was hypothesized to fail earlier at the discharge outlet, resulting in a less pronounced variability.

The data shown in **Figure 13** become more sporadic in magnitude and frequency, as the rotational frequency increases. The differences in these bounds are more clearly shown in S8, where the power consumption both increases dramatically in magnitude and deviation about a baseline consumption compared to the more well-behaved increased baseline observed in S7. The data for both the average flow rate and power consumption and their respective deviations are shown in **Table 6**. As the rotation frequency increases, so too does the flow rate and the power consumption. Because screw conveyors are designed to move a consistent volume of material with time based on the fractional filling of the flights, the resultant flow rate also follows similar qualitative trends as the material bulk density. These rates appear to deviate more with larger particles (S8 and S11), which is consistent with increased variance in particle packing within a confined, finite volume available to fill between flights. Comparatively, the smaller particles can more freely rotate, pack, and fill voids during the screw extraction from the bulk feed bin and result in higher space utilization and ultimately mass flow rate. The power draw during feeding increases with increasing particle size (S8 compared to S7, and S11 compared to S9). Here, it is interesting to note the large deviation in conveyance in particles produced from a hammermill (0.274 vs. 0.190 kW at 50%), compared to particles produced from the rotary shear process (0.207 vs. 0.167 kW). Here, the increase in power draw is lessened in addition to having less overall power draw, despite having larger-sized particle on average. This is hypothesized to occur due to a more uniform particle format in addition to having preferential internal, partial–particle, and partial–surface friction measurements. As a result, there is less energy dissipation or loss during the feeding. As noted above, this agrees with the

TABLE 5 | Hopper-specific flowrate through the wedge hopper per unit hopper opening.

Inclination angle (°)	Specific flowrate (Ton/hr/mm)				
	S7	S8	S9	S10	S11
28	0.2758	0.1986	0.1832	0.1778	0.1654
32	0.2636	0.2050	0.1969	0.1989	0.1813
36	0.2552	0.2030	0.1923	0.1958	0.1884
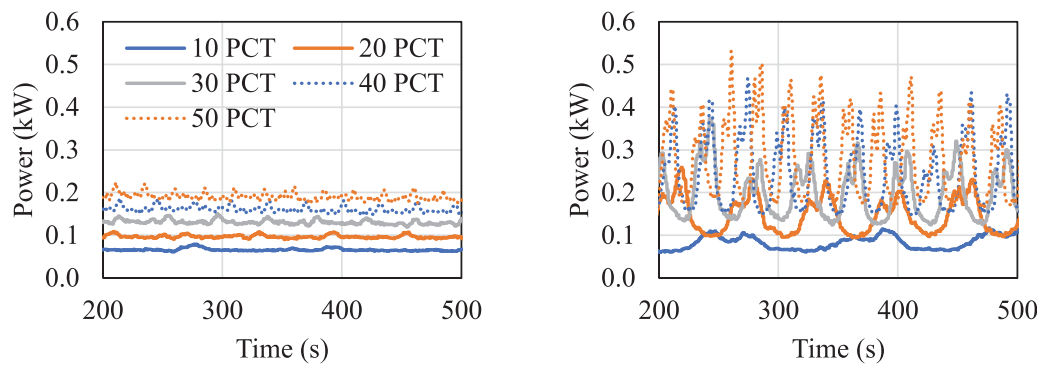
FIGURE 13 | Power consumption in the Acrison® screw feeder at a controlled speed for (left) S7 and (right) S8. The solid blue, orange, gray, dotted blue, and orange indicate results at auger rotational speeds of 10, 20, 30, 40, and 50%, respectively.

TABLE 6 | Summary of performance data for screw feeder in terms of flowrate and power consumption.

Auger frequency		Flowrate (LBH)					Power x 10^3 (kW)				
PCT (%)	RPM	S7	S8	S9	S10	S11	S7	S8	S9	S10	S11
10	6.4	31 ± 10	21 ± 9	26 ± 10	27 ± 11	25 ± 10	66 ± 3	83 ± 16	56 ± 1	57 ± 1	70 ± 5
20	12.3	59 ± 13	39 ± 13	46 ± 16	47 ± 15	47 ± 17	97 ± 4	146 ± 42	85 ± 2	89 ± 3	109 ± 9
30	18.3	87 ± 17	61 ± 14	67 ± 13	67 ± 13	66 ± 18	131 ± 5	197 ± 6	117 ± 3	116 ± 3	144 ± 12
40	24.2	117 ± 7	82 ± 14	93 ± 13	93 ± 11	90 ± 13	161 ± 7	243 ± 84	142 ± 3	141 ± 4	177 ± 15
50	30.0	145 ± 6	105 ± 13	119 ± 13	116 ± 9	113 ± 10	190 ± 9	274 ± 91	167 ± 4	168 ± 5	207 ± 17

observations of friction in respect to the particle scale, suggesting one potential source for these differences.

4 CONCLUSION

Various experimental shear and friction characterization techniques were investigated at multiple test and particle scales to examine the impact on the resulting shear characteristics. The critical material attributes, including particle size and distribution, were investigated as exploratory variables to describe the differential shear properties and behavior. To supplement these laboratory-scale properties, this work explored the flow properties through a pilot-scale wedge-shaped hopper and an Acrison® screw feeder. Several conclusions can be drawn from this study:

- Bulk cohesion was found to increase (from 0.68 to 1.3 kPa in an RST at 10 kPa preshear) with decreasing biomass particle size (D_{50} of 3.80–0.69 mm), except the largest test size. The measured internal friction was statistically constant with particle size and only varied by a few degrees when tested in the RST.
- The scale and type of characterization method were observed to be less sensitive as the particle size of the tested biomasses approached to that of more fine-milled powders (i.e., less than 1–2 mm) but diverged as the stress-chaining potential induced stochastic events to the testing protocols. In granular shear testers, it was found that the multi-scale feedstock properties

were more inclined to be influenced through the apparent bulk cohesion or unconfined microscale interactions compared to internal friction when investigating a specific material. Comparatively, the analysis performed in the smaller, more commonly available rheometers showed indeterminant trends of cohesive properties and nonlinear behavior with respect to the resulting effective internal friction. While the RST is a more robust primary characterization tool to provide shear flow property reference data for biomass material handling equipment design, lower-scale shear testers and rheometers are useful for cross-validation of the RST and qualitatively ranking materials, particularly for small-sized or fine-milled particles and are more widely available at research and industrial institutions.

- The mass discharge rate in a wedge hopper was proportionate to the discharge cross-sectional area and was largely dominated by the overall size of the biomass particles and their reduction technique, while the size distribution and the hopper inclination were comparatively minor. A positive regression relationship was observed when normalized with the discharge opening, suggesting some differences in the internal stresses governing forces distributed to the container walls and those in-line with the gravitational flow. The arching distance results had only modest positive correlation with inclination angle and were much less sensitive compared to even the relatively modest changes in the material type/format/size presented here. As a result, the style and consistency of biomass type, comminution, and

overall preparation should be critically considered when designing or adapting flow systems for biomass.

- Overall, wedge hopper mass discharge rates were explainable with the bulk density (positive correlation, from 0.26 to 0.19 tonne/hr/mm opening for S7 to S11 at 248 to 177 kg/m^3, for example, at 36°). Additionally, this suggests that the overall volumetric discharge rate is similar between similar materials such as the softwoods studied here. For the variable discharge geometries studied here, this suggest that as the particles approach states like what is studied in the unconfined bulk density tests.
- The screw feeder was found to be more consistent for the smaller and more uniform samples, which led to stable flow and less power consumption. This was also aligned with particle–particle anisotropic friction characterizations that found that overall energy dissipation was significantly less for smaller particles. As a result, the scale of mechanical conveyor (or particles being conveyed) must be well controlled to limit downstream "pulsing" flow, energy consumption, and excessive equipment wear as a result.

Overall, the direct understanding of how the shear properties of compressible, irregular, and anisotropic materials translate into flow performance at scale is still in the developing area; understanding how material attributes trend with both shear characteristics and flow performance provides some common qualitative linkages to build foundational knowledge.

DATA AVAILABILITY STATEMENT

The original contributions presented in the study are included in the article/**Supplementary Material**; further inquiries can be directed to the corresponding author.

AUTHOR CONTRIBUTIONS

JK, NS, TB, SC, RD, CB, OA, ZC, RN, and TS contributed to experimental investigation, methodology, and writing the original draft article. JK, WJ, YX, RD, OA, and TS contributed to conceptualization, project oversight, formal analysis, data curation, writing, reviewing, and editing.

FUNDING

ACKNOWLEDGMENTS

SUPPLEMENTARY MATERIAL

The Supplementary Material for this article can be found online at: https://www.frontiersin.org/articles/10.3389/fenrg.2022.855289/full#supplementary-material

REFERENCES

Barletta, D., Berry, R. J., Larsson, S. H., Lestander, T. A., Poletto, M., and Ramírez-Gómez, Á. (2015). Assessment on Bulk Solids Best Practice Techniques for Flow Characterization and Storage/handling Equipment Design for Biomass Materials of Different Classes. *Fuel Process. Technol.* 138, 540–554. doi:10.1016/j.fuproc.2015.06.034

Bilgili, F., Koçak, E., Bulut, Ü., and Kuşkaya, S. (2017). Can Biomass Energy Be an Efficient Policy Tool for Sustainable Development? *Renew. Sustain. Energy Rev.* 71, 830–845. doi:10.1016/j.rser.2016.12.109

Binder, J. B., and Raines, R. T. (2009). Simple Chemical Transformation of Lignocellulosic Biomass into Furans for Fuels and Chemicals. *J. Am. Chem. Soc.* 131 (5), 1979–1985. doi:10.1021/ja808537j

Chen, X., Xu, Y., Lu, H., and Guo, X. (2018). Effect of the Moisture Content of Straw on the Internal Friction Angle of a Granular Biomass-Coal System. *Fuel* 215, 266–271. doi:10.1016/j.fuel.2017.11.013

Cheng, Z., Leal, J. H., Hartford, C. E., Carson, J. W., Donohoe, B. S., Craig, D. A., et al. (2021). Flow Behavior Characterization of Biomass Feedstocks. *Powder Technol.* 387, 156–180. doi:10.1016/j.powtec.2021.04.004

Comanici, A. M., and Barsanescu, P. D. (2018). Modification of Mohr's Criterion in Order to Consider the Effect of the Intermediate Principal Stress. *Int. J. Plasticity* 108, 40–54. doi:10.1016/j.ijplas.2018.04.010

Dale, B. (2017). A Sober View of the Difficulties in Scaling Cellulosic Biofuels. *Biofuels, Bioprod. Biorefining* 1 (11), 5–7. doi:10.1002/bbb.1745

Dietmar, S. (2008). *Flow Properties of Powders and Bulk Solids*. Powders And Bulk Solids–Behavior, Characterization, Storage and Flow. Berlin, Germany: Springer-Verlag Berlin Heidelberg.

Falk, J., Berry, R. J., Broström, M., and Larsson, S. H. (2015). Mass Flow and Variability in Screw Feeding of Biomass Powders - Relations to Particle and Bulk Properties. *Powder Technol.* 276, 80–88. doi:10.1016/j.powtec.2015.02.023

Fanesi, A., Lavayssière, M., Breton, C., Bernard, O., Briandet, R., and Lopes, F. (2021). Shear Stress Affects the Architecture and Cohesion of Chlorella Vulgaris Biofilms. *Sci. Rep.* 11 (1), 4002–4011. doi:10.1038/s41598-021-83523-3

Faqih, A. M. N., Mehrotra, A., Hammond, S. V., and Muzzio, F. J. (2007). Effect of Moisture and Magnesium Stearate Concentration on Flow Properties of Cohesive Granular Materials. *Int. J. Pharm.* 336 (2), 338–345. doi:10.1016/j.ijpharm.2006.12.024

Fitzpatrick, J. J., Barringer, S. A., and Iqbal, T. (2004). Flow Property Measurement of Food Powders and Sensitivity of Jenike's Hopper Design Methodology to the Measured Values. *J. Food Eng.* 61 (3), 399–405. doi:10.1016/s0260-8774(03)00147-x

Guo, Z., Chen, X., Xu, Y., and Liu, H. (2015). Study of Flow Characteristics of Biomass and Biomass-Coal Blends. *Fuel* 141, 207–213. doi:10.1016/j.fuel.2014.10.062

Hernandez, S., Westover, T. L., Matthews, A. C., Ryan, J. C. B., and Williams, C. L. (2017). Feeding Properties and Behavior of Hammer- and Knife-Milled Pine. *Powder Technol.* 320, 191–201. doi:10.1016/j.powtec.2017.07.002

Hou, H., and Sun, C. C. (2008). Quantifying Effects of Particulate Properties on Powder Flow Properties Using a Ring Shear Tester. *J. Pharm. Sci.* 97 (9), 4030–4039. doi:10.1002/jps.21288

Ilic, D., Williams, K., Farnish, R., Webb, E., and Liu, G. (2018). On the Challenges Facing the Handling of Solid Biomass Feedstocks. *Biofuels, Bioprod. Bioref.* 12 (2), 187–202. doi:10.1002/bbb.1851

Krantz, M., Zhang, H., and Zhu, J. (2009). Characterization of Powder Flow: Static and Dynamic Testing. *Powder Technol.* 194 (3), 239–245. doi:10.1016/j.powtec.2009.05.001

Leturia, M., Benali, M., Lagarde, S., Ronga, I., and Saleh, K. (2014). Characterization of Flow Properties of Cohesive Powders: A Comparative Study of Traditional and New Testing Methods. *Powder Technol.* 253, 406–423. doi:10.1016/j.powtec.2013.11.045

Liu, Y., Lu, H., Guo, X., Gong, X., Sun, X., and Zhao, W. (2015). An Investigation of the Effect of Particle Size on Discharge Behavior of Pulverized Coal. *Powder Technol.* 284, 47–56. doi:10.1016/j.powtec.2015.06.041

Lu, H., Guo, X., Jin, Y., and Gong, X. (2018). Effect of Moisture on Flowability of Pulverized Coal. *Chem. Eng. Res. Des.* 133, 326–334. doi:10.1016/j.cherd.2018.03.023

Lu, Y., Jin, W., Klinger, J., and Dai, S. (2021a). Flow and Arching of Biomass Particles in Wedge-Shaped Hoppers. *ACS Sustain. Chem. Eng.* 9 (45), 15303–15314. doi:10.1021/acssuschemeng.1c05628

Lu, Y., Jin, W., Klinger, J., Westover, T. L., and Dai, S. (2021b). Flow Characterization of Compressible Biomass Particles Using Multiscale Experiments and a Hypoplastic Model. *Powder Technol.* 383, 396–409. doi:10.1016/j.powtec.2021.01.027

Miccio, F., Barletta, D., and Poletto, M. (2013). Flow Properties and Arching Behavior of Biomass Particulate Solids. *Powder Technol.* 235, 312–321. doi:10.1016/j.powtec.2012.10.047

Miccio, F., Silvestri, N., Barletta, D., and Poletto, M. (2011). Characterization of Woody Biomass Flowability. *Chem. Eng. Trans.* 24, 643–648.

Pachón-Morales, J., Colin, J., Casalinho, J., Perre, P., and Puel, F. (2020). Flowability Characterization of Torrefied Biomass Powders: Static and Dynamic Testing. *Biomass Bioenergy* 138, 105608. doi:10.1016/j.biombioe.2020.105608

Prescott, J. K., and Barnum, R. A. (2000). On Powder Flowability. *Pharm. Technol.* 24 (10), 60–85.

Ramírez-Gómez, Á. (2016). Research Needs on Biomass Characterization to Prevent Handling Problems and Hazards in Industry. *Part. Sci. Technol.* 34 (4), 432–441. doi:10.1080/02726351.2016.1138262

Rezaei, H., Sokhansanj, S., and Lim, C. J. (2018). Minimum Fluidization Velocity of Ground Chip and Ground Pellet Particles of Woody Biomass. *Chem. Eng. Process. - Process Intensif.* 124, 222–234. doi:10.1016/j.cep.2017.12.006

Senff, L., Barbetta, P. A., Repette, W. L., Hotza, D., Paiva, H., Ferreira, V. M., et al. (2009). Mortar Composition Defined According to Rheometer and Flow Table Tests Using Factorial Designed Experiments. *Constr. Build. Mater.* 23 (10), 3107–3111. doi:10.1016/j.conbuildmat.2009.06.028

Shi, H., Mohanty, R., Chakravarty, S., Cabiscol, R., Morgeneyer, M., Zetzener, H., et al. (2018). Effect of Particle Size and Cohesion on Powder Yielding and Flow. *KONA Powder Part. J.* 35, 226–250. doi:10.14356/kona.2018014

Stasiak, M., Molenda, M., Gancarz, M., Wiącek, J., Parafiniuk, P., and Lisowski, A. (2018). Characterization of Shear Behaviour in Consolidated Granular Biomass. *Powder Technol.* 327, 120–127. doi:10.1016/j.powtec.2017.12.037

Westover, T., and Hartley, D. S. (2018). *Biomass Handling and Feeding.* 86. doi:10.5772/intechopen.74606

Zhou, Q., Armstrong, B., Larson, I., Stewart, P. J., and Morton, D. A. V. (2010). Improving Powder Flow Properties of a Cohesive Lactose Monohydrate Powder by Intensive Mechanical Dry Coating. *J. Pharm. Sci.* 99 (2), 969–981. doi:10.1002/jps.21885

Advantages of publishing in Frontiers

OPEN ACCESS
Articles are free to read for greatest visibility and readership

FAST PUBLICATION
Around 90 days from submission to decision

HIGH QUALITY PEER-REVIEW
Rigorous, collaborative, and constructive peer-review

TRANSPARENT PEER-REVIEW
Editors and reviewers acknowledged by name on published articles

Frontiers
Avenue du Tribunal-Fédéral 34
1005 Lausanne | Switzerland

Visit us: www.frontiersin.org
Contact us: frontiersin.org/about/contact

REPRODUCIBILITY OF RESEARCH
Support open data and methods to enhance research reproducibility

DIGITAL PUBLISHING
Articles designed for optimal readership across devices

FOLLOW US
@frontiersin

IMPACT METRICS
Advanced article metrics track visibility across digital media

EXTENSIVE PROMOTION
Marketing and promotion of impactful research

LOOP RESEARCH NETWORK
Our network increases your article's readership